Structure and Bonding 164
Series Editor: D.M.P. Mingos

Song Gao *Editor*

Molecular Nanomagnets and Related Phenomena

Springer

164
Structure and Bonding

Aims and Scope

The series *Structure and Bonding* publishes critical reviews on topics of research concerned with chemical structure and bonding. The scope of the series spans the entire Periodic Table and addresses structure and bonding issues associated with all of the elements. It also focuses attention on new and developing areas of modern structural and theoretical chemistry such as nanostructures, molecular electronics, designed molecular solids, surfaces, metal clusters and supramolecular structures. Physical and spectroscopic techniques used to determine, examine and model structures fall within the purview of *Structure and Bonding* to the extent that the focus is on the scientific results obtained and not on specialist information concerning the techniques themselves. Issues associated with the development of bonding models and generalizations that illuminate the reactivity pathways and rates of chemical processes are also relevant

The individual volumes in the series are thematic. The goal of each volume is to give the reader, whether at a university or in industry, a comprehensive overview of an area where new insights are emerging that are of interest to a larger scientific audience. Thus each review within the volume critically surveys one aspect of that topic and places it within the context of the volume as a whole. The most significant developments of the last 5 to 10 years should be presented using selected examples to illustrate the principles discussed. A description of the physical basis of the experimental techniques that have been used to provide the primary data may also be appropriate, if it has not been covered in detail elsewhere. The coverage need not be exhaustive in data, but should rather be conceptual, concentrating on the new principles being developed that will allow the reader, who is not a specialist in the area covered, to understand the data presented. Discussion of possible future research directions in the area is welcomed.

Review articles for the individual volumes are invited by the volume editors.

In references *Structure and Bonding* is abbreviated *Struct Bond* and is cited as a journal.

More information about this series at
http://www.springer.com/series/430

Song Gao
Editor

Molecular Nanomagnets and Related Phenomena

With contributions by

M. Affronte · M.L. Baker · S.J. Blundell · L. Bogani · L.F. Chibotaru · R. Clérac · A. Cornia · C. Coulon · N. Domingo · M. Evangelisti · S. Gao · A. Ghirri · S. Hill · S.-D. Jiang · F. Luis · M. Mannini · C.J. Milios · V. Pianet · F. Troiani · M. Urdampilleta · R.E.P. Winpenny · B.-W. Wang

Springer

Editor
Song Gao
Coll. of Chemistry and Molecular Eng
Peking University
Beijing
China

ISSN 0081-5993 ISSN 1616-8550 (electronic)
Structure and Bonding
ISBN 978-3-662-45722-1 ISBN 978-3-662-45723-8 (eBook)
DOI 10.1007/978-3-662-45723-8

Library of Congress Control Number: 2015933274

Springer Heidelberg New York Dordrecht London

Printed on acid-free paper

Springer-Verlag GmbH Berlin Heidelberg is part of Springer Science+Business Media (www.springer.com)

Preface

The discovery of single-molecule magnets (SMMs) at the beginning of the 1990s opened a new interdisciplinary field in between chemistry, physics, materials, and nanoscience. The first SMM Mn12 cluster is a nanoscale molecule showing slow magnetic relaxation and quantum tunneling of magnetization. Some molecular nanowires with similar behaviors were found about 10 years later and named as single-chain magnets (SCMs). In the following decade, a few single-ion magnets (SIMs) were reported; they can be considered as a new family of molecular nanomagnets (MNs).

In 2006, volume 122 of Structure and Bonding had been devoted to "Single-Molecule Magnets and Related Phenomena," edited by Richard Winpenny. This is a continued volume and extended to more wide and comprehensive topics in the rapid growth field. Some authors of last volume also have their contributions to this volume. This volume covers various molecular nanomagnets, from materials to magnetism to device and from basis to method to application.

This volume consists of nine chapters: the first five chapters mainly focus on the different molecular nanomagnets, their synthesis, structures, intrinsic magnetic properties, theoretical and experimental methods; the followed four chapters mainly focus on related phenomena and potential applications.

The first chapter of this volume by Milios and Winpenny mainly focuses on the development of cluster-based SMMs since 2005 and summarizes astonishing number of beautiful new cluster-based SMMs, from 3d to 4d/5d, to 4f-elements. The clusters reported herein are categorized and commented in terms of their metal content from the synthetic chemist's point of view.

From 2003, SMMs have been extended from clusters to some mononuclear lanthanide coordination compounds or organometallics. In the second chapter Jiang, Wang, and Gao review four series of well-investigated lanthanide single-ion magnets, theoretical and experimental investigation methods, especially the advanced methods of the angle-resolved magnetometry measurement on lanthanide ions. Transition metal based SIMs are not included.

In the third chapter, the static and dynamic magnetic properties of single-chain magnets and related systems are reviewed by Coulon, Pianet, Urdampilleta, and Cleérac based on a theoretical point of view. Authors particularly focus on the so-called Ising limit, from simple regular chain of ferromagnetically coupled spins, to more complicated structures including chains of antiferromagnetically coupled magnetic sites. The section "from SCM to 3D ordered systems" provides a new insight into the single chain magnets.

The understanding of mechanisms of magnetic anisotropy in molecular nanomagnets became a task of primary importance in the last decade. In the fourth chapter, Chibotaru discusses the physical reasons for magnetic anisotropy and the mechanisms of its appearance in mononuclear and polynuclear metal complexes. Differences in the manifestation of magnetic anisotropy between complexes with weak and strong spin-orbit coupling are emphasized.

Following the theoretical chapter, four physicists Baker, Blundell, Domingo, and Stephen Hill present a fairly comprehensive review of some of the primary spectroscopic methods that have contributed to the current understanding of molecular nanomagnets. These include: electron paramagnetic resonance (EPR); optical spectroscopy, including magnetic and X-ray magnetic circular dichroism (MCD/XMCD); inelastic neutron scattering (INS); and muon spin rotation (μ+SR). Each section provides a background of the physics of the techniques before launching into some well-selected examples.

In the sixth chapter, Cornia and Mannini present a critical overview of the latest achievements in the deposition of SMMs as monolayers or submonolayers on native or prefunctionalized surfaces. Special emphasis is placed on the selection and design of molecular structures that withstand solution- or vapor-phase processing and maintain their magnetic functionality on a surface.

In the seventh chapter, Bogani reviews the experimental state of the art of molecular spintronics using molecular magnet. After a brief introduction to the fundamental concepts in the field, all possible approaches to fabricate molecular spintronic devices have been summarized. He also provides a brief discussion of the future directions and the considerable challenges that remain unexplored in the field.

Another potential application of molecular nanomagnets is quantum computation. Ghirri, Troiani, and Affronte introduce basic concepts, stressing analogies between the physics and the chemistry of molecular nanomagnets and the science of computing. They review main achievements, present challenges, and focus on two emerging topics: quantum simulators and hybrid systems made by resonant cavities and molecular nanomagnets.

Last chapter by Luis and Evangelisti review history, materials, and underlying physics that form a background common to magnetic refrigeration and spin–lattice relaxation. To illustrate how these subjects are profoundly interrelated with each other, they describe studies performed on two gadolinium-based single molecule magnets and their promising applications as low temperature magnetic refrigerants.

Last but not least, I am greatly indebted to all authors who have contributed to these important and exciting topics and I hope that the readers will find this volume useful, stimulating, and inspirational to their research. I also greatly appreciate the help of June Tang, Chemistry Editor of Springer, in organizing this volume.

Beijing, China Song Gao
October 2014

Contents

Struct Bond (2015) 164: 1–110
DOI: 10.1007/430_2014_149

Published online: 8 July 2014

Cluster-Based Single-Molecule Magnets

Constantinos J. Milios and Richard E.P. Winpenny

Abstract This review covers single-molecule magnets, not only focussing on developments since 2005 but also including coverage of earlier work where necessary for understanding of recent results. The enormous growth of the area has led to an astonishing number of beautiful new molecules, and these structures are described. While work on 3d-single-molecule magnets has continued to create new materials for study, the major new path for exploration is studies of elements from other areas of the periodic table, particularly the 4f-elements. Here much higher energy barriers for magnetic relaxation are observed, and a much more varied chemistry is possible due to the high stability of the +3 oxidation state of the lanthanides. The chapter does not cover single ion magnets, which are reviewed elsewhere in this volume.

Keywords Magnetic relaxation · Molecular magnetism · Polymetallic complexes · Single-molecule magnet

Contents

C.J. Milios (✉)
Department of Chemistry, The University of Crete, Voutes, 710 03 Herakleion, Crete, Greece
e-mail: komil@chemistry.uoc.gr

R.E.P. Winpenny (✉)
School of Chemistry and Photon Science Institute, The University of Manchester, Manchester M13 9PL, UK
e-mail: Richard.Winpenny@manchester.ac.uk

1 Introduction

"...such a complicated dodecameric unit should have interesting magnetic properties." [1] Perhaps the most prophetic words in the history of modern magnetochemistry written by Prof. Tadeusz Lis (Polish crystallographer) 33 years ago, concerning the magnetic behaviour of the dodecanuclear mixed-valent manganese cluster $[Mn_{12}O_{12}(MeCO_2)_{16}(H_2O)_4]\cdot 2MeCO_2H\cdot 4H_2O$ (**1**·$2MeCO_2H\cdot 4H_2O$) which contains eight Mn^{III} and four Mn^{IV} ions (Fig. 1). Due to limited instrumentation, little could they foresee back then that this cluster would change the way that discrete molecules can interact with an external magnetic field at very low temperatures, thus, leading to new adventures and horizons in the field of molecular magnetism. The beginning of the tale is actually much older; it began 92 years ago, in 1921, when Weinland and Fischer reporting on the "Über Manganiacetate und – benzoate" predicted the existence of such "deep-brown" coloured dodecanuclear species, based solely on elemental analysis [2]. This dodecanuclear manganese cluster waited for 59 years to be synthesised and structurally characterised by Lis, upon the reaction of manganese acetate and potassium permanganate in acetic acid.

The Odyssey was not over yet; it had to wait for further 11 years until Caneschi et al. established its magnetic properties, revealing a spin-ground state of $S = 10$ (which can be rationalised by assuming all Mn^{3+} ions being antiferromagnetically

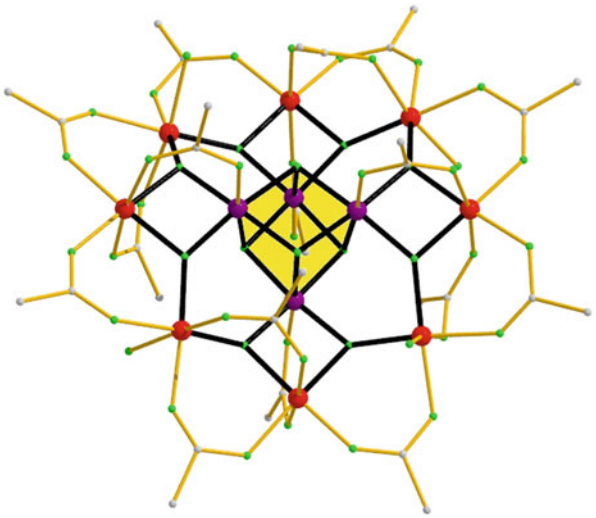

Fig. 1 The molecular structure of $[Mn_{12}O_{12}(CH_3COO)_{16}(H_2O)_4]$ (**1**), highlighting its $[Mn^{IV}{}_4Mn^{III}{}_8O_{12}]^{16+}$ core (in *bold*), as well its $\{Mn^{IV}{}_4O_4\}^{8+}$ sub-unit (in *yellow*). Hydrogen atoms are omitted for clarity. Colour code: Mn^{III} = *red*, Mn^{IV} = *purple*, O = *green*, C = *gold*

coupled to all Mn^{4+} ions) and zero-field splitting (ZFS) of this ground-state of $D = -0.5$ cm^{-1} [3]. But most importantly, they discovered that the molecules display frequency-dependent out-of-phase signals, χ'', analogous to those observed in superparamagnets [4] and spin glasses [5], since as they stated "...it is tempting to attribute these to factors analogous to those observed in superparamagnets...although the dimensions of the clusters are still much smaller than those observed in superparamagnets."; the trip to Ithaca was almost over. Indeed, 2 years later the magnetic bistability of **1**·2MeCO$_2$H·4H$_2$O, hereafter Mn_{12}OAc, was reported and magnetic hysteresis loops of molecular origin were observed for the first time, opening the door for potential magnetic data storage at the molecular level and signalling the era of Single-Molecule Magnets [6]. The term "Single-Molecule Magnet (SMM)" was introduced 3 years later [7], and it describes all molecules that can retain their magnetisation once magnetised under an external magnetic field upon removal of the external stimuli. Although this was not the first time that retention of magnetisation was observed at a molecular level (see for example: [8–14])' it was the first time that such behaviour was due to isolated, discrete molecules and not to domains of magnetically ordered or "frozen" spins.

The combination of a large spin ground state, S, and a negative zero-field splitting of that ground state, D, are the prerequisites for any molecule to display such properties, since they "raise" an energy barrier to magnetisation reversal via thermal deactivation (over the barrier), U, which is manifested in temperature and sweep-rate-dependent hysteresis loops in magnetisation versus field studies (Fig. 2); the height of this barrier is given by $U = |D| \cdot S^2$ and $U = |D| \cdot (S^2 - ¼)$, for integer and half-integer spin ground-states, respectively (Fig. 3). Furthermore,

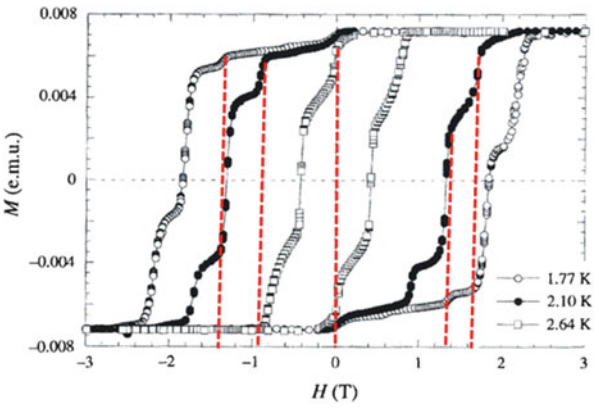

Fig. 2 Magnetisation (M) vs. applied field (H) curves, displaying magnetic hysteresis loops for a single crystal of **1**·$2CH_3COOH·4H_2O$ with the applied field along the easy axis of magnetisation. The dotted lines correspond to characteristic applied field's values which enhance the magnetic relaxation through QTM

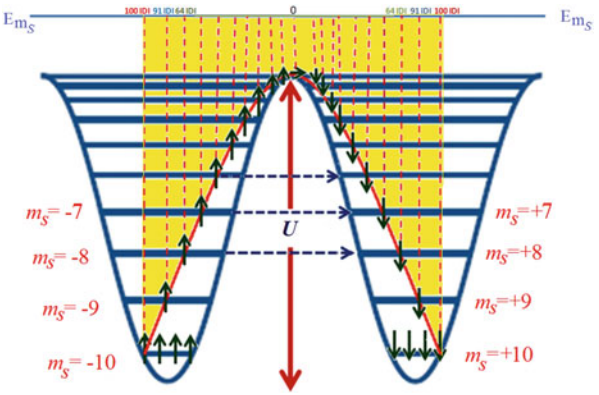

Fig. 3 Energy barrier to magnetisation reversal at zero-field; the *red line* indicates the course of thermal deactivation, while the *dotted blue arrows* indicate QTM transitions

SMMs provided the first clear-cut experimental observation of macroscopic quantum tunnelling of the magnetisation (QTM), displaying steps in the Magnetisation (M) vs. applied field (H) curves (hysteresis loops) in $Mn_{12}OAc$ below the blocking temperature of ~3 K (Fig. 3) [15, 16]. According to this phenomenon, the spins manage to "cheat" the energy barrier to magnetisation reversal, and instead of climbing over it, they transport from one side of the barrier to the other "through" it, resulting in a lowering of the theoretical energy barrier, U, to the experimentally observed, U_{eff}; the larger the U_{eff}, the slower the relaxation, and thus the more technological potential the molecule may display. The contribution of the QTM effect in the relaxation process may be estimated by single-crystal ultra-low temperature M vs. H measurements, at which the thermal deactivation is quenched, and, thus, any relaxation observed may be attributed to the QTM.

From Fig. 2, we can see that at zero applied field the magnetisation of the molecule, M, can take one of two values: either positive or negative. That indicates that the molecule "remembers" the sense of the field that was applied to it, suggesting the employment of such molecules for information storage. How far

are we from the technological application of such systems? A few years ago, the answer would have been "light-years", since the best SMM ($Mn_{12}OAc$) was working only at ~3.5 K, but in the last decade two examples of SMMs were reported to be able to retain their magnetisation above liquid He temperature once magnetised [17, 18], while just 2 years ago an example of an SMM operating at ~14 K was reported [19]. In 2012 information storage in isolated surface arrays of iron atoms was reported by IBM in *Science* [20]; this work was performed at very low temperature, but illustrates that industry is now taking this approach seriously. Very recently femto-second switching of magnetism via strongly correlated spin–charge quantum excitations was reported [21].

Nowadays, our knowledge regarding SMMs is growing exponentially; a phenomenon initially observed for a manganese-based dodecanuclear cluster now involves all paramagnetic metals, and numerous 3d-, 3d-4d, 3d-5d-, 4f- and 3d-4f clusters have been found to function as nanomagnets at low temperatures. This is due to two main reasons: (1) the well-orchestrated synthetic efforts of many coordination chemistry groups worldwide, and (2) the collaboration of physicists, synthetic chemists, theoretical chemists, spectroscopists, mathematicians and even engineers towards the deeper understanding of the factors that dictate the SMM behaviour. The development of new spectroscopic techniques, such as HF-EPR (High Frequency – and Field-Electron Paramagnetic Resonance) (see for example: [22–32])' FDMRS (Frequency Domain Magnetic Resonance Spectroscopy) (Representative refs: [33–37]) and INS (Inelastic Neutron Scattering) (see for example: [38–53]), are just a few of the new, modern and elegant techniques being used for the study of the relaxation dynamics of such complicated systems. The arsenal of SMMs is evolving rapidly; new clusters, new structures, new topologies and new synthetic approaches lead to better and deeper understanding of the SMM phenomenon via more advanced and sophisticated theories. These techniques are reviewed elsewhere in this volume.

1.1 Scope

The scope of this chapter is to gather as much information as possible regarding clusters that can function as SMMs to date, a task not trivial at all due to the vast literature concerning such systems; the number of SMMs has grown exponentially over the last two decades from a handful of compounds in the early 1990s to few hundreds today. Yet, in this laborious effort, our navigators are excellent reviews [54–64] and books [65, 66] that have been published over the years covering various aspects of SMMs, ranging from synthetic schemes to complicated theoretical matters. In addition, our approach is from the synthetic chemist's point of view; therefore, we will try not to engage in rather complicated physics and equations. The clusters reported herein are categorised in terms of their metal content.

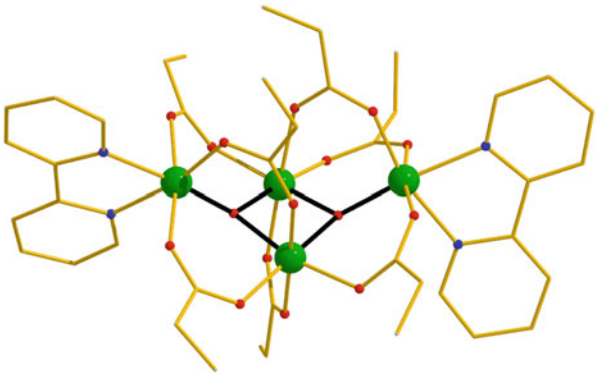

Fig. 4 The molecular structure of the cation of **2**, highlighting its $[V_4O_2]^{8+}$ "butterfly" motif (in *bold*)

2 3d-SMMs

2.1 Vanadium SMMs

2.1.1 $[V^{III}_4O_2(O_2CR)_7(L\text{-}L)_2]^z$: A Family of "Butterfly" V(III) SMMs

The first vanadium SMMs were reported in 1995 by the Christou group and belong to the family of $[V_4O_2(O_2CR)_7(L\text{-}L)_2]^{+1,0}$ clusters (L-L=bipy, R=Et, $z=+1$: **2**; R=Ph, $z=+1$: **5**, L-L = 4,4′-Me_2bpy, R=Et, $z=+1$: **3**; L-L = 5,5′-Me_2bpy, R=Et, $z=+1$: **4**; L-L = 2-picolinate, R=Et, $z=0$: **6**) [67, 68]. These clusters contain four trivalent vanadium $3d^2$ centres ($S=1$) arranged in a butterfly $[V_4O_2]^{8+}$ arrangement (Fig. 4). For complexes **2** and **6**, the ground-state was found $S=3$, due to competing J_{bb} (body–body) and J_{bw} (body–wingtip) interactions within the metallic core. Furthermore, fitting of the magnetisation data established a ZFS value of $D=-1.5$ cm^{-1} for both complexes, while finally, both of them display weak out-of-phase signals below 4.0 K, establishing their SMM behaviour. The same group in 1998 reported a similar cluster to **2**, complex $[NEt_4][V_4O_2(O_2CEt)_7(pic)_2]$ (**7**), which can also function as a SMM [69].

2.1.2 The Case of $[V^{IV}_{15}As_6O_{42}(H_2O)]^{6+}$: A Polyoxometallate SMM

The POM cluster $K_6[V_{15}As_6O_{42}(H_2O)]$ (**8**) which contains exclusively tetravalent ($3d^1$) vanadium centres is a "peculiar" example of an SMM. Although firstly synthesised in 1988 [70], its magnetic properties were investigated 3 years later [71, 72]. In this cluster the metal atoms are arranged in a quasi-spherical layered structure formed of a triangle, sandwiched between two hexagons. The molecule displays antiferromagnetic intramolecular interactions, allowing for a total spin of only $S=1/2$ ground-state. Yet, this molecule with a zero energy barrier presents unusual features, such as "butterfly-like" hysteresis loops due to the "phonon bottleneck" effect [73, 74] and, as theoretical estimates show, might demonstrate rather long decoherence times [75, 76].

2.2 Manganese SMMs

The Manganese family of SMMs is by far the largest and most extensively studied category of SMMs; not surprisingly, since: (1) it contains the prototype $Mn_{12}OAc$, (2) the relative easiness of making carboxylate analogues of the prototype SMM, as well as, reduced versions of it (approximately 60 [Mn_{12}] SMMs have been reported to date), (3) the large spin of the manganese centres in various oxidation states and the negative magnetoanisotropy of the Jahn–Teller elongated six-coordinate Mn^{III} ions, (4) the stability of the Mn complexes under aerobic conditions and (5) the availability of many manganese salts/complexes that can be employed as starting materials.

Given the vast literature regarding the Mn SMMs, we chose not to take the story from the very beginning, but to update the excellent review by Brechin and Aromi [56], as well as, the tutorial review by Bagai and Christou regarding the [Mn_{12}] field [57]. Yet, we feel it is appropriate to highlight and remind the readership of the major breakthroughs in Mn SMM history that had a great impact on the field of SMMs.

2.2.1 $[Mn^{IV}Mn^{III}_3O_3Cl_4(O_2CEt)_3(py)_3]$: Exchange-Biased Quantum Tunnelling in Dimers of [Mn_4] SMMs

Almost a decade after the premiere of the SMM act, a second major breakthrough happened; cubane cluster $[Mn^{IV}Mn^{III}_3O_3Cl_4(O_2CEt)_3(py)_3]\cdot 2.5MeCN$ (**9**·2.5MeCN) which contains three Mn^{III} and one Mn^{IV} ions, possessing an $S = 9/2$ ground-state, was found to display exchange-biased quantum tunnelling through intermolecular interactions between neighbouring [Mn_4] units [77]. Complex **9** was prepared upon the reaction of the $[Mn^{III}_3O(OCEt)_6(py)_3](ClO_4)$ starting material with the carboxylate abstracting reagent, Me_3SiCl, and was initially studied as a potential model for the Oxygen Evolving Center (OEC) of PSII [78]. The supramolecular structure of **9** consists of well-isolated dimers of [Mn_4]···[Mn_4] molecules arranged in a head-to-head fashion via six C–H···Cl hydrogen bonds. Magnetisation measurements on single crystals of **9** revealed the presence of weak but noticeable antiferromagnetic interactions within each [Mn_4]···[Mn_4] dimer, resulting in a total $S = 0$ of the exchange-coupled $S = 9/2$ [Mn_4] systems. As a result, a shift of the resonance tunnelling is observed from zero field, which is normally observed for the isolated cubanes, which is of fundamental importance for the technological application of SMMs, as in information storage devices.

2.2.2 $[Mn^{III}_2Mn^{II}_2(O_2CMe)_2(pdmH)_6](ClO_4)_2$: The First Tetranuclear Mn SMM

Complex $[Mn^{III}_2Mn^{II}_2(O_2CMe)_2(pdmH)_6](ClO_4)_2$ (**10**) was made from the reaction of $[Mn_3O(O_2CMe)_6(py)_3](ClO_4)$ with pyridine-2,6-dimethanol (H_2pdm) in CH_2Cl_2, followed by recrystallisation in MeCN; alternatively, **10** can be made

Table 1 Representative examples of $[Mn^{III}_2Mn^{II}_2]$ SMMs

Formula	S	U_{eff} (K)	References
$[Mn_4(O_2CMe)_2(pdmH)_6](ClO_4)_2$ (**10**)	9	17	[79]
$[Mn_4(O_2CMe)_2(pdmH)_6]$ $(ClO_4)_2{\cdot}2.5\ H_2O$ (**11**)	9	17	[79]
$[Mn_4(hmp)_6(NO_3)_4]$. MeCN (**12**)	9	–	[80]
$[Mn_4(hmp)_6(NO_3)_2(MeCN)_2](ClO_4)_2$ (**13**)	9	–	[80]
$[Mn_4(hmp)_4(acac)_2(MeO)_2](ClO_4)_2$ (**14**)	9	–	[80]
$[Mn_4(hmp)_6Br_2(H_2O)_2]Br_2$ (**15**)	9	16	[81]
$[Mn_4(hmp)_6(NO_3)_2(H_2O)_2](NO_3)_2{\cdot}2.5H_2O$ (**16**)	9	12	[82]
$[Mn_4(hmp)_6(H_2O)_4](ClO_4)_4{\cdot}2H_2O$ (**17**)	9	33	[82]
$[Mn_4(hmp)_6(NO_3)_2(H_2O)_2](ClO_4)_2{\cdot}4H_2O$ (**18**)	9	20	[83]
$[Mn_4(hmp)_6(N_3)_2](ClO_4)_2$ (**19**)	9	47	[83]
$[Mn_4(hmp)_6(NO_3)_2(dcn)_2]$. 2MeCN (**20**)	9	21	[84]
$[Mn_4(hmp)_6(dcn)_2](ClO_4)_2$ (**21**)	9	–	[84]
$[Mn_4(hmp)_6(Hpdm)_2(dcn)_2](ClO_4)_2{\cdot}2H_2O{\cdot}2MeCN$ (**22**)	9	13	[84]
$[Mn_4(hmp)_6Br_2(MeO)_2(dcn)_2]{\cdot}0.5H_2O{\cdot}2THF$ (**23**)	9	–	[84]
$[Mn_4(hmp)_6(MeCO_2)_2(H_2O)_2](ClO_4)_2{\cdot}4H_2O$ (**24**)	9	12	[85]
$[Mn_4(hmp)_6(PhCO_2)_2(H_2O)_2](ClO_4)_2{\cdot}4MeCN{\cdot}2H_2O$ (**25**)	9	14	[85]
$[Mn_4(hmp)_6(MeCO_2)_2](ClO_4)_2{\cdot}H_2O$ (**26**)	9	37	[85]
$[Mn_4(hmp)_6(ClCH_2CO_2)_2(H_2O)_2](ClO_4)_2{\cdot}2H_2O$ (**27**)	9	42	[85]
$[Mn_4(hmp)_6(MeCN)_2(H_2O)_2](ClO_4)_4{\cdot}2MeCN$ (**28**)	9	23	[86]
$[Mn_4(bdea)_2(bdeaH)_2(^tBuCO_2)_4]$ (**29**)	9	–	[87]
$[Mn_4(bdea)_2(bdeaH)_2(PhCO_2)_4]$ (**30**)	9	27	[87]
$[Mn_4(tea)_2(teaH)_2(^tBuCO_2)_4](^tBuCO_2)_2$ (**31**)	9	–	[88]
$[Mn_4(tea)_2(teaH)_2(MeCO_2)_4](MeCO_2)_2{\cdot}2H_2O$ (**32**)	9	22	[89]
$[Mn_4(tea)_2(teaH)_2(EtCO_2)_4](ClO_4)_2$ (**33**)	9	–	[89]
$[Mn_4(HL^6)_4Cl_2(MeOH)_4]{\cdot}2Et_2O$ (**34**)	9	–	[90]
$[Mn_4(HL^6)_4Br_2(MeOH)_4]{\cdot}2Et_2O$ (**35**)	9	–	[90]
$[Mn_4(hmp)_6Cl_2](ClO_4)_2$ (**36**)	9	–	[91]
$[Mn_4(O_2CPh)_4(mda)_2(mdaH)_2]$ (**37**)	9	15	[92]

H_2pdm 2,6-pyridinedimethanol, *Hhmp* 2-hydroxymethylpyridine, *dcn* dicyanoamide, *Hbdea* *N*-butyldiethanolamine, *H_3tea* triethanolamine, *HL^6* 2,6-bis(hydroxymethyl)-4-methylphenol, *H_2mda* *N*-methyldiethanolamine

directly from MeCN [79]. The structure of the molecule consists of a planar butterfly-like unit, with the two trivalent Mn ions located at the body and the two divalent Mn ions at the wings of the butterfly. The cluster is a ferromagnet with an $S = 9$ ground-state, while from reduced magnetisation and HFEPR studies a ZFS parameter of this ground-state of $D = -0.31\ cm^{-1}$ was found. The isolation and detailed study of **10** led to the formation of analogous complexes with similar behaviour (Table 1), thus forming one of the earliest "families" of SMMs. The impact of this family of SMMs was great for the development of the field; closely related clusters lead to the understanding of the magnetic properties in great depth and detail.

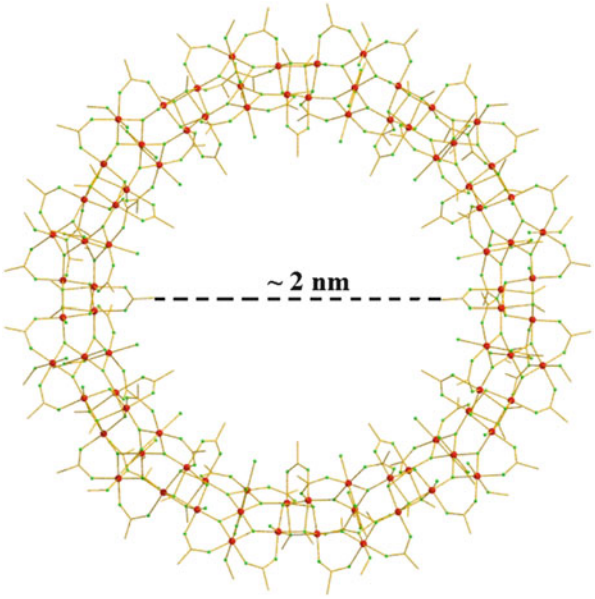

Fig. 5 The molecular structure of $[Mn^{III}_{84}O_{72}(OAc)_{78}(OMe)_{24}(OH)_6(MeOH)_{12}(H_2O)_{42}]$ (**38**). Hydrogen atoms are omitted for clarity

2.2.3 $[Mn^{III}_{84}O_{72}(OAc)_{78}(OMe)_{24}(OH)_6(MeOH)_{12}(H_2O)_{42}]$: A Colossal SMM

The largest SMM known to date was isolated in 2004 upon the reaction of the prototype SMM, $Mn_{12}OAc$, with tetrabutylammonium permanganate, NBu_4MnO_4, in MeOH that contained a little acetic acid, followed by filtration and layering of the filtrate with $CHCl_3$ [93]. Cluster $[Mn^{III}_{84}O_{72}(OAc)_{78}(OMe)_{24}(OH)_6(MeOH)_{12}(H_2O)_{42}]$ (**38**) consists of 84 trivalent Mn^{III} ions arranged in a torus-like topology possessing C_6 crystallographic symmetry, with alternating near-linear $[Mn_3O_4]^+$ and cubic $[Mn_4O_2(OMe)_2]^{6+}$ sub-units (Fig. 5). This impressive cluster is by far the largest Mn complex ever isolated in terms of nuclearity, with the second largest containing ~1/2 of the metal content of it $[Mn_{44}]$ [94]. The hole of the torus is ~2 nm, while its diameter is ~4.2 nm. Magnetic susceptibility studies reveal an $S = 6$ ground-state for the complex, while in addition low temperature single-crystal micro-SQUID measurements display temperature as well as and sweep-rate-dependent hysteresis loops confirming its SMM behaviour. Furthermore, an Arrhenius analysis of the *dc* and *ac* data yielded an energy barrier for the reorientation of the magnetisation of $U_{eff} = 18$ K and $\tau_0 = 5.7 \times 10^{-9}$ s.

2.2.4 $[Mn_{12}O_{12}(RCOO)_{16}L_4]$: The First and Largest Family of SMMs

As mentioned already, there are more than 60 analogues of the prototype $Mn_{12}OAc$ reported to date (Table 2). This is attributed to the fact that numerous carboxylate analogues of the acetate prototype have been synthesised, as well as reduced versions of the original SMM. The vast majority of the $\{Mn_{12}\}$ cages possess an $S = 10$ ground-state, due to the dominant antiferromagnetic interactions between the trivalent and tetravalent Mn ions. The zero-field splitting of this $S = 10$ ground-state was found by EPR [95] and INS [42] measurements to be $D \approx -0.50\ cm^{-1}$. This large and negative D value arises from the presence of the eight Jahn–Teller elongated six-coordinate Mn^{III} ions, which align their JT axes almost co-parallel. In fact, the relative orientation of the JT axes affects strongly the appearance of the out-of-phase *ac* susceptibility peaks of the $[Mn_{12}]$ analogues, as was proven that species with two different isomers regarding the JT orientation displayed two discrete out-of-phase peaks [109].

2.2.5 Oximate-Based Mn SMMs

Hexanuclear Manganese Salicyloximate-Based SMMs: Controlling the Spin and the Energy Barrier in an Extended Family of SMMs

In 2004, complex $[Mn^{III}{}_6O_2(O_2CPh)_2(sao)_6(EtOH)_4]\cdot EtOH$ (**101**·EtOH) ($saoH_2$= salicylaldoxime) was reported from the one-step reaction of manganese benzoate with salicylaldoxime in EtOH [136]. The structure of the complex describes two off-set stacked $[Mn^{III}{}_3O(sao)_3(O_2CPh)]$ triangles consisting of three $-$Mn-($-$N–O)$_{oximate}$- units forming a $\{$Mn-N-O–$\}_3$ ring. The linkage through the two triangular units occurs via two $O_{oximate}$ atoms, each one belonging to a $[Mn_3]$ unit, resulting in a $[Mn^{III}{}_6O_2(sao)_6(O_2CPh)_2]$ metallic core. In addition, each oximate ligand binds in a chelate mode to a metallic atom through the $O_{aromatic}$ atom and the $N_{oximate}$ atom. Therefore, four of the six oximate ligands are found in an $\eta^1{:}\eta^1{:}\eta^1{:}\mu$-fashion along the edges of each sub-unit, while the remaining two, responsible for the inter-triangular linkage are found in an $\eta^2{:}\eta^1{:}\eta^1{:}\mu_3$ mode. The two carboxylates are found in an $\eta^1{:}\eta^1{:}\mu$ mode, while the coordination environment of the metallic centres is completed by the presence of four terminal EtOH molecules (Fig. 6). Four metallic centres are six-coordinate adopting JT elongated octahedral geometry, while the remaining two are five-coordinate adopting square-pyramidal geometry. The acetate analogue, $[Mn^{III}{}_6O_2(O_2CMe)_2(sao)_6(EtOH)_4]\cdot 4EtOH$ (**102**·4EtOH), can be easily obtained upon switching to manganese acetate from manganese benzoate. Actually, the reaction forming **101** was initially carried out in MeCN, yielding the well-known mixed-valent hexanuclear $[Mn_6O_2(O_2CPh)_{10}(MeCN)_4]$ cluster (**103**) [137], while, surprisingly, from a very similar reaction-system, complex $[Mn^{III}{}_6O_2(O_2CPh)_2(sao)_6(H_2O)_2(MeCN)_2]$ (**104**) was reported a few years earlier in a pure form without the presence of **103** [138].

Table 2 Representative examples of the $Mn_{12}OAc$ family

Formula	S	D (cm^{-1})	U_{eff} (K)	τ_0 (s)	References
$[Mn_{12}O_{12}(CH_3COO)_{16}(H_2O)_4]\cdot 2CH_3COOH\cdot 4H_2O$ (**1**)	10	−0.50	70.3	2.1×10^{-7}	[1, 3, 6, 15, 42, 95]
$[Mn_{12}O_{12}(O_2CPh)_{16}(H_2O)_4]$ (**39**)	9	–	37/66	$3.2 \times 10^{-11}/4.7 \times 10^{-9}$	[96]
$[Mn_{12}O_{12}(O_2CCH_2Br)_{16}(H_2O)_4]\cdot 4CH_2Cl_2$ (**40**)	10	−0.38	74.6	3.3×10^{-9}	[97, 98]
$[Mn_{12}O_{12}(O_2CMe)_{16}(MeOH)_4]$ (**41**)	10	–	76	5.35×10^{-9}	[99]
$[Mn_{12}O_{12}(O_2CEt)_{16}(H_2O)_3]\cdot H_2O$ (**42**)	9	–	62	–	[100]
$[Mn_{12}O_{12}(O_2CCH_2{}^tBu)_{12}(NO_3)_4(H_2O)_4]$ (**43**)	10	−0.40	72	5.26×10^{-9}	[101]
$[Mn_{12}O_{12}(O_2CPh)_{12}(NO_3)_4(H_2O)_4]$ (**44**)	10	–	–	–	[101]
$[Mn_{12}O_{12}(O_2CCH_2Ph)_{16}(H_2O)_4]$ (**45**)	9-10	–	–	–	[102]
$[Mn_{12}O_{12}(O_2CMe)_8(O_2PPh_2)_8(H_2O)_4]\cdot 12CH_2Cl_2$ (**46**)	10	−0.41	60	–	[103]
$[Mn_{12}O_{12}(O_2CMe)_8(O_3SPh)_8(H_2O)_4]$ (**47**)	10	−0.34	67	6.6×10^{-9}	[104]
$[Mn_{12}O_{12}(O_2CCHCl_2)_8(O_2CH_2{}^tBu)_8(H_2O)_4]$ (**48**)	10	−0.45	71	7.7×10^{-9}	[105]
$[Mn_{12}O_{12}(O_2CCHCl_2)_8(O_2CEt)_8(H_2O)_4]$ (**49**)	10	−0.42	72	6.3×10^{-9}	[105]
$[Mn_{12}O_{12}(O_2CPh)_7(O_3PPh_2)_9(H_2O)_4]$ (**50**)	10	−0.42	40	5.9×10^{-9}	[106]
$[Mn_{12}O_{12}(O_2CPh\text{-}4\text{-}Cl)_{16}(H_2O)_4]\cdot 8CH_2Cl_2$ (**51**)	9–10	–	–	–	[107]
$[Mn_{12}O_{12}(O_2CPh\text{-}2\text{-}Cl)_{16}(H_2O)_4]$ (**52**)	10	–	–	–	[108]
$[Mn_{12}O_{12}(O_2CPh\text{-}2\text{-}Br)_{16}(H_2O)_4]$ (**53**)	10	–	–	–	[108]
$[Mn_{12}O_{12}(O_2CPh\text{-}4\text{-}Me)_{16}(H_2O)_4]\cdot 3H_2O$ (**54**)	9–10	–	–	–	[109]
$[Mn_{12}O_{12}(O_2CPh\text{-}4\text{-}Me)_{16}(H_2O)_4]\cdot HO_2CPh\text{-}4\text{-}Me$ (**55**)	9–10	–	–	–	[109]
$[Mn_{12}O_{12}(O_2CPh\text{-}4\text{-}Me)_{16}(H_2O)_3]\cdot(HO_2CPh\text{-}4\text{-}Me)$ (**56**)	9–10	–	37	2.2×10^{-10}	[109]
$[Mn_{12}O_{12}(O_2CPh\text{-}4\text{-}Me)_{16}(H_2O)_3]\cdot 3H_2O$ (**57**)	9–10	–	63	7.7×10^{-9}	[109]
$[Mn_{12}O_{12}(O_2CCF_3)_{16}(H_2O)_4]\cdot 2CF_3CO_2H\cdot 4H_2O$ (**58**)	10	−0.65	69	7.4×10^{-9}	[110]
$[Mn_{12}O_{12}(O_2CCF_3)_{16}(H_2O)_4]\cdot CF_3CO_2H\cdot 7H_2O$ (**59**)	10	−0.34	22	1.6×10^{-10}	[110]
$[Mn_{12}O_{12}(O_2CC_4H_3S)_{16}(HOCC_4H_3S)(H_2O)_2]$ (**60**)	10	−0.42	52/66	$5.3/6.7 \times 10^{-9}$	[111]
$[Mn_{12}O_{12}(O_2CC_4H_3S)_{16}(H_2O)_4]$ (**61**)	10	−0.45	67	7.6×10^{-9}	[111]
$[Mn_{12}O_{12}(O_2CCCH)_{16}(H_2O)_4]$ (**62**)	–	–	52	–	[112]
$[Mn_{12}O_{12}(O_2CCCC_6H_5)_{16}(H_2O)_4]$ (**63**)	–	–	61	–	[112]
$[Mn_{12}O_{12}(O_2CCHCHCH_3)_{16}(H_2O)_4]\cdot H_2O$ (**64**)	10	−0.44	65	2.43×10^{-9}	[113]

(continued)

Table 2 (continued)

Formula	S	D (cm^{-1})	U_{eff} (K)	τ_0 (s)	References
$[Mn_{12}O_{12}(O_2CC_6H_4C_6H_5)_{16}(H_2O)_4]$ (**65**)	10	−0.33	64	1.48×10^{-9}	[113]
$[Mn_{12}O_{12}(O_2CCF_3)_{16}(H_2O)_4]$ (**66**)	10	–	62	1.7×10^{-8}	[114]
$[Mn_{12}O_{12}(O_2CC_4H_3S)_{16}(H_2O)_4]$ (**67**)	10	–	69	3.8×10^{-9}	[115]
$[Mn_{12}O_{12}(O_2CEt)_{16}(H_2O)_4]\cdot H_2O$ (**68**)	9	−0.6	–	–	[116]
$[Mn_{12}O_{12}(O_2CCF_2Cl)_{16}(H_2O)_4]$ (**69**)	10	–	82/56	$1.33 \times 10^{-9}/5.2 \times 10^{-10}$	[117]
$[Mn_{12}O_{12}(O_2CCH_2NMe_3)_{16}(EtOH)_4](PF_6)_{14}$ (**70**)	11	−0.22	34	–	[118]
$[Mn_{12}O_{12}(O_2CC_6F_5)_{16}(H_2O)_4]\cdot 3CH_2Cl_2$ (**71**)	10	−0.40	59	8.1×10^{-9}	[119]
$[Mn_{12}O_{12}(O_2CC(CH_3)CH_2)_{16}(H_2O)_4]$ (**72**)	–	–	66	8.5×10^{-9}	[120]
$[Mn_{12}O_{12}(O_2CC_6H_4\text{-}2\text{-}CH_3)_{16}(H_2O)_4]\cdot CH_2Cl_2\cdot H_2O$ (**73**)	10	−0.47	29	–	[121]
$[Mn_{12}O_{12}(O_2CMe)_{12}(O_3SMe)_3(O_3SMe)(H_2O)_3]$ (**74**)	9	−0.38	34/67	–	[122]
$(PPh_4)[Mn_{12}O_{12}(O_2CEt)_{16}(H_2O)_4]$ (**75**)	19/2	−0.62	57	1.4×10^{-8}	[116]
$(PPh_4)[Mn_{12}O_{12}(O_2CPh)_{16}(H_2O)_4]$ (**76**)	19/2	−0.44	57	3.1×10^{-10}	[123]
$(PPh_4)_2[Mn_{12}O_{12}(O_2CH_2Cl)_{16}(H_2O)_3]$ (**77**)	10	−0.28	–	–	[124]
$(PPh_4)[Mn_{12}O_{12}(O_2CC_4H_3S)_{16}(H_2O)_4]$ (**78**)	19/2	−0.42	57	1.9×10^{-9}	[115]
$(PPh_4)_2[Mn_{12}O_{12}(O_2CHCl_2)_{16}(H_2O)_4]$ (**79**)	10	−0.27	32	–	[125]
$(PPh_4)_2[Mn_{12}O_{12}(O_2CHCl_2)_{16}(H_2O)_4]\cdot 4CH_2Cl_2\cdot H_2O$ (**80**)	10	−0.17	19	5.26×10^{-8}	[125]
$(PPh_4)_2[Mn_{12}O_{12}(O_2CHCl_2)_{16}(H_2O)_4]\cdot 6CH_2Cl_2$ (**81**)	10	−0.28	30	3.22×10^{-8}	[125, 126]
$[Mn_{12}O_{12}(O_2CMe)_{16}(dpp)_4]$ (**82**)	10	−0.42	62	–	[127]
$(NBu^n_4)[Mn_{12}O_{12}(O_2CPh)_{16}(H_2O)_3]$ (**83**)	19/2	−0.40	55	7.7×10^{-10}	[128]
$(NBu^n_4)_2[Mn_{12}O_{12}(OMe)_2(O_2CPh)_{16}(H_2O)_2]$ (**84**)	6	−0.37	50	2.77×10^{-9}	[128]
$(NMe_4)[Mn_{12}O_{12}(O_2CC_6F_5)_{16}(H_2O)_4]\cdot 4.5CH_2Cl_2$ (**85**)	19/2	−0.34	49/22	$3.0 \times 10^{-10}/1.3 \times 10^{-10}$	[119]
$(NMe_4)_2[Mn_{12}O_{12}(O_2CC_6F_5)_{16}(H_2O)_4]\cdot 6C_7H_8$ (**86**)	10	−0.29	24	9.1×10^{-8}	[119]
$(PPh_4)[Mn_{12}O_{12}(O_2CCF_2Cl)_{16}(H_2O)_4]$ (**87**)	21/2	–	65/32	$5.9 \times 10^{-10}/4.26 \times 10^{-9}$	[117]
$(NPr^n_4)[Mn_{12}O_{12}(O_2CHCl_2)_{16}(H_2O)_4]$ (**88**)	19/2	−0.35	–	–	[129]
$(NPr^n_4)_3[Mn_{12}O_{12}(O_2CHCl_2)_{16}(H_2O)_4]$ (**89**)	10	−0.28	–	–	[129]
$(NPr^n_4)_3[Mn_{12}O_{12}(O_2CHCl_2)_{16}(H_2O)_4]$ (**90**)	17/2	−0.25	–	–	[129]
$(NMe_4)_3[Mn_{12}O_{12}(O_2CHCl_2)_{16}(H_2O)_4]$ (**91**)	17/2	−0.23	–	–	[129]
$[Mn_{12}O_{12}(O_2CC_6H_4F)_{16}(EtOH)_4]\cdot 4.4CHCl_3$ (**92**)	–	–	–	–	[130]

$[Mn_{12}O_{12}(bet)_{16}(EtOH)_4](PF_6)_{14}{\cdot}4CH_3CN{\cdot}H_2O$ (**93**)	11	−0.22	37	2.1×10^{-10}	[131]
$[Mn_{12}O_{12}(bet)_{16}(EtOH)_3(H_2O)](PF_6)_{13}(OH){\cdot}6CH_3CN$ (**94**)	11	−0.31	36	4.7×10^{-9}	[131]
$[Mn_{12}O_{12}(O_2CCH_2Bu^t)_{16}(Bu^tOH)(H_2O)_3]$ (**95**)	10	−0.44	63	9.1×10^{-9}	[24]
$[Mn_{12}O_{12}(O_2CCH_2Bu^t)_{16}(C_5H_{11}OH)_4]$ (**96**)	10	−0.49	71	1.1×10^{-8}	[24]
$[Mn_{12}O_{12}(O_2CC_6H_4C_4H_3S)_{16}(H_2O)_3]{\cdot}14CH_2Cl_2$ (**97**)	10	−0.425	70	6.8×10^{-9}	[132]
$[Mn_{12}O_{12}(p\text{-}O_2CBnSMe)_{16}(H_2O)_4]$ (**98**)	10	–	64/30	$1.9 \times 10^{-9}/2.3 \times 10^{-10}$	[133]
$[Mn_{12}O_{12}(CN\text{-}C_6H_4CO_2)_{12}(CH_3CO_2)_4(H_2O)_4]{\cdot}CH_2Cl_2$ (**99**)	10	−0.39	59/35	$1.3 \times 10^{-8}/2 \times 10^{-9}$	[134]
$[Mn_{12}O_{12}(O_2CCH_2Bu^t)_{16}(MeOH)_4]{\cdot}MeOH$ (**100**)	10	−0.42	63	2.8×10^{-8}	[135]

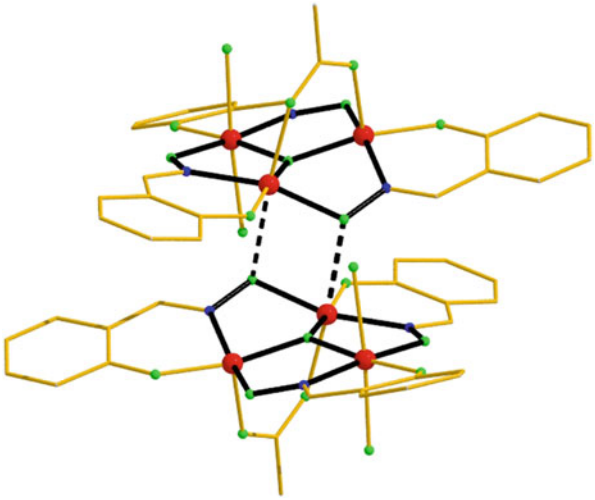

Fig. 6 The molecular structure of $[Mn^{III}_6O_2(O_2CMe)_2(sao)_6(EtOH)_4]$ (**102**), highlighting the triangular units, as well as, the inter-triangular linkage. Hydrogen atoms are omitted for clarity. Only the O atoms are shown from the coordinated EtOH molecules. Colour code: Mn^{III} = *red*, O = *green*, N = *blue*, C = *gold*

The magnetic susceptibility and reduced magnetisation data of both **101** and **102** were fitted to give an $S = 4$ ground-state and a zero-field splitting of this ground state of $D = -1.22$ cm^{-1} and $D = -1.21$ cm^{-1}, respectively. The $S = 4$ ground-state is due to: (1) the presence of competing AF interactions within each triangular sub-unit, establishing a local $S = 2$ within each triangle and (2) the presence of an inter-triangular ferromagnetic exchange interaction. Accordingly, the large and negative D value may be attributed to the parallel orientation of the four JT axes present in **101** and **102**. Both complexes displayed fully formed out-of-phase peaks in the 2–3.5 K temperature range, while an Arrhenius analysis yielded the energy barrier of the re-orientation of the magnetisation of $U_{eff} \sim 28$ K for both **101** and **102**. The magnetic behaviour of **104** appeared 5 years after the original report, while no single-molecule magnetism behaviour was reported [139].

One year after the report of **101** and **102**, cluster $[Mn^{III}_3O(mpko)_3(O_2CMe)_3]^+$ (**105**) (mpkoH=methyl 2-pyridyl ketone oxime) was reported (Fig. 7, left) [140]. The structure of **105** describes a $[Mn^{III}_3O(mpko)_3(O_2CMe)_3]$ triangle again consisting of three $-$Mn-($-$N-O)$_{oximate}$- units forming a {Mn-N-O–}$_3$ ring as in **101** and **102**, with the additional presence of three bridging carboxylates (vs. one in **101** and **102**) filling the coordination spheres of the metallic centres. Essentially, the core **105** can be considered as "half" the core of **101**–**102**, with the presence of the additional carboxylates. This molecule has an $S = 6$ ground-state due and a ZFS of this ground-state of $D = -0.34$ cm^{-1}, and displays out-of-phase peaks, χ_M'', although not fully formed, in ac magnetic susceptibility measurements. The SMM behaviour of **105** was established by single-crystal magnetisation measurements,

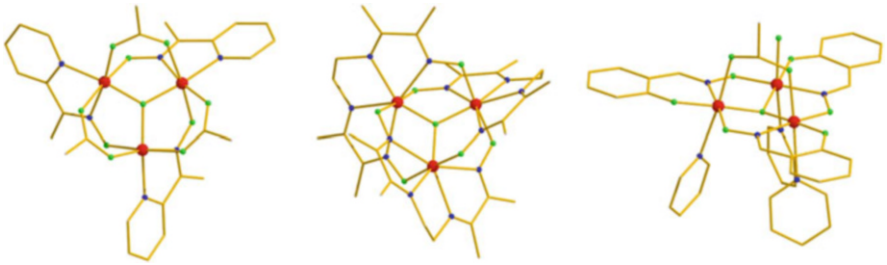

Fig. 7 The molecular structures of $[Mn^{III}_3O(mpko)_3(O_2CMe)_3]^+$ (**105**) (*left*), $Mn^{III}_3O(bamen)]^+$ (**106**) (*centre*) and $[Mn^{III}_3O(sao)_3(O_2CMe)(H_2O)(py)_3]$ (**107**) (*right*). Colour code: Mn^{III} = *red*, O = *green*, N = *blue*, C = *gold*

revealing an energy barrier of $U_{eff} = 11$ K for the magnetisation reversal and a pre-exponential factor of $\tau_0 = 5.7 \times 10^{-8}$ s, establishing **105** as the first example of a triangular trinuclear $[Mn^{III}_3]$ SMM. Furthermore, **105** was only the second ferromagnetically coupled oxo-centred $[Mn^{III}_3]$ cluster, with the first being again the oximate-based $[Mn^{III}_3O(bamen)]^+$ (**106**) (bamenH_2 = 1,2-bis(biacetylmonoxi-meimino)ethane) cluster published in 2002 [141], with all three metallic centres being seven-coordinate (Fig. 7, centre). The remarkable ferromagnetic character of **105** was attributed to the fact that the central μ_3-O^{2-} bridge was located 0.295 Å above the Mn_3 plane, thus weakening the strong AF interactions mediated by the μ_3-O^{2-} bridge when located on the same plane with the Mn^{3+} ions, a case always observed in all $[Mn^{II}_3O(O_2CR)_6L_3]$ (L: terminal ligand) triangles isolated to date. Yet, this hypothesis cannot explain the ferromagnetic character observed earlier in **106**, in which the central bridging oxide is marginally displaced by 0.015 Å by the Mn_3 plane, while in support of this hypothesis, there is a major difference between **105** and **106**; in **105** all Mn^{III} ions are six-coordinate, while in **106** they are seven-coordinate.

This reasonable explanation for the ferromagnetic character of **105** was put under pressure when a very similar cluster was isolated; complex $[Mn^{III}_3O(sao)_3(O_2CMe)(H_2O)(py)_3]$ (**107**) was isolated during the reaction that yielded **102** in pyridine under microwave conditions (Fig. 7, right) [142]. Its structure describes "half" the one of **102**, while the central μ_3-O^{2-} bridge is located 0.35 Å above the Mn_3 plane, i.e. even further away than in **105**. Yet, its magnetic ground state is dictated by antiferromagnetic interactions stabilising an $S \approx 2$ ground-state instead of the expected $S = 6$. This disappointing result, prompted the authors to investigate the reasons behind the different magnetic behaviour of **105** and **107**. A close comparison between the structures of **105** and **107** revealed that while in **107** the {Mn-O–N-Mn} unit is in the same plane as the Mn^{III}_3 triangle, in **105** it is clearly not. Therefore, the authors engaged in trying to make analogues of **107** that would not have the {Mn-N-O–Mn} unit in the same plane with the $[Mn_3]$ triangle, and their approach was simple: by using derivatised oxime ligands, R-saoH_2 (Fig. 8), they anticipated to "twist" the {Mn-N-O-Mn} unit and hopefully affect dramatically the magnetic behaviour of the clusters.

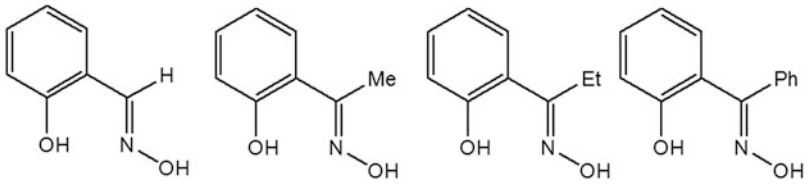

Fig. 8 The structures of the oxime ligands employed; (from *left* to *right*) $saoH_2$, Me-$saoH_2$, Et-$saoH_2$ and Ph-$saoH_2$

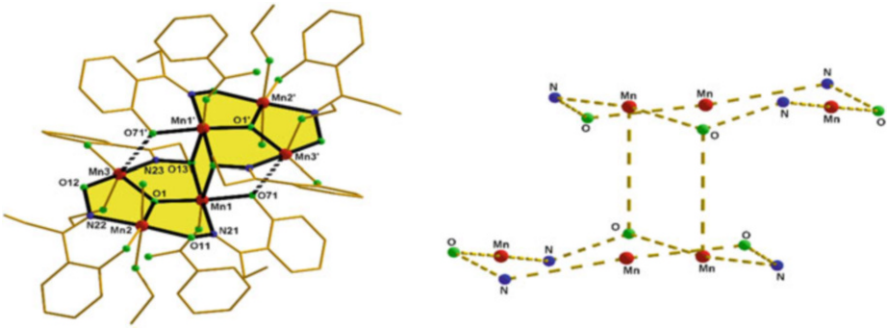

Fig. 9 (*Left*) The molecular structure of **108**, highlighting its core; (*right*) the "twisted" Mn-N-O-Mn arrangement in complex **108**. Reprinted with the permission from [143]. Copyright 2007 American Chemical Society

This turned out to be the case; the first complex isolated was cluster $[Mn^{III}_6O_2(Etsao)_6(O_2CPh)_2\ (EtOH)_4(H_2O)_2]\cdot 2EtOH$ (**108**·2EtOH) (which contains the ethyl-derivatised $saoH_2$ (Et-$saoH_2$) and does, indeed, display ferromagnetic exchange interactions with an $S = 12$ ground state [143]. The structure of the complex (Fig. 9, left) displays three significant differences to that of **101**/**102**: (1) the distance between the square-pyramidal Mn ion and the proximal phenolate O-atom has now decreased by ~1 Å, (2) the two carboxylates have become monodentate (vs. bridging in **101**/**102**), with the vacated coordination site on the neighbouring Mn ion now occupied by an additional solvent molecule and (3) the Mn-O-N-Mn torsion angles, *a*, have now increased significantly; more specifically, the three torsion angles have increased from 21.8, 35.4 and 11.4° for **101** to 39.9, 38.2, 31.2° for **108** (Fig. 9, right).

The magnetic susceptibility and reduced magnetisation data were fitted to give an $S = 12$ ground-state and a zero-field splitting of this ground state of $D = -0.43\ cm^{-1}$. Furthermore, single-crystal magnetisation versus field hysteresis loops measurements (Fig. 10, left) revealed an energy barrier of $U_{eff} = 53.1$ K with $\tau_0 = 8 \times 10^{-10}$ s. Complex **108** was the beginning of a wonderful adventure; a "chase" between ligands, torsion angles and magnetic properties that led to the formation of more than 30 [Mn^{III}_6/R-sao] SMMs with ground-states ranging from 4 up to 12 (Table 3) and with U_{eff} values between 23.8 and 85.4 K, resulting into

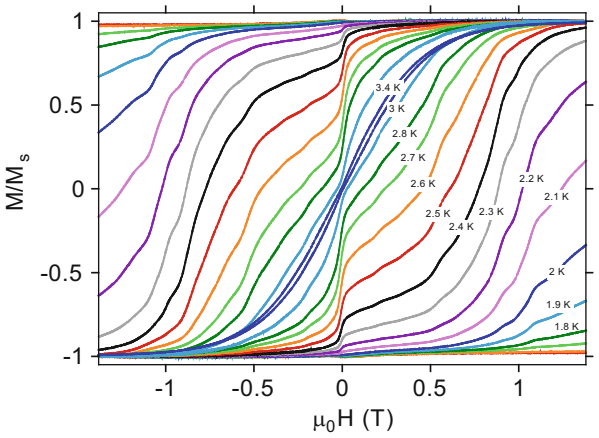

Fig. 10 Magnetisation versus field hysteresis loops for a single crystal of **108** at the indicated temperatures in a field sweep rate of 0.14 Ts^{-1}. M is normalised to its saturation value. Reprinted with the permission from [143]. Copyright 2007 American Chemical Society

two major findings: (1) the establishment of the first magnetostructural correlation for an extended family of hexanuclear [Mn^{III}_6] SMMs [145–148, 150, 152, 153] and (2) the synthesis of complex [Mn_6O_2(Et-sao)$_6$(O_2CPh(Me)$_2$)$_2$(EtOH)$_6$] (**109**) (Fig. 11) which holds the record for the energy barrier of $U_{eff} = 86.4$ K, for any transition metal-based SMM [17].

According to the magnetostructural correlation for the [Mn^{III}_6] family, the authors found out that*:* (1) in all cases the exchange *between* the [Mn_3] triangles appears to be ferromagnetic, (2) the exchange between Mn^{III}_2 pairs is dominated by the Mn-O-N-Mn torsion angles, *a*; the larger the torsion angle, the more ferromagnetic the pairwise interaction; the smaller the Mn-N-O-Mn torsion angle the more antiferromagnetic the pairwise interaction, (3) above a torsion angle of approximately 31° the exchange switches from antiferromagnetic to ferromagnetic, (4) it is the individual torsion angles between neighbouring Mn ions that dictates the behaviour of the complex, and not the average torsion angle, (5) the presence of the carboxylate in either coordinating mode (μ or terminally bonded) appears to have little effect on the sign of J [149], (6) if each Mn_2 exchange is ferromagnetic (i.e. an $S = 12$ complex), the larger the Mn-N-O-Mn torsion angle (α), the larger the barrier to magnetisation relaxation (U_{eff}) [154, 155].

Although cluster **109** possesses the same ground-state and ZFS with **108** ($S = 12$, $D = -0.43$ cm^{-1}), yet its U_{eff} is appreciably larger than that of **108** ($U_{eff} = 86.4$ K for **109** vs. $U_{eff} = 53.1$ K for **108**). Indeed, the U_{eff} value for **109** is very close to the theoretical value given by $U = |D| \cdot S^2 = 88.8$ K, while the corresponding for **108** is ~40 % smaller. The origin of this dramatic deviation between the two values, as confirmed by INS, FDMRS [35, 154, 156] and EPR [146, 157], should be attributed to the different magnitude of the isotropic exchange interaction present in **108** and **109**. More specifically, in **108** the exchange was found to be $J_{(108)} = +0.93$ cm^{-1} [143], while in **109** it was raised to $J_{(109)} = +1.6$ cm^{-1} [17]. The fact that $J_{(108)} < J_{(109)}$ results in the presence of many low-lying excited states closer to the ground-state for **108** than for **109**. In addition, it was shown that sublevels of

Table 3 Members of the $[Mn^{III}_6O_2(O_2CR)_2(R\text{-sao})_6L_x]$ family of SMMs

Formula	$Mn_{3plane} - (\mu_3-)O$ (Å)	α (°)	S	D (cm^{-1})	τ_0 (s)	U_{eff} (K)	References
$[Mn_6O_2(O_2CPh)_2(sao)_6(EtOH)_4]$ (**101**)	0.226	21.84, 11.40, 35.38	4	−1.22	2.3×10^{-8}	27.8	[136]
$[Mn^{III}_6O_2(O_2CMe)_2(sao)_6(EtOH)_4]$ (**102**)	0.212	22.83, 16.49, 10.70	4	−1.21	3.6×10^{-8}	27.9	[136]
$[Mn_6O_2(sao)_6(O_2CH)_2(MeOH)_4]$ (**110**)	0.226	25.57, 10.42, 18.01	4	−1.39	2.0×10^{-8}	28.0	[144]
$[Mn_6O_2(Me\text{-}sao)_6(O_2CCPh_3)_2(EtOH)_4]$ (**111**)	0.078	25.50, 42.44, 29.74	4	n.a.	6.8×10^{-10}	31.7	[145]
$[Mn_6O_2(sao)_6(ketoacetate)_2(EtOH)_2(H_2O)_2]$ (**112**)	0.211	19.06, 18.89, 11.92	4	n.a.	n.a.	n.a.	[146]
$[Mn_6O_2(sao)_6(O_2CPh)_2(MeCN)_2(H_2O)_2]$ (**113**)	0.186	28.18, 16.18, 8.36	4	−1.59	6.57×10^{-8}	23.8	[146]
$[Mn_6O_2(sao)_6(1\text{-Me-cyclohex})_2(MeOH)_4]$ (**114**)[a]	0.184/0.182	9.66, 29.83, 15.60 13.53, 23.80, 37.33	4	−1.18	1.70×10^{-8}	28.8	[146]
$[Mn_6O_2(Me\text{-}sao)_6(O_2C\text{-th})_2(EtOH)_4(H_2O)_2]$ (**115**)	0.025	27.40, 31.10, 36.35	n.a.	n.a.	n.a	n.a.	[145]
$[Mn_6O_2(Et\text{-}sao)_6(O_2CC_{12}H_{17})_2(EtOH)_4(H_2O)_2]$ (**116**)	0.100	27.83, 40.07, 41.46	5 ± 1	n.a.	9.3×10^{-10}	31.2	[145]
$[Mn_6O_2(Et\text{-}sao)_6(O_2CC(CH_3)_3)_2(MeOH)_6]$ (**117**)	0.107	26.93, 34.45, 40.70	5	n.a.	4.52×10^{-11}	59.2	[146]
$[Mn_6O_2(Et\text{-}sao)_6(O_2CC(CH_3)_3)_2(EtOH)_5]$ (**118**)[a]	0.072/0.105	36.92, 23.27, 42.12 32.33, 16.76, 42.24	6	−0.75	3.0×10^{-8}	30.0	[147]
$[Mn_6O_2(Et\text{-}sao)_6(O_2CPh^2OPh)_2(EtOH)_4]$ (**119**)	0.057	47.56, 31.76, 23.75	7 ± 1	−0.39	1.5×10^{-10}	43.2	[145]
$[Mn_6O_2(Et\text{-}sao)_6(O_2CPh^4OPh)_2(EtOH)_4(H_2O)_2]$ (**120**)	0.057	30.36, 38.38, 43.71	9 ± 1	−0.37	1.2×10^{10}	56.9	[145]

$[Mn_6O_2(Me\text{-}sao)_6(O_2CPhBr)_2(MeOH)_6]$ (**121**)	0.080	30.43, 42.94, 31.91	11 ± 1	−0.50	1.7×10^{-10}	50.2	[145]
$[Mn_6O_2(Me\text{-}sao)_6(O_2CC(Me)_3)_2(MeOH)_6]$ (**122**)	0.042	29.64, 38.51, 44.47	11 ± 1	n.a	3.58×10^{-10}	57.6	[146]
$[Mn_6O_2(Et\text{-}sao)_6(O_2CPh)_2(EtOH)_4(H_2O)_2]$ (**108**)	0.090	31.26, 38.20, 39.92	12	−0.43	8.0×10^{-10}	53.1	[143]
$[Mn_6O_2(Et\text{-}sao)_6(O_2CPh(Me)_2)_2(EtOH)_6]$ (**109**)	0.034	39.10, 43.04, 34.86	12	−0.43	2×10^{-10}	86.4	[17]
$[Mn_6O_2(Et\text{-}sao)_6(O_2C_{11}H_{15})_2(EtOH)_6]$ (**123**)	0.053	42.61, 36.73, 34.07	12	−0.43	2.5×10^{-10}	79.9	[148]
$[Mn_6O_2(Et\text{-}sao)_6(O_2CPh(Me))_2(EtOH)_4(H_2O)_2]$ (**124**)	0.081	47.16, 38.19, 30.37	12	−0.44	7.5×10^{-10}	69.9	[148]
$[Mn_6O_2(Et\text{-}sao)_6(O_2C\text{-}Napth)_2(EtOH)_4(H_2O)_2]$ (**125**)	0.103	41.09, 33.28, 40.50	12	−0.34	4.33×10^{-10}	60.1	[146]
$[Mn_6O_2(Et\text{-}sao)_6(O_2C\text{-}Anthra)_2(EtOH)_4(H_2O)_2]$ (**126**)	0.096	42.32, 39.28, 25.60	12	−0.44	3.99×10^{-10}	60.1	[146]
$[Mn_6O_2(Et\text{-}sao)_6(O_2CPh(C{\equiv}CH)_2(EtOH)_4(H_2O)_2]$ (**127**)	0.074	38.85, 38.67, 32.06	12	n.a.	6.23×10^{-11}	66.8	[146]
$[Mn_6O_2(Me\text{-}sao)_6(O_2CPh(C{\equiv}CH))_2(EtOH)_6]$ (**128**)	0.090	43.61, 33.72, 29.53	12	n.a.	4.37×10^{-10}	60.3	[146]
$[Mn_6O_2(Me\text{-}sao)_6(O_2CPh(Cl)_2)_2(MeOH)_6]$ (**129**)	0.081	43.24, 27.61, 30.94	12	−0.39	1.55×10^{-10}	48.5	[146]
$[Mn_6O_2(Et\text{-}sao)_6(Br)_2(EtOH)_6]$ (**130**)	0.014	33.40, 43.89, 33.00	12	−0.36	5.45×10^{-10}	54.1	[149]
$[Mn_6O_2(Me\text{-}sao)_6(I)_2(EtOH)_6]$ (**131**)	0.099	33.01, 31.28, 37.16	12	−0.36	n.a.	n.a.	[149]
$[Mn_6O_2(Ph\text{-}sao)_6(prop)_2\ (MeCN)_2]$ (**132**)	0.32	30.4, 1.6, 49.6	4	−0.70	1.7×10^{-8}	24.6	[150]
$[Mn_6O_2(Ph\text{-}sao)_6(prop)_2(EtOH)_4]$ (**133**)	0.09	48.7, 7.1, 26.0	4	−0.73	3.8×10^{-9}	28.9	[150]
$[Mn_6O_2(Ph\text{-}sao)_6(O_2C\text{-}ada)_2(MeOH)_4]$ (**134**)	0.07	26.59, 4.36, 47.79	4	−0.92	5.6×10^{-8}	25.6	[150]
$[Mn_6O_2(Ph\text{-}sao)_6(piv)_2(EtOH)_4]$ (**135**)	0.10	12.09, 27.87, 49.51	4	−0.92	7.8×10^{-8}	24.8	[150]
$Mn_6O_2(H_2N\text{-}sao)_6(py)_6(EtOH)_2](ClO_4)_2$ (**136**)	0.162	30.8, 39.4, 42.0	12	−0.34	5.3×10^{-9}	40	[151]

[a]These molecules possess no centre of symmetry

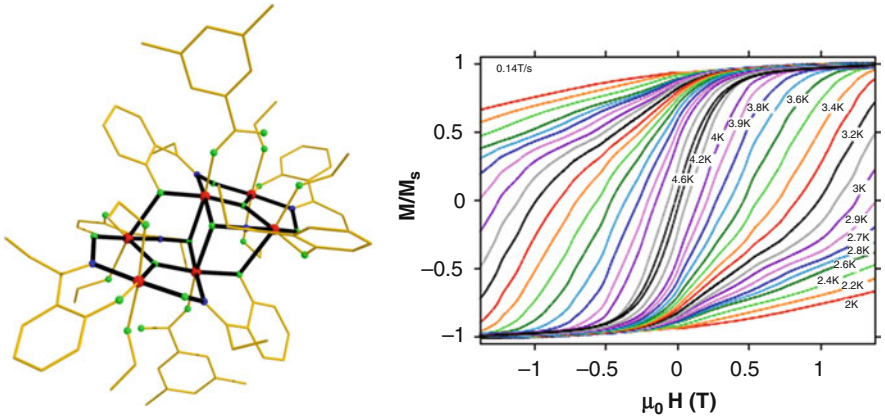

Fig. 11 The molecular structure of **109** (*left*) and magnetisation versus field hysteresis loops for a single crystal of **109** (*right*) at the indicated temperatures in a field sweep rate of 0.14 Ts^{-1}. *M* is normalised to its saturation value. Reprinted with the permission from [17]. Copyright 2007 American Chemical Society

several of the lowest lying excited spin-states are located within the manifold of the anisotropy split ground spin-state (Fig. 12) and that these excited-state sublevels admix, to varying extent in the different [Mn^{III}_6] systems, with the components of the ground spin-state [35, 154, 156, 158], leading to the breakdown of the *Giant Spin* model [154, 159]. As a result, the effective energy barrier for the reversal of the magnetisation crucially depends on the position of the excited multiplets.

Trinuclear Manganese Salicyloximate-Based SMMs

A similar situation with the [Mn^{III}_6] salicyloximate-based clusters, although more complicated, appears to be the case for trinuclear triangular [Mn^{III}_3] salicyloximate-based complexes, [Mn^{III}_3O(R-sao)$_3$(X)(sol)$_{3-4}$] {where R=H, Me, ^{t}Bu; X=$-O_2CR$ (R=H, Me, Ph, etc.); sol=py and/or H_2O} [160]. These molecules describe "half" the structure of their parent [$Mn^{III}_6O_2(O_2CR)_2$(R-sao)$_6L_x$] compounds. In addition, complexes with the general formulae of [Mn^{III}_3O(R-sao)$_3$(sol)$_3(XO_4)$] (where R=H, Et, Ph, naphth; sol=py, MeOH, b-pic, Et-py, ^{t}Bu-py; X=Cl, Re) were also isolated and characterised, in which small "pincer" type tripodal ligands (ClO_4^-, ReO_4^-, etc.) are now located above the triangular [Mn_3O] face. This time the strategy of "puckering" the magnetic core of these clusters has been employed and realised by three different ways: (1) by using R-saoH_2 ligands (as in the case of the [Mn^{III}_6] clusters), (2) by using tripodal ligands on the "upper" triangular face, and (3) by employing large sterically bulky ligands to occupy the "lower" triangular face. Yet, as the authors state "understanding the relationship between the structure and magnetic behaviour in these [Mn_3] triangles, however, is a difficult task since one must consider all contributions to the exchange". Still, it seems that the more

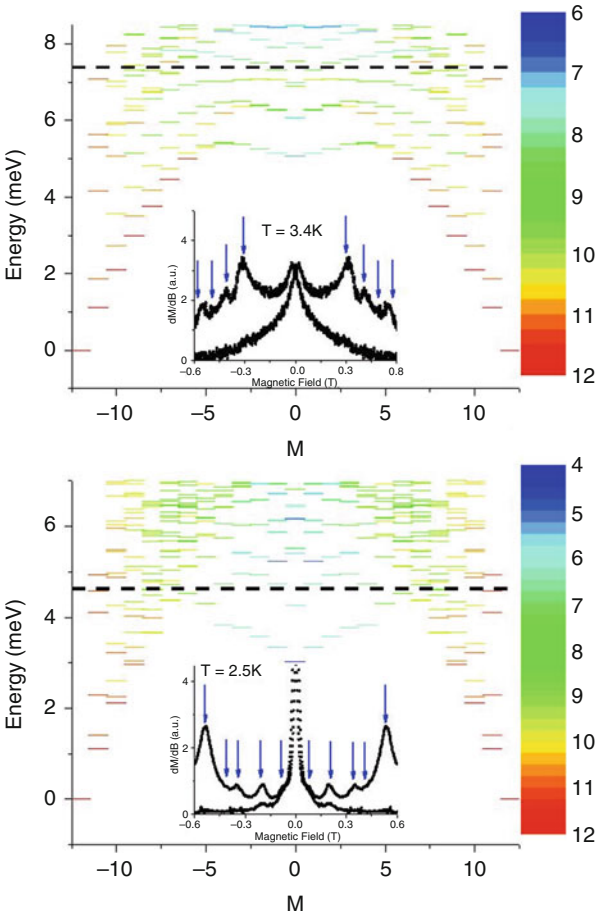

Fig. 12 Energy levels as a function of the z-component of the total spin for (**a**) **109** and (**b**) **108**. The colour maps S_{eff} , where $<S^2>:=S_{\text{eff}}(S_{\text{eff}}+1)$. The black dashed lines correspond to the observed value of U. *Insets*: examples of derivative of the hysteresis curves measured showing the presence of tunnelling peaks absent in a giant-spin model. For each value of field, there are two points corresponding to increasing or decreasing field in the hysteresis cycle. *Arrows* indicate the calculated (anti-)crossing positions. Reprinted with the permission from [154]. Copyright 2008 American Physical Society

puckered triangles display larger and more positive magnetic exchange interactions, J, while on the contrary, the more planar triangles favour more negative exchange constants, as is the case for their parent compounds. In addition, all $[Mn_3]$ clusters with $S=6$ ground-state display SMM behaviour with U_{eff} values between 25.7 and 57.04 K (Table 4).

Trinuclear Manganese Pyridyloximate-Based SMMs

The initial example of a triangular $[Mn^{III}{}_3]$ SMM, cluster **105**, was followed by the isolation and characterisation of two analogous compounds; clusters $[Mn^{III}{}_3O(mpko)_3(O_2CEt)_3](ClO_4)$ (**147**) and $[Mn^{III}{}_3O(mpko)_3(O_2CPh)_3](ClO_4)$ (**148**) both possess an $S=6$ ground-state, while from the fit of the reduced magnetisation data ZFS values of $D=-0.34$ cm^{-1} and $D=-0.35$ cm^{-1} were calculated for **147** and

Table 4 Members of the $[Mn^{III}_3O(R\text{-}sao)_3(X)(sol)_{3-4}]$ family of SMMs

Formula	$Mn_{3plane} - (\mu_3-)O$ (Å)	α (°)	S	D (cm^{-1})	τ_0 (s)	U_{eff} (K)	References
$[Mn_3O(Etsao)_3(O_2CPh(Cl)_2)(H_2O)(MeOH)_3]$(**137**)	0.2648	44.60, 38.17, 39.07	6	−0.59	1.27×10^{-9}	43.69	[160]
$[Mn_3O(Etsao)_3(MeOH)_3](ClO_4)$ (**138**)	0.1792	42.12	6	−0.77	1.98×10^{-9}	57.02	[160]
$[Mn_3O(Etsao)_3(O_2CPh)(C_6H_{16}NO_3)(O_2CPh)(H_2O)_2]$ (**139**)	0.2314	44.60, 35.76, 37.18,	6	−0.92	8.40×10^{-9}	25.73	[160]
$[Mn_3O(Etsao)_3(O_2CPh(CF_3)_2)(EtOH)(H_2O)_3]$.EtOH (**140**)	0.2274	46.66, 38.56, 40.35	6	−0.82	7.40×10^{-9}	42.53	[160]
$[Mn_3O(Etsao)_3(\beta\text{-pic})_3](ClO_4)$ (**141**)	0.2776	44.96	6	−0.52	2.97×10^{-8}	42.74	[160]
$[Mn_3O(Etsao)_3(Et\text{-py})_3](ClO_4)$ (**142**)	0.2754	46.78	6	−0.48	1.46×10^{-8}	47.97	[160]
$[Mn_3O(Etsao)_3(^tBu\text{-py})_3](ClO_4)$ (**143**)[a]	0.2664 0.2916	45.40 40.42	n.a.	n.a.	n.a.	n.a.	[160]
$[Mn_3O(Etsao)_3(EtOH)(H_2O)_2](ReO_4)\cdot 3EtOH$ (**144**)	0.0371	41.65, 40.25, 43.53	6	−0.75	5.55×10^{-9}	48.31	[160]
$[Mn_3O(Phsao)_3(O_2CC_{14}H_{19})(MeOH)_4](PhsaoH_2)$ (**145**)	0.1778	32.98, 34.41, 41.44	6	−0.51	n.a.	n.a.	[160]
$[Mn_3O(Phsao)_3(\beta\text{-pic})_3](ClO_4)$ (**146**)	0.2565	46.22, 39.31, 40.78	6	−0.37	n.a.	n.a.	[160]

[a]Two $[Mn^{III}_3]$ complexes in the asymmetric unit

148, respectively [161]. The ferromagnetic nature of the triangular [Mn^{II}_3] species was further investigated, suggesting that it is due to the structural distortion imposed on the molecules by the "replacement" of the three carboxylates present in the "normal" [$Mn^{III}_3O(O_2CR)_6(py)_3$] starting materials by three oximate ligands. This replacement leads to the structural distortion of the metallic core as dictated by: (1) the displacement of the central oxide out of the metallic plane and (2) the twist in the Mn-N-O-Mn bridging angle, ψ. Concerning the first reason, it is reasonable to assume that the displacement of the central oxide is important since such monoatomic bridges provide strong and primary exchange pathways in metal oxide complexes. For the later, the twist in the oxime will lead to a corresponding twist/tilting of the Mn coordinate axes, and, therefore affect the magnetic behaviour of the cluster. Finally, the magnitude of the exchange interactions, J, do not seem to correlate perfectly with the displacement of the central oxide, while on the contrary it correlates with the Mn-N-O-Mn torsion angle, since the largest torsion angle corresponds to the largest J values.

"Cube"-Like Manganese Oximate-Based SMMs

The use of derivatised salicyloxime ligands in manganese cluster chemistry led also to the isolation of the first ferromagnetic cube-like [Mn^{III}_4] SMM [162, 163]. The reaction between $Mn(OAc)_2{\cdot}4H_2O$ and Me-saoH$_2$ in MeCN led to the formation of cluster [Mn^{III}_4(Me-sao)$_4$(Me-saoH)$_4$] (**149**), which describes a cubane with alternating monoatomic, −O-, and diatomic, −N-O-, edges. The four trivalent manganese centres are ferromagnetically coupled to yield an $S = 8$ ground-state, while from magnetisation measurements the D value was estimated as $D = -0.34$ cm^{-1}. The SMM character of **149** was confirmed by single-crystal hysteresis loop measurements revealing hysteresis loops whose coercivity is temperature and sweep-rate dependent.

A Bi-tetrahedral "Frustrated" [$Mn^{III}_6Mn^{II}$] SMM

The reaction between $Mn(O_2CMe)_2{\cdot}4H_2O$, Et-saoH$_2$ and NMe_4NO_3 in EtOH gave cluster $(NMe_4)[Mn_7O_2(O_2CMe)_5(Et\text{-}sao)_6(EtOH)_{0.75}(H_2O)_{1.25}]{\cdot}0.25H_2O$ (**150**$\cdot 0.25H_2O$) (Fig. 13, left) [164]. Its structure describes two [Mn^{III}_3O]$^{7+}$ triangles linked to a central Mn^{II} ion, forming a [$Mn^{III}_6Mn^{II}(\mu_3\text{-}O^{2-})_2(\mu\text{-}O)_6$]$^{10+}$ core, with the central bridging occurring via three $\eta^2{:}\eta^2{:}\mu_3$-$MeCO_2^-$ ligands. The ground-state of **150** was found to be $S = 11/2$ with $D = -0.39$ cm^{-1}, while the first and second excited states of $S = 9/2$ and $S = 13/2$ are located at only 0.3 and 0.4 cm^{-1} above, respectively. Arrhenius analysis of the *dc* and *ac* magnetic susceptibility data yielded an energy barrier for the reorientation of the magnetisation of $U_{eff} = 32$ K and $\tau_0 = 2 \times 10^{-7}$ s. Finally, single-crystal magnetisation vs. field measurements display temperature and sweep-rate-dependent hysteresis loops, establishing its SMM behaviour (Fig. 13, right).

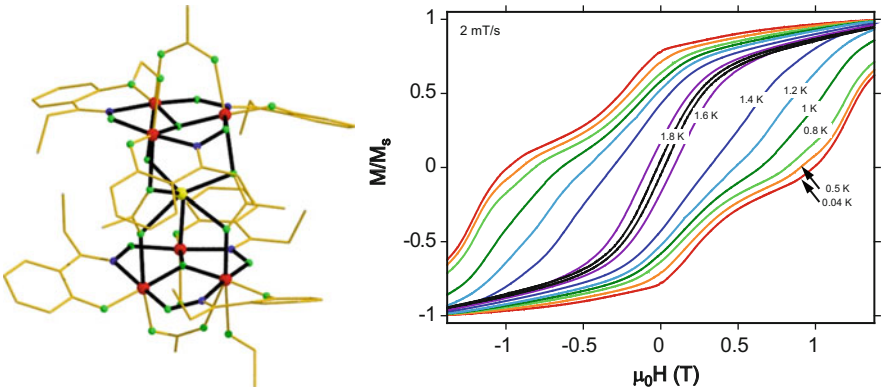

Fig. 13 The molecular structure of **150** (*left*) and magnetisation versus field hysteresis loops for a single crystal of **150** (*right*) at the indicated temperatures in a field sweep rate of 0.002 Ts^{-1}. *M* is normalised to its saturation value. Reprinted with the permission from [164]. Copyright 2007 American Chemical Society

An Octanuclear $[Mn^{III}_6Mn^{II}_2]$ SMM

Cluster $[Mn^{III}_6Mn^{II}_2O_2(napth\text{-}sao)_6(N_3)_6(MeOH)_8]\cdot 10MeOH$ (**151**·10MeOH) can be easily obtained upon the reaction of solution-stable $[Mn^{III}_6O_2(napth\text{-}sao)_6(O_2CPh)_2(EtOH)_6]$ (**152**) with 1 equiv. of both $Mn(ClO_4)_2\cdot 6H_2O$ and NaN_3 in MeOH [165, 166]. The cluster consists of a central $[Mn^{III}_6O_2(napth\text{-}sao)_6]^{2+}$ unit connected to its lower and upper triangular face with two metal "caps" through six *end-on* azide ligands, resulting in an overall $[Mn^{III}_6Mn^{II}_2O_2(napth\text{-}sao)_6(N_3)_6]$ core. The cluster possesses an $S = 7$ ground-state, as a result of: (1) ferromagnetic interaction within the central $[Mn^{III}_6O_2(napth\text{-}sao)_6]^{2+}$ unit due to the large Mn-N-O-Mn torsion angles present, stabilising a local spin of $S_{local} = 12$, and (2) antiferromagnetic interactions transmitted through the *end-on* azide ligands due to the large bridging angles [167]. Ac magnetic susceptibility measurements revealed nicely fully formed out-of-phase peaks in the 3–4 K temperature range, and thus, single-crystal magnetisation experiments were carried out revealing SMM behaviour of $U_{eff} = 40$ K and $\tau_0 = 1.2 \times 10^{-9}$ s.

Pentanuclear $[Mn^{III}_3Mn^{II}_2]$ SMMs

In 2010, clusters $[NEt_4]_3[Mn^{III}_3Mn^{II}_2(sao)_3O(N_3)_6Br_2]$ (**153**), $[NEt_4]_3[Mn^{III}_3Mn^{II}_2(Me\text{-}sao)_3O(N_3)_6Cl_2]$ (**154**) and $[NEt_4]_3[Mn^{III}_3Mn^{II}_2(sao)_3O(OCN)_6Cl_2]$ (**155**) were reported [168]. All three clusters display the same structure consisting of the triangular $[Mn^{III}_3O(R\text{-}sao)_3]^+$ unit which is "cupped" at each side by a divalent Mn ion via three *end-on* azide ligands (or monoatomic cyanate bridges in **155**). The ground-state of the complexes was found $S = 11$, $S = 6$ and $S = 1$, for **153**, **154** and **155**, respectively; the central $[Mn^{III}_3O(R\text{-}sao)_3]^+$ unit possesses an

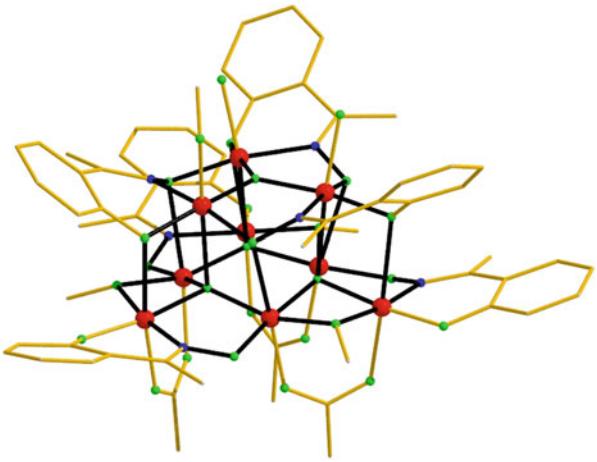

Fig. 14 The molecular structure of $[Mn_9O_4(OMe)_4(OAc)_3(Me\text{-}sao)_6(H_2O)_2]$(**156**). Hydrogen atoms are omitted for clarity

$S_{local} = 6$ ground-state due to the large Mn-N-O-Mn torsion angles present (i.e. all torsion angles above 31°), and as a result the total spin is dictated by the interactions mediated through the *end-on* azides/cyanate ligands. In the case of **153** the bridging angles of the azide ions favour ferromagnetic interactions stabilising the $S = 12$ ground-state, while in **154** there is a balance between FI and AFI (i.e. the bridging angle is 105° for the upper Mn^{II} and 112 for the lower Mn^{II} ion), thus retaining its $S = 6$ ground-state. Finally, for **155** the $S = 1$ ground-state is explained by the presence of AF interactions mediated by the cyanates, stabilising a total $S = 12–2 \times (5/2) = 1$. Both **153** and **154** possess large and negative ZFS values of $D = -0.20\ cm^{-1}$ and $D = -0.59\ cm^{-1}$, respectively, and display SMM behaviour with U_{eff} values of 36.4 and 39.4 K, respectively. Surprisingly enough, cluster **155** with an $S = 1$ ground-state also displays SMM behaviour with $U_{eff} = 33.9$ K, which according to the authors, should be attributed to the role of the low-lying excited states.

A Chiral $[Mn^{III}_9]$ Super-Tetrahedron SMM from Achiral Components

The reaction between $Mn(O_2CMe)_2{\cdot}4H_2O$, Me-saoH$_2$ and $Ln(NO_3)_3{\cdot}6H_2O$ in the presence of NEt_3 in a 1:1 mixture of MeOH and MeCN forms cluster $[Mn_9O_4(OMe)_4(OAc)_3(Me\text{-}sao)_6(H_2O)_2]{\cdot}1.5H_2O$ (**156**·1.5H$_2$O, Fig. 14) [169]. The core of **156** describes a partial Mn(III) super-tetrahedron in which the upper vertex is missing. The $[Mn^{III}_6]$ basal plane of the super-tetrahedron is linked to the upper $[Mn^{III}_3]$ plane via three μ_4-O^{2-} bridges. The molecule crystallises in the cubic space group *I*23, which is one of the 65 space groups containing only symmetry operations of the first kind (rotations and translations) and accommodates chiral molecules. In effect, the enneanuclear cluster exists in two enantiopure

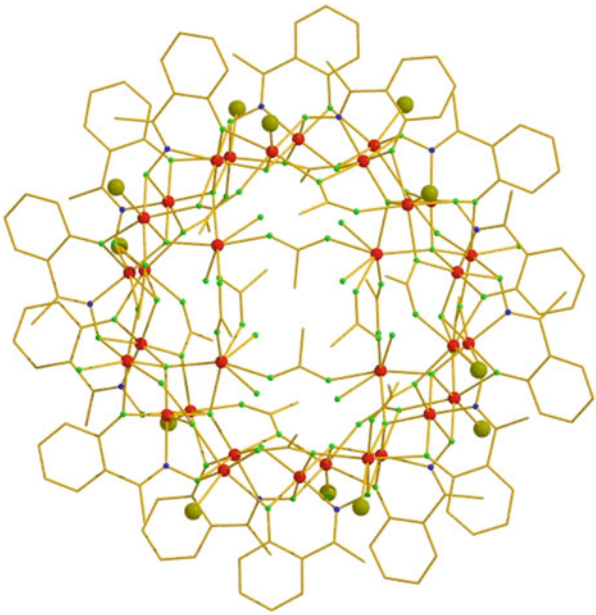

Fig. 15 The molecular structure of the dotriacontanuclear cluster **159**

forms one of which is present in the crystal of **156**. The spin ground-state of the cluster was found to be $S = 6$ with a ZFS of this ground-state of $D = -0.60$ cm^{-1}. The SMM behaviour of **156** was confirmed by temperature and sweep-rate-dependent hysteresis loops in single crystal magnetisation versus field measurements, while an Arrhenius analysis revealed an energy barrier for the re-orientation of the magnetisation of $U_{\text{eff}} = 30$ K. Finally, two very similar clusters, $[Mn_9O_4(OMe)_3(OAc)_4(Napth\text{-}sao)_6(H_2O)_x(MeOH)_y]$ (**157**) [170] and $[Mn_9O_4(OMe)_3(OH)(OAc)_3(Mesao)_6(MeOH)_2]\cdot 2.5DMF$ (**158**·2.5DMF) [171] were recently reported, with U_{eff} values of 67 K and 35.2 K, respectively.

A $[Mn^{II}{}_{18}Mn^{III}{}_{14}]$ Double-Decker Wheel SMM

The largest oxime-based Mn SMM came from the reaction of $MnBr_2\cdot 4H_2O$, NaO_2CMe, Ph-pdH_2 (=2-phenyl-1,2-propanediol) and Me-saoH_2 in MeCN, forming the impressive $[Mn_{32}(\mu_4\text{-}O)_8(\mu_3\text{-}OH)_6(Me\text{-}sao)_{14}(O_2CMe)_{18}Br_8(H_2O)_{10}](OH)_2$ (**159**) cluster [172]. This dotriacontanuclear mixed-valent $[Mn^{II}{}_{18}Mn^{III}{}_{14}]$ cluster describes a double-decker wheel consisting of two linked, parallel $[Mn^{II}{}_7Mn^{III}{}_7]$ crown-shaped wheels that house a $[Mn^{II}{}_4]$ rectangle in their inner cavity (Fig. 15). The molecule possesses an $S = 11$ or 12 ground-state, while fully formed out-of-phase peaks, χ_M'', are observed in the 2–3 K temperature range. In order to confirm the SMM behaviour, single-crystal magnetisation vs. fields experiments were carried out, revealing the presence of temperature and

sweep-rate-dependent loops with $U_{eff} = 44.5$ K, $\tau_0 = 3.5 \times 10^{-12}$ s and a blocking temperature of $T_b = 1.6$ K.

A $[Mn^{III}_{12}(sao)_{12}]$ SMM: Assembling $\{Mn^{III}_3O(sao)_3\}$ Triangles

In 2011 cluster $[Mn^{III}_{12}O_4(sao)_{12}(N_3)_4(MeOH)_4(H_2O)_2]$ (**160**) was synthesised upon the reaction of $Mn(hfac)_2$, $saoH_2$ and NaN_3 in MeOH, in the presence of NEt_3 [173]. Its structure consists of four triangular $\{Mn^{III}_3O(sao)_3\}$ units; two of them form the usual $\{Mn^{III}_6O_2(sao)_6\}^{2+}$ core, while the remaining two units cap the "lower" and "upper" face of the hexametallic unit via four *end-on* azide ligands. The ground-state of the complex was found to be $S = 8$, due to the presence of AFI within the cluster. More specifically, the central $\{Mn^{III}_6\}$ unit can be treated as an $S_{local} = 4$ unit, due to the presence of two Mn-N-O-Mn torsion angles lower than 30.4° (i.e. 13.4°, 16.9° and 33.2°). Each capping $\{Mn^{III}_3\}$ unit can be considered as an $S_{local} = 2$ unit, again due to the small Mn-N-O-Mn torsion angles, while, finally, the total $S = 8$ ground-state is due to the presence of the ferromagnetic interactions between the three sub-units via the *end-on* azide ligands. The molecule displays fully formed out-of-phase, χ_M'', peaks in the 3–4.5 K temperature range, while an Arrhenius analysis yielded an energy barrier for the re-orientation of the spins of $U_{eff} = 51$ K.

2.2.6 The Smallest Mn SMMs

Cluster $[Mn^{III}_2(saltmen)_2(ReO_4)_2]$ (**161**) ($saltmen^{2-}$=*N*,*N*′- (1,1,2,2-tetramethyl ethylene)bis(salicylideneiminate)) was the first dinuclear Mn-based SMM reported [174]. Each Mn^{III} centre is surrounded by an N_2O_2 environment of the $saltmen^{2-}$ ligand in the equatorial plane and two axial oxygen atoms from the perhenate anion and a neighbouring $\{Mn(saltmen)(ReO_4)\}$ moiety. The cluster possesses an $S = 4$ ground-state due to the presence of a ferromagnetic interaction, while the ZFS of this ground-state was found $D = -1.11$ cm^{-1}. Furthermore, single-crystal magnetisation vs. field measurements at temperatures below 1 K exhibit sweep-rate and temperature-dependent hysteresis loops, suggesting SMM behaviour. In addition, other members of this family were also found to function as SMMs, such as $[Mn(saltmen)(O_2CMe)]_2 \cdot 2MeCO_2H$ (**162**) [175], $[Mn(saltmen)(N_3)]_2$ (**163**) [175], [Mn(salen) (NCO)]$_2$ (**164**) [175], [Mn(3,5-Brsalen)(3,5-Brsalicylaldehyde)]$_2$ (**165**) [175], $[Mn(5\text{-}MeOsaltmen)(DCNNQI)]_2 \cdot MeOH$ (**166**) [176] and $[Mn(ins)(N_3)(MeOH)]_2$ (**167**) [177].

2.2.7 Enneanuclear Tripodal SMMs

The use of tripodal alcohol ligands, such as H_3thme (=1,1,1tris(hydroxymethyl) ethane), H_3tmp (=1,1,1tris(hydroxymethyl)propane), H_3cht (=1,3,5-cyclohaxanetriol)

and/or "tetrapodal" ligands, such as H_4peol (=pentaerythritol), in manganese cluster chemistry has led to the isolation of enneanuclear mixed-valent $[Mn^{IV}_3Mn^{III}_4Mn^{II}_2]$ clusters. The first example reported was cluster $[Mn^{IV}_3Mn^{III}_4Mn^{II}_2O_7(O_2CMe)_{11}(thme)(py)_3(H_2O)_2]$ (**168**) made from the reaction of the mixed-valent $[Mn_3O(O_2CMe)_6(py)_3]$ "starting material" with H_3thme in MeCN [178]. The structure of **168** describes a core of six Mn^{III} and two Mn^{II} centres surrounding a central $[Mn^{IV}_3]$ unit. The cluster has an $S = 17/2$ ground-state, as a result of antiferromagnetic exchange interactions between the Mn^{IV} and the $Mn^{III/II}$ centres, while the ZFS of this ground-state is $D = -0.29$ cm^{-1}. Single-crystal magnetisation vs. field measurements reveal nicely shaped temperature- and sweep-rate-dependent hysteresis loops in which QTM steps are clearly observed, while the U_{eff} was found to be 27 K [179]. Following this report, few other analogues were reported; for example, clusters $[Mn_9O_7(O_2CMe)_{11}(tmp)(py)_3(H_2O)_2]$ (**169**) [180], $[Mn_9O_7(O_2CMe)_{11}(Hpeol)(py)_3(H_2O)_2]$ (**170**) [180], $[Mn_9O_7(O_2CCMe_3)_{11}(Hpeol)(py)_3(H_2O)_2]$ (**171**) [180], $[Mn_9O_7(O_2CPh)_{11}(Hpeol)(py)_3(H_2O)_2]$ (**172**) [180] and $[Mn_9O_7(O_2CPh)_{11}(thmn)(py)_2(H_2O)_3]$ (**173**, H_3thmn = 1,1,1-tris(hydroxymethyl)nitromethane) [181] all display similar magnetic properties with complex **168**.

2.2.8 Disc-Like [Mn_7] SMMs

This small but growing family of SMMs started in 1998 with the characterisation of complex $[Mn^{II}_4Mn^{III}_3(teaH)_3(tea)_3](ClO_4)_2{\cdot}3MeOH$ (**174**·3MeOH) [182]. Its structure consists of a disc in which the central Mn^{III} ion is surrounded by three pairs of Mn^{II}-Mn^{III} centres. The ground-state of the cluster was found $S = 11$ due to the presence of both ferro- and antiferromagnetic interactions, while the zero-field splitting of the ground-state was found $D = -0.08$ cm^{-1}. Furthermore, the cluster displays fully formed out-of-phase, χ_M'', peaks under an *ac* field in the 1–2 K temperature range, while an Arrhenius analysis yielded $U_{eff} = 19.5$ K and $\tau_0 \approx 10^{-8}$ s. In 2005, a cluster with the same metal centred hexagonal structure with **174**, but with a reversed oxidation states' distribution, was reported; complex $[Mn^{II}_3Mn^{III}_4(5\text{-}NO_2\text{-}hbide)_6]{\cdot}5C_2H_4Cl_2$ (**175**·$5C_2H_4Cl_2$, H_3(5-NO_2-hbide) = *N*-(2-hydroxy-5-nitrobenzyl)iminodiethanol) was made from the reaction of Mn$(OAc)_2{\cdot}4H_2O$ with H_3(5-NO_2-hbide) in MeOH, followed by recrystallisation from 1,2-dichloroethane [183, 184]. Complex **175** has an $S = 19/2$ ground-state, while from magnetisation measurements the ZFS of this ground-state was found $D = -0.20$ cm^{-1}. Single-crystal magnetisation experiments showed temperature-dependent loops, verifying its SMM behaviour, with $U_{eff} = 18.1$ K and $\tau_0 = 1.63 \times 10^{-7}$ s. Another example of a heptanuclear [Mn_7] metallic disk SMM is cluster $\{Mn^{II}[Mn^{II}_2Mn^{III}_4Cl_6(L_3)_6]\}{\cdot}2CHCl_3$ (**176**·$2CHCl_3$, H_2L_3 = N-*n*-butyl diethanol amine) reported in 2007, with an $S = 27/2$ ground-state, $D = -0.005$ cm^{-1}, $U_{eff} \approx 10$ K and a blocking temperature of $T_b \approx 0.6$ K [185]. The latest example of a disc-like [Mn_7] SMM was reported in 2012 [186]; cluster $[Mn_7(heamp)_6](ClO_4)_2{\cdot}4CH_2Cl_2{\cdot}H_2O$ (**177**·$4CH_2Cl_2{\cdot}H_2O$, H_3heamp = 2-[*N*,*N*-di(2-hydroxyethyl)aminomethyl]phenol) contains a central divalent Mn

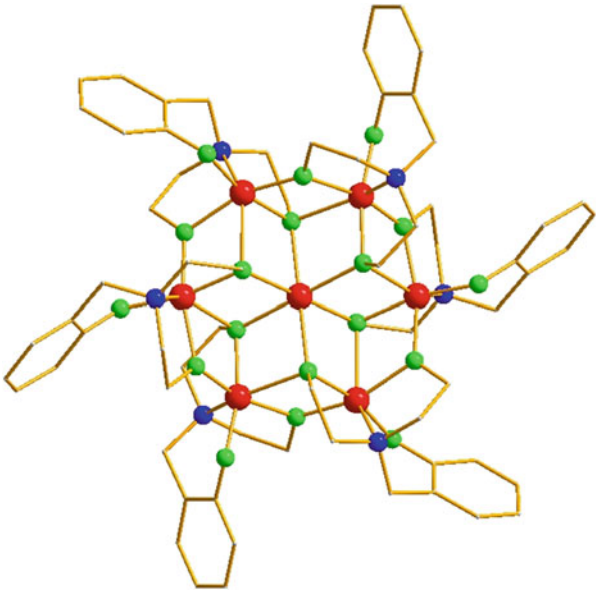

Fig. 16 The structure of the cationic part of **177**

centre encircled by six trivalent Mn ions that form a hexagonal disk (Fig. 16). This cluster has a half-integer, $S = 19/2 \pm 1$ ground-state, with an appreciable uniaxial zero-field splitting of $D = -0.16$ cm^{-1}, while from the Arrhenius analysis of the relaxation data the energy barrier of $U_{\text{eff}} \approx 13$ K was derived.

2.2.9 Octanuclear Manganese SMMs

This category contains only two members so far, excluding cluster **151**; cluster $[Mn^{III}_8O_2(OH)_2(OMe)_{12}(OAc)_2(Mesalim)_4]$ (**178**, MesalimH=methyl salicylimidate) [187] and complex $[Mn^{III}_4Mn^{II}_4O_4(Hpmide)_4(O_2CEt)_6]\cdot(ClO_4)_2$ (**179**, H_2pmide=*N*-(2-pyridylmethyl)-iminodiethanol) [188] The structure of **178** consists of six $[Mn^{III}_3O_4]$ defective cubane units, with the two central units sharing one face. Furthermore, each of the central partial cubanes shares a face with two of the four remaining units. The cluster possesses an intermediate $S = 8$ ground-state as a result of both ferromagnetic and antiferromagnetic interactions within the cluster, while the appearance of out-of-phase, χ_M'', peaks under an oscillating *ac* field reveals its SMM behaviour, with $U_{\text{eff}} = 36.0$ K and $\tau_0 = 4.39 \times 10^{-9}$ s. Likewise, complex **179** describes three face-sharing metal-oxo cubes with manganese ions located on alternate corners and oxygen atoms on the others (Fig. 17). The molecule possesses an $S = 4$ or $S = 5$ spin ground-state and displays out-of-phase peaks in the χ'' vs. log(v) diagram. Arrhenius analysis of the data revealed an $U_{\text{eff}} = 10.4$ K and a pre-exponential factor of $\tau_0 = 3.7 \times 10^{-7}$ s.

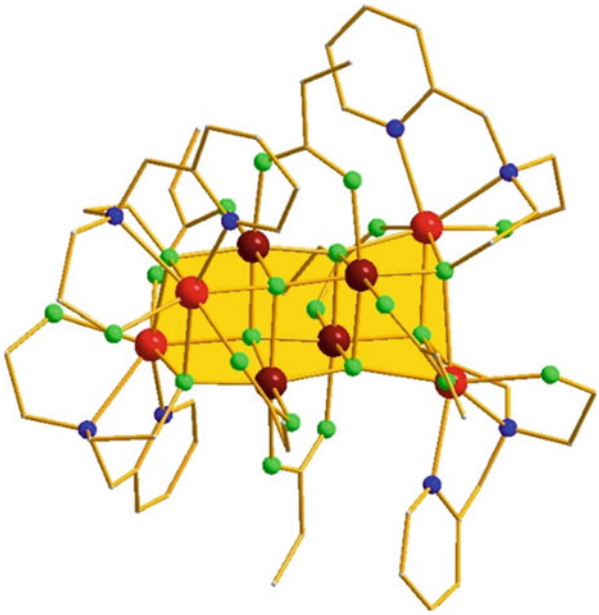

Fig. 17 The structure of the cationic part of **179**, highlighting its three face-sharing cubanes core. Colour code: Mn^{II} = *red*, Mn^{III} = *brown*, O = *green*, N = *blue*, C = *gold*

2.2.10 Decanuclear Manganese SMMs

Surprisingly enough, despite the large number of decanuclear [Mn_{10}] manganese clusters reported so far (more than 30) in various oxidation states only a handful of these clusters display SMM behaviour. The first example was cluster $[Et_3NH]_2[Mn^{II}(CH_3CN)_4(H_2O)_2][Mn^{III}{}_4Mn^{II}{}_6O_4(biphen)_4Br_{12}]\cdot 6CH_3CN\cdot 2.5H_2O\cdot C_6H_6$ (**180**·$6CH_3CN\cdot 2.5H_2O\cdot C_6H_6$, biphen$H_2$ = 2,2′-biphenoxide) reported in 1999 [189, 190]. The structure of the anion of **180** consists of an adamantane-like {Mn_6O_4} inner core to which four outer Mn^{II} ions are attached via the four oxo-bridges. The cluster has an $S = 12$ ground-state, while from EPR experiments the ZFS value of this ground-state was found $D = -0.037$ cm^{-1}. Furthermore, it displays fully formed out-of-phase peaks under an oscillating *ac* magnetic field in the 0.4–0.7 K temperature range, while the Arrhenius analysis yielded $U_{eff} = 7.0$ K and a pre-exponential factor of $\tau_0 = 1.7 \times 10^{-9}$ s. Indeed, this is the best characterised [Mn_{10}] SMM, since the following clusters $[Mn^{III}{}_6Mn^{II}{}_4O_3(O_2CCH_3)_6(tea)(teaH)_3(teaH_2)_3][NO_3]_2\cdot 3H_2O$ (**181**·$3H_2O$, H_3tea=triethanolamine [191], $[Mn^{II}{}_6Mn^{III}{}_4(teaH)_4(teaH_2)_2(tpaa)_6F_8]\cdot 2Et_2O\cdot 4MeCN$ (**182**·$2Et_2O$·4MeCN, tpaa=triphenylacetic acid) [192], $[Mn^{II}{}_6Mn^{III}{}_4(teaH)_4(teaH_2)_2(2\text{-bpca})_6F_8]\cdot 4MeCN$ (**183**·4MeCN, 2-bpca = 2-biphenylcarboxylic acid) [192], $[Mn^{II}{}_6Mn^{III}{}_4O_4(TBOC[3])_4Cl_4(DMF)_3]\cdot 3.3H_2O\cdot 1.5DMF$ (**184**·$3.3H_2O$·1.5DMF, TBOC[3]=*p*-^{t}Bu-Homooxacalix[3]arene) [193] and $[Mn^{II}{}_4Mn^{III}{}_9O_4(OH)_2(O_3PC_{10}H_7)_{10}(PhCO_2)_5(py)_8(H_2O)_6]$ (**185**, $C_{10}H_7PO_3H_2$ = 1-Naphthyl phosphonic acid) [194] all display *ac* magnetic susceptibility out-of-phase signals "going-up" and not fully formed out-of-phase peaks, and thus no further characterisation of their potential SMM behaviour was achieved.

2.2.11 Undecanuclear Manganese SMMs

This confined family of manganese clusters contains only four members of which only one behaves as an SMM; cluster $[Mn^{III}_7Mn^{II}_4O_2(OH)_2(nmpd)(pdmH)_5(pdm)_5Cl_6]\cdot 4MeCN$ (**186**, $nmpdH_2 = 2$-nitro-2-methyl-1,3-propanediol; $pdmH_2$=pyridine-2,6-dimethanol) was made upon the reaction of $MnCl_2$ with $pdmH_2$ and $nmpdH_2$ in a mixture of MeCN/MeOH in the presence of base [195]. The structure of the cluster consists of a central $[Mn_7(\mu_4\text{-}O)_2]$ core on which two dinuclear $\{Mn^{III}–Mn^{II}\}$ units are linked to each end through 13 alkoxide groups. *Dc* magnetic susceptibility measurements agree with an $S = 10$ spin ground-state, while from *ac* magnetic susceptibility studies no out-of-phase peaks (or even signals "going-up") were observed in the 1.8–10 K temperature range. Yet, **186** displays single-crystal magnetisation hysteresis loops below 0.7 K, whose coercivities increase with decreasing temperature, thus proving its SMM behaviour.

2.2.12 Dodecanuclear Manganese SMMs

Besides the well-known Mn_{12}OAc-like SMMs (Table 2), other dodecanuclear manganese clusters have been found to display SMM behaviour as well. For instance: (1) the wheel-shaped clusters $[Mn^{III}_6Mn^{II}_6(mdea)(O_2CMe)_{14}]$ (**187**, H_2mdea=*n*-methyldiethanol amine), $[Mn^{III}_6Mn^{II}_6(edea)(O_2CMe)_{14}]$ (**188**, H_2edea=*n*-ethyldiethanol amine) and $[Mn^{III}_6Mn^{II}_6(bdea)(O_2CMe)_{14}]$ (**189**, bdea=*n*-butyldiethanol amine) [196], (2) complex $[Mn^{IV}_4Mn^{III}_8O_{10}(OMe)_3(OH)(O_2CC_6H_3F_2)_{16}(MeOH)_2]\cdot 8MeOH$ (**190**·8MeOH) [197], (3) clusters $[Mn^{III}_4Mn^{II}_8O_2(OMe)_2(Hpeol)_4(O_2CPh_2)_{10}(H_2O)_2]\cdot 6MeCN$ (**191**·6MeCN, H_4peol= entaerythritol), $[Mn^{III}_4Mn^{II}_8O_2(OH)_2(Hpeol)_4(O_2CPh_2)_{10}(H_2O)_2]\cdot 12MeCN$ (**192**·12MeCN) and $Na[Mn^{III}_4Mn^{II}_8O_2(OH)(OMe)(Hpeol)_4(O_2CMe)_{11}(H_2O)_3]\cdot 4MeCN\cdot H_2O$ (**193**·4MeCN·H_2O) [198], (4) the "valence-sandwich" complex $[Mn^{II}_4Mn^{III}_4Mn^{II}_4O_2(OMe)_2(thme)_4(O_2CMe)_{10}(H_2O)_4]\cdot 2MeOH$ (**194**·2MeOH) [199], (5) cluster $[Mn_{12}O_4(OH)(N_3)_9(edte)_4](ClO_4)(N_3)\cdot 2H_2O$ (**195**·$2H_2O$, H_4edte=*N*,*N*,*N*′,*N*′′-tetrakis(2-hydroxyethyl)-ethylenediamine) [200] and (6) complexes $[Mn^{III}_6Mn^{II}_6(Adea)_8(CH_3COO)_{14}]\cdot 7CH_3CN$ (**196**·$7CH_3CN$, H_2Adea=*N*-allyl diethanolamine), $[Mn^{III}_6Mn^{II}_6(Edea)_8(CH_3CH_2COO)_{14}]$ (**197**), and $[Mn^{III}_6Mn^{II}_6(Edea)_8(CH_3COO)_2(CH_3CH_2COO)_{12}]$ (**198**) [201], are representative examples of non-Mn_{12}OAc-like SMMs, *albeit* with inferior magnetic properties to those of the prototype SMMs.

2.2.13 Large $[Mn_x]$ ($x > 12$) SMMs

Among the larger manganese clusters, few of them are found to display SMM behaviour (Table 5). A representative example is complex $[Mn^{IV}_6Mn^{III}_{10}O_{16}(OMe)_6(O_2CMe)_{16}(MeOH)_3(H_2O)_3]\cdot 6H_2O$ (**199**·$6H_2O$, Fig. 18), reported in 2007 upon the reaction of $^nBu_4NMnO_4$ with $Mn(NO_3)_2\cdot 4H_2O$ in a mixture of methanol and acetic

Table 5 "Large" $[Mn_x]$ $(x > 12)$ SMMs

Formula	S	D (cm^{-1})	τ_0 (s)	U_{eff} (K)	References
$[Mn_{84}O_{72}(OAc)_{78}(OMe)_{24}(OH)_6(MeOH)_{12}(H_2O)_{42}]$ (**38**)	6	–	5.7×10^{-9}	18	[93]
$[Mn_{32}(\mu_4\text{-}O)_8(\mu_3\text{-}OH)_6(Me\text{-}sao)_{14}(O_2CMe)_{18}Br_8(H_2O)_{10}](OH)_2$ (**159**)	11–12	–	3.5×10^{-12}	44.5	[172]
$[Mn_{20}O_{12}(OH)_2(O_3PCH_2Ph)_{12}(O_2CCMe_3)_{10}(py)_2]^{2-}$ (**200**)	19 ± 1	–	2×10^{-11}	43	[202]
$[Mn_{20}O_{10}(PhCH_2PO_3)_{14}(PhCO_2)_{12}(PhCO_2H)_{0.5}(CH_3CN)_2]$ (**201**)	14 ± 1	–	2×10^{-10}	17	[202]
$[Mn_{16}O_{16}(OMe)_6\ (O_2CMe)_{16}(MeOH)_3(H_2O)_3]$ (**199**)	–	–	3.00×10^{-9}	79.1	[203]
$[Mn_{14}O_2(OMe)_{12}(O_2CMe)_{10}(tmp)_8]$ (**202**)	14 ± 1	−0.04	9×10^{-11}	18.6	[204]
$[Mn_{15}O_{17}(O_2CCh)_{12}(OMe)_5(MeOH)_3(H_2O)_6]$ (**203**)	2	−1.58	5.25×10^{-7}	9	[205]
$[Mn_{18}O_{14}(O_2CMe)_{18}(hep)_4(Hhep)_2(H_2O)_2](ClO_4)_2$ (**204**)	13	−0.18	–	21.2	[206]
$[Mn_{20}O_6(OMe)_{14}(O_2CMe)_{16}(tmp)_8(HIm)_2]$ (**205**)	9 ± 1	−0.129	3×10^{-11}	18.6	[204]
$[Mn_{20}O_6(OMe)_{14}(O_2CMe)_{16}(Br\text{-}mp)_8(HIm)_2]$ (**206**)	9 ± 1	−0.165	2×10^{-11}	20	[204]
$[Mn_{21}O_{14}(OH)_2(O_2CMe)_{16}(hmp)_8(pic)_2(py)(H_2O)](ClO_4)$ (**207**)	17/2	−0.086	4.2×10^{-8}	13.2	[207]
$[Mn_{22}O_6(OMe)_{14}(O_2CMe)_{16}(tmp)_8(HIm)_2]$ (**208**)	10	−0.1	3×10^{-11}	18.6	[208]
$[Mn_{22}O_{12}(O_2CEt)_{22}(O_3PPh)_8(H_2O)_8]$ (**209**)	7	−0.16	9×10^{-7}	8.6	[209]
$[Mn_{25}O_{18}(OH)(OMe)(hmp)_6(pdm)_6(pdmH)_6](N_3)_2(ClO_4)_6$ (**210**)	$61/2 \pm 1$	−0.012	5×10^{-11}	9.2	[210]
$[Mn_{25}O_{18}(OH)_2(N_3)_{12}(pdm)_6(pdmH)_6](Cl)_2$ (**211**)	$51/2 \pm 1$	−0.022	–	11.5	[211]
$[Mn_{30}O_{24}(OH)_8(O_2CCH_2CMe_3)_{32}(H_2O)_2(MeNO_2)_4]$ (**212**)	5	−0.73	1.5×10^{-8}	14.3	[212]
$[Mn_{26}(pdol)_{12}(OMe)_{15}O_{16}(OH)_2(H_2O)]\cdot ClO_4$ (**213**)	–	–	5.3×10^{-14}	36.1	[213]
$[Mn_{26}(pdol)_{12}(OMe)_{12}O_{16}(N_3)_6]$ (**214**)	–	–	4.5×10^{-10}	16.5	[214]
$[Mn_{26}O_{17}(OH)_8(OMe)_4F_{10}(bta)_{22}(MeOH)_{14}(H_2O)_2]$ (**215**)	4	−0.9	3×10^{-9}	14.3	[215]
$[Mn_{18}O_{11}(OH)(OMe)(N_3)_{12}(tea)_3(teaH)_3(MeOH)]$ (**216**)	21/2	−0.073	10^{-7}	8.8	[216]
$[Mn_{17}NaO_{10}(OH)_2(N_3)_3(O_2CCMe_3)_{13}(tea)_3(teaH)(DMF)]$ (**217**)	17/2	−0.218	10^{-11}	19	[216]
$[Mn_{32}(OH)_{24}O_{14}(OMe)_6(O_2CC(CH_3)_3)_{24}(H_2O)_{2.6}]$ (**218**)	5	–	–	–	[217]
$[Mn_{16}O_8(OH)_2(O_2CPh)_{12}(hmp)_{10}(H_2O)_2](O_2CPh)_2$ (**219**)	8	−0.11	4×10^{-9}	8.1	[218]
$[Mn_{17}O_8(N_3)_4(O_2CMe)_2(pd)_{10}(py)_{10}(MeCN)_2(H_2O)_2](ClO_4)_3$ (**220**)	37	−0.009	1×10^{-13}	13	[219]
$[Mn_{16}O_8(O_2CPh)_{14}(mpko)_4(dpkd)_4]$ (**221**)	5	–	2.7×10^{-7}	12	[220]
$[Mn_{15}KO_4(O_2CEt)_{11}(pd)_{12}(py)_2]$ (**222**)	23/2	−0.071	–	–	[221]
$[Mn_{17}O_8Cl_4(O_2CMe)_2(DPD)_{10}Cl_{2.34}(O_2CMe)_{0.66}(py)_3(MeCN)_2]$ (**223**)	28 ± 1	–	2.0×10^{-10}	13.1	[222]
$[Mn_{24}O_{10}(N_3)_8(O_2CCMe_3)_{16}(dpkd)_{12}(DMF)_4]$ (**224**)	7	–	–	–	[223]

$[Mn_{26}O_8(OH)_4(N_3)_{12}(O_2CMe)_6(dpkd)_{14}(DMF)_4]$ (**225**)	8	–	3.4×10^{-11}	46	[223]
$[Mn_{26}O_{16}(OMe)_{12}(dpkd)_{12}(MeOH)_6](OH)_6$ (**226**)	6	–	3.0×10^{-12}	30	[224]
$[Mn_{16}(CH_3COO)_8(CH_3CH_2CH_2COO)_8(teaH)_{12}]$ (**227**)	12	−0.13	–	–	[225]
$[Mn_{16}((CH_3)_2CHCOO)_{16}(teaH)_{12}]$ (**228**)	11	−0.84	–	–	[225]
$[SrMn_{14}O_{11}(OMe)_3(O_2CPh)_{18}(MeCN)_2]$ (**229**)	9/2	−0.6	–	–	[226]

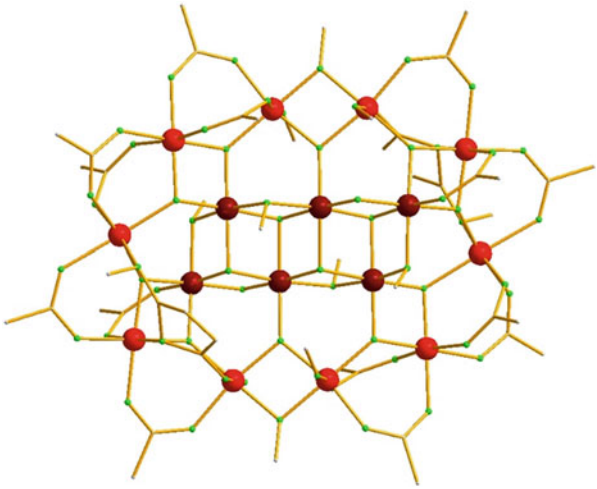

Fig. 18 The structure of the cationic part of **199**

acid [203]. Its structure contains a central $\{Mn^{IV}{}_6O_6(OMe)_4\}^{8+}$ unit encapsulated within a $\{Mn^{III}{}_{10}(\mu_3\text{-}O)_{10}\}^{10+}$ ring. Surprisingly, despite its overall antiferromagnetic interactions and its small *S* ground-state, this complex was reported to display *ac* fully formed out-of-phase, χ_M", peaks in the 5–8 K temperature range, while an Arrhenius analysis yielded an energy barrier of $U_{eff} = 79.1$ K with $\tau_0 = 3.00 \times 10^{-9}$ s.

Another impressive "large" SMM is the benzylphosphonate containing cage $[Et_3NH]_2$ $[Mn^{III}{}_{18}Mn^{II}{}_2O_{12}(OH)_2(O_3PCH_2Ph)_{12}(O_2CCMe_3)_{10}(py)_2]$ (**200**) [202]. The cage possesses an $S = 19 \pm 1$ ground-state, displaying fully formed *ac* out-of-phase peaks in the 2–4 K temperature range. Furthermore, single-crystal magnetisation vs. field measurements revealed temperature-dependent hysteresis loops, while an Arrhenius analysis yielded $U_{eff} = 43$ K with $\tau_0 = 2 \times 10^{-11}$ s.

2.3 *Iron SMMs*

This category was for many years the second largest family of SMMs after the family of manganese-based SMMs [227]. This is not surprising given the existence of iron in the oxidation states of 3+ ($3d^5$) and 2+ ($3d^6$), with five and four unpaired electrons in the high spin state, leading to ground-states of $S = 5/2$ and $S = 2$, for Fe(III) and Fe(II). Therefore, iron atoms can potentially lead to a large ground spin-state within a complex, which is a prerequisite for SMM behaviour, *albeit* this is not commonly the case since the nature of the magnetic exchange interaction between two neighbouring Fe atoms is rarely ferromagnetic. The pursuit of Fe-based SMMs was also due to the ferritin protein, which is responsible for storing iron in some organisms and can be considered as a magnetic nanoparticle [228]. In Table 6, the most representative examples of Fe SMM are presented, along with their magnetic properties.

Table 6 Representative examples of Fe-based SMMs

Formula	S	D (cm^{-1})	U_{eff} (K)	τ_0 (s)	References
$[Fe^{III}_8O_2(OH)_{12}(tacn)_6]^{8+}$ (**230**)	10	−0.27	22.1	1.9×10^{-7}	[229–232]
$[Fe^{III}_4(OMe)_6(dpm)_6]$ (**232**)	5	−0.2	3.5	1.1×10^{-6}	[233]
$[Fe^{III}_4(L_1)_2(dpm)_6]$ (**233**)	5	−0.445	15.6	3.4×10^{-8}	[234]
$[Fe^{III}_4(L_2)_2(dpm)_6]$ (**234**)	5	−0.432	16.6	1×10^{-8}	[30]
$[Fe^{III}_4(L_3)_2(dpm)_6]$ (**235**)	5	−0.421	15.6	1.9×10^{-8}	[30]
$[Fe^{III}_4(OEt)_3(L_4)(dpm)6]$ (**236**)	5	−0.430, −0.27, −0.22	5.95, 9.6	4.6×10^{-7}	[30]
$[Fe^{III}_4(L_5)_2(dpm)_6]$ (**237**)	5	−0.450	15.9	3.4×10^{-8}	[235]
$[Fe^{III}_4(L_6)_2(dpm)_6]$ (**238**)	5	−0.437	15.1	4.3×10^{-8}	[235]
$[Fe^{III}_4(L_7)_2(dpm)_6]$ (**239**)	5	−0.433(2)	15.7	3.5×10^{-8}	[236]
$Fe^{III}_4(esterC5)_2(dpm)_6]$ (**240**)	5	−0.421	11	6.8×10^{-8}	[237]
$[Fe^{III}_4(amideC5)_2(dpm)_6]$ (**241**)	5	−0.414	11	1.2×10^{-7}	[237]
$[Fe^{III}_4(azo)_2(dpm)_6]$ (**242**)	5	−0.406	14.98	7.6×10^{-7}	[238]
$[Fe^{III}_4(azoMe_2)_2(dpm)_6]$ (**243**)	5	−0.42	13.5	7.6×10^{-7}	[238]
$[Fe^{III}_4(thme)_2(C_3H_7OH)_6Cl_6]$ (**244**)	5	−0.32	8.5	3.7×10^{-8}	[239]
$[Fe^{II}_4(sae)_4(MeOH)_4]$ (**245**)	8	−0.64	28.4	2.06×10^{-9}	[240]
$[Fe^{II}_4(5\text{-}Br\text{-}sae)_4(MeOH)_4]$ (**249**)	8	−0.66	21.1	1.89×10^{-9}	[241]
$[Fe_4(3,5\text{-}Cl_2\text{-}sae)_4(MeOH)_4]$ (**250**)	8	−0.67	18.2	7.68×10^{-9}	[241]
$[Fe^{III}_{19}(metheidi)_{10}(OH)_{14}(O)_6(H_2O)_{12}]NO_3$ (**251**)	33/2	−0.035	–	–	[242]
$[Fe^{II}_9(N_3)_2(O_2CMe)_8\{(2\text{-}py)_2CO_2\}_4]$ (**252**)	14	–	41	3.4×10^{-12}	[243]
$[Fe^{II}_9(NCO)_2(O_2CMe)_8\{(2\text{-}py)_2CO_2\}_4]$ (**258**)	14	–	44	2.0×10^{-11}	[244]
$[Fe^{III}_9O_4(OH)_5(heia)_6(Hheia)_2]$ (**259**)	25/2	−0.07	7.6	6×10^{-10}	[245]
$[Fe^{III}_{10}Na_2O_6(OH)_4(O_2CPh)_{10}(chp)_6(H_2O)_2(Me_2CO)_2]$ (**260**)	11	–	5.3	–	[246]
$[NEt_4][Fe^{III}_{11}O_4(O_2CPh)_{10}(thme)_4(dmhp)_2Cl_4]$ (**261**)	11/2	−0.46	–	–	[247]
$[Fe^{II}_2(NCO)_3(acpypentO)]$ (**262**)	4	–	–	–	[248]
$(pyrH)_5[Fe_{13}F_{24}(OCH_3)_{12}O_4]$ (**263**)	–	–	13.1	7.5×10^{-13}	[249]
$[Fe^{III}_9O_4(OH)_4(O_2CPh)_{13}(heenH)_2]$ (**264**)	7/2	−0.85(1)	–	–	[250]
$\{Fe^{III}[Fe^{III}(L_1)_2]_3\}$ (**265**)	5	−0.57	14.25	–	[251]

(continued)

Table 6 (continued)

Formula	S	D (cm^{-1})	U_{eff} (K)	τ_0 (s)	References
$Na_{14}(NMe_4)_5[(Fe^{III}_4W_9O_{34}(H_2O))_2(Fe^{III}W_6O_{26})]$ (**266**)	15/2	$\|D\| = 0.24$	–	–	[252]
$Na_6(NMe_4)_4[Fe^{III}_4(H_2O)_2(Fe^{III}W_9O_{34})_2]$ (**267**)	5	$\|D\| = 0.49$	16.63	2.0×10^{-6}	[252]
$[Fe^{III}_{11}O_7(dea)_3(piv)_{12}]Cl$ (**268**)	13/2	−0.25	–	–	[253]

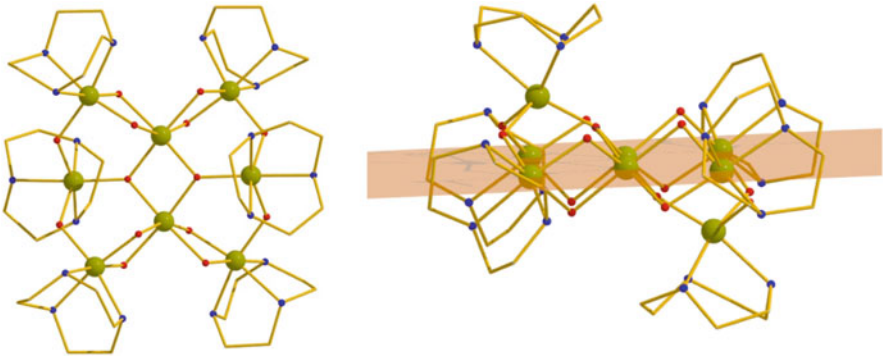

Fig. 19 The molecular structure of the cation of **230** (*left*); the planar arrangement of the central [Fe_6] unit (*right*).

2.3.1 $[Fe^{III}_8O_2(OH)_{12}(tacn)_6]Br_8 \cdot 9H_2O$: The First Fe-Based SMM

Complex $[Fe_8O_2(OH)_{12}(tacn)_6]^{8+}$ (**230**) (tacn = 1,4,7-triazacyclononane) was isolated as the bromide salt by Wieghardt in 1984, upon the hydrolysis of the corresponding monomeric unit [Fe(tacn)Cl_3] (**231**) at 20°C (pH 9) in the presence of bromide ions [254]. Its structure (Fig. 19) consists of eight Fe(III) centres arranged as following: two Fe(III) atoms form a dimeric [Fe^{III}_2] unit via the two μ_3-O^{2-} to give a central $[Fe^{III}_2O_2]^{2+}$ unit. Each iron centre from the dimer is further connected to two {Fe(tacn)} monomers via four μ-OH^- groups, while the dimer is connected to two more {Fe(tacn)} units via the μ_3-O^{2-} groups. Six of the eight Fe (III) centres are coplanar, while the remaining Fe(III) atoms are located ~ 1.98 Å above and below the plane (Fig. 19). Alternatively, the core of the [Fe^{III}_8] complex can be regarded as a [$Fe^{III}_4O_2$] "butterfly" unit to which four {Fe(tacn)} monomers are attached via eight μ-OH^- groups. Its magnetic properties were investigated few years later to reveal an $S = 10$ ground-state, which can be rationalised by assuming six spins up and two spins down [255]. Of course, such a hypothesis is oversimplified, since there are many triangular units within the cluster that should potentially lead to spin frustration phenomena. Yet, polarised neutron diffraction techniques showed that the two Fe(III) centres which are located above and below the [Fe_6] plane are spin-opposite to the ones located on the plane [256]. The splitting of the $S = 10$ ground-state was confirmed by HF-EPR, Mössbauer and AC magnetic susceptibility measurements [229], inelastic neutron scattering, INS, experiments [230], while this cluster was only the second example of an SMM displaying the QTM phenomenon, since it was reported that below 360 mK the relaxation of the magnetisation is temperature independent [231, 232]. Furthermore, this octanuclear iron-based SMM provided experimental confirmation for the first time of the topological part of the quantum spin phase (Berry phase) in a magnetic system [257]. This discovery is of fundamental importance, since it suggests that the magnetisation reversal can be completely controlled upon appropriately sweeping magnetic field in two dimensions.

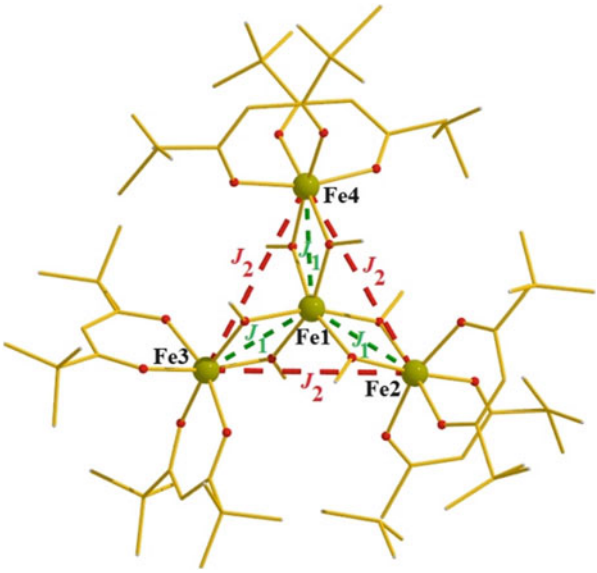

Fig. 20 The molecular structure of the cation of **232**, highlighting the 2-*J* interaction scheme employed for the fitting of its magnetic susceptibility data

2.3.2 $[Fe^{III}_4(OR)_6(dpm)_6]$: A Family of $[Fe_4]$ "Star" SMMs

The $[Fe_4(OMe)_6(dpm)_6]$ (**232**) (dpmH=dipivaloylmethane) complex was synthesised in 1999 by Barra et al. upon the reaction of $FeCl_3$ and dpmH in anhydrous MeOH in the presence of CH_3ONa [233]. Its structure (Fig. 20) consists of a central Fe(III) atom which is connected via three pairs of μ-OCH_3^- groups to three peripheral Fe(III) centres. Each peripheral Fe(III) atom is further capped by two chelate dionate monoanions. The three peripheral Fe(III) centres define an isosceles triangle, while the central metallic atom is located at its centre. Alternatively, the structure may be considered as a propeller of three {Fe-dpm} "wings", evolving around the central Fe atom via six μ-OCH_3^- groups.

The ground-state of **232** was found $S=5$, assuming one magnetic exchange interaction, J_1, between the central and the peripheral centres, and one, J_2, between the peripheral Fe(III) atoms (Fig. 20). A satisfactory fit was obtained upon the employment of the corresponding Hamiltonian, $\hat{H}=-2J_1\,(\hat{S_1}\cdot\hat{S_2}+\hat{S_1}\cdot\hat{S_3}+\hat{S_1}\cdot\hat{S_4})-2J_2\,(\hat{S_2}\cdot\hat{S_3}+\hat{S_3}\cdot\hat{S_4}+\hat{S_2}\cdot\hat{S_4})$, which afforded the parameters $J_1=21.1$ cm^{-1}, $J_2=-2.1$ cm^{-1} and $g=1.97$, with the first excited state of $S=4$ located ~60 cm^{-1} above the ground-state of $S=5$. Furthermore, HF-EPR studies showed that the system possesses uniaxial magnetic anisotropy, corresponding to a zero-field splitting parameter of the $S=5$ ground-state of $D=-0.2$ cm^{-1}, while ac magnetic susceptibility and magnetisation relaxation studies revealed an energy barrier of $U_{eff}=3.5$ K for the magnetisation reversal. This barrier is smaller than the theoretical value of $U\approx7.2$ K (arising from $U=|D|\cdot S^2$, for $S=5$ and $D=0.2$ cm^{-1}) and this may be attributed to the fact that the theoretical formula does not consider the QTM component in the magnetisation relaxation.

Compound **232** was the first of many star-like [Fe_4] clusters made in the following years, all of which display enhanced SMM properties compared to **232**; clusters [$Fe_4(L_1)_2(dpm)_6$] (**233**), [$Fe_4(L_2)_2(dpm)_6$] (**234**), [$Fe_4(L_3)_2(dpm)_6$]·Et_2O (**235**·Et_2O) and [$Fe_4(OEt)_3(L_4)(dpm)6$] (**236**) were prepared upon the reaction of **232** with the corresponding tripodal ligands R–$C(CH_2OH)_3$ (H_3L_1, R=) Me; H_3L_2, R=CH_2Br; H_3L_3, R=Ph; H_3L_4, R=^{t}Bu), with all clusters possessing an $S = 5$ ground-state as the parent compound [30, 234]. Yet, the zero-field splitting parameter was found $-0.445\ cm^{-1}$ in **233**, $-0.432\ cm^{-1}$ in **234**, $-0.42\ cm^{-1}$ in **235**·Et2O, and $-0.27\ cm^{-1}$ in **236**, leading to enhanced energy barriers of 17.0 K in **233**, 16.6 K in **234**, 15.6 K in **235**·Et2O and 5.95 K in **236** compared to 3.5 K for **232**.

A significant finding was that both $|D|$ and U_{eff} were found to increase with increasing helical pitch of the [$Fe(O_2Fe)_3$] core of the complexes induced by replacement of the initial μ-OCH_3^- groups found in **232** with the alkoxide groups of the tripodal ligands in **233–236**. Furthermore, by incorporating long-chain alkyl tethers at opposite sides and terminal "alligator clips" into the [Fe_4] clusters in the form of either alkenyl or thioacetyl groups, two new [Fe_4] derivatives, [$Fe_4(L_5)_2(dpm)_6$] (**237**) and [$Fe_4(L_6)_2(dpm)_6$] (**238**) (H_3L_5 = 2,2-Bis(hydroxymethyl)-10-undecen-1-ol; H_3L_6 = 11-(Acetylthio)-2,2-bis (hydroxylmethyl)undecan-1-ol) which can be used for deposition on silicon and gold substrates were prepared and characterised [235, 258]. In another example, again by substituting the initial μ-OCH_3^- groups found in **232** this time with the alkoxide groups of the monoether of pentaerythritol, complex [$Fe_4(L_7)_2(dpm)_6$] (**239**) (H_3L_7 = Ph-O–$CH_2C(CH_2OH)_3$) was formed, which possesses the lowest molecular symmetry among all [Fe_4] derivatives reported (C_1), retaining the same $S = 5$ ground spin state, but with an enhanced easy-axis anisotropy of $D = -0.433(2)\ cm^{-1}$, $E = 0.014(2)\ cm^{-1}$ and $B^0_4 = +1.5(1) \times 10^{-5}\ cm^{-1}$, leading to an energy barrier of $U_{eff} = 15.7(2)$ K [236]. Finally, the ester, [Fe_4(esterC5)$_2$(dpm)$_6$] (**240**), and amido, [Fe_4(amideC5)$_2$(dpm)$_6$]· Et_2O·4MeOH (**241**·Et_2O·4MeOH) (H_3esterC5=RC(O)$OCH_2C(CH_2OH)_3$ and H3amideC5=RC(O)$NHC(CH_2OH)_3$ with R=*n*-butyl), analogues were also prepared and characterised [237], in which the cluster core has been functionalised by ester and amido linkages, respectively, while just recently the azobenzene analogues, [$Fe_4(azo)_2(dpm)_6$] (**242**) and [$Fe_4(azoMe_2)_2(dpm)_6$] (**243**) (H_3azo = 2-(Hydroxymethyl)-2-(4-(phenyldiazenyl)phenyl)propane-1,3-diol; H_3azoMe_2 = 2-(4-((3,5-Dimethylphenyl) diazenyl)phenyl)-2-(hydroxymethyl)-propane-1,3-diol) were prepared, displaying both magnetic and optical bistability [238].

2.3.3 [$Fe^{III}_4(thme)_2(C_3H_7OH)_6Cl_6$]: A [$Fe_4$] "Star" SMM Based on a Triol Ligand

Cluster [$Fe_4(thme)_2(C_3H_7OH)_6Cl_6$] (**244**) was made upon the reaction of $FeCl_3$ and H_3thme (=1,1,1tris(hydroxymethyl)ethane) in MeOH in the presence of CH_3ONa [239]. Its core resembles the one of the classical [Fe_4/dpm] SMMs mentioned earlier, with the difference that now the central Fe atom is connected to the three

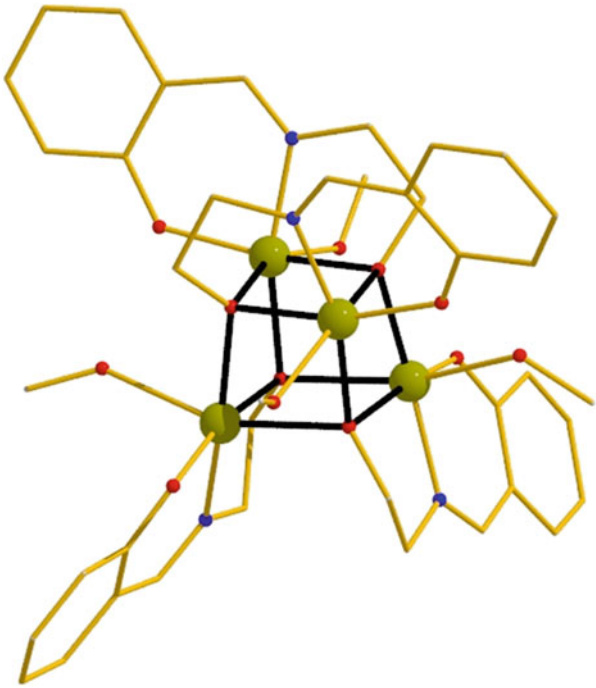

Fig. 21 The molecular structure of **245**, highlighting the cube-like topology (in *bold*)

peripheral Fe centres via two fully deprotonated $thme^{3-}$ ligands that provide six bridging alkoxide groups. Furthermore, two propanol molecules as well as two terminal Cl^{-} anions complete the coordination environment of the peripheral Fe atoms. The cluster possesses an $S = 5$ ground-state as evidenced by fitting of the magnetic susceptibility data to a model that assumes a magnetic exchange interaction of $J_1 = -28.2$ cm^{-1} between the central atom and the peripheral ones, and a weak intermolecular interaction of $J' = +0.05$ cm^{-1} between neighbouring clusters, while an interaction between the peripheral atoms was not introduced this time. Q-band EPR studies showed an axial anisotropy of $D = -0.32$ cm^{-1} and ac magnetic susceptibility studies confirmed the SMM behaviour, since out-of-phase frequency-dependent peaks were observed below 1 K. The SMM behaviour was further established by single crystal magnetisation measurements, revealing an energy barrier of $U_{eff} = 8.5$ K for the magnetisation reversal.

2.3.4 $[Fe^{II}_4(sae)_4(MeOH)_4]$: The First Fe(II)-Based SMM

Complex $[Fe_4(sae)_4(MeOH)_4]$ (**245**) was prepared upon the reaction of $FeCl_2{\cdot}4H_2O$ with H_2sae (=2-salicylideneamino-1-ethanol) in methanol under anaerobic conditions [240]. Complex **245** consists of four Fe^{II} centres ($3d^6$ ions, $S = 2$) held by four μ_3-OR groups in a cuboid arrangement, in which all Fe-O-Fe angles are in the 92.3–103.6° range (Fig. 21). Each iron centre adopts axially elongated octahedral geometry, with the coordination environment being tridentate sae^{-2-} ligands and

terminal MeOH molecules. The ground-state of **245** was found to be $S = 8$, presumably due to the small Fe-O-Fe angles present. Furthermore, the complex displays nicely formed out-of-phase peaks, χ_M'', at ~2.0–2.2 K, while the energy barrier for the re-orientation of the magnetisation was found to be 28.4 K with a pre-exponential factor of 2.06×10^{-9} s and a blocking temperature of ~1.1 K. Finally, the zero-field splitting parameter of the $S = 8$ ground-state was found to be $D = -0.64$ cm^{-1}, while the same authors managed to structurally control the magnetic anisotropy in similar [Fe^{II}_4] cubes [241]. More specifically, the synthesised complexes [Fe^{II}_4(sap)$_4$(MeOH)$_4$]·2H$_2$O (**246**·H$_2$O), [Fe^{II}_4(5-Br-sap)$_4$(MeOH)$_4$] (**247**), [Fe^{II}_4(3-MeO-sap)$_4$(MeOH)$_4$]·2MeOH (**248**·2MeOH), [Fe^{II}_4(5-Br-sae)$_4$(MeOH)$_4$]·MeOH (**249**·MeOH) and [Fe$_4$(3,5-Cl$_2$-sae)$_4$(MeOH)$_4$] (**250**) were found to possess an $S = 8$ ground-state with D values of +0.81, +0.80, +1.15, −0.66, and −0.67 cm^{-1}, respectively, with the appearance of out-of-phase peaks for **249** and **250** ($D < 0$).

2.3.5 [Fe^{III}_{19}(metheidi)$_{10}$(OH)$_{14}$(O)$_6$(H$_2$O)$_{12}$]NO$_3$·24H$_2$O: An Enneadecanuclear Fe(III) SMM

Cluster [Fe^{III}_{19}(metheidi)$_{10}$(OH)$_{14}$(O)$_6$(H$_2$O)$_{12}$]NO$_3$·24H$_2$O (**251**·24H$_2$O) represents the largest iron cluster to date displaying SMM behaviour and one of the largest SMMs of any metal type. It can be prepared upon the reaction of Fe(NO$_3$)$_3$·9H$_2$O with H$_3$metheidi (=*N*-(1-Hydroxymethylethyl)iminodiacetic acid) in H$_2$O/pyridine in relatively good yields (~35 %) [242]. This impressive Fe(III) cluster was made as an attempt of "creating engineered infinite arrays of zero-dimensional (nanoscale) aggregates", since the same group had reported on a co-crystallised [Fe_{17}]/[Fe_{19}] system with the ligand H$_3$heidi (=hydroxyethyliminodiacetic acid) [259], and it was important to "separate" the two polynuclear units for the elucidation of their magnetic properties, since the co-crystallised species displayed out-of-phase signals at ~1.1 K and a weak hysteresis loop at 0.1 K. Its structure consists (Fig. 22) of a central [Fe^{III}_7(μ_3-O)$_2$(μ_3-OH)$_6$(μ-OH)$_4$]$^{7+}$ purely "inorganic" planar disk, which is connected to: (1) four {Fe^{III}(metheidi)} units, each connected via a monoatomic carboxylate group from the metheidi^{-3} ligand and a μ-OH$^-$, and (2) two {Fe^{III}_4(metheidi)$_3$} units, each connected via three μ_3-O^{2-} groups. The cluster possesses an $S = 33/2$ ground-state, and a D parameter of −0.035 cm^{-1}, as was established by EPR experiments. Furthermore, the energy barrier for the re-orientation of the magnetisation was calculated to be ~15.7 K, while the cluster displays hysteresis loops in the 0.3–1.1 K temperature range.

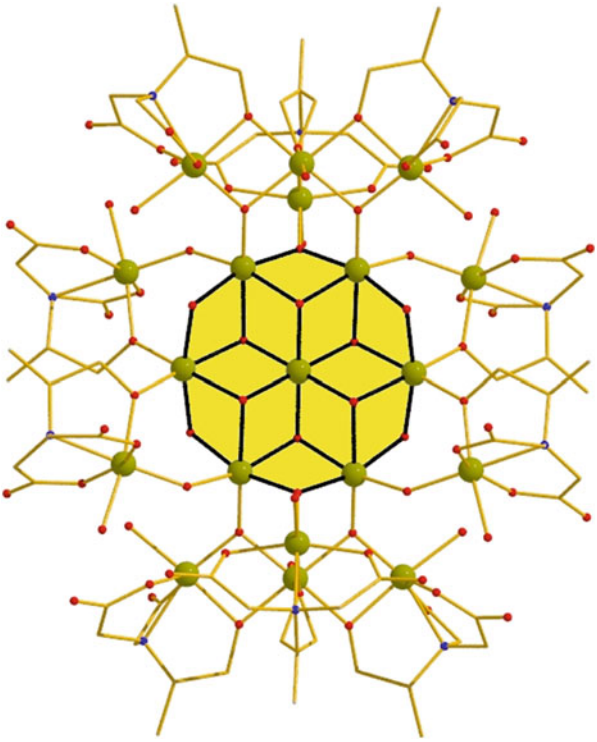

Fig. 22 The molecular structure of the cationic part of **251**, highlighting the central $[Fe^{III}_7(\mu_3\text{-}O)_2(\mu_3\text{-}OH)_6(\mu\text{-}OH)_4]^{7+}$ planar disk topology (in *yellow*). Colour code: Fe^{II} = *green*, O = *red*, C = *gold*

2.3.6 $[Fe^{II}_9(N_3)_2(O_2CMe)_8\{(2\text{-}py)_2CO_2\}_4]$: A Rational Design of a Fe(II) SMM

Complex $[Fe^{II}_9(N_3)_2(O_2CMe)_8\{(2\text{-}py)_2CO_2\}_4]$ (**252**) $((2\text{-}py)_2CO_2)^{2-}$=is the doubly deprotonated *gem*-diol form of di-2-pyridyl ketone) was prepared upon the rational replacement of the two μ_4-OH^- groups in the $[Fe^{II}_9(OH)_2(O_2CMe)_8\{(2\text{-}py)_2CO_2\}_4]$ (**253**) cluster by two μ_4-N_3^- azide ions in an *end-on* fashion [243]. Such strategy had been previously applied successfully by the Perlepes's group in two analogous and isostructural examples: (1) in the conversion of $[Co^{II}_9(OH)_2(O_2CMe)_8\{(2\text{-}py)_2CO_2\}_4]$ (**254**) to $[Co^{II}_9(N_3)_2(O_2CMe)_8\{(2\text{-}py)_2CO_2\}_4]$ (**255**) [260] and (2) in the conversion of $[Ni^{II}_9(OH)_2(O_2CMe)_8\{(2\text{-}py)_2CO_2\}_4]$ (**256**) to $[Ni^{II}_9(N_3)_2(O_2CMe)_8\{(2\text{-}py)_2CO_2\}_4]$ (**257**) [261], leading to a seven-fold and nine-fold increase in the spin ground-state, respectively (Fig. 23) [262, 263]. The structure of all **252**–**257** clusters consists of nine M(II) centres (M: Co, Ni, Fe) arranged in two square pyramids sharing a common apex. The nine centres are held in place by four η^3:η^3:η^1:η^1:μ_5 $(2\text{-}py)_2CO_2^{2-}$ ligands, eight *syn,syn* η^1:η^1:μ OAc^- ligands and two μ_4-N_3^- azide ions in an *end-on* fashion. The latter ones are responsible for the increase of the spin ground-state, since it is well known that azide ions can propagate ferromagnetic interactions when found in an *end-on* fashion. Cluster **252** possesses an $S = 14$ ground-state, while fully formed out-of-phase peaks, χ_M''', were observed

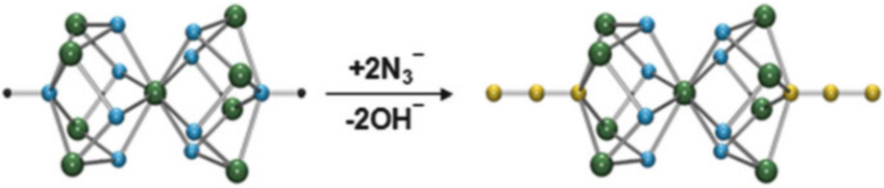

Fig. 23 Replacement of two μ_4-OH^- groups in the $[M^{II}_9(OH)_2(O_2CMe)_8\{(2\text{-py})_2CO_2\}_4]$ clusters by two μ_4-N_3^- azide ions. Colour code: M^{II} = *green*, O = *blue*, N = *gold*

in the ~2.0–2.3 K temperature range. From the Arrhenius equation plot, the energy barrier for the re-orientation of the magnetisation was found to be $U_{eff} = 41$ K with a pre-exponential factor of $\tau_0 = 3.4 \times 10^{-12}$ s.

In a similar manner, cluster $[Fe^{II}_9(NCO)_2(O_2CMe)_8\{(2\text{-py})_2CO_2\}_4]$ (**258**) in which the initial μ_4-OH^- groups have now been replaced by two μ_4-NCO^- ligands, possesses an $S = 14$ ground-state and functions as an SMM with $U_{eff} = 44$ K with a pre-exponential factor of $\tau_0 = 2.0 \times 10^{-11}$ [244]. This pioneering work by Perlepes led many scientists in the following years to engage into replacing bridging OH^- groups by *end-on* azides, as a means of deliberately enhancing the spin ground-states of many clusters.

2.3.7 $[Fe^{III}_9O_4(OH)_5(heia)_6(Hheia)_2]\cdot 3.5CH_3OH\cdot 8H_2O$: An Enneanuclear Fe(III) SMM

Cage $[Fe^{III}_9O_4(OH)_5(heia)_6(Hheia)_2]\cdot 3.5CH_3OH\cdot 8H_2O$ (**259**·$3.5CH_3OH\cdot 8H_2O$) was isolated upon the reaction of $Fe(NO_3)_3\cdot 9H_2O$ with H_2heia (=HN$\{CH_2COOH\}CH_2CH_2OH$) and $N(Me)_4OH$ in methanol, in the presence of the liquid drying agent diethoxymethane, as a means of blocking further hydrolysis [245]. This cage, in contrast to **252**, contains all iron centres in the ferric state. Its structure consists of a central tetrahedral Fe(III) ion connected by four μ_3-oxo bridges, to eight peripheral Fe(III) centres. Each of the outer meal centres is capped by a facially coordinated $heia^{2-}$ ligand, adopting distorted octahedral coordination geometry, while of great importance for its magnetic properties is the fact that the peripheral Fe(III) meal atoms are asymmetrically bridged. Magnetisation measurements for **259** gave an $S = 25/2$ ground-state, $g = 1.99$ and $D = -0.07$ cm^{-1}, while the cluster displays hysteresis loops in the 0.04–0.5 K temperature range. Finally, the fit to an Arrhenius law yielded $U_{eff} = 7.6$ K and $\tau_0 = 6 \times 10^{-10}$ s.

2.3.8 $[Fe^{III}10Na_2O_6(OH)_4(O_2CPh)_{10}(chp)_6(H_2O)_2(Me_2CO)_2]$: A Decanuclear Fe(III) SMM

Cluster $[Fe^{III}_{10}Na_2O_6(OH)_4(O_2CPh)_{10}(chp)_6(H_2O)_2(Me_2CO)_2]$ (**260**) (Hchp = 6-chloro-2-hydroxypyridine) was formed upon the reaction of $[NEt_4]_2[Fe_2OC1_6]$

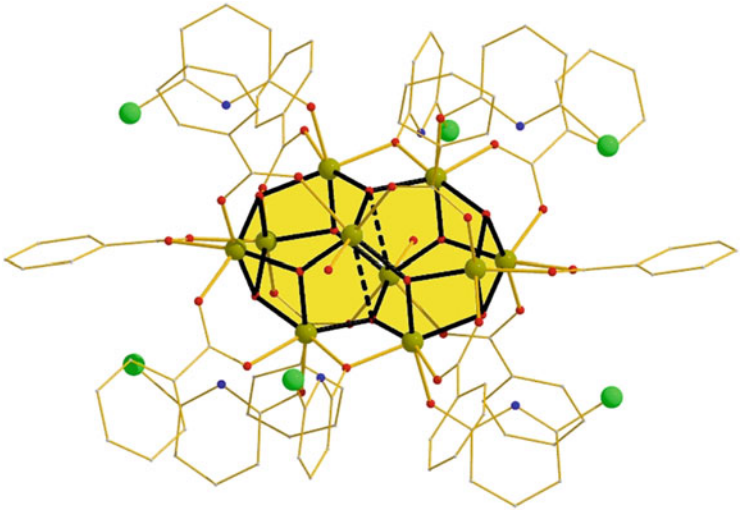

Fig. 24 View of the dianionic part of $[Fe^{III}_{10}O_6(OH)_4(O_2CPh)_{10}(chp)_6(H_2O)_2(Me_2CO)_2]^{2-}$ (**260**) highlighting the two distorted $\{Fe_6O_6\}$ hexagonal prisms sharing one "square" face

with NaO_2CPh and Nachp in MeCN/acetone [246]. The inorganic core of the cluster is described as two distorted $\{Fe_6O_6\}$ hexagonal prisms sharing one "square" face (Fig. 24). From magnetisation experiments the ground-state of the complex was found $S = 11$, while it displays frequency-dependent out-of-phase signals, χ_M'', below 1 K temperature range. Furthermore, from the fit of the Arrhenius plot the energy barrier for the re-orientation of the magnetisation was found $U_{eff} = 5.3$ K [264].

2.3.9 $[NEt_4][Fe^{III}_{11}O_4(O_2CPh)_{10}(thme)_4(dmhp)_2Cl_4]$: An Undecanuclear Fe(III) SMM with a Half-Integer Spin of $S = 11/2$

Cage $[NEt_4][Fe^{III}_{11}O_4(O_2CPh)_{10}(thme)_4(dmhp)_2Cl_4]$ (**261**) was made in a manner similar to that of cluster **260**, upon the reaction of $[NEt_4]_2[Fe_2OC1_6]$ with NaO_2CPh, 4,6-dimethyl-2-hydroxypyrimidine (dmhp), and 1,1,1-tris (hydroxymethyl)-ethane (H_3thme) in MeCN [247]. The metallic core of **261** consists of four fused butterfly $\{Fe_4O_2\}^{8+}$ motifs, with the two central units forming a planar $\{Fe_3O_4\}$ unit (Fig. 25). The complex was found to possess an $S = 11/2$ ground-state with a ZFS parameter of $D = -0.46$ cm^{-1} and a g value of 2.03, while below 1.2 K hysteresis loops were observed in magnetisation vs. field studies whose coercivities increase with decreasing temperature.

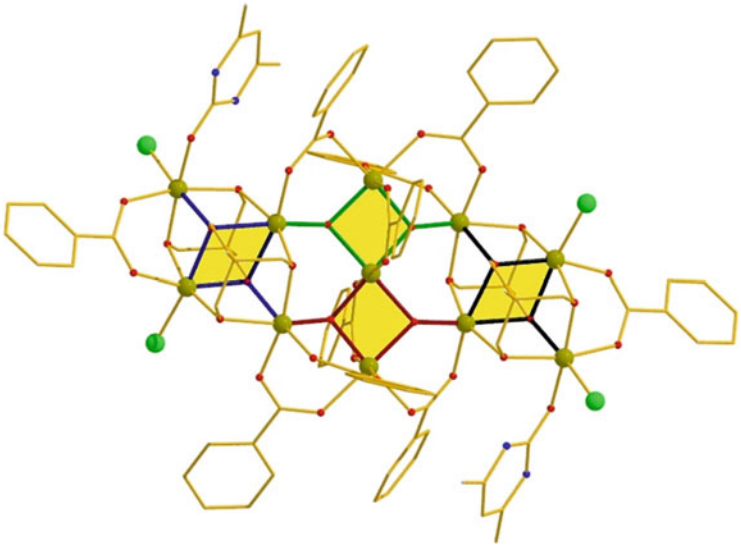

Fig. 25 The molecular structure of the anionic part of **261** highlighting its four fused butterfly $\{Fe_4O_2\}^{8+}$ units

2.3.10 $[Fe^{II}_2(NCO)_3(acpypentO)]$: A "Small" Iron-Based SMM

The dimer $[Fe^{II}_2(NCO)_3(acpypentO)]$ (**262**) was prepared upon the reaction of acpypentOH (=1,5-bis{[2-pyridyl(1-ethyl]imino)}pentane-3-ol) with $Fe(OAc)_2{\cdot}2H_2O$ and KOCN in a mixture of alcohols (MeOH/EtOH), in relatively good yields [248]. This complex was found to be ferromagnetic with $S = 4$, while in addition, single-ion anisotropies were present. Indeed, this cluster was confirmed to exhibit single-molecule magnetism behaviour, since ac magnetic susceptibility measurements revealed the presence of out-of-phase signals, χ_M'', below ~3.5 K, *albeit* not fully formed [265].

2.3.11 $(pyrH)_5[Fe_{13}F_{24}(OCH_3)_{12}O_4]{\cdot}CH_3OH{\cdot}4H_2O$: An "Open-Shell" Keggin-Type Fe(III) SMM

Cluster $(pyrH)_5[Fe_{13}F_{24}(OCH_3)_{12}O_4]{\cdot}CH_3OH{\cdot}4H_2O$ (**263**$\cdot CH_3OH{\cdot}H_2O$) was prepared from the reaction of $FeF_3{\cdot}3H_2O$ and pyridine in hot methanol under anaerobic conditions [249]. The cage which adopts an ideal α-Keggin structure with 12 surrounding iron atoms and a central tetrahedral $\{FeO_4\}$ core displays frequency-dependent out-of-phase signals, χ_M'', below 1.0 K, suggesting single-molecule magnetism behaviour with $U_{eff} = 13.1$ K and $\tau_0 = 7.5 \times 10^{-13}$ s [266].

2.3.12 $[Fe^{III}_9O_4(OH)_4(O_2CPh)_{13}(heenH)_2]\cdot 9MeCN$: Fe(III) SMM

Cluster $[Fe^{III}_9O_4(OH)_4(O_2CPh)_{13}(heenH)_2]\cdot 9MeCN$ (**264**·9MeCN) was made from the reaction of $FeCl_3$, NaO_2CPh and $heenH_2$ (= *N*,*N*′-bis(2-hydroxyethyl)-ethylene diamine) in MeCN [250]. The structure of **264** consists of two $\{Fe_4(\mu_3\text{-}O)(\mu_3\text{-}OH)\}^{9+}$ "butterfly" units fused at a body atom, while two additional Fe atoms are connected by two μ_3-OH^- and two μ_3-O^{2-} groups. Dc magnetic susceptibility and magnetisation data yielded an $S = 7/2$ ground-state and a zero-field splitting of this ground-state of $D = -0.85(1)\ cm^{-1}$. Cluster **264** displays frequency-dependent out-of-phase signals, χ_M'', below 3.0 K and its SMM behaviour was further established by the presence of hysteresis loops at magnetisation vs. dc field scans on single crystals.

2.3.13 $\{Fe^{III}[Fe^{III}(L_1)_2]_3\}$: A Ferric "Star" SMM

Complex $\{Fe^{III}[Fe^{III}(L_1)_2]_3\}$ (**265**) was synthesised in 2006 by Saalfrank et al. from the reaction of anhydrous $FeCl_3$ and H_2L_1 (=*N*-methyldiethanolamine) in the presence of NaH in anhydrous THF followed by extraction into CH_2Cl_2 [251]. The complex describes a star-like topology of four ferric centres, leading to an $S = 5$ ground-state, as all its predecessors with the same topology, while EPR measurements yielded the zero-field splitting value of the $S = 5$ ground-state to be $D = -0.57$ K. Finally, **265** displays hysteresis loops below 1.2 K, while the energy barrier for reversing magnetisation was found $U = 14.3$ K.

2.3.14 $Na_{14}(NMe_4)_5[(Fe^{III}_4W_9O_{34}(H_2O))_2(Fe^{III}W_6O_{26})]\cdot 50H_2O$ and $Na_6(NMe_4)_4[Fe^{III}_4(H_2O)_2(Fe^{III}W_9O_{34})_2]\cdot 45H_2O$: Two Polyoxometallate Fe(III) SMMs

Complexes $Na_{14}(NMe_4)_5[(Fe^{III}_4W_9O_{34}(H_2O))_2(Fe^{III}W_6O_{26})]\cdot 50H_2O$ (**266**·$50H_2O$) and $Na_6(NMe_4)_4[Fe^{III}_4(H_2O)_2(Fe^{III}W_9O_{34})_2]\cdot 45H_2O$ (**267**·$45H_2O$) were made upon the reaction of $Na_2WO_4\cdot 2H_2O$, $FeCl_3\cdot 6H_2O$, and NMe_4Br at pH 7 under hydrothermal conditions. The first product out of the reaction is **266**·$50H_2O$, while upon removal of it from the mother liquor crystals of **267**·$45H_2O$ start forming after two days [252]. Both cages fall in the POM (polyoxometallate) category. Yet, their properties fit nicely in the classic SMM behaviour: for cage **266** variable-field and temperature magnetisation experiments yield a ground-state of $S = 15/2$ with $|D| = 0.24\ cm^{-1}$, while for cage **267** the same parameters were $S = 5$ with $|D| = 0.49\ cm^{-1}$. Single-crystal magnetisation vs. dc field scans studies were performed on an array of micro-SQUIDs [267] for single crystals of both **266** and **267**, revealing hysteresis loops in the 0.04–0.5 K and 0.04–1.1 K, respectively. Furthermore, the blocking temperature for **266** was found $T_b \approx 0.6$ K, while for **267** a two-fold increase was observed ($T_b \approx 1.2$ K). Finally, for **267** the energy for the magnetisation's reorientation was found to be $U_{eff} = 16.6$ K.

2.3.15 $[Fe^{III}_{11}O_7(dea)_3(piv)_{12}]Cl{\cdot}5MeCN$: A Half-Integer $[Fe^{III}_{11}]$ SMM

The reaction between $FeCl_3{\cdot}6H_2O$ and pivH (=pivalic acid) with $deaH_2$ (=diethanolamine) in MeCN affords cluster $[Fe^{III}_{11}O_7(dea)_3(piv)_{12}]Cl{\cdot}5MeCN$ (**268**·5MeCN) in good yield [253]. Its structure consists of a $[Fe^{III}_{11}O_7]^{19+}$ central metallic core held together by three μ_4-O^{2-} and four μ_3-O^{2-} bridges. Around the core twelve bridging pivalate and three chelating dea^{2-} ligands are positioned, forming the organic shell of the cluster. Magnetisation data revealed an $S = 13/2$ ground-state with a zfs parameter of $D = -0.25$ cm^{-1}. In addition, single-crystal magnetisation measurements showed hysteresis loops, whose coercivity increases with both decreasing T and increasing sweep rate, thus proving the SMM character of **268**.

2.4 Cobalt SMMs

Cobalt SMMs, first reported in 2002, have attracted a lot of interest during the last few years, despite the fact that theoretical treatment of the magnetic data for octahedral Co^{II} is difficult and complicated. The reason for the latter is that octahedral Co^{II} ions possess $^4T_{1g}$ ground term that splits to a doublet ground-state at low temperature when in distorted environment due to spin–orbit coupling [268]. Furthermore, Co(II) is highly anisotropic and the magnetic exchange interactions in such systems are mainly dictated by the orientation of the local magnetic moments [269]. In addition, one should remember that Co(II) ions in octahedral symmetry may be treated as pseudo "$S_{eff} = ½$" systems at low temperature due to the splitting of the Kramer's doublets. A review of cobalt SMMs was recently published [270]; the most representative examples of cobalt SMMs are given in Table 7.

2.4.1 $[Co^{II}_4(hmp)_4(MeOH)_4Cl_4]$: The First Co-Based SMM

Cluster $[Co^{II}_4(hmp)_4(MeOH)_4Cl_4]$ (**269**) was prepared upon the reaction of $CoCl_2{\cdot}6H_2O$ with Hhmp (=hydroxymethylpyridine) in MeOH in the presence of sodium methoxide [271]. The molecule adopts a $\{Co_4(OR)_4\}$ cubane-like structure with the alkoxide groups belonging to four hmp^- monoanionic ligands, while all Co^{II} centres are six-coordinate with an O_4NCl coordination sphere, adopting octahedral geometry. Fitting of the magnetisation data gave an $S = 6$ ground-state, with a zero-field splitting of this ground-state of $D = -2.79$ cm^{-1}. The cluster was studied by means of single-crystal magnetisation techniques in order to examine if it could function as a SMM. Indeed, **269** displays temperature-dependent hysteresis loops below 1.2 K, while the size of the loops does not really

Table 7 Representative examples of co-based SMMs

Formula	S'	D (cm^{-1})	U_{eff} (K)	τ_0 (s)	References
$[Co^{II}_4(hmp)_4(MeOH)_4Cl_4]$ (**269**)	6 (S)	−2.79	–	–	[271]
$(NMe_4)_3Na[Co^{II}_6(cit)_4(H_2O)_{10}]$ (**270**)	3	–	26	8.2×10^{-9}	[272]
"$(NMe_4)_4[Co^{II}_6(cit)_4(H_2O)_{10}]$" (**271**)	3	–	32	2.1×10^{-9}	[272]
$[Co^{II}_7(bzp)_6(N_3)_9(CH_3O)_3](ClO_4)_2$ (**272**)	7/2	–	–	–	[273]
$[Co^{II}_7(hdeo)_6(N_3)_6][ClO4]_2$ (**273**)	7/2	–	–	–	[274]
$[Co^{II}_4Co^{III}_3(HL)_6(NO_3)_3(H_2O)_3](NO_3)_2$ (**274**)	2	–	–	–	[275]
$[Co^{II}_4L_4]$ (**276**)	–	–	38.8	5.4×10^{-9}	[276]
$[Co^{II}_5(\mu_4\text{-}N_3)(piv)(^t bdea)_2(piv)_4(MeCN)_2]$ (**277**)	–	–	14.3	1.7×10^{-7}	[277]
$[Et_3NH][Co^{II}_8(chp)_{10}(O_3PPh)_2(NO_3)_3(Hchp)_2]$ (**280**)	–	–	84	1.8×10^{-12}	[278]
$[Co^{II}_{12}(bm)_{12}(NO_3)(O_2CMe)_6(EtOH)_6](NO_3)_5$ (**281**)	6	–	15	1.94×10^{-7}	[279]
$[Co^{II}_8Co^{III}(L)_6](BF_4)_7$ (**282**)	4	–	12.7	9.03×10^{-7}	[280]
$[Co^{II}_7(bhqe)_3(OH)_2(H_2O)_6]$ (**283**)	7/2	–	21, 13	2.7×10^{-7}, 3.9×10^{-6}	[281]
$[GuH]_8[Co^{II}_4(cit)_4]$ (**284**)	–	–	24	3.4×10^{-8}	[282, 283]
$[Co^{II}_{20}(OH)_6(O_2CMe)_{22}(HL)_4(DMF)_2]$ (**285**)	4	–	–	–	[284]
$[Co^{III}Co^{II}_6(OH)_6(L)_6](ClO_4)_3$ (**286**)	–	–	–	–	[285]
$[Co^{II}_4(phen)_4Cl_8]$ (**287**)	–	–	8.41	5.29×10^{-9}	[286]
$Na_{22}Rb_6[\{Co^{II}_4(OH)_3PO_4\}_4(A\text{-}\alpha\text{-}PW_9O_{34})_4]$ (**288**)	8	–	26.1	3.5×10^{-8}	[287]

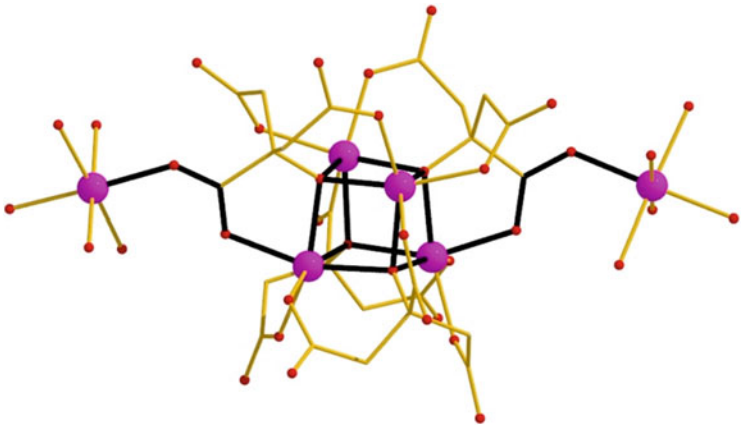

Fig. 26 The molecular structure of the anionic part of **270**

depend on the field sweep rate, probably indicating that resonant quantum tunnelling is hindered by small intermolecular exchange interactions.

2.4.2 $(NMe_4)_3Na[Co^{II}_6(cit)_4(H_2O)_{10}]$: A "Citrus" Co-Based SMM

The second example of Co-based SMM was reported in 2003, just one year after **269**, and was prepared upon reacting Hcit (=citric acid) with $CoSO_4{\cdot}7H_2O$ in the presence of NMe_4OH and Na_2SO_4, yielding cage $(NMe_4)_3Na[Co^{II}_6(cit)_4(H_2O)_{10}]$ (**270**) [272]. The structure of the molecule (Fig. 26) can be described as a $\{Co_4(OR)_4\}$ cubane with two $\{Co(H_2O)_5\}$ units attached via *syn, anti*- $COO^-_{citrate}$ groups. Each Co^{II} centre is six-coordinate adopting twisted trigonal prismatic geometry. The ground-state of the complex was found $S' = 3$, treating each Co^{II} centre as an "$S_{eff} = ½$" system at very low temperature, while from *ac* magnetic susceptibility experiments frequency-dependent out-of-phase peaks were observed in the 1.8–3 K temperature range. An Arrhenius analysis of the *ac* data yielded an energy barrier for the reorientation of the magnetisation of $U_{eff} = 26$ K and a pre-exponential factor $\tau_0 = 8.2 \times 10^{-9}$ s. Interestingly enough, the same reaction in the absence of Na^+ cations forms cluster "$(NMe_4)_4[Co^{II}_6(cit)_4(H_2O)_{10}]{\cdot}16H_2O$" (**271**$\cdot 16H_2O$) as evidenced by means of IR spectroscopy and elemental analysis. Complex **271** can also function as an SMM, with a slightly improved $U_{eff} = 32$ K compared to **270**, and a pre-exponential factor $\tau_0 = 2.1 \times 10^{-9}$ s.

2.4.3 $[Co^{II}_7(bzp)_6(N_3)_9(CH_3O)_3]^{2+}$

Complex $[Co^{II}_7(bzp)_6(N_3)_9(CH_3O)_3](ClO_4)_2{\cdot}2H_2O$ (**272**$\cdot 2H_2O$) was made upon the reaction of NaN_3 with $Co(ClO_4)_2{\cdot}6H_2O$ and bzp (=2-benzoyl pyridine) in MeOH

[273]. The molecule contains a six-member $\{Co_6\}$ ring, with the seventh Co ion located at its centre. The heptametallic disc is planar with all Co^{II} centres in a distorted octahedral geometry, while all azide ions are found in an end-on fashion. The *dc* magnetic susceptibility data above ~100 K obeys the Curie law with $\theta = +37.3$ K, indicating the presence of dominant ferromagnetic interactions within the disc. Fitting of the magnetisation data confirms the overall ferromagnetic nature of **272**, yielding an $S' = 7/2$ ground-state for the complex (assuming each Co^{II} centre as an $S_{eff} = ½$ metal). Furthermore, cage **272** displays frequency-dependent out-of-phase signals below ~3.5 K, which are not fully formed. Yet, the fully formed peaks can be observed upon employment of a *dc* field since it is well known that the applied *dc* field decreases the amount of quantum tunnelling [288]. Finally, single-crystal magnetisation hysteresis loops were performed on a micro-SQUID set-up showing hysteresis loops, albeit very small, most probably due to the phonon-bottleneck effect [73] and/or small intercluster AF interactions.

Similar magnetic behaviour is displayed by another heptanuclear $[Co^{II}_7]$ complex, $[Co^{II}_7(hdeo)_6(N_3)_6][ClO_4]_2$ (**273**) (Hhdeo = 2-hydroxy-[1,2-di(pyridin-2-yl)] ethane-1-one), which possess an $S' = 7/2$ ground-state and displays frequency-dependent, not fully formed, out-of-phase signals below ~1.9 K [274].

2.4.4 $[Co^{II}_4Co^{III}_3(HL)_6(NO_3)_3(H_2O)_3](NO_3)_2$: A Mixed-Valent $Co^{II/III}$ SMM

In 2007 the first mixed-valent $Co^{II/III}$ SMM was reported [275]; cluster $[Co^{II}_4Co^{III}_3(HL)_6(NO_3)_3(H_2O)_3](NO_3)_2$ (**274**) (H_3L=$H_2NC(CH_2OH)_3$) was prepared from the reaction of $Co(NO_3)_2{\cdot}6H_2O$ with the ligand in H_2O in the presence of NMe_4OH. The four Co^{II} centres are arranged in a star-like topology, with the trivalent ones being located at the periphery of the $\{Co^{II}_4\}$ star (Fig. 27). All metallic centres adopt distorted octahedral geometry, are coplanar and bridged exclusively by alkoxide groups of the doubly deprotonated ligands. The molecule behaves as a ferromagnetically coupled $[Co^{II}_4]$ cage, possessing an $S' = 2$ (again each Co^{II} ion is treated as an ½ spin system). The cluster displays out-of-phase frequency-dependent tails "going up" below ~4 K, but no peaks are observed. In order to further investigate for SMM behaviour, single-crystal magnetisation studies were carried out on **274** verifying its SMM character, since it displayed temperature and sweep-rate-dependent hysteresis loops.

Interestingly enough, a very similar complex to **274**, complex $[Co^{II}_4Co^{III}_3(dea)_6(OAc)_3][ClO_4]_{0.75}[OAc]_{1.25}$ (**275**) (dea=the monoanionic form of diethanolamine) displaying the same core, the same oxidation states' distribution and the same $S' = 2$ ground-state was not found to function as an SMM, most probably due to the different space group (cubic for **275** vs. trigonal for **274**) [289].

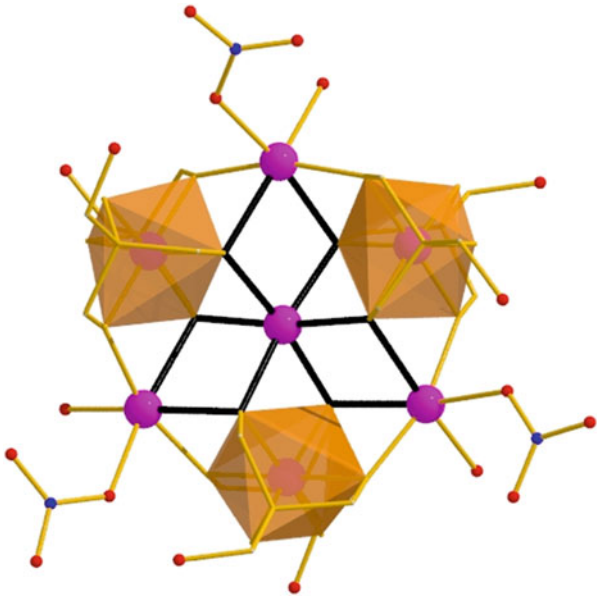

Fig. 27 The molecular structure of the dicationic part of **274**. Colour code: Co^{II} = *pink*, O = *red*, C = *gold*. The Co^{III} ions are given inside their polyhedra

2.4.5 $[Co^{II}_4L_4]$: A Square Co^{II} SMM

Complex $[Co^{II}_4L_4]\cdot 0.5H_2O$ (**276**·$0.5H_2O$) (H_2L=*N*,*N*′-di[1-(2-hydroxyphenyl) ethlidene]-hydrazone) was made upon the reaction of $Co(ClO_4)_2\cdot 6H_2O$ and the corresponding ligand in MeOH under N_2 atmosphere [276]. The tetranuclear molecule adopts a square topology (all four Co···Co···Co angles fall in the 88.1–92° range), in which the four five-coordinate Co^{II} centres are bridged by μ-O_R groups belonging to the doubly deprotonated ligands. Each Co^{II} centre is in a distorted trigonal bipyramidal coordination environment, while the complex has S_4 symmetry. *Dc* magnetic susceptibility measurements suggest ferromagnetic behaviour, while frequency-dependent fully formed out-of-phase peaks were observed in the *ac* magnetic susceptibility measurements in the 2.2–4.5 K temperature range. Arrhenius analysis of the *ac* data revealed an energy barrier for the reversal of the magnetisation of $U_{eff} = 38.8$ K and $\tau_0 = 5.4 \times 10^{-9}$ s, while more detailed *ac* measurements revealed a distribution of single relaxation processes.

2.4.6 $[Co^{II}_5(N_3)(piv)(^t bdea)_2(piv)_4(MeCN)_2]$: A Square-Pyramidal Co^{II} SMM

Complex $[Co^{II}_5(\mu_4\text{-}N_3)(piv)(^t bdea)_2(piv)_4(MeCN)_2]$ (**277**) (^{t}bdeaH$_2$=*N*-tertbutyl-diethanol amine, Hpiv=pivalic acid) was obtained in 2009 from the reaction between $[Co^{II}_2(OH_2)(piv)_4(pivH)_4]$ [290] with NaN_3 and ^{t}bdeaH$_2$ in CH_3CN

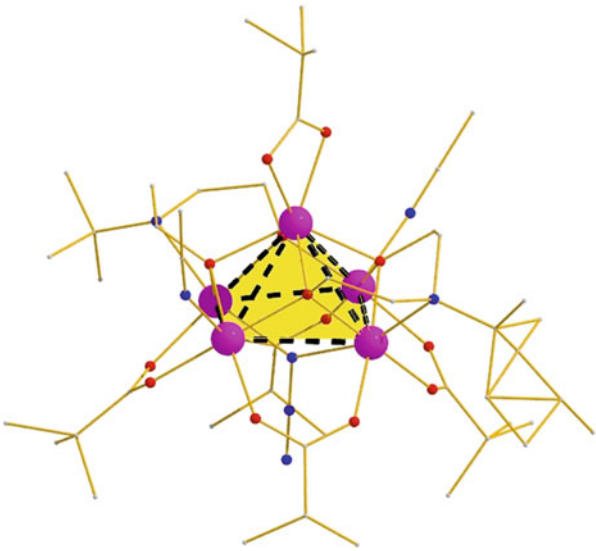

Fig. 28 The molecular structure of **277**

[277]. Furthermore, by using different Co^{II} starting materials, clusters $[Co^{II}_5(\mu_4\text{-Cl})(Cl)(^t\text{bdea})_2(piv)_4(pivH)_2]$ (**278**) and $[Co^{II}_5(\mu_4\text{-N}_3)(Cl)(^t\text{bdea})_2(piv)_4(pivH)_2]$ (**279**) may also be obtained. The structure of all analogues (Fig. 28) consists of five Co^{II} atoms arranged at the corners of a square pyramid, with the basal dimensions in the 3.15–3.21 Å range and the apical centre at 2.19 Å above the base of the pyramid. From these three analogues, only **277** displays ferromagnetic interactions within the metallic centres, as evidenced by *dc* and magnetisation experiments, while on the contrary antiferromagnetic interactions were observed for **278** and **279**. In addition, **277** displays frequency-dependent fully formed out-of-phase peaks in the 1.8–3.5 K temperature range, and further analysis of this data following the Arrhenius law gave $U_{eff} = 14.3$ K and $\tau_0 = 1.7 \times 10^{-7}$ s. Finally, complex **279** displays only a very weak out-of-phase, χ_M'', signal.

2.4.7 $[Et_3NH][Co^{II}_8(chp)_{10}(O_3PPh)_2(NO_3)_3(Hchp)_2]$: An Octanuclear Phosphonate Co^{II} SMM

Cluster $[Et_3NH][Co^{II}_8(chp)_{10}(O_3PPh)_2(NO_3)_3(Hchp)_2]$ (**280**) (Hchp = 6-chloro-2-hydroxypyridine) was made upon the reaction of Hchp, $PhPO_3H_2$ and $Co(NO_3)_2{\cdot}6H_2O$ in MeCN in the presence of NEt_3 [278], and it displays an irregular structure; two P-atoms from phosphonate ligands and four Co^{II} atoms lie on the vertices of a central trigonal prism, while the remaining four Co^{II} atoms lie above the triangular faces of the prism. Furthermore, the $[Co^{II}_8]$ clusters are not isolated and form H-bonds with the triethylammonium, NEt_3H^+, cations. *Dc* magnetic susceptibility and magnetisation data indicate the presence of competing antiferromagnetic interactions leading to a magnetic spin ground-state, although of

unknown S. In *ac* magnetic susceptibility measurements, a frequency-dependent maximum is found in both the in-phase and out-of-phase susceptibility in the 4–6 K temperature range; the latter being ~1/10 of the former, indicating that only a fraction of the magnetisation is relaxing slowly. Employment of the Arrhenius law gave a very high energy barrier of $U_{\text{eff}} \sim 84$ K with $\tau_0 = 1.8 \times 10^{-12}$ s. Yet, for such a high energy barrier hysteresis loops of appreciable size should be observed at single-crystal magnetisation experiments. Indeed, hysteresis was observed below 4 K, but the loops were rather small and displayed an usual feature; at temperatures lower than 0.5 K the hysteresis narrows and adopts a "butterfly" shape, which was later attributed to single-chain magnetism behaviour [291].

2.4.8 $[Co^{II}_{12}(bm)_{12}(NO_3)(O_2CMe)_6(EtOH)_6](NO_3)_5$: A Dodecanuclear Co^{II} SMM

The reaction between $Co(NO_3)_2{\cdot}6H_2O$, $Co(O_2CMe)_2{\cdot}4H_2O$, Hbm (=1H-benzimidazol-2-yl)methanol) and NEt_3 in ethanol under solvothermal conditions, forms cluster $[Co^{II}_{12}(bm)_{12}(NO_3)(O_2CMe)_6(EtOH)_6](NO_3)_5$ (**281**) in moderate yields [279]. The dodecanuclear cluster consists of three $\{Co^{II}_4O(R)_4\}$ cubane units bridged by a rare μ_6-NO_3^- ligand, while all Co^{II} ions are in distorted octahedral geometry. The cluster behaves as a ferromagnet consisting of 12 $S_{\text{eff}} = ½$ centres, while from *ac* measurements the parameters of $U_{\text{eff}} = 15$ K and $\tau_0 = 1.94 \times 10^{-7}$ s were derived.

2.4.9 $[Co^{II}_8Co^{III}(L)_6](BF_4)_7$: a [3 × 3] Mixed-Valent $Co^{II/III}$ Grid SMM

Cluster $[Co^{II}_8Co^{III}(L)_6](BF_4)_7$ (**282**) is an unusual example of an SMM of any metal type [280]. This cluster which can be made upon the reaction of H_2L (=2,6-bis [5-(2-pyridinyl)-1H-pyrazole-3-yl]pyridine) with $Co(BF_4)_2{\cdot}6H_2O$ and NEt_3 in MeOH/MeCN adopts a grid-like structure (Fig. 29) in which the central cobalt ion has an octahedral coordination geometry, the four cobalt ions on the edges have square-pyramidal coordination environments and the remaining four corner cobalt ions have highly distorted tetrahedral coordination environments. From the eight divalent cobalt centres the ones located at the corners of the grid are high-spin Co^{II} centres ($S = 3/2$), while the ones located at the edges are low-spin Co^{II} centres ($S = 1/2$). Alternatively, cluster **282** can be considered as an eight-membered paramagnetic ring, since the central metal atom is diamagnetic. From magnetic susceptibility data, an $S = 4$ ground-state was found, while under an oscillating *ac* field fully formed out-of-phase peaks are seen in the 2–3 K temperature range. Employment of the Arrhenius law gave $U_{\text{eff}} = 12.7$ K and $\tau_0 = 9.03 \times 10^{-7}$ s.

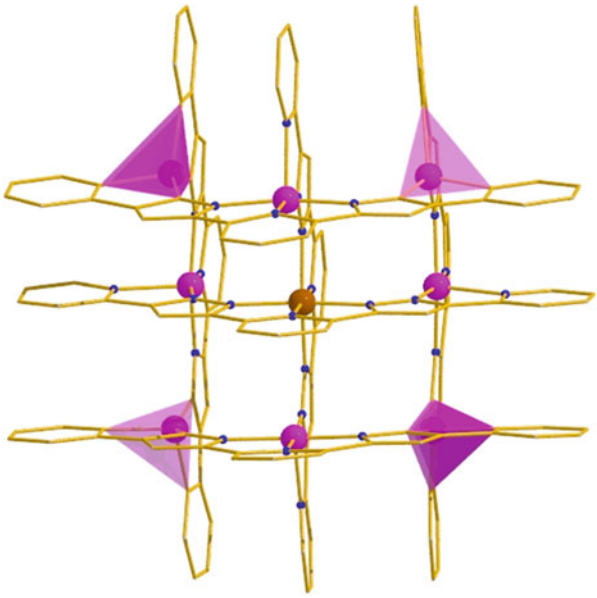

Fig. 29 The molecular structure of the heptacation of **282**. Colour code: Co^{II} = *pink*, Co^{III} = *brown*, N = *blue*, C = *gold*. The high-spin Co^{II} are displayed within their polyhedra

2.4.10 $[Co^{II}_7(bhqe)_3(OH)_2(H_2O)_6]$: A Heptanuclear Dicubane Co^{II} SMM

Cage $[Co^{II}_7(bhqe)_3(OH)_2(H_2O)_6]\cdot 2EtOH\cdot 2H_2O$ (**283**$\cdot 2EtOH\cdot 2H_2O$) was made from the in situ generation of H_4bhqe (=1,2-bis(8-hydroxyquinolin-2-yl)ethane-1,2-diol) from 2-(hydroxymethyl)quinolin-8-ol, in the presence of $Co(NO_3)_2\cdot 6H_2O$ and NEt_3 under solvothermal conditions [281]. The metallic core consists of a cluster of seven cobalt atoms disposed at the corners of two cubes with one shared at one vertex. The cluster possesses an $S' = 7/2$ ground-state due to the ferromagnetic coupling between neighbouring Co^{II} centres which are only bridged by alkoxide groups with an average angle of approximately 95°. Furthermore, the cluster displays fully formed out-of-phase peaks 2–4 K temperature range, while a Debye analysis revealed two activated regimes; above and below 2.7 K, with ${U_{\text{eff}}}^{I} = 21$ K and ${\tau_0}^{I} = 2.7 \times 10^{-7}$ s and ${U_{\text{eff}}}^{2} = 13$ K and ${\tau_0}^{2} = 3.9 \times 10^{-6}$ s, respectively.

2.4.11 $[GuH]_8[Co^{II}_4(cit)_4]$: A Guanidine-Based Cubane Co^{II} SMM

A cluster similar to **269** was reported in 2008 [282, 283]; complex $[GuH]_8[Co^{II}_4(cit)_4]$ (**284**) forms cubane structures which are connected by an extensive hydrogen bonding network involving the guanidinium counterions. Ac susceptibility measurements show fully formed out-of-phase peaks in the 2–4 K temperature range, while employment of the Arrhenius law yielded an energy barrier of $U_{\text{eff}} = 24$ K and $\tau_0 = 3.4 \times 10^{-8}$ s.

2.4.12 $[Co^{II}_{20}(OH)_6(O_2CMe)_{22}(HL)_4(DMF)_2]$: An Icosanuclear Co^{II} SMM

The impressive icosanuclear cluster $[Co^{II}_{20}(OH)_6(O_2CMe)_{22}(HL)_4(DMF)_2]$ (**285**) (HL^{3-}=pyC(O^-)(OH)pyC(O^-)$_2$py) was synthesised upon the reaction of cobalt (II) acetate and dpcp (=2,6-bis(2-pyridylcarbonyl)pyridine) in hot DMF [284]. Its structure consists of a central double cubane with two missing vertices connected to two warped $\{Co_6O_6\}$ rings through two $\{Co_2O_4\}$ moieties, while the dpcp ligand has undergone hydrolysis of both carbonyl groups, in a similar manner that its "parent" ligand dpK (=di-2-pyridyl ketone) has been found to undergo [260–262, 292]. The molecule seems to possess an $S = 4$ ground-state, while frequency-dependent out-of-phase "tails going up" were observed below 4 K.

2.4.13 $[Co^{III}Co^{II}_6(OH)_6(L)_6](ClO_4)_3$: A Disk-Like $Co^{III}Co^{II}_6$ SMM

In 2011, the mixed-valent disc-like $[Co^{III}Co^{II}_6(OH)_6(L)_6](ClO_4)_3 \cdot 1.6\ H_2O$ (**286**·1.6 H_2O) was reported (L^-=the anion of 2-(pyridine-2-yl)pentane-2-ol-4-one) [285]. The cluster was made straightforward from the reaction of Co$(ClO_4)_2 \cdot 6H_2O$, (py)(Me)CO and NBu_4OMe in acetone, under normal laboratory conditions. The molecule adopts a disc-like topology with the trivalent Co atom at the centre of the disc. Alternatively, it describes as a six-member ring consisting of divalent high-spin Co^{II} atoms. From *ac* measurements, it becomes clear that the molecule displays frequency-dependent out-of-phase "tails going up" below ~2.2 K, while single-crystal magnetisation vs. *dc* field studies display the characteristic temperature-dependent and sweep-rate hysteresis loops, albeit with small coercivity.

2.4.14 $[Co^{II}_4(phen)_4Cl_8]$: A Linear Co^{II} SMM

In 2010 the first linear cobalt SMM was reported; cluster $[Co_4(phen)_4Cl_8]$ (**287**) can be made from the reaction of $CoCl_2 \cdot 6H_2O$ and phen (=1,10-phenanthroline) in EtOH under solvothermal conditions [286]. The structure of the molecule consists of a zig-zag backbone of $\{Co(\mu\text{-}Cl)_2Co\}$ planes (Fig. 30). The two central cobalt (II) ions reside in slightly distorted octahedral, whereas the two terminal Co sites are five-coordinated adopting an intermediate between square-pyramidal and trigonal-bipyramidal ($\tau = 0.41$). Under an oscillating *ac* field, the molecule displays frequency-dependent out-of-phase "tails going up" below ~3 K. Since no fully formed out of peaks were observed, the authors used the τ values obtained from fitting the frequency-dependent ac susceptibility data to a generalised Debye model to fit the Arrhenius law, yielding an energy barrier of $U_{eff} = 8.41$ K and $\tau_0 = 5.29 \times 10^{-7}$ s.

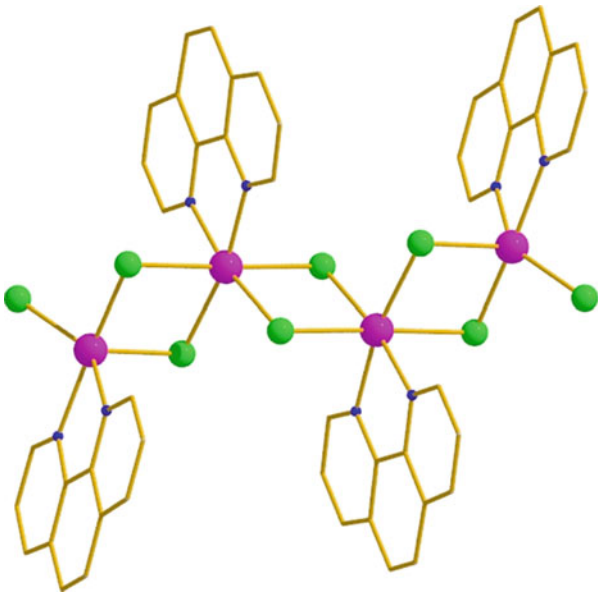

Fig. 30 The molecular structure of **287**

2.4.15 $Na_{22}Rb_6[\{Co^{II}_4(OH)_3PO_4\}_4(A\text{-}\alpha\text{-}PW_9O_{34})_4]$: A POM Phosphonate Co^{II} SMM

Cluster $Na_{22}Rb_6[\{Co^{II}_4(OH)_3PO_4\}_4(A\text{-}\alpha\text{-}PW_9O_{34})_4]\cdot 76H_2O$ (**288**·$76H_2O$) was made in a simple one-step reaction of $CoCl_2\cdot 6H_2O$ with $Na_9[A\text{-}\alpha\text{-}PW_9O_{34}]\cdot 7H_2O$ in aqueous solution at pH 8 and crystallised as the hydrated sodium–rubidium salt [287]. Cluster-POM **288** consists of a central $\{Co^{II}_4O_4\}$ cubane unit which is capped by four tricobalt(II)-substituted Keggin fragments $[\{Co(OH)\}_3(A\text{-}\alpha\text{-}PW_9O_{34})]^{6-}$ and four phosphate linkers. The hexadecametallic cobalt metallic core possesses an $S' = 8$ ground-state, and in addition the molecule shows nicely formed, frequency-dependent out-of-phase peaks under an *ac* field in the 1.8–4 K temperature range. The relaxation data derived from the dynamic behaviour of **288** are $U_{eff} = 26.1$ K and $\tau_0 = 3.5 \times 10^{-8}$ s.

2.5 Nickel SMMs

Nickel SMMs is a relatively small, although growing family of SMMs, given that the first example was reported in 2001. The reasons why Ni(II) ions should be good "ingredients" for constructing SMMs are mainly three: (1) the large ZFS of the Ni^{II} ions in certain coordination geometries [293–296], (2) the super-exchange magnetic interaction between neighbouring nickel centres is often ferromagnetic and (3) the ease with which a large number of polynuclear Ni^{II} clusters can be made. In Table 8 the most representative examples of nickel SMMs are shown.

Table 8 Representative examples of Ni-based SMMs

Formula	S	D (cm^{-1})	U_{eff} (K)	τ_0 (s)	References
$[Ni^{II}_{12}(chp)_{12}(O_2CMe)_{12}(thf)_6(H_2O)_6]$ (**289**)	12	−0.05	9.6	–	[297]
$[Ni^{II}_4(hmp)_4(MeOH)_4Cl_4]$ (**290**)	4	−0.60	–	–	[298, 299]
$[Ni^{II}_4(hmp)_4(EtOH)_4Cl_4]$ (**291**)	4	−0.60	–	–	[298, 299]
$[Ni^{II}_4(hmp)_4(dmb)_4Cl_4]$ (**292**)	4	−0.61	2	–	[298, 299]
$[Ni^{II}_4(H_2thme)_4(MeCN)_4](NO_3)_4$ (**293**)	4	−0.43	–	–	[300]
$[Ni^{II}_4(hmp)_4(chp)_4Cl_4]$ (**294**)	4	−0.59	–	–	[299]
$[Ni^{II}_4(hmp)_4(dmb)_4Br_4]$ (**295**)	4	−0.56	–	–	[299]
$[Ni^{II}_4(^tBuhmp)_4(dmb)_4Cl_4]$ (**296**)	4	−0.68	–	–	[299]
$[Ni^{II}_4Cl_4(HL)_4]$ (**297**)	4	−0.75	–	–	[301]
$[Ni^{II}_4Cl_8(HL)_4]$ (**298**)	4	−0.88	–	–	[302]
$[Ni^{II}_4(OH)_4Cl_4(HL)_4]$ (**299**)	4	−0.63	–	–	[302]
$[Ni^{II}_4(OH)(OMe)_3$ (Hphpz)$_4(MeOH)_3]$ (**300**)	4	−0.263	4.21	–	[303]
$[Ni^{II}_8Na_2(N_3)_{12}(PhCO_2)_2(mpo)_4(Hmpo)_6(EtOAc)_6]$ (**301**)	8	−0.066	4	–	[304]
$Na_2(NMe_4)_{14}$ $[Ni^{II}_{21}(cit)_{12}(OH)_{10}(H_2O)_{10}]$ (**303**)	3	−0.22	2.9	4.0×10^{-7}	[305]
$(NMe_4)_{16}[Ni^{II}_{21}(cit)_{12}(OH)_{10}(H_2O)_{10}]$ (**303a**)	3	−0.22	2.9	4.0×10^{-7}	[305]
$[Ni^{II}_{10}(tmp)_2(N_3)_8(acac)_6(MeOH)_6]$ (**304**)	10	−0.14	14	–	[306, 307]
$[Ni^{II}_3L_3(OH)(Cl)](ClO_4)$ (**305**)	3	−1.324	9.6	3×10^{-8}	[308]
$[Ni^{II}_3L_3(OH)(OCN)](ClO_4)$ (**306**)	3	−1.241	10.5	3×10^{-8}	[308]
$[Ni^{II}_3L_3(OH)(N_3)](ClO_4)$ (**307**)	3	−1.164	10.6	3×10^{-8}	[308]
$[Ni^{II}_8(thme)_2(O_2CPh)_4(Cl)_6(MeCN)_6(H_2O)_2]$ (**308**)	8	−0.22	–	–	[307]
$[Ni^{II}_7(OH)_8(hfac)_6(py)_6]$ (**309**)	6–7	−0.18	–	–	[309]
$[Ni^{II}_5\{pyCOpyC(O)(OMe)py\}_2(O_2CMe)_4(N_3)_4(MeOH)_2]$ (**311**)	5	–	–	–	[310]

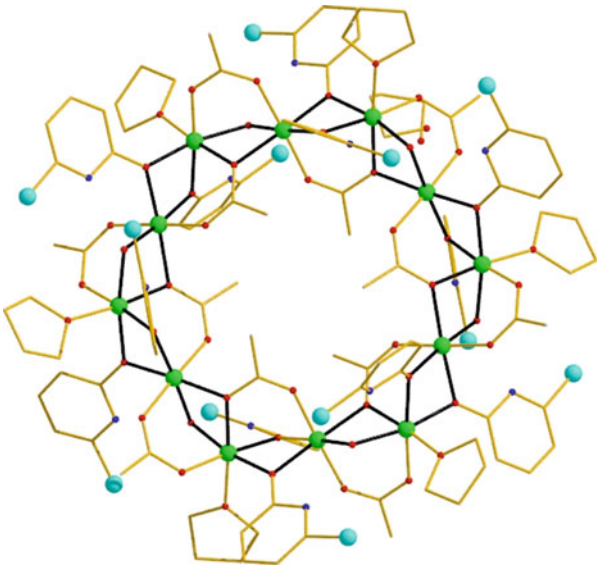

Fig. 31 The molecular structure of **289**

2.5.1 $[Ni^{II}_{12}(chp)_{12}(O_2CMe)_{12}(thf)_6(H_2O)_6]$: The First Ni SMM

Cluster $[Ni^{II}_{12}(chp)_{12}(O_2CMe)_{12}(thf)_6(H_2O)_6]$ (**289**) (Hchp = 6-chloro-2-hydroxypyridine) first reported in 1994 [297] can be synthesised upon the addition of $Ni(OAc)_2{\cdot}4H_2O$ in an excess of Hchp "melt" under nitrogen at 130°C, followed by recrystallisation from tetrahydrofurane. The molecule (Fig. 31) has a crystallographic S_6 symmetry and consists of a closed-chain of intersecting $\{Ni_2(OR_{chp})_2\}$ rings, with each ring being additionally strapped by an acetate ligand. The acetate ligands found can be categorised in two categories: (1) the internal ones pointing towards the centre of the molecule adopting an 3.21 coordination mode and (2) the external ones pointing away from the cavity of the molecule found in a 2.11 manner. The initial magnetic measurements revealed a ferromagnetic interaction between the metal centres of $J = +4.7\ cm^{-1}$ leading to an $S = 12$ ground-state, while following magnetisation studies at 150 mK verified the $S = 12$ ground-state and yielded a ZFS value of $D = -0.07$ K [311]. Dynamic studies of the molecule under an oscillating *ac* field revealed the presence of frequency-dependent out-of-phase in the 0.2–0.7 K temperature range, while single-crystal magnetisation vs. *dc* magnetic field experiments showed temperature-dependent hysteresis loops below ~0.4 K, manifesting the SMM behaviour of the molecule. Finally, an Arrhenius treatment of the data gave an energy barrier of $U_{eff} = 9.6$ K.

2.5.2 $[Ni^{II}_4(hmp)_4(ROH)_4Cl_4]$: Exchange-Bias in $[Ni^{II}_4]$ SMMs

Complexes $[Ni^{II}_4(hmp)_4(ROH)_4Cl_4]$ (R=CH_3, **290**; R=CH_3CH_2, **291**; $(CH_3)_3CCH_2CH_2$, **292**) can be synthesised from the one-pot reaction of $NiCl_2{\cdot}6H_2O$ with Hhmp (=2-hydroxymethylpyridine) in the presence of sodium methoxide in the corresponding alcohol media [298]. The core of each cluster describes a distorted cubane $\{Ni^{II}_4(OR)_4\}$ formed by the Ni^{II} ions and four deprotonated alkoxide groups belonging to the hmp^- ligands. Fitting of the magnetic susceptibility measurements for **292** adopting a 1-*J* model revealed an $S=4$ ground-state for the complex with $J=+5.2$ cm^{-1} and $g=2.02$, while analogous behaviour was displayed by the other two similar clusters. Fitting of the magnetisation data using the full matrix diagonalisation method gave $S=4$, $g=2.16$ and $D=-0.61$ cm^{-1} for **292**, $S=4$, $g=2.12$ and $D=-0.60$ cm^{-1} for **291** and $S=4$, $g=2.09$ and $D=-0.60$ cm^{-1} for **290**.

These results were confirmed by single-crystal HFEPR measurements, which additionally showed a series of more-or-less evenly spaced double peaks, due to either different environments about the $[Ni_4]$ species in the crystal, or the presence of inter-molecular magnetic exchange interactions between neighbouring $[Ni_4]$ species. In order to investigate this hypothesis, single-crystal magnetisation vs. *dc* magnetic field experiments were performed, firstly proving that complexes **290**–**292** are SMMs since they displayed time and temperature-dependent hysteresis loops. In addition, the hysteresis loops show the first step at −0.72 T, which is highly uncommon for SMMs, since the vast majority of SMMs displays the first resonant tunnelling step at zero field. This rare feature is attributed to the presence of an exchange bias present for the complexes affecting the field at which magnetisation tunnelling occurs, as in the case of the $[Mn_4]$ species [227].

A similar cubane-like cluster was reported in 2004; complex $[Ni^{II}_4(H_2thme)_4(MeCN)_4](NO_3)_4{\cdot}1.33NaNO_3$ (**293**·$1.33NaNO_3$) was obtained upon the reaction between $Ni(NO_3)_2{\cdot}6H_2O$, H_3thme and $NaOCH_3$ in methanol followed by extraction in MeCN [300]. The complex has an $S=4$ ground-state, due to the presence of two ferromagnetic exchange interactions, $J_1=+15$ cm^{-1} and $J_2=+8$ cm^{-1}, arising from the small Ni-O_R-Ni angles (below 98°) [312–314]. From magnetisation measurements a *D* value of -0.43 cm^{-1} of the $S=4$ ground-state was derived, while hysteresis loops featuring steps caused by quantum tunnelling of the magnetisation were also observed in single crystal μ-SQUID measurements.

Similar complexes displaying analogous behaviour have been reported throughout the last years, thus, making SMM behaviour not that uncommon for $[Ni_4]$ cubanes; for instance, clusters $[Ni^{II}_4(hmp)_4(chp)_4Cl_4]$ (**294**) (chp = 3-cyclohexyl-1-propanol) and $[Ni^{II}_4(hmp)_4(dmb)_4Br_4]$ (**295**) (dmb = 3,3′-dimethyl-1-butanol), $[Ni^{II}_4(^tBuhmp)_4(dmb)_4Cl_4]$ (**296**) (^tBuhmpH = 4-tert-butyl-2-hydroxy methylpyridine) [299], $[Ni^{II}_4Cl_4(HL)_4]$ (**297**) $\{H_2L=HN(CH_2CH_2\ OH)_2\}$ [301], $[Ni^{II}_4Cl_8(HL)_4]$ (**298**) and $[Ni^{II}_4(OH)_4Cl_4(HL)_4]$ (**299**) (HL = 2-methyl-1-(pyridin-2-yl)-propan-2-ol) [302] and $[Ni^{II}_4(OH)(OMe)_3(Hphpz)_4(MeOH)_3]{\cdot}MeOH$ (**300**·MeOH) (H_2phpz = 3-methyl-5-(2-hydroxyphenyl) pyrazole) [303] have all been found to possess an $S=4$ ground-state displaying SMM behaviour.

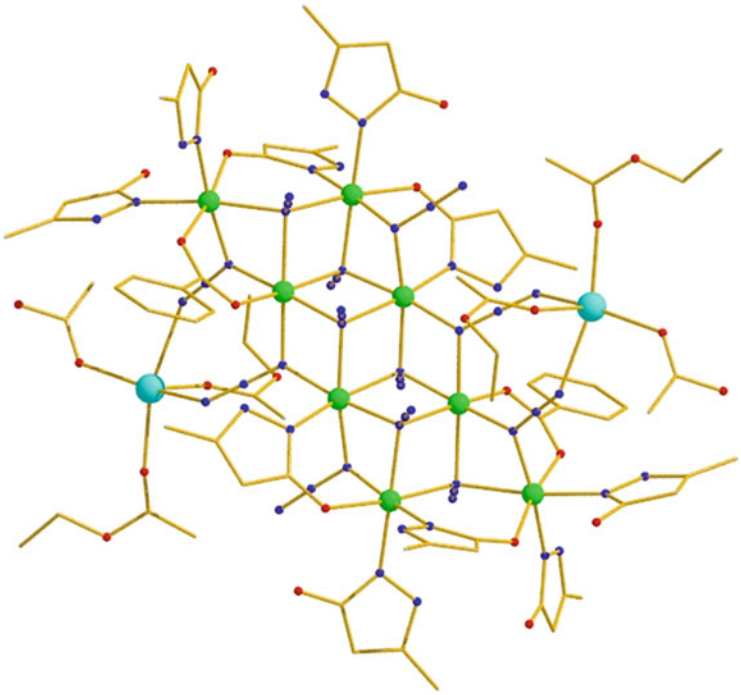

Fig. 32 The molecular structure of **301**

2.5.3 $[Ni^{II}_8Na_2(N_3)_{12}(PhCO_2)_2(mpo)_4(Hmpo)_6(EtOAc)_6]$: An Octanuclear Azide-Bridged Ni^{II} SMM

Cluster $[Ni^{II}_8Na_2(N_3)_{12}(PhCO_2)_2(mpo)_4(Hmpo)_6(EtOAc)_6]$ (**301**) can be synthesised upon the reaction of nickel(II) tetrafluoroborate, Hmpo (=2-methylpyrazolinone) and benzoic acid in methanol, in the presence of NaOMe and excess NaN_3 under reflux for 72 h, followed by recrystallisation from ethyl acetate [304]. This cluster was synthesised in an attempt of substituting the μ_4-OH^- groups found in its parent cluster $Na[Ni^{II}_8Na(OH)_2F_8(^tBuPhCO_2)_8(Hmpo)_8]$ (**302**) with N_3^- ligands in order to enhance its magnetic behaviour. Yet, due to solubility problems for **302**, the formation of **301** came from the in situ reaction of its ingredients, leading to a different octanuclear metallic topology. The eight nickel ions in **301** are arranged as six edge-sharing azide-centred triangles in a 4×2 rod (Fig. 32). The nickel ions are almost coplanar with the sodiums either side of this pseudo plane. From the twelve azide ligands found in **301**, six bridge in an μ_3-end-on fashion, four in an η^2: η^1: μ_3 fashion bridging two nickel centres and one sodium cation, and two in a μ- end-on fashion. Magnetic susceptibility measurements revealed ferromagnetic exchange interactions leading to a ground-state of $S = 8$ with $D = -0.066$ cm^{-1}, while its SMM behaviour was established by the presence of temperature and sweep-rate-dependent hysteresis loops at very low temperatures, with a small estimated energy barrier of $U \sim 4$ K.

2.5.4 $Na_2(NMe_4)_{14}[Ni^{II}_{21}(cit)_{12}(OH)_{10}(H_2O)_{10}]$: A "Citrus" Ni-Based SMM

One year before the cobalt "citrus" SMM (**270**) was reported [272], the nickel "citrus" analogue was isolated [305]. From the reaction of $Ni(OH)_2$ with citric acid monohydrate in the presence of $NMe_4OH{\cdot}5H_2O$ in aqueous solution, complex $Na_2(NMe_4)_{14}$ $[Ni^{II}_{21}(cit)_{12}(OH)_{10}(H_2O)_{10}]$ (**303**) was synthesised. The core of the structure contains a $\{Ni_7(\mu_3\text{-}OH)_6\}$ unit, which resembles the ones found in layers of $Ni(OH)_2$, where the hydroxide ions are hexagonal close-packed and the Ni^{2+} ions occupy the octahedral holes. The remaining metallic centres are attached to the central core via twelve citrate ligands in four different coordination modes, binding three, four, or five metal atoms. In addition, cluster **303** contains two chiral nickel centres and is found in its $\Delta-\Lambda$ isomer, while the cluster $(NMe_4)_{16}[Ni^{II}_{21}(cit)_{12}(OH)_{10}(H_2O)_{10}]$ (**303a**) which contains the enantiomeric pair $\Delta-\Delta+\Lambda-\Lambda$ was also be obtained. Both **303** and **303a** display the same magnetic properties and possess an $S=3$ ground-state, while frequency-dependent out-of-phase peaks are observed below ~0.8 K, suggesting SMM behaviour with an energy barrier of $U_{eff}\sim 2.9$ K and $\tau_0=4.0\times10^{-7}$ s.

2.5.5 $[Ni^{II}_{10}(tmp)_2(N_3)_8(acac)_6(MeOH)_6]$: The Highest U_{eff} For Any Ni SMM

The reaction of $Ni(acac)_2$ with H_3tmp (=1,1,1-tris(hydroxymethyl)propane) and NaN_3 in CH_2Cl_2/MeOH gave cluster $[Ni^{II}_{10}(tmp)_2(N_3)_8(acac)_6(MeOH)_6]{\cdot}H_2O$ (**304**$\cdot H_2O$) [306], which describes a planar decametallic disk held together by a combination of fully deprotonated tmp^{-3} and N_3^- ligands (Fig. 33). All azide ligands are found in an *end-on* fashion bridging two or three metal atoms. The complex has an $S=10$ ground-state, while from magnetisation measurements it seems to have an appreciable magnetic anisotropy, since the various isofield lines do not superimpose. Furthermore, its magnetic dynamic behaviour displays frequency-dependent out-of-phase ac susceptibility signals, "tails going up" below ~2.5 K. Single-crystal magnetisation vs. *dc* field measurements showed hysteresis loops whose coercivity was temperature and sweep-rate dependent (Fig. 34), while an Arrhenius analysis gave $U_{eff}\sim 14$ K, which is the highest energy barrier displayed to date for any Ni SMM.

2.5.6 $[Ni^{II}_3L_3(OH)(Cl)](ClO_4)$: The Smallest Ni^{II} SMM

The latest addition in Ni SMMs is complex $[Ni^{II}_3L_3(OH)(Cl)](ClO_4)$ (**305**) (HL = 2-[(3-dimethylaminopropylimino)methyl]phenol), which was recently reported [308]. The complex can be made upon the reaction of $Ni(ClO_4)_2{\cdot}6H_2O$ with the Schiff base in a methanolic solution followed by the addition of an aqueous

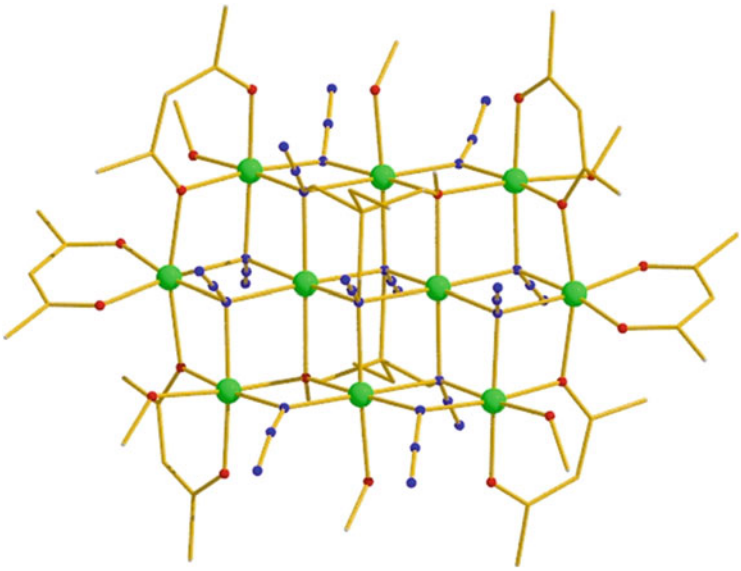

Fig. 33 The molecular structure of **304**

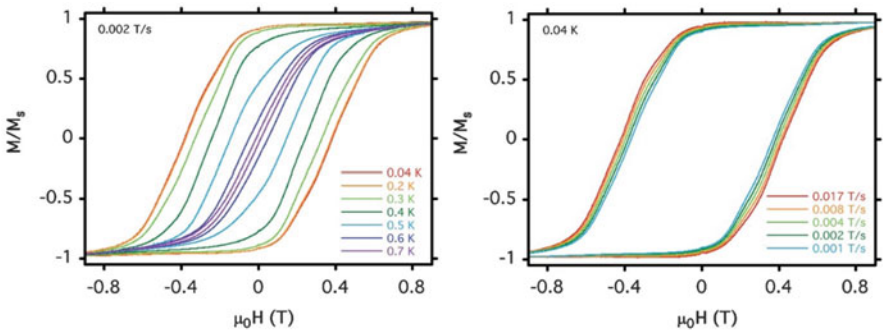

Fig. 34 Single crystal magnetisation (M) versus field (H) hysteresis loops for complex **304** at the indicated field sweep rates and temperatures; the magnetisation is normalised to its saturation value. Reprinted with the permission from [306]. Copyright 2005 Royal Society of Chemistry

solution of NaCl in the presence of NEt_3. Furthermore, complexes $[Ni^{II}{}_3L_3(OH)(OCN)](ClO_4)$ (**306**) and $[Ni^{II}{}_3L_3(OH)(N_3)](ClO_4)$ (**307**) can also be isolated upon replacement of NaCl with NaOCN and NaN_3, respectively. All **305–307** are isomorphous and consist of $[Ni_3L_3(\mu_3\text{-}OH)X]^+$ (X=Cl^-, OCN^-, or $N_3{}^-$) units (Fig. 35). The three Ni^{II} ions form an isosceles triangle and are bridged by one central μ_3-hydroxide group and three μ_3-phenoxide groups belonging to three deprotonated ligands, L^-. Finally, there is an X ligand (X=Cl^-, OCN^-, or $N_3{}^-$) bridging the metal centres at the base of the isosceles triangle in a monoatomic

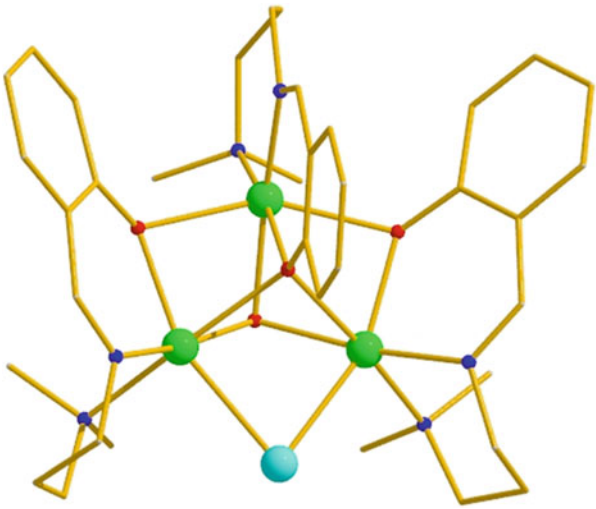

Fig. 35 The molecular structure of the cation of **305**

fashion. The magnetic behaviour of all **305–307** is the same; all possess an $S = 3$ ground-state, while from HFEPR experiments the *zfs* of this ground-state was found $D = -1.324$ cm^{-1} for **305**, $D = -1.241$ cm^{-1} for **306** and $D = -1.164$ cm^{-1} for **307**. Under an oscillating *ac* field at various frequencies, all three clusters display frequency-dependent out-of-phase "tails going up" below ~3 K, while employment of the Arrhenius law gave $U_{\text{eff}} = 9.6$ K with $\tau_0 = 3 \times 10^{-8}$ s for **305**, $U_{\text{eff}} = 10.5$ K with $\tau_0 = 3 \times 10^{-8}$ s for **306** and $U_{\text{eff}} = 10.6$ K with $\tau_0 = 3 \times 10^{-8}$ s for **307**.

2.5.7 $[Ni^{II}_8(thme)_2(O_2CPh)_4(Cl)_6(MeCN)_6(H_2O)_2]\cdot H_2O\cdot 3.5MeCN$: An Octametallic Ni^{II} SMM

The reaction between $NiCl_2\cdot 6H_2O$ with one equivalent of H_3thme (=1,1,1-tris (hydroxymethyl)ethane) and NaO_2CPh in MeCN produced the octanuclear cluster $[Ni^{II}_8(thme)_2(O_2CPh)_4(Cl)_6(MeCN)_6(H_2O)_2]\cdot H_2O\cdot 3.5MeCN$ (**308**·H_2O·MeCN) [307]. The core of the cluster contains a planar $[Ni^{II}_8(\mu_3\text{-}O)_6(\mu\text{-}O)_4(_\mu\text{-}Cl)_4]$ unit of six edge-sharing $[Ni^{II}_3]$ triangles, which is held together by fully deprotonated thme^{3-} and carboxylate ligands. The two triols are located one above and one below the $[Ni^{II}_8]$ plane, each one bridging six Ni^{II} ions in a 6.333 coordination mode. The molecule possesses an $S = 8$ ground-state, while a *zfs* value of $D = -0.22$ cm^{-1} was extracted by magnetisation measurements. Despite the $S = 8$ ground-state and the relatively large and negative D value, the molecule does not display out-of-phase signals; yet, it displays temperature and sweep-rate-dependent hysteresis loops in single-crystal magnetisation vs. *dc* field experiments, *albeit* with small coercivity. In addition, the *S* shape of the hysteresis loops (Fig. 36) indicates the presence of intermolecular interactions between neighbouring $[Ni^{II}_8]$ species, in good agreement with the X-ray crystal structure.

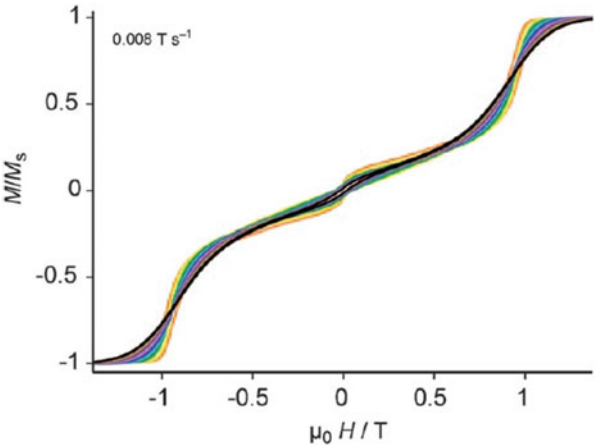

Fig. 36 Single crystal magnetisation (M) versus field (H) hysteresis loops for complex **308** at the indicated field sweep rates in the 1.0 (*black*) – 0.04 K (*red line*) temperature range. Reprinted with the permission from [307]. Copyright 2007 Wiley

2.5.8 $[Ni^{II}_7(OH)_8(hfac)_6(py)_6]$: A Heptanuclear Ni^{II} SMM

Complex $[Ni^{II}_7(OH)_8(hfac)_6(py)_6]\cdot 2py$ (**309**·2py) was prepared upon drying complex $[Ni^{II}_4(hfac)_4(CH_3OH)_4(CH_3O)_4]$ (**310**) at high temperature, followed by treatment in pyridine [309]. The metallic $[Ni^{II}_7(OH)_4]$ core of **309** can be described as the result of the "condensation" of two $\{Ni^{II}_4(OH)_4\}$ cubanes sharing one metallic corner. Magnetisation studies indicate an $S = 7$ ground-state, while, magnetic susceptibility as well as HFEPR measurements suggests a ground-state spin of $S = 6$. Furthermore, from the latter a *zfs* value of $D = -0.18$ cm^{-1} for the $S = 6$ ground-state was found. Finally, for **309** micro-SQUID magnetometry measurements were carried out, showing smooth hysteresis loops below 0.5 K with coercivities which increase upon cooling to reach 200 Oe at 40 mK.

2.5.9 $[Ni^{II}_5\{pyCOpyC(O)(OMe)py\}_2(O_2CMe)_4(N_3)_4(MeOH)_2]$: a pentanuclear Ni^{II} SMM

Cluster $[Ni^{II}_5\{pyCOpyC(O)(OMe)py\}_2(O_2CMe)_4(N_3)_4(MeOH)_2]\cdot 2MeOH\cdot 2.6H_2O$ (**311**·2MeOH·2.6H_2O) was made in an attempt to further investigate the chemistry of the dpcp (=2,6-bis(2-pyridylcarbonyl)pyridine) ligand in Ni^{II} chemistry [310], after the synthesis of the SMM complex $[Co^{II}_{20}(OH)_6(O_2CMe)_{22}(HL)_4(DMF)_2]$ (**284**) (HL^{3-}=pyC(O^-)(OH)pyC(O^-)$_2$py). Its structure describes a helix containing the five six-coordinate Ni^{II} ions, in which each pair of neighbouring Ni^{II} is bridged by *end-on* N_3^-, acetate and dpcp ligands. In addition, only one carbonylic group of the ligand has been alcoholysed to the hemiacetal form, while the other has retained its carbonyl character, thus, leading to the carbonyl-hemiacetal form of the ligand. *Dc* magnetic susceptibility measurements reveal an $S = 5$ ground-state, while from

Table 9 Members of the 3d-4d/5d family of SMMs

Formula	S	D (cm^{-1})	τ_0 (s)	U_{eff} (K)	References
$K[(Me_3tacn)_6Mn^{II}Mo^{III}_6(CN)_{18}](ClO_4)_3$ (**312**)	13/2	−0.33	7×10^{-7}	14.3	[316]
$\{Co^{II}_9[W^{V}(CN)_8]_6{\cdot}(CH_3OH)_{24}\}{\cdot}19H_2O$ (**314**)	21/2	–	7.39×10^{-11}	27.8	[317]
$\{Co^{II}_9[Mo^{V}(CN)_8]_6{\cdot}(CH_3OH)_{24}\}{\cdot}4CH_3OH{\cdot}16H_2O$ (**315**)	21/2	–	–	–	[317]
$(NBu_4)_4[Ni\{ReCl_4(ox)\}_3]$ (**316**)	11/2	−0.46	–	–	[318]
$\{[W^{V}(bpy)(CN)_6]_2[Mn^{III}(L)]_2\}$ (**317**)	5	−0.90	5.1×10^{-12}	32	[319]
$[Ni\{Ni(bpy)(H_2O)\}_8\{W(CN)_8\}_6]$ (**319**)	12	–	1.5×10^{-13}	47.3	[320]
$[\{Mn^{II}Cl\}_4\{Re^{II}(triphos)(CN)_3\}_4]$ (**320**)	8	−0.391	3.25×10^{-7}	12.6	[321]
$[\{Mn^{II}I\}_4\{Re^{II}(triphos)(CN)_3\}_4]$ (**321**)	–	–	–	–	[322]
$\{Ni^{II}[Ni^{II}(tmphen)(MeOH)]_6[Ni(H_2O)_3]_2[CN]_{30}[W^{V}(CN)_3]_6\}$ (**322**)	12	−0.039	–	–	[323]
$[Co^{II}_9\{Re^{V}(CN)_8\}\{Mo^{V}(CN)_8\}_5{\cdot}(CH_3OH)_{24}]$ (**323**)	20	–	–	–	[324]
$[Co^{II}_9\{Re^{V}(CN)_8\}\{W^{V}(CN)_8\}_5{\cdot}(CH_3OH)_{24}]$ (**324**)	20	–	–	–	[324]
$[(PY5Me_2)_4Mn^{II}_4Re^{IV}(CN)_7](PF_6)_5$ (**325**)	21/2	−0.44	2.4×10^{-8}	47.3	[325]
(Net_4) $[Mn^{III}_2(5\text{-}Brsalen)_2(MeO\text{-}H)_2Os^{III}(CN)_6]$ (**326**)	–	–	5.0×10^{-7}	19	[326]
$[(PY5Me_2)_4Ni^{II}_4Re^{IV}(CN)_7](PF_6)_5$ (**327**)	9/2	−0.93	1.4×10^{-7}	24.4	[327]
$[(PY5Me_2)_4Cu^{II}_4Re(CN)_7](PF_6)_5$ (**328**)	5/2	−1.33	–	–	[327]
$[(Mo^{IV}(CN)_8)_2(Cu^{II}LTb^{III})_4)][Mo^{IV}(CN)_8]$ (**329**)	–	–	2.12×10^{-6}	19.25	[328]
$[L^{Me2}Ni^{II}Tb^{III}\{W^{V}(CN)_8\}]$ (**330**)	–	–	4.5×10^{-7}	15.3	[329]

magnetisation experiments the D value was found -3.2 cm^{-1}. Ac measurements display fully formed out-of-phase signals in the 3.3–5 K temperature range, while an Arrhenius analysis of the data revealed two magnetisation relaxation processes.

3 3d-4d/5d SMMs

Another successful, if unusual, way of synthesising SMMs is the employment of both 3d and 4d (or 5d) metals. This recently employed strategy takes advantage of the inherent properties of the heavier 4d and 5d metal atoms, such as the diffuse nature of their d-orbitals that leads to stronger magnetic exchange interactions between the metallic centres, their spin–orbit coupling rising magnetic anisotropy, and their diverse redox properties. An excellent review highlighting the use of such species in the field of molecular magnetism was published only two years ago [315]. In this section we highlight some representative examples of 3d-4d/5d SMMs, while in Table 9 all such species reported to date are presented.

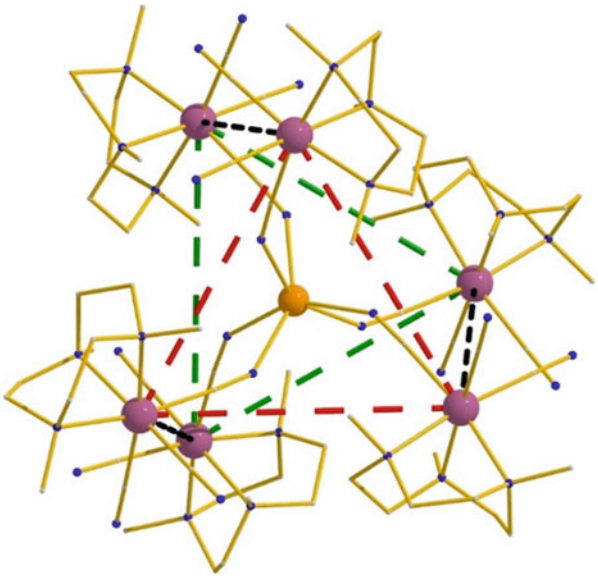

Fig. 37 The molecular structure of $K[(Me_3tacn)_6Mn^{II}Mo^{III}{}_6(CN)_{18}](ClO_4)_3$ (**312**). Hydrogen atoms are omitted for clarity. Colour code: Mn^{II} = *orange*, Mo^{III} = *plum*, N = *blue*, C = *gold*

3.1 $K[(Me_3tacn)_6Mn^{II}Mo^{III}{}_6(CN)_{18}](ClO_4)_3$: the initial example of a 3d-4d SMM

Cluster $K[(Me_3tacn)_6Mn^{II}Mo^{III}{}_6(CN)_{18}](ClO_4)_3$ (**312**, Me_3tacn=*N*,*N*′,*N*″trimethyl-1,4,7-triaza cyclononane) was prepared upon the deliberate "substitution" of the central Cr^{III} centre in the $[(Me_3tacn)_6Mn^{II}Cr^{III}{}_6(CN)_{18}]^{2+}$ cluster (**313**) [330] with Mo^{III} [316]. The structure of **312** consists of a central Mn^{II} ion encapsulated within a distorted trigonal prism of six Mo^{III} centres via six cyanide ligands (Fig. 37). *Dc* magnetic susceptibility studies revealed an $S = 13/2$ ground-state for the cluster due to the presence of antiferromagnetic exchange interactions between the central Mn^{II} atom and the peripheral Mo^{III} centres ($S_{Mo(III)} = 3/2$). Furthermore, the ZFS value of the $S = 13/2$ ground-state was calculated $D = -0.33$ cm^{-1} from reduced magnetisation measurements. Given the S and D values of **312**, *ac* magnetic susceptibility experiments were carried out showing the presence of fully formed out-of-phase peaks, in the lower temperature limit of the instrument, while the Arrhenius analysis yielded a magnetisation energy barrier of $U_{eff} = 14.3$ K with $\tau_0 = 7 \times 10^{-7}$ s.

3.2 $\{Co^{II}_9M^{V}_6\}$ (M=W, Mo) SMMs

Three years after the inaugural example of a 3d-4d SMM, complexes $\{Co^{II}_9[W^{V}(CN)_8]_6\cdot(MeOH)_{24}\}\cdot 19H_2O$ (**314**) and $\{Co^{II}_9[Mo^{V}(CN)_8]_6\cdot(MeOH)_{24}\}\cdot 4MeOH\cdot 16H_2O$ (**315**) were reported [317]. Both clusters are isostructural and describe a six-capped body-centred cube in which two of the six $\{M^{V}(CN)_8\}^{3-}$ units ions adopt bicapped trigonal prismatic geometry, while the remaining four favour dodecahedral geometry. Each $\{M^{V}(CN)_8\}^{3-}$ unit connects to Co^{II} ions via five bridging CN^{-} ligands, with eight Co^{II} centres located at the corners of the cube and the ninth occupying its centre. Cluster **314** seems to possess an $S = 21/2$ ground-state, assuming $S_{Co(II)} = 3/2$, and in addition it displays fully formed *ac* out-of-phase, χ_M'', peaks in the 2.0–2.5 K temperature range. Employing an Arrhenius analysis of the *ac* data yielded $U_{eff} = 27.8$ K with a very small $\tau_0 = 7.39 \times 10^{-11}$ s for **314**. Analogous analysis for **315** was not possible, since there were no out-of-phase peaks under an *ac* oscillating field.

3.3 $(NBu_4)_4[Ni\{ReCl_4(ox)\}_3]$: A Tetranuclear $[Ni^{II}Re^{IV}_3]$ SMM

In 2006, cluster $(NBu_4)_4[Ni\{ReCl_4(ox)\}_3]$ (**316**, ox=oxalate(−2)) was synthesised upon the reaction of $Ni(NO_3)_2\cdot 6H_2O$ with $(NBu_4)_2[ReCl_4(ox)]$ [5]. Its structure describes a "star-like" molecule in which the central Ni^{II} atom is connected to the three peripheral Re^{IV} atoms via three η^1: η^1: η^1: η^1: μ oxalate(−2) ligands. The *dc* magnetic susceptibility data were fitted to a model including isotropic exchange interactions, ZFS and Zeeman effects, to produce a ferromagnetic interaction between the central Ni atom and the three Re^{IV} atoms, yielding $S = 11/2$ and $D = -0.46$ cm^{-1}. Furthermore, magnetisation data confirmed the negative D value (-0.50 cm^{-1}). Frequency-dependent out-of-phase *ac* signals were observed, *albeit* without reaching their maxima values in the absence of an external *dc* field. However, applying a *dc* magnetic field (500, 1000 and 2000 G) leads to the full formation of the χ_M'' peaks in the 2.0–2.6 K temperature range. Furthermore, single-crystal magnetisation vs. field measurements revealed sweep-rate and temperature-dependent hysteresis loops verifying its SMM character (Fig. 38).

3.4 $\{[W^{V}(bpy)(CN)_6]_2[Mn^{III}(L)]_2\}\cdot 3H_2O$: a $[W^{V}_2Mn^{III}_2]$ SMM

Cluster $\{[W^{V}(bpy)(CN)_6]_2[Mn^{III}(L)]_2\}\cdot 3H_2O$ (**317**·$3H_2O$, L=*N*,*N*′-bis(2-hydroxy acetophenylidene)-1,2-diaminopropane] was prepared upon the reaction of $(AsPh_4)[W(CN)_6(bpy)]_5$ with $[Mn(L)(H_2O)]_2(ClO_4)_2\cdot H_2O$ (**318**·H_2O) [331] in

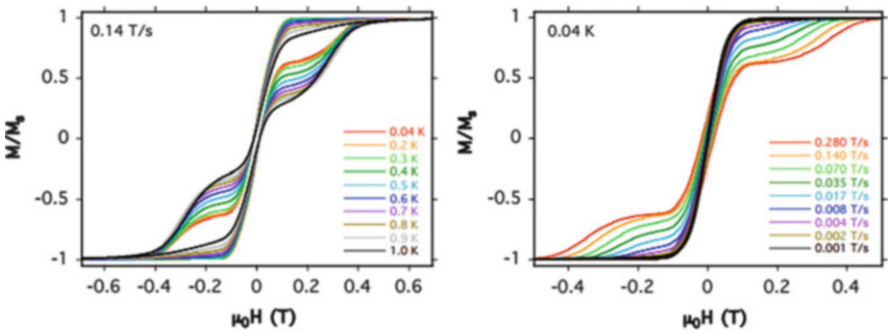

Fig. 38 Temperature-dependent (*left*) and sweep-rate-dependent (*right*) hysteresis loops for **316**. Reprinted with the permission from [318]. Copyright 2006 American Chemical Society

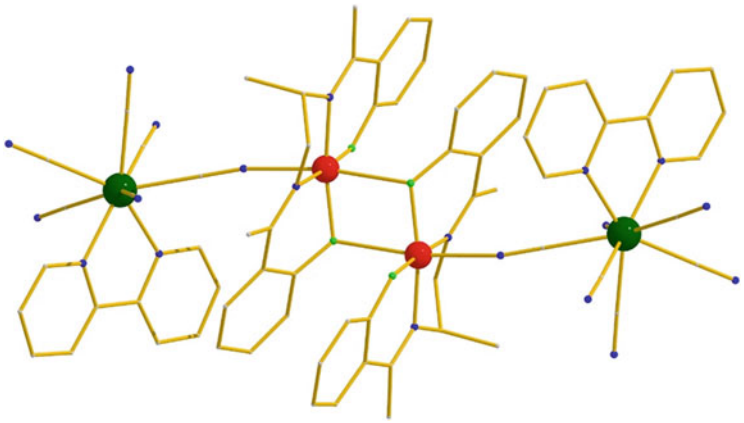

Fig. 39 The molecular structure of $\{[W^{V}(bpy)(CN)_6]_2[Mn^{III}(L)]_2\}\cdot 3H_2O$ (**317**·$3H_2O$). Hydrogen atoms are omitted for clarity

H_2O/MeCN [319]. The structure of **317** (Fig. 39) contains a central bis-phenoxide bridged $\{Mn^{III}{}_2\}$ dimer which is further connected to two $\{W^{V}(bpy)\}^{5+}$ units, one at each side, via two bridging cyanide ligands. The cluster was found to display ferromagnetic exchange interactions between the W^{V}-Mn^{III} pairs ($J_1 = +0.83$ cm^{-1}), as well as within the central $\{Mn^{III}{}_2\}$ unit ($J_2 = +0.95$ cm^{-1}), leading to an $S = 5$ ground-state ($S_{W(V)} = ½$) for the complex. The cluster displays fully formed out-of-phase peaks under an oscillating magnetic field, in the 2.0–2.4 K temperature range, while an Arrhenius analysis gave $U_{eff} = 32$ K with a very small τ_0 value of 5.1×10^{-12} s.

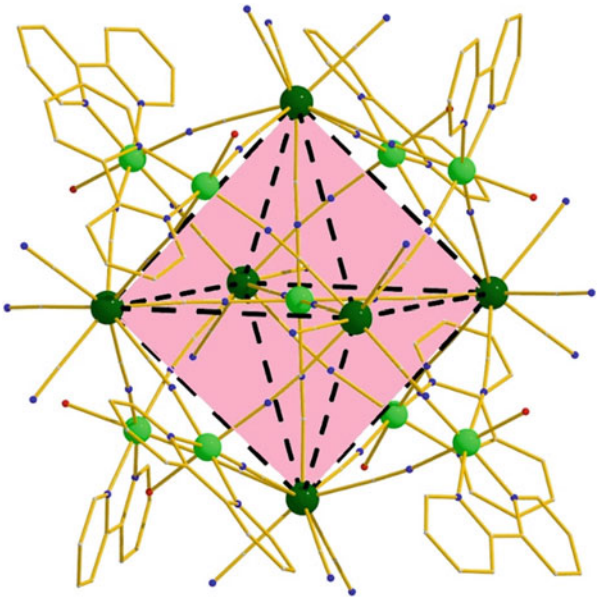

Fig. 40 The molecular structure of **319**. Hydrogen atoms are omitted for clarity. Colour code: Ni^{II} = *green*, W^{V} = *dark-green*, N = *blue*, O = *red*, C = *gold*

3.5 *[Ni{Ni(bpy)(H_2O)}$_8${W(CN)$_8$}$_6$]: A Six-Capped Body-Centred Cube [$Ni^{II}_9W^{V}_6$] SMM*

Complex [Ni{Ni(bpy)(H_2O)}$_8${W(CN)$_8$}$_6$]·23H_2O (**319**·23H_2O), reported in 2006, was synthesised upon reacting $(Bu_4N)_3$[W(CN)$_8$] with [Ni(bpy)(H_2O)$_4$]·(SO_4)·2H_2O [332] in H_2O/MeCN [320]. Its structure consists of a central Ni^{II} ion located at the centre of a {W^{V}_6} octahedron (Fig. 40), which is further face-capped by eight Ni^{II} atoms, resulting in an overall six-capped body-centred cube structure. The molecule possesses a ferromagnetic $S = 12$ ground-state, while it displays frequency and temperature-dependent fully formed out-of-phase peaks under an oscillating magnetic field, in the 2.5–3.0 K temperature range. Employment of the Arrhenius law yielded $U_{eff} = 47.3$ K with an extremely small value of $\tau_0 = 1.5 \times 10^{-13}$ s.

3.6 *[{Mn^{II}Cl}$_4${Re^{II}(triphos)(CN)$_3$}$_4$]: A [$Mn^{II}_2Re^{II}_2$] Cube SMM*

In 2004 Schelter et al. reported the synthesis of complex [{Mn^{II}Cl}$_4${Re^{II}(triphos)(CN)$_3$}$_4$] (**320**, triphos = 1,1,1-tris(diphenylphosphine ethyl)methane) upon the reaction of $MnCl_2$ with [Et_4N][Re(triphos)(CN)$_3$] [333] in MeCN/$(Me)_2CO$ [321]. The structure of **320** consists of a distorted cube with alternating corners of Mn^{II} and Re^{II} centres bridged by cyanide ligands. Each Mn^{II} is four-coordinate

adopting distorted tetrahedral geometry, while all Re^{II} centres are six-coordinate adopting octahedral geometry. *Dc* magnetic susceptibility measurements reveal a spin ground-state of $S' = 8$, but this should be taken with caution since the Re^{II} centres exhibit an orbital ^2E ground state and, as such, cannot be described using the classical spin, *S*. Following *ac* magnetic susceptibility measurements displayed out-of-phase peaks under an *ac* oscillating magnetic field in the 5–25 kHz frequency, in the 2.5–3.0 K temperature range, while an Arrhenius analysis gave $U_{eff} = 12.6$ K with $\tau_0 = 3.25 \times 10^{-7}$ s. Compound **320** was the first SMM characterised containing a 5d metal centre. The iodide analogue, $[\{Mn^{II}I\}_4\{Re^{II}(triphos)(CN)_3\}_4]$ (**321**) is also an SMM, albeit at lower temperatures (<1.8 K) [322].

3.7 *{Ni^{II}[Ni^{II}(tmphen)(MeOH)]$_6$[Ni(H$_2$O)$_3$]$_2$[CN]$_{30}$[W^{V}(CN)$_3$]$_6$}: A Pentadecanuclear [Ni$^{II}_9$W$^{V}_6$] SMM*

The impressive pentadecanuclear cluster $\{Ni^{II}[Ni^{II}(tmphen)(MeOH)]_6[Ni(H_2O)_3]_2[CN]_{30}[W^{V}(CN)_3]_6\}$ (**322**) is the second example of $[Ni^{II}_9W^{V}_6]$ SMM [323], with **319** the first. Complex **322** contains a six-capped body-centred cube arrangement as in **319**, with a central Ni^{II} ion encapsulated within a $\{W^{V}_6\}$ octahedron, which is further face-capped by eight Ni^{II} atoms. All Ni^{II} centres adopt pseudo-octahedral geometry, while the W^{V} atoms are eight-coordinate adopting bicapped trigonal prismatic geometry. The $S = 12$ ground-state was realised in terms of ferromagnetic interactions between the Ni^{II}-W^{V} pairs with $J = +12$ cm^{-1}. Furthermore, the $S = 12$ ground-state was verified by reduced magnetisation measurements that in addition yielded the *zfs* value of $D = -0.039$ cm^{-1}. The SMM character of **322** was confirmed by single-crystal magnetisation vs. field measurements at a micro-SQUID device, revealing temperature and sweep-rate-dependent hysteresis loops below 1 K (Fig. 41).

4 Lanthanide-Based SMMs

One of the most active areas in research into SMMs involves lanthanide complexes. Such species consist of either mixed-metal 3d-4f clusters or purely 4f-based complexes. The introduction of 4f centres in the field of SMM was based mainly on two fundamental lanthanide properties: (1) their large magnetic moment, since they can provide up to seven unpaired electrons in the metallic cluster and (2) the large spin–orbit coupling induced magnetic anisotropy. Both of these properties provide a solid keystone for the construction of magnetic nanoclusters, while the last few years many detailed reviews have focused on the use of lanthanide centres for the preparation of SMMs [64, 334–336].

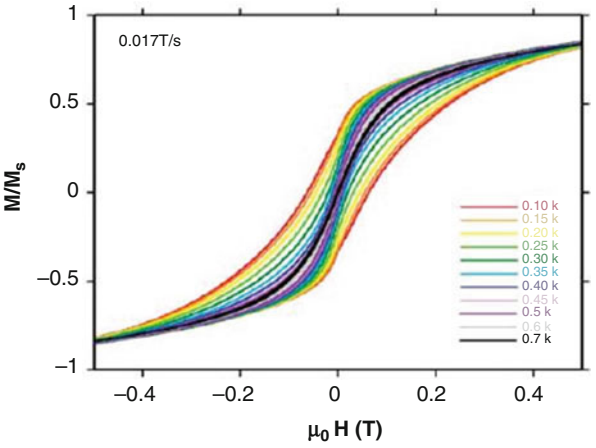

Fig. 41 Temperature-dependent magnetisation hysteresis loops for **322**. Reprinted with the permission from [323]. Copyright 2009 Royal Society of Chemistry

4.1 3d-4f SMMs

4.1.1 $[Cu^{II}Tb^{III}L(hfac)_2]_2$: The First 3d-4f SMM

The first 3d-4f SMM was complex $[Cu^{II}Tb^{III}L(hfac)_2]_2$ (**331**) (H_3L = 1-(2-hydroxybenzamido)-2-(2-hydroxy-3-methoxy-benzylideneamino)-ethane), reported in 2004 [337, 338]. Its structure describes a "cyclic" molecule, in which alternating square-planar Cu^{II} centres and $[Tb^{III}(hfac)_2]^+$ species are bridged by two trianions, L^{3-}. The complex displays frequency-dependent out-of-phase, χ_M'', peaks, in the 2.0–2.8 K temperature range, establishing its SMM behaviour with $U_{eff} = 21$ K and $\tau_0 = 2.7 \times 10^{-8}$ s. Furthermore, in order for the authors to investigate whether the SMM character was solely lanthanide-based or not, they synthesised the Ni^{II} analogue, cluster $[Ni^{II}Tb^{III}L(hfac)_2]_2$ (**332**), with diamagnetic square-planar Ni^{II} centres replacing the square-planar Cu^{II} centres in **331**, which was not found to display SMM behaviour, thus establishing the participation of the 3d metal centre in the SMM characteristic feature of **331**. In addition, the authors characterised the Dy^{III} analogue, cluster $[Cu^{II}Dy^{III}L(hfac)_2]_2$ (**333**), which also displays frequency-dependent out-of-phase peaks, *albeit* at lower temperatures. This seminal work, established the three main advantages of 3d-4f clusters as SMM candidates: "(1) the d-f polynuclear molecule can be easily synthesised by the assembly reaction of the d-component exhibiting a donor coordination ability and the f-component exhibiting an acceptor coordination ability, (2) the high-spin ground state can be generated by a smaller number of metal ions than the d polynuclear complex and (3) the molecular magnetic anisotropy is easily derived from the f-component". Indeed, this work led to an incredible growth and characterisation of numerous 3d-4f SMMs, and in this section we will try to highlight some representative examples, while in Table 10 most species reported to date are presented.

Table 10 Members of the 3d-4f family of SMMs

Formula	τ_0 (s)	U_{eff} (K)	References
$[Cu^{II}Tb^{III}L(hfac)_2]_2$ (**331**)	2.7×10^{-8}	21	[337, 338]
$[Dy^{III}_6Mn_6(H_2shi)_4(Hshi)_2(shi)_{10}(CH_3OH)_{10}(H_2O)_2]$ (**334**)	–	–	[339]
$[L^7Cu^{II}Tb^{III}(NO_3)_2(DMF)]_2$ (**335**)	1×10^{-5}	4.2	[340]
$[L^4Cu^{II}Tb^{III}(NO_3)_2]_2$ (**336**)	–	–	[340]
$[Fe^{III}_2Ho^{III}_2(OH)_2(teaH)_2(O_2CPh)_4(NO_3)_2]$ (**337**)	–	–	[341]
$[Fe^{III}_2Dy^{III}_2(OH)_2(teaH)_2(O_2CPh)_6]$ (**338**)	–	–	[341]
$[Mn_5Tb^{III}_4O_6(mdea)_2(mdeaH)_2(piv)_6(NO_3)_4(H_2O)_2]$ (**340**)	–	–	[342]
$[Mn_5Dy^{III}_4O_6(mdea)_2(mdeaH)_2(piv)_6(NO_3)_4(H_2O)_2]$ (**341**)	3.0×10^{-9}	38.6	[342]
$[Mn_5Ho^{III}_4O_6(mdea)_2(mdeaH)_2(piv)_6(NO_3)_4(H_2O)_2]$ (**342**)	–	–	[342]
$[Mn_5Y^{III}_4O_6(mdea)_2$ $(mdeaH)_2(piv)_6(NO_3)_4(H_2O)_2]$ (**343**)	–	–	[342]
$[\{Dy^{III}(hfac)_3\}_2\{Ni(dpk)_2(phen)\}]$ (**344**)	–	–	[343]
$[\{Dy^{III}(hfac)_3\}_2\{Ni(dpk)_2(py)_2\}]$ (**345**)	–	–	[343]
$[\{Dy^{III}(hfac)_3\}_2\{Cu(dpk)_2\}]$ (**346**)	1.1×10^{-7}	47	[344]
$[Mn^{III}_9Mn^{II}_2Gd^{III}_2O_8(OH)_2(piv)_{10.6}(fca)_{6.4}(NO_3)_2(H_2O)]$ (**347**)	2×10^{-12}	18.4	[345]
$[LCuDy^{III}(hfac)_2(DMF)]_2$ (**348**)	1.7×10^{-7}	14.7	[346]
$[LCuTb^{III}(hfac)_2(DMF)]_2$ (**349**)	–	–	[346]
$[Dy^{III}_3Cu^{II}_6L_6(OH)_6(H_2O)_{10}]Cl_2$ (**350**)	1.5×10^{-7}	25	[347]
$[Dy^{III}_3Fe^{III}_7O_2(OH)_2(mdea)_7(O_2CPh)_4(N_3)_6]$ (**351**)	1.3×10^{-7}	30.9	[348]
$[Mn_5Tb^{III}_6O_4(OH)_4(OMe)_2(bemp)_2(OAc)_{10}(NO_3)_4]$ (**352**)	4.76×10^{-8}	17.8	[349]
$[\{(S)P[N(Me)N{=}CH\text{-}C_6H_3\text{-}2\text{-}O\text{-}3\text{-}OMe]_3\}_2Co^{II}_2Tb^{III}]$ NO_3 (**354**)	5.5×10^{-6}	18.9	[350]
$[\{(S)P[N(Me)N{=}CH\text{-}C_6H_3\text{-}2\text{-}O\text{-}3\text{-}OMe]_3\}_2Co^{II}_2Dy^{III}]$ NO_3 (**355**)	5.1×10^{-6}	14.2	[350]
$[\{(S)P[N(Me)N{=}CH\text{-}C_6H_3\text{-}2\text{-}O\text{-}3\text{-}OMe]_3\}_2Co^{II}_2Ho^{III}]$ NO_3 (**356**)	13×10^{-5}	8	[350]
$[Mn^{III}_{12}Mn^{II}_6Dy^{III}O_8Cl_{6.5}(N_3)_{1.5}(HL)_{12}(MeOH)_6]Cl_3$ (**357**)	–	–	[351]
$[Mn_{12}Gd^{III}O_9(O_2CPh)_{18}(O_2CH)(NO_3)(HO_2CPh)]$ (**359**)	2.4×10^{-12}	15.9	[352]
$[Zn_2Dy^{III}_3(m\text{-}salen)_3(N_3)_5(OH)_2]$ (**360**)	3.3×10^{-7}	13.4	[353]
$[Mn^{III}_4Sm^{III}_4(^n$Bu-dea$)_4(HCOO)_4(OMe)_4(O_2CE$ $t)_4(O_2CEt)_4(MeOH)_4]$ (**361**)	–	–	[354]
$[Mn^{III}_4Tb^{III}_4(^n$Bu-dea$)_4(HCOO)_4(OMe)_4(O_2CE$ $t)_4(O_2CEt)_4(MeOH)_4]$ (**362**)	–	–	[354]
$[Mn^{III}_4Dy^{III}_4(^n$Bu-dea$)_4(HCOO)_4(OMe)_4(O_2CE$-$t)_4(O_2CEt)_4(MeOH)_4]$ (**363**)	3.5×10^{-7}	12	[354]
$[Cr^{III}_4Dy^{III}_4(OH)_4(N_3)_4(mdea)_4(piv)_4]$ (**365**)	1.9×10^{-7}	15	[355]
$[Mn^{III}_6O_3(sao)_6(CH_3O)_6La^{III}_2(CH_3OH)_4(H_2O)_2]$ (**366**)	5.8×10^{-10}	32.8	[356]
$[Mn^{III}_6O_3(sao)_6(CH_3O)_6Tb^{III}_2(CH_3OH)_4(H_2O)_2]$ (**367**)	1.6×10^{-10}	103	[356]
$[Dy^{III}_2Co^{III}_2(OMe)_2(teaH)_2(O_2CPh)_4(MeOH)_4](NO_3)_2$ (**368**)	5.64×10^{-8}	88.8	[357]
$[Fe_4Dy^{III}_4(teaH)_8(N_3)_8(H_2O)]$ (**369**)	2.0×10^{-9}	30.5	[358]
$[Mn_4Tb^{III}_2O_2(O_2CBu^t)_6(edteH_2)_2(NO_3)_2]$ (**370**)	1.4×10^{-11}	20.3	[359]
$[Cu^{II}_5Tb^{III}_4O_2$ $(teaH)_4\{O_2CC(CH_3)_3\}_2(NO_3)_4(OMe)_4]$ (**371**)	9×10^{-6}	11.9	[360]

(continued)

Table 10 (continued)

Formula	τ_0 (s)	U_{eff} (K)	References
$[Cu^{II}_5Dy^{III}_4O_2$ (teaH)$_4\{O_2CC(CH_3)_3\}_2(NO_3)_4(OMe)_4]$ (**372**)	1.3×10^{-5}	7	[360]
$[Cu^{II}_5Ho^{III}_4O_2$ (teaH)$_4\{O_2CC(CH_3)_3\}_2(NO_3)_4(OMe)_4]$ (**373**)	3.2×10^{-6}	10	[360]
$[Ni^{II}_2Dy^{III}_3(LH)_4]Cl$ (**374**)	5.9×10^{-7}/ 2.3×10^{-8}	85/53.5	[361]
$[Dy^{III}_2Co^{III}_2(OMe)_2$(teaH)$_2$(acac)$_4(NO_3)_2]$ (**375**)	8.1×10^{-6}	27	[362]
$[Dy^{III}_2Co^{III}_2(OH)_2$(teaH)$_2$(acac)$_4(NO_3)_2]$ (**376**)	7.4×10^{-6}	28	[362]
$[Dy^{III}_2Co^{III}_2(OMe)_2$(mdea)$_2$(acac)$_4(NO_3)_2]$ (**377**)	2.6×10^{-6}	38	[362]
$[Mn^{III}_2$ Nd^{III}_2(bdea)$_2$(bdeaH)$_2$(piv)$_6]$ (**378**)	1.4×10^{-6}	10	[363]
$[Ni^{II}_3Dy^{III}\{$(py)$_2$C(H)O$\}_6](ClO_4)_3$ (**379**)	–	–	[364]
$[\{$(S)P[N(Me)N=CH-C_6H_3-2-O-3-OMe]$_3\}_2Co^{II}_2Gd^{III}]$ (NO_3) (**380**)	1.5×10^{-7}	27.4	[365]
$[Mn^{III}_2Dy^{III}_2(LH)_4(OAc)_2](NO_3)_2$ (**381**)	8.3×10^{-9}	24	[366]
$[Mn^{III}_2Tb^{III}_2(LH)_4(OAc)_2](NO_3)_2$ (**382**)	1.63×10^{-8}	48.5	[366]
$[Dy^{III}_3Ni^{II}_5L_5$(PhCOO)$_3$(OH)$_5$(OCH$_3$)(CH$_3$OH)$_4$(H$_2$O)] (**383**)	–	–	[367]

4.1.2 $[Dy_6Mn_6(H_2shi)_4(Hshi)_{10}(CH_3OH)_{10}(H_2O)_2]$: A $[Dy^{III}_6Mn^{IV}_4Mn^{III}_2]$ SMM

The second 3d-4f SMM synthesised was $[Dy_6Mn_6(H_2shi)_4(Hshi)_2(shi)_{10}(MeOH)_{10}(H_2O)_2]\cdot 9MeOH\cdot 8H_2O$ (**334**·9MeOH·8H$_2$O, H$_3$shi=salicylhydroxamic acid), reported in 2006 upon the reaction of $Dy(NO_3)_3\cdot 5H_2O$, $Mn(OAc)_2\cdot 4H_2O$ and salicylhydroxamic acid in MeOH [339]. Its structure contains a nearly planar hexagon of Dy^{III} centres attached to a $[Mn^{III}_2Mn^{IV}]$ trimer on either end. The cluster displays frequency-dependent out-of-phase peaks under an *ac* oscillating field, although not fully formed, suggesting the presence of SMM behaviour. Furthermore, the authors synthesised both the Gd^{III} and the Tb^{III} analogues, which did not show hysteresis features, thus proving the role and the contribution of the Dy^{III} centres in the SMM behaviour of **334**.

4.1.3 Two Tetranuclear $[Cu^{II}_2Tb^{III}_2]$ SMMs

In 2006, the two tetranuclear clusters $[L^7Cu^{II}Tb^{III}(NO_3)_2(DMF)]_2$ (**335**, H_3L^7=the Schiff base resulting from the condensation of *N*-(2-aminoethyl)-2-hydroxy-3-methoxybenzamide with salicylaldehyde), and $[L^4Cu^{II}Tb^{III}(NO_3)_2]_2\cdot 2MeOH$ (**336**, H_3L^4=the Schiff base resulting from the condensation of *N*-(2-amino-2-methylpropyl)-2-hydroxy-3-methoxybenzamide with orthovanillin) were reported [340]. Both clusters display similar structures with heterodimeric Cu-Tb units

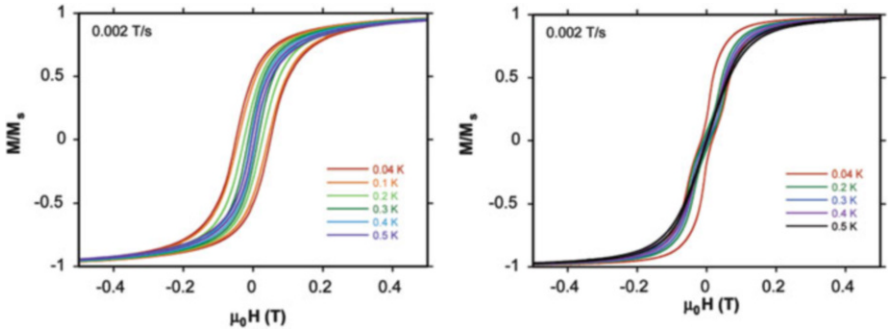

Fig. 42 Temperature-dependent magnetisation hysteresis loops for complexes **335** (*left*) and **336** (*right*). Reprinted with the permission from [340]. Copyright 2006 American Chemical Society

assembled through the oxygen atoms of the ligands' amido groups to form a double {Cu-N-C-O-Tb} bridge, which leads to the formation of the tetranuclear species. Both complexes display typical temperature and sweep-rate-dependent hysteresis loops (Fig. 42), thus establishing their SMM behaviour. Furthermore, for complex **335** the SMM parameters $U_{\text{eff}} = 4.2$ K and $\tau_0 = 1 \times 10^{-5}$ s were extracted upon the employment of the Arrhenius law.

4.1.4 The First Fe^{III}-4f SMMs

Complexes $[Fe^{III}{}_2Ho^{III}{}_2(OH)_2(teaH)_2(O_2CPh)_4(NO_3)_2]\cdot 6MeCN$ (**337**·6MeCN) and $[Fe^{III}{}_2Dy^{III}{}_2(OH)_2(teaH)_2(O_2CPh)_6]\cdot 4MeCN\cdot 3H_2O$ (**338**·4MeCN·$3H_2O$) were made upon the reaction of the starting material $[Fe^{III}{}_3O(O_2CPh)_6(H_2O)_3](O_2CPh)$ (**339a**) with H_3tea (=triethanolamine) and the corresponding lanthanide nitrate salt in MeCN/MeOH [341]. Both complexes can be described as consisting of two face-sharing $[M_4O_4]$ cubanes with a metal atom missing from one vertex in each cubane, resulting in a rhombus-like planar $\{Fe^{III}{}_2Ln^{III}{}_2\}$ arrangement with six-coordinate Fe^{III} centres and nine-coordinate Ln^{III} centres. Despite the fact that neither complex showed a clear out-of-phase, χ_M'', signal above 1.8 K, both **337** and **338** established their SMM character via single-crystal magnetic hysteresis measurements.

4.1.5 A Family of $[Mn^{III}{}_4Mn^{IV}Ln^{III}{}_4]$ SMMs

The reaction of $[Mn_6O_2(piv)_{10}(4\text{-Me-py})_{2.5}(pivH)_{1.5}]$ (**339b**) with $mdeaH_2$ (=*N*-methyldiethanolamine) with various lanthanide nitrate salts in MeCN led to the formation of a family of nonanuclear compounds with the formula $[Mn_5Ln_4O_6(mdea)_2(mdeaH)_2(piv)_6(NO_3)_4(H_2O)_2]\cdot 2MeCN$ (Ln^{III}=Tb (**340**), Dy (**341**), Ho (**342**), Y (**343**)), with all of them displaying SMM behaviour [342]. All complexes are isostructural, consisting of two distorted $\{Mn^{IV}Mn^{III}Ln^{III}{}_2O_4\}$

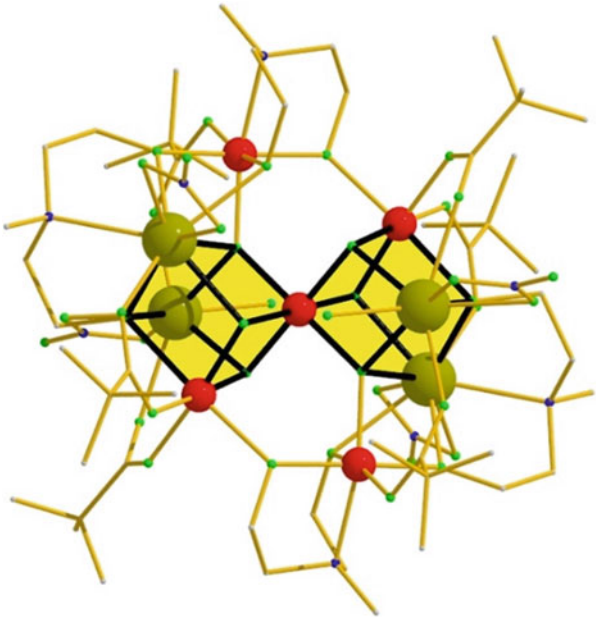

Fig. 43 The crystal structure of **341**. Hydrogen atoms are omitted for clarity. Colour code: Dy^{III} = *dark-yellow*, Mn = *red*, N = *blue*, O = *green*, C = *gold*

cubanes sharing a common Mn^{IV} vertex, with a further Mn^{III} centre attached to each cubane via a μ_3-O^{2-}ligand and mdeaH$^-$ ligands (Fig. 43). The magnetic properties of all clusters were investigated in detail, while an $S = 3/2$ ground-state was revealed for the Y^{III} analogue, cluster **343**, as a result of antiferromagnetic interactions between the trivalent manganese centres. Furthermore, all **340**–**343** clusters display frequency-dependent out-of-phase signals, χ_M'', with their SMM character strongly depending on the Ln^{III} centre present in each species. Among these, the Dy^{III} analogue displays a high energy barrier for the reorientation of the magnetisation of $U_{eff} = 38.6$ K with $\tau_0 = 3.0 \times 10^{-9}$ s, displaying beautiful out-of-phase peaks in the 2–4 K temperature range under oscillating fields at various frequencies (Fig. 44 left), and hysteresis loops up to 1.8 K (Fig. 44, right), thus, establishing its molecular magnetic origin. Most importantly, the Y^{III} analogue also (**343**) displays out-of-phase peaks, albeit not fully formed, but upon replacement of the Y^{III} centres with Dy^{III} ions a dramatic improvement of the SMM characteristics was evidenced, possibly due to (1) an increase of the "spin ground state" and (2) an increase of the magnetic anisotropy induced by the Dy^{III} centres.

4.1.6 Tetranuclear $[Dy^{III}_3Ni^{II}]$ Oximate SMMs

The tetranuclear clusters $[\{Dy(hfac)_3\}_2\{Ni(dpk)_2(phen)\}]$ (**344**) and $[\{Dy(hfac)_3\}_2\{Ni(dpk)_2(py)_2\}]$ (**345**) (dpk=di-2-pyridyl ketoximate; phen = 1, 10-phenanthroline) were made upon reacting $[Ni(dpk)_2(phen)]$ (or $[Ni(dpk)_2(py)_2]$) [368] with $[Dy(hfac)_3(H_2O)_2]$ [369] in dry CH_2Cl_2 [343]. Both

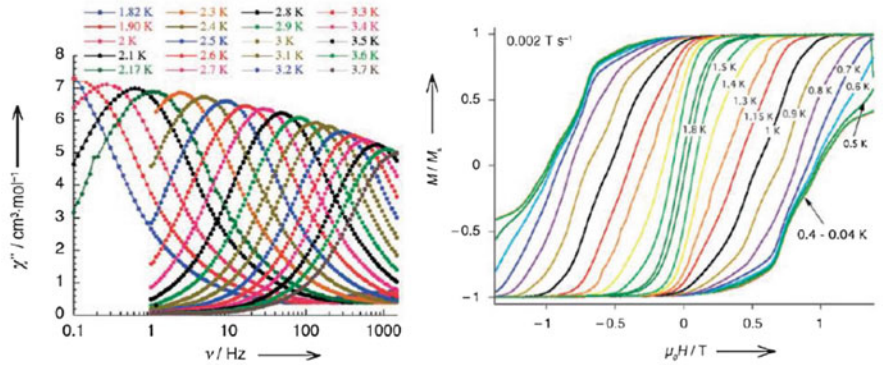

Fig. 44 Out-of-phase ac susceptibility plot as a function of the frequency at different temperatures for **341** (*left*); single-crystal hysteresis loops at various temperatures for **341** (*right*). Reprinted with the permission from [342]. Copyright 2008 Wiley

clusters adopt very similar structures, with a linear arrangement of the three metallic centres in **345** and an almost collinear arrangement in **344**, with six-coordinate Ni^{II} and eight-coordinate Dy^{III} centres. The magnetic investigation revealed that for both **344** and **345** out-of-phase "tails-going-up" were observed under ~1.8 K, therefore suggesting SMM character. A major development of this work was the synthesis of the Cu^{II} analogue, cluster $[\{Dy(hfac)_3\}_2\{Cu(dpk)_2\}]$ (**346**), which was synthesised in an analogous manner to **345** [344]. Cluster **346** shows fully formed out-of-phase peaks in the 4–9 K temperature range, while the Arrhenius analysis yielded an impressive $U_{eff} = 47$ K with $\tau_0 = 1.1 \times 10^{-7}$ s.

4.1.7 A Bell-Shaped Tridecanuclear $[Mn^{III}_9Mn^{II}_2Gd_2]$ SMM

Complex $[Mn^{III}_9Mn^{II}_2Gd_2O_8(OH)_2(piv)_{10.6}(fca)_{6.4}(NO_3)_2(H_2O)]\cdot 13CH_3CN\cdot H_2O$ (**347**·13MeCN·H_2O; fcaH = 2-furan-carboxylic acid) was reported in 2007, upon the reaction of **339** with $Gd(NO_3)_3\cdot 6H_2O$ in the presence of fcaH in MeCN [345]. Its structure may be described as bell-shaped; five manganese centres form the shell of the bell, while the remaining six manganese atoms form the rim of the bell, and the two Gd centres consist of the bell's clapper (Fig. 45). Ac magnetic susceptibility measurements reveal the existence of not fully formed out-of-phase signals, while single-crystal magnetisation measurements down to 40 mK showed hysteresis loops whose coercivity increased with decreasing temperature, confirming the SMM character of **347**, with $U_{eff} = 18.4$ K and $\tau_0 = 2 \times 10^{-12}$ s.

4.1.8 Tetranuclear $[Cu^{II}_2Ln^{III}_2]$ (Ln=Tb, Dy) SMMs

The use of the trianionic ligand H_3L (=2-hydroxy-N-(2-{[(2-hydroxyphenyl) methylene]amino}-2-methylpropyl)-benzamide), that possesses an inner N_2O_2

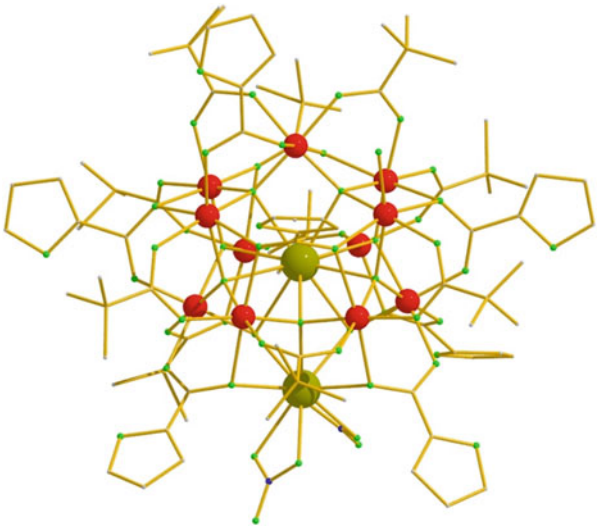

Fig. 45 The crystal structure of **347**. Hydrogen atoms and solvate molecules are omitted for clarity

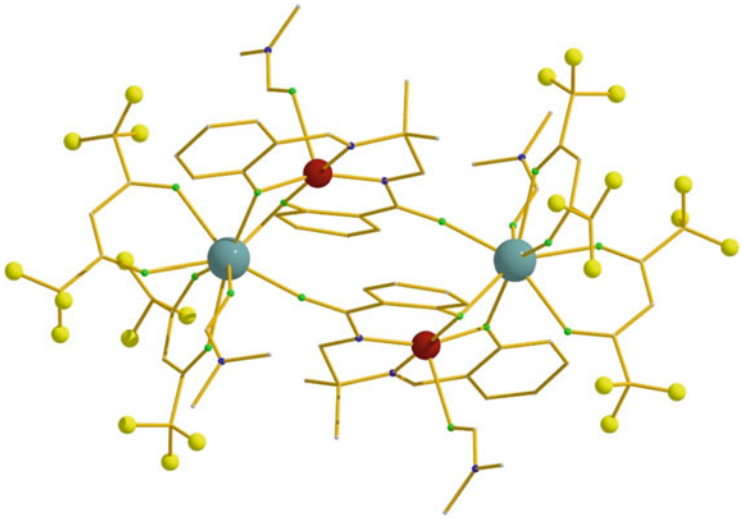

Fig. 46 The crystal structure of **348**. Hydrogen atoms are omitted for clarity

coordination site and an oxygen atom from an amide function not involved in this site, in Cu^{II}-Ln^{III} chemistry led to the formation of complexes [LCuDy $(hfac)_2(DMF)]_2$ (**348**) and [LCuTb$(hfac)_2(DMF)]_2$ (**349**), both of which display SMM behaviour [346]. The structure of the complexes can be described as two heteronuclear [Cu–Dy] dimers assembled through the oxygen atoms of the amido groups to form a double {Cu–N–C–O–Dy} bridge which leads to the centrosymmetric tetranuclear complexes (Fig. 46). The Cu^{II} ions adopt square-pyramidal

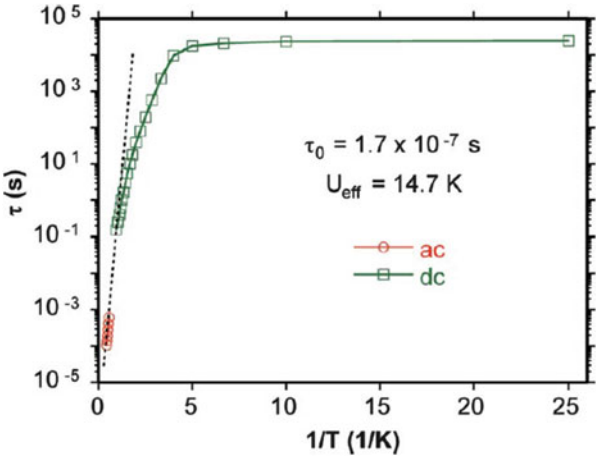

Fig. 47 Arrhenius plot using powder (*ac*) and single-crystal (*dc*) data for cluster **348**. The *dashed line* is the fit of the thermally activated region. Reprinted with the permission from [346]. Copyright 2008 Royal Society of Chemistry

geometry, while the Dy^{III} centres are eight-coordinate. The magnetic properties of both clusters were studied in detail revealing SMM behaviour for both of them. Complex **348** shows slow magnetic relaxation, which is evidenced by large singe-crystal hysteresis loops, whose coercivity is temperature and sweep-rate dependent, increasing with decreasing temperature and increasing field sweep rate, with $U_{\text{eff}} = 14.7$ K and $\tau_0 = 1.7 \times 10^{-7}$ s, as extracted upon employment of the Arrhenius law (Fig. 47). On the other hand, cluster **349** relaxes much faster than **348**, as evidenced by the smaller hysteresis loops displayed.

4.1.9 A Nonanuclear $[Cu^{II}_6Dy^{III}_3]$ SMM

Cluster $[Dy^{III}_3Cu^{II}_6L_6(OH)_6(H_2O)_{10}]Cl_2{\cdot}ClO_4{\cdot}3.5H_2O$ (**350**·3.5H_2O, $LH_2 = 1,1,1$-trifluoro-7-hydroxy-4-methyl-5-azahept-3-en-2-one) was prepared from the reaction of $Dy(ClO_4)_3{\cdot}6H_2O$ with LH_2 and $CuCl_2{\cdot}2H_2O$ in MeOH in the presence of NEt_3 [347]. The structure of the cationic part of **350** consists of three Dy^{III} ions arranged in a triangular fashion with $\{Cu^{II}_2L_2\}$ dimeric units on each edge of the triangle (Fig. 48). Furthermore, six alkoxo oxygen atoms of the deprotonated ligands L^{2-} and six hydroxo groups bridge the different metal ions in a μ_3 fashion, forming distorted $\{Cu_2L_2Dy_2(OH)_2\}$cubanes. The three Dy^{III} ions have the same eight-coordinate environment, while all Cu^{II} centres adopt square-pyramidal geometry. *Ac* measurements showed a strong frequency dependence of in-phase, χ', and out-of-phase, χ'', magnetic susceptibility below ~5 K, strongly suggesting SMM behaviour. This was further investigated by means of single-crystal magnetisation studies, which revealed hysteresis loops with large coercive field widening upon cooling. Finally, an Arrhenius analysis yielded $U_{\text{eff}} = 25$ K and $\tau_0 = 1.5 \times 10^{-7}$ s.

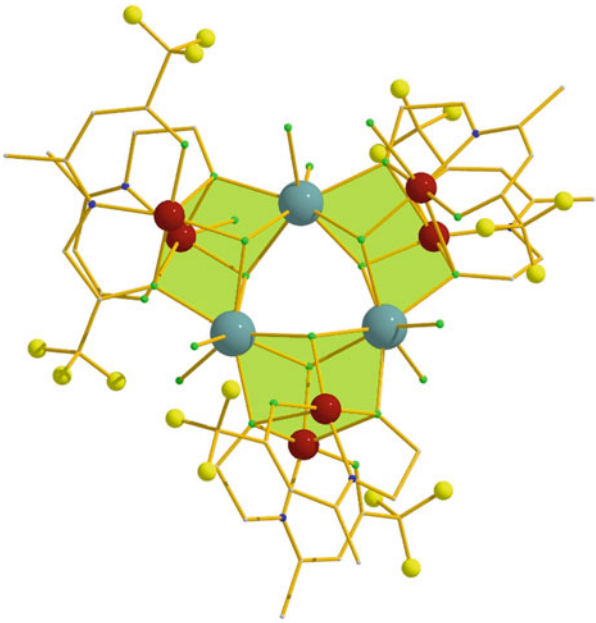

Fig. 48 The crystal structure of the cationic part of **350**, highlighting the three $\{Cu_2L_2Dy_2(OH)_2\}$ cubane units. Hydrogen atoms are omitted for clarity. Colour code: Dy^{III} = *cyan*, Cu^{II} = *red*, N = *blue*, O = *green*, C = *gold*, F = *yellow*

4.1.10 A Decanuclear $[Fe^{III}_7Dy^{III}_3]$ SMM

Cluster $[Dy^{III}_3Fe^{III}_7O_2(OH)_2(mdea)_7(O_2CPh)_4(N_3)_6]\cdot 2H_2O\cdot 7CH_3OH$ (**351**$\cdot 2H_2O\cdot 7CH_3OH$) was made from the reaction of $DyCl_3\cdot 6H_2O$, PhCOOH, $FeCl_3$, NaN_3, and $mdeaH_2$ (=*N*-methyldiethanolamine) in MeOH, under reflux conditions [348]. The metallic core consists of seven Fe(III) centres, each of which is chelated by a doubly deprotonated $mdea^{2-}$ ligand and three Dy(III) atoms. The structure is built up by two distorted edge-sharing $\{Dy_2Fe_2\}$ tetrahedra, with two further Fe(III) centres attached on each tetrahedron, to form the final decametallic unit. *Ac* magnetic susceptibility measurements show beautiful out-of-phase peaks in the 2–6 K temperature range, while single crystal magnetisation vs. field studies reveal magnetic hysteresis loops, establishing the SMM character of **351**. Following an Arrhenius analysis gave $U_{eff} = 30.9$ K with $\tau_0 = 1.3 \times 10^{-7}$ s.

4.1.11 An Undecanuclear $[Mn^{III}_4Mn^{IV}Tb^{III}_6]$ SMM

The reaction between $Mn(OAc)_2\cdot 4H_2O$, $Tb(NO_3)_3\cdot 6H_2O$ and H_3bemp (=2,6-bis[*N*-(2-hydroxyethyl)iminomethyl]-4-methylphenol) in MeOH in the presence of NEt_3 yielded complex $[Mn_5Tb_6O_4(OH)_4(OMe)_2(bemp)_2(OAc)_{10}(NO_3)_4]$ (**352**) [349]. The complex describes two corner-shared $\{Mn_4Tb_4\}$ cubanes, while charge balance considerations necessitate a $Mn^{III}_4Mn^{IV}$ oxidation-state distribution for the manganese atoms. The complex displays χ_M'' peaks under an oscillating magnetic field in the 2–3 K temperature range, while the energy barrier for the reorientation

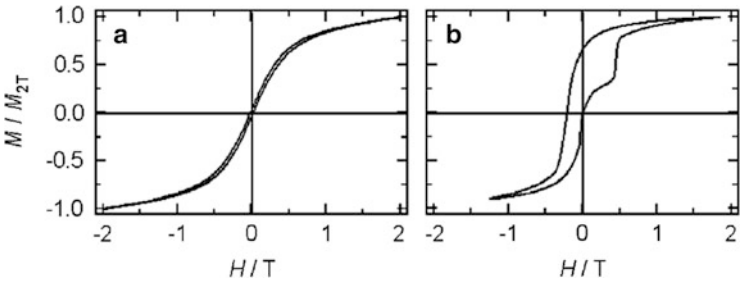

Fig. 49 Hysteresis loops of aligned single crystals of **352** at 0.5 K under (**a**) static and (**b**) pulsed magnetic field. Reprinted with the permission from [349]. Copyright 2009 Royal Society of Chemistry

of magnetisation of $U_{\text{eff}} = 17.8$ K with $\tau_0 = 4.76 \times 10^{-8}$ s was deducted upon the Arrhenius employment. Furthermore, the authors characterised the Gd^{III} analogue, cluster $[Mn_5Gd_6O_4(OH)_4(OMe)_2(bemp)_2(OAc)_{10}(NO_3)_4]$ (**353**) which does not display SMM behaviour, thus strongly suggesting that the SMM character of **352** is based on the magnetic anisotropy induced by the Tb^{III} centres. Finally, on **352** magnetisation experiments on a single crystal were performed under static and pulsed magnetic fields at 0.5 K (Fig. 49). In the first case, no steps were observed, while in the second case distinctive stepped hysteresis loops were observed.

4.1.12 A family of $[Co^{II}_2Ln^{III}]$ (Ln=Tb, Dy, Ho) SMMs

In 2009, a new family of 3d-4f SMMs was reported [350]; clusters $[\{(S)P[N(Me)N{=}CH\text{-}C_6H_3\text{-}2\text{-}O\text{-}3\text{-}OMe]_3\}_2Co_2Ln]NO_3{\cdot}2CHCl_3$ (Ln=Tb, **354**; Dy, **355**; Ho, **356**) were synthesised upon the reaction of the ligand LH_3(= $(S)P[N(Me)N{=}CH\text{-}C_6H_3\text{-}2\text{-}OH\text{-}3\text{-}OMe]_3$) with $Co(OAc)_2{\cdot}4H_2O$ and the corresponding lanthanide nitrate in $MeOH/CHCl_3$. All clusters are isostructural and describe a linear arrangement of the three metallic atoms, with the lanthanide located in the centre. The two terminal Co^{II} ions possess a *fac*-N_3O_3 coordination environment comprising three imino nitrogen atoms and three phenolate oxygen atoms, forcing a severely distorted octahedral geometry around the Co^{II} atoms, while the lanthanide centre is 12-coordinate adopting an icosahedral coordination sphere. The *dc* magnetic susceptibility for all **354**–**356** reveals an increase of the $\chi_M T$ product upon cooling, suggesting possibly the presence of ferromagnetic interactions within the clusters. Under an *ac* oscillating magnetic field, clusters **354**–**356** display out-of-phase χ_M'' peaks, with the Arrhenius analysis yielding U_{eff}/τ_0 pairs of 18.9 K/5.5×10^{-6} s, 14.2 K/5.1×10^{-6} s and 8 K/13×10^{-5} s, respectively. Furthermore, the authors studied the effect of applying small *dc* fields while measuring *ac* magnetic susceptibility, in order to elucidate the relaxation of the cluster between the thermal and the quantum SMM regimes; for **354**, as anticipated the application of a small *dc* field slows down the relaxation for the cluster, since the relaxation mode is going

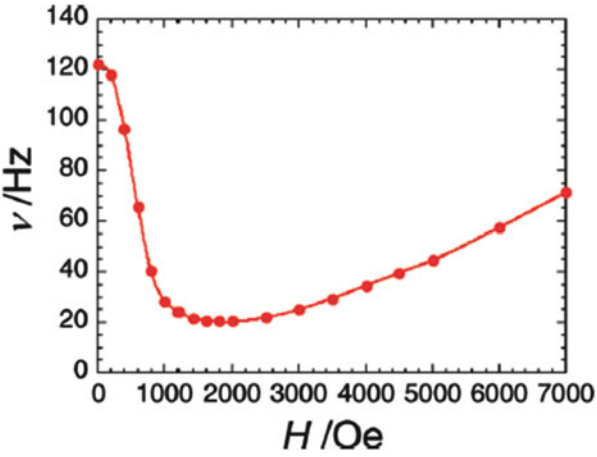

Fig. 50 Field dependence of the characteristic frequency at 3.5 K for **354**. Reprinted with the permission from [350]. Copyright 2009 American Chemical Society

down in frequency with an increasing dc field (Fig. 50), while on the contrary for **355–356**, even at low fields, the relaxation becomes faster than in zero *dc* field, suggesting the absence or the negligible influence of the QTM effects.

4.1.13 A $[Mn^{III}_{12}Mn^{II}_{6}Dy^{III}]$ SMM

The impressive cluster $[Mn^{III}_{12}Mn^{II}_{6}Dy^{III}O_8Cl_{6.5}(N_3)_{1.5}(HL)_{12}(MeOH)_6]Cl_3{\cdot}25MeOH$ (**357**·25MeOH) was made upon the reaction of H_3L (=2,6-bis-(hydroxymethyl)-4-methylphenol) with $MnCl_2{\cdot}4H_2O$, NaN_3, and $NaO_2CMe{\cdot}3H_2O$ in MeCN/MeOH followed by the addition of $Dy(NO_3)_3{\cdot}6H_2O$ [351]. The synthesis was based on the "parent" compound $[Mn^{III}_{12}Mn^{II}_{7}O_8(N_3)_8(HL)_{12}(MeCN)_6]Cl_2{\cdot}10MeOH{\cdot}MeCN$ (**358**·10MeOH·MeCN) [370], which holds the record for the highest spin ground-state of $S = 83/2$, while it does not display SMM behaviour [371]. More specifically, the authors managed to replace the central eight-coordinate Mn^{II} ion in **358** with a Dy^{III} ion, therefore introducing uniaxial magnetic anisotropy, as seen from the slow relaxation of the magnetisation observed above 1.8 K (vide infra). The structure of the trication consists of two supertetrahedral units, each made up of an octahedron of Mn^{III} ions inscribed in a tetrahedron of Mn^{II} ions, which share a common central eight-coordinate Dy^{III} vertex (Fig. 51). The cluster displays frequency- and temperature-dependent out-of-phase, χ_M'', signals, *albeit* not fully formed, suggesting its SMM origin. In order to prove the latter, single-crystal magnetisation vs. field experiments were carried out, showing hysteresis loops below 0.5 K, thus establishing its SMM behaviour.

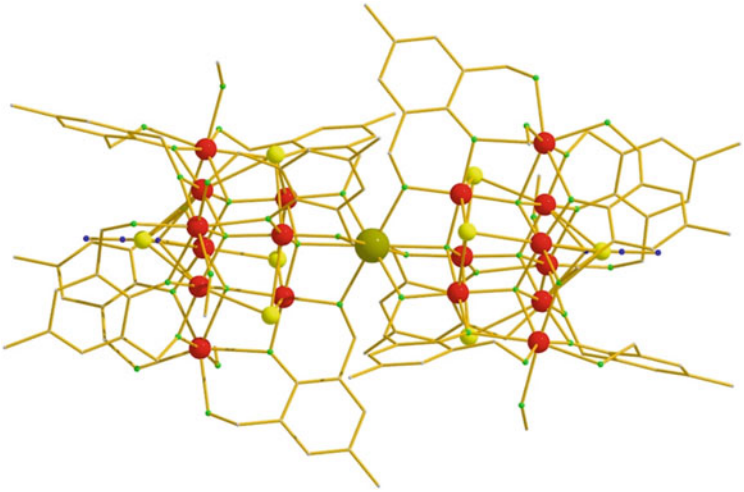

Fig. 51 The crystal structure of the cationic part of **357**. Hydrogen atoms are omitted for clarity. Colour code: Dy^{III} = *dark yellow*, Mn = *red*, N = *blue*, O = *green*, C = *gold*, Cl = *yellow*

4.1.14 Observing QTM Steps in a $[Mn^{III}_{11}Mn^{II}Gd^{III}]$ SMM

Cluster $[Mn_{12}GdO_9(O_2CPh)_{18}(O_2CH)(NO_3)(HO_2CPh)]$ (**359**) was synthesised upon reacting $Mn(O_2CPh)_2$, $^nBu_4NMnO_4$, $Gd(NO_3)_3{\cdot}6H_2O$ and $PhCO_2H$ in CH_3NO_2 [352]. Its core consists of a central nine-coordinate $\{O_9\}$ Gd^{III} atom, encapsulated within a $\{Mn_{12}\}$ shell. The ground-state of the complex was found to be $S = 9$, upon fitting the magnetisation data, while a zero-field splitting of this ground-state was calculated of $D = -0.163$ cm^{-1}. The cluster shows out-of-phase signals (not fully formed) under an *ac* magnetic field below ~3 K, while single-crystal magnetisation vs. field experiments revealed beautiful step-shaped hysteresis loops (Fig. 52). Such steps are diagnostic of the QTM effect, and this was the first time that such steps were seen for a 3d-4f SMM. Following an Arrhenius analysis gave $U_{eff} = 15.9$ K with $\tau_0 = 2.4 \times 10^{-12}$ s.

4.1.15 A Salen-Based $[Zn^{II}_2Dy^{III}_3]$ SMM

Cluster $[Zn_2Dy_3(\text{m-salen})_3(N_3)_5(OH)_2]$ (**360**, H_2m-salen=*N*,*N*′-ethylenebis (3-methoxy salicylideneamine)) was synthesised from the reaction of H_2m-salen, NaN_3, $ZnCl_2$, and $Dy(NO_3)_3{\cdot}3H_2O$ in MeOH/MeCN, in the presence of NEt_3 [353]. Cluster **360** can be described as a V-shaped molecule, consisting of three m-salen^{2-} ligands coordinated to two Zn^{II} ions in the inner pocket and three Dy^{III} ions (one in the inner pocket and two in the outer pocket) (Fig. 53). The cluster displays out-of-phase signals, below ~2.6 K, while an Arrhenius treatment yielded $U_{eff} = 13.4$ K with $\tau_0 = 3.3 \times 10^{-7}$ s. Furthermore, the authors performed *ac*

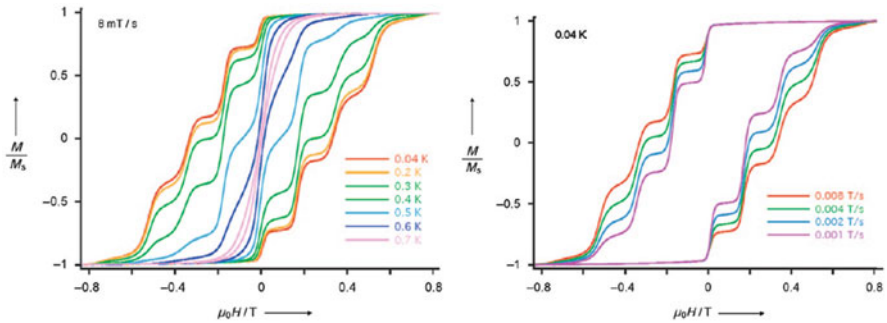

Fig. 52 Magnetisation versus field hysteresis loops for a single crystal of **359** at the indicated temperatures (*left*) and field sweep rates (*right*). M is normalised to its saturation value. Reprinted with the permission from [352]. Copyright 2009 Wiley

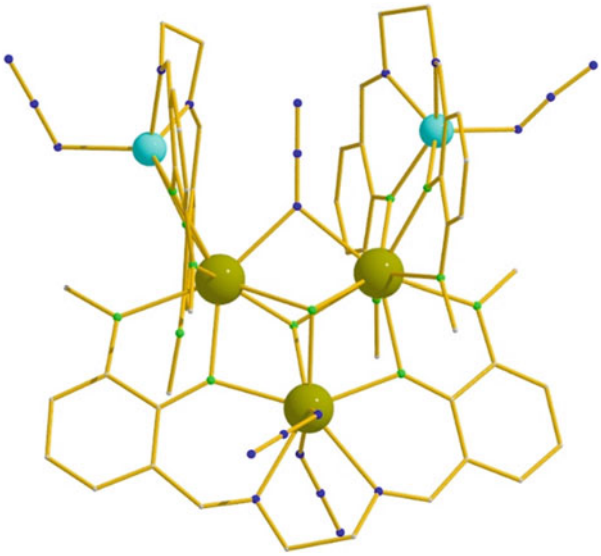

Fig. 53 The crystal structure of **360**. Hydrogen atoms are omitted for clarity

measurements under various applied *dc* fields, but, unfortunately, the magnetic relaxation of the cluster remained unchanged. In addition, single-crystal *dc* relaxation measurements were performed on a micro-SQUID, revealing "unusual" three-step shaped hysteresis loops with a narrow opening, possibly due to weak exchange interactions and the orientation of the applied magnetic field with respect to the plane defined by the three Dy^{III} centres [372, 373].

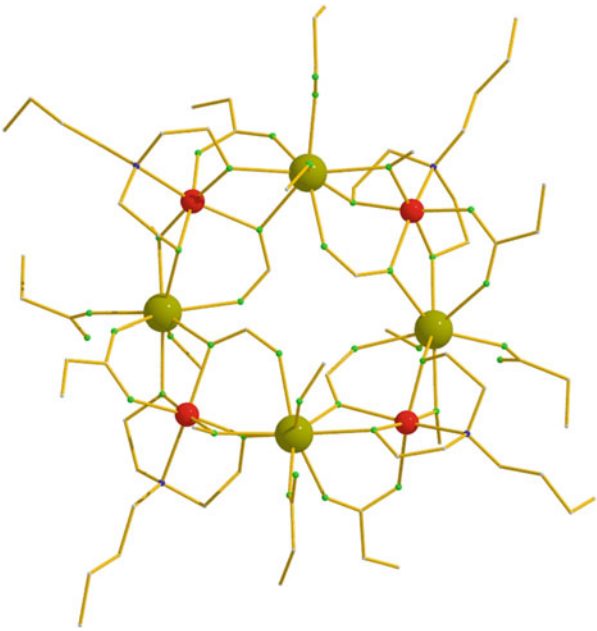

Fig. 54 The crystal structure of **361**. Hydrogen atoms are omitted for clarity

4.1.16 A Family of $[Mn^{III}_4Ln^{III}_4]$ (Ln=Sm, Tb, Dy) SMMs

The 3d-4f family of clusters with the general formulae of $[Mn^{III}_4Ln_4(^n\text{Bu-dea})_4(HCOO)_4(OMe)_4(O_2CEt)_4(O_2CEt)_4(MeOH)_4]$ (^{n}Bu-deaH$_2$=*N*-^{n}butyl-diethanol amine, Ln=Sm, **361**; Tb, **362**; Dy, **363**) was prepared upon the reaction of $Mn(O_2CEt)_2{\cdot}2H_2O$, HCOONa, ^{n}Bu-deaH$_2$ and the corresponding lanthanide nitrate salt in MeOH, in the presence or absence of NEt_3 [354]. All clusters are isostructural, and describe a saddle-like core in which the 3d and 4f centres are alternating (Fig. 54). All manganese centres are six-coordinate, adopting JT distorted octahedral geometry, with the JT axes alternately tilted with respect to each other, while the lanthanide centres are eight-coordinate. All **361**–**363** clusters exhibit clear frequency-dependent out-of-phase, χ_M'', signals, with only the Dy^{III} analogue (**363**) displaying fully-formed peaks, suggesting SMM behaviour, while the Y^{III} analogue, cluster $[Mn^{III}_4Y_4(^n\text{Bu-dea})_4(HCOO)_4(OMe)_4(O_2CEt)_4(O_2CEt)_4(MeOH)_4]$ (**364**) displays very weak out-of-phase signal, suggesting that the SMM behaviour of **361**–**363** is mainly, but not exclusively, due to the lanthanide centres present in the molecules. The energy barrier for the reorientation of the magnetisation was found for **363**, upon employment of the Arrhenius law, to be $U_{eff} = 12$ K with $\tau_0 = 3.5 \times 10^{-7}$ s.

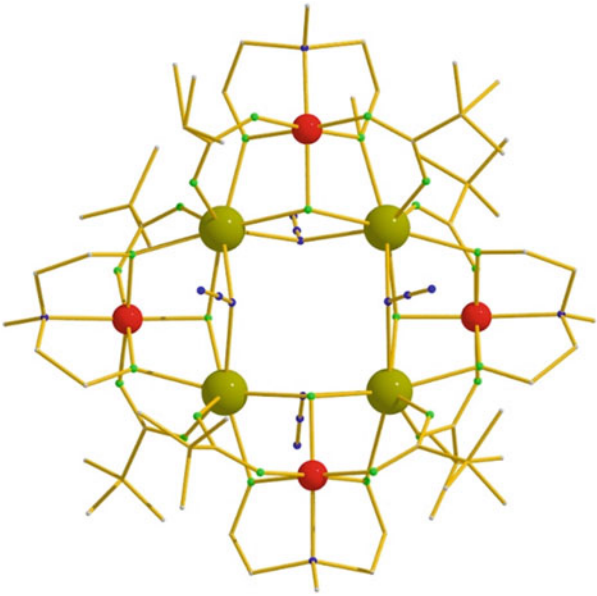

Fig. 55 The crystal structure of **365**. Hydrogen atoms and solvate molecules are omitted for clarity

4.1.17 The First Cr^{III}-4f SMM

In 2010, the first Cr^{III} containing 3d-4f SMM was reported [355]; cluster $[Cr^{III}_4Dy^{III}_4(OH)_4(N_3)_4(mdea)_4(piv)_4]\cdot 3CH_2Cl_2$ (**365**$\cdot 3CH_2Cl_2$, H_2mdea=methyl diethanolamine) was synthesised upon the reaction of H_2mdea and NaN_3 with $CrCl_2$ in MeCN under inert atmosphere, followed by addition of $Dy(NO_3)_3\cdot 6H_2O$, pivalic acid, and CH_2Cl_2. The structure consists of a central metallic square of Dy^{III} ions, at which each pair of neighbouring Dy centres is further bridged by a μ_3-OH^- ligand to a Cr^{III} atom, with the four Cr^{III} located alternately above and below the {Dy_4} square (Fig. 55). The complex displays frequency- and temperature-dependent out-of-phase, χ_M'', signals, with the maximum signal appearing at ~2.2 K for the frequency of 1500 Hz. In order to prove its SMM character, single-crystal magnetisation vs. field studies were carried out, revealing, indeed, its SMM origin (Fig. 56), with $U_{eff} = 15$ K and $\tau_0 = 1.9 \times 10^{-7}$ s. Finally, by employing the Cole–Cole analysis, the parameter of $\alpha = 0.42$–0.5 was calculated, suggesting that more than one relaxation processes are operational in **365**.

4.1.18 Going Above 100 K for a $[Mn^{III}_6Tb^{III}_2]$ SMM

In 2011 clusters $[Mn^{III}_6O_3(sao)_6(CH_3O)_6Ln_2(CH_3OH)_4(H_2O)_2]$ ($saoH_2$= salicylaldoxime; Ln=La, **366**; Tb, **367**) were reported, upon the reaction of $MnCl_2\cdot 4H_2O$, $saoH_2$ and the corresponding $Ln(NO_3)_3\cdot 6H_2O$ in MeOH, in the presence of NEt_4OH [356]. Both complexes are isostructural and consist of an

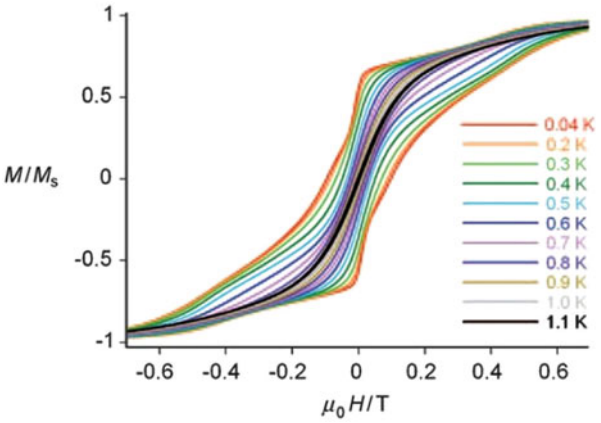

Fig. 56 Magnetisation versus field hysteresis loops for a single crystal of **365** at the indicated temperatures. M is normalised to its saturation value. Reprinted with the permission from [355]. Copyright 2010 Wiley

$\{(CH_3OH)_2(H_2O)Ln\}$-$(\mu_4$-$O)_3$-$\{Ln(CH_3OH)_2(H_2O)\}$ linear motif with a synperiplanar conformation, attached to a surrounding $\{Mn^{III}{}_6\}$ wheel on an equatorial position of the Mn sites. From fitting the magnetic susceptibility data for **366** an $S = 11$ ground-state was calculated, while from the comparison of the magnetic susceptibility data between **366** and **367** ferromagnetic interactions were qualitatively found between the Mn^{III} and Tb^{III} ions for the latter. Both clusters display fully formed out-of-phase peaks under an *ac* field, with a blocking temperature of ~3 K for **366**, and ~9 K for **367**. Their SMM behaviour was further proved by single-crystal magnetisation measurements, which indeed displayed temperature and sweep-rate-dependent hysteresis loops. Furthermore, the energy barriers for both clusters were found as $U_{eff} = 32.8$ K with $\tau_0 = 5.8 \times 10^{-10}$ s for **366** and $U_{eff} = 103$ K with $\tau_0 = 1.6 \times 10^{-10}$ s for **367**.

4.1.19 Suppressing QTM in a $[Co^{III}{}_2Dy^{III}{}_2]$ SMM

In 2012, clusters $[Dy^{III}{}_2Co^{III}{}_2(OMe)_2(teaH)_2(O_2CPh)_4(MeOH)_4](NO_3)_2{\cdot}MeOH{\cdot}H_2O$ (H_3tea: triethanolamine; **368a**·MeOH·H_2O) and $[Dy^{III}{}_2Co^{III}{}_2(OMe)_2(teaH)_2(O_2CPh)_4(MeOH)_2(NO_3)_2]{\cdot}MeOH{\cdot}H_2O$ (**368b**·MeOH·H_2O) were synthesised upon the reaction of $Co(NO_3)_2{\cdot}6H_2O$, $Dy(NO_3)_3{\cdot}6H_2O$, H_3tea and benzoic acid in MeCN in the presence of NEt_3, followed by recrystallisation in MeOH [357], with both clusters found within the asymmetric unit of the crystal structure. Both complexes are almost isostructural and describe a planar $\{Co^{III}{}_2Dy^{III}{}_2\}$ butterfly unit, with the 4f ions occupying the body positions and the 3d centres located at the wing, held together by two μ_3-OMe^- ligands, both bridging to two Dy^{III} ions and one Co^{III} ion. The differences between the two clusters lie on: (1) the presence of two terminal MeOH molecules on a Dy^{III} centre in **368a**·MeOH·H_2O, and (2) the presence of a NO_3^- in the lattice of **368a**·MeOH·H_2O, while in **368b**·MeOH·H_2O the NO_3^- is now coordinated on the Dy^{III} centre that has one coordinated MeOH molecule, resulting in a cationic species for **368a**·MeOH·H_2O and neutral species for **368b**·MeOH·H_2O. *Ac* magnetic susceptibility measurements reveal features typical of SMM behaviour for

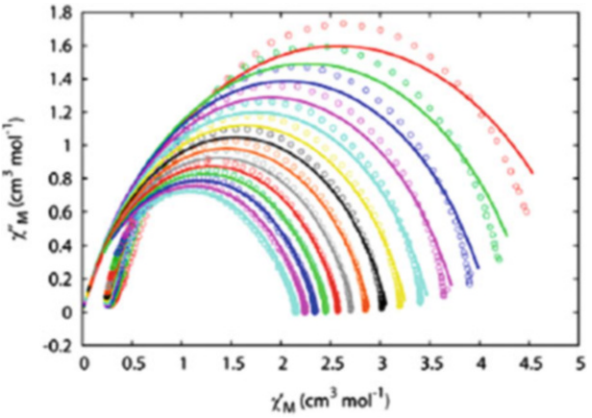

Fig. 57 Cole–Cole plots between 4 and 10.5 K for **368**, with the *solid lines* being best fits to the experimental data. Reprinted with the permission from [357]. Copyright 2012 American Chemical Society

the Dy complex **368**, with both the in-phase (χ_M') and out-of-phase (χ_M'') susceptibilities displaying frequency and temperature dependence below ~20 K, signalling the blocking of the magnetisation. Employment of the Arrhenius law yielded $U_{eff} = 88.8$ K with $\tau_0 = 5.64 \times 10^{-8}$ s. Furthermore, the Cole–Cole diagram (Fig. 57) was fitted to a generalised Debye model to determine α values and relaxation times (τ) in the temperature range 4–10.5 K, and the plots reveal relatively symmetrical semicircles, indicating a single relaxation process, with α values ranging from 0.29 to 0.24, indicating a broad distribution of relaxation times in this single relaxation process. Finally, an important point is the fact that the relaxation time, τ, does not become temperature independent in the temperature range studied, indicating the absence of a pure quantum regime down to 2.5 K (when the tunnelling rate becomes faster than the thermally activated relaxation). Indeed, upon applying a static *dc* field, no significant shift in the χ_M'' vs. T plot was observed in fields up to 1,000 Oe, further supporting that QTM is inefficient in this system.

5 4f SMMs

Studies of SMMs were revolutionised in 2003 by the report by Ishikawa et al. of a terbium bisphthalocyanine (Pc) complex that had an energy barrier for magnetic relaxation of ~330 K [374], which is far higher than those found for the 3d-block SMMs. This observation has led to a huge increase in the studies of the magnetic behaviour of complexes of the heavier lanthanides, especially terbium and dysprosium. This was recently comprehensively reviewed to the end of 2012, and we do not intend to repeat that discussion which would make this review excessively long [336]. Here we merely update that review, including the new 4f-SMMs reported in 2013. There is also a division between monometallic SMMs, which are now frequently termed "single ion magnets" (SIMs) and polymetallic SMMs. Progress in research on SIMs is reviewed elsewhere in this volume [375], and we do not cover these fascinating molecules.

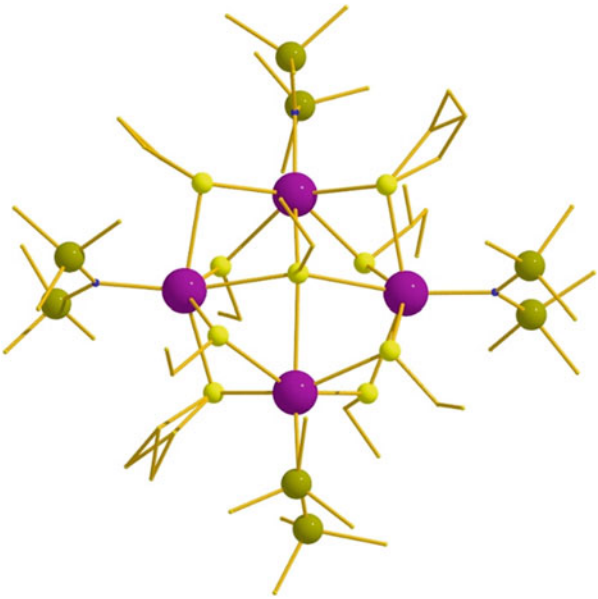

Fig. 58 The crystal structure of the anion of **384**. Hydrogen atoms and solvate molecules are omitted for clarity

5.1 Terbium SMMs in 2013

Although the first significant 4f-SMM was a terbium complex, and most of the very high energy barriers are for terbium phthalocyanine complexes [375] there are very few polymetallic terbium SMMs. The most significant is the dimer bridged by N_2^{3-} reported by Rinehart et al. in 2011 [19]. In 2013 only two new terbium SMMs have been reported. Cluster $[Li(THF)_4][Tb_4\{N(SiMe_3)_2\}_4(\mu_4\text{-SEt})(\mu\text{-SEt})_8]$ (**384**, Fig. 58), which contains a square of Tb centres, bridged on each edge by two thiolates, with a central μ_4-SEt and four terminal $N(SiMe_3)_2^-$ ligands. The energy barrier is very small (see Table 11) [376].

The second example is a $\{Tb_4\}$ triple-decker involving a central fused phthalocyanines [377]. $[Tb(obPc)_2]Tb(Fused\text{-}Pc)Tb[Tb(obPc)_2]$ **385** (obPc = 2, 3, 9, 10, 16, 17, 23, 24-octabutoxyphthalocyaninato, Fused-Pc=bis{7^2, 8^2, 12^2, 13^2, 17^2, 18^2-hexabutoxytribenzo[*g*, *l*, *q*]-5, 10, 15, 20-tetraazaporphirino}[*b*,*e*] benzenato) contains two $\{Tb_2\}$ units on either side of the central fused phthalocyanine. This molecule shows slow relaxation of magnetisation, with 213 K and τ_0 of 2.7×10^{-8} s. More importantly, the paper shows that the magnetic relaxation is influenced by dipole–dipole interactions between the Tb centres.

5.2 Dysprosium SMMs in 2013

Most papers in the 4f-SMMs area continue to be concerned with dysprosium SMMs.

Table 11 Most recent members of the 4f family of SMMs

Formula	U_{eff} (K)	τ_0 (s)	References
$[Li(thf)_4][Tb_4\{N(SiMe_3)_2\}_4(Set)_9]$ (**384**)	6.6	1.5×10^{-5}	[376]
$[Tb(obPc)_2]Tb(Fused\text{-}Pc)Tb[Tb(obPc)_2]$ (**385**)	213	2.7×10^{-8}	[377]
$\{[TCIPP]Y[Pc(Oph)_8]Dy[Pc(Oph)_8]\}$ (**386**)	24.9[a]	1.52×10^{-7}	[378]
$[(Pc)Dy(L^1)Dy(Pc)]$ (**390**)	13.8	5.3×10^{-6}	[379]
$[(Me_5trenCH_2)Dy(\mu\text{-}H)_3Dy(Me_6tren)]$ (**391**)	94	1.04×10^{-7}	[380]
$[Dy(notpH_4)(NO_3)(H_2O)]_2 \cdot 8\ H_2O$ (**392**·$8H_2O$)	49[a]	6.75×10^{-9}	[381]
$[Dy(notpH_4)(NO_3)(H_2O)]_2$ (**392** dehydrated)	81.8	1.19×10^{-7}	[381]
$[Dy(HL^2)(O_2CPh)(MeOH)]_2$ (**393**)	94	2.1×10^{-7}	[382]
$[Dy(\mu\text{-}OH)(\gamma\text{-}SiW_{10}O_{36})]_2^{12}$ (**394**)	65.7	3.11×10^{-7}	[383]
$[Dy(hfac)_3(L^3)]$ (**397**)	ca. 100[a]	0.4×10^{-8}	[384]
	ca. 100[a]	9×10^{-8}	
$[Dy_3(OH)(HL^4)_3(NO_3)_3(MeOH)_2(H_2O)]\ (NO_3)$ (**398**)	6.0[a]	9.5×10^{-5}	[385]
	53.8[a]	2.4×10^{-7}	
$[Dy_3(OH)(HL^5)_3(Cl)_2(MeOH)(H_2O)_3]\ [Dy_3(OH)(HL^5)_3(Cl)_2(H_2O)_4]\ (Cl)_4$ (**399**)	21.7	1.3×10^{-5}	[385]
$[Dy_3(OH)(L^6)(HL^6)_4](ClO_4)_2$ (**400**)	13	8.3×10^{-6}	[386]
$[Dy_4(OH)_2(L^7)_2(acac)_6]$ (**401**)	13.95	5.0×10^{-6}	[387]
$[Dy_4(bpt)_4(\mu_3\text{-}OH)_2(\mu\text{-}Ome)_2(NO_3)_4]$ (**402**)	116	2.89×10^{-7}	[388]
$[Li(thf)_4][Dy_4\{N(SiMe_3)_2\}_4(Set)_9]$ (**403**)	66	4.3×10^{-6}	[376]
$[Dy_4K_2(\mu_6\text{-}O)(O^tBu)_{12}]$ (**404**)	692	6.6×10^{-11}	[389]
	316	2.6×10^{-9}	
$Dy@[Y_4K_2(\mu_6\text{-}O)(O^tBu)_{12}]$ (**405**)	842	1.54×10^{-11}	[389]
$Dy@[Y_5(\mu_5\text{-}O)(O^iPr)_{13}]$ (**406**)	804	2.69×10^{-11}	[389]
$[Dy_5(\mu_3\text{-}OH)_3(L^8)_6(H_2O)_3]$ (**407**)	8.1	1.7×10^{-5}	[390]
	37.9	9.7×10^{-8}	
$Dy_5(\mu_3\text{-}OH)_3(L^8)_4(HL^8)_2(MeOH)(H_2O)_2](ClO_4)_2$ (**408**)	197	3.2×10^{-9}	[390]
$[Dy_6(L^9)_4(\mu_4\text{-}O)(NO_3)_4(MeOH)]$ (**410**)	33.9	5.8×10^{-8}	[391]
	40.7	1.2×10^{-7}	
$[Yb(tta)_2(L^{11})(L^{12})]_2$ (**411**)	14.7	1.7×10^{-6}	[392]

[a]Measured in presence of an external *dc* field

5.2.1 Dimetallic Dysprosium SMMs

Among the new dimetallic dysprosium SMMs are two reported based on expansion of the phthalocyanine structures. Four dimers involving both phthalocyanine and porphyrin ligands have been reported: $\{[TCIPP]M[Pc(Oph)_8]M'[Pc(Oph)_8]\}$ (**386**–**389**), where TClPP=dianion of meso–tetrakis(4-chlorophenyl)porphyrin; Pc(Oph)$_8$=dianion of 2,3,9,10,16,17,23,24-octa(phenoxyl)phthalocyanine, and where M and M′ are varied between Dy and Y [378]. The structure contains two metal sites – one sandwiched between two phthalocyanines, and a second sandwiched between a phthalocyanine and a porphyrin. For the compound where Dy is in the former site and Y in the latter site (**386**), a small energy barrier is derived in a small external field (Table 11). The di-dysprosium complex (**387**) also shows some slow relaxation of magnetisation, but no energy barrier was derived, while the compound with Dy in the heteroleptic site did not show any SMM behaviour.

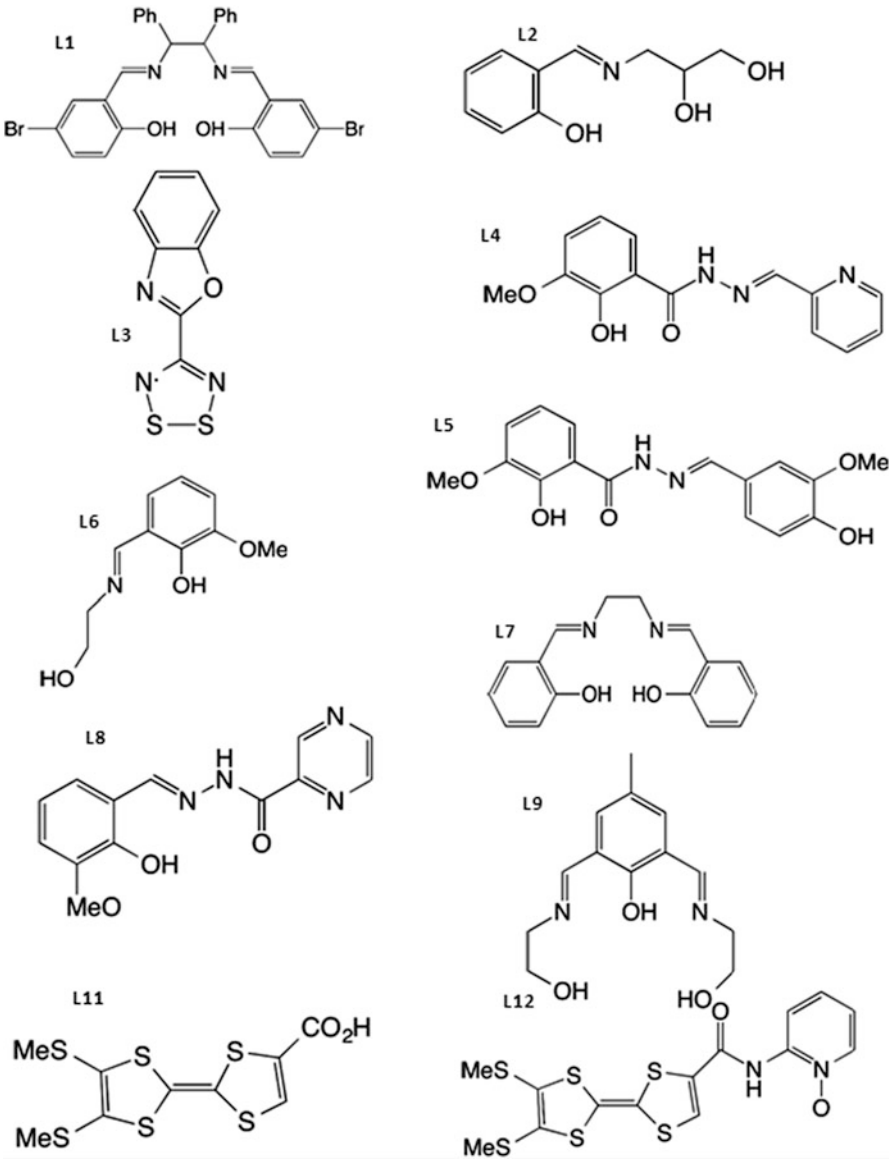

Scheme 1 Few of the ligands employed for the synthesis of 4f-SMMs

A second triple-decker involves a Schiff-base ligand (H_2L^1) (see Scheme 1), with this interposed between two Dy phthalocyanine fragments, to give [(Pc)Dy(L^1)Dy(Pc)] (**390**) [379]. The energy barrier found is small; the Cole–Cole plots on the compound are somewhat irregular, indicating a distribution of energy barriers probably associated with the two Dy sites in the structure being subtly inequivalent.

A more unusual dimer is found where two Dy centres are bridged by hydride ligands, $[(Me_5trenCH_2)Dy(\mu\text{–}H)_3Dy(Me_6tren)]$ (**391**) [380], (where Me_6tren=tris {2-(dimethylamino)ethylamine). This is the first hydride-bridged SMM and shows how the stability of the +3 oxidation state for the lanthanides allows very unusual ligands to be used in this chemistry. There are two distinct coordination sites in the molecule, and ab initio calculations show that the slow relaxation observed is associated with the eight-coordinate Dy site. The U_{eff} measured in zero-field is 94 K, but by applying an external field of 800 G fast quantum tunneling can be suppressed and this U_{eff} rises to 122 K [380].

Use of a tris-phosphonate derived from 1,4-7-triazacyclononane-1,4,7-triyl-tris (methylenephosphonic acid) ($notpH_6$) gives a dimetallic SMM $[Dy(notpH_4)(NO_3)(H_2O)]_2{\cdot}8\ H_2O$ (**392**$\cdot 8H_2O$) [381]; an energy barrier can only be obtained for this SMM in the presence of an external dc field. This compound can be dehydrated, to give a different phase but where EXAFS studies show that the Dy coordination environment is not significantly changed. The dehydrated compound is also an SMM, with a higher U_{eff}, and the energy barrier can be derived in zero-external field (Table 11). This study shows the importance of the solvation state of SMMs.

A new dimetallic Schiff-base complex SMM has also been reported [382]. The compound $[Dy(HL^2)(O_2CPh)(MeOH)]_2$ (**393**; HL^2 shown in Scheme 1) has an inversion centre, and is eight-coordinate. Five donor atoms from Schiff-base ligands occupy an equatorial plane on each Dy site, with a bidentate benzoate in an axial site, *trans* to a coordinated MeOH. The U_{eff} found is moderate (Table 11).

A polyoxometallate ligand is used in another di-dysprosium SMM [383]. The ligand used is a lacunary $[\gamma\text{-}SiW_{10}O_{36}]^{8-}$, forming the compound $[Dy(\mu\text{-}OH)(\gamma\text{-}SiW_{10}O_{36})]_2^{12-}$ (**394**) via deprotonation of $[Dy(OH_2)(\gamma\text{-}SiW_{10}O_{36})]_2^{10-}$ (**395**). The former compound has an energy barrier of 66 K (Table 11). Interestingly, the thermal energy barrier did not change when Dy was doped into $[Y(\mu\text{-}OH)(\gamma\text{-}SiW_{10}O_{36})]_2^{12-}$ (**396**), indicating that the Dy···Dy interaction in the compound has little influence on the magnetic behaviour.

One further spin system should be discussed here. Fatila et al. have reported a Dy-radical compound that forms supramolecular dimers in the solid state [384]. The compound $[Dy(hfac)_3(L^3)]$ (**397**; hfac = 1, 1, 1, 5, 5, 5-hexafluoroacetylacetonate, L^3 shown in Scheme 1) has a chelating dithiadiazoyl radical coordinated to the Dy centre. The compound crystallises with an interaction between pairs of molecules in the solid state through stacking of the dithiadiazoyls. In zero external magnetic fields the magnetic relaxation is dominated by quantum tunneling; however, this relaxation path can be lifted by application of a d.c. field of 700 Oe. Two thermally activated processes are then seen, both with a U_{eff} around 100 K, but with different values for τ_o (Table 11).

5.2.2 Higher Nuclearity Dy SMMs

Three new $\{Dy_3\}$ triangular SMMs were reported in 2013 [385, 386]. The ligands used are shown in Scheme 1. $[Dy_3(OH)(HL^4)_3(NO_3)_3(MeOH)_2(H_2O)](NO_3)$ (**398**)

and $[Dy_3(OH)(HL^5)_3(Cl)_2(MeOH)(H_2O)_3]$ $[Dy_3(OH)(HL^5)_3(Cl)_2(H_2O)_4](Cl)_4$ (**399**) have been studied in some detail. The former compound shows two relaxation processes, with $U_{eff} = 6.0$ and 53.8 K (Table 11) measured in a small external field, while the latter compound shows only one relaxation process. In $[Dy_3(OH)(L^6)(HL^6)_4](ClO_4)_2$ (**400**) the magnetic studies again show one relaxation process, with a small energy barrier.

A $\{Dy_4\}$ butterfly SMM has been reported featuring acetylacetonate and the Schiff base *N*,*N*′-bis(salicylidene)-1,2-ethanediamine (H_2L^7) [387]. $[Dy_4(OH)_2(L^7)_2(acac)_6]$ (**401**) has a small energy barrier and a τ_o value that suggests quantum tunneling is important in magnetic relaxation in this compound. Further tetranuclear dysprosium Schiff base complexes have also been reported to be SMMs, with remarkably low U_{eff} barriers claimed [393].

A much more unusual $\{Dy_4\}$ SMM has been reported by Guo et al. using the ligand 3,5-bis(pyridine-2-yl)-1,2,4-triazole (Hbpt) [388]. The compound $[Dy_4(bpt)_4(\mu_3\text{-}OH)_2(\mu\text{-}Ome)_2(NO_3)_4]$ (**402**) again contains a butterfly of Dy centres. The energy barrier found is moderately high, at 116 K, and the compound also shows both photo- and electro-luminescence. The paper is therefore a significant step towards multifunctional lanthanide-based molecular magnets, albeit there is no attempt to couple the magnetic and luminescent properties.

Two further tetrametallic dysprosium SMMs have been reported with much simpler ligands. The first is a thiolate bridged square, $[Li(THF)_4][Dy_4\{N(SiMe_3)_2\}_4(\mu_4\text{-}Set)(\mu\text{-}Set)_8]$ (**403**) [376], which is isostructural with the $\{Tb_4\}$ square described in Sect. 5.1. The energy barrier is unremarkable (Table 11), but the use of S-donors in an SMM is unusual, again illustrating the variety of chemistry available in lanthanide molecular magnets. The second is $[Dy_4K_2(\mu_6\text{-}O)(O^tBu)_{12}]$ (**404**), which contains four Dy and two K ions forming an oxo-centred octahedron, with a *cis*-arrangement of the two K ions [389]. The compound is closely related to a $\{Dy_5\}$ alkoxide reported in 2011 [394]. The pure compound shows two thermal relaxation mechanisms, with remarkable U_{eff} values of 692 and 316 K. Even more remarkably, doping Dy into the equivalent $\{Y_4K_2\}$ (**405**) and $\{Y_5\}$ (**406**) alkoxides gives compounds with U_{eff} values of 842 and 804 K [389]. The very high energy barriers observed are due to a strongly axial crystal field at the Dy sites, caused by the central oxide and terminal alkoxide groups. This disfavours relaxation via the first excited state of the compounds, leading to the surprisingly high energy barriers.

Two pentametallic Dy butterflies have also been reported [390], using a ligand related to those used in $\{Dy_3\}$ triangles [385]. $[Dy_5(\mu_3\text{-}OH)_3(L^8)_6(H_2O)_3]$ (**407**, Fig. 59) and $[Dy_5(\mu_3\text{-}OH)_3(L^8)_4(HL^8)_2(MeOH)(H_2O)_2](ClO_4)_2$ (**408**; H_2L^8 shown in Scheme 1) have very similar structures, but very different magnetic behaviour. In the neutral complex two relaxation processes are seen, with small energy barriers, the smaller of which is consistent with quantum tunneling. The dicationic complex has a large energy barrier of 197 K. This large difference for a subtle structural change illustrates the complexity of lanthanide-based SMMs.

One of the most intriguing dysprosium molecular nanomagnets is the $\{Dy_3\}$ triangle reported by Lin et al. which shows a toroidal magnetic moment [395]. The Powell group reported an extension of this work to a $\{Dy_6\}$ compound in 2013

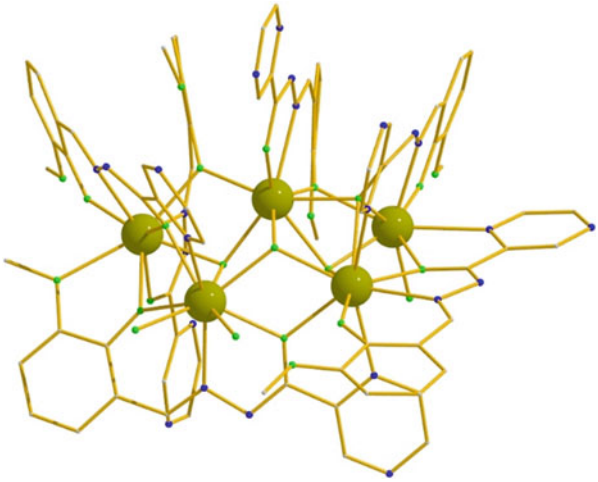

Fig. 59 The crystal structure of the anion of **407**. Hydrogen atoms and solvate molecules are omitted for clarity

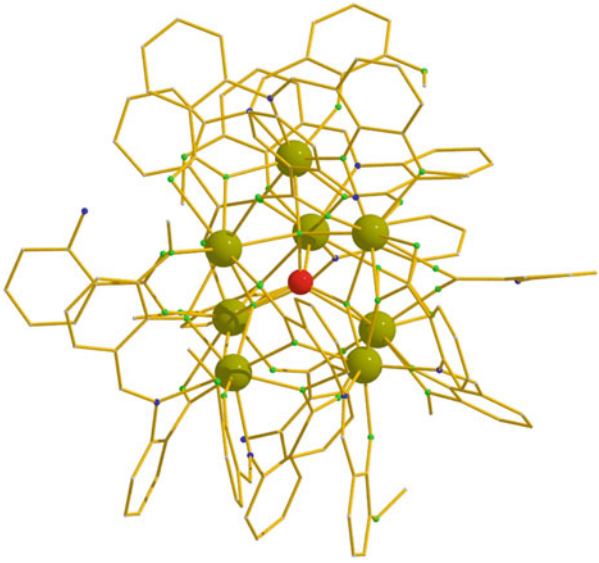

Fig. 60 The crystal structure of the anion of **410**. Hydrogen atoms are omitted for clarity

[391]. The compound $[Dy_6(L^9)_4(\mu_4\text{-}O)(NO_3)_4(MeOH)]$ (**409**; H_3L^9 shown in Scheme 1) contains two $\{Dy_3\}$ triangles, linked by the μ_4-oxide. The changes from the parent $\{Dy_3\}$ compound are intriguing, with a larger crossing field between the diamagnetic moment in ground state and the toroidal moment, and larger magnetic hysteresis. Two relaxation processes are found for the excited state, with U_{eff} values of 33.9 and 40.7 K. It is clear that coupling toroidal moments in lanthanide molecular magnets could produce interesting new physics.

One of the most structurally intriguing new Dy SMMs is $[Dy_8(L^{10})_8(C_6H_4NH_2CO_2)_4(SiO_4)]$ (**410**, Fig. 60; H_2L^{10} = 2-{[(2-hydroxy-3-

methoxyphenyl) methylidene]amino}benzoic acid; $C_6H_4NH_2CO_2H$=anthranilic acid) [396]. The compound contains a central SiO_4^{4-} unit, which adopts the 8.3333 binding mode, bridging to the eight Dy sites, which are described as a three-layer polyhedron. The compound appears to show slow relaxation of magnetisation, but a peak is only seen in χ'' at the highest frequency measured, and therefore no energy barrier is reported.

5.3 New Ytterbium SMMs in 2013

Only one new ytterbium SMM has been reported in 2013, a dimetallic compound $[Yb(tta)_2(L^{11})(L^{12})]_2$ (**411**; structures of HL^{11} and HL^{12} given in Scheme 1; $tta^- = 2$-thenoyltrifluoroacetonate) [392]. The compound has a small energy barrier to magnetic relaxation (Table 11) and also shows a Yb-based luminescence, and redox-activity at the ligand. The compound is therefore another example of a multi-functional Ln SMM, although again there is no link between the magnetism and the other interesting physical behaviour.

5.4 Discussion of 4f-SMMs

The progress in 10 years in lanthanide SMMs (and SIMs) is remarkable. There are now compounds of Tb phthalocyanine compounds with $U_{eff} > 900$ K [397]; Dy compounds with $U_{eff} > 800$ K [389]; Ho compounds with $U_{eff} \approx 400$ K [398]; Er compounds with $U_{eff} > 300$ K [399]. Therefore for most of the heavier lanthanides energy barriers have been achieved that far exceed those found for 3d-block compounds.

There is an increasing need to understand and hence predict the energy barriers and relaxation paths seen. Excellent work has been published recently on using computer programs to calculate U_{eff} in lanthanide SIMs with high symmetry using a crystal field approach [400]. The difficulty in a crystal field approach is the need for high symmetry to allow a sensible number of parameters to be used; as the symmetry falls the number of parameters becomes unmanageable. This also assumes that very high symmetry is important. This latter assumption also leads to some cases where high symmetry is claimed which is simply not present. The use of *quasi-* ahead of a point group term is not particularly helpful. The rules being applied only apply when the symmetry is strictly obeyed, not in *quasi*-symmetric cases.

In fact the axial symmetry being used may be missing the key point, which is that in most of the high energy barriers SMMs and SIMs, there is a very strong axial field leading to one direction being very different to the others, regardless of the point group symmetry. Recently an electrostatic approach has been proposed to calculate the anisotropy axes in Dy SMMs [401]. This approach is pleasingly

simplistic, based on a charge partition using valence bond theory that could be carried out by an intelligent first year chemistry undergraduate. It is also limited, producing no energetics to this point and only being applicable to one lanthanide.

Many of the papers above involve high level ab initio calculations using CASSCF; in most cases, these have been performed in the group led by Prof. Liviu Chibotaru. These calculations are clearly immensely valuable in guiding synthetic chemists towards better Ln-based SMMs. Whether a simpler approach can be adopted which will be easier to understand, and which is less computationally demanding, remains to be seen.

A major issue remains the low temperatures at which magnetic hysteresis is found in most Ln-based SMMs, regardless of the very high energy barriers. This is a direct consequence of quantum tunneling of magnetisation, which is favoured by the strong spin–orbit coupling. Work from Long's group [19] suggests that proximity to an organic radical can reduce the tunneling and hence raise the temperature at which hysteresis is observed. There is some evidence that local fields that are transverse to the direction of magnetic anisotropy increase tunneling rates [389] and dipolar interactions between Ln-SMMs in crystals and powders is clearly an important factor in deciding both the apparent energy barriers and the tunneling. Whether careful and designed positioning of local magnetic moments, e.g. organising organic or d-block paramagnets about the Ln-SMM, can reduce tunneling remains to be proven. However this route needs to be explored. In Ln-SMMs we now have a very high energy barrier to loss of magnetisation; we now need to learn to block the tunnel through this barrier.

6 ADDENDA

The following SMMs were missed in our original survey and we would like to thank Prof. Song Gao for bringing them to our attention.

6.1 [$NaMn_3(^tBuSao)_6$]: A Linear Oximate-Based SMM

A linear mixed-valent [$Mn^{IV}{}_2Mn^{III}$] oximate cluster was reported in 2012, [$NaMn_3(^tBuSao)_6$] (**412**), featuring the bulky oximate ligand 3,5-di-tert-butylsalicylaldoxime ($^tBuSaoH_2$) [402]. Its structure describes a linear trinuclear {$Mn^{IV}{}_2Mn^{III}$} core capped by six bulky doubly deprotonated $^tBuSao^{2-}$ ligands. The cluster possesses an $S = 5$ ground-state, due to the presence of dominant ferromagnetic interactions within the cluster between the trivalent and the tetravalent ions. The complex displays out-of-phase peaks at ~2.0 K, leading to an energy barrier of ~9 K with $\tau_0 = 2.0 \times 10^{-7}$ s.

6.2 An Enantiopure [Fe^{III}_4] SMM

Complexes $[Fe_4(L_R)_6]\cdot 5DMF\cdot H_2O$ (**413**R·5DMF·H_2O) and $[Fe_4(L_s)_6]\cdot 5DMF\cdot H_2O$ (**413**S·5DMF·H_2O) were synthesised upon the reaction of $FeCl_2$ with H_2L (=((R or S)-2-((2-hydroxy-1-phenylethyliminomethyl)phenol) in the presence of NEt_3 in MeOH, followed by recrystallisation in DMF [403]. Both complexes are enantiomers and their structure describes a typical [Fe_4] star-like complex. Both enantiomers exhibit identical magnetic behavior, with each possessing an $S = 5$ ground-state as a result of the antiferromagnetic interactions between the central and the peripheral iron atoms, while from magnetisation studies the zero-field splitting of the ground-state parameter, D, was found to be $-0.34\ cm^{-1}$. The cluster displays fully formed out-of-phase peaks below ~1 K, while the Arrhenius analysis yielded an $U_{eff} \sim 10$ K.

6.3 [$Fe_{12}Sm_4O_{10}(OH)_4(PhCO_2)_{24}$]: A Decatetranuclear Fe/Sm SMM

Cluster $[Fe^{III}_{12}Sm_4O_{10}(OH)_4(PhCO_2)_{24}]$ (**414**) was made upon reacting $[Fe_3O(PhCO_2)_6(H_2O)_3](PhCO_2)$ with $Sm(NO_3)_3\cdot 9H_2O$ in MeCN under solvothermal conditions [404]. In **414** all iron centres are found in a distorted octahedral coordination environent, while the Sm^{III} ions display distorted square-antiprism geometry. The structure consists of two $\{Fe_4O_2(OH)_2\}$ cubane units which "sandwich" four Fe^{III} centres forming a dodecanuclear ferric core on which the four Sm^{III} centres are attached via six μ_3-O^{2-} groups. The cluster displays fully formed "out-of-phase" peaks in *ac* magnetic susceptibility measurements below ~2.5 K, while the Arrhenius analysis yielded $U_{eff} = 16$ K with $\tau_0 = 2 \times 10^{-8}$ s.

References

1. Lis T (1980) Acta Cryst B36:2042
2. Weinland RF, Fischer G (1921) Z Anorg Allg Chem 120:161
3. Caneschi A, Gatteschi D, Sessoli R, Barra AL, Brunel LC, Guillot M (1991) J Am Chem Soc 113:5873
4. Richardson JT, Milligan WD (1956) Phys Rev B 102:1289
5. Nagata S, Keesom PH, Harrison HN (1979) Phys Rev B 19:1363
6. Sessoli R, Gatteschi D, Caneschi A, Novak MA (1993) Nature 365:141
7. Aubin SMJ, Wemple MW, Adams DM, Tsai H-L, Christou G, Hendrickson DN (1996) J Am Chem Soc 118:7746
8. Wickman HH, Trozzolo AM, Williams HJ, Hull GW, Merritt FR (1967) Phys Rev 155:563
9. Wickman HH (1972) J Chem Phys 56:976
10. Arai N, Sorai M, Suga H, Seki S (1977) J Phys Chem Solids 38:1341

11. Miller JS, Calabrese JC, Rommelmann H, Chittipeddi SR, Zhang JH, Reiff WM, Epstein AJ (1987) J Am Chem Soc 109:769
12. Miller JS, Epstein AJ (1987) J Am Chem Soc 109:3850
13. Manriquez JM, Yee GT, McLean RS, Epstein AJ, Miller JS (1991) Science 252:1415
14. Ferlay S, Mallah T, Quahés R, Veillet P, Verdaguer M (1995) Nature 378:701
15. Friedman JR, Sarachik MP, Tejada J, Ziolo R (1996) Phys Rev Lett 76:3830
16. Thomas L, Lionti F, Ballou R, Gatteschi D, Sessoli R, Barbara B (1996) Nature 383:145
17. Milios CJ, Vinslava A, Wernsdorfer W, Moggach S, Parsons S, Perlepes SP, Christou G, Brechin EK (2007) J Am Chem Soc 129:2754
18. Rinehart JD, Fang M, Evans WJ, Long JR (2011) Nat Chem 3:539
19. Rinehart JD, Fang M, Evans WJ, Long JR (2011) J Am Chem Soc 133:14236
20. Loth S, Baumann S, Lutz CP, Eigler DM, Heinrich AJ (2012) Science 335:196
21. Li T, Patz A, Mouchliadis L, Yan J, Lograsso TA, Perakis IE, Wang J (2013) Nature 496:69
22. Datta S, Milios CJ, Brechin EK, Hill S (2008) J App Phys 103:07B913
23. Bouwen A, Caneschi A, Gatteschi D, Goovaerts E, Schoemaker D, Sorace L, Stefan M (2001) J Phys Chem B 105:2658
24. Lampropoulos C, Redler G, Data S, Abboud KA, Hill S, Christou G (2010) Inorg Chem 49:1325
25. Hill S, Anderson N, Wilson A, Takahashi S, Chakov NE, Murugesu M, North JM, Dalal NS, Christou G (2005) J App Phys 97(10):M510
26. Hill S, Edwards RS, Jones SI, North JM, Dalal NS (2003) Phys Rev Lett 90:217204
27. Takahashi S, Edwards RS, North JM, Hill S, Dalal NS (2004) Phys Rev B 70:094429
28. Barra A-L, Caneschi A, Cornia A, Gatteschi D, Gorini L, Heiniger L-P, Sessoli R, Sorace L (2007) J Am Chem Soc 129:10754
29. Wilson A, Lawrence J, Yang EC, Nakano M, Hendrickson DN, Hill S (2006) Phys Rev B 74:140403
30. Accorsi S, Barra AL, Caneschi A, Chastanet G, Cornia A, Fabretti AC, Gatteschi D, Mortalò C, Olivieri E, Parenti F, Rosa P, Sessoli R, Sorace L, Wernsdorfer W, Zobbi L (2006) J Am Chem Soc 128:4742
31. Hill S, Murugesu M, Christou G (2009) Phys Rev B 80:174416
32. Barra AL, Caneschi A, Gatteschi D, Sessoli R (1995) J Am Chem Soc 117:8855
33. Kirchner N, van Slageren J, Brechin EK, Dressel M (2005) Polyhedron 24:2400
34. van Slageren J, Vongtragool S, Gorshunov B, Mukhin AA, Karl N, Krzystek J, Telser J, Muller A, Sangregorio C, Gatteschi D, Dressel M (2003) Phys Chem Chem Phys 5:3837
35. Pieper O, Guidi T, Caretta S, van Slageren J, El Hallak F, Lake B, Santini P, Amoretti G, Mutka H, Koza M, Russina M, Schnegg A, Milios CJ, Brechin EK, Julià A, Tejada J (2010) Phys Rev B 81:174420
36. van Slageren J, Vongtragool S, Gorshunov BP, Mukhin AA, Dressel M (2009) Phys Rev B 79:224406
37. El Hallak F, van Slageren J, Gómez-Segura J, Ruiz-Molina D, Dressel M (2007) Phys Rev B 75:104403
38. Andres H, Basler R, Güdel HU, Aromi G, Christou G, Buttner H, Ruffle B (2000) J Am Chem Soc 122:12469
39. Zhong Y, Sarachik MP, Friedman JR, Robinson RA, Kelley TM, Nakotte H, Christianson AC, Trouw F, Aubin SMJ, Hendrickson DN (1999) J Appl Phys 85:5636
40. Hennion M, Pardi L, Mirebeau I, Suard E, Sessoli R, Caneschi A (1997) Phys Rev B 56:8819
41. Basler R, Sieber A, Chaboussant G, Güdel HU, Chakov NE, Soler M, Christou G, Desmedt A, Lechner R (2005) Inorg Chem 44:649
42. Mirebeau I, Hennion M, Casalta H, Andres H, Güdel H-U, Irodova AV, Caneschi A (1999) Phys Rev Lett 83:628
43. Andres H, Basler R, Blake AJ, Cadiou C, Chaboussant G, Graig M, Güdel HU, Murrie M, Parson S, Paulsen C, Semadini F, Villar V, Wernsdorfer W, Winpenny REP (2002) Chem Eur J 8:21

44. Basler R, Chaboussant G, Canada-Vilalta C, Christou G, Mutka H, Janssen S, Altorfer F, Güdel H-U (2003) Polyhedron 22:2471
45. Carretta S, Livotti E, Amoretti G, Caciuffo R, Caneschi A, Gatteschi D (2002) Phys Rev B 65:052411
46. Amoretti G, Caciuffo R, Combet J, Murani A, Caneschi A (2000) Phys Rev B 62:3022
47. Waldmann O, Carver G, Dobe C, Biner D, Sieber A, Güdel H-U, Mutka H, Ollivier J, Chakov NE (2006) Appl Phys Lett 88:042507
48. Waldmann O, Bircher R, Carver G, Sieber A, Güdel HU, Mutka H (2007) Phys Rev B 75:174438
49. Waldmann O, Carver G, Dobe C, Sieber A, Güdel HU, Mutka H (2007) J Am Chem Soc 129:1526
50. Sieber A, Foguet-Albiol D, Waldmann O, Ochsenbein ST, Carver G, Mutka H, Fernandez-Alonso F, Mezouar M, Weber HP, Christou G, Güdel HU (2006) Phys Rev B 74:024405
51. Stuiber S, Wu G, Nehrkorn J, Dreiser J, Lan Y, Novitchi G, Anson CE, Unruh T, Powell AK, Waldmann O (2011) Chem Eur J 17:9094
52. Ochsenbein ST, Tuna F, Rancan M, Davies RSG, Muryn CA, Waldmann O, Bircher R, Sieber A, Carver G, Mutka H, Fernandez-Alonso F, Podlesnyak A, Engelhardt LP, Timco GA, Güdel HU, Winpenny REP (2008) Chem Eur J 14:5144
53. Waldmann O, Güdel HU (2005) Phys Rev B 72:094422
54. Christou G, Gatteschi D, Hendrickson DN, Sessoli R (2000) Mater Res Bull 25:66
55. Sessoli R, Gatteschi D (2003) Angew Chem Int Ed 42:268
56. Aromí G, Brechin EK (2006) Struct Bond 122:1
57. Bagai R, Christou G (2009) Chem Soc Rev 38:1011
58. Dei A, Gatteschi D (2011) Angew Chem Int Ed 50:11852
59. Winpenny REP (ed) (2006) Single-molecule magnets and related phenomena. Struct Bond 122
60. Friedman JR, Sarachik MP (2010) Annu Rev Condens Matter Phys 1:109
61. Sorace L, Benelli C, Gatteschi D (2011) Chem Soc Rev 40:3092
62. Brooker S, Kitchen JA (2009) Dalton Trans 7331
63. Habib F, Murugesu M (2013) Chem Soc Rev 42:3278
64. Guo Y-N, Xu G-F, Guo Y, Tang J (2011) Dalton Trans 40:9953
65. Winpenny REP, McInnes EJL (2010) In: Walton RI, Bruce DW O'Hare D (eds) Molecular nanomagnets. "Inorganic Materials" "Molecular Materials", vol 3. Wiley, Chichester, UK
66. Gatteschi D, Sessoli R, Villain R (2006) Molecular nanomagnets. Oxford University Press, Oxford
67. Castro SL, Sun Z, Bollinger JD, Hendrickson DN, Christou G (1995) Chem Soc Chem Commun 1995:2517
68. Castro SL, Sun Z, Grant CM, Bollinger JC, Hendrickson DN, Christou G (1998) J Am Chem Soc 120:2365
69. Sun ZM, Grant CM, Castro SL, Hendrickson DN, Christou G (1998) Chem Commun 1998:721
70. Müller A, Döring J (1988) Angew Chem Int Ed Engl 27:1721
71. Gatteschi D, Pardi L, Barra AL, Müller A, Döring J (1991) Nature (Lond) 354:465
72. Barra A-L, Gatteschi D, Pardi L, Müller A, Döring J (1992) J Am Chem Soc 114:8509
73. Chiorescu I, Wernsdorfer W, Müller A, Bögge H, Barbara B (2000) Phys Rev Lett 84:3454
74. Chiorescu I, Wernsdorfer W, Barbara B (2000) J Appl Phys 87:5496
75. Dobrovitski VV, Katsnelson MI, Harmon BN (2000) Phys Rev Lett 84:3458
76. Yang J, Wang Y, Wang Z, Rong X, Duan C-K, Su JH, Du J (2012) Phys Rev Lett 108:230501
77. Wernsdorfer W, Aliaga-Alcalde N, Hendrickson DN, Christou G (2002) Nature 146:406
78. Hendrickson DN, Christou G, Schmitt EA, Libby E, Bashkin JS, Wang SY, Tsai HL, Vincent JB, Boyd PDW, Huffman JC, Folting K, Li QY, Streib WE (1992) J Am Chem Soc 114:2455
79. Yoo J, Brechin EK, Yamaguchi A, Nakano M, Huffman JC, Maniero AL, Brunel LC, Awaga K, Ishimoto H, Christou G, Hendrickson DN (2000) Inorg Chem 39:3615

80. Yang EC, Harden N, Wernsdorfer W, Zakharov L, Brechin EK, Rheingold AL, Christou G, Hendrickson DN (2003) Polyhedron 22:1857
81. Yoo J, Yamaguchi A, Nakano M, Krzystek J, Streib WE, Brunel LC, Ishimoto H, Christou G, Hendrickson DN (2001) Inorg Chem 40:4604
82. Lecren L, Wernsdorfer W, Li Y-G, Roubeau O, Miyasaka H, Clérac R (2005) J Am Chem Soc 127:11311
83. Lecren L, Roubeau O, Coulon C, Li Y-G, Le Goff XF, Wernsdorfer W, Miyasaka H, Clérac R (2005) J Am Chem Soc 127:17353
84. Miyasaka H, Nakata K, Lecren L, Coulon C, Nakazawa Y, Fijisaki T, Sugiura K-I, Yamashita M, Clérac R (2006) J Am Chem Soc 128:3770
85. Lecren L, Roubeau O, Li Y-G, Le Goff XF, Miyasaka H, Richard F, Wernsdorfer W, Coulon C, Clérac R (2008) Dalton Trans 2008:755
86. Lecren L, Li Y-G, Wernsdorfer W, Roubeau O, Miyasaka H, Clérac R (2005) Inorg Chem Commun 8:626
87. Ako AM, Mereacre V, Hewitt IJ, Clérac R, Lecren L, Anson CE, Powell AK (2006) J Mater Chem 16:2579
88. Wittick LM, Jones LF, Jensen P, Moubaraki B, Spiccia L, Berry KJ, Murray KS (2006) Dalton Trans 2006:1534
89. Wittick LM, Murray KS, Moubaraki B, Batten SR, Spiccia L, Berry KJ (2004) Dalton Trans 2004:1003
90. Yang C-I, Lee G-H, Wur C-S, Lin JG, Tsai H-L (2005) Polyhedron 24:2215
91. Yoo J, Wernsdorfer W, Yang E-C, Nakano M, Rheingold AL, Hendrickson DN (2005) Inorg Chem 44:3377
92. Foguet-Albiol D, O'Brien TA, Wernsdorfer W, Moulton B, Zaworotko MJ, Abboud KA, Christou G (2005) Angew Chem Int Ed 44:897
93. Tasiopoulos AT, Vinslava A, Wernsdorfer W, Abboud KA, Christou G (2004) Angew Chem Int Ed 43:2117
94. Moushi EE, Lampropoulos C, Wernsdorfer W, Nastopoulos V, Christou G, Tasiopoulos AJ (2010) J Am Chem Soc 132:16146
95. Barra AL, Gatteschi D, Sessoli R (1997) Phys Rev B 56:8192
96. Sessoli R, Tsai HL, Schake AR, Wang SY, Vincent JB, Folting K, Gatteschi D, Christou G, Hendrickson DN (1993) J Am Chem Soc 115:1804
97. Tsai H-L, Chin D-M, Yang C-I, Jwo T-Y, Wur C-S, Lee G-H, Wang Y (2001) Inorg Chem Commun 4:511
98. Chakov NE, Lee S-C, Harter AG, Kuhns PL, Reyes AP, Hill SO, Dalal NS, Wernsdorfer W, Abboud KA, Christou G (2006) J Am Chem Soc 128:6975
99. Bian G-Q, Kuroda-Sowa T, Gunjima N, Maekawa M, Munakata M (2005) Inorg Chem Commun 8:208
100. Eppley HJ, Tsai H-L, De Vries N, Folting K, Christou G, Hendrickson DN (1995) J Am Chem Soc 177:301
101. Artus P, Boskovic C, Yoo J, Streib WE, Brunel L-C, Hendrickson DN, Christou G (2001) Inorg Chem 40:4199
102. Sun Z, Ruiz D, Rumberger E, Incarvito CD, Folting K, Rheingold AL, Christou G, Hendrickson DN (1998) Inorg Chem 37:4758
103. Boskovic C, Pink M, Huffman JC, Hendrickson DN, Christou G (2001) J Am Chem Soc 123:9914
104. Chankov NE, Wernsdorfer W, Abboud KA, Hendrickson DN, Christou G (2003) Dalton Trans 2003:2243
105. Soler M, Artus P, Folting K, Huffman JC, Hendrickson DN, Christou G (2001) Inorg Chem 40:4902
106. Brockman JT, Abboud KA, Hendrickson DN, Christou G (2003) Polyhedron 22:1765
107. Aubin SMJ, Spagna S, Eppley HJ, Sanger RE, Folting K, Christou G, Hendrickson DN (1997) Mol Cryst Liq Cryst 305:181

108. Ruiz D, Sun Z, Albela B, Folting K, Ribas J, Christou G, Hendrickson DN (1998) Angew Chem Int Ed 37:300
109. Aubin SMJ, Sun ZM, Eppley HJ, Rumberger EM, Guzei IA, Folting K, Gantzel PK, Rheingold AL, Christou G, Hendrickson DN (2001) Inorg Chem 40:2127
110. Zhao H, Berlinguette CP, Bacsa J, Prosvirin AV, Bera JK, Tichy SE, Schelter EJ, Dunbar KR (2004) Inorg Chem 43:1359
111. Lim JM, Do Y, Kim J (2006) Eur J Inorg Chem 2006:711
112. Gómez-Segura J, Campo J, Imaz I, Wurst K, Veciana J, Gerbier P, Ruiz-Molina D (2007) Dalton Trans 2007:2450
113. Ruiz-Molina D, Gerbier R, Rumberger E, Amabilino DB, Guzei IA, Folting K, Huffman JC, Rheingold A, Christou G, Veciana J, Hendrickson DN (2002) J Mater Chem 12:1152
114. Gómez-Segura J, Lhotel E, Paulsen C, Luneau D, Wurst K, Veciana J, Ruiz-Molina D, Gerbier P (2005) New J Chem 29:499
115. Kuroda-Sowa T, Nogami T, Konaka H, Maekawa M, Munekata M, Miyasaka H, Yamashita M (2003) Polyhedron 22:1795
116. Tsai H-L, Eppley HJ, de Vries N, Folting K, Christou G, Hendrickson DN (1995) Mol Cryst Liq Cryst 274:167
117. Tsai H-L, Shiao H-A, Jwo T-Y, Yang C-I, Wur C-S, Lee G-H (2005) Polyhedron 24:2205
118. Coronado E, Forment-Aliaga A, Gaita-Ariño A, Giménez-Saiz C, Romero FM, Wernsdorfer W (2004) Angew Chem Int Ed 43:6152
119. Chakov NE, Soler M, Wernsdorfer W, Abboud KA, Christou G (2005) Inorg Chem 44:5304
120. Willemin S, Donnadieu B, Lecren L, Henner B, Clérac R, Guérin C, Meyer A, Pokrovskii AV, Larionova J (2004) New J Chem 2004:919
121. Rumberger EM, del Barco E, Lawrence J, Hill S, Kent AD, Zakharov LN, Rheingold AL, Hendrickson DN (2005) Polyhedron 24:2557
122. Kuroda-Sowa T, Handa T, Kotera T, Maekawa M, Munakata M, Miyasaka H, Yamashita M (2004) Chem Lett 33:540
123. Aubin SMJ, Sun Z, Pardi L, Krzystek J, Folting K, Brunel L-C, Rheingold AL, Christou G, Hendrickson DN (1999) Inorg Chem 38:5329
124. Soler M, Chandra SK, Ruiz D, Huffman JC, Hendrickson DN, Christou G (2001) Polyhedron 20:1279
125. Soler M, Wernsdorfer W, Abboud KA, Huffman JC, Davidson ER, Hendrickson DN, Christou G (2003) J Am Chem Soc 125:3576
126. Soler M, Wernsdorfer W, Abboud KA, Hendrickson DN, Christou G (2003) Polyhedron 22:1777
127. Bian G-Q, Kuroda-Sowa T, Konaka H, Hatano M, Maekawa M, Munakata M, Miyasaka H, Yamashita M (2004) Inorg Chem 43:4790
128. Tasiopoulos AJ, Wernsdorfer W, Abboud KA, Christou G (2005) Inorg Chem 44:6324
129. Bagai R, Christou G (2007) Inorg Chem 46:10810
130. Burgert M, Voss S, Herr S, Fonin M, Groth U, Rüdiger U (2007) J Am Chem Soc 129:14363
131. Clemente-Juan JM, Coronado E, Forment-Aliaga A, Gaita-Ariño A, Giménez-Saiz C, Romero FM, Wernsdorfer W, Biagi R, Corradini V (2010) Inorg Chem 49:386
132. George SM, Mamun SI, Kim J (2010) Inorg Chem Commun 13:429
133. Pineider F, Mannini M, Sangregorio C, Gorini L, Sessoli R (2008) Inorg Chim Acta 361:3944
134. Kushch LA, Sasnovskaya VD, Dmitriev AI, Yagubskii EB, Koplak OV, Zorina LV, Boukhvalov DW (2012) Dalton Trans 41:13747
135. Lampropoulos C, Murugesu M, Harter AG, Wernsdofer W, Hill S, Dalal NS, Reyes AP, Kuhns PL, Abboud KA, Christou G (2013) Inorg Chem 52:258
136. Milios CJ, Raptopoulou CP, Terzis A, Lloret F, Vicente R, Perlepes SP, Escuer A (2004) Angew Chem Int Ed 43:210
137. Halcrow MA, Streib WE, Folting K, Christou G (1995) Acta Crystallogr C51:1263
138. Chaudhuri P, Hess M, Rentschler E, Weyhermüller T, Flörke U (1998) New J Chem 22:553
139. Chaudhuri P (2003) Coord Chem Rev 241:143

140. Stamatatos TC, Foguet-Albiol D, Stoumpos CC, Raptopoulou CP, Terzis A, Wernsdorfer W, Perlepes SP, Christou G (2005) J Am Chem Soc 127:15380
141. Sreerama SG, Pal S (2002) Inorg Chem 41:4843
142. Milios CJ, Gavin Whittaker A, Brechin EK (2007) Polyhedron 26:1927
143. Milios CJ, Vinslava A, Wood PA, Parsons S, Wernsdorfer W, Christou G, Perlepes SP, Brechin EK (2007) J Am Chem Soc 129:8
144. Milios CJ, Vinslava A, Whittaker AG, Parsons S, Wernsdorfer W, Christou G, Perlepes SP, Brechin EK (2006) Inorg Chem 45:5272
145. Milios CJ, Inglis R, Vinslava A, Bagai R, Wernsdorfer W, Parsons S, Perlepes SP, Christou G, Brechin EK (2007) J Am Chem Soc 129:12505
146. Inglis R, Jones LF, Milios CJ, Datta S, Collins A, Parsons S, Wernsdorfer W, Hill S, Perlepes SP, Piligkos S, Brechin EK (2009) Dalton Trans 2009:3403
147. Milios CJ, Vinslava A, Wernsdorfer W, Prescimone A, Wood PA, Parsons S, Perlepes SP, Christou G, Brechin EK (2007) J Am Chem Soc 129:6547
148. Milios CJ, Inglis R, Bagai R, Wernsdorfer W, Collins A, Moggach S, Parsons S, Perlepes SP, Christou G, Brechin EK (2007) Chem Comm 2007:3476
149. Jones LF, Inglis R, Cochrane ME, Mason K, Collins A, Parsons S, Perlepes SP, Brechin EK (2008) Dalton Trans 2008:6205
150. Kotzabasaki V, Inglis R, Siczek M, Lis T, Brechin EK, Milios CJ (2011) Dalton Trans 40:1693
151. Martínez-Lillo J, Dolan N, Brechin EK (2013) Dalton Trans. doi:10.1039/c3dt51512e
152. Milios CJ, Piligkos S, Brechin EK (2008) Dalton Trans 2008:1809
153. Inglis R, Milios CJ, Jones LF, Brechin EK (2012) Chem Comm 48:181
154. Carretta S, Guidi T, Santini P, Amoretti G, Pieper O, Lake B, Van Slageren J, Mutka H, Russina M, Milios CJ, Brechin EK (2008) Phys Rev Lett 100:157203
155. Bahr S, Milios CJ, Brechin EK, Mosser V, Wernsdorfer W (2008) Phys Rev B 78:132401
156. Carretta S, Guidi T, Santini P, Amoretti G, Pieper O, Lake B, van Slageren J, El Hallak F, Wernsdorfer W, Mutka H, Russina M, Milios CJ, Brechin EK (2009) Polyhedron 28:1940
157. Datta S, Bolin E, Inglis R, Milios CJ, Brechin EK, Hill S (2009) Polyhedron 28:1788
158. Piligkos S, Bendix J, Weihe H, Milios CJ, Brechin EK (2008) Dalton Trans 2008:2277
159. Carretta S, Liviotti E, Magnani N, Santini P, Amoretti G (2004) Phys Rev Lett 92:207205
160. Inglis R, Taylor SM, Jones LF, Papaefstathiou GS, Perlepes SP, Datta S, Hill S, Wernsdorfer W, Brechin EK (2009) Dalton Trans 2009:9157
161. Stamatatos TC, Foguet-Albiol D, Lee S-C, Stoumpos CC, Raptopoulou CP, Terzis A, Wernsdorfer W, Hill SO, Perlepes SP, Christou G (2007) J Am Chem Soc 129:9484
162. Milios CJ, Prescimone A, Mishra A, Parsons S, Wernsdorfer W, Christou G, Perlepes SP, Brechin EK (2007) Chem Comm 2007:153
163. Inglis R, Stoumpos CC, Prescimone A, Siczek M, Lis T, Wernsdorfer W, Brechin EK, Milios CJ (2010) Dalton Trans 10:4777
164. Milios CJ, Gass IA, Vinslava A, Budd L, Parsons S, Wernsdorfer W, Perlepes SP, Christou G, Brechin EK (2007) Inorg Chem 46:6215
165. Milios CJ, Inglis R, Vinslava A, Prescimone A, Parsons S, Perlepes SP, Christou G, Brechin EK (2007) Chem Comm 2007:2738
166. Milios CJ, Inglis R, Jones LF, Prescimone A, Parsons S, Wernsdorfer W, Brechin EK (2009) Dalton Trans 2009:2812
167. Escuer A, Aromi G (2006) Eur J Inorg Chem 2006:4721
168. Feng PL, Stephenson CJ, Amjad A, Ogawa G, del Barco E, Hendrickson DN (2010) Inorg Chem 49:1304
169. Inglis R, White F, Piligkos S, Wernsdorfer W, Brechin EK, Papaefstathiou GS (2011) Chem Commun 47:3090
170. Hołynska M, Frank N, Pichon C, Jeon I-R, Clérac R, Dehnen S (2013) Inorg Chem 52:7317
171. Wang S, Kong L, Yang H, He Z, Zheng J, Li D, Zeng S, Niu M, Song Y, Dou J (2011) Inorg Chem 50:2705

172. Manoli M, Inglis R, Manos MJ, Nastopoulos V, Wernsdorfer W, Brechin EK, Tasiopoulos AJ (2011) Angew Chem Int Ed 50:4441
173. Cordero B, Roubeau O, Teat SJ, Escuer A (2011) Dalton Trans 40:7127
174. Miyasaka H, Clérac R, Wernsdorfer W, Lecren L, Bonhomme C, Sugiura K-I, Yamashita M (2004) Angew Chem Int Ed 43:2801
175. Lu Z, Yuan M, Pan F, Gao S, Zhang D, Zhu D (2006) Inorg Chem 45:3548
176. Kachi-Terajima C, Miyasaka H, Sugiura K-I, Clérac R, Nojiri H (2006) Inorg Chem 45:4381
177. Ge C-H, Cui A-L, Ni Z-H, Jiang Y-B, Zhang L-F, Ribas J, Kou H-Z (2006) Inorg Chem 45:4883
178. Brechin EK, Soler M, Davidson J, Hendrickson DN, Parsons S, Christou G (2002) Chem Commun 2002:2252
179. Piligkos S, Rajaraman G, Soler M, Kirchner N, van Slageren J, Bircher R, Parsons S, Güdel H-U, Kortus J, Wernsdorfer W, Christou G, Brechin EK (2005) J Am Chem Soc 127:5572
180. Murugesu M, Wernsdorfer W, Christou G, Brechin EK (2007) Polyhedron 26:1845
181. Mondal KC, Song Y, Mukherjee PS (2007) Inorg Chem 46:9736
182. Pilawa B, Kelemen MT, Wanka S, Geisselmann A, Barra AL (1998) A L Europhys Lett 43:7
183. Koizumi S, Nihei M, Nakano M, Oshio H (2005) Inorg Chem 44:1208
184. Koizumi S, Nihei M, Shiga T, Nakano M, Nojiri H, Bircher R, Waldmann O, Ochsenbein ST, Güdel HU, Fernandez-Alonso F, Oshio H (2007) Chem Eur J 13:8445
185. Saalfrank RW, Scheurer A, Prakash R, Heinemann FW, Nakajima T, Hampel F, Leppin R, Pilawa B, Rupp H, Müller P (2007) Inorg Chem 46:1586
186. Chen S-Y, Beedle CC, Gan P-R, Lee G-H, Hill S, Yang E-C (2012) Inorg Chem 51:4448
187. Godbole MD, Roubeau O, Clérac R, Kooijman H, Spek AL, Bouwman E (2005) Chem Commun 2005:3715
188. Wu C-C, Datta S, Wernsdorfer W, Lee G-H, Hill S, Yang E-C (2010) Dalton Trans 39:10160
189. Goldberg DP, Caneschi A, Delfs CD, Sessoli R, Lippard SJ (1995) J Am Chem Soc 117:5789
190. Barra AL, Caneschi A, Gatteschi D, Goldberg DP, Sessoli R (1999) J Solid State Chem 145:484
191. Langley SK, Berry KJ, Moubaraki B, Murray KS (2009) Dalton Trans 2009:973
192. Langley SK, Moubaraki B, Berry KJ, Murray KS (2010) Dalton Trans 39:4848
193. Taylor SM, McIntosh RD, Rezé J, Dalgarno SJ, Brechin EK (2012) Chem Commun 48:9263
194. Li J-T, Ma Y-S, Li S-G, Cao D-K, Li Y-Z, Song Y, Zheng L-M (2009) Dalton Trans 2009:5029
195. Murugesu M, Wernsdorfer W, Abboud KA, Christou G (2005) Polyhedron 24:2894
196. Rumberger EM, Shah SJ, Beedle CC, Zakharov LN, Rheingold AL, Hendrickson DN (2005) Inorg Chem 44:2742
197. King P, Wernsdorfer W, Abboud KA, Christou G (2005) Inorg Chem 44:8659
198. Murugesu M, Wernsdorfer W, Abboud KA, Brechin EK, Christou G (2006) Dalton Trans 2006:2285
199. Li Y, Wernsdorfer W, Clérac R, Hewitt IJ, Anson CE, Powell AK (2006) Inorg Chem 45:2376
200. Zhou A-J, Qin L-J, Beedle CC, Ding S, Nakano M, Leng J-D, Tong M-L, Hendrickson DN (2007) Inorg Chem 46:8111
201. Shah SJ, Ramsey CM, Heroux KJ, DiPasquale AG, Dalal NS, Rheingold AL, del Barco E, Hendrickson DN (2008) Inorg Chem 47:9569
202. Maheswaran S, Chastanet G, Teat SJ, Mallah T, Sessoli R, Wernsdorfer W, Winpenny REP (2005) Angew Chem Int Ed 44:5044
203. Price DJ, Batten SR, Moubaraki B, Murray KS (2007) Polyhedron 26:305
204. Manoli M, Prescimone A, Bagai R, Mishra A, Murugesu M, Parsons S, Wernsdorfer W, Christou G, Brechin EK (2007) Inorg Chem 46:6968
205. Zheng Y-Z, Xue W, Zhang W-X, Tong ML, Chen X-M (2007) Inorg Chem 46:6437

206. Brechin EK, Sañudo EC, Wernsdorfer W, Boskovic C, Yoo J, Hendrickson DN, Yamaguchi A, Ishimoto H, Concolino TE, Rheingold AL, Christou G (2005) Inorg Chem 44:502
207. Sañudo EC, Wernsdorfer W, Abboud KA, Christou G (2004) Inorg Chem 43:4137
208. Murugescu M, Raftery J, Wernsdorfer W, Christou G, Brechin EK (2004) Inorg Chem 43:4203
209. Brockman JT, Stamatatos TC, Wernsdorfer W, Abboud KA, Christou G (2007) Inorg Chem 46:9160
210. Stamatatos TC, Abboud KA, Wernsdorfer W, Christou C (2007) Angew Chem Int Ed 46:884
211. Murugescu M, Habrych M, Wernsdorfer W, Abboud KA, Christou G (2004) J Am Chem Soc 126:4766
212. Soler M, Wernsdorfer W, Folting K, Pink M, Christou G (2004) J Am Chem Soc 126:2156
213. Zaleski CM, Depperman EC, Dendrinou-Samara C, Alexiou M, Kampf JW, Kessissoglou DP, Kirk ML, Pecoraro VL (2005) J Am Chem Soc 127:12862
214. Dendrinou-Samara C, Alexiou M, Zaleski CM, Kampf JW, Kirk ML, Kessissoglou DP, Pecoraro VL (2003) Angew Chem Int Ed 42:3763
215. Jones LF, Rajaraman G, Brockman J, Murugesu M, Sañudo EC, Raftery J, Teat SJ, Wernsdorfer W, Christou G, Brechin EK, Collison D (2004) Chem Eur J 10:5180
216. Stamatatos TC, Foguet-Albiol D, Wernsdorfer W, Abboud KA, Christou G (2011) Chem Commun 47:274
217. Langley SK, Stott RA, Chilton NF, Moubaraki B, Murray KS (2011) Chem Commun 47:6281
218. Taguchi T, Wernsdorfer W, Abboud KA, Christou G (2010) Inorg Chem 49:10579
219. Moushi EE, Stamatatos TC, Wernsdorfer W, Nastopoulos V, Christou G, Tasiopoulos AJ (2009) Inorg Chem 48:5049
220. Wang H-S, Zhang Z-C, Song X-J, Zhang J-W, Zhou H-B, Wang J, Song Y, You X-Z (2011) Dalton Trans 40:2703
221. Moushi EE, Masello A, Wernsdorfer W, Nastopoulos V, Christou G, Tasiopoulos AJ (2010) Dalton Trans 39:4978
222. Nayak S, Beltran LMC, Lan Y, Clérac R, Hearns NGR, Wernsdorfer W, Anson CE, Powell AK (2009) Dalton Trans 2009:1901
223. Stamatatos TC, Abboud KA, Wernsdorfer W, Christou G (2008) Angew Chem Int Ed 47:6694
224. Stamatatos TC, Nastopoulos V, Tasiopoulos AJ, Moushi EE, Wernsdorfer W, Christou G, Perlepes SP (2008) Inorg Chem 47:10081
225. Shah SJ, Ramsey CM, Heroux KJ, O'Brien JR, DiPasquale AG, Rheingold ADL, del Barco E, Hendrickson DN (2008) Inorg Chem 47:6245
226. Mishra A, Pushkar Y, Yano J, Yachandra VK, Wernsdorfer W, Abboud KA, Christou G (2008) Inorg Chem 47:1940
227. Gatteschi D, Sessoli R, Cornia A (2000) Chem Commun 2000:725
228. Xu B, Chasteen ND (1991) J Biol Chem 266:19965
229. Barra AL, Debrunner P, Gatteschi D, Schulz CE, Sessoli R (1996) Europhys Lett 35:133
230. Caciuffo R, Amoretti G, Murani A, Sessoli R, Caneschi A, Gatteschi D (1998) Phys Rev Lett 81:4744
231. Sangregorio C, Ohm T, Paulsen C, Sessoli R, Gatteschi D (1997) Phys Rev Lett 78:4645
232. Wernsdorfer W, Ohm T, Sangregorio C, Sessoli R, Mailly D, Paulsen C (1999) Phys Rev Lett 82:3903
233. Barra A-L, Caneschi A, Cornia A, Fabrizi de Biani F, Gatteschi D, Sangregorio C, Sessoli R, Sorace L (1999) J Am Chem Soc 121:5302
234. Cornia A, Fabretti AC, Garrisi P, Mortal C, Bonacchi D, Gatteschi D, Sessoli R, Sorace L, Wernsdorfer W, Barra A-L (2004) Angew Chem Int Ed Engl 43:1136
235. Barra A-L, Bianchi F, Caneschi A, Cornia A, Gatteschi D, Gorini L, Gregoli L, Maffini M, Parenti F, Sessoli R, Sorace L, Talarico AM (2007) Eur J Inorg Chem 2007:4145

236. Cornia A, Gregoli L, Danieli C, Caneschi A, Sessoli R, Sorace L, Barra A-L, Wernsdorfer W (2008) Inorg Chim Acta 361:3481
237. Rodriguez-Douton MJ, Cornia A, Sessoli R, Sorace L, Barra A-L (2010) Dalton Trans 39:5851
238. Prasad TK, Poneti G, Sorace L, Rodriguez-Douton MJ, Barra A-L, Neugebauer P, Costantino L, Sessoli R, Cornia A (2012) Dalton Trans 41:8368
239. Moragues-Canovas M, Riviere P, Ricard L, Paulsen C, Wernsdorfer W, Rajaraman G, Brechin EK, Mallah T (2004) Adv Mater 16:1101
240. Oshio H, Hoshino N, Ito T (2000) J Am Chem Soc 122:12602
241. Oshio H, Hoshino N, Ito T, Nakano M (2004) J Am Chem Soc 126:8805
242. Goodwin JC, Sessoli R, Gatteschi D, Wernsdorfer W, Powell AK, Heath SL (2000) J Chem Soc Dalton Trans 2000:1835
243. Boudalis AK, Donnadieu B, Nastopoulos V, Modesto Clemente-Juan J, Mari A, Sanakis Y, Tuchagues J-P, Perlepes SP (2004) Angew Chem Int Ed 43:2266
244. Boudalis AK, Sanakis Y, Clemente-Juan JM, Donnadieu B, Nastopoulos V, Mari A, Coppel Y, Tuchagues J-P, Perlepes SP (2008) Chem Eur J 14:2514
245. Powell GW, Lancashire HN, Brechin EK, Collison D, Heath SL, Mallah T, Wernsdorfer W (2004) Angew Chem Int Ed 43:5772
246. Benelli C, Parsons S, Solan GA, Winpenny REP (1996) Angew Chem Int Ed Engl 35:1825
247. Jones LF, Brechin EK, Collison D, Helliwell M, Mallah T, Piligkos S, Rajaraman G, Wernsdorfer W (2003) Inorg Chem 42:6601
248. Boudalis AK, Clemente-Juan JM, Dahan F, Tuchagues J-P (2004) Inorg Chem 43:1574
249. Bino A, Ardon M, Lee D, Spingler B, Lippard SJ (2002) J Am Chem Soc 124:4578
250. Bagai R, Wernsdorfer W, Abboud KA, Christou G (2007) J Am Chem Soc 129:12918
251. Saalfrank RW, Scheurer A, Bernt I, Heinemann FW, Postnikov AV, Schünemann V, Trautwein AX, Alam MS, Rupp H, Müller P (2006) Dalton Trans 2006:2865
252. Compain J-D, Mialane P, Dolbecq A, Mbomekallé IM, Marrot J, Sécheresse F, Rivière E, Rogez G, Wernsdorfer W (2009) Angew Chem Int Ed 48:3077
253. Ako AM, Mereacre V, Lan Y, Wernsdorfer W, Clérac R, Anson CE, Powell AK (2010) Inorg Chem 49:1
254. Wieghardt K, Pohl K, Jibril I, Huttner G (1984) Angew Chem Int Ed Engl 23:77
255. Delfs C, Gatteschi D, Pardi L, Sessoli R, Wieghardt K, Hanke D (1993) Inorg Chem 32:3099
256. Pontillon Y, Caneschi A, Gatteschi D, Sessoli R, Ressouche E, Schweizer J, Lelievre-Berna E (1999) J Am Chem Soc 121:5342
257. Wernsdorfer W, Sessoli R (1999) Science 284:133
258. Condorelli GG, Motta A, Pellegrino G, Cornia A, Gorini L, Fragalà IL, Sangregorio C, Sorace L (2008) Chem Mater 20:2405
259. Price DJ, Lionti F, Ballou R, Wood PT, Powell AK (1999) Philos Trans R Soc Lond Ser A Math Phys Eng Sci 357:3099
260. Papaefstathiou GS, Escuer A, Vicente R, Font-Bardia M, Solans X, Perlepes SP (2001) Chem Commun 2001:2414
261. Tsohos A, Dionyssopoulou S, Raptopoulou CP, Terzis A, Bakalbassis EG, Perlepes SP (1999) Angew Chem Int Ed 38:983
262. Papaefstathiou GS, Perlepes SP, Escuer A, Vicente R, Font-Bardia M, Solans X (2001) Angew Chem Int Ed 40:884
263. Papaefstathiou GS, Boudalis AK, Stamatatos TC, Milios CJ, Efthymiou CG, Raptopoulou CP, Terzis A, Psycharis V, Sanakis Y, Vicente R, Escuer A, Tuchagues J-P, Perlepes SP (2007) Polyhedron 26:2089
264. Benelli C, Cano J, Journaux Y, Sessoli R, Solan GA, Winpenny REP (2001) Inorg Chem 40:188
265. Boudalis AK, Sanakis Y, Clemente-Juan JM, Mari A, Tuchagues J-P (2007) Eur J Inorg Chem 2007:2409

266. van Slageren J, Rosa P, Caneschi A, Sessoli R, Casellas H, Rakitin YV, Cianchi L, Del Giallo F, Spina G, Bino A, Barra A-L, Guidi T, Carretta S, Caciuffo R (2006) Phys Rev B 73:014422
267. Wernsdorfer W (2001) Adv Chem Phys 118:99
268. Kahn O (1993) Molecular magnetism. New York, Wiley-VCH
269. Boeer AB, Barra A-L, Chibotaru LF, Collison D, McInnes EJL, Mole RA, Simeoni GC, Timco GA, Ungur L, Unruh T, Winpenny REP (2011) Angew Chem Int Ed 50:4007
270. Murrie M (2010) Chem Soc Rev 39:1986
271. Yang EC, Hendrickson DN, Wernsdorfer W, Nakano M, Zakharov LN, Sommer RD, Rheingold AL, Ledezma-Gairaud M, Christou G (2002) J Appl Phys 91:7382
272. Murrie M, Teat SJ, Stoeckli-Evans H, Güdel HU (2003) Angew Chem Int Edit 42:4653
273. Zhang Y-Z, Wernsdorfer W, Pan F, Wang Z-M, Gao S (2006) Chem Commun 2006:3302
274. Wang X-T, Wang B-W, Wang Z-M, Zhang W, Gao S (2008) Inorg Chim Acta 361:3895
275. Ferguson A, Parkin A, Sanchez-Benitez J, Kamenev K, Wernsdorfer W, Murrie M (2007) Chem Commun 2007:3473
276. Wu D, Guo D, Song Y, Huang W, Duan C, Meng Q, Sato O (2009) Inorg Chem 48:854
277. Klöwer F, Lan Y, Nehrkorn J, Waldmann O, Anson CE, Powell AK (2009) Chem Eur J 15:7413
278. Langley SJ, Helliwell M, Sessoli R, Rosa P, Wernsdorfer W, Winpenny REP (2005) Chem Commun 2005:5029
279. Zeng M-H, Yao M-X, Liang H, Zhang W-X, Chen X-M (2007) Angew Chem Int Ed 46:1832
280. Shiga T, Matsumoto T, Noguchi M, Onuki T, Hoshino N, Newton GN, Nakano M, Oshio H (2009) Chem Asian J 4:1660
281. Chen Q, Zeng M-H, Zhou Y-L, Zou H-H, Kurmoo M (2010) Chem Mater 22:2114
282. Galloway KW, Whyte AM, Wernsdorfer W, Sanchez-Benitez J, Kamenev KV, Parkin A, Peacock RD, Murrie M (2008) Inorg Chem 47:7438
283. Moubaraki B, Murray KS, Hudson TA, Robson R (2008) Eur J Inorg Chem 2008:4525
284. Boudalis AK, Raptopoulou CP, Abarca B, Ballasteros R, Chadlaoui M, Tuchagues J-P, Terzis A (2006) Angew Chem Int Ed 45:432
285. Kitos AA, Efthymiou CG, Papatriantafyllopoulou C, Nastopoulos V, Tasiopoulos AJ, Manos MJ, Wernsdorfer W, Christou G, Perlepes SP (2011) Polyhedron 30:2987
286. Zheng Y-Z, Speldrich M, Schilder H, Chen X-M, Kögerler P (2010) Dalton Trans 39:10827
287. Ibrahim M, Lan Y, Bassil BS, Xiang Y, Suchopar A, Powell AK, Kortz U (2011) Angew Chem Int Ed 50:4708
288. Hernández JM, Zhang XX, Luis F, Bartolomé J, Tejada J, Ziolo R (1996) Europhys Lett 35:301
289. Tudor V, Marin G, Lloret F, Kravtsov VC, Simonov YA, Julve M, Andruh M (2008) Inorg Chim Acta 361:3446
290. Aromi G, Batsanov AS, Christian P, Helliwell M, Parkin A, Parsons S, Smith AA, Timco GA, Winpenny REP (2003) Chem Eur J 9:5142
291. Langley S, Helliwell M, Sessoli R, Teat SJ, Winpenny REP (2008) Inorg Chem 47:497
292. Tangoulis V, Raptopoulou CP, Paschalidou S, Bakalbassis EG, Perlepes SP, Terzis A (1997) Angew Chem Int Ed Engl 36:1083
293. Rogez G, Rebilly JN, Barra AL, Sorace L, Blondin G, Kirchner N, Duran M, van Slageren J, Parsons S, Ricard L, Marvilliers A, Mallah T (2005) Angew Chem Int Ed 44:1876
294. Krzystek J, Park J-H, Meisel MW, Hitchman MA, Stratemeier H, Brunel L-C, Telser J (2002) Inorg Chem 41:4478
295. Vongtragool S, Gorshunov B, Dressel M, Krzystek J, Eichhorn DM, Telser J (2003) Inorg Chem 42:1788
296. Boča R (2004) Coord Chem Rev 248:757
297. Blake AJ, Grant CM, Parsons S, Rawson JM, Winpenny REP (1994) J Chem Soc Chem Commun 1994:2363

298. Yang EC, Wersdorfer W, Hill S, Edwards RS, Nakano M, Maccagnano S, Zakharov LN, Rheingold AL, Christou G, Hendrickson DN (2003) Polyhedron 22:1727
299. Yang E-C, Wernsdorfer W, Zakharov LN, Karaki Y, Yamaguchi A, Isidro RM, Lu G-D, Wilson SA, Rheingold AL, Ishimoto H, Hendrickson DN (2006) Inorg Chem 45:529
300. Moragues-Canova M, Helliwell M, Ricard L, Riviere E, Wernsdorfer W, Brechin EK, Mallah T (2004) Eur J Inorg Chem 2004:2219
301. Ferguson A, Lawrence J, Parkin A, Sanchez-Benitez J, Kamenev KV, Brechin EK, Wernsdorfer W, Murrie M (2008) Dalton Trans 2008:6409
302. Hameury S, Kayser L, Pattacini R, Rogez G, Wernsdorfer W, Braunstein P (2013) Dalton Trans 42:5013
303. Aromí G, Bouwman E, Burzurí E, Carbonera C, Krzystek J, Luis F, Schlegel C, van Slageren J, Tanase S, Teat SJ (2008) Chem Eur J 14:11158
304. Bell A, Aromí G, Teat SJ, Wernsdorfer W, Winpenny REP (2005) Chem Commun 2005:2808
305. Ochsenbein ST, Murrie M, Rusanov E, Stoeckli-Evans H, Sekine C, Güdel HU (2002) Inorg Chem 41:5133
306. Aromí G, Parsons S, Wernsdorfer W, Brechin EK, McInnes EJL (2005) Chem Commun 2005:5038
307. Scott RTW, Jones LF, Tidmarsh IS, Breeze B, Laye RH, Wolowska J, Stone DJ, Collins A, Parsons S, Wernsdorfer W, Aromí G, McInnes EJL, Brechin EK (2009) Chem Eur J 15:12389
308. Biswas R, Ida Y, Baker ML, Biswas S, Kar P, Nojiri H, Ishida T, Ghosh A (2013) Chem Eur J 19:3943
309. Petit S, Neugebauer P, Pilet G, Chastanet G, Barra A-L, Antunes AB, Wernsdorfer WG, Luneau D (2012) Inorg Chem 51:6645
310. Boudalis AK, Pissas M, Raptopoulou CP, Psycharis V, Abarca B, Ballesteros R (2008) Inorg Chem 47:10674
311. Cadiou C, Murrie M, Paulsen C, Villar V, Wernsdorfer W, Winpenny REP (2001) Chem Commun 2001:2666
312. Barnes JA, Hatfield WE (1971) Inorg Chem 10:2355
313. Gladfelter WL, Lynch MW, Schaefer WP, Hendrickson DN, Gray HB (1981) Inorg Chem 20:2390
314. Halcrow MA, Sun J-S, Huffman JC, Christou G (1995) Inorg Chem 34:4167
315. Wang X-Y, Avendaño C, Dunbar KR (2011) Chem Soc Rev 40:3213
316. Sokol JJ, Hee AG, Long JR (2002) J Am Chem Soc 124:7656
317. Song Y, Zhang P, Ren X-M, Shen X-F, Li Y-Z, You X-Z (2005) J Am Chem Soc 127:3708
318. Martínez-Lillo J, Armentano D, De Munno G, Wernsdorfer W, Julve M, Lloret F, Faus J (2006) J Am Chem Soc 128:14218
319. Yoon JH, Lim JH, Kim HC, Hong CS (2006) Inorg Chem 45:9613
320. Lim JH, Yoon JH, Kim HC, Hong CS (2006) Angew Chem Int Ed 45:7424
321. Schelter EJ, Prosvirin AV, Dunbar KR (2004) J Am Chem Soc 126:15004
322. Schelter EJ, Karadas F, Avendano C, Prosvirin AV, Wernsdorfer W, Dunbar KR (2007) J Am Chem Soc 129:8139
323. Hilfiger MG, Zhao H, Prosvirin A, Wernsdorfer W, Dunbar KR (2009) Dalton Trans 2009:5155
324. Freedman DE, Bennett MV, Long JR (2006) Dalton Trans 2006:2829
325. Freedman DE, Jenkins DM, Iavarone AT, Long JR (2008) J Am Chem Soc 130:2884
326. Pedersen KS, Schau-Magnussen M, Bendix J, Weihe H, Palii AV, Klokishner SI, Ostrovsky S, Reu OS, Mutka H, Tregenna-Piggott PLW (2010) Chem Eur J 16:13458
327. Zadrozny JM, Freedman DE, Jenkins DM, David Harris T, Iavarone AT, Mathonière C, Clérac R, Long JR (2010) Inorg Chem 49:8886
328. Long J, Chamoreau LM, Marvaud V (2010) Dalton Trans 39:2188
329. Sutter JP, Dhers S, Rajamani R, Ramasesha S, Costes JP, Duhayon C, Vendier L (2009) Inorg Chem 48:5820

330. Heinrich JL, Sokol JJ, Hee AG, Long JR (2001) J Solid State Chem 159:293
331. Karmakar R, Choudhury CR, Bravic G, Sutter J-P, Mitra S (2004) Polyhedron 23:949
332. Healy PC, Patrick JM, White AH (1984) Aust J Chem 37:921
333. Schelter EJ, Bera JK, Bacsa J, Galan-Mascaros JR, Dunbar KR (2003) Inorg Chem 42:4256
334. Sessoli R (2009) a, A. K. Powell. Coord Chem Rev 253:2328
335. Rinehart JD, Long JR (2011) Chem Sci 2:2078
336. Woodruff DN, Winpenny REP, Layfield RA (2013) Chem Rev 113:5110
337. Osa S, Kido T, Matsumoto N, Re N, Pochaba A, Mrozinski J (2004) J Am Chem Soc 126:420
338. Hamamatsu T, Yabe K, Towatari M, Osa S, Matsumoto N, Re N, Pochaba A, Mrozinski J, Gallani J-L, Barla A, Imperia P, Paulsen C, Kappler J-P (2007) Inorg Chem 46:4458
339. Zaleski CM, Depperman EC, Kampf JW, Kirk ML, Pecoraro VL (2004) Angew Chem Int Ed 43:3912
340. Costes J-P, Auchel M, Dahan F, Peyrou V, Shova S, Wernsdorfer W (2006) Inorg Chem 45:1924
341. Murugesu M, Mishra A, Wernsdorfer W, Abboud KA, Christou G (2006) Polyhedron 25:613
342. Mereacre V, Ako AM, Clérac R, Wernsdorfer W, Hewitt IJ, Anson CE, Powell AK (2008) Chem Eur J 14:3577
343. Mori F, Ishida T, Nogami T (2005) Polyhedron 24:2588
344. Mori F, Nyui T, Ishida T, Nogami T, Choi K-Y, Nojiri H (2006) J Am Chem Soc 128:1440
345. Mereacre VM, Ako AM, Clérac R, Wernsdorfer W, Filoti G, Bartolomé J, Anson CE, Powell AK (2007) J Am Chem Soc 129:9248
346. Costes J-P, Shova S, Wernsdorfer W (2008) Dalton Trans 2008:1843
347. Aronica C, Pilet G, Chastanet G, Wernsdorfer W, Jacquot J-F, Luneau D (2006) Angew Chem Int Ed 45:4659
348. Abbas G, Lan Y, Mereacre V, Wernsdorfer W, Clérac R, Buth G, Sougrati MT, Grandjean F, Long GJ, Anson CE, Powell AK (2009) Inorg Chem 48:9345
349. Shiga T, Onuki T, Matsumoto T, Nojiri H, Newton G, Hoshino N, Oshio H (2009) Chem Commun 2009:3568
350. Chandrasekhar V, Pandian BM, Vittal JJ, Clérac R (2009) Inorg Chem 48:1148
351. Ako AM, Mereacre V, Clérac R, Wernsdorfer W, Hewitt IJ, Anson CE, Powell AK (2009) Chem Commun 2009:544
352. Stamatatos TC, Teat SJ, Wernsdorfer W, Christou G (2009) Angew Chem 121:521
353. Burrow CE, Burchell TJ, Lin P-H, Habib F, Wernsdorfer W, Clérac R, Murugesu M (2009) Inorg Chem 48:8051
354. Li M, Lan Y, Ako AM, Wernsdorfer W, Anson CE, Buth G, Powell AK, Wang Z, Gao S (2010) Inorg Chem 49:11587
355. Rinck J, Novitchi G, den Heuvel WV, Ungur L, Lan Y, Wernsdorfer W, Anson CE, Chibotaru LF, Powell AK (2010) Angew Chem Int Ed 49:7583
356. Hołyńska M, Premužić D, Jeon I-R, Wernsdorfer W, Clérac R, Dehnen S (2011) Chem Eur J 17:9605
357. Langley SK, Chilton NF, Ungur L, Moubaraki B, Chibotaru LF, Murray KS (2012) Inorg Chem 51:11873
358. Schray D, Abbas G, Lan Y, Mereacre V, Sundt A, Dreiser J, Waldmann O, Kostakis GE, Anson CE, Powell AK (2010) Angew Chem Int Ed 49:5185
359. Saha A, Thompson M, Abboud KA, Wernsdorfer W, Christou G (2011) Inorg Chem 50:10476
360. Langley SK, Ungur L, Chilton NF, Moubaraki B, Chibotaru LF, Murray KS (2011) Chem Eur J 17:9209
361. Chandrasekhar V, Bag P, Kroener W, Gieb K, Müller P (2013) Inorg Chem 52:13078
362. Langley SK, Chilton NF, Moubaraki B, Murray KS (2013) Inorg Chem 52:7183
363. Akhtar MN, Lan Y, Mereacre V, Clérac R, Anson CE, Powell AK (2009) Polyhedron 28:1698

364. Efthymiou CG, Stamatatos TC, Papatriantafyllopoulou C, Tasiopoulos AJ, Wernsdorfer W, Perlepes SP, Christou G (2010) Inorg Chem 49:9737
365. Chandrasekhar V, Pandian BM, Azhakar R, Vittal JJ, Clérac R (2007) Inorg Chem 46:5140
366. Chandrasekhar V, Bag P, Speldrich M, van Leusen J, Kögerler P (2013) Inorg Chem 52:5035
367. Wang H, Ke H, Lin S-Y, Guo Y, Zhao L, Tang J, Li Y-H (2013) Dalton Trans 42:5298
368. Crause RA, Busch DH (1960) J Am Chem Soc 82:4830
369. Richardson MF, Wagner WF, Sands DE (1968) J Inorg Nucl Chem 30:1275
370. Ako AM, Hewitt IJ, Mereacre V, Clérac R, Wernsdorfer W, Anson CE, Powell AK (2006) Angew Chem 118:5048
371. Waldmann O, Ako AM, Güdel HU, Powell AK (2008) Inorg Chem 47:3486
372. Chibotaru LF, Ungur L (2008) A, Soncini. Angew Chem 47:4126
373. Luzon J, Bernot K, Hewitt IJ, Anson CE, Powell AK, Sessoli R (2008) Phys Rev Lett 100:247205
374. Ishikawa N, Sugita M, Ishikawa T, Koshihara S, Kaizu Y (2003) J Am Chem Soc 125:8694
375. Jiang S-D, Wang B-W, Gao S (2014) Advances in lanthanide single-ion magnets. Struct Bond. doi:10.1007/430_2014_153
376. Woodruff DN, Tuna F, Bodensteiner M, Winpenny REP, Layfield RA (2013) Organomet 32:1224
377. Morita T, Katoh K, Breedlove BK, Yamashita M (2013) Inorg Chem 52:13555
378. Kan J, Wang H, Sun W, Cao W, Tao J, Jiang J (2013) Inorg Chem 52:8505
379. Gao F, Li Y-Y, Liu C-M, Li Y-Z, Zuo J-L (2013) Dalton Trans 42:11043
380. Venugopal A, Tuna F, Spaniol TP, Ungur L, Chibotaru LF, Okuda J, Layfield RA (2013) Chem Commun 49:901
381. Ren M, Bao S-S, Hoshino N, Akutagawa T, Wang B, Ding Y-C, Wei S, Zheng L-M (2013) Chem Eur J 19:9619
382. Zhang P, Zhang L, Lin S-Y, Xue S, Tang J (2013) Inorg Chem 52:4587
383. Suzuki K, Sato R, Mizuno N (2013) Chem Sci 4:596
384. Fatila EM, Rouzières M, Jennings MC, Lough AJ, Clérac R, Preuss KE (2013) J Am Chem Soc 135:9596
385. Xue S, Chen X-H, Zhao L, Guo Y-N, Tang J (2013) Inorg Chem 52:13264
386. Shen S, Xue S, Lin S-Y, Zhao L, Tang J (2013) Dalton Trans 42:10413
387. Sun W-B, Han B-L, Lin P-H, Li H-F, Chen P, Tian Y-M, Murugesu M, Yan P-F (2013) Dalton Trans 42:13397
388. Guo P-H, Liu J-L, Jia J-H, Wang J, Guo F-S, Chen Y-C, Lin W-Q, Leng J-D, Bao D-H, Zhang X-D, Luo J-H, Tong M-L (2013) Chem Eur J 19:8769
389. Blagg RJ, Ungur L, Tuna F, Speak J, Comar P, Collison D, Wernsdorfer W, McInnes EJL, Chibotaru LF, Winpenny REP (2013) Nat Chem 5:673
390. Tian H, Zhao L, Lin H, Tang J, Li G (2013) Chem Eur J 19:13235
391. Lin S-Y, Wernsdorfer W, Ungur L, Powell AK, Guo Y-N, Tang J, Zhao L, Chibotaru LF, Zhange H-J (2013) Angew Chem Int Ed 51:12767
392. Pointillart F, Le Guennic B, Golhen S, Cador O, Maury O, Ouahab L (2013) Chem Commun 49:615
393. Zhang L, Zhang P, Zhao L, Lin S-Y, Xue S, Tang J, Liu Z (2013) Eur J Inorg Chem 2013:1351
394. Blagg RJ, Muryn CA, McInnes EJL, Tuna F, Winpenny REP (2011) Angew Chem Int Ed 50:6530
395. Tang J, Hewitt I, Madhu NT, Chastanet G, Wernsdorfer W, Anson CE, Benelli C, Sessoli R, Powell AK (2006) Angew Chem Int Ed 45:1729
396. She S-X, Zaworotko MJ, Liu W, Zhang Z-X, Li Y (2013) CrystEngComm 15:5003
397. Ganivet CR, Ballesteros B, de la Torre G, Clemente-Juan JM, Coronado E, Torres T (2013) Chem Eur J 19:1457
398. Blagg RJ, Muryn CA, McInnes EJL, Tuna F, Winpenny REP (2011) Chem Commun 47:10587

399. Jiang S, Wang B, Sun H, Wang Z, Gao S (2011) J Am Chem Soc 133:4730
400. Baldovi JJ, Cardona-Serra S, Clemente-Juan JM, Coronado E, Gaita-Ariño A, Palii A (2013) J Comp Chem 34:1961
401. Chilton NF, Collison D, McInnes EJL, Winpenny REP, Soncini A (2013) Nat Comm 4:2551. doi:10.1038/ncomms3551
402. Zhou C-L, Wang Z-M, Wang B-W, Gao S (2012) Dalton Trans 41:13620
403. Zhu Y-Y, Guo X, Cui C, Wang B-W, Wang Z-M, Gao S (2011) Chem Commun 47:8049
404. Zeng Y-F, Xu G-C, Hu X, Chen Z, Bu X-H, Gao S, Sañudo EC (2010) Inorg Chem 49:9734

Struct Bond (2015) 164: 111–142
DOI: 10.1007/430_2014_153

Published online: 4 July 2014

Advances in Lanthanide Single-Ion Magnets

Shang-Da Jiang, Bing-Wu Wang, and Song Gao

Abstract We present an overview of the investigation methods of lanthanide-based single-ion magnet. The electronic structure of lanthanide ions is described in the picture of electron–electron interaction, spin–orbit coupling, and ligand-field effects. The ligand-field Hamiltonian is introduced in cooperation with equivalent operator method. In the part of experimental methods, we review the advanced methods of the angle-resolved magnetometry measurement and magnetic resonance spectroscopy on lanthanide ions. In the part of theoretical approaches, we describe the lanthanide-ion electron-density distribution anisotropy using the multipole-moment model, which is able to qualitatively describe the magnetic anisotropy behavior of various lanthanide ions. We introduce three approaches of determining ligand-field parameters. Additionally, we review four series of well-investigated lanthanide single-ion magnets.

Keywords Angular resolved magnetometer · Lanthanide · Ligand-field Hamiltonian · Magnetic anisotropy · Magnetic resonance · Single-ion magnet

Contents

S.-D. Jiang
1. Physikalisches Institut, Universität Stuttgart, Pfaffenwaldring 57, 70550, Stuttgart, Germany
e-mail: jiang@pi1.physik.uni-stuttgart.de

B.-W. Wang and S. Gao (✉)
Beijing National Laboratory of Molecular Science, State Key Laboratory of Rare Earth Materials Chemistry and Applications, College of Chemistry and Molecular Engineering, Peking University, Beijing 100871, P.R. China
e-mail: wangbw@pku.edu.cn; gaosong@pku.edu.cn

The last two decades have been the prominent period for the development of molecular nanomagnetism because of the discovery and investigation of single-molecule magnets (SMMs) [1] and single-chain magnets (SCMs) [2]. An SMM is able to maintain its magnetic moment in the scale of an individual molecule at low temperature due to its Ising-type anisotropy, therefore offering the opportunity of molecule-based information storage, quantum computing and opening a new area of molecular spintronics [3]. The chemical syntheses, physical characterizations, and applications to material science of these magnetic molecules are an interdisciplinary subject drawing the attentions of chemists, physicists, crystallographers, and material scientists.

The lanthanides, the 4f-block series elements, are involved in molecular nanomagnets in a fascinating way. The largely unquenched orbital moment of lanthanides gives rise to their highly anisotropic magnetic properties in a ligand field, thus making them one of the hottest candidates for the synthesis of single-molecule magnets (SMMs) [4, 5]. Some of the lanthanide ions are able to exhibit magnetic hysteresis and slow relaxation without coupling to other spin carriers. This feature can partially overcome the complexity of polynuclear SMMs where the magnetic easy axes of the spin centers are differently oriented and the magnetic coupling properties between them are difficult to control [6, 7]. Consequently, mononuclear SMMs, nowadays frequently denoted single-ion magnets (SIMs), are well investigated. The employment of lanthanides in molecular nanomagnets has improved the slow relaxation energy barrier to nearly 1,000 K and the hysteresis temperature to liquid hydrogen temperatures [8, 9]. These records greatly exceed the observation of 3d-block SMMs [10]. It is now known, however, that the SMM behaviors of lanthanide-based SIMs (Ln-SIMs), where the strong spin–orbit coupling plays an important role, are fundamentally different from those of polynuclear 3d-block SMMs.

Instead of collecting all the published Ln-SIMs, which can be found in reviews elsewhere [11], herein we intend to provide an overview of the research on this topic, including the basic properties of lanthanide electronic structures, an introduction to ligand-field Hamiltonian, experimental and theoretical analysis methods, a few well-investigated Ln-SIMs and their major conclusions, and a short perspective.

1 The Electronic Structure of Lanthanide Ions

As 4f-block elements, lanthanide ions have magnetic properties that are dramatically different from those of transition metal ions and are dominated by the intrinsic nature of f orbitals. The different behaviors can be basically attributed to three aspects as described below.

1. The 4f electrons are mostly localized in the inner shell in contrast to d electrons, so that the ligand-field effects on the electronic structure are much smaller. The ligand-field effect is able to slightly remove the degeneracy of the 4f orbital, affording large unquenched orbital momentum [12]. It is commonly accepted that the orbital contribution to the magnetic behavior is much larger for lanthanides than to that of 3d-block ions;
2. As a consequence of the largely saved orbital momentum and stronger relativistic effect, the spin–orbit coupling of lanthanides is much stronger than that of 3d-block ions. It is so strong that the spin momentum is not an observable quantity and the total angular quantum number J is thus a well-defined quantum number instead of S. It is proper to describe the magnetic property of lanthanide with J rather than S;
3. Also because of the inner shell 4f orbit of lanthanides, magnetic coupling between lanthanides is much weaker. In the absence of coupling pathways, the magnetic interaction via superexchange between lanthanide ions can be neglected. However, once the lanthanide ion achieves its Ising limit state, the dipole–dipole interaction can be of several wavenumbers with a distance of 5 Å, which is not negligible any longer.

Because of the above reasons, the effects of electron–electron interactions, spin–orbit couplings, and ligand-field effects are different for 3d and 4f ions as tabulated below (Table 1).

It is clear that the ligand-field effect on 4f ions is always a minor effect compared to spin–orbit coupling, while the spin–orbit coupling is the weaker effect for most of 3d ions because of the largely quenched orbital momentum.

The trivalent lanthanide ions are characterized by f^n configurations, which give rise to ^{2S+1}L terms, further split by spin–orbit coupling providing J multiplets. The corresponding multiplets energy can be calculated by

$$E_{^{2S+1}L_J} = \frac{\lambda}{2}[J(J+1) - L(L+1) - S(S+1)], \quad (1)$$

where J is defined by the angular momentum summation rules $|L–S| \leq J \leq |L+S|$ and $\lambda = \pm\zeta/2S$. ζ is the spin–orbit coupling constant which ranges from 600 to 3,000 cm^{-1} throughout the lanthanide series (Table 2), with the highest values corresponding to the heaviest lanthanide ions. The "+" sign in the summation rule applies for $n < 7$ and the "–" sign for $n > 7$ according to Hund's rule. The sign of the spin–orbit coupling constant λ implies that in the ground-state $J = L - S$ for $n < 7$

Table 1 Effects of electron–electron interactions (H_{ee}), spin–orbit couplings (H_{SO}), and ligand-field effects (H_{LF}) in 3d and 4f ions

3d	H_{ee}	>	H_{LF}	>	H_{SO}	Weak field
	H_{LF}	>	H_{ee}	>	H_{SO}	Strong field
	H_{LF}	≈	H_{ee}	>	H_{SO}	Intermediate field
4f	H_{ee}	>	H_{SO}	>	H_{LF}	Strong field
	H_{ee}	>	H_{SO}	>>	H_{LF}	Weak field

Table 2 Lanthanide free ions: f electron numbers, ground-state terms, spin–orbit coupling constants ζ (cm^{-1}), g_J, $\chi_m T$ (emu mol^{-1} K), $\langle r^k \rangle$ (a.u.^{k}) and Q_2 (a.u.^{2})

Ln^{3+}	$4f^N$	$^{2S+1}L_J$	ζ	g_J	$\chi_m T$[a]	$\langle r^2 \rangle$[b]	$\langle r^4 \rangle$[b]	$\langle r^6 \rangle$[b]	Q_2[c]
Ce^{3+}	$4f^1$	$^2F_{5/2}$	625	6/7	0.80	1.456	5.437	42.26	–0.832
Pr^{3+}	$4f^2$	$^3H_4$	758	4/5	1.60	1.327	4.537	32.65	–0.781
Nd^{3+}	$4f^3$	$^4I_{9/2}$	884	8/11	1.64	1.222	3.875	26.12	–0.283
Pm^{3+}	$4f^4$	$^5I_4$	1,000	3/5	0.90	1.135	3.366	21.46	0.245
Sm^{3+}	$4f^5$	$^6H_{5/2}$	1,157	2/7	0.09	1.061	2.964	17.99	0.438
Eu^{3+}	$4f^6$	$^7F_0$	1,326	0	0	0.997	2.638	15.34	0
Gd^{3+}	$4f^7$	$^8S_{7/2}$	1,450	2	7.88	0.942	2.381	13.36	0
Tb^{3+}	$4f^8$	$^7F_6$	1,709	3/2	11.82	0.893	2.163	11.75	–0.595
Dy^{3+}	$4f^9$	$^6H_{15/2}$	1,932	4/3	14.17	0.849	1.977	10.44	–0.566
Ho^{3+}	$4f^{10}$	$^5I_8$	2,141	5/4	14.07	0.810	1.816	9.345	–0.216
Er^{3+}	$4f^{11}$	$^4I_{15/2}$	2,369	6/5	11.48	0.773	1.677	8.431	0.206
Tm^{3+}	$4f^{12}$	$^3H_6$	2,628	7/6	7.15	0.740	1.555	7.659	0.493
Yb^{3+}	$4f^{13}$	$^2F_{7/2}$	2,870	8/7	2.57	0.710	1.448	7.003	0.473

[a] $\chi_m T \approx \frac{1}{8} g_J{}^2 [J(J+1)]$
[b] $\langle r^k \rangle$ is from [14]
[c] Q_2 is calculated from Eq. (11)

and $J = L + S$ for $n > 7$. For f^7 ions like Gd^{3+}, $L = 0$ and $S = 7/2$, the orbital momentum is completely quenched in the ground state.

Figure 1 provides a qualitative description of the energy levels of lanthanide considering electron–electron interactions, spin–orbit couplings, and ligand-field effects. The first column is the electron excitation. The second column is the energy separation of the order of 10^4 cm^{-1} due to electron–electron interaction. The third column is the spin–orbit coupling separation in the scale of 10^3–10^4 cm^{-1}. The last column is the ligand-field splitting in the scale of 10^2 cm^{-1}.

As described above, the influence from the ligand field is typically one order of magnitude smaller than of the effect arising from spin–orbit coupling. Therefore the energy splitting of the $^{2S+1}L_J$ multiplets of each lanthanide ion in different environments should not change much, so that one can calculate or determine this splitting from spectroscopy. Dieke has tabulated these energy splittings of all the lanthanide multiplets, and the corresponding energy diagram is known as Dieke's diagram [13], which can be used as a reference for lanthanide spectroscopic researches.

The Landé factor of lanthanide ions is determined by both spin and orbit quantum number by

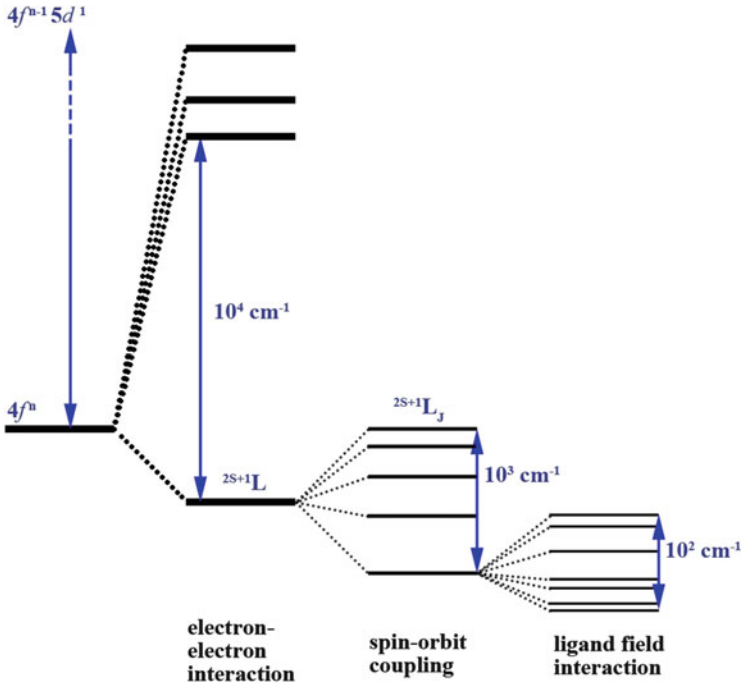

Fig. 1 Energy scale of the electronic structures of lanthanide ions. From *left* to *right*, electron–electron interaction, spin–orbit coupling, and ligand field are shown

$$g_J = 1 + \frac{J(J+1+S(S+1)-L(L+1))}{2J(J+1)}. \tag{2}$$

Table 2 summarizes some important constants of lanthanide ions.

2 Introduction to Ligand-Field Hamiltonian Fomalism

The effective spin Hamiltonian is often employed in the description of the 3d-block polynuclear SMMs, which is a model mapping the low-energy part of the spectrum to a linear combination of spin operators. In most cases the spin Hamiltonian is able to describe the magnetic behaviors of 3d-block SMMs very precisely within two orders of anisotropy terms, and the higher-order anisotropy is always much weaker (smaller than three orders in magnitude). This is because the orbital momentum is majorly quenched and the excited state mixing plays a role in the zero-field splitting in 3d-block ions. This is not true for lanthanide ions, however because of the large residual orbital momentum and strong spin–orbit coupling. A deduction of the ligand-field Hamiltonian can be found elsewhere [15–17]; herein, we aim at an

overview of this approach rather than focusing on every equation in detail. The ligand-field perturbation of lanthanide ions can be described by the ligand-field potential

$$H_{LF} = -e\sum_{i=1}^{n} V\left(\vec{r}_i\right), \tag{3a}$$

where $V\left(\vec{r}_i\right)$ is the potential felt by the ith electron, and $\vec{r}_i$ is the position vector of the electron [18]. This potential $V\left(\vec{r}_i\right)$ describes the electrostatic environment, which is considered to be generated via point charges at $\vec{R}_L$ as follows:

$$V\left(\vec{r}_i\right) = \sum_{L} \frac{(-Ze)_L}{\left|\vec{R}_L - \vec{r}_i\right|}, \tag{3b}$$

where $\frac{1}{\left|\vec{R}_L - \vec{r}_i\right|}$ can be expanded as a series summation of Legendre polynomials, which can be further expanded by spherical harmonics via the spherical harmonic addition theorem [19]. Thus, the ligand-field potential can be expressed as a linear combination of spherical harmonics, and the ligand-field Hamiltonian becomes

$$\begin{aligned}\widehat{H}_{LF} = V(r_i) = \sum_{k=0}^{\infty}\Bigg[B_0^k C_0^k(i) + \sum_{q=1}^{k}\Big(B_q^k\left(C_k^{-q}(i) + (-1)^q C_k^q(i)\right) \\ + B'^k_{\mathrm{q}} i\left(C_k^{-q}(i) - (-1)^q C_k^q(i)\right)\Big)\Bigg],\end{aligned} \tag{4}$$

where B_q^k are the ligand-field parameters, and $C_k^q(i)$ are the Racah operators noted as follows:

$$C_k^q(i) = \sqrt{\frac{4\pi}{2k+1}} Y_k^q(i). \tag{5}$$

Only terms with even rank ($k = 0, 2, 4, 6$) are responsible for the ligand-field splitting, and terms with $k > 7$ vanish for lanthanide ions. A higher symmetry environment of the lanthanide ion can reduce the complexity a lot, since some terms of the Hamiltonian vanish in a specific symmetry. The ligand-field Hamiltonian expressions in various point groups are tabulated in handbooks [16]. With the Wigner–Eckart theorem one is able to calculate the matrix elements in the full excitation Hilbert space. Since this ligand-field Hamiltonian approach is systematically developed by Racah and summarized by Wybourne [20], Eq. (4) is frequently noted as Racah notation or Wybourne notation.

Table 3 The frequently used equivalent operators[a]

k	q	$\widehat{O}_k^q$
2	0	$3J_z^2 - j$
	2	$\frac{1}{2}\left(J_+^2 + J_-^2\right)$
4	0	$35J_z^4 - 30jJ_z^2 + 25J_z^2 - 6j + 3j^2$
	2	$\frac{1}{2}\left\{\left(7J_z^2 - j - 5\right), \left(J_+^2 + J_-^2\right)\right\}$
	3	$\frac{1}{2}\left\{J_z, \left(J_+^3 + J_-^3\right)\right\}$
	4	$\frac{1}{2}\left(J_+^4 + J_-^4\right)$
6	0	$231J_z^6 - 315jJ_z^4 + 735J_z^4 + 105j^2J_z^2 - 525jJ_z^2 + 294J_z^2 - 5j^3 + 40j^2 - 60j$
	3	$\frac{1}{2}\left\{\left[11J_z^2 - (3j + 59)J_z\right], \left(J_+^3 + J_-^3\right)\right\}$
	4	$\frac{1}{2}\left\{\left(11J_z^2 - j - 38\right), \left(J_+^4 + J_-^4\right)\right\}$
	6	$\frac{1}{2}\left(J_+^6 + J_-^6\right)$

[a] j denotes $J(J+1)$ and $\{A, B\}$ denotes $\frac{1}{2}(AB + BA)$ for short

It can be proven that spherical harmonics are irreducible tensor operators and the following two Racah relations hold [21–23]:

$$\left[\widehat{J}_z, \widehat{Y}_k^q\right] = q\widehat{Y}_k^q, \tag{6a}$$

$$\left[\widehat{J}_\pm, \widehat{Y}_k^q\right] = \sqrt{k(k+1) - q(q \pm 1)}\widehat{Y}_k^{q\pm1}. \tag{6b}$$

By taking the advantage of these relations, one can substitute the spherical harmonics in Eq. (4) for momentum operators. The equivalent operators $\widehat{O}_k^q$ are denoted as Stevens operators [24], firstly introduced in 1952 [25]. By substituting, one obtains

$$H_{LF} = \sum_{k=2,4,6} \sum_{q=-k}^{k} a_k A_k^q \langle r^k \rangle \widehat{O}_k^q = B_k^q \widehat{O}_k^q, \tag{7}$$

where a_k are the Stevens' coefficients $\langle J\|\alpha\|J\rangle$, $\langle J\|\beta\|J\rangle$, and $\langle J\|\gamma\|J\rangle$ tabulated in [24, 25], $\langle r^k \rangle$ is the expectation value of r^k tabulated in Table 2 [14], A_k^q are the ligand-field parameters in Stevens notation. The transformation between Wybourne notation and Stevens notations [Eqs. (4) and (7)] can be found in [20]. Table 3 lists some frequently used equivalent operators $\widehat{O}_k^q$. The extended equivalent operators to higher orders with $k > 6$ can be useful in high-spin SMMs within the giant spin model, which are available in publication elsewhere [26].

The transformation of the irreducible operator [Eq. (4)] into operator equivalents [Eq. (7)] is actually the change from the ligand-field Hamiltonian, where the operators have physical meanings, into the effective Hamiltonian. Equivalent operators are of great convenience in dealing with the energy splitting by the ligand-field effect within one spectroscopic branched term $^{2S+1}L_J$, when no

configuration interaction is considered. The absence of multiplet mixings is a good approximation for the description of the magnetic behavior of heavy lanthanide ions at low temperatures (below room temperature), since the first excited multiplet is more than 2,000 cm^{-1} higher and the multiplets mixing can be neglected.

Within one multiplet, the ligand-field Hamiltonian in Stevens notation is very similar to the effective spin Hamiltonian. It is normally the case that in the spin Hamiltonian of 3d-block ions the higher-order anisotropy terms are much smaller than the first-order terms. This is not true, however, for lanthanide ions, where the higher-order terms are not necessarily smaller than first-order ones. Moreover, the transverse anisotropy terms can be even larger than the axial terms.

Like the investigation of 3d-block ions SMMs, the key to understand the magnetic anisotropic behavior of lanthanide ions is the determination of the ligand-field parameters to reproduce the electronic fine structure, so that one can simulate the temperature dependence of the magnetic susceptibility, the field dependence of the magnetization, the magnetic-susceptibility tensor, EPR and far-infrared spectra, luminescence fine structure, etc., and simulate the corresponding spectra also.

One of the difficulties in the extraction of the lanthanide ions' ligand-field parameters is low symmetry. Since some terms vanish in specific point groups of lanthanide ions, a higher-symmetry lanthanide ion can be described by fewer ligand-field parameters. D_{4d} local symmetry, for instance, contains only three axial anisotropy terms $B_2^0\widehat{O}_2^0$, $B_4^0\widehat{O}_4^0$, and $B_6^0\widehat{O}_6^0$ [Eq. (7)], while there are nine terms in a C_{2v} local symmetry [16]. Lanthanide ions normally possess large ionic radii and thus the coordination number and geometry vary a lot. Most of the lanthanide coordination complexes crystallize in a very low symmetry making the extraction of ligand-field parameters challenging and consequently hinders understanding their magnetic anisotropy behaviors.

3 Experimental Methods

As a special case of SMMs, Ln-SIMs exhibit similar magnetic properties compared to 3d-block SMM clusters. The experimental analysis methods in normal SMMs investigation also hold for Ln-SIMs, which are very well described previously. However, some unconventional applications of the standard methods are necessary to suit the Ln-SIMs research because of the special properties of lanthanide. Herein we focus on the applications of angular resolved magnetometer research on Ln-SIMs single crystals, HFEPR (high-frequency electron paramagnetic resonance) and FIR (far-infrared spectroscopy) methods in the investigation of Ln-SIMs. Some other spectroscopic methods like high resolution luminescence spectroscopy, MCD (magnetic circular dichroism) [27], and INS (inelastic neutron scattering) [28] can also be very helpful in the Ln-SIMs research, especially in the determination of the ligand-field parameters. There are some reviews elsewhere available, and we do not cover these methods.

3.1 Angular Resolved Magnetometry Method

Since the lanthanide-containing molecules are often of low symmetry, the prediction of magnetic principal axes based on magneto-structure correlation is not straightforward. Even though the lanthanide ion local symmetry sometimes can be approximated by a higher one, the magnetic anisotropy of lanthanide ions is not directly related to the approximated high-symmetry environment; one remarkable example is reviewed in Sect. 5.3. Therefore an experimental determination of the molecular magnetic principal axes is necessary and of fundamental importance in understanding the magnetic anisotropy behavior of lanthanide ion. An angle-resolved magnetometry measurement can be very helpful in this determination. Unfortunately there are few examples demonstrating this method [29–33].

The full description of the response of a magnetic system to an external magnetic field is given by the magnetic-susceptibility tensor in a Cartesian system. As a measurement of magnetization responses to the magnetic field, the magnetic susceptibility is the second derivative of the partition function's logarithm ($\ln Z$) with respect to the magnetic field (H), which always exists and is continuous in the paramagnetic region [34]. According to the Schwarz theorem, this second derivative has the symmetry property, $\partial^2 \ln Z/\partial H_x \partial H_y = \partial^2 \ln Z/\partial H_y \partial H_x$, indicating that the magnetic-susceptibility tensor is a symmetric matrix($\chi_{ij} = \chi_{ji}$). The expression of the magnetic susceptibility 3×3 second-rank tensor depends on the selection of the Cartesian system. It is straightforward that these different susceptibility tensor expressions in their corresponding Cartesian systems are a group of matrix similarity ($\widetilde{\chi}_{ij}{}' = S^{-1}\widetilde{\chi}_{ij}S$) and the matrix S of the same dimension is the transformation matrix between different Cartesian systems. The selection of the magnetic principal axes as Cartesian systems falls in a diagonal form of the susceptibility tensor and the three nonzero matrix elements are the susceptibility along the magnetic principal axes. Intuitively, the selection of the Cartesian system will not affect the magnetic susceptibility and magnetic principal axes directions, since the group of matrix similarity shares the same set of eigenvalues and their eigenvectors in different systems can be changed into the same principal axes after a proper coordinate system transformation S. It is also interesting to realize that as a symmetric matrix the susceptibility tensor always possesses only real, rather than complex, eigenvalues.

With the basic ideas discussed above, one is able to determine the magnetic principal axes by an arbitrary selection of experimental framework in the ease of operation. With the crystal face indexing information, one can deduce the transformation matrix from the crystal unit-cell framework of the experimental system, so that the magnetic principal-axis orientations can be expressed in the unit cell with respect to the relative locations of the atoms. A horizontal rotator whose rotation axis is perpendicular to the static magnetic field direction (Fig. 2a) can be implemented into the MPMS-XL SQUID magnetometer, so that one can record an angularly resolved magnetization of the single crystal mounted on the rotator platform. Since the magnetometer measures the magnetic moment rather than the

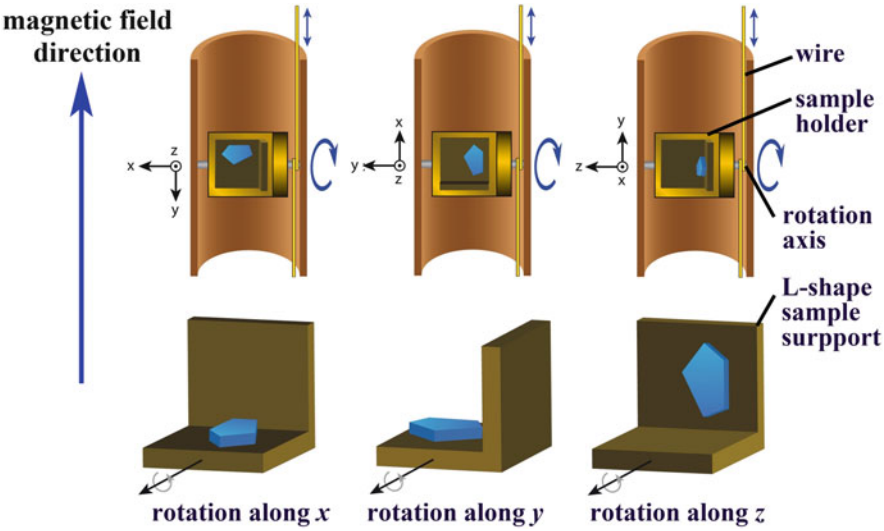

Fig. 2 Description of the angular resolved magnetometry operations. The higher row describes the structure of a horizontal rotator. The rotation axis is perpendicular to the static magnetic field direction. The rotation is performed via the stretching of the Cu–Be wire bonded on the pulley, which shares the rotation axis with the sample holder. The lower row is the orientation of an L-shaped Cu–Be support with respect to the three rotation axes. The three orthogonal directions on the support are employed as the experimental framework

susceptibility directly, the latter has to be extracted by the low-field approximation, where the magnetization of the sample has a linear response to the field and susceptibility is independent of the field. As a result, a standard magnetic characterization of the powder sample is necessarily prior to the single crystal research to confirm the validity of the low-field assumption.

Within the low-field limit, the susceptibility tensor in a specific Cartesian system is contained in the following equation,

$$M = H_0 \begin{pmatrix} \sin\theta\cos\phi \\ \sin\theta\sin\phi \\ \cos\theta \end{pmatrix}^T \begin{pmatrix} \chi_{xx} & \chi_{xy} & \chi_{xz} \\ \chi_{yx} & \chi_{yy} & \chi_{yz} \\ \chi_{zx} & \chi_{zy} & \chi_{zz} \end{pmatrix} \begin{pmatrix} \sin\theta\cos\phi \\ \sin\theta\sin\phi \\ \cos\theta \end{pmatrix}, \tag{8}$$

where the crystal susceptibility tensor χ_{ij} (i and j being axis labels) is expressed in the laboratory coordinate system $\boldsymbol{x}$, $\boldsymbol{y}$, $\boldsymbol{z}$, while the magnetic field $\boldsymbol{H}(H_0, \theta, \varphi)$, with magnitude H_0, is provided in the spherical coordinate system expressed by θ (polar angle between $\boldsymbol{H}$ and $\boldsymbol{z}$) and φ (azimuthal angle between $\boldsymbol{x}$ and the projection of $\boldsymbol{H}$ on the $\boldsymbol{xy}$ plane) (Fig. 3a). The two direction vectors before and after the tensor describe the magnetization and magnetic-field direction, respectively. These two directions coincide because the collected magnetization from MPMS is a scalar along the magnetic-field direction. In principle, the six independent tensor elements (three diagonal ones and three off-diagonal ones) can be extracted by fitting the

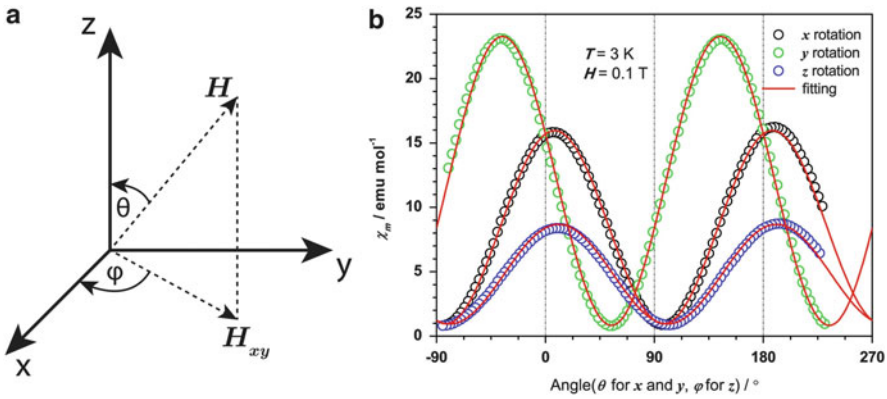

Fig. 3 (**a**) The definition of the spherical coordinate system with polar angle θ and azimuthal angle φ with respect to the Cartesian system. (**b**) Independent magnetization rotation curves intersect at $n\pi/2$ position where geometrical coincidence happens

magnetization data from the rotation around at least three independent axes that are able to span the experimental space. From the convenience perspective, the rotations around $\boldsymbol{x}$, $\boldsymbol{y}$, and $\boldsymbol{z}$ are frequently employed (Fig. 2b), and additionally either θ or φ vanish in each rotation above, which enhances the precision of fitting.

The internal consistency and accuracy of the measurements can be verified by the points where the three rotation curves cross and by symmetry considerations. Firstly, it should be noticed that the rotations around the three orthogonal axes necessarily cross at $n\pi/2$, where n is an integer (Fig. 3b). This is what is expected from the geometry consideration, where rotation around one axis leads to points of geometrical coincidence with the other two rotations and the magnetic field is applied along the same direction of the crystal. Secondly, the positions where the rotation goes through the symmetric axis of the crystal must be a maximum or minimum according to Neumann's principle, which states that the symmetry elements of any physical property of a crystal must include the symmetry elements of the point group of the crystal.

The aforementioned method is actually the determination of the crystal magnetic-susceptibility tensor. The molecular magnetic-susceptibility tensor can be extracted from the crystal one according to the symmetry relations. When the crystal asymmetric unit contains only one magnetic molecule, p, the magnetic-susceptibility tensor of any other molecule q in the crystal cell can be related to p by $\chi_{ij}^{m_q} = \left(A_p^q\right)\chi_{ij}^{m_p}\left(A_p^q\right)^{\dagger}$, where $\chi_{ij}^{m_i}$ are the molecular susceptibility-tensor elements and (A_p^q) is the symmetry operator matrix relating p and q. The response of the crystal is then given by the summation over all the molecules in the unit cell:

$$\chi_{ij}^{C} = \sum_{q} \chi_{ij}^{m_q} = \sum_{q} \left(A_p^q\right) \chi_{ij}^{m_p} \left(A_p^q\right)^{\dagger}. \tag{9}$$

Accordingly, the molecular susceptibility tensor can be extracted from the crystal one if there is only one symmetrically independent molecule in the unit cell. Nevertheless, in general some elements of the molecular susceptibility tensors will cancel out in the summation of Eq. (9) when the molecular symmetry is lower than the crystal lattice one. In this case, the molecular tensor can only be partially determined, with some missing elements due to symmetry reasons. This leads to the fact that the molecular magnetic susceptibility can be determined if and only if there is one symmetrically independent molecule in the unit cell and the molecules are related by an inversion center or located at the position of highest symmetry. Most of the lanthanide-ion-containing molecules are of very low symmetry C_1, and the only possibility to precisely determine the magnetic anisotropy axes of these low-symmetry molecules is by observing that the molecule crystallizes in a triclinic system, which means that there is only one molecule in the unit cell of P1 space group or two molecules in the unit cell of P-1 space group.

In the investigation of Ln-SIMs, the angular resolved single-crystal magnetometry method is able to, besides determine the orientation of the principal axes, provide the information about the ground state. This is possible when the lanthanide ion is of strong Ising-type anisotropy and the first excited ligand-field state is well separated. In the low-temperature region the ground state is well isolated, which fulfills the Curie law that there are no thermally accessible states whose populations vary with changing temperature. The effective g value along the quantized axis with consideration of effective spin 1/2 can then be extracted from the determined magnetic susceptibility along the easy-axis direction according to $\chi_{//}T = \frac{1}{8} g_{//}^{eff\,2} [\frac{1}{2}(\frac{1}{2}+1)]$. The effective g factor is directly related to the property of the ground state by $g_{//}^{eff} = 2g_J \langle \pm J_z | \widehat{J}_z | \pm J_z \rangle$ [24], so that one is able to determine the ground state expectation value when a pure $|\pm J_z\rangle$ is not the eigenstate of the system.

3.2 Magnetic Resonance Methods

3.2.1 High Frequency Electron Paramagnetic Resonance

There is no doubt that the application of HFEPR into molecular nanomagnets, which has direct access to the molecular zero-field splitting, has been of great importance. Normally the HFEPR spectrum on a powder sample is able to provide the anisotropy parameters up to second order to a very high precision, and the higher order anisotropy parameters can be determined via a single-crystal measurement [35, 36]. Well-resolved higher-order transverse anisotropy parameters allow

scientists to understand the quantum tunneling of magnetization which is due to states mixing caused by the transverse anisotropy terms [37, 38]. It is also possible to gain insight into the molecular anisotropy origin by simulating the single-crystal HFEPR spectrum with multi-spin Hamiltonians [35–37]. Nevertheless, these advantages are not applicable to lanthanide-ion-containing molecules, even with a very high symmetry. The problem comes from the aforementioned very large spin–orbit coupling, which results in a much larger zero-field splitting (ligand-field splitting), as compared to 3d-block SMMs. The energy gap between $\Delta M_s = \pm 1$ states of Mn_{12} is not larger than 10 cm^{-1}. An HFEPR with a frequency of 250 GHz is able to cover all the possible transitions within the ground multiplet, while typical ligand-field splittings of a lanthanide ion are in the range of 10^2 cm^{-1}, demanding frequencies in the THz range. There are, nonetheless, some possible applications of HFEPR to Ln-SIMs. It is still possible to observe the transition between low-lying states when the energy gap is in the HFEPR frequency range and the transition is allowed. In some higher-symmetry lanthanide complexes, some forbidden transitions can be observed by applying the field perpendicular to the quantized axis to mix the two ground states. The field dependence of the ground-state splitting is directly related to the eigenstates' nature, and this information could provide an insight into the magnetic anisotropy of the lanthanide ions.

3.2.2 Frequency-Domain Magnetic Resonance

Compared to the HFEPR method, some of the unconventional EPR measurements can provide more information about the ligand-field splitting of Ln-SIMs [39].

The frequency-domain magnetic resonance (FDMR) spectroscopy sweeps the electromagnetic radiation spectrum, rather than the magnetic field, and the external field is fixed at a certain value (which may be zero) [40, 41]. One of the advantages is that it is possible to observe the magnetic transitions in the absence of a static field, which can be a perturbation in conventional magnetic measurements. The most important improvement of FDMR spectroscopy is the employment of backward-wave oscillators (BWOs) as monochromatic and continuously tunable sources, a dozen of whose wavelengths can cover the range of 1 cm^{-1} to 50 cm^{-1}(30 GHz to 1.5 THz). The power output of BWOs varies from several hundreds of mW for the long-wavelength sources (100 GHz) to 1 mW at the short-wavelength (1.5 THz). The radiation generated by BWOs is coherent, highly monochromatic, and linearly polarized to a high degree (99.99%). The frequency resolution is able to reach $\Delta v/v$ up to 10^{-6}, making it possible to study narrow magnetic-absorption lines and to investigate the line-shape in detail.

The resonance signal is detected as an absorption peak when the frequency matches an allowed transition. The procedure can then be repeated in an applied magnetic field to obtain the complete field dependence of the energy levels. This field dependence, as mentioned in the HFEPR part, is closely related to the eigenstates' properties, and the magnetic-anisotropy properties can be extracted in a wider frequency range with allowed transitions, as compared to conventional

HFEPR. The linearly polarized source makes it possible to research angularly resolved polarization-dependence spectroscopy on a single crystal sample. This polarization is very useful in the determination of the state nature of the lanthanide ions. In a D_{3h} symmetry of a non-Kramers ion, the $B_6^3\hat{O}_6^3$ term [Eq. (4)] can be larger than the axial anisotropy terms. The $|\pm 3\rangle$ state can be split by this term into $|+3\rangle + |-3\rangle$ and $|+3\rangle - |-3\rangle$. The "$\Delta M_s = 0$" transition applies here and is permitted for the oscillating magnetic field parallel to the quantization axis. This is very different from 3d-block SMMs whose higher-order transverse anisotropy terms are normally very small, and this kind of transition is not observable in conventional HFEPR spectroscopy [42].

In addition to FDMR spectroscopy, the application of Fourier-transform infrared spectrometers could cover even a wider range of frequencies. Some of the Ln-SIMs ligand-field splitting transitions can be detected in the far-infrared range. The existence of phonon absorption in far infrared sometimes hinders the observation of magnetic transitions. Magnetic transitions can be identified from a group of phonon peaks by comparison of the spectroscopy with and without static field. Nevertheless, it is very difficult to resolve the magnetic transition once it is covered by the phonon peaks.

4 Theoretical Approaches

The theoretical approach in understanding the electronic structures of Ln-SIMs can be very helpful in the exploration of the origin of magnetic anisotropy of lanthanide ions in conjunction with the experimental technique. Specifically, the theoretical approach is the ab initio calculation of the electronic structures by solving the Schrödinger equation using only the atomic coordination input and no other experimental information. The post Hartree–Fock ab initio calculations on lanthanide ions are well developed with consideration of relativistic effects in the MOLCAS program package [43]. With the calculated low-lying energy state, it is possible to simulate the temperature dependence of the magnetic-susceptibility tensor in a certain Cartesian system, or the magnetization vector. Mapping the energy levels of the spin Hamiltonian for 3d-block clusters or of the ligand-field Hamiltonian for lanthanide ions, one is also able to obtain the corresponding magnetic parameters, providing a reference for the experimental investigation. This post Hartree–Fock method has already been found to be an accurate tool to predict the anisotropy of lanthanide-based molecular compounds. A detailed introduction of the ab initio method is available elsewhere in this book volume.

More generally, the theoretical consideration includes the semiempirical method and the experimental data analysis and fitting based on ligand-field Hamiltonian.

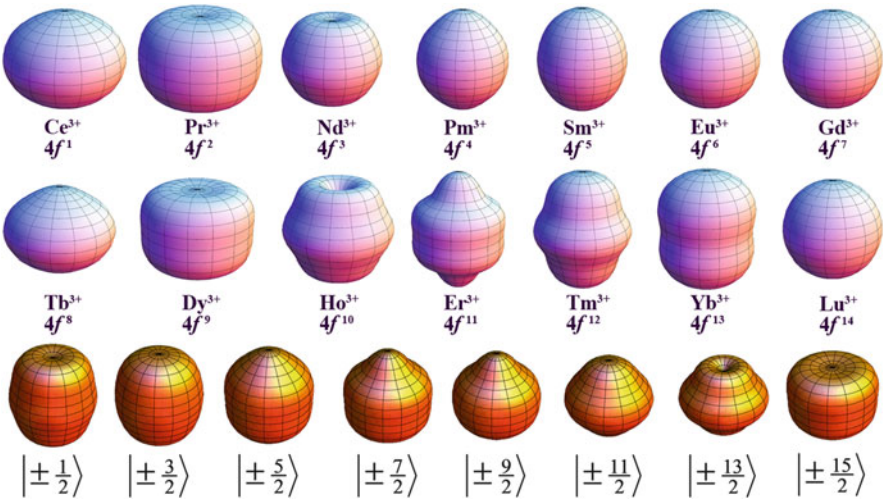

Fig. 4 The first two rows are the anisotropy of the electron-density distribution of lanthanide ions in their Ising-limit state with an expansion of 2^2-, 2^4-, and 2^6-multipolmoment. Ce^{3+}, Pr^{3+}, Nd^{3+}, Tb^{3+}, Dy^{3+}, and Ho^{3+} are oblate ions (axially pressed); Pm^{3+}, Sm^{3+}, Er^{3+}, Tm^{3+}, and Yb^{3+} are prolate ions (axially elongated); Eu^{3+}, Gd^{3+}, and Lu^{3+} are isotropic ion (spherical). The last row shows the electron-density distribution of Dy^{3+} changes from typically prolate in $\left|\pm\frac{1}{2}\right\rangle$ to oblate in the Ising limit

4.1 Anisotropy of the Electron-Density Distribution

The spherical electron-density distribution of lanthanide ions can be broken by the existence of asymmetric ligand field charges. Since the 4f obitals are in the inner shell of the ion, the ligand-field effect is dramatically screened by 5d and 6s orbitals. The electron-density distribution of lanthanide ions in an axial ligand field can be represented by a multipole moment expansion. The description of the asphericity of the 4f-shell was first introduced by the pioneering work of Sievers in 1980s [44], who proposed that the electron-density distribution of a certain J_z state can be expanded as a linear combination of the spherical harmonics Y_k^q ($k \leq 6$) and the combination coefficients can be calculated by the Wigner–Eckart theorem and the reduced-matrix element. This spherical-harmonic expansion implies that the 4f electron density possesses up to 2^k-multipolemoments feature. Since the electron density behaves like a rotational symmetry in a pure J_z state, terms with $q \neq 0$ vanish and only axial terms Y_2^0, Y_4^0, and Y_6^0 play a role. The first two rows of Fig. 4 show plots of lanthanide-ion electron-cloud shapes in the Ising limit by expansion of the multipole model up to sixth order.

Skomski has further simplified the above aspherical model with the consideration of the dominated quadrupole moment of the Ising-limit ground state [45]. By substituting the equivalent operator, this quadrupole moment can be calculated as

$$\langle Q_2 \rangle = \alpha \langle r^2 \rangle \langle 3J_z^2 - J(J+1) \rangle, \tag{10}$$

where the angle brackets on Q_2 represent the thermally averaged quadrupole moment of the charge cloud. In the Ising limit, $J_z = J$, and the above equation collapse to

$$Q_2 = \alpha \langle r^2 \rangle (2J^2 - J), \tag{11}$$

where α is the Stevens coefficient $\langle J \| \alpha \| J \rangle$, and $\langle r^2 \rangle$ was defined in the Stevens notation above. A positive Q_2 represents prolate (axially elongated) electron density and a negative one means an oblate (axially compressed) electron distribution on 4f shell (see Fig. 4 in [46]). The Q_2 are calculated and listed in Table 2. It is explicit that in the Ising-limit state, the Ce^{3+}, Pr^{3+}, Nd^{3+}, Tb^{3+}, Dy^{3+}, Ho^{3+} are oblate ions, while Pm^{3+}, Sm^{3+}, Er^{3+}, Tm^{3+}, Yb^{3+} are prolate ions. Gd^{3+} is an isotropic ion since the orbital momentum is quenched. Skomski's model clearly distinguishes the lanthanide ions of Ising limit into different anisotropy types in an axial ligand field, indicating that a rational selection of lanthanide ions in the synthesis of Ln-SIMs is possible.

It is inadequate to attribute simply, for instance, Dy^{3+} to an oblate ion or Er^{3+} to a prolate ion. The geometry of electron-density distribution for a certain lanthanide ion depends on the J_z state. As can be seen in the last row of Fig. 4, the electron-density distribution of Dy^{3+} ion changes gradually from typically oblate ($J_z = \pm 15/2$) to typically prolate ($J_z = \pm 1/2$).

Rinehart and Long extended Skomski's model to the idea of maximizing the anisotropy of the two types of ions [46]. For instance, the ligand-field negative charges are supposed to be located outside the equator plane to maximize the anisotropy of oblate ions, while the charges concentrating on the polar are able to enhance the anisotropy of prolate ions. This extension provides us the idea in rational design of Ln-SIMs. A lucid choice of the ligand from the negative-charge perspective enables increasing the anisotropy of the lanthanide ions.

A further step of Rinehart and Long's idea is exactly the opposite. Once the negative charges in the ligand field are placed in the polar orientation of a prolate ion, easy-plane anisotropy can be generated since the negative lanthanide electron density is repelled, and the magnetization is forced to the equatorial plane.

Based on Skomski's quadrupole model, the easy-axis orientation of magnetization can be predicted according to the arrangement of ligand negative charges with respect to the lanthanide ion once the Ln-SIM is structured. The easy-axis orientation of prolate ions prefers the direction of the sparse electron density, while that of oblate ions points to the dense negative-charge orientation so as to minimize the overall energy of the molecule. This conclusion is very useful in the initial guess of the principal axis in low-symmetry Ln-SIMs.

One promising improvement of this anisotropic electron-density distribution of lanthanide ions is recently achieved by Chilton, Soncini, and their coworkers, who have developed an electrostatic model to determine the magnetic anisotropy of

Dy^{3+} containing complexes [47]. The basic idea of this quantitative method is to minimize the potential energy of the atomic orbital corresponding to $J_z = \pm 15/2$ in the ligand field. Rather than considering the overall electron-density geometry of Dy^{3+} in the ground multiplet, Chilton's model deals with only one pure Kramers doublet, since many of the low-symmetry Dy^{3+} containing Ln-SIMs show an Ising-limit ground state. A simple fractional charge distribution on the ligand atoms can be calculated via the valence-bond model, and thus the ground-state electrostatic potential energy can be calculated based on the orientation of the coordinating atoms based on the single-crystal structure. The energy minimization can be done via the full space searching the orientation of the strongly axial $M_J = \pm 15/2$ atomic orbital since the present model is based on a classical mechanics theory and the calculation is not time consuming. The results turn to be surprisingly good comparable to an ab initio calculation. It turns out that the easy-axis orientation of Dy^{3+} SIMs always prefers the dense negative-charge orientation. This is an obvious result since the Ising-limit assumption of Dy^{3+} enhances the oblate electron-density distribution of the $^6H_{15/2}$ ion.

4.2 *Determination of Ligand-Field Parameters from Magnetization Data*

The determination of ligand-field parameters is the key to understanding the lanthanide anisotropy behavior. As discussed in the experimental section, however, an exact extraction of the ligand-field parameters based on the spectroscopic methods is not easy because of low symmetry and the many-parameter problem. Aside from the spectrum approach, fitting the magnetization data of lanthanide complexes to certain high symmetries is an alternative option.

4.2.1 Linear Response to the Atomic Radii

In the development of the first Ln-SIM, $[LnPc_2]^-[TBA]^+$, where Pc is dianion of phthalocyanine and TBA is tetra-*n*-butylammoniumcation, whose symmetry was approximated to be D_{4d} (Fig. 5a), Ishikawa has proposed a method to determine ligand-field parameters based on simultaneously fitting of ^1H NMR paramagnetic shift and magnetic susceptibility [48, 49]. The axial anisotropy parameters in Stevens notation are assumed to be a linear response to the atomic number, since the lanthanide contraction effect affords a weaker ligand potential on decreasing the atomic radii of the lanthanide ions in the same structure. The three axial terms of the ligand-field parameters $A_2^0\langle r^2\rangle$, $A_4^0\langle r^4\rangle$, and $A_6^0\langle r^6\rangle$ are expressed as a linear function of the atomic numbers, n:

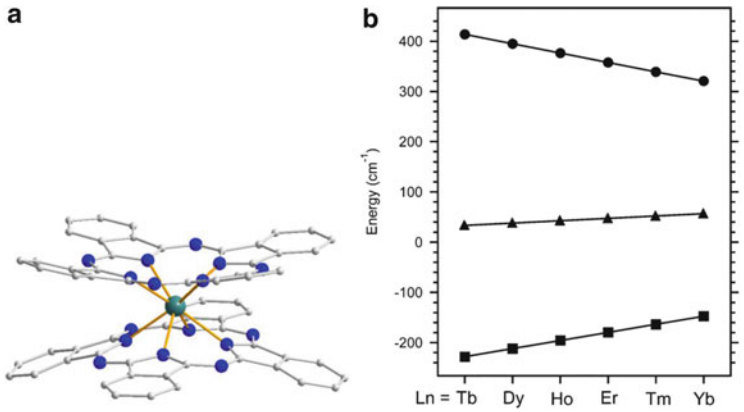

Fig. 5 (**a**) The $LnPc_2$ anion is a typical double-decker structure. The lanthanide ion is coordinated by eight nitrogen atoms from both ligands. The locations of the nitrogen atoms form an approximate square-antiprismatic geometry. (**b**) Ligand-field parameters $A_2^0\langle r^2\rangle$, $A_4^0\langle r^4\rangle$, and $A_6^0\langle r^6\rangle$ are linearly related to the atomic number. Figure 5b is reprinted with the permission from [49]. Copyright © 2002 American Chemical Society

$$A_k^q\langle r^k\rangle(n) = a_k^q + b_k^q(n-10) \tag{12}$$

where $n = 8, 9, \ldots, 13$ represent Tb^{3+}, Dy^{3+}, Ho^{3+}, Er^{3+}, Tm^{3+}, and Yb^{3+}. With a certain initial guesses of the three groups of coefficients $\{a_k^q, b_k^q\}$ for the three axial terms, the ligand-field parameters are found that provide the least-square fit to magnetic-susceptibility data at seven temperatures below 150 K and the chemical shifts of a hydrogen atom on the phthalocynine ring.

Other than the temperature dependence of magnetic susceptibility, this method has taken into account the chemical shift of the ^1H NMR information, which is closely related to the magnetization along the quantization axis. This approach can be very helpful for magnetic-anisotropy research without information on single-crystal magnetization data. Furthermore, instead of fitting the 18 parameters of the six complexes independently, Ishikawa related them via the linear function above and reduced the fitting parameters down to 6, which avoids the over-parameterization problem.

Nevertheless, this method cannot easily be extended to other systems, because of the over-fitting of low-symmetry systems, on the one hand, and the complexity of the hydrogen interaction with the paramagnetic center on the other. One of the weak parts of this method is the linear relation above, since it seems not to be a general rule for lanthanides. The ligand-field parameters of lanthanide ions determined from the spectroscopic data independently do not show such a linear response to the atomic number as well as the ionic radii [24].

4.2.2 CONDON Program

Schilder and Lueken have developed the computational program CONDON to fit the ligand-field parameters to magnetic-susceptibility data of either a single-crystal or powder samples [50]. One advantage of CONDON is that the ligand-field Hamiltonian employs the Wybourne notation rather than the operator equivalent, affording that the calculation is based on the full Hilbert space considering all the microstates. This selection of basis makes it possible to consider the multiplet interaction and multiplet mixing, which is typical for light lanthanide ions. Besides the ligand-field Hamiltonian terms, the interelectronic repulsion, spin–orbit coupling, and Zeeman terms are also taken into account for a mononuclear lanthanide system. Within the scope of molecular-magnetism investigations, the CONDON program is also applicable to spin–coupling systems, like d^n–d^n, f^n–f^n, d^n–S, and f^n–S, although they are not concerned with Ln-SIMs investigations. With a certain selection of the lanthanide-ion environment, where a proper approximation is necessary for low-symmetry systems, and initial guess of the ligand-field parameters, the susceptibility is calculated and embedded in the fitting procedure of Levenberg–Marquardt by varying the ligand-field parameters till the self-consistent condition is achieved. There are two problems frequently encountered in using CONDON. Since the magnetic susceptibility is the second partial derivative of the partition function's logarithm with respect to the magnetic field, it is not very sensitive to slight changes in energy levels. Reliable experiment data, including magnetization data from the magnetometer and the mass of the sample, are necessary for a reliable fitting. On the other hand, over-fitting for low-symmetry systems or multi-solutions can always happen with the magnetic susceptibility data.

4.2.3 Effective Point-Charge Model

As another operator equivalent approach, a ligand-field Hamiltonian method with an effective point-charge consideration was developed by Coronado, Gaita-Ariño, and their coworkers to calculate the ground multiplet splittings [51, 52]. The ligand-field parameters A_k^q in Stevens notation can be calculated by the following expression,

$$A_k^q = \frac{4\pi}{2k+1} c_{kq} (-1)^q \sum_{i=1}^{N} \frac{Z_i e^2 Y_k^q(\theta_i, \phi_i)}{R_i^{k+1}}, \tag{13}$$

where R_i, θ_i, φ_i are the polar coordinates of the point charge, Z_i is the effective point charge of the ligands, e is the electron charge, c_{kq} is the transformation coefficient between spherical harmonics and operator equivalents.

The very rough approach is to take the Mulliken charges and location as charge values and coordinates, respectively, to calculate the ligand-field parameters and finally obtain the energy levels. Coronado and his coworkers, however, took the

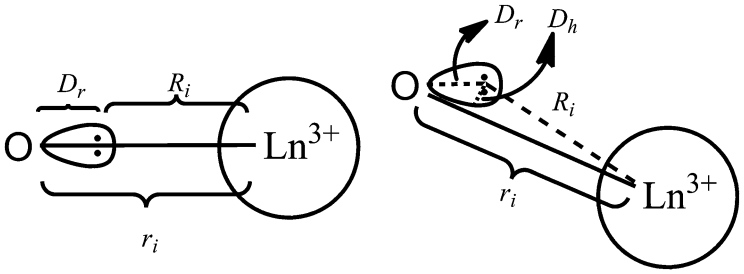

Fig. 6 The two types of electron pairs of the ligand with respect to the lanthanide ion. *Left*: The electron pair orients directly to the lanthanide ion, thus the location of the effective charge is modified by the displacement vector (D_r). *Right*: The lone-pair points slightly off the lanthanide ion, and the effective charge is modified by two vectors D_h and D_r. In both cases R_i is the value adapted in Eq. (13)

radial effective charge and lone-pair effective charge into account to demonstrate the real point charge felt by the lanthanide ions. In the covalent-bond-sharing mode, for example (radial effective charge model, REC): the effective charge locates between the lanthanide and coordination atom rather than exactly on the atom. This covalent-bonding nature of coordination requires a displacement vector (D_r), where the location of the effective charge is varied. In the lone-pair-coordinating mode (lone-pair effective charge model, LPEC), the effective charge does not point directly to the lanthanide ion, and thus a horizontal displacement (D_h) is introduced in addition to D_r, which describes the location of the negative charge. Therefore, in an Ln-SIM complex with N coordination atoms in the REC model without any symmetry considerations (C_1 point group), there are $2N$ parameters (D_r and Z for each atom) that determine the whole set of ligand-field parameters. Furthermore, the values of these parameters are desired by the chemical and structural information (Fig. 6).

This is a big advantage compared to other methods if one performs a fitting to some available experimental data, like temperature dependence of magnetic susceptibility, field dependence of magnetization, or even angular resolved magnetization on a single crystal sample. It is worth noting that the calculation of the ligand-field parameters is heavily based on the precise determination of the molecular structure, since the coordinate information of the coordination atoms is included in Eq. (13). This leads to a discussion of the condition obtaining the crystal structure. It is necessary to determine the single-crystal structure at low temperatures, like the liquid helium range, since the special magnetic properties arise at that range. Actually, the structure deviation between 100 K and 5 K is in the D_r or D_h range (~0.01 Å), and some researches are available showing that a ligand–metal coordination bond distortion of the range 0.005 Å is able to introduce comparable quantized axis distortion. This crucial demand might introduce some inconvenience since a determining single-crystal structure at very low temperatures is difficult.

5 A Few Examples of Ln-SIMs

Investigation of Ln-SIMs started in 2003 with the report of $LnPc_2$ by Ishikawa and his coworkers. This observation led to an explosion of research on lanthanide-ion magnetic behaviors. Herein we will not cover all the Ln-SIMs on hand, but rather pick up several typical ones in order to further illustrate the methods reviewed in the previous sections.

5.1 The First Ln-SIM: $[TbPc_2]^-$

In the series of LnPc2 complexes only the Tb and Dy analogues exhibit like SMM behavior. The magnetic slow relaxation barrier of Tb complex is as high as 260 cm^{-1}, which is significantly higher than 3d-block SMMs [53, 54]. The measurement for the diluted sample in the diamagnetic iso-structural yttrium complex $[Pc_2Y]^- \cdot TBA^+$ showed that the χ_M''/χ_M peaks remained. This clearly proves that the slow magnetization relaxation is the single-olecular property of $[Pc_2Tb]^-$, rather than resulting from intermolecular interactions and magnetic order. Applying the ligand-field Hamiltonian analysis by Ishikawa introduced above, the ground state is determined to be an Ising limit doublet $|\pm 6\rangle$, and the first excited state is $|\pm 5\rangle$ lying over 400 cm^{-1} higher in energy. With the effective point charge approach by Coronado, the ground state is still in the Ising limit, while the first excited state is dominated by $|0\rangle$ and slightly mixed with $|\pm 4\rangle$ [51]. This disagreement is due to the differently assumed symmetries. As pointed out above, the symmetry of these double-decker molecules are approximated to be D_{4d}, in which the ligand-field Hamiltonian is only composed by axial anisotropy terms. Without consideration of the interaction between multiplets, the off-diagonal elements of the Hamiltonian matrix vanish, thus the electronic fine structure resolved by Ishikawa contains only pure state. However, the double-decker molecules of heavy lanthanides crystallize in the P-1 space group, which is of low symmetry, suggesting that the molecule is in C_1 point group. Mapping the energy levels, which is calculated by CASSCF/RASSI on MOLCAS based on the molecular crystal structure, to the ligand-field Hamiltonian with C_1 symmetry, one can find some non-negligible transverse anisotropy parameters, B_2^1, B_2^2, B_4^1, B_4^4 and B_6^6, confirming the low symmetry of these molecules [55].

The most distinguished property of this, and actually many of the reported Ln-SIMs, is the huge energy barrier compared to 3d-blocked cluster SMMs. The energy barrier of typical SMMs is climbing up the double well potential generated by the zero-field splitting of the ground multiplets combining with quantum tunneling of magnetization. While this is not possible for lanthanide, on the one hand, the ligand-field splitting is in the 10^2 cm^{-1} range for 4f ions, the observed energy barrier is smaller than this; the excitation of the moment is necessarily to obey the selection rule of $\Delta M_J = \pm 1$, and this can only be achieved with a dominating $B_2^0\widehat{O}_2^0$

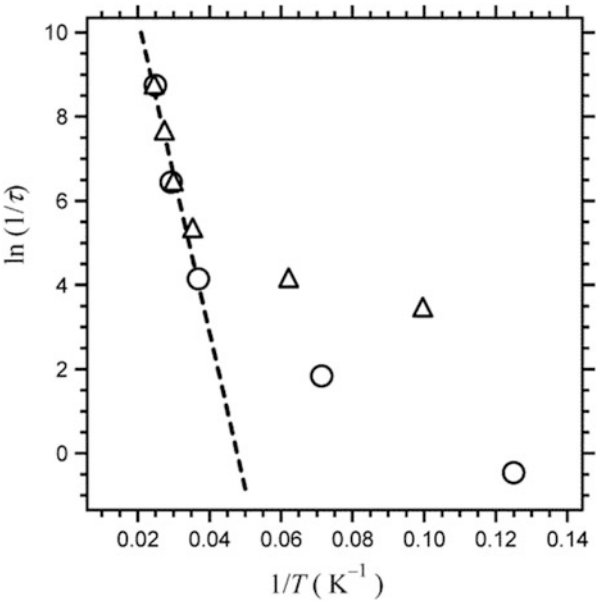

Fig. 7 Logarithm of the relaxation time of both pure (*triangles*) and diluted (*circles*) sample of $[Pc_2Tb]^-$ with respect to the inverse of the temperature shows a linear response, indicating that the relaxation process is a typical spin-lattice relaxation dominated by the Orbach process. Reprinted with the permission from [54]. Copyright © 2004 American Chemical Society

term. Ishikawa related the linear relation between logarithm of relaxation time and the inverse of temperature, concluding the relaxation process is a typical spin-lattice relaxation dominated by the Orbach process (Fig. 7). Further evidence is that the magnetic relaxation barrier is directly comparable to the ground and first excited state energy gap.

Wernsdorfer, Ishikawa, and their coworkers have performed a micro-SQUID measurement on the magnetic diluted sample of Tb and Dy complexes [56]. It is surprising to observe quantum tunneling of magnetization at zero magnetic field in the Dy complex which is a Kramers ion, while no such process was observed in the non-Kramers Tb analogue (Fig. 8). According to Kramers theorem, the Kramers doublets always keep their degeneracy in the absent of a magnetic field perturbation independent of ligand field symmetry. The Landau–Zener–Stückelberg model demands a tunnel splitting for the quantum tunneling of magnetization in the avoided crossing of the energy levels [57]. The observation of magnetization tunneling of Dy complex near zero field indicates that the Kramers doublet is spitted in the absence of field perturbation. This behavior is attributed to the effect of the isotope ^{161}Dy and ^{163}Dy, whose nuclear spins are $I = 5/2$. The hyperfine coupling of $J = 15/2$ and $I = 5/2$ leads to an integer total spin, which can be split in certain low symmetries. Due to similar reason, the hyperfine coupled Tb ion ($I = 3/2$) behaves like a Kramers ion, and no tunneling of magnetization can be observed at zero field.

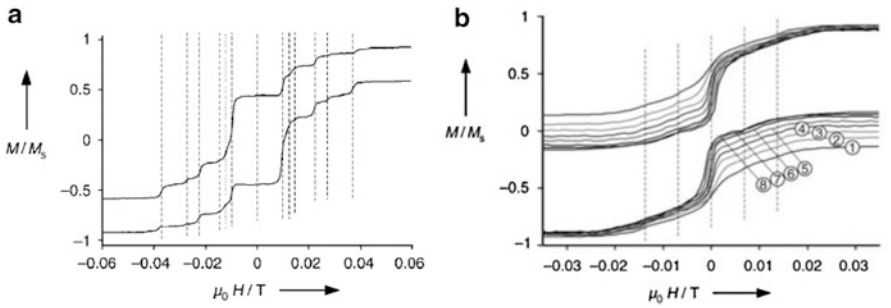

Fig. 8 The hysteresis at 0.04 K for a single crystal samples of diluted Tb (**a**) and Dy (**b**) analogues of $[Pc_2Ln]^-$ complex. The Tb one does not show a tunneling in the absence of a magnetic field, while the Dy one is the contrary. This behavior is attributed to the nuclear effect. Reprinted with the permission from [56]. Copyright © 2005 Wiley-VCH Verlag GmbH & Co. KGaA, Weinheim

5.2 *The Low Symmetry Series: Dy/β-Diketonates*

Gao, Wang, and their coworkers have reported a mononuclear Dy^{3+} containing complex. Crystal analysis shows that the isomorphous complexes consist of a neutral mononuclear $[Dy(acac)_3(H_2O)_2]$ together with an uncoordinated water and ethanol molecule [58], where acac is acetylacetonate. The eight coordinating oxygen atoms form an approximate square-antiprismatic coordination polyhedron, and the local symmetry of Dy^{3+} was approximated to be D_{4d}.

Very similar to the $[DyPc_2]^-$ complex, the complex shows a typical SMM behavior. The magnetic relaxation time was determined to show a crossover at 8 K. Below this crossing temperature, the relaxation time is temperature independent indicating quantum tunnelling of magnetization. This kind of quantum relaxation behavior is normally found in SMM clusters at very low temperature. The origin of this Kramers ion tunnelling behavior is also attributed to the hyperfine coupling. The frequency-dependent ac susceptibility of magnetic site diluted samples reveals the single-ion origin of the slow relaxation behavior. The tunnelling of magnetization is found to be less prominent in diluted samples, indicating that the dipole–dipole interaction may be taken as such a perturbation to enhance the tunnelling process. On measuring the diluted sample, a butterfly-shaped magnetization hysteresis can be observed at 0.5 K. The butterfly-shaped hysteresis loop does not show remanent and coercive fields. This is owing to the sweep rate (150 Oe/min) of the loop that is slow compared with the fast zero field relaxation between the ground state. The ligand field analysis was carried out by means of CONDON in the D_{4d} approximation yielding an Ising type ground state $|\pm 15/2\rangle$.

Similar to this Dy containing complex with β-diketonate as ligands, many other analogues were reported with a similar coordination mode [59–64]. The magnetic hysteresis can be observed at even higher temperatures. It is promising that one of the analogues crystallizes in a P-1 space group, and the magnetic easy axis is

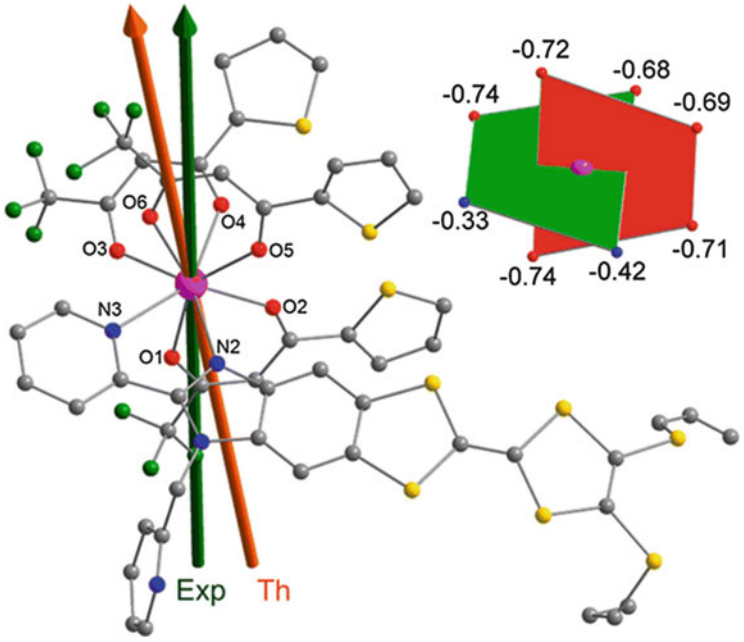

Fig. 9 The structure and magnetic easy-axis orientation (*green*: from the experiment, *red*: from the ab initio calculation) of a dysprosium/β-diketonate analogues. Reprinted with the permission from [33]. Copyright © 2013 American Chemical Society

determined to be away from the pseudo C_4 axis [33]. A reconsideration of the local symmetry is thus necessary. In the series of molecules, one can always find that the Dy ion rides at the intersection between two planes: one defined by the oxygens of two opposite β-diketonates, and the other one formed by the oxygens of the third β-diketonates and an assistant ligand (Fig. 9). The two generated planes are almost perpendicular to each other. The symmetry of the first coordination sphere with respect shall thus be considered as C_{2v}.

The determined easy axis nearly lies in the plane defined by the two opposite β-diketonates and Dy^{III}. This orientation shows a large deviation from the pseudo C_4 axis in the commonly employed D_{4d} local symmetry of Dy/β-diketonate SIMs reported. This experimental determination agrees also with recent predictions of the electrostatic model approach by Chilton [47]. From the local geometry perspective, it is worth stressing that the D_{4d} local symmetry is not a good approximation for dysprosium coordinated to β-diketonates systems. The model structure is a two-plane (each generated by two anti-side ligands) intersection (C_{2v}, where C_2 axis is the intersection of the two planes), rather than a more symmetric, double-decker like (D_{4d}) in the first coordination sphere.

As reviewed above, the easy axis of the oblate Dy^{3+} ion prefers to lie along the direction of high electron density. Since the intersection of the two planes is in a direction of low electron density, the quantized axis of Dy^{3+} must be perpendicular

to this intersection. More precisely, the easy axis lies in one of the *trans*-ligand planes. A detailed investigation of the charge distribution in the two planes is necessary to identify the easy axis location. This easy-axis orientation determination shows that, in Dy/β-diketonate systems, a crude approximation to a square-antiprism model is totally insufficient, so that the easy-axis shows a big deviation from the pseudo symmetry axis in D_{4d} approximation.

5.3 Break Down of Pseudo Symmetry: Dy^{3+}/DOTA

In the previous two examples, it has been shown that a slight distortion of the ideal geometry can influence the magnetic properties. The research on the Dy/DOTA complex by Sessoli and her coworkers provides the most promising example on this issue [31]. The anion of H_4DOTA, 1,4,7,10-tetraazacyclododecane *N*,*N*′,*N*″,*N*‴-tetraacetic acid, is able to provide a psuedo tetragonal symmetry in the coordination of the lanthanide as a square-antiprism model, where the four N atoms from the cyclododecane form one plane and four O atoms from the carboxylic acids form another. One water molecule coordinates to the lanthanide ion from the oxygen plane side generating capped square-antiprism coordination geometry in pseudo C_{4v} symmetry.

A magneto-structure prediction will straightforwardly lead to the conclusion that the C_4 axis must be one of the principal axis and the other two are identical lying in the plane perpendicular to it. The previous magnetic characterization has identified that the Dy^{3+} containing molecule shows typical SMM behavior and the magnetic anisotropy must be of strong Ising type, indicating that the C_4 axis is necessarily the magnetic easy axis and the plane parallel to N and O planes is the hard plane.

The angular resolved single crystal magnetization measurement did confirm the uniaxial anisotropy with the Ising direction effective *g* value of 17.0, which is a bit smaller than the Ising limit value of 20. Nevertheless, the principal axis orientations demonstrate that the easy axis lies in the originally proposed hard plane, while perpendicular to the pseudo C_4 axis. This result is also confirmed by the ab initio calculations (Fig. 10, second column).

The ab initio calculations have shown some surprising results. By manually removing the capping coordinating water molecule, the calculated easy axis rotates nearly 90° in the plane but still perpendicular to the C_4 axis. The operation, by rotating the hydrogen atoms on the water molecule around the C_4 for 90°, can also affect the orientation of the easy axis in the plane. These ab initio results clearly show that the capping water molecule, including the two hydrogen atoms, has a massive influence on the Dy^{3+} anisotropy. The theoretical calculation proposed a possible explanation that a π interaction between oxygen atom and the Dy^{3+} can affect the relative population of the 5d orbitals.

This molecule crystallizes in P-1 space group, indicating that no crystallographic symmetry element exists in the molecule. However, as shown above, slight deviation from the ideal point group can lead to a big effect of the principal axis of the

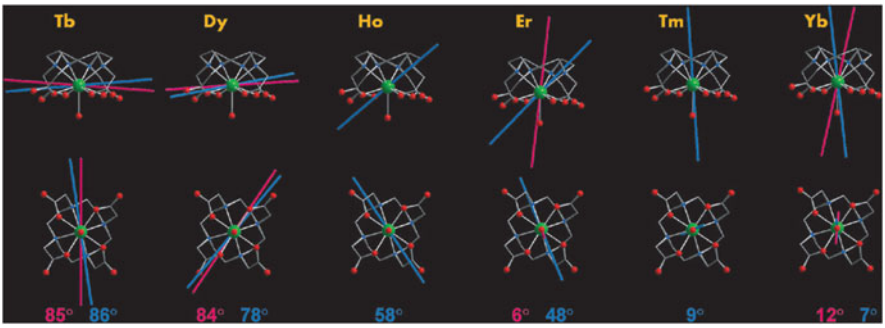

Fig. 10 The magnetic easy-axis orientation of the Ln/DOTA series. (*pink*: experimental determination, *blue*: ab initio calculation) As visible, the easy axes rotate from the horizontal plane to the axial direction by gradually changing the electron-density distribution from oblate to prolate. Reprinted with the permission from [32]. Copyright © 2013 Wiley-VCH Verlag GmbH & Co. KGaA, Weinheim

lanthanide ions. This investigation provides a remarkable example that it is necessary to carefully take the simple magneto-structural correlations based on the lanthanide local environment.

A further step of this work is the analysis of all the heavy lanthanide ion analogues [32]. The angular resolved single crystal magnetization measurements, on the Tb, Dy, Er, and Yb analogues with large single crystals available, show easy axis of magnetization with strong rhombic anisotropy. Ab initio calculation results coincide with experiment and identify that the Ho and Tm analogues anisotropy is also of Ising type. Both the theoretical and experimental results show that the magnetization easy axes exhibit a rotation from the perpendicular towards parallel direction of the pseudo C_4 axis. This gradual change is directly related to the lanthanide ion electron-density distribution introduced in the previous section. Since the Q_2 value increases from –0.6 to 0.5 for Tb^{3+} to Yb^{3+}, the electron-density distribution geometry goes from a strong oblate shape to a prolate one step by step, which is the driving force of the observed easy-axis orientation changing due to the fact that the negative charges of the DOTA ligand concentrates in the equatorial plane throughout the series of analogues.

In addition to the single crystal magnetometer measurement, a well-resolved luminescence spectroscopy of the Dy analogue is also recorded at room temperature [31]. The transitions from $^7F_{9/2}$ to $^6H_{15/2}$ are observed at around 20,800 cm^{-1}. Since the measurement is performed at rather high temperature, the excited doublets of $^7F_{9/2}$ are also involved in the emission. Sessoli and her coworkers distinguished the "hot transitions" from the shape of the peaks in the $^7F_{9/2} \rightarrow {}^6H_{15/2}$ band. By deconstruction the transition band into eight Gaussian lines, they were able to resolve the electron fine structures. The ground and first excited state energy gap was determined to be 53 ± 8 cm^{-1}.

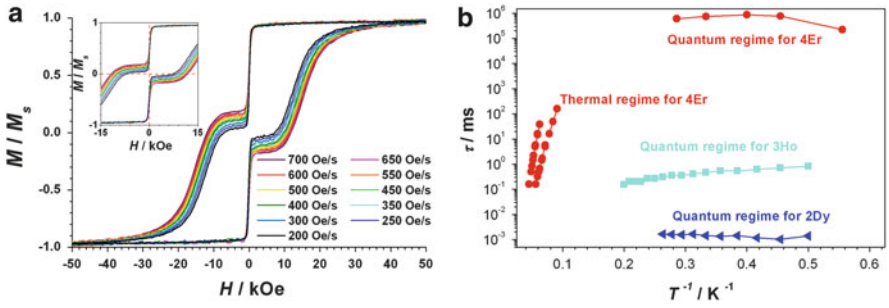

Fig. 11 (**a**) Magnetic hysteresis at 1.6 K on the magnetically diluted sample at different sweeping rates. (**b**) The tunneling rate of the Dy, Ho, and Er analogues decreases with respect to the bending angle

5.4 The Prolate Ion: Organometallic Er^{3+}

As an organometallic molecule, (COT)ErCp*, reported by Gao, Wang and their coworkers has opened a new access to the construction of Ln-SIMs, where COT^{2-} stands for cyclooctatetraene dianion, and Cp^{*-} represents the pentamethylcyclopentadiene anion [65]. The two aromatic rings are not parallel, but with a tilting angle of 8°. Magnetic hysteresis can be recorded at 5 K with a coercive field of 1.3 T at a sweeping rate of 700 Oe/s on a magnetically diluted sample (Fig. 11a). It is interesting to observe the thermally activated relaxation with two processes, caused by the two conformers of the disordered COT ring. The rate of quantum tunneling of magnetization in the Dy, Ho, and Er analogues changes along with the deviation of the idealized $C_{\infty v}$ [66]. A larger bending angle leads to a faster tunneling rate. This is straightforward since the tunneling rate highly depends on the transverse anisotropy terms (Fig. 11b).

As is discussed in Sect. 3.1, it is not possible to extract the molecular magnetic-susceptibility tensor when the symmetry of the molecule is lower than that of the crystal unit cell. Sessoli and her coworkers have measured an angular resolved magnetization on the single crystal of this compound. The crystal possesses easy plane anisotropy due to the highly tilted orientation of the molecular easy axis (Fig. 12a). It is not possible to determine the magnetic easy-axis orientation experimentally. The ab initio calculation indicates that it is along the pseudo axial direction. The single crystal magnetization measurement below the blocking temperature shows that the 180° periodicity of the rotation sine curve breaks down (Fig. 12b). This asymmetric behavior is due to the very slow relaxation at a 0.1 T static magnetic field as can be viewed in the hysteresis measurement. A measurement with long time decays was able to restore the symmetric sine curve during rotation.

Meihaus and Long have reported a complex $[Er(COT)_2]^-$ in addition to the sandwich organometallic family [67]. The magnetic hysteresis can be observed even at 10 K and the relaxation energy barrier is determined to be 150 cm^{-1}.

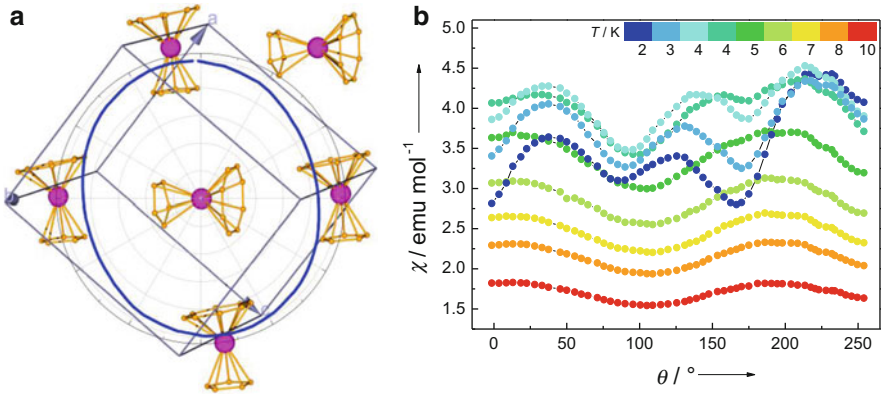

Fig. 12 (**a**) The polar plot of the magnetization along the hard axis of the crystal. This crystal shows an easy plane anisotropy due to the highly tilted molecular easy axes. (**b**) The single crystal magnetization measurements below the blocking temperature shows an asymmetric sine, since the magnetization of the crystal relaxes slow in the experimental condition due to the existence of hysteresis

These Er^{3+} containing complexes are very different compared to the previously reported Tb^{3+} and Dy^{3+} ones. From the perspective of lanthanide ion electron-density distribution geometry, the latter two are typical oblate ions while Er^{3+} is a prolate one. In the SIM complex of Er^{3+}, the ground Kramers doublet is dominated by $|\pm 15/2\rangle$, which enhances the prolate property of the electron density. One argument against the Skomski's quadrupole model is that the calculated magnetic easy axis points toward the two aromatic rings, where the electron charge density is dense, and this will cause a higher potential energy. This can be overcome by the consideration of the π-bonding nature of the molecular orbitals. The π-bond enriches the electron density above and below the aromatic rings, so as to generate an equatorial ligand field, which is able to stabilize the Ising type prolate Er^{3+} ions.

6 Conclusions

The last decade has been the renaissance of research on molecular magnetism based on lanthanides. Aside from the research on Ln-SIMs, there is an exploding increase on the reports of lanthanide-based SMMs. However, the understanding and controlling of their properties remain to be improved. This will have to be based on better comprehension of the magnetic properties of Ln-SIMs. This review tries to briefly present some theories and methods in understanding the Ln-SIMs behaviors so as to promote the development of this area.

The ligand field analysis is definitely one of the most basic and important approaches to understand the magnetic anisotropy of lanthanide ions. However, due to the low symmetry and experimental limitation, this analysis is very difficult

to perform. In the heavy lanthanide series, from where most of the Ln-SIMs arise, the excited multiplet mixing is weak, therefore the employment of operator equivalent can be convenient to reduce the difficulty of the ligand-field Hamiltonian. Nevertheless, the determination of ligand-field parameters is not easy. It is necessary to synthesize more highly symmetric Ln-SIMs to reduce the variance of parameters. On the other hand, a combination of multiple experimental methods, like magnetic measurement and spectroscopic methods, is required to achieve the purpose.

Qualitatively, the electron-density distribution geometry consideration provides an intuitive picture in understanding and designing Ln-SIMs. The oblate and prolate geometry of the lanthanide ion electron density is normally enhanced in the Ising anisotropy of Ln-SIMs. In the method developed by Chilton et al., the orientation of the magnetic easy axis can even be calculated by the classic static electric model. Quantitatively, the ab inito calculations including relativistic effects provide a promising alternative in understanding the electronic structures in contrast to the ligand-field Hamiltonian approach. The application of these calculations to explain the relaxation behaviors of polynuclear complexes is an advantage compared to experimental method, since the spectroscopy can become very complex in that case.

At least two aspects in the investigation of Ln-SIMs are debatable. There is an increasing trend relating the magnetic relaxation barrier to the energy gap between the ground and first excited state. This relation is valid when the slow magnetic relaxation is dominated by the spin lattice relaxation via Orbach process. However, it is not necessary that the spin lattice relaxation in Ln-SIMs always proceeds via Orbach process. A detailed investigation of the relaxation time upon temperature and magnetic field is required to exclude the direct and Raman process before one relates the relaxation barrier to the energy gap. This argument applies to the field-induced magnetic relaxation of lanthanide ions as well. Actually the origin of the energy barrier in the magnetic relaxation process is still an open question, demanding well-determined electronic structures and the elaborated description of the relaxation process. Recently, Sorace and his coworkers have demonstrated that the magnetization dynamics is not necessarily related to the magnetic anisotropy in lanthanides [68].

The magnetic dipole interaction is not negligible in the magnetic properties consideration at low temperature in some of the Ln-SIMs crystal lattice. The dipolar coupling constant can be as large as several wavenumbers when the lanthanide ion is in the Ising limit. A proper employment of the low temperature magnetic data considering the dipole effect can improve the reliability.

In conclusion, as an interdisciplinary field, the study of molecular nanomagtism of lanthanides attracts the interests of scientists from synthetic chemistry, magnetochemistry, crystal engineering, theoretical chemistry, material chemistry, magnetophysics, condensed matter physics, theoretical physics, surface physics, materials science, and more. It is of course necessary to combine all these methods to explore the properties of these molecules. We expect that the step achieved on Ln-SIMs will enhance the development of molecular nanomagnetism in the recent future.

Reference

1. Sessoli R, Gatteschi D, Caneschi A, Novak MA (1993) Nature 365:141
2. Caneschi A, Gatteschi D, Lalioti N, Sangregorio C, Sessoli R, Venturi G, Vindigni A, Rettori A, Pini MG, Novak MA (2001) Angew Chem Int Ed 40:1760
3. Bogani L, Wernsdorfer W (2008) Nat Mater 7:179
4. Sessoli R, Powell AK (2009) Coordin Chem Rev 253:2328
5. Sorace L, Benelli C, Gatteschi D (2011) Chem Soc Rev 40:3092
6. Bencini A, Gatteschi D (2012) EPR of exchange coupled systems. Dover, Heidelberg
7. Gatteschi D, Sorace L (2001) J Solid State Chem 159:253
8. Ganivet CR, Ballesteros B, de la Torre G, Clemente-Juan JM, Coronado E, Torres T (2013) Chem Eur J 19:1457
9. Rinehart JD, Fang M, Evans WJ, Long JR (2011) Nat Chem 3:538
10. Milios CJ, Vinslava A, Wernsdorfer W, Moggach S, Parsons S, Perlepes SP, Christou G, Brechin EK (2007) J Am Chem Soc 129:2754
11. Woodruff DN, Winpenny REP, Layfield RA (2013) Chem Rev 113:5110
12. Figgis BN (2000) Ligand field theory and its applications. Wiley-VCH, New York
13. Dieke GH, Crosswhite HM, Crosswhite H (1968) Spectra and energy levels of rare earth ions in crystals. Interscience, New York
14. Edvardsson S, Klintenberg M (1998) J Alloy Compd 275:230
15. Newman DJ, Ng B (2000) Crystal field handbook. Cambridge University Press, New York
16. Görller-Walrand C, Binnemans K (1996) Rationalization of crystal-field parametrization. In: Karl A, Gschneidner Jr., LeRoy E (eds) Handbook on the physics and chemistry of rare earths. Amsterdam, Lausanne, New York
17. Gerloch M (2009) Magnetism and ligand-field analysis. Cambridge University Press, London/New York
18. Bethe H (1929) Ann Phys Berlin 3:133
19. Griffith JS (1961) The theory of transition-metal ions. Cambridge University Press, New York
20. Wybourne BG (1965) Spectroscopic properties of rare earths. Interscience, New York/London/Sydney
21. Racah G (1942) Phys Rev 61:186
22. Racah G (1942) Phys Rev 62:438
23. Racah G (1943) Phys Rev 63:0367
24. Abragam A, Bleaney B (1970) Electron paramagnetic resonance of transition ions. OUP Oxford, New York
25. Stevens KWH (1952) P Phys Soc Lond A 65:209
26. Rudowicz C, Chung CY (2004) J Phys Condens Mat 16:5825
27. Görller-Walrand C, Fluyt L (2010) Magnetic circular dichroism of lanthanides. In: Karl A, Gschneidner JJ-CGBn, Vitalij KP (eds) Handbook on the physics and chemistry of rare earths. Oxford, Shannon, Tokyo
28. McInnes EL (2006) Spectroscopy of single-molecule magnets. In: Winpenny R (ed) Structure and bonding. Springer, Berlin Heidelberg
29. Luzon J, Sessoli R (2012) Dalton Trans 41:13556
30. Bernot K, Luzon J, Bogani L, Etienne M, Sangregorio C, Shanmugam M, Caneschi A, Sessoli R, Gatteschi D (2009) J Am Chem Soc 131:5573
31. Cucinotta G, Perfetti M, Luzon J, Etienne M, Car PE, Caneschi A, Calvez G, Bernot K, Sessoli R (2012) Angew Chem Int Ed 51:1606
32. Boulon ME, Cucinotta G, Luzon J, Degl'Innocenti C, Perfetti M, Bernot K, Calvez G, Caneschi A, Sessoli R (2013) Angew Chem Int Ed 52:350
33. da Cunha TT, Jung J, Boulon M-E, Campo G, Pointillart F, Pereira CLM, Le Guennic B, Cador O, Bernot K, Pineider F, Golhen S, Ouahab L (2013) J Am Chem Soc 135:16332
34. Kahn O (1993) Molecular magnetism. VCH, New York

35. Barra AL, Caneschi A, Cornia A, Gatteschi D, Gorini L, Heiniger LP, Sessoli R, Sorace L (2007) J Am Chem Soc 129:10754
36. Sorace L, Boulon ME, Totaro P, Cornia A, Fernandes-Soares J, Sessoli R (2013) Phys Rev B 88:104407
37. Hill S, Datta S, Liu J, Inglis R, Milios CJ, Feng PL, Henderson JJ, del Barco E, Brechin EK, Hendrickson DN (2010) Dalton Trans 39:4693
38. del Barco E, Kent AD, Hill S, North JM, Dalal NS, Rumberger EM, Hendrickson DN, Chakov N, Christou G (2005) J Low Temp Phys 140:119
39. van Slageren J (2012) New directions in electron paramagnetic resonance spectroscopy on molecular nanomagnets. In: Drescher M, Jeschke G (eds) EPR Spectroscopy, topics in current chemistry. Springer, Berlin Heidelberg
40. van Slageren J, Vongtragool S, Gorshunov B, Mukhin AA, Dressel M (2004) J Magn Magn Mater 272:E765
41. van Slageren J, Vongtragool S, Gorshunov B, Mukhin AA, Karl N, Krzystek J, Telser J, Muller A, Sangregorio C, Gatteschi D, Dressel M (2003) Phys Chem Chem Phys 5:3837
42. Weil JA, Bolton JR (2007) Electron paramagnetic resonance: elementary theory and practical applications. Wiley, Hoboken
43. Aquilante F, De Vico L, Ferre N, Ghigo G, Malmqvist PA, Neogrady P, Pedersen TB, Pitonak M, Reiher M, Roos BO, Serrano-Andres L, Urban M, Veryazov V, Lindh R (2010) J Comput Chem 31:224
44. Sievers J (1982) Z Phys B Con Mat 45:289
45. Skomski R (2008) Simple models of magnetism. OUP Oxford, New York
46. Rinehart JD, Long JR (2011) Chem Sci 2:2078
47. Chilton NF, Collison D, McInnes EJL, Winpenny REP, Soncini A (2013) Nat Comm 4:3551
48. Ishikawa N, Iino T, Kaizu Y (2002) J Phys Chem A 106:9543
49. Ishikawa N, Sugita M, Okubo T, Tanaka N, Lino T, Kaizu Y (2003) Inorg Chem 42:2440
50. Schilder H, Lueken H (2004) J Magn Magn Mater 281:17
51. Baldoví JJ, Borrás-Almenar JJ, Clemente-Juan JM, Coronado E, Gaita-Ariño A (2012) Dalton Trans 41:13705
52. Baldoví JJ, Cardona-Serra S, Clemente-Juan JM, Coronado E, Gaita-Ariño A, Palii A (2013) J Comput Chem 34:1961
53. Ishikawa N, Sugita M, Ishikawa T, Koshihara S, Kaizu Y (2003) J Am Chem Soc 125:8694
54. Ishikawa N, Sugita M, Ishikawa T, Koshihara S, Kaizu Y (2004) J Phys Chem B 108:11265
55. Chibotaru LF, Ungur L (2013) Magnetic anisotropy in complexes and its ab initio description. In: European conference on molecular magnetism 2013 satellite workshop on magnetic anisotropy, Karlsruhe
56. Ishikawa N, Sugita M, Wernsdorfer W (2005) Angew Chem Int Ed 44:2931
57. Gatteschi D, Sessoli R (2003) Angew Chem Int Ed 42:268
58. Jiang SD, Wang BW, Su G, Wang ZM, Gao S (2010) Angew Chem Int Ed 49:7448
59. Chen G-J, Guo Y-N, Tian J-L, Tang J, Gu W, Liu X, Yan S-P, Cheng P, Liao D-Z (2012) Chem Eur J 18:2484
60. Chen GJ, Gao CY, Tian JL, Tang JK, Gu W, Liu X, Yan SP, Liao DZ, Cheng P (2011) Dalton Trans 40:5579
61. Bi Y, Guo YN, Zhao L, Guo Y, Lin SY, Jiang SD, Tang JK, Wang BW, Gao S (2011) Chem Eur J 17:12476
62. Li DP, Wang TW, Li CH, Liu DS, Li YZ, You XZ (2010) Chem Commun 46:2929
63. Li DP, Zhang XP, Wang TW, Ma BB, Li CH, Li YZ, You XZ (2011) Chem Commun 47:6867
64. Mei XL, Ma Y, Li LC, Liao DZ (2012) Dalton Trans 41:505
65. Jiang SD, Wang BW, Sun HL, Wang ZM, Gao S (2011) J Am Chem Soc 133:4730
66. Jiang SD, Liu SS, Zhou LN, Wang BW, Wang ZM, Gao S (2012) Inorg Chem 51:3079
67. Meihaus KR, Long JR (2013) J Am Chem Soc 135:17952
68. Lucaccini E, Sorace L, Perfetti M, Costes JP, Sessoli R (2014) Chem Commun 50:1648

Struct Bond (2015) 164: 143–184
DOI: 10.1007/430_2014_154

Published online: 29 July 2014

Single-Chain Magnets and Related Systems

Claude Coulon, Vivien Pianet, Matias Urdampilleta, and Rodolphe Clérac

Abstract In this chapter, the static and dynamic magnetic properties of single-chain magnets and related systems are reviewed. We will particularly focus on the so-called Ising limit for which the magnetic anisotropy energy is much larger than the energy of the intrachain exchange interactions. The simple regular chain of ferromagnetically coupled spins will be first described. Static properties will be summarized to introduce the dominant role of domain walls at low temperature. The slow relaxation of the magnetization will be then discussed using a stochastic description. The deduced dynamic critical behavior will be analyzed in detail to explain the observed magnet behavior. In particular, the effect of applying a magnetic field, often ignored in the literature, will be discussed. Then, more complicated structures including chains of antiferromagnetically coupled magnetic sites will be discussed. Finally, the importance of interchain couplings will be introduced to discriminate between a "real" single-chain magnet and a sample presenting both a magnet-type property and a three-dimensional antiferromagnetic ordered state at low temperature.

Keywords Ising model · Low-dimensional magnetic systems · Magnetic phase transition · Magnetically ordered phase · Single-chain magnet · Slow dynamics of the magnetization

C. Coulon (✉), V. Pianet, and R. Clérac (✉)
CNRS, CRPP, UPR 8641, 33600 Pessac, France

Univ. Bordeaux, CRPP, UPR 8641, 33600 Pessac, France
e-mail: coulon@crpp-bordeaux.cnrs.fr; clerac@crpp-bordeaux.cnrs.fr

M. Urdampilleta
London Centre for Nanotechnology, University College London, WC1H 0AH London, UK

Contents

Abbreviations

1-D	One-dimensional
2-D	Two-dimensional
3-D	Three-dimensional
ac	Alternating current
C	Curie constant
dc	Direct current
eiao$^-$	1-Ethylimidazole-2-aldoximate
H	Magnetic field
Hhmp	2-Hydroxymethylpyridine
JT	Jahn-Teller
LEA	Local equilibrium approximation
LZ	Landau-Zener
M	Magnetization
miao$^-$	1-Methylimidazole-2-aldoximate
pao$^-$	Pyridine-2-aldoximate
py	Pyridine
Rsaltmen^{2-}	*N*,*N*′–(1,1,2,2-Tetramethylethylene)-bis(5-Rsalicylideneiminate)
saltmen^{2-}	*N*,*N*′–(1,1,2,2-Tetramethylethylene)-bis(salicylideneiminate)
SCM	Single-chain magnet
SMM	Single-molecule magnet
T	Temperature
ξ	Correlation length
χ	Magnetic susceptibility

1 Introduction

In the last 10 years, considerable research effort has been devoted to the synthesis of nanometer-scale magnetic systems with the ultimate goal to reduce the size of the magnetic units that store information. Quite generally, such a magnetic unit is able to show a bistable behavior at some temperatures and values of the applied magnetic field. A typical magnetic signature of this bistability is a hysteresis loop as shown in Fig. 1.

Depending on its magnetic history, the sample can be prepared in different metastable states presenting either a positive or negative magnetization. This type of magnetic behavior is commonly observed in materials which present a ferromagnetic or ferrimagnetic long-range order, but is also observed in many types of less conventional magnetic systems. The hysteresis loop may have different origins depending on the sample, but it always reveals the existence of magnetization slow dynamics, and thus this whole class of materials is called *magnets*. In bulk-ordered materials, several magnetic domains are present and displacements of the walls separating these domains are at the origin of the slow relaxation of the magnetization. In samples of smaller size, these domain walls no longer exist and a single magnetic domain is found. In this case, the slow relaxation of the magnetization takes its origin in the existence of an energy barrier due to the magnetic anisotropy. As this energy is proportional to the volume of the sample, there is a size limit down which bistability is no longer observed (at a given temperature). This so-called super-paramagnetic limit imposes a lower limit to the size of the magnetic units used for magnetic storage using conventional materials.

The beginning of the 1990s marked the discovery of single-molecule magnets (SMMs) [1–7] which gave the hope to store information on a single molecule [8–13]. In the 25 years since, numerous SMMs have been discovered and a broad community currently works on new systems with improved magnetic characteristics, although it seems difficult to obtain a magnet behavior at high temperature with such systems. However, SMMs illustrate that the existence of a long-range magnetic order is not a necessary condition to obtain a magnet (i.e., a slow relaxation of the magnetization). In fact, these systems remain in a paramagnetic phase at any temperature.

More recently, one-dimensional (1-D) systems [14, 15], termed single-chain magnets (SCMs) [15, 16], have been discovered to exhibit slow relaxation of the magnetization and thus magnetic properties comparable to SMMs. While most of the previous reviews on SCMs are describing their chemistry and synthetic strategies to obtain this type of systems [17–24], this report is mainly focusing on the magnetic properties of single-chain magnets and related systems. It summarizes the current knowledge on a theoretical point of view and illustrates the different aspects with selected experimental data. In SCM materials, the slow relaxation of the magnetization is not the signature of isolated anisotropic complexes like for SMMs, but arises from the magnetic interactions between anisotropic repeating units along a single chain. As a result, the SCM phenomenon is due to the critical

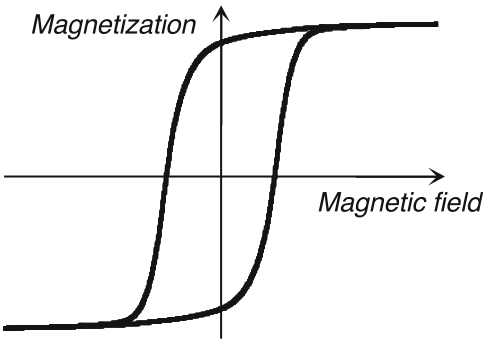

Fig. 1 Scheme of the hysteresis effect on the field dependence of the magnetization at a fixed temperature. At zero magnetic field, the magnetization can have two values depending on the magnetic history of the sample. This kind of systems with a hysteresis effect (also called memory effect) is called bistable

slowing down observed at the neighborhood of a second-order magnetic transition occurring at 0 K in the one-dimensional case. Hence, the presence of a short-range order along the chain induces a slowing down of the spin dynamics over a broad range of temperatures. This dynamic was first described by R. J. Glauber in 1963 in the frame of the Ising model [25]. Since the increase of the intrachain interaction is much easier to control experimentally than the intrinsic magnetic anisotropy in SMMs, SCMs are a promising alternative for information storage [15–24].

For the first time in 2002, a chain of ferromagnetically coupled units, as imagined by R. J. Glauber [25] ($[Mn_2(saltmen)_2Ni(pao)_2(py)_2](ClO_4)_2$; $saltmen^{2-}$: *N*,*N*′–(1,1,2,2-tetramethylethylene)-bis(salicylideneiminate); pao^-: pyridine-2-aldoximate; py: pyridine), was synthesized and its SCM properties studied in detail [15]. In this system shown in Fig. 2, the choice of the precursor building blocks ($[Mn_2(saltmen)_2(H_2O)_2](ClO_4)_2$ and $[Ni(pao)_2(py)_2]$) allowed a premeditated control of the structural dimensionality and opened the possibility to design a large series of one-dimensional systems of general formula: $[Mn_2(5\text{-}Rsaltmen)_2Ni(L1)_2(L2)_x](X)_2$ (noted in the following $[Mn_2Ni]$ chains; $Rsaltmen^{2-}$: *N*,*N*′–(1,1,2,2-tetramethylethylene)-bis(5-Rsalicylideneiminate); R: H or MeO; L1: pao^-: pyridine-2-aldoximate or $miao^-$: 1-methylimidazole-2-aldoximate or $eiao^-$: 1-ethylimidazole-2-aldoximate; L2: $x = 2$ for pyridine, 4-picoline, 4-*tert*-butylpyridine or *N*-methylimidazole, $x = 1$ for 1,10 phenanthroline; X^-: $[ClO_4]^-$, $[ReO_4]^-$, $[BPh_4]^-$, $[PF_6]^-$, $[BF_4]^-$) [15, 26–28]. In this family of compounds, the strong antiferromagnetic coupling between Mn^{III} and Ni^{II} spin carriers leads at low temperatures (typically below 25 K) [15, 26–28] to $S = 3$ macrospin units, which are ferromagnetically coupled along the chain. Up to date, this system appears to be one of the simplest experimental illustrations of a SCM made of ferromagnetically coupled anisotropic spins in the Ising limit (i.e., large anisotropy energy in comparison to the intrachain exchange energy). The first part of this book chapter (Sect. 2) is summarizing the theoretical description of this type of SCMs and

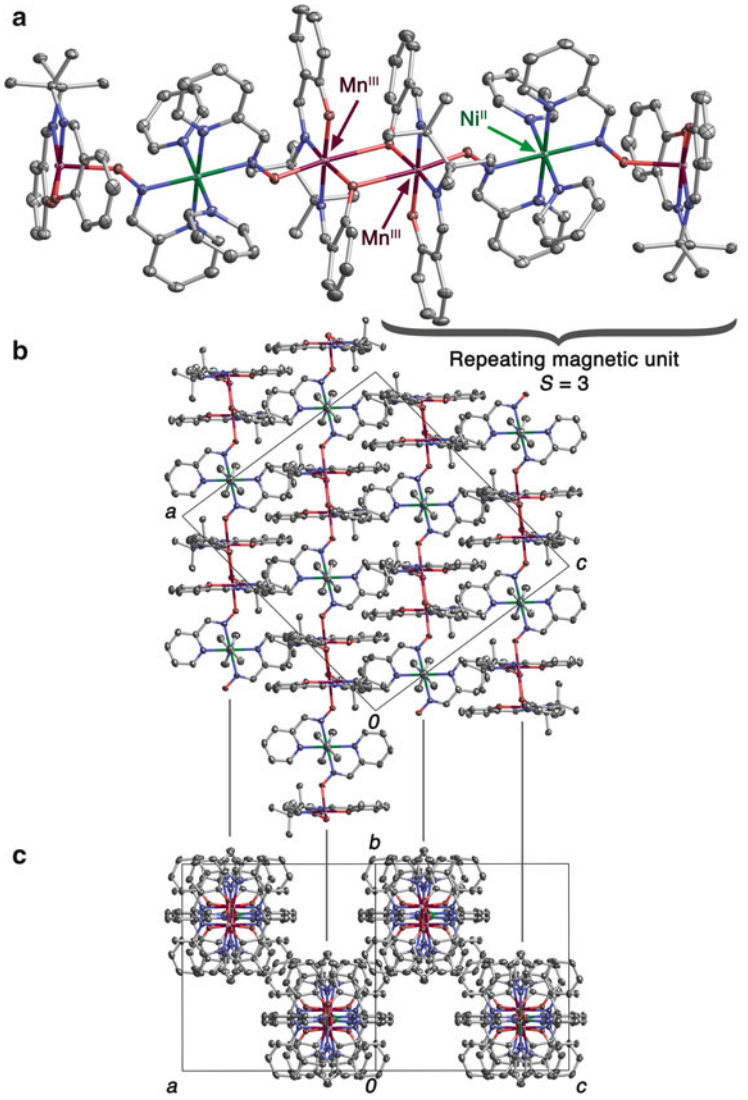

Fig. 2 Views of the crystal structure of $[Mn_2(saltmen)_2Ni(pao)_2(py)_2](ClO_4)_2$; (**a**) the one-dimensional arrangement, (**b**) a projection in the (ac) plan, and (**c**) a projection along the chain axis. The hydrogen atoms and perchlorate anions located between the chains have been omitted for clarity. Color code: *blue* N, *red* O, *pink* Mn, *green* Ni, *grey* C. Adapted from Clérac et al. [15]

selected experimental data from the $[Mn_2(5\text{-}Rsaltmen)_2Ni(L2)_2(L1)_x](X)_2$ compounds have been chosen to illustrate the key conclusions [15, 26–28].

In Sect. 3, the magnetic properties of regular chains of antiferromagnetically coupled anisotropic spins will be described and discussed in relation with the dual

ferromagnetic case presented in Sect. 2. Indeed, slow relaxation of the magnetization is also expected in this type of chain due to finite-size effects. Experimental data from the $[Mn_4(hmp)_6(L)_2](ClO_4)_2$ compounds (Hhmp: 2-hydroxymethylpyridine; L^-: N_3^-, CH_3COO^-, $ClCH_2COO^-$) made of antiferromagnetically coupled $S = 9$ anisotropic $[Mn_4(hmp)_6]^{4+}$ motifs [29, 30] will be used to illustrate this part.

The fourth part of this chapter is devoted to the effect of the interchain interactions and the possibility to stabilize three-dimensional magnetic orders of chains that, individually, would behave as a SCM. In contradiction with what was usually believed, it has been recently demonstrated both theoretically and experimentally (e.g., in $[Mn_2(5\text{-MeOsaltmen})_2Ni(pao)_2(phen)](PF_6)_2$) [31] that slow relaxation of the magnetization, i.e., magnet-type behavior induced by the presence of the chains, is still present in the magnetically ordered state, even in the case of an antiferromagnetic ground state [32, 33].

Concluding remarks and perspectives will be finally given in Sect. 5. In particular, the case of single-chain magnets that display more complex structure or spin topologies will be evoked.

2 Regular Chain of Ferromagnetically Coupled Anisotropic Spins

As mentioned in the introduction, numerous systems have been recently described as single-chain magnets. However, many of them have been characterized only in a very preliminary manner and then it is not excluded that some of them may present a 3-D long-range magnetic order and not SCM properties (see Sect. 4). To fully characterize a SCM, detailed static (thermodynamic) and dynamic magnetic measurements are required. To illustrate this argument, we will take the example of the $[Mn_2Ni]$ chain [15, 26–28], already mentioned in the introduction. In fact, this family of one-dimensional coordination polymers can be considered as a model system from which theoretical arguments and experimental results can be nicely compared. The dynamic properties and in particular the slow relaxation of the magnetization are essential. However, the static properties should be in priority and extensively described since they are at the origin of the magnetization dynamics of the chain.

2.1 Basic Arguments

Figure 2 shows different views of the crystal structure of the $[Mn_2(saltmen)_2Ni(pao)_2(py)_2](ClO_4)_2$ chain [15]. Thanks to the organic ligands, the different chains are well isolated from each others in the crystal structure and, therefore, they can be

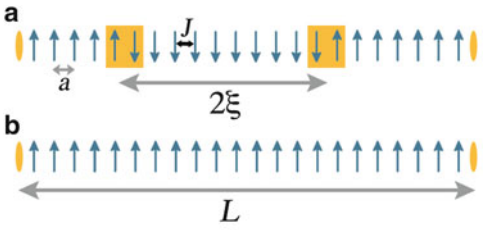

Fig. 3 Schematic views of a chain of ferromagnetically coupled Ising-type spins in zero dc field in the case of $2\xi < L$ (**a**) and $2\xi \gg$ L (**b**). L is the distance between two defects (*orange ellipses*). 2ξ is the size of the magnetic domains separated by two domain walls (*orange squares*) with ξ being the correlation length

considered as magnetically isolated. However, the magnitude of the interchain interactions cannot be easily quantified by a simple examination of the structure and thus this hypothesis should be verified by a detailed analysis of the static magnetic properties of the material (*vide infra*). Considering a single chain, Fig. 2a shows that the complex organization can be described either in terms of Mn-Ni-Mn trinuclear units or Mn-Mn dinuclear complexes linked by [Ni $(pao)_2(py)_2$] modules. For the magnetic analysis, the first description is the most appropriate as the exchange interaction within the Mn-Ni-Mn moieties is known to be about 2 orders of magnitude stronger than the Mn-Mn exchange coupling [15]. Consequently, only the ground state of the Mn-Ni-Mn trinuclear unit should be populated at low temperature allowing its approximation to an effective $S = 3$ macrospin. The coupling between Mn metal ions, J, being ferromagnetic ($J > 0$), the system can be described using this approximation as regular chain of ferromagnetically coupled effective $S = 3$ spins (Fig. 3).

Due to the well-known Jahn-Teller (JT) distortion of the Mn^{III} coordination sphere, these effective spins should be described as anisotropic magnetic centers with a local easy axis oriented along the JT axis. In the crystal structure (Fig. 2), the magnetic easy axes are ideally oriented along a unique orientation coinciding with the chain direction. The relevant Hamiltonian (called anisotropic Heisenberg Hamiltonian) to describe this $[Mn_2Ni]$ chain in the absence of an applied field is given by Eq. (1), in which the S_i spins are considered as classical spins.

$$H = -2J\sum_{-\infty}^{+\infty} \vec{S}_i \vec{S}_{i+1} - D\sum_{-\infty}^{+\infty} S_{iz}^2 \tag{1}$$

With the convention adopted in this Hamiltonian, Eq. (1), $D > 0$ corresponds to an easy axis. In the simple limit where $D \gg J$, the magnetic anisotropy forces the effective spin to align with the local easy axis and the above Hamiltonian is thus reduced to the Ising model (Eq. (2), where $\sigma_i = \pm 1$ specifies the orientation of the ith spin).

$$H = -2JS^2 \sum_{-\infty}^{+\infty} \sigma_i \sigma_{i+1} \tag{2}$$

In the next subsections, we will describe the static and dynamic properties of the regular chain of ferromagnetically coupled anisotropic spins (Fig. 3).

2.2 *Infinite Chain Length Regime*

In this part, the simplest description of the chain will be presented in the absence of an applied magnetic field and considering a chain of infinite length (Fig. 3a; at this level of description, the unavoidable presence of defects is ignored).

2.2.1 Static Properties

General considerations can be given for the anisotropic Heisenberg model. First, as for any 1-D system (with short-range interactions), no long-range magnetic order can be present at a finite temperature. However, a critical point does exist at $T = 0$ K, and for this reason, short-range order develops at low temperature. Independently of the D/J ratio, a general description of these one-dimensional spin systems with magnetic correlations can be done. In the low-temperature limit, the equilibrium state of these chains consists of large oriented magnetic domains separated by narrower domain walls (Fig. 3a). As domains with positive or negative magnetization are equally probable in absence of an applied magnetic field, the average net magnetization of a chain is zero. The size of these domains is by definition equal to 2ξ, where ξ is the correlation length. In the low-temperature limit, the temperature dependence of the correlation length can be easily deduced from a simple argument: the domain walls are well isolated from each other and therefore, they follow a Boltzmann statistics. Their number decreases exponentially as $\exp(-E/k_BT)$ where E is the creation energy of a domain wall [16]. Consequently, the correlation length also increases exponentially as $\exp(E/k_BT)$ when the temperature is lowered. The profile of a domain wall has been calculated for regular chain of ferromagnetically coupled classical spins (at $T = 0$ K) [34]. This work has been recently revisited to include more complex configurations of the chain (Coulon C, Pianet V Unpublished results). Figure 4 gives the equilibrium profile for the regular ferromagnetic chain with different D/J ratios. While "broad" domain walls are found for small D/J values (Fig. 4a), a discontinuity appears in the center of the domain wall for intermediate values (Fig. 4b). Finally, as soon as $D/J > 4/3$ (Fig. 4c), the domain wall is remarkably identical to the one predicted for the Ising limit and implies only two spins of opposite orientations (Fig. 3). This crossover is also emphasized when plotting the equilibrium angle, θ_0, of the first spin situated on the right part of the domain wall ($n = 0$). Figure 5a gives the evolution of this angle as a function of D/J.

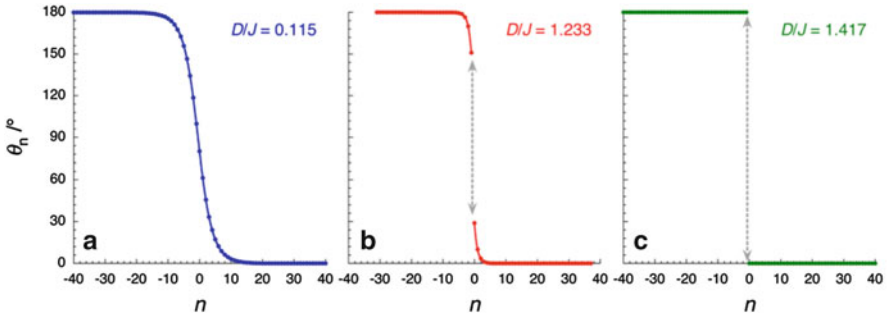

Fig. 4 Angular equilibrium profile of the spin orientation (n is the index of a given spin along the chain) on both sides of a domain wall (as in [34], $n = -1/2$ corresponds the center of the domain wall) in (**a**) the broad domain wall limit, for (**b**) an intermediate value of D/J, and in (**c**) the Ising limit with $D/J > 4/3$

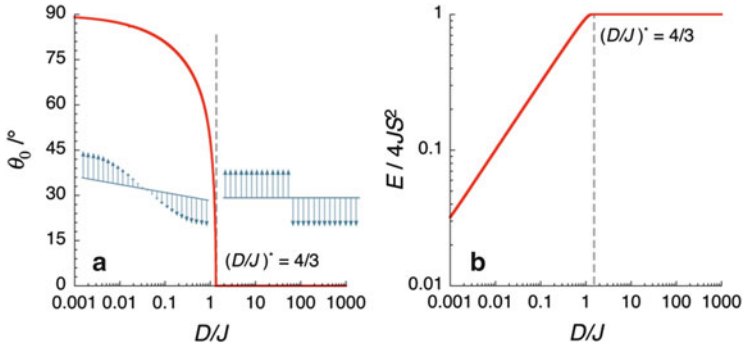

Fig. 5 (**a**) Variation of the equilibrium angle of the $n = 0$ spin and (**b**) the corresponding energy E of the domain wall (normalized to $4JS^2$) as a function of D/J

The corresponding creation energy of the domain wall is given in Fig. 5b. Although first increasing with D/J, this energy becomes constant and equal to $4JS^2$ as soon as D/J is larger than 4/3. The crossover between these two regimes, also evidenced by Fig. 5a, has been described at zero temperature as a phase transition [35]. The energy to create a domain wall, E, can be probed experimentally measuring the parallel magnetic susceptibility ($\chi_{//}$) in the zero dc-field limit that is proportional to the correlation length as shown in Eq. (3) (C is the Curie constant and a is the unit cell parameter along the chain; Fig. 3) [16] (A general demonstration of the relation between the correlation length and the zero-field magnetic susceptibility is made by Fisher [36]. In this reference, his demonstration is then applied to the classical Heisenberg model). Experimentally as illustrated by Fig. 6, the semilog plot of χT versus $1/T$ at low temperature gives a thermally activated behavior with an energy gap usually called Δ_ξ (Eq. (3)).

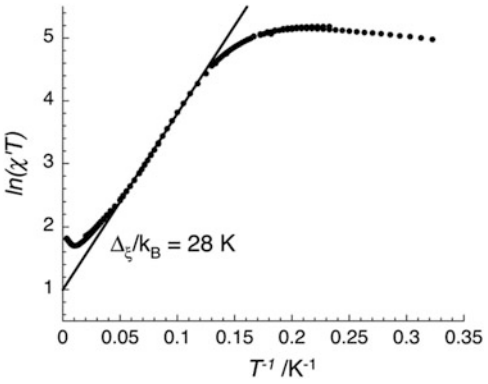

Fig. 6 Plot of $\ln(\chi' T)$ *versus* $1/T$ for $[Mn_2(saltmen)_2Ni(pao)_2(py)_2](ClO_4)_2$ (χ' is the in-phase component of the ac susceptibility measured in zero dc field at 1 Hz). Adapted from Coulon et al. [41]

$$\frac{\chi_{//} T}{C} = \frac{2\xi}{a} = \exp(\Delta_\xi / k_B T) \tag{3}$$

In the Ising limit ($D \gg J$), this experimental activation energy, Δ_ξ, is directly equal to the energy of the domain wall, $E = 4JS^2$. In the case of a finite anisotropy, Δ_ξ is still equal to E (Fig. 5b), at enough low temperature, as proved analytically by Nakamura et al. [37, 38]. However, other magnetic excitations, like spins waves, may be relevant at higher temperatures and the activation energy of the relaxation time may be affected [39]. This latter point has been recently discussed based on numerical calculations by Vindigni et al. [40].

Figure 6 gives an example of this kind of experimental results for the $[Mn_2Ni]$ chain [41]. Between 7.5 and 25 K, a linear dependence is clearly observed with $\Delta_\xi / k_B = 28$ K. Above 25 K, the effective spin approximation fails and the $\ln(\chi T)$ value deviates from a straight line. Below 7.5 K, a saturation of the χT product is observed due to the finite-size effects, as discussed in Sect. 2.3. The deduced Δ_ξ value is consistent with the estimation of $4JS^2$, indeed expected for these $[Mn_2Ni]$ chain systems, which fall in the Ising limit i.e., $D/J > 4/3$. In the rest of this section, including the dynamic properties, the discussion will be developed within the Ising limit.

Note that the data shown in Fig. 6 are obtained on a polycrystalline sample. Hence, the measured magnetic susceptibility, χ, should contain both parallel (to the easy magnetic axis, Eq. (3)) and perpendicular contributions as shown in Eq. (4).

$$\chi = \frac{2\chi_\perp + \chi_{//}}{3} = \frac{2}{3}\chi_\perp + \frac{C}{3T}\exp\left(4JS^2/k_B T\right) \tag{4}$$

However, the perpendicular contribution is negligible at low temperature as the parallel component becomes large. The thermally activated behavior is thus readily observed on a polycrystalline sample without any significant correction due to the transverse susceptibility.

2.2.2 Dynamic Properties

The application of a dc field on a SCM system generates a finite magnetization. When this applied field is suppressed, the induced magnetization decreases with time to finally relax to zero as expected at the thermal equilibrium. In order to understand these relaxation properties, it is thus necessary to describe the time dependence of the magnetization. Alternatively, the dynamics of the magnetization can be studied when probing the magnetic response with a small alternative (ac) field applied at a given frequency, ν. As the frequency dependence of the ac susceptibility is the Fourier transform of the time response, this ac technique gives the same information as the time resolved dc measurement. Indeed, most of the experimental studies reported on SCMs have been performed with ac susceptibility measurements on polycrystalline samples.

In the simplest case, the magnetic relaxation corresponds to the existence of a single mode, i.e., to a Debye model [42]. In this approximation, the real and imaginary parts of the ac complex susceptibility are given by Eq. (5) (where χ_{dc} is the static magnetic susceptibility and $\omega = 2\pi\nu$).

$$\chi'(\omega) = \frac{\chi_{dc}}{1+\omega^2\tau^2} \quad \text{and} \quad \chi''(\omega) = \frac{\chi_{dc}\omega\tau}{1+\omega^2\tau^2} \tag{5}$$

The position of the $\chi''(\omega)$ maximum readily gives the relaxation time at a given temperature as $\omega_{max}\tau = 1$ with $\omega_{max} = 2\pi\nu_{max}$ (ν_{max} is the frequency at which the maximum of χ'' is observed). Figure 7 gives selected ac data measured for the [Mn_2Ni] chain (Clérac R Unpublished results). As a first approximation, the $\chi''(\nu)$ curves follow a generalized Debye model. In this case, the expressions given above (Eq. (5)) are generalized introducing a third parameter, α, that takes into account a distribution of relaxation times [42]. This parameter being small, the assumption of a single relaxation time remains reasonable. The frequency position of the $\chi''(\nu)$ maximum and therefore the relaxation time, τ, are both temperature dependent and thus these measurements (Fig. 7) can be used to estimate the temperature dependence of τ.

It should be noted that in most publications, the temperature dependence of χ' and χ'' at a given frequency is reported. In order to determine the temperature dependence of the relaxation time, the maximum of $\chi''(T)$ at a given frequency is identified as the blocking temperature T_B. The deduced T_B *versus* ν plot is then reversed to obtain τ *versus* $1/T_B$. This measurement strategy is not without danger. Considering that both χ_{dc} and τ are temperature dependent, the maximum of $\chi''(T)$ (Eq. (6)) does not give the right answer unless the temperature dependence of χ_{dc} is much weaker than the one of τ [43]. The determination of $\tau(T)$ by this method becomes completely wrong if several relaxation modes are present.

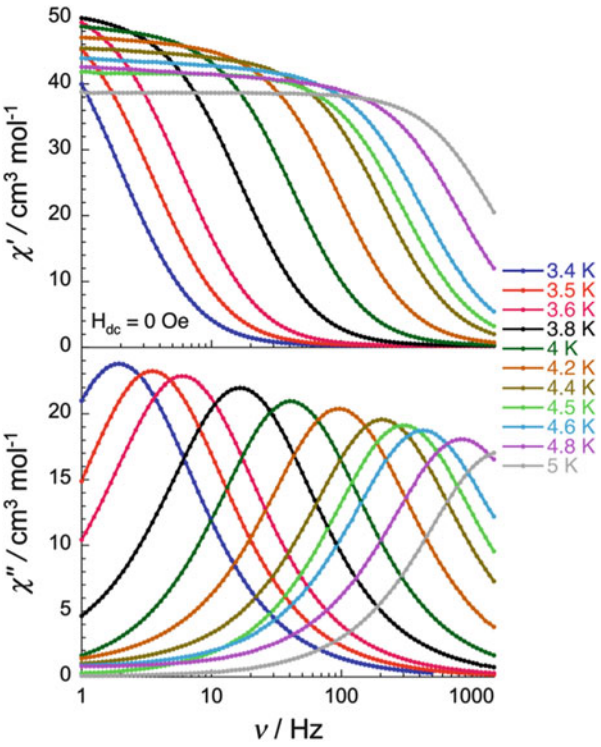

Fig. 7 Frequency dependence between 1 and 1500 Hz of the in-phase and out-of-phase ac susceptibility between 3.4 and 5 K for $[Mn_2(saltmen)_2Ni(pao)_2(py)_2](ClO_4)_2$ (Clérac R Unpublished results)

$$\chi''(T) = \frac{\chi_{dc}(T)\tau(T)\omega}{1+\omega^2\tau(T)^2} \tag{6}$$

For a theoretical description of the relaxation, the simplest approach relies on stochastic models, which have essentially been developed for Ising systems. Following the pioneering work of Glauber [25], most of the theoretical works assumes the occurrence of single-spin flips during the relaxation process. In this case, the dynamic is described by elementary steps where the transition probability, $W_i(\sigma_i)$, to flip the ith spin from σ_i to $-\sigma_i$ depends on the local field, E_i, seen by this spin. This local field is assumed to depend only on the spin state of the σ_i first neighbors. In the one-dimensional Ising case (Eq. (2)), E_i is given by Eq. (7).

$$E_i = 2JS^2(\sigma_{i-1} + \sigma_{i+1}) \tag{7}$$

Indeed, several choices for $W_i(\sigma_i)$ can be made with the only condition being that the detailed balance relation should be verified, to be consistent with the equilibrium probabilities shown in Eq. (8).

$$\frac{W_i(\sigma_i)}{W_i(-\sigma_i)} = \frac{\exp(-E_i\sigma_i/k_BT)}{\exp(E_i\sigma_i/k_BT)} = \frac{1-\sigma_i\tanh(E_i/k_BT)}{1+\sigma_i\tanh(E_i/k_BT)} \tag{8}$$

where the right part equality of Eq. (8) is obtained only when $\sigma_i = \pm 1$. For the same reason, the most general way to express the transition probability is given in Eq. (9) with f being an even function of the local field.

$$W_i(\sigma_i) = f(E_i/k_BT)(1-\sigma_i\tanh(E_i/k_BT)) \tag{9}$$

The simplest choice for $W_i(\sigma_i)$ was suggested by Glauber [25] and corresponds to $f = 1/2\tau_0$, where τ_0 is the spin flip time for a spin in absence of interactions. In this case, Eq. (10) (with $\gamma = \tanh(4JS^2/k_BT)$ [25]) gives an equivalent expression of the transition probability (as $\sigma_i = \pm 1$).

$$W_i(\sigma_i) = \frac{1}{2\tau_0}\left(1 - \frac{\gamma}{2}\sigma_i(\sigma_{i-1}+\sigma_{i+1})\right) \tag{10}$$

Nevertheless, the choice of the transition probability made by Glauber is arbitrary with the only motivation to be able to find an exact mathematical solution of this equation system in absence of an applied dc field. In fact, a more physical probability law would be an Arrhenius law [44–46]. In this case the transition probability is given by Eq. (11) for $f(E_i/k_BT) = \cosh(E_i/k_BT)/(2\tau_0)$.

$$W_i(\sigma_i) = \frac{1}{2\tau_0}\exp(-E_i\sigma_i/k_BT) \tag{11}$$

In the one-dimensional case, a general expression of $W_i(\sigma_i)$ can be established (Eq. (12)) independently of the transition probability choice.

$$W_i(\sigma_i) = \frac{1}{2\tau_0(1-\rho)}\left(1 + \rho\sigma_{i-1}\sigma_{i+1} - \frac{\gamma}{2}(1+\rho)\sigma_i(\sigma_{i-1}+\sigma_{i+1})\right) \tag{12}$$

In Eq. (12), ρ is a function of the temperature, which depends on the probability law. While $\rho = 0$ in the particular case of the Glauber probability, ρ is equal to $\tanh^2(2JS^2/k_BT)$ in the Arrhenius case. Independently of ρ, the next step to calculate the relaxation time is the determination of dynamic equations (Eq. (13)) for the average correlation functions.

$$\frac{\mathrm{d} < \sigma_i\sigma_j \ldots \sigma_r >}{\mathrm{dt}} = -2 < \sigma_i\sigma_j \ldots \sigma_r\left(W_i(\sigma_i) + W_j(\sigma_j) + \ldots + W_r(\sigma_r)\right) > \tag{13}$$

Equation (13) contains indeed a large number of coupled differential equations, with the first of these equations given by Eq. (14).

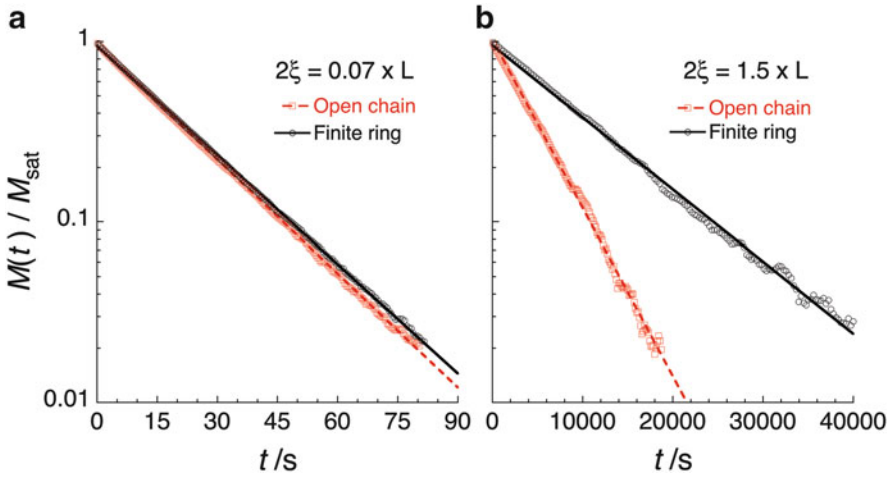

Fig. 8 Time decay of the normalized magnetization considering the Arrhenius probability law simulated by Monte Carlo approach (for $N = 100$) showing the single exponential behavior, when (**a**) $2\xi < L$ and (**b**) $2\xi > L$ (i.e., at lower temperature). *Solid* and *dashed lines* are the best fits of the numerical results by exponential laws

$$\tau_0(1-\rho)\frac{\mathrm{d} < \sigma_i >}{\mathrm{dt}} + (1-\gamma(1+\rho)) < \sigma_i > +\rho < \sigma_{i-1}\sigma_i\sigma_{i+1} >= 0 \qquad (14)$$

When $\rho = 0$ (Glauber probability), Eq. (14) describes the dynamics of the magnetization decoupled from the rest of the equation system. Only in this particular case, this dynamic equation is exactly solvable leading to an exponential time decay of the magnetization with a single relaxation time given by Eq. (15). In the low-temperature limit, Eq. (15) can be simplified and τ is then given by Eq. (16).

$$\tau = \frac{\tau_0}{1 - \tanh\left(4JS^2/k_\mathrm{B}T\right)} \qquad (15)$$

$$\tau = \frac{\tau_0}{2}\exp\left(8JS^2/k_\mathrm{B}T\right) \qquad (16)$$

On the other hand, no obvious analytical solution can be found even in the Arrhenius case, even in zero dc field, as the dynamics of the magnetization is coupled to the one of a three-spin correlation function that is itself coupled to higher-order terms! To discuss the effect of the probability law, numerical calculations are then necessary. Recent results include solutions from (i) the diagonalization of the whole dynamic linear equations system (Eq. (13)) on small chains (up to 10 spins) and (ii) Monte Carlo simulations on larger systems of N spins with different boundary conditions: either finite rings or open chains (Coulon C, Pianet V Unpublished results). Figure 8 shows typical magnetization relaxations calculated in the Arrhenius case for $N = 100$ (note that these results are

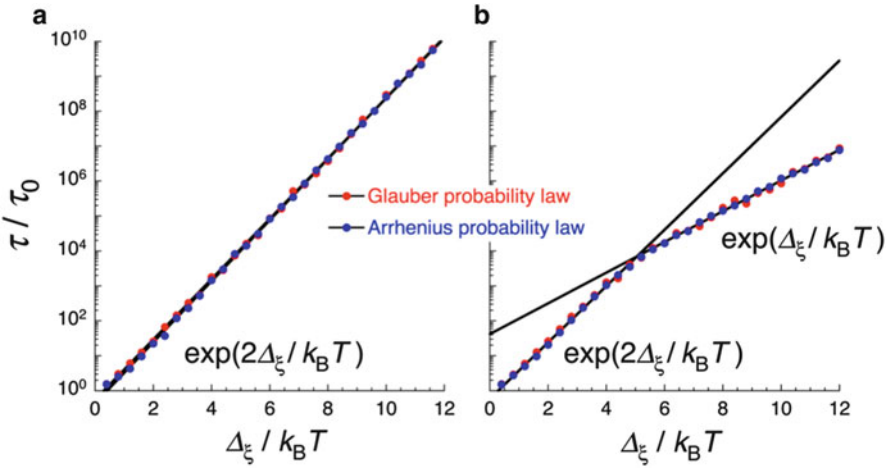

Fig. 9 Deduced normalized relaxation time (for $N = 100$; from Fig. 8) as a function of the inverse of the normalized temperature for (**a**) finite ring and (**b**) open chain. The *black solid lines* indicate the exponential laws for the different regimes of relaxation

representative of any chain length). Single exponential relaxations are found with both boundary conditions. No significant difference in Fig. 8a can be found between open chains and finite rings when the correlation length, 2ξ, is smaller than the chain length, $L = aN$ (Fig. 3), while different relaxation times are clearly observed for $2\xi > L$ (Fig. 8b). This latter point highlights the presence of finite-size effects that will be discussed in the next Sect. 2.3.

As single exponential relaxations of the magnetization are obtained (Fig. 8), a single relaxation time is readily deduced from these numerical data. It is important to note that τ is normalized by τ_0 in Fig. 9 and thus only the contribution due to the magnetic correlations is shown. It is absolutely remarkable to observe in Fig. 9 that the obtained relaxation time and its temperature dependence are essentially the same for the Glauber and Arrhenius probability laws. In contrast with what was claimed in previous publications on the subject, these simulations demonstrate that the slow relaxation of the magnetization in SCM systems is not necessary a Glauber dynamics! As it will be discussed in Sect. 2.4, it is indeed not possible to discriminate between the probability laws with experimental results at zero dc field.

For the finite ring, the relaxation time is following a single thermally activated law in agreement with Eq. (16) (Fig. 9a). In contrast, as seen in Fig. 9b, a crossover is observed for open chains. At high temperature, the relaxation time follows the same exponential law as for the finite ring, while the activated energy is reduced by two below the crossover temperature, T^*. This crossover, also related to the presence of finite-size effects, will be discussed in Sect. 2.3.

These simulations show clearly that the relaxation of the magnetization exhibits a universal behavior at zero field and low temperatures that is independent of the chosen probability law. Indeed, this result can be inferred from simple scaling arguments (omitting numerical factors). The relaxation time is the characteristic

time for a domain wall to diffuse on the length ξ of a magnetic domain. The elementary time unit being τ_0, one gets immediately $\tau \propto \tau_0(\xi/a)^2$ [47]. Therefore, considering Eq. (3), the relaxation time in the Ising limit is thermally activated with an energy gap of $2\Delta_\xi$ (Eq. (17)).

$$\tau = \frac{\tau_0}{2}\exp(2\Delta_\xi/k_B T) \tag{17}$$

The observed universality is also consistent with the vicinity of a critical point for $T = 0$ K in absence of magnetic field for which the dynamic behavior is no longer dependent on the details of the model, like the expression of the probability law. This important, although often ignored, argument has a straightforward consequence: the experimental data obtained only at zero dc field cannot be used to claim that the Glauber model has been verified. Only the above scaling arguments, valid for a whole class of probability laws, are probed with such experiments.

Finally, to compare with experimental data, it should be mentioned that τ_0 is also expected to follow an activated law (Eq. (18)) with an energy gap, Δ_A, that is the energy barrier experienced by a spin unit in absence of interaction, i.e., inside a domain wall [41].

$$\tau_0(T) = \tau_i \exp(\Delta_A/k_B T) \tag{18}$$

In the Ising limit (for narrow domain walls), Δ_A is equal to DS^2. Finally from Eqs. (17) and (18), the relaxation time for the infinite chain at low temperature can be deduced as shown by Eq. (19) (the prefactor τ_i describes the intrinsic dynamics of the spin in contact with the thermal bath, in the absence of an energy barrier).

$$\tau = \frac{\tau_i}{2}\exp((2\Delta_\xi + \Delta_A)/k_B T) \tag{19}$$

This relation is expected to be also true for a finite anisotropy, at least in the low-temperature limit. Of course in this case, the expressions of Δ_ξ and Δ_A may be more complicated that the one found in the Ising limit (where $\Delta_\xi = 4JS^2$ and $\Delta_A = DS^2$). For example, the expression of Δ_A in the large domain wall limit ($D \ll J$) is still controversial [40].

The temperature dependence of the experimental relaxation time for the [Mn_2Ni] chain is given in Fig. 10. As expected theoretically (*vide supra*), two thermally activated regimes are observed with $\Delta_{\tau 1}/k_B = 74$ K and $\Delta_{\tau 2}/k_B = 55$ K, respectively. As DS^2 can be determined, for example, from *M versus H* data on an oriented single crystal when the magnetic field is applied along the hard axis, the above relation (Eq. (19)) can be tested experimentally [41]. In the case of the [Mn_2Ni] chain (Fig. 10), the equality $\Delta_{\tau 1} = 2\Delta_\xi + \Delta_A$ is experimentally verified with $\Delta_\xi/k_B = 28$ K and $\Delta_A/k_B = 23$ K. The low-temperature regime where $\Delta_{\tau 2} = \Delta_\xi + \Delta_A$ will be discussed in the next section.

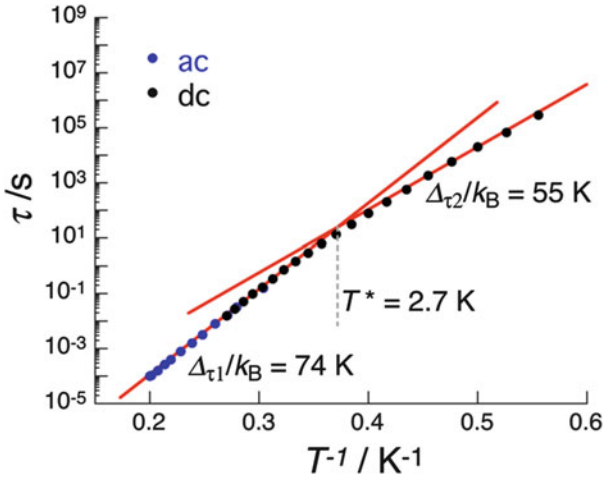

Fig. 10 Semilog plot of the relaxation time τ versus $1/T$ for $[Mn_2(saltmen)_2Ni(pao)_2(py)_2](ClO_4)_2$. The *blue* and *black dots* were obtained from ac and dc measurements, respectively. The *red straight lines* are the Arrhenius laws in the infinite and finite-size chain regimes. Adapted from Coulon et al. [41]

2.3 *Finite-Size Effects*

As noticed in the previous section for the $[Mn_2Ni]$ chain, the experimental results (Figs. 6 and 10) deviate significantly from the expected infinite chain behavior at low temperatures. This feature, which is quite general in SCM systems, reveals the presence of defects along the spin chain. Defining L as the average distance between two defects (Fig. 3b), it is clear that the magnetic correlations along the chain should saturate below the temperature for which $L \approx 2\xi$ (where ξ is the theoretical correlation length of the chain without defects) inducing, for $2\xi \gg L$, the presence of only one magnetic domain between two defects. This crossover generated by finite-size effects can be predicted by Monte Carlo simulations (Figs. 8b and 9b) as well as observed experimentally (Figs. 6 and 10). Therefore, both static and dynamic properties of SCM systems will be revisited in the following paragraphs when $L > 2\xi$.

2.3.1 Static Properties

The simplest approach to describe the finite-size effects in SCMs is to consider the "monodisperse description". At this approximation, the chains are identical finite segments of size L, i.e., the distance L between two defects is assumed to be a constant. Below the crossover temperature, T^*, when $2\xi \gg L$, the magnetic susceptibility is given by Eq. (20).

$$\frac{\chi T}{C} = \frac{L}{a} \tag{20}$$

In this limit, as there is only one magnetic domain per segment of size L, it can be considered as an effective LS/a spin. Thus, the above expression (Eq. (20)) is simply the Curie law for these effective spins. Therefore, a saturation of the χT product is expected in presence of finite-size effects as observed experimentally for the [Mn_2Ni] chain below 7.5 K (Fig. 6) [41]. In this case, the weak decrease of χT observed at low temperature has been attributed to small antiferromagnetic interactions between segments [41].

A polydisperse approach can also be developed [48, 49] considering the probability c of finding a defect in the chain. Then, the probability of finding a chain of n spins is proportional to $c^2(1-c)^n$ for missing sites and $c^2(1-c)^{n-1}$ for missing links or interactions. In this case, the magnetic susceptibility can be calculated in the Ising limit for a chain of ferromagnetically coupled spins (S). Equation (21) gives the analytical expressions of the χT product with $\eta = 1$ for missing links and $\eta = 1-c$ for missing sites.

$$\frac{\chi T}{C} = \eta \frac{1 + (1-c)\tanh\left(2JS^2/k_B T\right)}{1 - (1-c)\tanh\left(2JS^2/k_B T\right)} \tag{21}$$

At the low-temperature limit ($2JS^2 \gg k_B T$) and when c is small (i.e., small number of defects), Eq. (21) can be simplified to a unique expression given by Eq. (22).

$$\frac{\chi T}{C} = \frac{2}{c + 2\exp\left(-4JS^2/k_B T\right)} \tag{22}$$

The polydisperse approach also predicts a saturation of the χT product at low temperature at a value giving the average number of sites between two defects. It is worth mentioning that the temperature dependences of the magnetic susceptibility deduced from the monodisperse and polydisperse models are very similar and thus static measurements cannot help to detect the presence of polydispersity for a chain with ferromagnetically coupled spins [16].

2.3.2 Dynamic Properties

Finite-size effects on the relaxation time of one-dimensional systems have also been discussed using a monodisperse model and the Glauber probability law [50]. In this case, the relaxation time of the magnetization is governed by the longest characteristic time of a segment of size L. As previously discussed, τ experiences a crossover when $L \approx 2\xi$ (Figs. 9b and 10). Below this crossover, when $L \ll 2\xi$, the expression of the relaxation time is given in the Ising limit by

Eq. (23) or in the general case by Eq. (24). Introducing the expression of τ_0 (Eq. (18)), Eq. (24) can be simplified to Eq. (25).

$$\tau = \frac{\tau_0 L}{2a}\exp\left(4JS^2/k_{\mathrm{B}}T\right) \tag{23}$$

$$\tau = \frac{\tau_0 L}{2a}\exp(\Delta_\xi/k_{\mathrm{B}}T) \tag{24}$$

$$\tau = \frac{\tau_i L}{2a}\exp((\Delta_\xi + \Delta_A)/k_{\mathrm{B}}T) \tag{25}$$

This theoretical result can be readily compared with the low-temperature properties of the [Mn_2Ni] chain shown in Fig. 10. The experimental activation energy, $\Delta_{\tau 2}/k_{\mathrm{B}} = 55$ K, is in fact close to the expected $\Delta_\xi + \Delta_{\mathrm{A}}$ sum, with $\Delta_\xi/k_{\mathrm{B}} = 28$ K and $\Delta_{\mathrm{A}}/k_{\mathrm{B}} = 23$ K [41].

Dynamic properties have also been discussed in the frame of the polydisperse approach. In contrast with the monodisperse case, the theory predicts a non-exponential relaxation of the magnetization but the temperature dependence of the characteristic relaxation time is still given by the equations obtained from the monodisperse approach (Eqs. (23), (24), and (25)) [51]. For this reason, the experimental results in the finite-size regime are generally analyzed using the monodisperse approach.

Finally, it should be noted that the above conclusions are again independent of the probability law as shown by Fig. 9b, which compares the Glauber and Arrhenius results for a finite chain of 100 spin units.

2.4 Effect of the Applied Magnetic Field

Only a very few experiments on SCMs have been performed in the presence of an applied magnetic field. However, the obtained data are essential to prove the SCM properties and to exclude the occurrence of a 3-D magnetic order. It is important to keep in mind that the slow relaxation of the magnetization in 1-D systems is due to the presence of a critical point located at $T_{\mathrm{C}} = 0$ K and $H_{\mathrm{C}} = 0$. Therefore, important variations of the static and dynamic properties should occur not only by changing the temperature for $H = 0$, but also by increasing the applied magnetic field at a constant low temperature. In this latter case, a maximum of the magnetic susceptibility and of the relaxation time should be observed at $H = 0$ and an associated critical behavior should be present at low field. For the Ising model, the nature of this critical behavior has been extensively discussed, in particular to analyze the helix-coil transition in biopolymers [52–59]. The effect of an applied dc field on the SCM properties has been also described in a recent publication [60] and analyzed from numerical calculations (Coulon C, Pianet V Unpublished results). The main results will be summarized in the next paragraphs.

2.4.1 Static Properties

The field dependence of the magnetization can be exactly determined for an infinite chain of spins. In the Ising limit, the normalized magnetization, M/M_{sat}, and the associated magnetic susceptibility, χ, are given by Eqs. (26) and (27) respectively, with $M_{sat} = N\mu$ being the magnetization at saturation for N spins possessing an individual magnetic moment $\mu = g\mu_B S$.

$$\frac{M}{M_{sat}} = \frac{\sinh(\mu H/k_B T)}{\sqrt{\sinh^2(\mu H/k_B T) + \exp\left(-8JS^2/k_B T\right)}} \tag{26}$$

$$\chi = \frac{\partial M}{\partial H} = \frac{M_{sat}\mu}{k_B T} \frac{\cosh(\mu H/k_B T)\exp\left(-8JS^2/k_B T\right)}{\left(\sinh^2(\mu H/k_B T) + \exp\left(-8JS^2/k_B T\right)\right)^{3/2}} \tag{27}$$

This expression of the magnetic susceptibility emphasizes the existence of a critical regime at low field ($\mu H \ll k_B T$) for which Eq. (27) simplifies into Eq. (28).

$$\begin{aligned} \chi &= \frac{N\mu^2}{k_B T} \frac{\exp\left(4JS^2/k_B T\right)}{\left(1 + (\mu H/k_B T)^2 \exp\left(8JS^2/k_B T\right)\right)^{3/2}} \\ &= \frac{\chi(H=0)}{\left(1 + (\mu H/k_B T)^2 \exp\left(8JS^2/k_B T\right)\right)^{3/2}} \\ &= \frac{\chi(H=0)}{(1+x^2)^{3/2}} \end{aligned} \tag{28}$$

Equation (28) shows the existence of a reduced variable $x = (\mu H/k_B T)\exp(4JS^2/k_B T) = 2\mu H\xi/(ak_B T)$ that controls the field dependence of the magnetic susceptibility. At low temperature and as expected, the susceptibility is maximum at $H = 0$ (and $x = 0$) and is drastically reduced even at low fields (for $x \approx 1$).

For a spin segment of size L, finite-size effects are predicted by the theory. In the simple limit where $2\xi \gg L$, all the spins are parallel within the segments. Each segment is then equivalent to a giant spin $nS = LS/a$. As an assembly of monodispersed segments follows a Boltzmann statistics, its magnetization and magnetic susceptibility can be easily expressed by Eqs. (29) and (30) with a new reduced variable $x' = L\mu H/(ak_B T)$ (with the segment length, L, replacing 2ξ). In the low-field limit ($x' \ll 1$), Eq. (30) can be simplified into Eq. (31). A critical effect is still observed with a maximum of the susceptibility at $H = 0$ ($x' = 0$) and its reduction at low fields (for $x' > 0$).

$$\frac{M}{M_{\text{sat}}} = \tanh(L\mu H/(ak_{\text{B}}T)) \tag{29}$$

$$\chi = \frac{LN\mu^2}{ak_{\text{B}}T}\left(1 - \tanh^2(L\mu H/(ak_{\text{B}}T))\right) \tag{30}$$

$$\chi = \frac{LN\mu^2}{ak_{\text{B}}T}\left(1 - x'^2\right) \tag{31}$$

2.4.2 Dynamic Properties

To discuss the effect of an applied magnetic field on the dynamic of SCMs, the transition probability should be adapted under dc field. In its pioneer work [25], Glauber reported a new expression of the transition probability given by Eq. (32) with $Q = \tanh(\mu H/k_{\text{B}}T)$.

$$W_i(\sigma_i) = \frac{1}{2\tau_0}(1 - Q\sigma_i)\left(1 - \frac{\gamma}{2}\sigma_i(\sigma_{i-1} + \sigma_{i+1})\right) \tag{32}$$

It should be mentioned that Eq. (32) was used by Glauber to describe only small applied fields. For higher fields, the above expression is no longer a simple function of the local field. For this reason, an alternative expression, Eq. (33), was introduced by Suzuki and Kubo [61] (with E_i defined by Eq. (7)). It is worth noting that Eq. (33) becomes identical to the Glauber expression in zero field (Eq. (32)).

$$W_i(\sigma_i) = \frac{1}{2\tau_0}\left(1 - \sigma_i \tanh\left(\frac{E_i + \mu H}{k_{\text{B}}T}\right)\right) \tag{33}$$

Finally in the Arrhenius case, the transition probability can also be written in presence of an applied field as shown by Eq. (34) [45, 46].

$$W_i(\sigma_i) = \frac{1}{2\tau_0}\exp\left(-\frac{2JS^2}{k_{\text{B}}T}\sigma_i(\sigma_{i-1} + \sigma_{i+1}) - \frac{\mu H}{k_{\text{B}}T}\sigma_i\right) \tag{34}$$

In each case, the relaxation of the magnetization can be calculated solving a system of coupled dynamic equations, exemplified by Eq. (35) for the Glauber transition probability.

$$\tau_0 \frac{\mathrm{d} < \sigma_i >}{\mathrm{dt}} + (1 - \gamma) < \sigma_i > + \gamma Q < \sigma_i\sigma_{i+1} > - Q = 0 \tag{35}$$

Even in this simple case, this equation is not decoupled from the rest of the system and thus an exact solution is no longer available. Unfortunately, this remark is also true for the Suzuki–Kubo and Arrhenius probability laws. Although the Glauber model is no longer exactly soluble for $H \neq 0$, simple approximations like the local equilibrium approximation (LEA) have been used to obtain a solution [60].

The spirit of this approximation is to consider first the linear response of the system. The linearized version of Eq. (35) is given by Eq. (36) introducing $m = <\sigma_i>, \Gamma = <\sigma_i \sigma_{i+1}>$ and $\delta m = m(t) - m_{\mathrm{eq}}$ (m_{eq} being the equilibrium value of m). The relaxation time is thus easily expressed as a function of γ, Q, and $\mathrm{d}\Gamma/\mathrm{d}m$ in Eq. (37).

$$\tau_0 \frac{\mathrm{d}\delta m}{\mathrm{d}t} + \left(1 - \gamma + \gamma Q \frac{\mathrm{d}\Gamma}{\mathrm{d}m}\right)\delta m = 0 \tag{36}$$

$$\frac{\tau_0}{\tau} = 1 - \gamma + \gamma Q \frac{\mathrm{d}\Gamma}{\mathrm{d}m} \tag{37}$$

The LEA consists in introducing the equilibrium value of $\mathrm{d}\Gamma/\mathrm{d}m$ in Eq. (37), considering that the relaxation of the correlation function Γ is much quicker than the relaxation of the magnetization.

As for the static properties, a critical regime is found at low fields. For the infinite chain, the deduced relaxation time is given by Eq. (38).

$$\tau(H) = \frac{\tau(H=0)}{1 + (\mu H/k_{\mathrm{B}}T)^2 \exp\left(8JS^2/k_{\mathrm{B}}T\right)} = \frac{\tau(H=0)}{1 + x^2} \tag{38}$$

Therefore, as concluded for the magnetic susceptibility, the relaxation time of the magnetization for a SCM is expected to be maximum at $H = 0$ ($x = 0$) and to decrease rapidly when a magnetic field is applied. This conclusion holds also in the finite-size regime for which the relaxation is given by Eq. (39) at low fields.

$$\tau(H) = \frac{\tau(H=0)}{1 + 2(\mu H/k_{\mathrm{B}}T)^2 L^2/3a^2} = \frac{\tau(H=0)}{1 + 2x'^2/3} \tag{39}$$

Omitting the numerical factors, the two expressions are similar and emphasize the role of x or x' as reduced variables to describe the critical effects.

To avoid these approximations, numerical results have been recently obtained (Coulon C, Pianet V Unpublished results). Although they confirm qualitatively the scaling laws deduced from the LEA, they show that the field dependence found in Eqs. (38) and (39) is overestimated by a factor of 2. The origin of this discrepancy is found in the calculation of $\mathrm{d}\Gamma/\mathrm{d}m$ that appears in Eq. (37).[1] Then, Eqs. (38) and (39) for the Glauber case must be replaced by the corrected expressions, Eqs. (40) and (41), for the infinite and finite-size regimes, respectively.

[1] The equilibrium value of Γ is an even function of m and Γ is proportional to m^2 or Hm at low field. The estimation of $\mathrm{d}(Hm)$ at the LEA gives $H\mathrm{d}m + m\mathrm{d}H = 2H\mathrm{d}m$ (as m is proportional to H at equilibrium and low field). On the other hand, the dynamic calculation requires the estimation of $\mathrm{d}(Hm)$ for a constant value of H, which is exactly half of the LEA result.

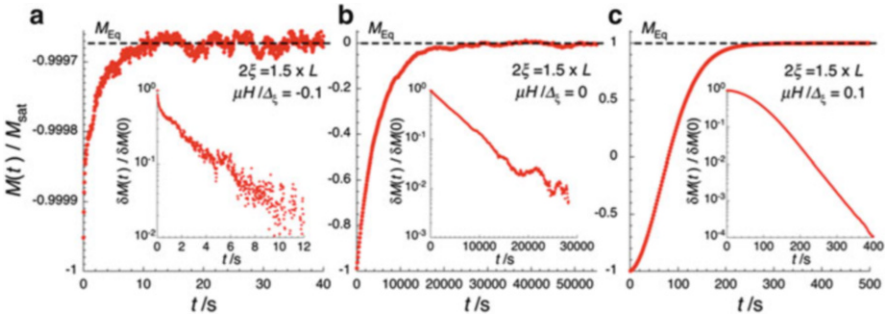

Fig. 11 Relaxation of the normalized magnetization at a fixed temperature ($\Delta_\xi/k_BT = 5$) obtained by Monte Carlo simulations in the finite-size regime ($2\xi > L$) starting from a completely saturated negative magnetization. The time decay of the reduced magnetization ($\delta M(t)/\delta M(0) = (M(t) - M(t \to \infty))/(M(t=0) - M(t \to \infty))$) in semilogarithmic plot is given in *inset*, (**a**) for a negative applied field ($\mu H/\Delta_\xi = -0.1$), (**b**) in absence of applied field ($\mu H/\Delta_\xi = 0$), and (**c**) for a positive applied field ($\mu H/\Delta_\xi = 0.1$)

$$\tau(H) = \frac{\tau(H=0)}{1 + x^2/2} \tag{40}$$

$$\tau(H) = \frac{\tau(H=0)}{1 + x'^2/3} \tag{41}$$

Indeed, the field dependence of the relaxation time is not strongly modified by the choice of the probability law as expected in a critical regime, i.e., when x or $x' \ll 1$, for which a universal behavior must be observed. Outside the critical regime, the expressions of the relaxation time can also be established. Relying on the local equilibrium approximation, theoretical results have been obtained in the Glauber case. The main conclusion of this work demonstrates that τ becomes of the order of τ_0 for $x \gg 1$ or $x' \gg 1$ [60]. More recently, Monte Carlo simulations have been used to study the effect of the different probability laws on the magnetization relaxation under dc field (Coulon C, Pianet V Unpublished results). Typical numerical data of the magnetization relaxation in the finite-size regime ($2\xi > L$) are shown in Fig. 11 starting from an initial state being completely saturated with a negative magnetization.

The presented relaxation curves are at the same temperature ($\Delta_\xi/k_BT = 5$), respectively, for $H < 0$ (Fig. 11a), $H = 0$ (Fig. 11b), and $H > 0$ (Fig. 11c) and coherently in inset of these plots is given the time decay of the reduced magnetization ($\delta M(t)/\delta M(0) = M(t) - M(t \to \infty))/(M(t=0) - M(t \to \infty))$). The theoretical relaxation of the magnetization under dc field is no longer a single exponential although a unique relaxation time can still be extracted at long time scale. As shown in Fig. 12, this deduced normalized relaxation time, τ/τ_0, is plotted as a function of the normalized inverse of the temperature (Δ_ξ/k_BT) and for different values of the normalized magnetic field ($\mu H/\Delta_\xi$) in order to evidence the different thermally activated regimes. As previously mentioned, only the correlation contribution to

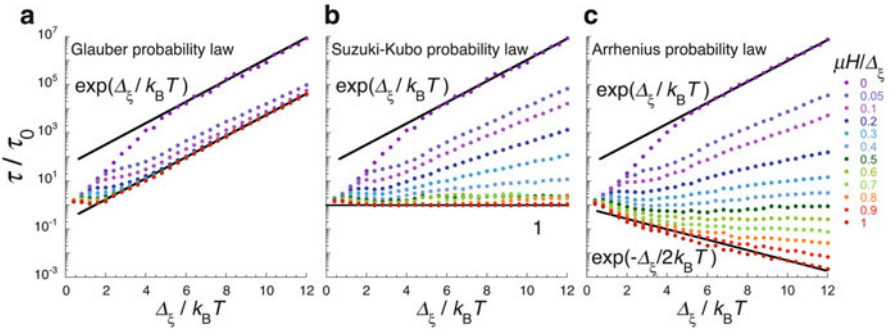

Fig. 12 Normalized relaxation time as a function of the inverse of the normalized temperature determined by Monte Carlo simulations ($N = 100$) for different values of the reduced magnetic field ($\mu H/\Delta_\xi$) in the case of the (**a**) Glauber, (**b**) Suzuki–Kubo, and (**c**) Arrhenius probability laws. *Solid lines* emphasize the low-temperature activated regimes

the relaxation time, τ/τ_0, is reported. Thus, when the obtained activation energy, $\Delta_{\tau/\tau 0}$, is negative, it simply indicates that the activation energy for the relaxation time, Δ_τ, is smaller than Δ_A. In contrast with the obtained properties at zero (Fig. 9) or small applied fields, these numerical data suggest that, at higher fields, the temperature dependence of the relaxation time is strongly dependent of the introduced probability law (Fig. 12). This result is indeed expected since the previous argument of universality is no longer valid far from the critical point. From Fig. 12, the contribution of the activation energy due to the magnetic correlations, $\Delta_{\tau/\tau 0}$, can be deduced as a function of the applied magnetic field (Fig. 13). As already concluded from Fig. 12, very different activation energies are obtained for the three investigated probability laws for finite reduced magnetic field, $\mu H/\Delta_\xi$. Moreover, the comparison between Monte Carlo simulations for $N = 100$ and numerical estimation with $N = 10$ using diagonalization of the dynamic linear equations (Eq. 13) allows to conclude that the obtained theoretical results are essentially independent of the chain length in the low-temperature limit. These theoretical results strongly suggest that experimental dynamic properties under high applied magnetic fields should be able to specify the probability law that governs SCM systems. Such experiments are presently missing in the literature.

Experimentally, the effect of the applied dc field has been studied in detail for only two different SCMs, including the [Mn_2Ni] chain [60]. As theoretically expected, the relaxation time of the magnetization is maximum in zero dc field and the low-field critical regime is well reproduced. At larger fields, the experimental results suggest that the field dependence of τ_0 should be responsible for the limited variation of τ. Other perturbations, like the influence of interchain couplings, may also be relevant to discuss the field dependence of the relaxation time. As far as we know, [60] constitutes the only detailed study of a SCM under field in the literature. Obviously, more experimental work probing the influence of a dc field would certainly be useful to test the theoretical predictions summarized here

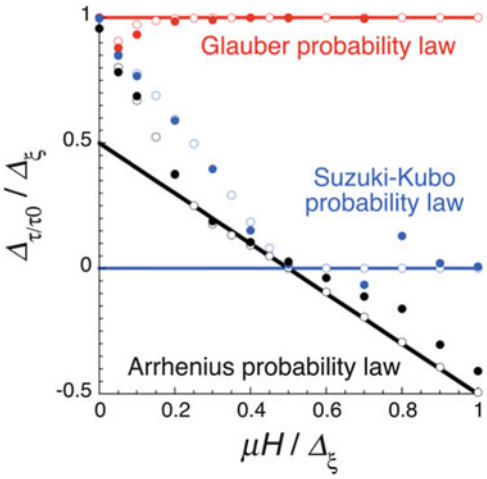

Fig. 13 Variation of the normalized correlation activation energy, $\Delta_{\tau/\tau 0}/\Delta_\xi$, obtained at low temperature as a function of the reduced applied field, $\mu H/\Delta_\xi$, from numerical results for $N = 10$ (full diagonalization, *open symbols*) and for $N = 100$ (Monte Carlo approach; full symbols, from Fig. 12) in the case of the Glauber (*red*), Suzuki-Kubo (*blue*), and Arrhenius (*black*) probability laws. *Solid lines* emphasize the linear field dependence obtained at high field

and in particular to demonstrate if the SCMs follow or not a Glauber dynamics. It should be also mentioned that this type of study is essential to distinguish between systems exhibiting a 3-D magnetically ordered phase and a real SCM behavior (see Sect. 4).

2.5 *Quantum Regime*

In the previous subsections, the experimental results have been analyzed using classical models. Indeed, as SCMs are mesoscopic objects, the influence of quantum mechanics remains marginal, for example, in comparison with single-molecule magnet systems. Quantum effects can however be observed and discussed at very low temperatures as long as a magnetic field is applied to lower the energy barrier [62, 63]. In the case of the $[Mn_2Ni]$ chain chosen as the archetype SCM in this book chapter, the field sweep rate ($v = dH/dt$) and temperature dependence of the magnetization reversal have been studied below 2.6 K. The coercive or nucleation field, H_n, increases with decreasing temperature and increasing v as expected for a thermally activated process above 1 K. Below this temperature, H_n becomes temperature independent but remains strongly sweep rate dependent. This behavior and the detailed analysis of the $H_n(v,T)$ data reveals that in this very low-temperature region, the reversal of the magnetization is induced by a quantum nucleation of a domain wall that then propagates due to the applied field [62].

2.5.1 Quantum Tunneling of the Magnetization

As discussed previously, SCMs are built with spin units presenting, in general, a strong uniaxial anisotropy or in some cases SMM properties [64, 65] like for instance in the case of the [Mn_2Ni] chains. These 1-D coordination polymers result from the self-assembly of $[Mn_2(Rsaltmen)_2Ni(L_1)_2(L_2)_x]^{2+}$ moieties, which act individually as SMMs [66]. At low temperature, this SMM unit behaves like a giant $S = 3$ spin with a uniaxial magnetic anisotropy, D/k_B, equal to 2.5 K [15, 26–28, 66]. In a SMM, the strong uniaxial anisotropy creates an energy barrier, Δ_A, that can be overcome by temperature which in this case promotes spin reversal. This spin relaxation follows an Arrhenius law (Eq. (18)) above a characteristic temperature, T^*. Below T^*, the classical magnetization dynamic becomes too slow and a faster mechanism of relaxation by quantum tunneling takes over.

Tunneling through a barrier is the archetypical effect of quantum mechanics. It happens when two states separated by an energy barrier are coupled and brought into resonance. The system can then tunnel from one state to the other.

A formal explanation of this mechanism is given by the Landau–Zener (LZ) theory. To illustrate this theory, a simple Hamiltonian given in Eq. (42), including rhombic magnetic anisotropy and Zeeman terms, should be considered (D and E being the longitudinal and transverse anisotropy, H_z the magnetic field along the z axis, and S_z, S_+ and S_- the Pauli operators).

$$H = -DS_z^2 + E\left(S_+^2 + S_-^2\right) + g\mu_B\mu_0 H_z S_z \tag{42}$$

In the case of $E = 0$, the spin eigenstates are the m_S states ($m_S = -3, \ldots +3$ for the $[Mn_2Ni]^{2+}$ SMMs) and then quantum tunneling is impossible since by definition eigenstates are stationary states. In the case of $E \neq 0$, S_+^2 and S_-^2 elements couple m_S states that satisfy the $\Delta m = \pm 2n$ rule (n being an integer number). In consequence, when two coupled m_S states are brought into resonance (Fig. 14), the spin can tunnel from one state to the other. When the temperature increases and reaches the separation energy between two m_S states with $\Delta m = \pm 1$, the absorption of a phonon can promote the spin from the ground state to an excited state where tunneling through the barrier can occur (Fig. 14b pathway). This phenomenon is called thermally assisted tunneling.

The tunneling probability between two states is given by the Landau–Zener probability, P_{LZ}, (Eq. (43); α is a coefficient that depends on the total spin number, Δ is the tunnel splitting that depends on the anisotropy parameters and v is the magnetic field sweep rate) [67].

$$P_{LZ} = 1 - \exp\left(-\alpha\frac{\Delta^2}{v}\right) \tag{43}$$

The LZ theory has been used to determine the different anisotropy parameters of SMMs [68] as well as to understand their quantum behavior such as quantum

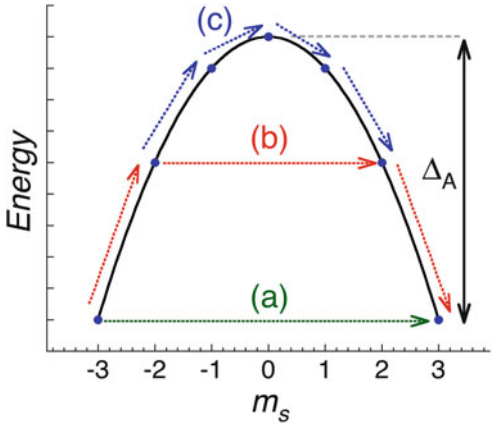

Fig. 14 Representation of the different spin reversal mechanisms for an $S = 3$ SMM. The energy separating 0 from ± 3 states is the anisotropy barrier, Δ_A. Three possible mechanisms exist: (*a*) the system can tunnel directly through the barrier from $m_S = -3$ to +3; (*b*) the spin can be thermally promoted to an excited state and then tunnel, for example, from $m_S = -2$ to +2, it is the thermally assisted tunneling; or (*c*) the spin gets enough thermal energy to pass over the energy barrier

interferences [69, 70]. In the following, we will describe how the LZ tunneling occurs and how it affects the magnetic behavior of SCM systems at very low temperature.

2.5.2 Nucleation of Domain Wall

At low temperature, a magnetic field can be applied in order to lower the energy barrier of a SCM system. When the field approaches a certain value, a domain wall can nucleate when a spin is reversed either by thermal activation or by quantum tunneling. Once triggered, the domain walls propagate due to the applied magnetic field, which induces a complete reversal of the SCM magnetization. Figure 15 presents the field dependence of the magnetization for the $[Mn_2Ni]$ chain at $T = 1.4$ K and 0.04 K for different sweep rates v. The nucleation field H_n corresponds here to the coercive field for which the magnetization reaches zero. Down to 0.5 K, H_n depends strongly on the temperature and the sweeping rate v (Fig. 16) that cannot be explained solely by the LZ theory.

Indeed at a given magnetic field, the probability of having a nucleation induced by thermal fluctuations depends on how long the system stays at this field and hence depends on v. In order to discriminate between both regimes of nucleation (induced by thermal fluctuation *versus* LZ tunneling), Wernsdorfer et al. proposed a phenomenological law that has been successfully used to explain magnetization reversal at low temperature in various low-dimensional magnetic systems [71, 72]. The temperature and sweep rate dependence of the nucleation field is expressed by Eq. (44) in which H_n^0 is the nucleation field at $T = 0$ K, E_0 the energy barrier, and b a constant that depends on the Arrhenius prefactor of Eq. (25).

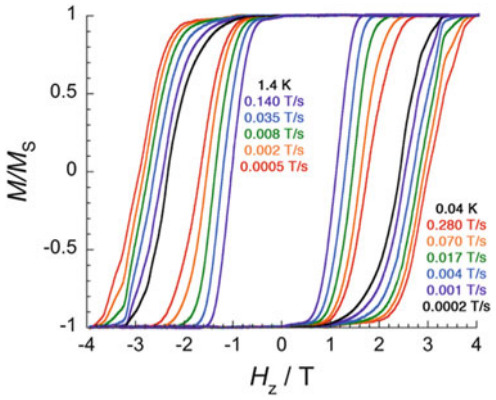

Fig. 15 Field dependence of the magnetization on a single crystal of $[Mn_2(saltmen)_2Ni(pao)_2(py)_2](ClO_4)_2$ at 1.4 and 0.04 K. The magnetic field is applied along the easy magnetic direction, and the hysteresis loops are recorded at different sweep rates. Adapted from Wernsdorfer et al. [62]

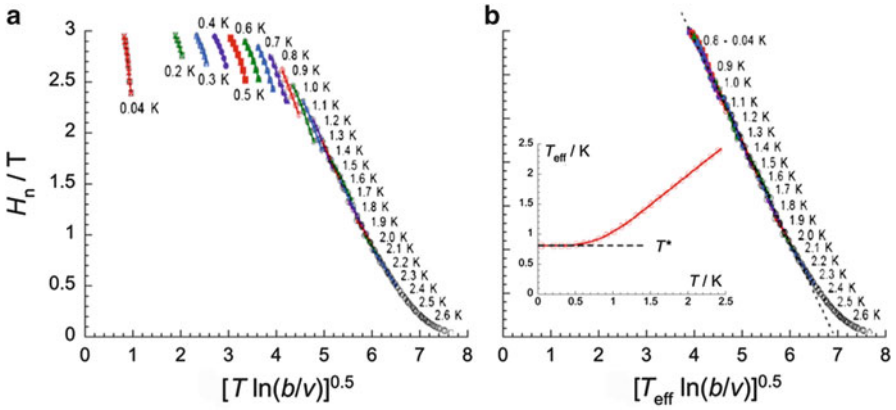

Fig. 16 Scaling plots of the nucleation field H_n for $[Mn_2(saltmen)_2Ni(pao)_2(py)_2](ClO_4)_2$ for different sweep rates (**a**) at different temperatures and (**b**) at different effective temperature T_{eff}. The *inset* gives T_{eff} as a function of T. Adapted from Wernsdorfer et al. [62]

$$H_n \approx H_n^0 \left(1 - \sqrt{\frac{k_B T}{E_0} \ln\left(\frac{b}{v}\right)}\right) \tag{44}$$

Measuring the nucleation field for different sweep rates at different temperatures allows to plot H_n as a function of a reduced variable $(T \ln(b/v))^{1/2}$ in Fig. 16a. These experimental plots show that above 1 K all the data points collapse on a single master curve. The deviation from this regime at lower temperatures reveals LZ quantum tunneling. As introduced in the previous section, the LZ probability is

independent of the temperature. As a result, when replacing T by an effective temperature T_{eff} that is constant below 1 K, all experimental data now collapse on the same master curve shown Fig. 16b. This behavior is unequivocally the signature of quantum nucleation of domain walls [62].

This phenomenological approach highlights the key role of LZ tunneling in the nucleation of the domain walls at very low temperature in SCM systems [62, 63]. However, a unified theory is still missing to fully describe the SCM dynamic at very low temperatures. Moreover, extended experiments in which the tunnel splitting Δ is tuned through the modification of the transverse anisotropy or the application of a transverse field would certainly improve the understanding of quantum nucleation of domain walls in SCMs.

3 Regular Chain of Antiferromagnetically Coupled Anisotropic Spins

For most of the magnetic problems, the only difference between ferromagnetic and antiferromagnetic cases is simply the sign of the exchange constant. Hence, the duality of the two systems allows to directly transpose the theoretical results obtained in the ferromagnetic case to the antiferromagnetic one. This very general rule can of course be applied to the regular chain of magnetically coupled anisotropic spins transposing the results obtained for the ferromagnetic case in the previous sections to the antiferromagnetic case that will be described in the following paragraphs.

3.1 Infinite Chain Length Regime

3.1.1 Static Properties

As expected, the equilibrium properties of the antiferromagnetic and ferromagnetic chain models are the same and a simple change of the interaction sign is necessary. As a result, the net magnetization of the ground state is zero but the magnetization oscillates in space, i.e., staggered magnetization, with a wave vector $q_0 = \pi/a$ (where a is the unit cell parameter; Fig. 17a). In the low-temperature limit, the equilibrium state consists of large oriented magnetic domains separated by narrower domain walls (Fig. 17b). Therefore, for decreasing temperature, the parallel susceptibility in zero field decreases exponentially and the response for a polycrystalline sample is given by Eq. (45) in the Ising limit. This relation can be generalized beyond the Ising limit by Eq. (46).

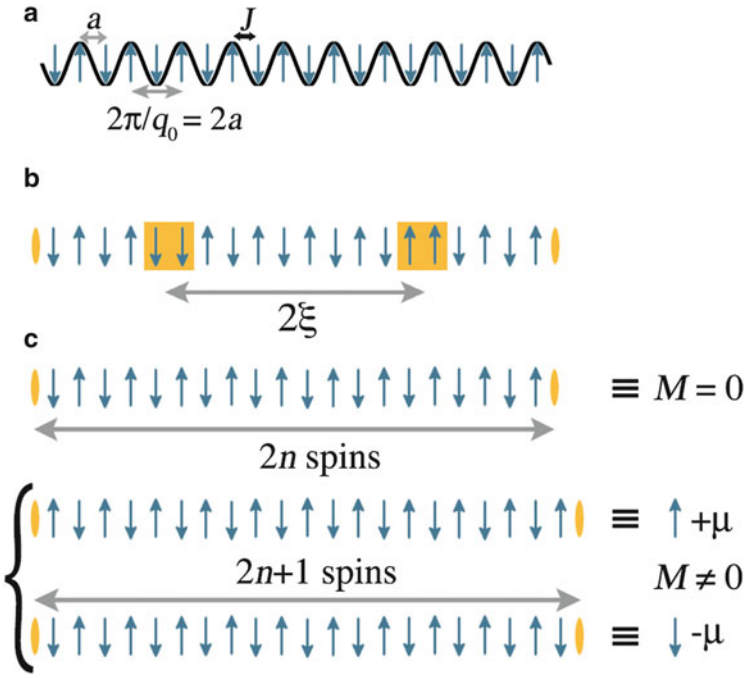

Fig. 17 Schematic views of a chain of antiferromagnetically coupled Ising-type spins in zero dc field: (**a**) the representation of the ground state (staggered magnetization: *sinusoid black line*); at a finite temperature in the cases of (**b**) $2\xi < L$ and (**c**) $2\xi \gg$ L (L is the distance between two defects, i.e., *orange ellipses*)

$$\chi = \frac{2}{3}\chi_{\perp} + \frac{C}{3T}\exp\left(-4|J|S^2/k_{\mathrm{B}}T\right) \tag{45}$$

$$\chi = \frac{2}{3}\chi_{\perp} + \frac{C}{3T}\exp(-\Delta_{\xi}/k_{\mathrm{B}}T) \tag{46}$$

Nevertheless, an essential difference appears in these relations. As the parallel component of the susceptibility decreases exponentially, the transverse contribution is no longer negligible (like it was in the ferromagnetic case, Eq. (4)) and therefore this parameter should be introduced in the fitting procedure of experimental data on polycrystalline samples. In the antiferromagnetic case, the correlation length is still diverging at low temperature but the corresponding susceptibility is now the response to a "staggered magnetic field," i.e., to a field which oscillates in space with a wave vector $q_0 = \pi/a$. The staggered susceptibility, $\chi(q_0)$, describes the response to a staggered magnetic field and is thus proportional to the correlation length as shown by Eq. (47).

$$\frac{\chi(q_0)T}{C} = \frac{2\xi}{a} \tag{47}$$

Equation (47) is the strict equivalent of Eq. (3) found for the static susceptibility in the ferromagnetic case. The expression of the correlation length is given by Eqs. (48) and (49) in the Ising limit and in the general case, respectively.

$$\frac{\xi}{a} = \exp\left(4|J|S^2/k_\mathrm{B}T\right) \tag{48}$$

$$\frac{\xi}{a} = \exp(\Delta_\xi/k_\mathrm{B}T) \tag{49}$$

3.1.2 Dynamic Properties

To make the parallel with the ferromagnetic case, it should be realized that the slow relaxation in chains of antiferromagnetically coupled spins concerns the relaxation of the staggered magnetization (Fig. 17a). On the other hand, the static magnetization relaxes even more quickly than for noninteracting spins. For the relaxation of this mode ($q_0 = \pi/a$), the expression of the relaxation time given in Eq. (50) is exactly the same as the one found for an infinite chain of ferromagnetically coupled spins (Eq. (19)).

$$\tau(q_0) = \frac{\tau_i}{2}\exp((2\Delta_\xi + \Delta_\mathrm{A})/k_\mathrm{B}T) \tag{50}$$

However, as the static susceptibility probes the relaxation of the uniform magnetization ($q = 0$), this kind of measurement is not appropriate to study the slow relaxation in the antiferromagnetic case. Note that experimentally the staggered magnetization can be deduced from the NMR relaxation time. This method has been extensively used to study organic conductors and probe the occurrence of a 3-D antiferromagnetic order ([73] and references therein).

3.2 Finite-Size Regime

3.2.1 Static Properties

As for the ferromagnetic case, the magnetic susceptibility of a finite chain can be exactly obtained [48, 49] and the same expression of the parallel susceptibility can be used (Eq. (21)) for antiferromagnetic interactions ($J < 0$). A simplified expression of $\chi T/C$, Eq. (51), is obtained at low temperature when c, the number of defects, is small. At this approximation, the average susceptibility for polycrystalline samples is given by Eq. (52).

$$\frac{\chi_{//}T}{C} = \frac{c + 2\exp\left(-4|J|S^2/k_BT\right)}{2} \tag{51}$$

$$\chi = \frac{C}{3T}\left(\frac{c + 2\exp\left(-4|J|S^2/k_BT\right)}{2}\right) + \frac{2}{3}\chi_{\perp} \tag{52}$$

At low temperature, the parallel susceptibility saturates to a limit value given by Eq. (53).

$$\frac{\chi_{//}T}{C} = \frac{c}{2} \tag{53}$$

Indeed, this result can be easily understood. In a polydisperse description, segments of all sizes are found (Fig 17c). For those containing an odd number of spins, a non-compensated magnetization equal to the magnetic moment of one spin unit is found, independently of the length of the segment. The percentage of defects associated with odd segments is in fact $c/2$, which gives directly the Curie component written above. It is worth to emphasize in this case that the monodisperse description would be artificial as the statistic of segment lengths becomes at low temperature a major contribution of the magnetic susceptibility (Eq. (51), (52), and (53)).

3.2.2 Dynamic Properties

As for the infinite chain (Sect. 3.1.2), the expression of the relaxation time for the staggered magnetization in the finite-size regime, Eq. (54), can be deduced from the ferromagnetic case (Eq. (25)).

$$\tau(q_0) = \frac{\tau_i L}{2a}\exp((\Delta_\xi + \Delta_A)/k_BT) \tag{54}$$

Remarkably, the dynamics of the finite chain of antiferromagnetically coupled spins can be observed even by standard *M versus time* or ac measurements. Figure 17c describes schematically the reversal of the staggered magnetization of an odd segment at low temperature. The net magnetization of these segments goes from $+\mu$ to $-\mu$ between the initial and final states. Then the total magnetization of the material changes with time and a mode can be detected with the ac susceptibility with however a weak intensity proportional to the number of defects. It is astonishing to realize that the dynamic of these chains is detected only in finite-size regime ($2\xi > L$), thanks to the defects present in the system. This argument has obviously no counterpart in the infinite chain case ($2\xi < L$).

It exists in the literature experimental data illustrating these arguments in three different materials containing one-dimensional coordination polymer of $S = 9$ $[Mn_4(hmp)_6]^{4+}$ SMMs [29, 30]: $[Mn_4(hmp)_6(L)_2](ClO_4)_2$; L^-: N_3^-, CH_3COO^-,

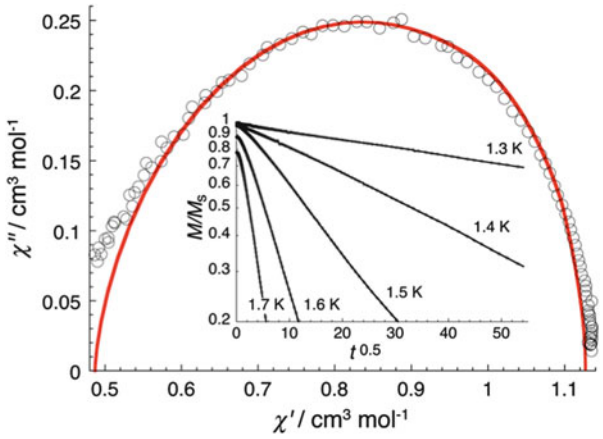

Fig. 18 Cole–Cole plot deduced from the ac susceptibility components at 2.7 K for $[Mn_4(hmp)_6(N_3)_2](ClO_4)_2$. The *solid line* gives the theoretical prediction from the polydisperse model [29, 51]. *Inset*: selected *M* versus *time* data plotted as a function of $t^{0.5}$ to emphasize the non-exponential relaxation of the magnetization. Adapted from Lecren et al. [29]

$ClCH_2COO^-$. The amount of defects has been deduced from the modeling of the static magnetic susceptibility as described in the previous paragraph (Sect. 3.2.1). As expected from the theory, the activation energy deduced for the temperature dependence of the relaxation time is consistent only with finite chains and not with the expected intrinsic dynamics of the isolated SMM units. Finally, the polydisperse character of these systems has also been emphasized through the characteristic asymmetric shape of the Cole-Cole plots and the non-exponential decay of the magnetization [29] in coherence with the theoretical prediction of [51] (Fig. 18).

4 From SCM to 3-D Ordered Systems

It was previously believed that the slow relaxation of the magnetization observed for SMM or SCM systems no longer exists if a 3-D magnetic order is present. For this reason, many systems have been described in the literature as SCMs based solely on zero field magnetic data, as soon as a slow dynamics was evidenced, for example, by ac susceptibility measurements. However, it has been recently demonstrated, both experimentally and theoretically, that slow relaxation of the magnetization and 3-D antiferromagnetic order can coexist [31–33].

As interchain couplings are antiferromagnetic in most of the cases, the simplest system, which generalizes the discussion made in Sect. 2, corresponds to ferromagnetically coupled anisotropic spins organized in regular chains, which antiferromagnetically interact. Experimentally, the simultaneous presence of a 3-D antiferromagnetic order and a slow relaxation of the magnetization has been clearly

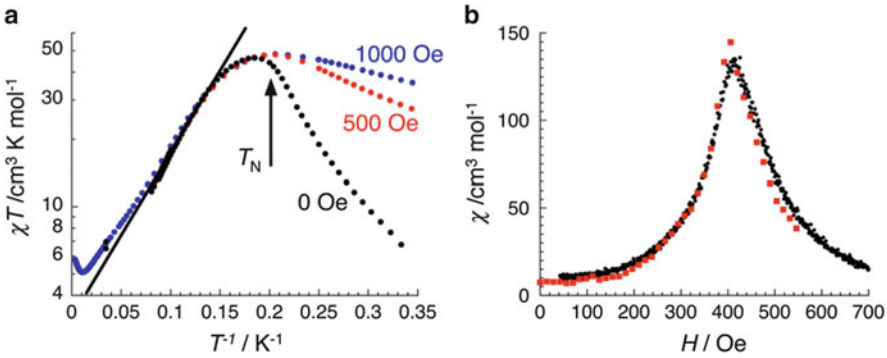

Fig. 19 Experimental data for $[Mn_2(5\text{-MeOsaltmen})_2Ni(pao)_2(phen)_2](PF_6)_2$ (with 5-MeOsaltmen and phen being the *N*,*N*′-(1,1,2,2-tetramethylethylene) bis(5-methoxy salicylideneiminate) and 1,10-phenanthroline ligands): (**a**) magnetic susceptibility data on a polycrystalline sample at different applied fields; (**b**) field dependence of the single crystal susceptibility deduced from magnetization measurements at 2.9 K (*black dots*) with a field sweeping rate of 22 Oe/s. The susceptibility deduced from relaxation data after normalization is also shown (*red squares*). Adapted from Coulon et al. [31]

demonstrated for the first time in $[Mn_2(5\text{-MeOsaltmen})_2Ni(pao)_2(phen)](PF_6)_2$ that is composed of the same type of $[Mn_2Ni]$ chain described in Sect. 2. The essential difference between the different $[Mn_2Ni]$ chain based compounds resides only in the magnitude of the antiferromagnetic interchain couplings. When strong enough, these interactions induce a 3-D antiferromagnetic order without destroying the intrinsic slow dynamics of the chains. Like in the rest of this book chapter, the $[Mn_2Ni]$ chain system will be used as an example to illustrate the theoretical arguments given in this section.

4.1 Static Properties

Figure 19a shows the χT product obtained on a polycrystalline sample for different (low) values of the applied magnetic field. Above 5 K, the χT value is independent of the dc field and clearly thermally activated as expected for SCM (Eq. (3), Fig. 6). However, at lower temperatures, the strong field dependence of the susceptibility and its noticeable decrease in zero dc field are characteristic of a 3-D antiferromagnetic ordered state.

At the same time, experiments on an oriented single crystal (Fig. 19b) show that the maximum of the susceptibility (dM/dH), at a given temperature, occurs at a finite field, H_C, of about 400 Oe, while theoretically it should be located at $H = 0$ for a SCM (Eqs. (28) and (30)). Consistent results were obtained on oriented single crystals and polycrystalline samples. It is worth mentioning that the maximum of susceptibility on polycrystalline samples is, in theory, always slightly higher (by a

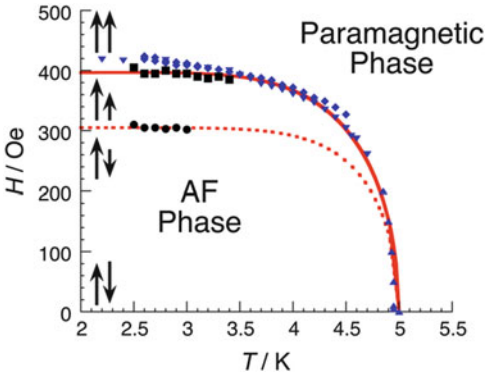

Fig. 20 Phase diagram for $[Mn_2(5\text{-MeOsaltmen})_2Ni(pao)_2(phen)_2](PF_6)_2$. Position of the susceptibility maximum from the *M versus H* data, (*black diamond*) single crystal and (*inverted filled triangle*) powder measurements, or from the temperature dependence of the powder ac susceptibility at a given dc field (*filled triangle*). Experimental points deduced from the dynamics measurements, (*filled square*) location on the main maximum of the relaxation time, and (*filled circle*) location of the second maximum (inversion point). The continuous line is the theoretical prediction of the antiferromagnetic-paramagnetic phase transition and the dashed line gives the line of inversion points. The arrows are schematizing the orientation and magnitude of the two order parameters of the problem. Adapted from Coulon et al. [31]

factor of about 1.15) than H_C accurately obtained from single-crystal measurements (see supporting information of [31]).

These static magnetic properties have been analyzed in the frame of a simple model for which antiferromagnetic interchain interactions are introduced and treated within the mean-field approximation. The resulting phase diagram is given in Fig. 20 with a comparison between experimental and theoretical results. The theory specifies the existence of two characteristic fields: (i) a critical field, H_C, associated to the antiferromagnetic-paramagnetic phase transition and (ii) an inversion field H_{inv}, located in the antiferromagnetic phase, which corresponds to the cancelation of the magnetization of one of the two sublattices. Both fields are temperature dependent and vanish at T_N, the transition temperature at zero field (Fig. 20). The temperature dependence of H_C can be followed experimentally from the maximum of dM/dH and is perfectly in agreement with the theory.

The magnitude of the interchain coupling can be deduced from the extrapolation of H_C at zero temperature, while T_N depends both on the intrachain correlation length and the interchain couplings. As the intrachain correlation length can be estimated independently from the temperature dependence of the χT product in the paramagnetic phase (Figs. 6 and 19a), the consistency between the experiment and the theoretical analysis can be completely verified.

To conclude, it should be mentioned that the inversion and critical fields are small as they essentially correspond to the situation where the external field (i.e., the Zeeman energy, which draws all chains in the same orientation) compensates the small interchain coupling (which favors the antiferromagnetic order of the

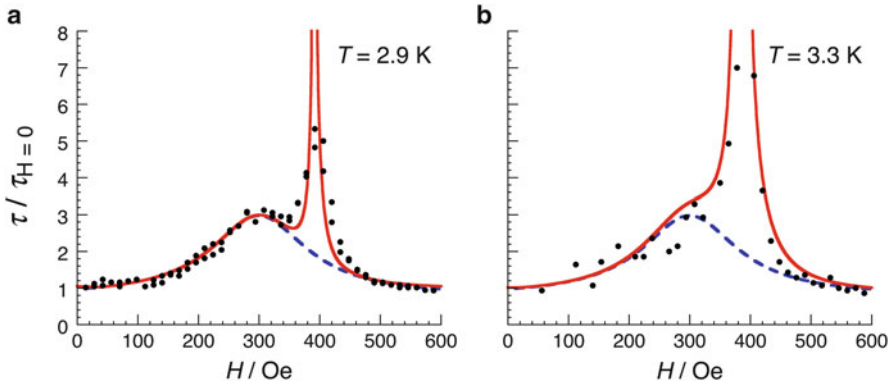

Fig. 21 Field dependence of the deduced relaxation time (normalized at zero field) for $[Mn_2(5\text{-MeOsaltmen})_2Ni(pao)_2(phen)_2](PF_6)_2$: *black dots* (**a**) at $T = 2.9$ K, (**b**) at $T = 3.3$ K. The *dashed line* shows the expected relaxation time when the magnetization m_1 of the sublattice #1 is saturated. The *continuous line* gives the calculated relaxation time using a mean-field approach. Adapted from Coulon et al. [31]

chains). As soon as the interchain coupling is small, these magnetic fields are small and the system remains strongly influenced by the intrinsic single-chain properties. This argument can also be applied to the dynamic properties as it is shown in the following subsection.

4.2 Dynamic Properties

The dynamic properties of this $[Mn_2Ni]$ compound have also been studied and analyzed [31]. Strictly speaking, the relaxation of the magnetization is no longer following a simple single exponential law when a magnetic field is applied. Nevertheless for a first analysis, the characteristic time has been deduced considering $M(t)$ data measured on single crystals and taking the time where the normalized magnetization is equal to 1/e. Figure 21 shows the field dependence of the deduced relaxation time at two different temperatures.

A maximum of the relaxation time is no longer obtained at zero field as expected for SCMs (Eqs. (38), (39), (40), and (41)). On the other hand, it reaches a maximum close to the critical field H_C (Figs. 19b and 21). Nevertheless, a thermally activated behavior of the relaxation time is still observed with an activation energy consistent with the infinite chain regime of a SCM (Eq. (19)). As a consequence, it should be emphasized that the plot of $\ln(\tau)$ *versus* $1/T$ does not really help to make the difference between a real SCM and a sample exhibiting both slow relaxation of the magnetization and a 3-D antiferromagnetically ordered system. This remark highlights the key importance of the field dependence of the relaxation time to discriminate between the two magnetic states.

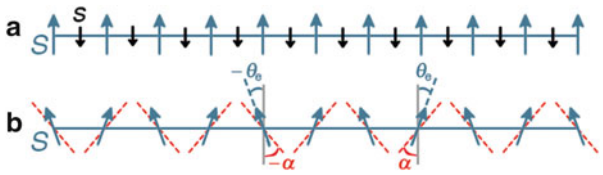

Fig. 22 Schematic representation of the structure of more complex chains: (**a**) a mixed ferrimagnetic chain composed of an alternation of isotropic (*black*) and anisotropic (*blue*) spins and (**b**) a canted chain where an alternation of the easy axis orientation is found (defining the α angle). In the latter case, the easy axes are visualized by *red dashed lines*. The spins are oriented in the direction of equilibrium (defining θ_e in the (**b**) case) in absence of domain walls

The mean-field theory used to describe the static properties (Fig. 20) was also applied to analyze these dynamic results. Although it may be too simple (in particular the non-exponential relaxation of the magnetization is not described in this approximation), this first theoretical approach shows that slow relaxation of the magnetization and 3-D antiferromagnetically order are not incompatible and can coexist. Moreover, a good agreement between the mean-field theory and the experimental results was obtained as illustrated in Fig. 21.

To conclude this section, we should emphasize that many compounds have been described as SCMs based only on studies performed in zero dc field. Indeed, this section underlines that in these experimental conditions, it is difficult to make the difference between real SCM properties and a magnetic behavior that implies a long-range ordered magnetic ground state. This is the reason why in the literature many materials were described erroneously as SCMs.

5 Conclusions and Opened Questions

In this book chapter, SCMs with simple spin architectures have been described on a theoretical point of view and illustrated by selected experimental data. Nevertheless, one-dimensional magnetic systems with a more complex spin and interaction topologies have also been synthesized and are, indeed, the most common in the literature. In all these cases, the theory is much less developed as both static and dynamic properties are more complicated to describe.

In any case, as soon as some Ising-type magnetic anisotropy is present, the low-temperature properties are always strongly influenced by the presence of domain walls. As a consequence, the first step to understand static and dynamic properties is certainly to specify the structure of these domain walls. As shown in Sect. 2.2.1 for a regular chain of ferromagnetically coupled anisotropic spins, narrow profiles are always found as soon as $D/J > 4/3$. A recent theoretical work shows a different scenario as soon as the chain topology becomes more complex (Coulon C, Pianet V Unpublished results). To illustrate this argument, two examples shown in Fig. 22 have been selected: (a) a chain composed of an alternation of

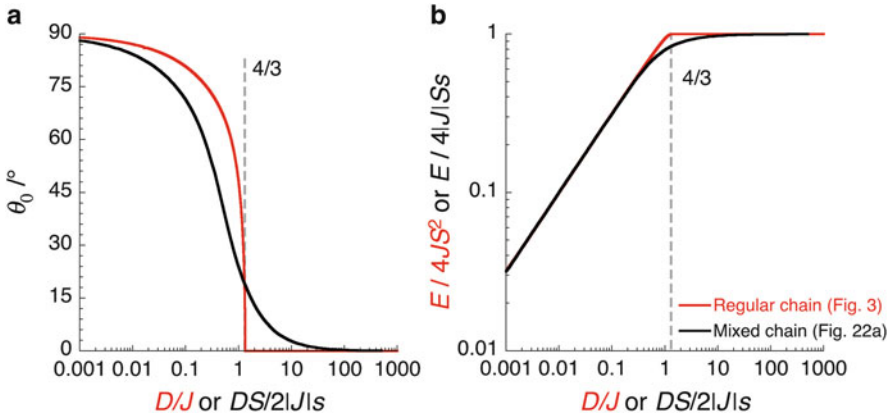

Fig. 23 (**a**) Variation of the equilibrium angle of the $n = 0$ spin, θ_0, and (**b**) the corresponding normalized energy, E, of the domain wall as a function of the anisotropy-exchange energy ratio, for the mixed chain (Fig. 22a; *black line*) compared to the regular chain of ferromagnetically coupled spins (Fig. 3; *red line*). For a better comparison, the energy of the mixed chain is normalized by $4|J|Ss$ (instead of $4JS^2$ for the regular chain) and $D/|J|$ has been multiplied by $S/2\,s$ for the mixed chain to obtain a superposition of the two curves in the broad and Ising limits

isotropic s spins and anisotropic S spins in antiferromagnetic interactions and (b) a chain of canted anisotropic spins.

For the chain with a ferrimagnetic spin topology, Fig. 23a gives the calculated angle, θ_0, of the first spin located in the right part of the domain wall, as a function of the anisotropy-exchange energy ratio ($DS/2|J|s$). These theoretical data can be readily compared with their analogues for the regular chain (Fig. 5a). The striking difference is that strictly narrow domain walls no longer exist.

For any value of $DS/2|J|s$, the width of the domain wall is larger than a simple unit cell. This result points out that the transition observed at $D/J = 4/3$ for the regular chain does not exist anymore for this type of "ferrimagnetic" chains (Fig. 22a). The same conclusions can be drawn from the variation of the domain wall energy (Fig. 23b) that does not show any cusp at any value of $DS/2|J|s$.

Similar theoretical data on the domain wall are also available for a chain of canted anisotropic spins (Fig. 22b). In this case, two different angles should be introduced to characterize the profile of a domain wall, each of them having a nonzero equilibrium value. Therefore, to specify the topology of the domain wall in this case, it is easier to use a single angular parameter, $\delta\theta_0$, obtained from the subtraction of this equilibrium value, θ_e, to the angle, θ_0 (the angle of the first spin located in the right part of the domain wall). Figure 24a reports the variation of $\delta\theta_0 = \theta_0 - \theta_e$ (Fig. 22b) as a function of $D/|J|$. As for the previous type of chain, the transition observed at $D/J = 4/3$ for the regular chain (Fig. 5) is also suppressed when introducing any value of the canting angle (α, Fig. 22b) and thus strictly narrow domain walls no longer exist. Figure 24b gives the corresponding calculated energy of the domain wall that has been normalized to $4|J|S^2\cos(2\alpha)$, the expected

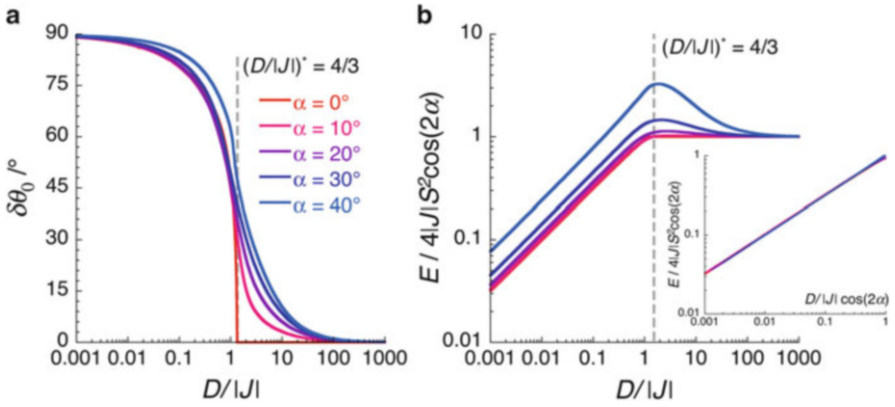

Fig. 24 (**a**) Variation of the differential angle, $\delta\theta_0 = \theta_0 - \theta_e$, and (**b**) the corresponding normalized energy of the domain wall as a function of $D/|J|$ (*inset*: as a function of the $D/|J|\cos(2\alpha)$) for the canted chain (Fig. 22b) compared to the regular chain ($\alpha = 0°$) of ferromagnetically coupled spins (Figs. 3 and 5; *red line*)

value of this energy in the Ising limit. These theoretical data show that the Ising limit is only reached for very large values of D/J as α increases. This limit is thus inappropriate to describe most of real systems. Moreover, a unique limit is found for small values of $D/|J|$ when this ratio is normalized by $\cos(2\alpha)$, showing that $|J|\cos(2\alpha)$ plays the role of an effective exchange energy in this case.

These selected results highlight that novel and original results are expected from one-dimensional magnetic systems with more complex spin and interaction topologies. However, either theoretical or experimental data on such systems remain very preliminary. In particular, this book chapter shows that magnetic experiments should explore the temperature and field dependence of both static and dynamic properties for a detailed and convincing analysis. Returning to the simple "ferromagnetic" chain described in Sect. 2, it should also be emphasized that the SCM properties in the broad domain wall limit (i.e., $D/|J| \ll 4/3$) is far from being completely understood. In this regime, other excitations, like spin waves, should compete with domain walls at finite temperature, and both static and dynamic properties are certainly more difficult to understand [39, 40, 74–79]. On the other hand, we have shown that the properties of the SCMs in the narrow domain wall limit ($D/|J| > 4/3$) are more accessible, but even in this case, a lot of work remains to be done. For example, experimental results at "high dc field" (Sect. 2.4) are still missing to discriminate between the different possible probability laws in contrast with the universal results obtained near the critical point (i.e., near $T = 0$ and $H = 0$).

To conclude this book chapter, it appears important to reinforce the idea of the universality of the physics near this critical point. This strongly suggests that the relations between the different activation energies obtained at zero field, $\Delta_{\tau 1} = 2\Delta_\xi + \Delta_A$ and $\Delta_{\tau 2} = \Delta_\xi + \Delta_A$, must be valid, at least for large values of the anisotropy energy and at low temperature. As these relations were deduced from

general scaling arguments, they can probably be transposed to more exotic chains. Following the same idea, the critical regime obtained at low field is expected to be universal. On the other hand, results at higher dc fields should be more sensitive to the spin and interaction topologies of the chain. This part of the problem remains also unexplored, both theoretically and experimentally.

Last but not least, it was remarkable to discover that the SCM behavior is preserved for systems exhibiting a long-range magnetic order, at least when the interchain couplings are weaker than the intrachain interactions. This result opens the possibility to prepare new quasi one-dimensional compounds presenting slow relaxation of the magnetization at higher temperature. But at the same time, the experimentalist is now forced to perform detailed magnetic studies and analyses (with and without applying a magnetic field) to fully characterize a potential SCM and more importantly to differentiate between a true SCM system and a 3-D magnetic order. In this respect, it would probably be useful to reinvestigate with critical eyes some published systems described as SCMs based only on a limited amount of experimental results.

Acknowledgements We are grateful to all our co-workers, past students, and friends who have contributed to our scientific adventures. In addition, the authors thank the Conseil Régional d'Aquitaine, the University of Bordeaux, the CNRS, and the ANR.

References

1. Boyd PDW, Li Q, Vincent JB, Folting K, Chang H-R, Streib WE, Huffman JC, Christou G, Hendrickson DN (1988) J Am Chem Soc 110:8537
2. Caneschi A, Gatteschi D, Sessoli R (1991) J Am Chem Soc 113:5873
3. Sessoli R, Tsai H-L, Schake AR, Wang S, Vincent JB, Folting K, Gatteschi D, Christou G, Hendrickson DN (1993) J Am Chem Soc 115:1804
4. Sessoli R, Gatteschi D, Caneschi A, Novak MA (1993) Nature 365:141
5. Thomas L, Lionti F, Ballou R, Gatteschi D, Sessoli R, Barbara B (1996) Nature 383:145
6. Gatteschi D, Sessoli R, Villain J (2006) Molecular nanomagnets. Oxford University Press, Oxford
7. Pedersen KS, Bendix J, Clérac R (2014) Chem Commun 50:4396
8. Leuenberger MN, Loss D (2001) Nature 410:789
9. Bogani L, Wernsdorfer W (2008) Nat Mater 7:179
10. Afronte M (2008) J Mater Chem 19:1731
11. Winpenny REP (2008) Angew Chem Int Ed 47:7992
12. Wernsdorfer W (2008) CR Chimie 11:1086
13. Mannini M, Pineider F, Sainctavit P, Danieli C, Otero E, Sciancalepore C, Talarico AM, Arrio MA, Cornia A, Gatteschi D, Sessoli R (2009) Nat Mater 8:194
14. Caneschi A, Gatteschi D, Lalioti N, Sangregorio C, Sessoli R, Venturi G, Vindigni A, Rettori A, Pini MG, Novak MA (2001) Angew Chem Int Ed 40:1760
15. Clérac R, Miyasaka H, Yamashita M, Coulon C (2002) J Am Chem Soc 124:12837
16. Coulon C, Miyasaka H, Clérac R (2006) Struct Bond 122:163
17. Miyasaka H, Clérac R (2005) Bull Chem Soc Jpn 78:1725
18. Xu G, Wang Q, Liao D, Yang G (2005) Prog Chem 17:970

19. Lescouëzec R, Toma LM, Vaissermann J, Verdaguer M, Delgado FS, Ruiz-Pérez C, Lloret F, Julve M (2005) Coord Chem Rev 249:2691
20. Bogani L, Vindigni A, Sessoli R, Gatteschi D (2008) J Mater Chem 18:4750
21. Miyasaka H, Julve M, Yamashita M, Clérac R (2009) Inorg Chem 48:3420
22. Brooker S, Kitchen JA (2009) Dalton Trans 7331
23. Sun H-L, Wang Z-M, Gao S (2010) Coord Chem Rev 254:1081
24. Zhang W-X, Ishikawa R, Breedlove B, Yamashita M (2013) RSC Adv 3:3772
25. Glauber J (1963) J Math Phys 4:294
26. Miyasaka H, Clérac R, Mizushima K, Sugiura K, Yamashita M, Wernsdorfer W, Coulon C (2003) Inorg Chem 42:8203
27. Saitoh A, Miyasaka H, Yamashita M, Clérac R (2007) J Mater Chem 17:2002
28. Miyasaka H, Saitoh A, Yamashita M, Clérac R (2008) Dalton Trans 2422
29. Lecren L, Roubeau O, Coulon C, Li Y-G, Le Goff XF, Wernsdorfer W, Miyasaka H, Clérac R (2005) J Am Chem Soc 127:17353
30. Lecren L, Roubeau O, Li Y-G, Le Goff XF, Miyasaka H, Richard F, Wernsdorfer W, Coulon C, Clérac R (2008) Dalton Trans 755
31. Coulon C, Clérac R, Wernsdorfer W, Colin T, Miyasaka H (2009) Phys Rev Lett 102:167204
32. Miyasaka H, Takayama K, Saitoh A, Furukawa S, Yamashita M, Clérac R (2010) Chem Eur J 16:3656
33. Bhowmick I, Hillard EA, Dechambenoit P, Coulon C, Harris TD, Clérac R (2012) Chem Commun 48:9717
34. Barbara B (1994) J Magn Magn Mater 129:79
35. Lajzerowicz J, Niez JJ (1979) J Phys Lett 40:L165
36. Fisher ME (1964) Am J Phys 32:343
37. Nakamura K, Sasada T (1978) J Phys C 11:331
38. Nakamura K, Sasada T (1977) Solid State Commun 21:891
39. Sakai T, Matsumoto M, Asakura K, Sato M (2005) Progr Theor Phys Suppl 159:308
40. Billoni O, Pianet V, Pescia D, Vindigni A (2011) Phys Rev B 84:064415
41. Coulon C, Clérac R, Lecren L, Wernsdorfer W, Miyasaka H (2004) Phys Rev B 69:132408
42. Cole KS, Cole RH (1941) J Chem Phys 9:341
43. Sun Z-M, Prosvirin AV, Zhao H-H, Mao J-G, Dunbar KR (2005) J Appl Phys 97:10B305
44. Huang HW (1973) Phys Rev A 8:2553
45. Saito Y, Kubo R (1976) J Stat Phys 15:233
46. Boukheddaden K, Shteto I, Hoo B, Varret F (2000) Phys Rev B 62:14806
47. Cordery R, Sarker S, Tobochnik J (1981) Phys Rev B 24:5402
48. Wortis M (1974) Phys Rev B 10:4665
49. Matsubara F, Yoshimura K (1973) Can J Phys 51:1053
50. Luscombe JH, Luban M, Reynolds JP (1996) Phys Rev E 53:5852
51. Dhar D, Barma M (1980) J Stat Phys 22:259
52. Schwarz G (1965) J Mol Biol 11:64
53. Pipkin AC, Gibbs JH (1996) Biopolymers 4:3
54. Craig ME, Crothers DM (1968) Biopolymers 6:385
55. Schwarz G (1968) Biopolymers 6:873
56. Schwarz G (1968) Rev Mod Phys 40:206
57. Schwarz G (1972) J Theor Biol 36:569
58. Schwarz M Jr, Poland D (1976) J Chem Phys 65:2620
59. Baumgärtner A, Binder K (1979) J Chem Phys 70:429
60. Coulon C, Clérac R, Wernsdorfer W, Colin T, Saitoh A, Motokawa N, Miyasaka H (2007) Phys Rev B 76:214422
61. Suzuki M, Kubo R (1968) J Phys Soc Jpn 24:51
62. Wernsdorfer W, Clérac R, Coulon C, Lecren L, Miyasaka H (2005) Phys Rev Lett 95:237203
63. Toma LM, Lescouëzec R, Pasan J, Ruiz-Perez C, Vaissermann J, Cano J, Carrasco R, Wernsdorfer W, Lloret F, Julve M (2006) J Am Chem Soc 128:4842

64. Roubeau O, Clérac R (2008) Eur J Inorg Chem 4313:4480
65. Jeon IR, Clérac R (2012) Dalton Trans 41:9569
66. Miyasaka H, Nezu T, Sugimoto K, Sugiura K-I, Yamashita M, Clérac R (2005) Chem Eur J 11:1592
67. Zener C (1932) Proc R Soc A 137:696
68. Wernsdorfer W, Bhaduri S, Vinslava A, Christou G (2005) Phys Rev B 72:4429
69. Wernsdorfer W, Sessoli R (1999) Science 284:133
70. Lecren L, Wernsdorfer W, Li Y-G, Roubeau O, Miyasaka H, Clérac R (2005) J Am Chem Soc 127:11311
71. Wernsdorfer W, Bonet Orozco E, Hasselbach K, Benoit A, Barbara B, Demoncy N, Loiseau A (1997) Phys Rev Lett 78:1791
72. Wernsdorfer W, Murugesu M, Tasiopoulos T, Christou G (2005) Phys Rev B 72:212406
73. Miyagawa K, Kanoda K, Kawamoto A (2004) Chem Rev 104:5635
74. Miyasaka H, Madanbashi T, Sugimoto K, Nakazawa Y, Wernsdorfer W, Sugiura K-I, Yamashita M, Coulon C, Clérac R (2006) Chem Eur J 12:7028
75. Harris TD, Bennett MV, Clérac R, Long JR (2010) J Am Chem Soc 132:3980
76. Feng X, Harris TD, Long JR (2011) Chem Sci 2:1688
77. Ishikawa R, Katoh K, Breedlove BK, Yamashita M (2012) Inorg Chem 51:9123
78. Tomkowicz Z, Rams M, Balanda M, Foro S, Nojiri H, Krupskaya Y, Kataev V, Bücher B, Nayak SK, Yakhmi JV, Haase W (2012) Inorg Chem 51:9983
79. Zhang Y-Q, Luo C-L, Wu X-B, Wang B-W, Gao S (2014) Inorg Chem 53:3503

Struct Bond (2015) 164: 185–230
DOI: 10.1007/430_2014_171

Published online: 22 November 2014

Theoretical Understanding of Anisotropy in Molecular Nanomagnets

Liviu F. Chibotaru

Abstract The study of magnetic anisotropy in metal complexes is at the forefront of current molecular magnetism research because it represents the key property for potential application of molecular materials in spintronics, memory storage, and quantum computing. The anisotropy adds an order of complexity to magnetic properties of complexes, requiring more refined experimental techniques and the use of theoretical tools, especially, of new ab initio approaches for their description. In this review, we discuss the physical reasons for magnetic anisotropy and the mechanisms of its appearance in different metal complexes. Differences in the manifestation of magnetic anisotropy between complexes with weak and strong spin–orbit coupling as well as between single-ion and polynuclear compounds will be emphasized.

Keywords Ab initio calculations · Magnetic anisotropy · Magnetic properties · Magnetization blocking · Metal complexes · Single-molecule magnets

Contents

L.F. Chibotaru (✉)
Theory of Nanomaterials Group, KU Leuven, Leuven, Belgium
e-mail: Liviu.Chibotaru@chem.kuleuven.be

Abbreviations

ac	Alternative current
Ac	Acetyl
BS-DFT	Broken-symmetry DFT
CASPT2	Complete active space second-order perturbation theory
CASSCF	Complete active space self-consistent field
COT	Cyclooctatetraene
CPT	Capped trigonal prisms
Cr_2Dy_2	$[Cr^{III}_2Dy^{III}_2(OMe)_2(O_2CPh)_4(mdea)_2(NO_3)_2]$
DFT	Density functional theory
Dy_2	$[Dy_2(ovph)_2Cl_2(MeOH)_3]$
Fe_8	$[Fe_8O_2(OH)_{12}(tacn)_6]^{8+}$
H_2ovph	Pyridine-2-carboxylic acid [(2-hydroxy-3-methoxyphenyl)methylene] hydrazide
ITO	Irreducible tensor operator
KD	Kramers doublet
L	*N*,*N*′,*N*″-Tris(2-hydroxy-3-methoxybenzylidene)-2-(aminomethyl)-2-methyl-1,3-propanediamine
Ln	Lanthanide
$mdeaH_2$	*N*-Methyldiethanolamine
Me	Methyl
$Mn_{12}ac$	$[Mn_{12}O_{12}(CH_3COO)_{16}(H_2O)_4]$
Pc	Phthalocyanine
Ph	Phenyl
QTM	Quantum tunneling of magnetization
R	Radical
RASSI-SO	Restricted active space state interaction for spin–orbit coupling
SCM	Single-chain magnet
SIM	Single-ion magnet
SMM	Single-molecule magnet
tacn	1,4,7-Triazacyclononane
TM	Transition metal
ZFS	Zero-field splitting

1 Introduction

The discovery of magnetic bistability in the Mn_{12}ac complex [1], qualified nowadays as first single-molecule magnet (SMM) [2], has sparked much interest in the effects of magnetic anisotropy in metal complexes, whose investigation became a mainstream in magnetochemistry research [3–5]. Following Olivier Kahn, we can say today that the magnetic anisotropy represents "a new dimension" in the field of molecule-based magnets [6]. Indeed, with the addition of magnetic anisotropy, the phenomenology of magnetic properties becomes much richer compared to isotropic (spin) magnetic complexes [7]. For example, a magnetic state in strongly anisotropic magnetic complexes is characterized not only by the total magnetic moment, like in isotropic systems [8], but also by local magnetic moments on the metal sites, especially, their relative directions, a feature playing a crucial role in the magnetism of such compounds [9]. Even more complex is the description of anisotropic magnetic properties. While the description of magnetism in isotropic complexes reduces to the knowledge of one single g factor in the case of mononuclear compounds and one exchange parameter per pair of exchange-coupled magnetic centers in polynuclear compounds [8], the theoretical modeling of anisotropic magnetic complexes requires tens of parameters [7]. This makes the approaches for the investigation of magnetic properties in isotropic and (strongly) anisotropic metal complexes radically different. In the former case, the structure of spin multiplets responsible for magnetism can be derived from measured static magnetic properties, temperature-dependent Van Vleck susceptibility, and field-dependent magnetization, by simulating these experiments with Heisenberg exchange models containing few fitting exchange parameters [8]. In the second case, these experimental data are by far unsufficient to elucidate the magnetism, and new experiments like luminescence and far-infrared spectroscopy [10, 11], inelastic neutron scattering [12], magnetic circular dichroism [13], and electron and nuclear paramagnetic resonances [14, 15] should be done in order to acquire additional information over the systems. The quest for additional data is especially stringent in the case of lanthanides, where recently performed single-crystal angular-dependent magnetic susceptibility proved to be very informative [16, 17]. The complexity of magnetic interactions in strongly anisotropic complexes prompted the wide use of various theoretical approaches for their description, ranging from traditional crystal-field models [18, 19] to new ab initio methodologies [20, 21]. The ultimate goal of these combined experimental and theoretical studies is the elucidation of the structure of the ground and low-lying magnetic states responsible for anisotropic magnetic properties of complexes, as well as their control via the geometry and atomic (ligand) structure of the compounds. In this review, we discuss the physical reasons for magnetic anisotropy and the mechanisms of its appearance in different metal complexes. Differences in the manifestation of magnetic anisotropy between weakly and strongly anisotropic compounds as well as between single-ion and polynuclear complexes will be emphasized.

2 Physical Reasons and Manifestations of Magnetic Anisotropy

Magnetic anisotropy is generally understood as the dependence of magnetic properties of a system on the *direction* of applied magnetic field. In bulk magnetic materials, it is also associated with preferential directions of spontaneous magnetization (magnetic ordering) and to the existence of non-collinear magnetization density distribution [22]. These are the bulk materials where the magnetic anisotropy was first observed and the physical reasons for its appearance first investigated. Next followed the magnetic nanoparticles elucidated in the seminal work of Néel [23] and, finally, two decades ago – the magnetic complexes called SMMs showing magnetic bistability at low temperature [1]. To the class of nanomagnets also belong the magnetic chains, called single-chain magnets (SCMs) [24]. All mentioned groups of magnetic systems exhibit blocking of magnetization, for which the magnetic anisotropy plays an increasing role when passing from bulk magnetic materials to SMMs. In this chapter, we discuss the origin of magnetic anisotropy in metal complexes and emphasize its different effect on magnetization blocking from magnetic nanoparticles.

2.1 Lift of Degeneracy as Reason for Anisotropy

Consider an isolated atom or ion. If it is characterized by a nonzero spin S or total angular momentum J, which is the sum of spin and orbital angular momenta, $\mathbf{J} = \mathbf{S} + \mathbf{L}$, it also possesses a magnetic moment given by the gyromagnetic relation $\boldsymbol{\mu} = -\mu_B g_s \mathbf{S}$ or $\boldsymbol{\mu} = -\mu_B g_J \mathbf{J}$, respectively, where μ_B is the Bohr magneton, $g_s = 2.0023$ is the spin, and g_J is the Landé gyromagnetic factor [25]. Being in a state with definite S or J, the atom is $2S+1$ ($2J+1$) degenerate after the projection of the angular momentum on a chosen axis. In applied magnetic field H, this degenerate manifold splits into nondegenerate levels (Zeeman splitting):

$$\begin{aligned} &E_M = \mu_B g_s H M,\ M = -S,\ -S+1,\ \ldots S \\ &\text{or} \\ &E_M = \mu_B g_J H M,\ M = -J,\ -J+1,\ \ldots J \end{aligned} \tag{1}$$

The corresponding eigenfunctions, $|SM\rangle$ or $|JM\rangle$, are just suitable components of atomic term S or multiplet J, having definite angular momentum projections M on the direction of applied field (z):

$$\hat{S}_z|SM\rangle = M|SM\rangle, \quad \hat{J}_z|JM\rangle = M|JM\rangle \tag{2}$$

We want to emphasize that the obtained Zeeman spectrum (1) does not depend on the direction of applied field $\mathbf{H}$, i.e., it is *isotropic*. The only difference arising with

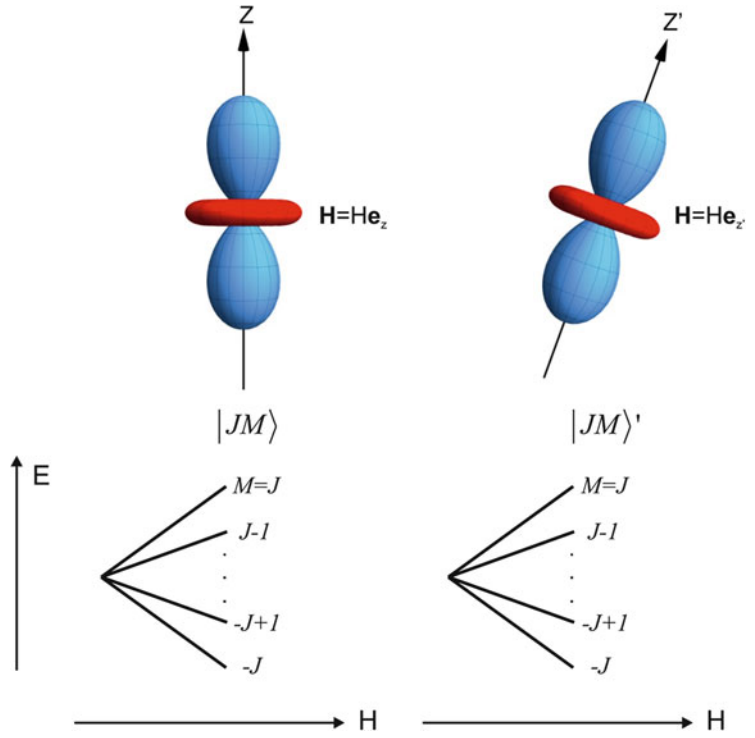

Fig. 1 Zeeman splitting of an atomic J-multiplet for different directions of applied magnetic field

the change of the direction of **H** is the new quantization axis (z'), along which the angular momentum has a definite projection M:

$$\hat{S}_{z'}|SM\rangle' = M|SM\rangle', \quad \hat{J}_{z'}|JM\rangle' = M|JM\rangle' \tag{3}$$

that always follows the direction of the field (Fig. 1). Moreover, the eigenfunctions of momentum projection along different quantization axes look equivalently (Fig. 1), i.e., can be obtained from each other via mere rotations of corresponding coordinate systems. Since both sets, (2) and (3), are eigenfunctions of the same degenerate term S or multiplet J, respectively, they are linear combinations of each other:

$$|SM_1\rangle' = \sum_{M_2=-S}^{S} D_{M_1M_2}(\alpha\beta\gamma)|SM_2\rangle, \quad |JM_1\rangle' = \sum_{M_2=-J}^{J} D_{M_1M_2}(\alpha\beta\gamma)|JM_2\rangle \tag{4}$$

The coefficients of the linear combinations, $D_{M_1M_2}(\alpha\beta\gamma)$, are the Wigner functions [26], and $\alpha\beta\gamma$ are the Euler angles relating two coordinate systems. We should stress that *all* $2S+1$ $(2J+1)$ term (multiplet) eigenfunctions should enter the

right-hand side of Eq. (4) in order to achieve the suitable combinations, $|SM_1\rangle'$ and $|JM_1\rangle'$, describing their free rotations toward arbitrary quantization axes z'. This is only possible if all these eigenfunctions correspond to the same eigenvalue, i.e., are degenerate. Thus the perfect *degeneracy* of angular momentum eigenfunctions corresponding to its given eigenvalue is the necessary and sufficient condition for the space isotropy of angular momentum and – via Eq. (1) – is the reason for *magnetic isotropy*.

Then it is clear that lifting the degeneracy of angular momentum eigenfunctions, for instance, removing one of them from the sums in the right-hand sides of Eq. (4), will not allow anymore to reproduce the shape of eigenfunctions and the Zeeman-splitting pattern (Fig. 1) for arbitrary orientations of magnetic field (rotations of quantization axis z'). This allows us to conclude that the *lift of degeneracy* of eigenfunctions of an angular momentum is the only reason for *magnetic anisotropy*.

Consider as an example a V^{3+} ion having a $3d^2$ electronic configuration. Its ground-state term is characterized by $S=1$ and $L=3$, while spin–orbit interaction couples these two momenta into the total $J=L-S=2$. In an axial crystal field (Fig. 2a), the $J=2$ multiplet splits into two Kramers doublets, $|2,\pm 2\rangle$ and $|2,\pm 1\rangle$, and a nondegenerate state $|2,0\rangle$ (Fig. 2b). In these multiplets, the axial crystal field conserves the projection of total angular momentum on the main axis Z (Fig. 2a). In the basis of the two components of the ground Kramers doublet, $|2,\pm 2\rangle$, the Zeeman operator, $\hat{V}_{\text{Zeeman}} = -\hat{\boldsymbol{\mu}}_{\text{at}} \cdot \mathbf{H} = \mu_B g_J \hat{\mathbf{J}} \cdot \mathbf{H}$, is represented by the matrix:

$$\hat{V}_{\text{Zeeman}} = \begin{pmatrix} 2\mu_B g_J H_z & 0 \\ 0 & -2\mu_B g_J H_z \end{pmatrix}, \tag{5}$$

where $H_z = H cos\theta$ and θ is the angle between the main symmetry axis and the direction of applied field (Fig. 2c). The Zeeman splitting resulting from Eq. (5) in

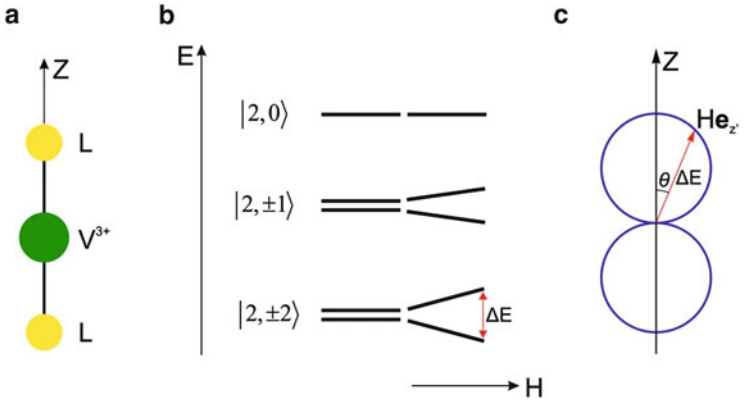

Fig. 2 Effect of lift of degeneracy on magnetic anisotropy. (**a**) Example of ligand configuration leading to axial crystal field. (**b**) Splitting of the ground-state atomic multiplet $J=2$ of V^{3+} ion into Kramers doublets in an axial crystal field. (**c**) Zeeman splitting of the ground-state crystal-field doublet $|2,\pm 2\rangle$ in function of the angle between the anisotropy axis (Z) and the direction of applied magnetic field (Z')

function of angle θ is shown in Fig. 2c. We may notice a very strong anisotropy of Zeeman splitting, which even vanishes completely for $\theta = 90°$. The reason for this anisotropy is the lift of fivefold degeneracy of $J = 2$ multiplet by the crystal field of the ligands.

The smallest angular momenta $S = 1/2$ and $J = 1/2$ belong to a special case since the twofold degeneracy of their eigenstates cannot be removed in virtue of Kramers theorem [25]. Nevertheless, these Kramers doublets can become anisotropic too in complexes of low symmetry. The anisotropy arises in this case via spin–orbit (for S) and crystal-field (for J) admixture of excited states. The necessary condition that such an admixture leads to anisotropy is the removal of degeneracy after angular momentum projection of the excited states. Thus, as in the cases discussed above, the lift of degeneracy is the ultimate reason for the observed anisotropy in this case too. However, now this lift of degeneracy is manifested in the second order of perturbation theory implying that the resulting anisotropy is not strong. Examples of this kind are Cu^{2+} complexes in orbitally nondegenerate ground state [25]. Compared to them, the anisotropy arising from the splitting of the ground manifold can be much stronger, as shown in Fig. 2.

2.2 Basic Manifestations of Magnetic Anisotropy

In mononuclear complexes, there are three basic manifestations of magnetic anisotropy, which we will illustrate here on the example of spin complexes (S-complexes). These are complexes characterized by orbitally nondegenerate ground state with a total spin S, in which spin–orbit coupling leads to the following effects:

1. $2S + 1$ – degenerate spin levels, corresponding to $S > 1/2$, become split into:
   - Kramers doublets for half-integer spin
   - Nondegenerate levels for integer spin

   This effect called zero-field splitting (ZFS) is described by the following spin Hamiltonian:

$$\hat{H}_{\mathrm{ZFS}} = \sum_{\alpha,\beta} \hat{S}_{\alpha} D_{\alpha\beta} \hat{S}_{\beta}, \quad \alpha, \beta = x, y, z \tag{6}$$

   where $\mathbf{D}$ is the ZFS tensor and the spin operators $\hat{S}_{\alpha}$, $\hat{S}_{\beta}$ act on the spin wave functions of the ground molecular term.
2. The Zeeman interaction becomes anisotropic, and the gyromagnetic factor becomes a tensor:

$$g \rightarrow g_{\alpha\beta}, \quad \alpha,\beta = x,y,z \tag{7}$$

3. The magnetization becomes anisotropic, and the susceptibility function becomes a tensor:

$$\chi(T,H) \rightarrow \chi_{\alpha\beta}(T,H), \quad M_\alpha = \sum_\beta \chi_{\alpha\beta} H_\beta, \quad \alpha,\beta = x,y,z \tag{8}$$

In polynuclear complexes, the spins localized at different magnetic centers interact with each other via Heisenberg exchange interaction [8]. In the case of two centers, this interaction is described by the following Heisenberg Hamiltonian:

$$\hat{H}_{\text{ex}} = -J\hat{\mathbf{S}}_1 \cdot \hat{\mathbf{S}}_2 \tag{9}$$

where S_1 and S_2 are ground-state spins of the two centers and J is the exchange coupling constant. The scalar product form of (9) is dictated by the requirement of conservation of the total spin of the complex, $\mathbf{S} = \mathbf{S}_1 + \mathbf{S}_2$. This is a particular case of a general property: the total spin of a multielectronic system is conserved in the absence of spin–orbit coupling and of an externally applied magnetic field [26]. Indeed, one can check directly that $\hat{H}_{\text{ex}}$ commutes with the square of the total spin, $\hat{\mathbf{S}}^2$, and with any of its projections, e.g., $\hat{S}_z$. This means, in particular, that the eigenvalues of the exchange operator (9) are $(2S+1)$ degenerate after the projection of total spin on arbitrary axis. Then again, as in the case of Zeeman splitting in isolated atoms discussed above, the eigenfunctions of total spin S defined with respect to different quantization axes, $|SM\rangle$ and $|SM\rangle'$, are obtained from each other by rotations of the corresponding coordinate systems (cf Fig. 1). On this reason, the exchange interaction described by Eq. (9) is called isotropic. The spin–orbit coupling on the metal ions makes the spins of the corresponding magnetic centers anisotropic, as reflected in Eqs. (6, 7, and 8). This anisotropy is imprinted also on the exchange interaction between the spins localized at the metal ions, which is not described anymore by a pure Heisenberg model (9). Actually, as shown by Morya [7, 27], the exchange Hamiltonian between two spins is described by the operator:

$$\hat{H}_{\text{ex}} = -J\hat{\mathbf{S}}_1 \cdot \hat{\mathbf{S}}_2 + \hat{\mathbf{S}}_1 \cdot \mathbf{D}_{12} \cdot \hat{\mathbf{S}}_2 + \mathbf{d}_{12} \cdot \hat{\mathbf{S}}_1 \times \hat{\mathbf{S}}_2 \tag{10}$$

which besides the Heisenberg term contains the symmetric anisotropic (second term) and the antisymmetric (last term) contributions to the exchange interaction. The symmetric anisotropic part is defined by the symmetric traceless tensor $\mathbf{D}_{12}$, involving five independent parameters, while the antisymmetric part – by the vector $\mathbf{d}_{12}$, involving three independent parameters. These two contributions to the exchange interaction do not conserve the total spin $\mathbf{S}$ of the pair, which can be checked straightforwardly by calculating their commutators with $\hat{\mathbf{S}}^2$ and $\hat{S}_z$. As a result, the eigenvalues of (10) will not be characterized anymore by $(2S+1)$-fold

degeneracy after the total spin projection. Accordingly, the corresponding eigenfunctions will not be $|SM\rangle$ states but rather their arbitrary combinations, i.e., will manifest space and magnetic anisotropy (cf Fig. 2).

In the case when spin–orbit coupling is stronger than the crystal-field splitting of the orbitally degenerate term (this is a typical situation for lanthanides), the ground and low-lying excited states can be seen as arising from the crystal-field splitting of the ground atomic J-multiplet. The crystal-field states of such J-complexes will manifest magnetic anisotropy as exemplified in Fig. 2. Polynuclear complexes involving J-ions will be characterized by strongly anisotropic exchange interactions, which are generally more complex than in S-complexes (Eq. 10).

2.3 Relation to Magnetization Blocking

As was mentioned in the introduction, one of the most intriguing manifestations of magnetic anisotropy in complexes is the phenomenon of magnetization blocking or, generally, slowing down of magnetic relaxation in nanomolecules [3]. Magnetization blocking is ubiquitous in bulk magnetic materials, where it simply corresponds to ordering (freezing) of localized magnetic moments below some critical temperature [28]. In these ordered phases, the steady orientation of magnetic moments at the metal sites is caused by the presence of low-symmetry molecular field arising from exchange interaction with neighbor sites (Weiss field), which persists due to the macroscopic size of the material. For smaller pieces of material, containing a few metal sites, or in magnetic complexes, such a field does not develop, and the magnetization relaxes quickly to its equilibrium value, i.e., to zero in the absence of an applied constant magnetic field. This occurs because the internal magnetic field, e.g., created by other spins in the system, induces quantum transitions between the eigenstates of the nanoparticle $|SM\rangle$ with neighboring values of momentum projection, $M' = M \pm 1$. Due to these transitions, a paramagnetic nanoparticle prepared in a state $|SM\rangle$, i.e., having initially a magnetization M, will lose it via a thermodynamic equilibration with all states $|SM'\rangle$, $M' = -S, \ldots, S$ within a relaxation time which can be as short as 10^{-9} s in concentrated systems [3].

On the other hand, any removal of $(2S+1)$ degeneracy of the ground-state spin S, resulting in magnetic anisotropy of the smaller ground-state manifold, will suppress the transition between the eigenstates entering this manifold. This is illustrated in Fig. 2 for a J-complex. As in the case of fully degenerate S term, an external magnetic field will induce transitions between all eigenstates $|JM\rangle$ of the J-multiplet. However, this transition is suppressed in the ground crystal-field manifold, $|2, \pm 2\rangle$ (Fig. 2b). The reason is the large difference between the angular momentum projections of the two eigenstates, $M_1 - M_2 = \pm 4$, which forbids matrix elements of any angular momenta between these two states. Thus the strong magnetic anisotropy suppresses the direct transition between the states of the ground manifold. The indirect transition between these states involves the excited states of the complex (Fig. 2b) and goes via Raman and/or activation relaxation

mechanism [25]. The efficiency of these relaxation processes depends on the ratio between the temperature and the excitation energy (U) of the state via which the transition occurs, kT/U. Thus U plays the role of a height of barrier which stops the indirect transitions between ground states and, therefore, the relaxation of magnetization.

The height of the barrier, U, is not necessarily equal to the energy of the lowest excited multiplet but can correspond instead to the top of a stair of states involved in the relaxation transition. To find out what states will make up the barrier of reversal of magnetization, one needs to analyze the rates of electron–phonon and tunneling transitions between the ground and low-lying eigenstates of the complex [3]. Both these rates are expressed via the squares of matrix elements of angular momenta and their powers [29–31]. Therefore, on the reasons given above, the largest transition matrix elements will arise between $|SM\rangle$ (or $|JM\rangle$) states with smallest difference of momentum projection, $M_1 - M_2 = \pm 1$. Thus, one can predict for the example given in Fig. 2 that the relaxation between the two ground states will be of activation type (for not very low temperatures) and will proceed via the chain of transitions: $|2,2\rangle \rightarrow |2,1\rangle \rightarrow |2,0\rangle \rightarrow |2,-1\rangle \rightarrow |2,-2\rangle$. In the subsequent sections, the origin of the blocking barriers in mononuclear and polynuclear complexes of both S and J types will be considered.

2.4 Nanoparticles Versus Nanomolecules

Magnetic nanoparticles were the first nano-objects where the blocking of magnetization has been investigated [23, 32, 33]. Magnetic nanoparticles are obtained by reducing the size of magnetic grains until they become single magnetic domains. That such a critical size should exist was predicted long time ago [34] and estimated to be in the range between 10 and 1,000 nm for different magnetic materials [35]. The interest for these systems arose considerably in the last decades due to the quest of miniaturization of magnetic units of information storage devices [36, 37].

Even small nanoparticles, with sizes of 5–10 nm, contain hundreds and thousands of metal ions and exhibit, therefore, a magnetic ordering at a temperature close to the corresponding critical temperature in bulk material (Curie temperature in the case of ferromagnetic ordering). This temperature is usually much higher than the temperature of magnetization blocking T_B. Then the magnetic dynamics of nanoparticles reduces to the dynamics of one single magnetization vector for temperatures not exceeding much T_B. The magnetization comprises the magnetic moments of all metal ions of the nanoparticle, amounting to thousands of Bohr magnetons. This implies classical dynamics and relaxation of magnetization in nanoparticles. Accordingly, the over-barrier relaxation is the basic mechanism of reversal of magnetization at all temperatures. There are four relevant contributions to the barrier of reversal of magnetization [38]: (1) magnetocrystalline anisotropy, (2) shape anisotropy, (3) strain anisotropy, and (4) surface anisotropy. Note that the second contribution is not related to the presence of spin–orbit coupling but

originates from magnetic dipole interaction between metal ions, whose energy depends on the direction of magnetization in the case of non-spherical nanoparticles.

Contrary to nanoparticles, the magnetization blocking in nanomolecules is basically contributed by ZFS on the metal sites (6) and by anisotropic exchange interaction between metal ions (10) (both responsible for magnetocrystalline anisotropy in nanoparticles), which are entirely due to spin–orbit coupling. One should stress that although nanoparticles possess T_B of several tens of Kelvins, reducing their size to the nuclearity of typical SMMs (usually <10 metal ions) will significantly diminish their blocking properties compared to the latter. Another important property of nanomolecules is their exact identity to each other, a feature hardly achieved for metallic nanoparticles. These properties of magnetic nanomolecules can represent an important advantage for their potential applications.

2.5 Theoretical Description

Magnetic anisotropy in complexes has a long history of theoretical description by different phenomenological models. In the case of weak spin–orbit coupling effects, the model description is based on spin Hamiltonians as in Eqs. (6) and (10) [7, 8, 25]. In the case of moderate and strong spin–orbit coupling effects, the energies and wave functions of low-lying multiplets of the complex are described by effective spin (pseudospin) Hamiltonians [25, 39]. The pseudospin $\widetilde{S}$ is not related to a physical angular momentum of the complex. Its size is defined by the dimension N of the manifold of states which is chosen for the model description: $2\widetilde{S}+1 = N$. For example, in the case of doublet states arising from crystal-field splitting of an atomic J-multiplet (Fig. 2b), the corresponding pseudospin is $\widetilde{S} = 1/2$ ($2\widetilde{S}+1 = 2$). Despite its formal nature, the pseudospin vector $(\widetilde{S}_x, \widetilde{S}_y, \widetilde{S}_z)$ can be related to real space coordinate system, i.e., completely defined, when it is close to a true spin (S-pseudospin) or a true total angular momentum (J-pseudospin) or corresponds to a degenerate irreducible representation of high-symmetry group (-Γ-pseudospin) [40]. Contrary to spin Hamiltonians used for the description of Zeeman, ZFS, and exchange interactions in complexes with weak spin–orbit coupling effects, the number of parameters entering the corresponding pseudospin Hamiltonians increases tremendously with the size of pseudospins. For the description of ionic anisotropy in mononuclear complexes and fragments, also crystal (ligand)-field models have been applied [41]. As in the case of pseudospin Hamiltonians, they can involve many parameters. For instance, to describe the crystal-field spectrum arising only from the ground atomic multiplet of a Ln ion, one needs to use up to 27 crystal-field parameters if the complexes have low symmetry [25].

At the early stage, when the theory was not able to provide the parameters of pseudospin Hamiltonians with sufficient accuracy, the latter were efficiently

constructed as invariants of given symmetry groups of the complexes [39]. Indeed, written in a coordinate system related to the symmetry axes of the complex, they involve a minimal number of parameters which can in principle be extracted from experiment. To this end, the eigenvalues of pseudospin Hamiltonians are fitted to the observed transition energies, while their eigenfunctions are used to simulate the experimental probabilities of transitions between different energy levels [25, 39]. Experimentally, the parameters of the spin Hamiltonians are most often extracted from EPR spectroscopy [7, 25, 39].

The intrinsic limitation of phenomenological models prompted the use of quantum chemistry methods, which have been first applied to the evaluation of spin Hamiltonian parameters, suitable for the description of most *S*-complexes. Thus it became possible to determine the Zeeman-splitting g tensor either perturbatively [42] or straightforwardly from DFT (for a review, see, e.g., [43]) [44] and Dirac–Fock (four-component) calculations [45, 46]. The parameters of the zero-field-splitting D tensor have been extracted from DFT calculations via a direct perturbative approach [47], by analyzing the second-order spin–orbit coupling contributions to the magnetic anisotropy energy [48, 49], via a DFT-based ligand-field model [50], and from explicitly correlated ab initio calculations by analyzing the zero-field splitting of spin levels [44, 51–56]. The effect of weak spin–orbit coupling on the exchange interactions was also studied [57–59].

Recently, the increased power of explicitly correlated ab initio methods made the accurate determination of the parameters of pseudospin Hamiltonians for experimentally investigated complexes feasible. Contrary to spin Hamiltonians, the pseudospin description requires *a nonperturbative* treatment of spin–orbit coupling, i.e., the latter should be included in the quantum chemistry calculations from the very beginning. The second important aspect is the essentially multiconfigurational character of the corresponding wave functions, which excludes the use of DFT methods for most complexes requiring a pseudospin description. The method of choice, which meets these requirements, proved to be the complete active space self-consistent field (CASSCF) approach [60], often followed by second-order perturbation treatment of dynamic electronic correlation (CASPT2) [61] implemented in the MOLCAS package [62]. In these calculations, relativistic effects are taken into account via the Douglas–Kroll Hamiltonian [63], first as scalar ones in the CASSCF/CASPT2 calculations and then via spin–orbit mixing of the obtained molecular terms within the spin–orbit restricted active space state interaction code (RASSI-SO) [64]. The methodology for the extraction of pseudospin magnetic Hamiltonians from ab initio calculations has been recently developed [21, 40].

The efficiency of this ab initio approach for the description of the effects of strong magnetic anisotropy has been first demonstrated on the nonperturbative calculations of the g tensor for the ground Kramers doublet of strongly anisotropic $[Mo(CN)_7]^{4-}$ complexes and fragments [65]. Table 1 shows that the obtained g tensor strongly depends on the geometry of the complex, i.e., whether the heptacyano environment forms a pentagonal bipyramid (PBP) or a capped trigonal prism (CTP) or has no symmetry at all being a fragment of an extended network. In

Table 1 The g tensors of $Mo(CN)_7^{4-}$ complexes in different geometries

PBP (D_{5h})	CTP (C_{2v})	$K_2[Mn(H_2O)_2]_3[Mo(CN)_7]_2 \cdot 6H_2O$ fragment (C_1)
$g_{\|\|} = 3.20$	$g_y = 2.23$	$g_1 = 2.53$
$g_\perp \approx 0.00$	$g_x = 1.88$	$g_2 = 1.41$
$\zeta = 489\ cm^{-1}$	$g_z = 1.87$	$g_3 = 1.39$
$k = 0.60$	$\zeta = 317\ cm^{-1}$	$\zeta = 310\ cm^{-1}$
	$k = 0.39$	$k = 0.38$

the former case, $g_\perp = 0$, i.e., the g tensor is of Ising type, which is the consequence of high axial symmetry of the PBP complex and of the orbitally degenerate ground state leading to unquenched orbital moment. In the CTP complex, the relatively large difference between the g factors is due to quasidegeneracy of the two lowest terms (Fig. 3a). To achieve the correct order of the lowest two terms, $^2B_1$ and $^2A_1$, in the ligand-field simulations (Fig. 3b), a *different* Racah parameter A for the lowest d orbitals was needed: $\Delta A_{xz} = 829\ cm^{-1}$ and $\Delta A_{x^2-y^2} = -3,922\ cm^{-1}$ [65]. The obtained smaller A for $d_{x^2-y^2}$ reflects a stronger covalency of this orbital as compared to that of d_{xz}. Since in phenomenological ligand/crystal-field models a single Racah parameter A is used for the entire d or f shell, this example shows severe limitations of these models for a correct description of ligand-field spectrum in complexes with important metal–ligand covalency. Finally, the geometry of the low-symmetry $[Mo(CN)_7]^{4-}$ fragment can be characterized as being in-between

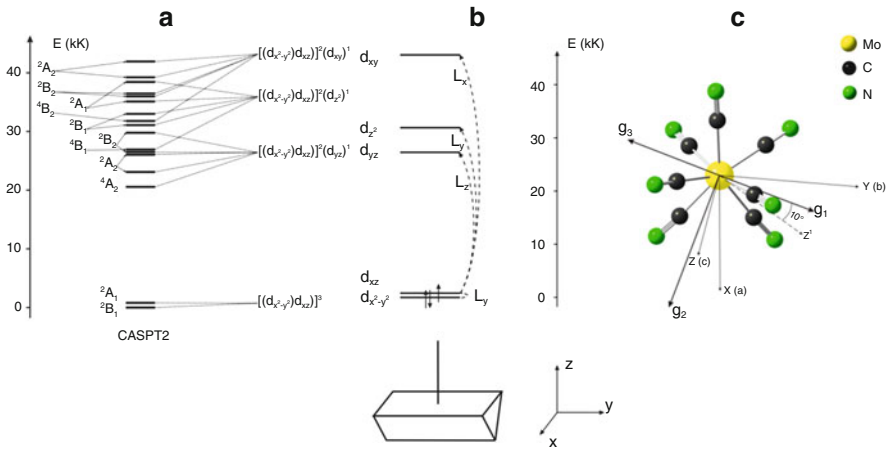

Fig. 3 Ab initio calculated g tensors for the $Mo(CN)_7^{4-}$ complex and fragment. (**a**) Ab initio spectrum of low-lying terms of CTP complex (C_{2v}). (**b**) Single-electron excitations (orbital splitting) in the CTP complex from the ground electronic configuration $\left(d_{x^2-y^2}\right)^2\left(d_{xz}\right)^1$ (*dashed arrows*) obtained in the ligand-field simulation of ab initio spectrum. Orbital moment projection contributing to the spin–orbit admixture of the corresponding excited state is indicated. (**c**) Principal magnetic axes, g_1, g_2, and g_3, of the fragment of $K_2[Mn(H_2O)_2]_3[Mo(CN)_7]_2 \cdot 6H_2O$. Reprinted with permission from Chibotaru et al. [65]. Copyright 2005 American Chemical Society

PBP and CTP geometry, which is fully reflected in the values of the calculated g factors (Table 1). The calculated main magnetic axes in this low-symmetry complex point in arbitrary directions, not passing through any ligand atom (Fig. 3c).

Calculations of this type have been done for other transition metal complexes with strong magnetic anisotropy [66–68], as well as for lanthanide [9, 69–71] and actinide [72, 73] complexes. The implementation and application of ab initio methodology for the description of anisotropic magnetic properties of lanthanides (J-complexes) has been recently reviewed [74].

3 Mononuclear Complexes

The interest for the effects of magnetic anisotropy first arose in connection with single-molecule magnet behavior of Mn_{12}ac [1], while their study in mononuclear complexes started a decade later, after the discovery of SMM behavior in $[Tb(Pc)_2]^-$ [18]. This is because the magnetization blocking is easier to achieve in polynuclear than in mononuclear complexes. On the other hand, the anisotropic magnetic interactions are obviously less complex in the latter.

3.1 Weak Spin–Orbit Coupling Effects

In transition metal complexes, the effects of spin–orbit coupling are usually weak. Indeed, a typical situation in these complexes is an orbitally nondegenerate electronic ground term, characterized by the total spin S and well separated from excited states, so that the effect of spin–orbit coupling can be considered as a perturbation (Fig. 4a). This is the case in most of the first-row transition metal complexes involving ions like Cr^{3+}, Mn^{2+}, Fe^{3+}, Ni^{2+}, etc., where the spin–orbit coupling is of the order of several hundred wavenumbers, while the crystal-field splitting is of the order of several thousand wavenumbers, so that the perturbational approach works rather well [75]. Due to the orbital nondegeneracy of the ground term, the effect of spin–orbit coupling on its energy levels arises only in the second order of perturbation theory, so the ZFS Hamiltonian is always bilinear in S, having the form given by Eq. (6). The Zeeman interaction in the lowest, first-order perturbation theory after spin–orbit coupling is always linear in S and is described by the g tensor (7) [25]:

$$\hat{H}_{\mathrm{Zee}} = \mu_{\mathrm{B}} \sum_{\alpha,\beta} H_{\alpha} g_{\alpha\beta} \hat{S}_{\beta}, \qquad \alpha,\beta = x,y,z \tag{11}$$

The **D** and **g** tensors entering magnetic Hamiltonians (6) and (11), respectively, were straightforwardly derived for various levels of description of electronic terms of complexes. The simplest description is provided by the crystal-field theory [25,

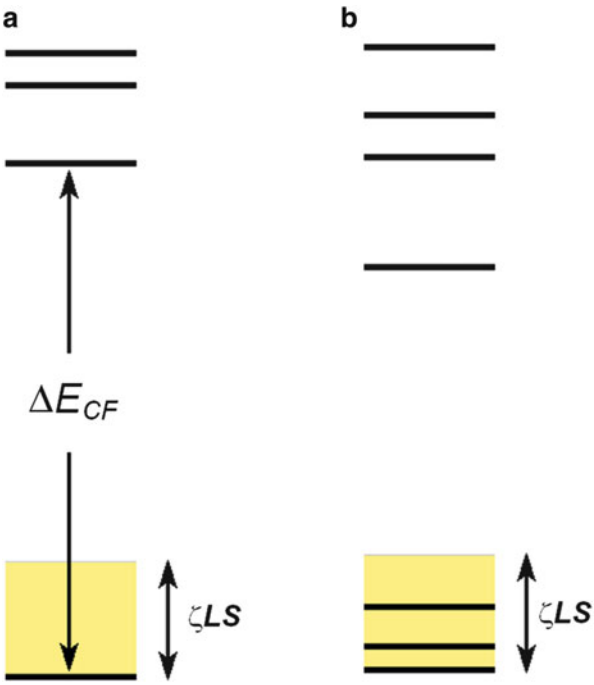

Fig. 4 Scheme of electronic energy levels of the complex in the case of (**a**) weak spin–orbit coupling effects and (**b**) strong spin–orbit coupling effects

39, 41, 75]. Thus, in the case of weak and intermediate crystal field, when the lowest terms of the complexes can be thought as arising from the ground atomic *LS* term of the corresponding metal ion, the spin–orbit coupling acquires a simple form:

$$\hat{H}_{\mathrm{so}}(LS) = \lambda \mathbf{L} \cdot \mathbf{S}, \quad \lambda = \pm\kappa\frac{\xi}{2S}, \tag{12}$$

where ζ is the spin–orbit coupling constant of the metal ion [25]; κ is the orbital reduction factor, taking into account the effect of metal–ligand covalency on the spin–orbit coupling [25, 76]; and λ is the projected spin–orbit coupling constant for a given spin S [25, 26, 76]. The two signs in the expression for λ correspond to less than half-filled and more than half-filled shell of magnetic electrons on the metal site, respectively. Perturbation theory applied to the operator (12) leads to spin Hamiltonians (6 and 11) with the following parameters:

$$\begin{aligned}&\mathbf{g} = g_e\mathbf{1} + \lambda\mathbf{\Lambda},\\ &\mathbf{D} = \lambda^2\mathbf{\Lambda},\\ &\Lambda_{\alpha\beta} = \sum_{\nu}\frac{\langle\Psi_{SM}|\hat{L}_\alpha|\Psi_{\nu SM}\rangle\langle\Psi_{\nu SM}|\hat{L}_\beta|\Psi_{SM}\rangle}{E_S - E_{\nu S}}, \quad \alpha,\beta = x,y,z\end{aligned} \tag{13}$$

where $\hat{L}_\alpha$, $\hat{L}_\beta$ are Cartesian components of the total orbital momentum, Ψ_{SM} and E_S are the wave function and energy of the ground term, while $\Psi_{\nu SM}$ and $E_{\nu S}$ – of the ν-th excited term of the same spin S. The fact that no terms of other spin admix in Eq. (13) is the consequence of the form (12) of the spin–orbit coupling, i.e., of the LS approximation [25]. A general spin–orbit coupling operator [26, 77] will admix also terms with $S' = S \pm 1$ [47, 78, 79].

By proper choice of the directions of coordinate axes (X, Y, Z), one can bring the tensors **g** and **D** to diagonal form. These coordinate systems define the *main magnetic* axes for **g** and the *main anisotropy* axes for **D**. The eigenvalues are called main values of the g tensor (g_X, g_Y, g_Z), or simply g factors, and main values of D tensor (D_X, D_Y, D_Z). Since the latter define the splitting of the S-multiplet, choosing the zero of energy in the center of gravity of the split levels makes **D** traceless, i.e., $D_X + D_Y + D_Z = 0$. Then the ZFS Hamiltonian, written in the coordinate system of main anisotropy axes, is defined by only two independent parameters:

$$\begin{aligned}&\hat{H}_{\mathrm{ZFS}} = D\left(\hat{S}_Z^2 - S(S+1)/3\right) + E\left(\hat{S}_X^2 - \hat{S}_Y^2\right),\\ &D = 3D_Z/2, \quad E = (D_X - D_Y)/2.\end{aligned} \tag{14}$$

D is the called parameter of axial magnetic anisotropy because it defines the ZFS splitting of S in complexes with axial symmetry (possessing main rotational axis of order higher than two, e.g., C_3 or S_4); E is the parameter of rhombic magnetic anisotropy because it is nonzero only in non-axial low-symmetry groups, e.g., D_2.

In the crystal-field approximation, both **g** and **D** tensors are expressed via a common tensor $\mathbf{\Lambda}$. Therefore, the main axes of these tensors coincide for any symmetry of the complex since in both cases they are the main axes of the tensor $\mathbf{\Lambda}$ ($\mathbf{1}$ in Eq. (13) is a unity matrix). This is an artifact of the simplified description of spin–orbit coupling (12), having a perfect spherical symmetry, i.e., being unrelated to the actual symmetry of the complex. Derivations based on true wave functions of the electronic terms and realistic spin–orbit coupling give "quantum chemistry" expressions for **g** and **D** which are free of this drawback [40, 47, 79]. As an example, Fig. 5 shows the main magnetic and main anisotropy axes of a Ni(II) complex [80] obtained with SINGLE_ANISO module on the basis of CASSCF/CASPT2 /RASSI-SO calculations [21]. We can see that despite the fact that this complex is in a weak spin–orbit coupling regime, the direction of its main magnetic and main anisotropy axes differs significantly. Note that the two sets of axes will coincide in complexes with symmetry not lower than orthorhombic [25, 40].

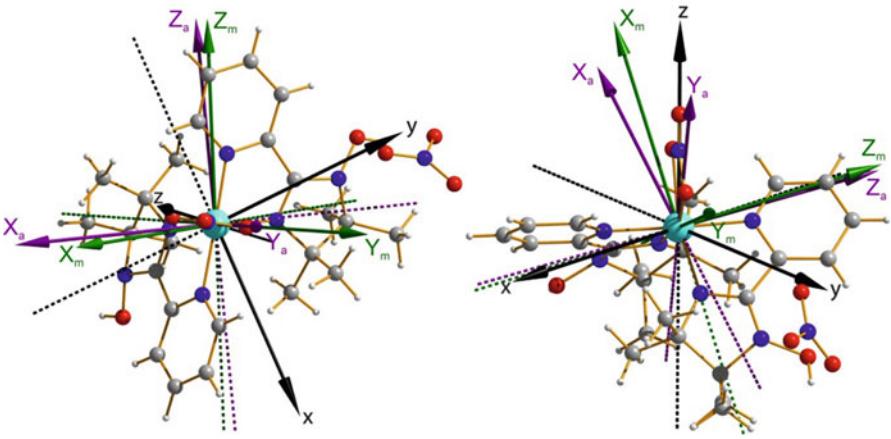

Fig. 5 Molecular structure of the Ni(II) complex. Orientation of the main magnetic axes (X_m, Y_m, Z_m) (*green arrows*) and the main anisotropy axes (X_a, Y_a, Z_a) (*purple arrows*) calculated ab initio. *Color scheme*: turquoise Ni, red O, blue N, gray C, white H. Reprinted with permission from Chibotaru and Ungur [21]. Copyright 2012 AIP Publishing LLC

3.2 Strong Spin–Orbit Coupling Effects

This is the case of complexes containing lanthanides (except Gd^{3+}), actinides, most of 4d and 5d, and some of 3d transition metals (e.g., Co^{2+}, Fe^{2+}, etc. in some geometries). In these complexes, the low-lying terms are often closely spaced, so that their spin–orbit mixing cannot be treated within the perturbation theory (Fig. 4b). As a result, the spin of the ground term cannot be considered as a good quantum number even approximately. Therefore, contrary to the case of weak spin–orbit coupling effects, the Zeeman and ZFS Hamiltonians cannot be expressed via ground term's spin but should be formulated instead via the pseudospin (see Sect. 2.5). The main difference from the spin description is that the pseudospin ($\widetilde{S}$) does not have the meaning of a physical angular momentum of the complex and its size is defined by the number N of low-lying multiplets involved in the model description ($2\widetilde{S} + 1 = N$).

The magnetic Hamiltonians expressed in terms of pseudospin operators formally look similar to spin Hamiltonians but contain much more terms and independent parameters. Thus the spin ZFS Hamiltonian (6 and 14) contains only bilinear terms in spin operators and five independent parameters (three angular parameters defining the main anisotropy axes, X_a, Y_a, and Z_a, and two ZFS parameters, E and D, in Eq. (14)). The spin Zeeman Hamiltonian contains only linear terms in S_α and six parameters (three angles defining the directions of main magnetic axes, X_m, Y_m, and Z_m, and three main values of the g tensor, g_X, g_Y, and g_Z). In the case of pseudospin description, these Hamiltonians keep their form (with $\hat{S}_\alpha$ replaced by $\hat{\widetilde{S}}_\alpha$) for $\widetilde{S} \leq 1$ in the case of Zeeman and for $\widetilde{S} \leq 3/2$ in the case of ZFS interaction, respectively

[21, 40]. For larger pseudospins, terms of higher order in $\hat{\tilde{S}}_\alpha$ should be added for full description of corresponding interactions. In order to construct possible independent (irreducible) combination of polynomials in $\hat{\tilde{S}}_\alpha$, the technique of irreducible tensor operators (ITO) is conveniently applied for the construction of pseudospin magnetic Hamiltonians [40]. It can be shown that independent combinations of polynomial terms of a rank l can be represented by $2l+1$ familiar spherical harmonics $Y_{lm}(\theta,\varphi)$, $m=-l,-l+1,\ldots l$, in which the spherical angular coordinates defining the direction of an electron in space, $\mathbf{r}/r$, are replaced by pseudospin unit vector $\hat{\tilde{\mathbf{S}}}/\tilde{S}$. These can be replaced by more simple expressions, the Stevens operators [25, 39, 81], $\hat{O}_{n,m}\left(\hat{\tilde{\mathbf{S}}}\right) \sim \hat{Y}_{n,m}\left(\hat{\tilde{\mathbf{S}}}/\tilde{S}\right)$, or their Hermitian combinations ($m>0$):

$$\hat{O}_n^m \sim \frac{1}{2}\left((-1)^m \hat{O}_{n,+m} + \hat{O}_{n,-m}\right), \quad \hat{\Omega}_n^m \sim \frac{i}{2}\left(\hat{O}_{n,-m} - (-1)^m \hat{O}_{n,m}\right) \tag{15}$$

Since the operator of magnetic moment, $\hat{\boldsymbol{\mu}}$, defining the Zeeman interaction, $\hat{H}_{\text{Zee}} = -\hat{\boldsymbol{\mu}}\cdot\mathbf{H}$, is a time-odd operator, which changes its sign under time inversion [25], its ITO decomposition will involve only irreducible operators of odd rank:

$$\hat{\boldsymbol{\mu}}=\hat{\boldsymbol{\mu}}^{\mathbf{1}}+\hat{\boldsymbol{\mu}}^{\mathbf{3}}+\hat{\boldsymbol{\mu}}^{\mathbf{5}}+\ldots, \quad \hat{\mu}_\alpha^n = \sum_{m=0}^{n}\left(b_{nm}^\alpha \hat{O}_n^m + c_{nm}^\alpha \hat{\Omega}_n^m\right), \quad \alpha = x,y,z \tag{16}$$

On the other hand, the ZFS Hamiltonian is a time-even operator; therefore, it will contain only even-rank irreducible tensors in its decomposition:

$$\hat{H}_{\text{ZFS}} = \hat{H}_{\text{ZFS}}^2 + \hat{H}_{\text{ZFS}}^4 + H_{\text{ZFS}}^6 + \cdots + \hat{H}_{ZFS}^n = \sum_{m=0}^{n}\left(e_{nm}^\alpha \hat{O}_n^m + f_{nm}^\alpha \hat{\Omega}_n^m\right) \tag{17}$$

The highest rank of ITO entering the decomposition of Eqs. (16) and (17) is defined by the condition $n_{\max} \le 2\tilde{S}$, which gives structure of Zeeman and ZFS Hamiltonians as function of the size of pseudospin $\tilde{S}$ shown in Table 2. We can see that the number of independent parameters describing the Zeeman interaction (b_{nm}^α and c_{nm}^α in Eq. (16)) and the ZFS interaction (e_{nm}^α and f_{nm}^α in Eq. (17)) increases quickly with the size of pseudospin in the case of low-symmetry complexes. However, in high-symmetry complexes, their number can be strongly reduced. For example, the Zeeman Hamiltonian for pseudospin $\tilde{S}=3/2$ will include in a general case 6 parameters in the first-rank part and 21 parameters in the third-rank part (see Table 2), while only one parameter for contributions of each rank in the case of cubic symmetry of the complex [25, 40].

A useful tool for theoretical investigation of magnetic anisotropy, especially in lanthanide complexes, is the crystal-field analysis of the lowest multiplets [18, 19,

Table 2 ITO decomposition of Zeeman and ZFS pseudospin Hamiltonians

$\widetilde{S}$	$\hat{H}_{\text{Zee}} = -\hat{\boldsymbol{\mu}} \cdot \mathbf{H}$	$\hat{H}_{\text{ZFS}}$
1/2	$\hat{\boldsymbol{\mu}}^1$	–
1	$\hat{\boldsymbol{\mu}}^1$	$\hat{H}^2_{\text{ZFS}}$
3/2	$\hat{\boldsymbol{\mu}}^1 + \hat{\boldsymbol{\mu}}^3$	$\hat{H}^2_{ZFS}$
2	$\hat{\boldsymbol{\mu}}^1 + \hat{\boldsymbol{\mu}}^3$	$\hat{H}^2_{\text{ZFS}} + \hat{H}^4_{\text{ZFS}}$
5/2	$\hat{\boldsymbol{\mu}}^1 + \hat{\boldsymbol{\mu}}^3 + \hat{\boldsymbol{\mu}}^5$	$\hat{H}^2_{\text{ZFS}} + \hat{H}^4_{\text{ZFS}}$
3	$\hat{\boldsymbol{\mu}}^1 + \hat{\boldsymbol{\mu}}^3 + \hat{\boldsymbol{\mu}}^5$	$\hat{H}^2_{\text{ZFS}} + \hat{H}^4_{\text{ZFS}} + \hat{H}^6_{\text{ZFS}}$
7/2	$\hat{\boldsymbol{\mu}}^1 + \hat{\boldsymbol{\mu}}^3 + \hat{\boldsymbol{\mu}}^5 + \hat{\boldsymbol{\mu}}^7$	$\hat{H}^2_{\text{ZFS}} + \hat{H}^4_{\text{ZFS}} + \hat{H}^6_{\text{ZFS}}$
4	$\hat{\boldsymbol{\mu}}^1 + \hat{\boldsymbol{\mu}}^3 + \hat{\boldsymbol{\mu}}^5 + \hat{\boldsymbol{\mu}}^7$	$\hat{H}^2_{\text{ZFS}} + \hat{H}^4_{\text{ZFS}} + \hat{H}^6_{\text{ZFS}} + \hat{H}^8_{\text{ZFS}}$

74]. This theory describes the splitting of an *nl* shell of the metal ions in the field of surrounding ligands' atoms. Given the spherical symmetry of the $|nlm\rangle$ orbitals on the metal ion, the expansion of crystal-field potential in spherical harmonics $Y_{km}(\theta,\varphi)$, $m = -k,-k+1,\ldots k$, will involve only terms with even $k \leq 2l$, which in the case of lanthanides and actinides ($l = 3$) reduce to $k = 2, 4, 6$ [25]. For the description of magnetic properties of lanthanide complexes, including its anisotropy, it is sufficient to describe the crystal-field splitting of the ground atomic *J*-multiplet of the corresponding Ln^{3+} ion. This is achieved by the projection of electronic operators $Y_{km}(\theta,\varphi)$ onto the ITO $\hat{O}_{k,m}(\hat{\mathbf{J}})$ and their Hermitian combinations (15), where $\hat{\mathbf{J}} = (\hat{J}_x, \hat{J}_y, \hat{J}_z)$ is the operator of total angular momentum. Thus the crystal-field Hamiltonian acting in the space of $2J+1$ wave functions ($|JM\rangle$) of the ground atomic *J*-multiplet has the form [25]:

$$\hat{H}^{J}_{\text{CF}} = \sum_{n=2,4,6} \left(\sum_{m=0}^{n} B^{c}_{nm} \hat{O}^{m}_{n} + \sum_{m=1}^{n} B^{s}_{nm} \hat{\Omega}^{m}_{n} \right) \tag{18}$$

Such projected Hamiltonian is less justified in the case of actinides, where important mixing of excited terms takes place due to a much stronger metal–ligand covalency than in lanthanide complexes.

In the absence of point group symmetry, which is a typical situation in lanthanides, the Hamiltonian (18) involves 27 independent parameters, whose correct determination poses the main problem in the application of crystal-field theory to lanthanides. The traditional approach to crystal-field description is based on the extraction of these parameters from available experiments. This approach becomes feasible when the number of crystal-field parameters is reduced due to a high symmetry of the complex [18, 19, 82]. For example, in the case of complexes with square-antiprism geometry, such as $[LnPh_2]^-$ with Pc = phthalocyanine [18] (Fig. 6a) and polyoxometalates [19], having a D_{4d} symmetry in the absence of distortions (ideal geometry), only the parameters B^c_{20}, B^c_{40}, and B^c_{60} enter Eq. (18) and can be determined from magnetic data. Recently, an ab initio methodology of calculation of crystal-field parameters for lanthanides has been proposed [84, 85] and implemented [83] in the module SINGLE_ANISO of MOLCAS package [62]. As an example, Fig. 6 shows the ab initio calculated magnetic susceptibility

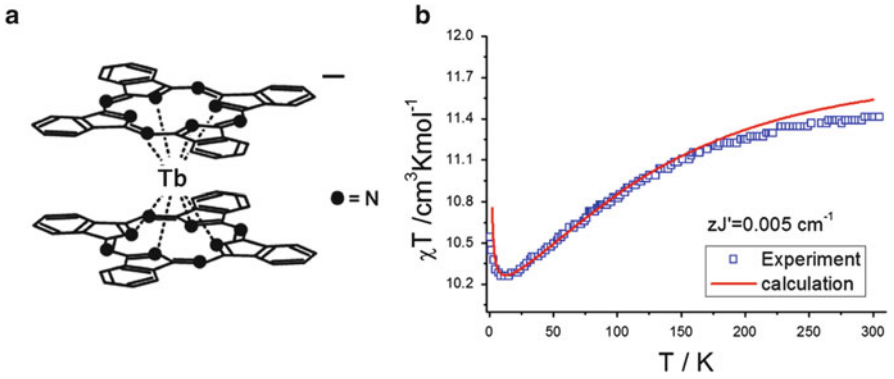

Fig. 6 Atomic structure of the $[Tb(Pc)_2]^-$ complex (**a**) and the temperature dependence of magnetic susceptibility multiplied by temperature (**b**). Experimental points are taken from Ishikawa et al. [18] and the line corresponds to ab initio calculations [83]. The bending up of the curve at $T < 10$ K is due to ferromagnetic intermolecular coupling which was simulated with effective exchange parameter zJ'

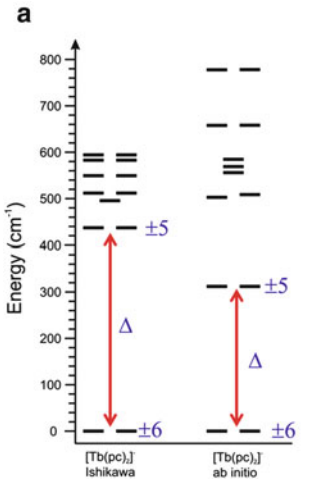

b

n	m	Real geometry B^c_{nm}	Real geometry B^s_{nm}	Ideal geometry B^c_{nm}	Ideal geometry B^s_{nm}	Ishikawa [18] B^c_{nm}	Ishikawa [18] B^s_{nm}
2	0	566	–	574	–	414	–
	1	90	−58				
	2	19	−317				
4	0	−102	–	−116	–	−228	–
	1	49	−33				
	2	3	−54				
	3	1	−5				
	4	−17	−5			10	–
6	0	−18	–	−20	–	33	–
	1	3	−4				
	2	−1	−21				
	3	1	0				
	4	−5	−4				
	5	−5	−3				
	6	14	−18				

Fig. 7 Crystal-field spectrum of the $[Tb(Pc)_2]^-$ complex. (**a**) Phenomenological crystal field [18] (*left*) versus ab initio (*right*) [83] calculations. *Red arrows* show the lowest excitation in the spectrum which was extracted in experiment as $\Delta = 260$ cm^{-1} [18]. (**b**) Crystal-field parameters (cm^{-1}) calculated ab initio for the real [18] and ideal D_{4d} geometry of the complex [83] and extracted from fitting of experimental data by Ishikawa et al. [18] (Color figure online)

of $[LnPh_2]^-$ complex, while Fig. 7 shows the corresponding spectrum of lowest multiplets and the calculated crystal-field parameters [83]. We can notice that although the real geometry of the complex deviates from the ideal one only slightly, many non-axial crystal-field parameters become important.

3.3 Axiality and Magnetization Blocking

The *axiality* of spin–orbit multiplets of magnetic complexes characterizes the difference of magnetic properties along the main magnetic/anisotropy axes in these multiplets [86]. Strong axiality is achieved when the magnetism along one of these axes (principal axis Z) differs significantly from the other two (transversal axes X, Y). Strongly axial multiplets always appear as spin–orbit *doublets*. In complexes with odd numbers of electrons, these are simply Kramers doublets, whose degeneracy in the absence of applied magnetic field is guaranteed by the Kramers theorem [25]. The axiality of a Kramers doublet is measured by the ratio of the principal g factor, g_Z, which exceeds the transversal g factors, g_X and g_Y. The highest possible (perfect) axiality corresponds to vanishing values of two transverse g factors, $g_X = g_Y = 0$. This situation is realized in the case of pure axial crystal field, containing in Eq. (18) only terms $\sim B^c_{n0}$, where $n = 2, 4, 6$ in the case of lanthanides and actinides and $n = 2, 4$ in the case of transition metal complexes [25]. In this case, the Kramers doublets are characterized by definite projections M of the total angular momentum J on the axis Z (we take a lanthanide as an example). The corresponding wave functions are $|JM\rangle$ and $|J-M\rangle$, i.e., are described by equal projections of opposite sign which is a requirement imposed by time reversal symmetry [25]. As explained in Sect. 2.3, the angular momentum eigenfunctions $|JM_1\rangle$ and $|JM_2\rangle$ with the difference $|M_1 - M_2| > 1$ will have zero matrix elements of angular momentum projection operators, $\langle JM_1|\hat{J}_\alpha|JM_2\rangle = 0$. This means that the Kramers doublets $|J \pm M\rangle$ for $M > 1$ will have zero matrix elements from transverse components of the angular momentum resulting in $g_X = g_Y = 0$, i.e., will be characterized by a perfect axiality. As an example, Fig. 8 shows the ab initio calculated [86] spectrum of low-lying Kramers doublets in the axial diatomic complex $[DyO]^+$. The crystal field in this complex stabilizes the Kramers doublets with large values of M, the main contribution in (18) coming from the term $B^c_{20}[3\hat{J}_Z^2 - J(J+1)]$, where $J = 15/2$. This term is equivalent to the axial ZFS term for S-complexes, Eq. (14), where $S, \hat{S_Z}$ are to be replaced by $J, \hat{J_Z}$. However, in the present case, we have also non-negligible contributions from crystal-field terms $\sim B^c_{40}$ and B^c_{60}, containing even powers of $\hat{J_Z}$ up to fourth and sixth order, respectively. In the case of complexes with even number of electrons, the multiplets in strongly axial crystal fields form Ising doublets. An example of the latter are the crystal-field eigenstates $|2 \pm 1\rangle$ and $|2 \pm 2\rangle$ in Fig. 2. A perfect axiality in these complexes corresponds to zero energy gap (tunneling gap) between the components of the doublet. This is particularly the case of the Ising doublets shown in Fig. 2.

Strong axiality of the ground doublet is the necessary condition for the observation of magnetization blocking (SMM behavior) in a complex. Indeed, the smallest rate of reversal of magnetization (magnetization relaxation rate) is achieved at low temperature, when only the ground doublet state is populated. In this case, relaxation of magnetization takes place via the tunneling of magnetic moment into the opposite direction, $M \leftrightarrows -M$ [3]. In the case of Kramers doublets, the tunneling splitting (Δ_{tun}) can arise only due to Zeeman interaction of transversal

a

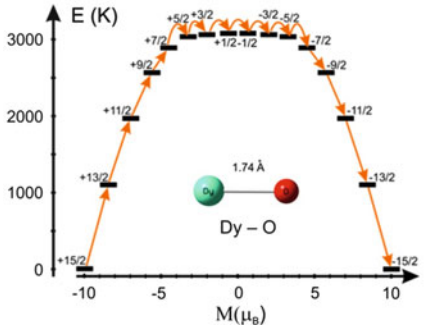

b

KD	$\|M_J\|$	E (cm^{-1})	$g_{\|\|}$	$g(Dy^{3+})$
1	15/2	0.0	19.908	20.000
2	13/2	767.2	16.869	17.333
3	11/2	1371.5	14.100	14.667
4	9/2	1783.5	11.541	12.000
5	7/2	2013.0	9.064	9.333
6	5/2	2108.8	6.562	6.667
7	1/2	2132.1	1.337	1.333
8	3/2	2132.5	3.984	4.000

Fig. 8 Splitting of the ground atomic multiplet $J = 15/2$ in the $[DyO]^+$ complex in equilibrium geometry revealed by ab initio calculations. (**a**) Individual states of the Kramers doublets (KD) arranged according to their magnetic moment projection on the main symmetry axis of the complex (Dy–O bond). The *arrows* show the relaxation paths outlining the activation barrier for reversal of magnetization. (**b**) The energies' main g factors for the $[DyO]^+$ complex (third and fourth column) and main g factors for an isolated Dy^{3+} ion (last column). Reproduced from Ungur and Chibotaru [86] with permission from the PCCP Owner Societies

magnetic moments with external magnetic field (from surrounding nuclear spins and other magnetic complexes), $\Delta_{\text{tun}} = \mu_B \left(g_X \hat{\tilde{s}}_X H_X + g_Y \hat{\tilde{s}}_Y H_Y \right)$, where $\hat{\tilde{s}}_X$ and $\hat{\tilde{s}}_Y$ are operators of transversal components of pseudospin $\tilde{s} = 1/2$ corresponding to the ground Kramers doublet ($2\tilde{s} + 1 = 2$). Strong axiality is characterized by vanishing values of g_X and g_Y and, therefore, $\Delta_{\text{tun}} \approx 0$, which leads to the quenching of quantum tunneling of magnetization in the ground doublet. At higher temperature, the spin–lattice relaxation via excited Kramers doublets becomes possible (see Sect. 2.3); however, this will not proceed via the tunneling of magnetization in the excited doublets if they are strongly axial too. In this case, the relaxation process will go via consecutive transition between $|JM\rangle$ states with close values of magnetic moment projection M thus outlining an activation barrier of reversal of magnetization. An example of such a situation is shown in Fig. 8 for the $[DyO]^+$ complex. In the case of Ising doublets, realized in complexes with even number of electrons, Δ_{tun} is an intrinsic gap, always present if the symmetry is not high enough. High axiality of the complex means in this case disappearance of this tunneling gap, i.e., again the quenching of quantum tunneling of magnetization.

3.4 SIM: Role of Symmetry and Hybridization

Single-ion magnets (SIM) are complexes containing one single anisotropic metal ion and exhibiting blocking of magnetization. At variance to $[DyO]^+$ considered above, the complexes studied to date have nonlinear geometry. Therefore, the

crystal-field eigenstates are usually not characterized by definite projections of angular momentum (M). Nevertheless, if the complex possesses a symmetry belonging to an axial point group (containing a main symmetry axis of order higher than two), then the corresponding doublets can be perfectly axial if they belong to special irreducible representations [86]. This is particularly the case of the first synthesized SIM, the double-decker phthalocyanine complex $[Tb(Pc)_2]^-$ [18], having the symmetry close to D_{4d} with the main symmetry axis of order eight directed perpendicularly to the plane of two phthalocyanines (Fig. 6a). The complexes in crystals, especially the lanthanides, rarely have a geometry corresponding to an ideal symmetry but exhibit small deformations from the latter. A crucial issue for magnetization blocking is the influence of these deformations on the axiality of low-lying doublets. Lucky examples are the complexes of late lanthanide series (Tb^{3+}, Dy^{3+}, Ho^{3+}, Er^{3+}) which exhibit high axiality of the ground doublet and blocking of magnetization for practically any geometry of surrounding ligand atoms [86]. This is explained by two basic reasons:

1. In lanthanides, there is often a direction along which the axial components of the crystal field, the $B^c_{20}, B^c_{40}, B^c_{60}$ ones in Eq. (18), are predominant. This can be due to a stronger chemical bonding of Ln with one of the ligand atoms [87] or with an entire ligand group. In the last case, the main magnetic/anisotropy axis will be directed toward the center of the ligand group as, e.g., in $[Ln(Ph)_2]^-$ (Fig. 6) and $[Ln^{III}(COT)_2]^-$ (Fig. 9). The axial part of the ligand field will stabilize the corresponding doublet state $|J \pm M\rangle$ (Sect. 3.3), which will be further intermixed by weaker low-symmetry terms in (18). The coefficients of admixture of other states are proportional to the ratio of corresponding matrix elements of low-symmetry crystal field to the energy separation of the admixed $|J \pm M\rangle$ states. In the case of dominant axial crystal field, these coefficients are small.
2. The value of the opened gap in Ising doublets or of induced transversal g factors in Kramers doublets by low-symmetry components of the crystal field depends crucially on the size of magnetic moment M in the corresponding doublet state $|J \pm M\rangle$. Indeed, a larger value of M will require a higher order of perturbation theory with respect to low-symmetry crystal-field components in order to achieve these deviations from the perfect axiality. For example, the first reported SIM complex $[Tb(Pc)_2]^-$ in ideal D_{4d} symmetry has the ground Ising doublet $|6 \pm 6\rangle$ [18], which is perfectly axial on symmetry grounds [86]. The low-symmetry components of the second rank, the terms $\sim B^c_{2m}, B^s_{2m}$, $m \neq 0$ in (18), will connect the wave functions $|6, 6\rangle$ and $|6, -6\rangle$, i.e., will open the tunneling gap, in an order of perturbation theory not lower than six. This means that the value of Δ_{tun} will be very small even for non-negligible components of low-symmetry crystal field. This is indeed confirmed by experiment, which shows a tunneling gap of $\sim 10^{-6}$ cm^{-1} for this complex [89]. Large values of J arise in the ground atomic multiplets of the late lanthanide series (Ln > Gd). In these Ln ions, the ground-state multiplets are "inverted" [26], i.e., the spin and orbital momenta are coupled parallel to each other, $J = L + S$. On the contrary, in the ions from earlier lanthanide series (Ln < Gd), the ground-state multiplets are

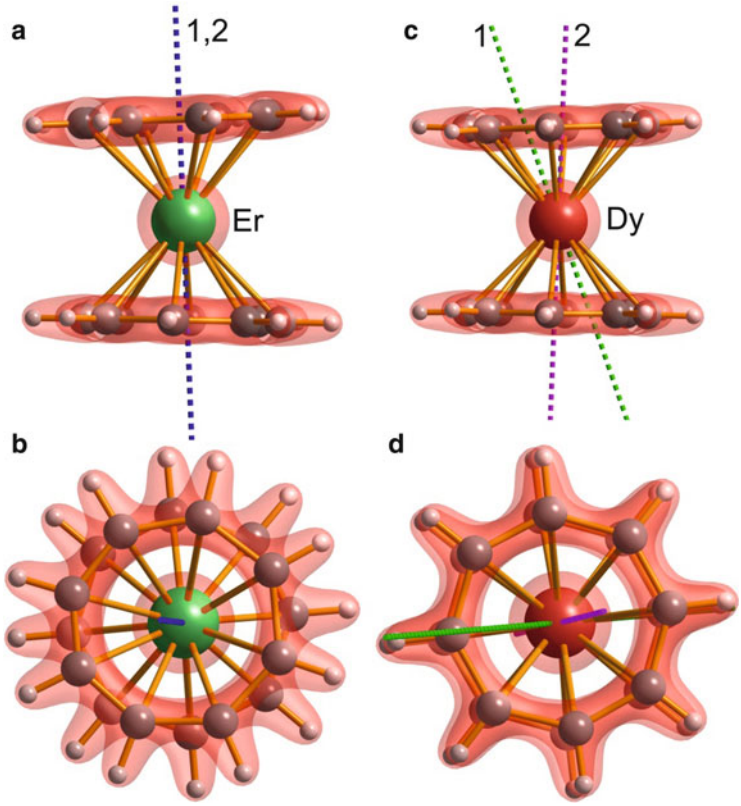

Fig. 9 Molecular structure of $[Ln^{III}(COT)_2]^-$ magnetic anions. (**a**) Side and (**b**) top view for Ln=Er; (**c**) side and (**d**) top view for Ln=Dy. Coordinated to one of the COT rings $[K(18\text{-crown-}6)]^+$ cation is not shown for clarity. *Color scheme*: Er green, Dy red, C gray, H white. Structural details: distance between centers of COT rings: 3.74 Å (Er); 3.81 Å (Dy); mean angle between COT planes: 3.5° (Er) and 2.8° (Dy). *Transparent red surface* shows the calculated electronic density in the ground state. Note the higher rotational symmetry of the electronic cloud close to the Ln ion than expected from an octagonal group. *Dashed lines* show the calculated orientation of the main magnetic axis on Ln ions in the ground (1) and first excited (2) Kramers doublet. For Er: $g_{X,Y} = 3.5 \times 10^{-6}$, $g_Z = 17.96$ for the ground doublet and $g_{X,Y} = 5.4 \times 10^{-4}$, $g_Z = 15.53$ for the first excited doublet; the angle between corresponding g_Z axes is ~1.0°. For Dy: $g_{X,Y} = 1.6 \times 10^{-1}$; $g_Z = 12.64$ for the ground doublet (*green dashed line*) and $g_{X,Y} = 5.8 \times 10^{-2}$; $g_Z = 13.84$ for the first excited doublet (*purple dashed line*); the angle between corresponding g_Z axes is ~21°. Reproduced with permission from Ungur et al. [88]. Copyright 2014 John Wiley & Sons, Inc

"normal," i.e., the spin and orbital momenta are coupled antiparallel to each other, $J = |L - S|$. The smaller ground-state momenta are the reason why the corresponding complexes are not efficient SIMs as a rule.

The exceptional ability of lanthanides to possess large J is entirely due to the weak crystal-field regime, always realized in lanthanide complexes. In this regime, the crystal-field splitting of the ground atomic J-multiplet (of the order of several

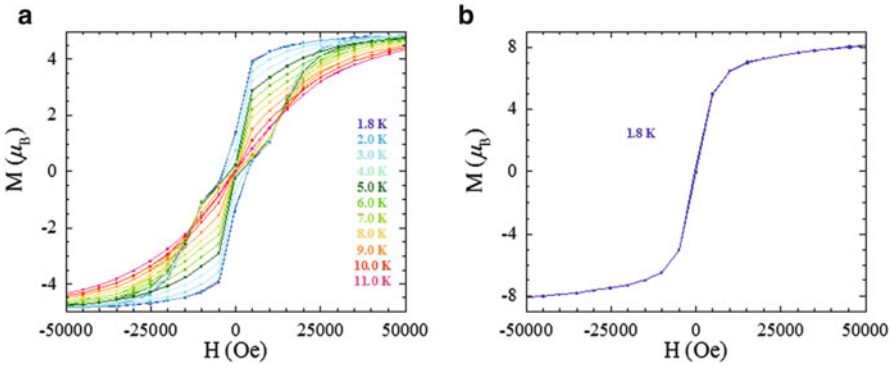

Fig. 10 Magnetization hysteresis loops for $[Ln(COT)_2]^-$ complexes. (**a**) M(H) for $[Er(COT)_2]^-$ measured on a SQUID array at 35 Oe/s sweep rate and at indicated temperatures. At $T = 2$ K the coercivity (distance between M(H) points at $M = 0$) is ca. 8,000 Oe. (**b**) Equivalent measurement for $[Dy(COT)_2]^-$ at 1.8 K. Reproduced with permission from Ungur et al. [88]. Copyright 2014 John Wiley & Sons, Inc

hundred wavenumbers) is much smaller than the Hund rule coupling stabilizing the maximal total spin S in the ground term of a given f^n configuration and is also much smaller than the spin–orbit coupling within the f shell leading to unquenched total orbital momentum L and to its coupling with S into the total angular momentum J. However, to show SIM behavior, the complex should possess a doublet with preponderant $|J \pm M\rangle$ component with large M as discussed above. Whether the crystal field stabilizing the component with largest possible M should be axial or equatorial depends entirely on the character of 4f-shell electron distribution in a given Ln [90]. If this distribution is oblate with respect to quantization axis (Z), then the state with largest projection of the total moment is stabilized by an axial crystal field. An example of such a situation is depicted in Fig. 8a, where the ground Kramers doublet of Dy^{3+} in the field of a single oxygen ion is obtained as $|15/2 \pm 15/2\rangle$. On the contrary, in the case of prolate distribution of 4f electrons, like in Er^{3+}, the state with maximal M is stabilized by equatorial crystal field [90].

As an illustration of above principles, consider the recently investigated complexes $[Ln^{III}(COT)_2]^-$ with Ln = Er,Dy and COT = cyclooctatetraene (Fig. 9) [88]. The erbium compound is the first SIM showing large coercivity (Fig. 10), which further increases through dilution with Y [91], approaching in efficiency of magnetization blocking the best polynuclear SMMs [3]. At the same time, the isostructural dysprosium complex is a much weaker SIM, showing negligible hysteresis loops (Fig. 10). The spectrum of calculated low-lying Kramers doublets in the two complexes is shown in Fig. 11. The ground state of Er compound corresponds to $M = \pm 15/2$, which testifies about preponderant equatorial component of the crystal field. The small distortions of the structure from ideal D_{8d} geometry and relatively large energy of the first excited Kramers doublet (Fig. 11) make the admixture of components different from $M = \pm 15/2$ in the ground state very small (weight $<10^{-4}$) [88], which explains exceptional blocking

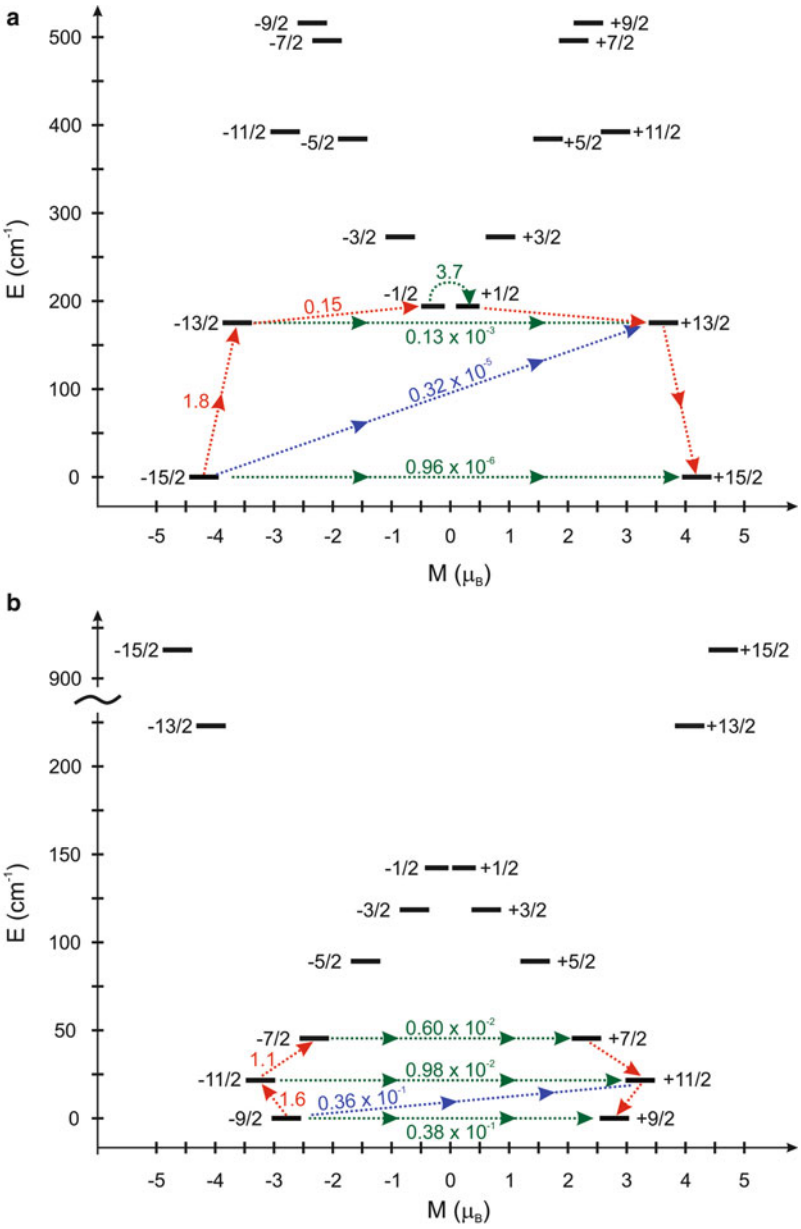

Fig. 11 Ab initio calculated multiplet spectrum and the magnetization blocking barriers in Er (**a**) and Dy (**b**) compounds from Fig. 10]. The *thick black lines* represent the KDs as a function of their magnetic moment along the axis connecting the centers of COT rings. The *green dashed lines* correspond to diagonal quantum tunneling of magnetization (QTM); the *blue dashed lines* represent possible Orbach relaxation processes. The numbers at each *arrow* stand for the mean absolute value of the corresponding matrix element of transition magnetic moment $((|\mu_X| + |\mu_Y| + |\mu_Z|)/3)$. The path shown by the *red arrows* represents the most probable path for magnetic relaxation in the corresponding compounds. Reproduced with permission from Ungur et al. [88]. Copyright 2014 John Wiley & Sons, Inc

property of the complex at low temperatures. On the same reason, the first excited state is also very axial and has the main magnetic axis almost parallel to the ground state (Fig. 9), which raises the activation barrier for magnetic relaxation till the second excited state (Fig. 11). In the dysprosium complex, the signs of the main crystal-field parameters, B^c_{20} and B^c_{40}, are opposite to the dysprosium complex (due to the opposite signs of the corresponding Stevens parameters α and β for $J = 15/2$ in Dy^{3+} and Er^{3+} ions [25]), which leads to an almost reversed crystal-field spectrum in $[Dy(COT)_2]^-$ compared to $[Er(COT)_2]^-$ (Fig. 11). We can see that the ground state of the dysprosium complex is preponderantly of $\pm 9/2$ type and is separated by small gaps with excited Kramers doublets (Fig. 11b). As a result, the weight of admixed other states, with $M \neq \pm 9/2$, amounts to 4.5%, reducing strongly the axiality of the ground Kramers doublet of this complex with respect to $[Er(COT)_2]^-$, making it a weak SIM (Fig. 10b).

In contrast to lanthanide complexes, the transition metal and actinide complexes are in intermediate and strong crystal-field regimes. Therefore, their low-lying states are not characterized by large angular momenta. As a result, the corresponding complexes usually show SIM behavior when their geometry is close to a high-symmetry axial point group. As an example, the actinide complex $[Np^{IV}(COT)_2]$, being isostructural to $[Er(COT)_2]^-$ and having the D_{8h} geometry, is a much weaker SIM compared to the latter [92]. Blocking behavior was observed in pentavalent [93] and trivalent [94, 95] uranium complexes but with significantly shorter relaxation times and lower heights of activation barriers compared to most lanthanide-based SIMs. Mononuclear transition metal complexes also can exhibit magnetization blocking; that was demonstrated for the first time on Fe (II) complexes [96]. However, a stronger crystal field in these complexes compared to actinides puts rigorous demands for an ideal axial geometry which would provide unquenched orbital moment on the transition metal ion. This was achieved in bivalent iron complexes with a perfect C_{3v} [96] and D_{3d} [97] symmetry. Although the latter complex shows a relaxation barrier exceeding 200 cm^{-1}, no magnetic remanence was observed in the hysteresis loops [97], in contrast to lanthanide complexes (Fig. 11a). Even stronger crystal fields are achieved in 4d and 5d transition metal complexes, for which no compounds exhibiting SIM behavior have been yet reported. However, high-symmetry fragments of these metal ions were used as building blocks for the design of polynuclear SMMs (see the next section). Although these blocks still look as high-symmetry units in some polynuclear complexes, especially those built by cyanide bridges [98, 99], the real symmetry of the crystal field on the corresponding transition metal ions is much lower than the geometry of nearest neighbor ligand atoms might suggest. The reason is the strong metal–ligand covalency present in such transition metal fragments, which hybridize efficiently the 4d/5d orbitals of the metal with the orbitals of distant ligand atoms, thus imposing the low crystal-field symmetry matching the low site symmetry of the metal ion in the entire complex. An example of such situation is the heptacyanomolybdate building block in a cyano-bridged magnetic network, for which the calculated crystal-field spectrum within the reduced

structural model in Fig. 3c [65] might not be exactly in view of strong hybridization with more distant atoms of the network. In this respect, lanthanides occupy an exceptional place, since their 4f orbitals have a much weaker hybridization with surrounding ligand orbitals.

4 Polynuclear Compounds

The anisotropic magnetic properties of polynuclear complexes are characterized by the interplay of ionic anisotropy on the individual metal sites and the anisotropic exchange interaction between different pairs of metal ions. The model description of complexes with strongly anisotropic metal sites can involve a large number of parameters thus complicating their extraction from experiment.

4.1 Complexes in Strong Exchange Limit

In function of the relative strength of ionic anisotropy on the metal sites and of the exchange interactions, the polynuclear complexes belong to one of the two groups. The first one corresponds to the case of weak ZFS on the metal sites compared to the spread of exchange spectrum. This is the case of strong exchange limit [7], involving most of transition metal complexes, which will be reviewed here. As was discussed in Sect. 3, the situation of weak ZFS, Eqs. (6 and 13), is achieved in the case when the crystal-field splitting of the lowest states exceeds considerably the strength of spin–orbit interaction (Fig. 4a). In this case, the exchange interaction between arbitrary metal sites is described by the generic exchange Hamiltonian (10). In this Hamiltonian, the isotropic exchange part is by far the main term, while the antisymmetric and the symmetric anisotropic contributions depend on the extent of spin–orbit admixture of excited terms on the metal sites [27] and are, therefore, much smaller. In many complexes of this limit, the exchange multiplets arising from isotropic Heisenberg interaction (9), and characterized by the total spin S of the complex, are separated by energy gaps exceeding the anisotropic contributions to the exchange interaction (last two terms in (10)) and the ZFS on the metal sites. Then the spectrum of spin–orbit multiplets of such complexes merely corresponds to the splitting of isotropic exchange terms S by anisotropic contributions (Fig. 12). This splitting is described in a good approximation by the ZFS Hamiltonian, Eq. (14), in which the spin projection operators refer to the ground exchange term S of the complex [1, 3]. An example of spectrum of multiplets resulting from the ZFS splitting of ground exchange term is shown in Fig. 12 for the complex $[Fe_8O_2(OH)_{12}(tacn)_6]^{8+}$, where tacn = 1,4,7-triazacyclononane [3, 100]. One of the distinctive features of complexes in strong exchange limit is an almost collinear arrangement of local magnetic moments on the metal sites in all multiplets. Figure 12a shows that the magnetic moments on the Fe(III) centers in the Fe_8

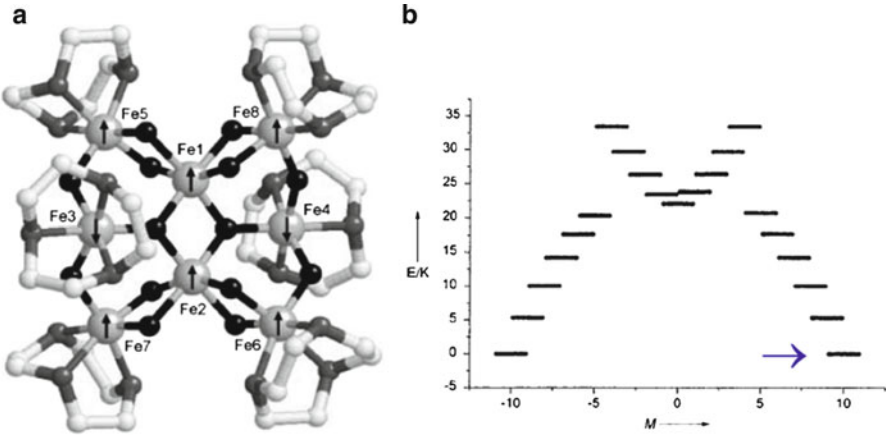

Fig. 12 Molecular structure of the Fe_8 complex [3] and the ordering of local magnetic moments on the Fe(III) sites in the ground exchange doublet (**a**). The structure of ZFS levels of the ground exchange term ($S = 10$) in function of their saturated magnetic moment along the main anisotropy axis of the complex (Z in Eq. (14))

complex are all aligned along the main anisotropy axis of the ground $S = 10$ term of that complex. This is the result of much stronger isotropic exchange interaction in this compound, stabilizing collinear arrangement of magnetic moments, compared to anisotropic contributions which might induce their non-collinear arrangement.

Magnetization blocking in complexes of strong exchange limit is determined entirely by the character of ZFS splitting of its ground exchange term. Best SMMs are obtained in the case when only the axial component of ZFS Hamiltonian for the S term, $D\hat{S}_Z^2$ in Eq. (14) is present, which is guaranteed if the polynuclear complex possesses an axial symmetry. This was precisely the case for the first discovered SMM, $[Mn_{12}O_{12}(CH_3COO)_{16}(H_2O)_4]$ (or Mn_{12}ac) [1–3], which possesses an S_4 symmetry axis. A second important feature is the negative sign of axial ZFS constant ($D < 0$) which ensures the stabilization of a doublet state with maximal spin projection on the anisotropy axis ($|10 \pm 10\rangle$ in the case of Mn_{12}ac) [3]. Since the axial ZFS provides a high degree of axiality of the ground and the low-lying spin–orbit doublets of the complex, the reversal of magnetization will proceed via relaxation steps involving multiplets with close values of spin (momentum) projection, as described in Sect. 2.3. In the case of very strong axiality of all doublets, this chain of relaxation transitions can accede the state with minimal spin projection ($M = 0$ for integer S and $M = \pm 1/2$ for half-integer S), which will be the highest in energy for $D < 0$. In this case, the reversal of magnetization between the states $|SS\rangle$ and $|S - S\rangle$ of the ground doublet will require overcoming of a barrier of a height equal to the ZFS splitting of the term S. The situation is similar to axial crystal-field splitting of atomic multiplet $J = 15/2$ of Dy^{3+} (Fig. 8a), where an almost parabolic barrier of reversal of magnetization was obtained due to a predominant negative second-rank component of the crystal field (see Sect. 3.3). In the present case, the amplitude of ZFS splitting of the term S depends on the way the individual ionic and

exchange anisotropic contributions are projected into the ZFS Hamiltonian of this term [7]. For example, in the case of ferromagnetic ground exchange term, the contribution of ZFS at individual metal ions to the negative D will be maximal when the local anisotropy parameters on the metal sites will be all negative ($D_i < 0$), while the corresponding local anisotropy axes (Z_i) will be all parallel to the main anisotropy axis of the complex. In the case of Mn_{12}ac, such contribution from ionic anisotropy to D, as well as to fourth- and sixth-rank ZFS tensors (which are operative for $S = 10$, see Table 2), is expected to be predominant [101]. We note that the Ising doublets $|10 \pm M\rangle$ in Mn_{12}ac are not ideally axial (Sect. 3.3) even in the case of an ideal D_{2d} geometry of the complex, then the fourth- and sixth-rank ZFS contributions and the interaction with transverse magnetic field can lead to small Δ_{tun} in these doublets [3]. However, the opening of the tunneling gaps occurs via several perturbation steps, their number being proportional to M. Therefore, the large value of S is necessary to have suppressed QTM in the low-lying multiplets. The tunneling splitting in the multiplets $|S \pm M\rangle$ increases quickly with the deviation of M from S, leading sometimes to the shortcutting of the relaxation path at some intermediate value $M_0 < M_{min}$, thus effectively reducing the height of blocking barrier from the highest possible value [30]. This is because in higher-lying exchange doublets, corresponding to $M < S$, the opening of the tunneling gap arises via a lesser number of perturbation steps than in the ground exchange doublet ($M = S$). On the other hand, the arguments based on perturbation theory and large ground-state spin explain why the low-lying doublets of Fe_8 complex ($S = 10$) [3] remain axial despite a relatively strong rhombic contribution ($|E/D| = 0.19$) to the ZFS interaction (14) [100]. This is also confirmed in Fig. 12b showing an almost parabolic momentum dependence of the energy of low-lying multiplets, similarly to Mn_{12}ac [3], suggesting predominant axial anisotropy for these levels.

4.2 Complexes in Weak Exchange Limit

When the spin–orbit coupling effects on the metal sites become stronger, i.e., the separation of the low-lying local terms becomes of the order or smaller than the spin–orbit energy (Fig. 4b), the magnetic interaction on the metal sites and the exchange interaction between them is described in terms of pseudospins (see Sect. 3.2). The reason why the total spin of the complex is not a good quantum number anymore is the strong mixing of several spin terms, which cannot be described via perturbation theory with respect to spin–orbit coupling. One of the consequences of this situation was a large number (compared to the case of weak spin–orbit coupling effects) of parameters of ZFS and Zeeman pseudospin Hamiltonians describing the magnetic interactions on individual magnetic centers, which a priori are of comparable order of magnitude. As the corresponding Eqs. (16) and (17) show, the number of independent parameters, equal to the number of allowed tensorial components, increases quickly with the size of pseudospin $\widetilde{S}$. The situation

becomes even more dramatic in the case of exchange interaction between two metal ions with strong spin–orbit coupling effects. Similarly to magnetic pseudospin Hamiltonians of individual metal sites, the exchange interaction will include a priori all allowed tensorial forms of two pseudospin operators. The only constraints imposed on these forms are (1) the overall odd tensorial ranks of all contributions to the exchange interaction, which is the consequence of invariance of the exchange Hamiltonian with respect to time inversion, and (2) the order of polynomials of pseudospin operators ($\hat{\tilde{S}}_\alpha$) should not exceed $2\tilde{S}$, which is the consequence of general property of spin and pseudospin operators. Then the general form (in the absence of symmetry) of exchange interaction between magnetic centers A and B, described by the pseudospins $\tilde{S}_A$ and $\tilde{S}_B$, respectively, is the following:

$$\hat{H}_{\text{ex}} = \sum_{k}^{\leq 2\tilde{S}_A} \sum_{p=0}^{k} \sum_{l}^{\leq 2\tilde{S}_B} \sum_{q=0}^{l} \left[J^{cc}_{kp,lq} \hat{O}^{\,p}_{k}\left(\tilde{\mathbf{S}}_A\right) \hat{O}^{\,q}_{l}\left(\tilde{\mathbf{S}}_B\right) + J^{cs}_{kp,lq} \hat{O}^{\,p}_{k}\left(\tilde{\mathbf{S}}_A\right) \hat{\Omega}^{\,q}_{l}\left(\tilde{\mathbf{S}}_B\right) + J^{sc}_{kp,lq} \hat{\Omega}^{\,p}_{k}\left(\tilde{\mathbf{S}}_A\right) \hat{O}^{\,q}_{l}\left(\tilde{\mathbf{S}}_B\right) + J^{ss}_{kp,lq} \hat{\Omega}^{\,p}_{k}\left(\tilde{\mathbf{S}}_A\right) \hat{\Omega}^{\,q}_{l}\left(\tilde{\mathbf{S}}_B\right) \right] \tag{19}$$

where the ranks of the ITOs in each term can be simultaneously odd, $k, l = 1, 3, \ldots$, or simultaneously even, $k, l = 2, 4, \ldots$ and $\Omega^0_k = \Omega^0_l = 0$. We can see that the number of independent parameters $J^{ab}_{kp,lq}$ in this exchange Hamiltonian can amount to many tens, even in the case of pseudospins of moderate size. On the contrary, the exchange interaction between metal ions with weak spin–orbit coupling effects, Eq. (10), involves one isotropic (J), three antisymmetric (Dzyaloshinsky–Morya vector $\mathbf{d}$), and five symmetric anisotropic ($D_{\alpha\beta}$ of zero trace) exchange parameters, i.e., nine independent parameters at most for any size of interacting spins. These contributions correspond to first-rank terms ($k = l = 1$) in Eq. (19).

In the case of very strong spin–orbit coupling effects, the ZFS on the metal sites exceeds the exchange interaction between them. The corresponding complexes belong to the so-called weak exchange limit [7]. This is the case of almost all lanthanide complexes (except Gd) and also actinides and transition metal complexes in special geometries allowing for orbital (quasi)degeneracy which leads to unquenched orbital momenta on the metal sites [102]. Hence the hierarchy of interactions is opposite to the case of complexes in strong exchange limit. Figure 13 shows the spectrum of low-lying exchange multiplets of a trinuclear Dy_3 complex. The levels denoted by Dy_1–Dy_3 in the left-hand side of Fig. 13b correspond to single crystal-field excitations on the corresponding Dy sites (Fig. 13a). The exchange interaction between metal centers broadens the crystal-field levels into bands (right-hand side of Fig. 13b). However, the width of these exchange bands is much smaller than the separation between the crystal-field levels. The latter usually amounts to several tens cm^{-1}, while the exchange splitting for a pair of two lanthanide ions is of the order of a few cm^{-1}. As a result, the spectrum of levels arising from exchange interaction of ground multiplets on Ln sites is well separated

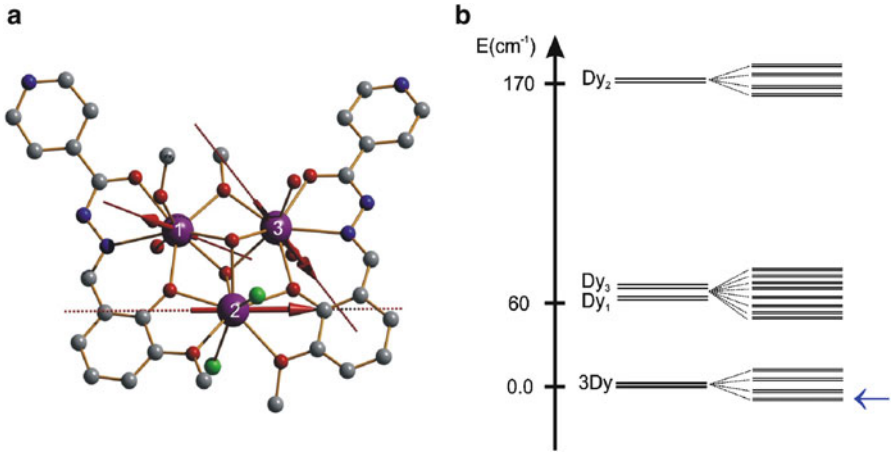

Fig. 13 (**a**) Molecular structure of a Dy_3 complex (Murugesu et al., unpublished) and the arrangement of local magnetic moments on the Dy(III) sites along the corresponding principal magnetic axes (*dashed lines*) in the ground exchange Kramers doublet. (**b**) The ab initio calculated energies of low-lying crystal-field multiplets (*left*) and their splitting by the exchange and dipolar interaction (*right*)

from the exchange multiplets of excited local multiplets, which is seen in Fig. 13b. Then the low-lying exchange spectrum can be described as exchange interaction between ground doublets on Ln ions, i.e., between corresponding pseudospins $\widetilde{s} = 1/2$. According to general rules described above, only terms of first rank will be retained in the corresponding exchange Hamiltonian (19), i.e., will have the generic form (10) in which $\hat{\mathbf{S}}_1$ and $\hat{\mathbf{S}}_2$ are to be replaced by $\hat{\widetilde{\mathbf{s}}}_1$ and $\hat{\widetilde{\mathbf{s}}}_2$, respectively. As was discussed in Sect. 3.4, the ground doublets on Ln sites in complexes are usually strongly axial. This allows to simplify the description of interaction in these systems further. Given the high current interest for lanthanide complexes, we discuss in detail this exchange interaction and its effect on magnetization blocking in the next sections.

4.3 Magnetization Blocking in Pure Lanthanide Complexes

The high axiality on the lanthanide sites in combination with the weak exchange limit in the corresponding complexes leads to a situation where, at least in the ground and low-lying exchange multiplets, the local magnetic moments on Ln sites will be directed along the corresponding principal magnetic axes. The latter are defined as having the largest g factor among the three main magnetic axes of the corresponding doublet on the metal site, denoted by g_Z in Sect. 3.3. Figure 13a shows the arrangement of local magnetic moments in the ground exchange Kramers doublet of a Dy_3 complex. We can see a strong non-collinearity of magnetic

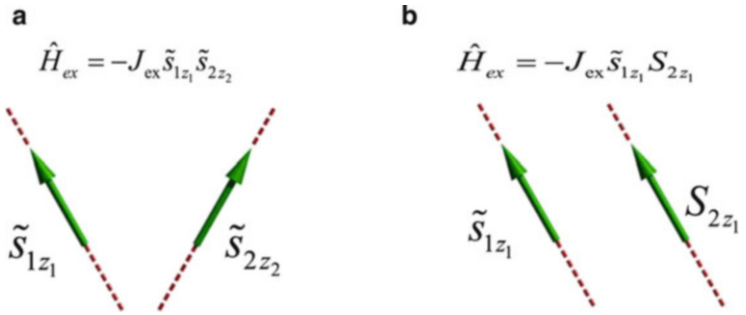

Fig. 14 Exchange interaction between two strongly axial doublets $\tilde{s}_1$ and $\tilde{s}_2$ (**a**) and between an axial doublet $\tilde{s}_1$ and an isotropic spin S_2 (**b**). *Dashed lines* show principal magnetic axes (z_i) of the corresponding axial doublets *i*

moments on Dy sites, which is a fingerprint of complexes in weak exchange limit. The exchange interaction between strongly axial doublet states of two Ln ions, described by pseudospins $\tilde{s}_1 = \tilde{s}_2 = 1/2$, reduces to Ising exchange interaction between the projection of pseudospins on the corresponding principal magnetic axes, z_1 and z_2 of the two doublets (Fig. 14a). When these axes are not parallel to each other, the exchange is of *non-collinear* Ising type, which is the case in most polynuclear lanthanide complexes [74]. This interaction is derived straightforwardly on the basis of microscopic models of electronic structure of interacting metal pairs [103], in full analogy with the derivation of Anderson's superexchange interaction between isotropic spins [104]. Therefore, if the directions of principal magnetic axes are known, either from ab initio calculations [74] or from magnetic measurements [16, 17], then the simulation of exchange interaction between the corresponding strongly axial Ln ions will require knowledge of one single exchange parameter (J_{ex} in Fig. 14a), i.e., will be as simple as the Heisenberg exchange interaction for two spins (10). This is a great simplification for the theory which allowed to rationalize a large number of polynuclear lanthanide complexes [9, 74, 87].

The exchange interaction between lanthanide doublets amounts to few wavenumbers in most cases. At the same time, the magnetic moments in the ground doublet states can reach values up to 10 μ_B. In this situation, the dipolar interaction between local magnetic moments on Ln sites is of the order of or larger than the net exchange interaction and should be taken into account together with the latter in the description of magnetic properties of lanthanide complexes. The dipolar interaction has the form:

$$\hat{H}_{\text{dip}} = -\frac{\hat{\boldsymbol{\mu}}_1 \cdot \hat{\boldsymbol{\mu}}_2 - 3(\hat{\boldsymbol{\mu}}_1 \cdot \mathbf{n}_{12})(\hat{\boldsymbol{\mu}}_2 \cdot \mathbf{n}_{12})}{r_{12}^3}, \tag{20}$$

where r_{12} is the distance between the magnetic moments and $\mathbf{n}_{12}$ is the unit vector along the axis connecting them. Substituting for magnetic moments their

expressions in term of pseudospins: ($\widetilde{s}_i = 1/2$), $\boldsymbol{\mu}_i = -\mu_B g^{(i)}_{Z_i} \hat{\widetilde{s}}_{iz_i} \mathbf{e}_{Z_i}$, $i = 1, 2$, we obtain again an expression for non-collinear Ising interaction of pseudospins (Fig. 14a) with the coefficient which should be identified as the parameter of dipolar magnetic interaction ($J_{\rm dip}$). Then the total magnetic interaction between two strongly axial Ln doublets has the form:

$$\hat{H}_{\rm int} = -\left(J_{\rm ex} + J_{\rm dip}\right) \hat{\widetilde{s}}_{1z_1} \hat{\widetilde{s}}_{2z_2}, \tag{21}$$

with

$$J_{\rm dip} = \mu_B^2 g^{(1)}_{Z_1} g^{(2)}_{Z_2} \frac{\cos\theta_{12} - 3\cos\theta_{1n}\cos\theta_{2n}}{r_{12}^3}, \tag{22}$$

where θ_{12} is the angle between the principal anisotropy axes on the two Ln sites and θ_{in}, $i = 1, 2$, is the angle between the principal magnetic axis on the center i and the vector $\mathbf{n}_{12}$ connecting the two Ln ions. Note that knowledge of principal magnetic axes ($\mathbf{e}_{Z_i}$) and principal values of the g tensors ($g^i_{Z_i}$), e.g., from ab initio calculations of mono-lanthanide fragments, allows to calculate the parameter $J_{\rm dip}$ in Eq. (22) from the first principles. Thus the only quantity which requires extraction from other data is the exchange parameter $J_{\rm ex}$. The latter is either extracted from the fitting of the experimental temperature-dependent magnetic susceptibility and field-dependent magnetization of the complex [9, 74, 105] or from broken-symmetry DFT calculations [106].

Consider as an example the asymmetric binuclear Dy_2 complex which is one of the first reported binuclear lanthanide SMMs [105]. Figure 15a shows a different environment for two Dy ions in this complex, which leads to different spectra of local Kramers doublets at the corresponding metal sites. In particular, the ab initio calculations give different orientations of principal magnetic axes on two Dy sites (red dashed lines in Fig. 15a), although both being directed closely to the Dy–Dy bond. Then, according to Eq. (22), the dipolar interaction between these Kramers doublets is ferromagnetic ($J_{\rm dip} > 0$). Ab initio calculation finds very strong axiality of ground-state Kramers doublets on both Dy sites implying the applicability of non-collinear Ising model (21) for the description of their exchange interaction. From ab initio results, we obtain $J_{\rm dip} = 5.36$ cm^{-1}, while simulation of magnetic susceptibility (Fig. 15b) gave for the exchange contribution in (22) $J_{\rm dip} = 0.52$ cm^{-1}, i.e., a ten times smaller value. One consequence of the almost ferromagnetic arrangement of two Dy magnetic moments in the ground exchange doublet (coupled into a total magnetic moment of ca 20 μ_B) is the very strong dipolar magnetic interaction between neighbor complexes, implying an unusually large effective exchange parameter between corresponding exchange doublets on neighbor complexes (zJ in Fig. 15b). The corresponding calculated stray field $H_{\rm bias}$ is shown in Fig. 16a (upper plot). The almost net Ising exchange interaction between Dy sites, together with strong axiality of their Kramers doublets, is the reason for a very strong axiality of the resulting two exchange Ising doublets,

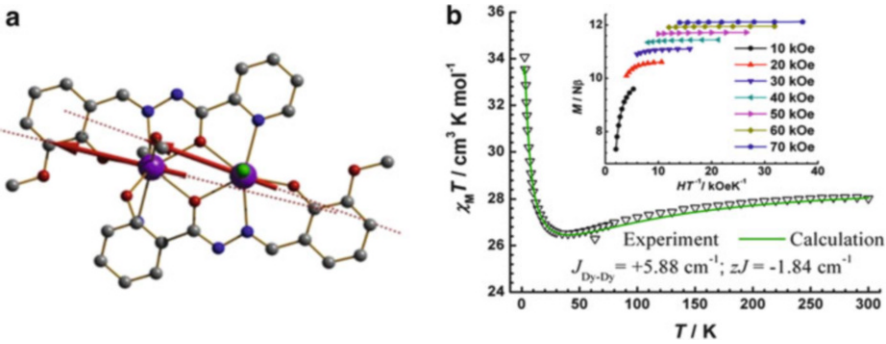

Fig. 15 (**a**) Molecular structure of asymmetric Dy_2 complex. *Color legend*: Dy purple, C gray, N blue, O red, Cl green. *Dashed lines* show principal magnetic axes on Dy sites and *arrows* show the local magnetic moment in the ground exchange doublet. (**b**) Molar magnetic susceptibility multiplied by temperature versus T for the Dy_2 complex. The *inset* is a plot of the reduced magnetization versus H/T. The *solid lines* are guides for the eye. Reprinted with permission from Guo et al. [105]. Copyright 2011 American Chemical Society

showing a negligible tunneling splitting Δ (Fig. 16a, lower plot). The latter is the reason for the quenching of QTM in this complex which leads to the observed hysteresis loops of magnetization (Fig. 16a, upper plot) and long relaxation times at low temperatures (Fig. 16b). The reversal of magnetization in the low-temperature domain goes via over-barrier relaxation mechanism. At temperatures considerably exceeding the separation between two lowest exchange doublets (≈ 3 cm^{-1}, as evidenced in the lower plot of Fig. 16a), the magnetic relaxation occurs via excited Kramers doublets on individual Dy sites. The fact that two relaxation times are observed in this temperature region (left-hand side of the lower plot in Fig. 16a) is an additional evidence for non-equivalent Dy sites having, in particular, different energies of the first excited Kramers doublets and, therefore, different activation barriers of on-site reversal of magnetization.

4.4 Magnetization Blocking in Mixed Ln–TM Complexes

In the case of mixed Ln–TM complexes, the high axiality (if present) of the ground-state doublet of the lanthanide ion will lead again to the Ising exchange interaction. However, contrary to the previous case, this interaction involves now the projection of Ln pseudospin $\widetilde{s}_1 = 1/2$ on the corresponding principal magnetic axis (Z_1) and the projection of the true spin S_2 of the transition metal ion on the same axis Z_1 (Fig. 14b), i.e., it is of *collinear* Ising type. An analysis based on a microscopic model [103] shows that this is indeed the form of exchange interaction when the strongly axial Ln doublet is close to have a maximal projection of the total moment J on the principal magnetic axis, i.e., to be $\approx |J, \pm J\rangle$. This is, in particular, the situation in most lanthanide ions with low site symmetry in the complex. For

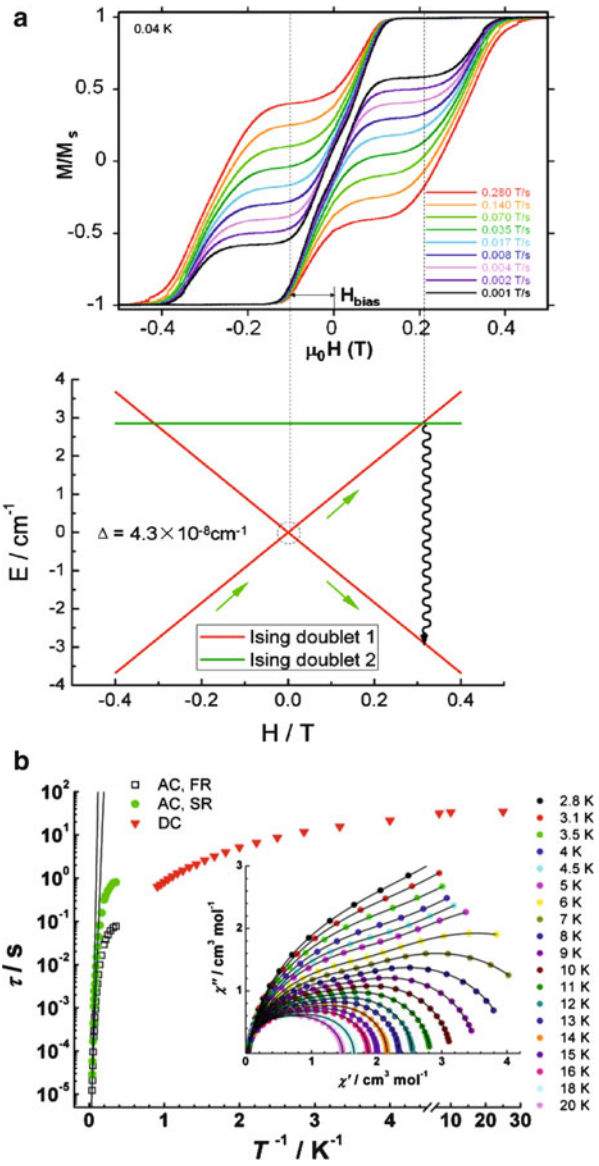

Fig. 16 (**a**) *Upper plot*: Magnetization loops in the asymmetric Dy_2 SMM at 0.04 K and different field sweep rates. *Lower plot*: Zeeman diagrams calculated for the field applied along the principal magnetic axis of the ground exchange doublet. The *arrows* show the magnetization relaxation pathways when the field is swept from left to right. (**b**) Arrhenius plot constructed using out-of-phase ac susceptibility and dc magnetization decay data [105]. *Inset*: Cole–Cole plots showing two relaxation times at high temperatures. Reprinted with permission from Guo et al. [105]. Copyright 2011 American Chemical Society

doublets characterized by lower projections of the total moment, e.g., $\approx |J, \pm (J-1)\rangle$, their exchange interaction with transition metals involves also transversal components of S which are, however, relatively small [103]. Another difference from the previous case is that the magnetic dipolar interaction between a strongly axial Ln doublet and an isotropic TM spin is not reduced to an Ising form as in Eq. (21). Indeed, substituting in Eq. (20) the expression for $\boldsymbol{\mu}_1$ given in Sect. 4.3 and taking $\boldsymbol{\mu}_2 = -\mu_B g^{(2)} \mathbf{S}_2$, we obtain the following contribution:

$$\hat{H}_{\text{dip}} = -J_{\text{dip}}\left(\hat{\tilde{s}}_{1z_1}\hat{S}_{2z_1} - 3\cos\theta_{1n}\hat{\tilde{s}}_{1z_1}\hat{S}_{2n}\right), \tag{23}$$

with

$$J_{\text{dip}} = \mu_B^2 g_{Z_1}^{(1)} g^{(2)}/r_{12}^3, \tag{24}$$

where S_{2n} is the projection of the TM spin on the axis $\mathbf{n}_{12}$ connecting the two metal ions and the angle θ_{1n} is the same as in Eq. (22).

Compared to Ln–Ln pairs, the Ln–TM exchange interaction is usually one order of magnitude larger due to more diffuse 3d orbitals of transition metals compared to 4f orbitals of lanthanides. Then the description of the Ln–TM exchange interaction involving one single (ground) doublet on Ln site is only justified when the resulting exchange splitting is significantly smaller than the energy of the first excited multiplet at the lanthanide ion. If this condition is not fulfilled, more multiplets on the Ln sites should be involved in the description of exchange interaction, which taken together will correspond to a larger pseudospin [40] and will lead to a more complex exchange interaction according to Eq. (19). On the contrary, the dipolar magnetic interaction within Ln–TM pairs is expected to be several times smaller than in Ln–Ln pairs due to much smaller magnetic dipole moments of TM ions compared to lanthanide ions. Then the dominant collinear Ising Ln–TM interaction (Fig. 14b) will impose a collinear alignment of all local magnet moments to the principal magnetic axes of Ln ions present in the complex if the latter are parallel to each other. At the same time, the effect of other contributions to the exchange and dipolar magnetic interactions, favoring a non-collinear arrangement of local magnetic moments, will be effectively suppressed by the collinear Ising contribution.

An example of such situation is the tetranuclear complex $[Cr^{III}_2Dy^{III}_2(OMe)_2(O_2CPh)_4(mdea)_2(NO_3)_2]$ shown in Fig. 17a [106]. This complex has an inversion center which interconnects the pairs of dysprosium and chromium atoms. Ab initio calculations have shown that the ground Kramers doublet at Dy sites is very axial. The principal magnetic axes (Z) on the two Dy ions are indicated in Fig. 17a by dashed lines and are parallel to each other because of the inversion symmetry of the complex. The calculated exchange parameters by broken-symmetry DFT methods are shown in Table 3 (they refer to $\tilde{s}_{\text{Dy}} = 1/2$, $S_{\text{Cr}} = 3/2$, see Langley et al. [106] for the details of these calculations). We can see from the table that for Cr–Dy pairs J_{ex} is several times larger than J_{dip}, calculated with Eq. (24) on the basis of ab initio results. Varying the values of exchange parameters in order to fit the experimental temperature-dependent susceptibility (Fig. 17b) does not modify them drastically, as can be seen in Table 3. The large value of obtained J_{ex} is the reason for an almost collinear arrangement of magnetic moments on the metal sites in the ground (Fig. 17a) and the low-lying exchange doublets. For these states, the general Hamiltonian of magnetic interaction between metal centers:

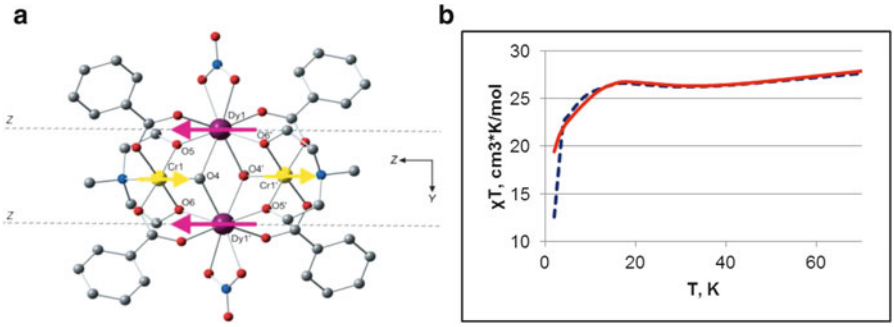

Fig. 17 (**a**) Molecular structure of Cr_2Dy_2 complex. *Color legend*: Dy purple, Cr yellow, C gray, N blue, O red. *Dashed lines* show principal magnetic axes on Dy sites and *arrows* show the local magnetic moment in the ground exchange doublet. (**b**) Molar magnetic susceptibility multiplied by temperature versus T: experiment (*dashed line*) and theory (*solid line*). Reproduced with permission from Langley et al. [106]. Copyright 2013 John Wiley & Sons, Inc

Table 3 Magnetic coupling parameters (cm^{-1}) for different metal pairs of Cr_2Dy_2 complex

	Calculated		Fitted	
Metal pairs (M_1-M_2)	J_{dip}	J_{ex} (BS-DFT)	J_{ex}	J_{M1-M2} in Eq. (26)
Dy1–Dy1′	2.5	1.00	1.00	−1.5
Cr1–Cr1′	0.34	0.12	0.10	0.12
Dy1–Cr1	5.2	−26.0	−20.5	−20.3
Dy1–Cr1′	5.2	−32.5	−17.0	−16.7

$$\hat{H} = \sum_{i=1}^{4}\sum_{j>i}^{4}\left(\hat{H}_{ex}^{ij} + \hat{H}_{dip}^{ij}\right) \tag{25}$$

reduces to a collinear Ising one

$$\begin{aligned}\hat{H} = &-J_{Dy1-Dy1'}\,\hat{\tilde{s}}_{Dy1,z}\hat{\tilde{s}}_{Dy1',z} - J_{Dy1-Cr1}\left(\hat{\tilde{s}}_{Dy1,z}\hat{S}_{Cr1,z} + \hat{\tilde{s}}_{Dy1',z}\hat{S}_{Cr1',z}\right)\\ &- J_{Cr1-Cr1'}\,\hat{S}_{Cr1,z}\hat{S}_{Cr1',z} - J_{Dy1-Cr1'}\left(\hat{\tilde{s}}_{Dy1,z}\hat{S}_{Cr1',z} + \hat{\tilde{s}}_{Dy1',z}\hat{S}_{Cr1,z}\right)\end{aligned} \tag{26}$$

with the parameters which include the effect of exchange and dipolar magnetic interaction between the four metal ions (last column in Table 3). The resulting spectrum of low-lying exchange doublets is shown in Fig. 18 together with the structure of blocking barrier for magnetization. We can see that the high axiality of low-lying exchange doublets, blocking the QTM relaxation in these excited states, is the reason for relatively high value of blocking barrier, amounting to ca 50 cm^{-1}. This value matches nicely the activation energy for relaxation of magnetization extracted from the measurements of ac susceptibility [106]. We would like to emphasize that the barrier shown in Fig. 18 is of exchange type, since it is built

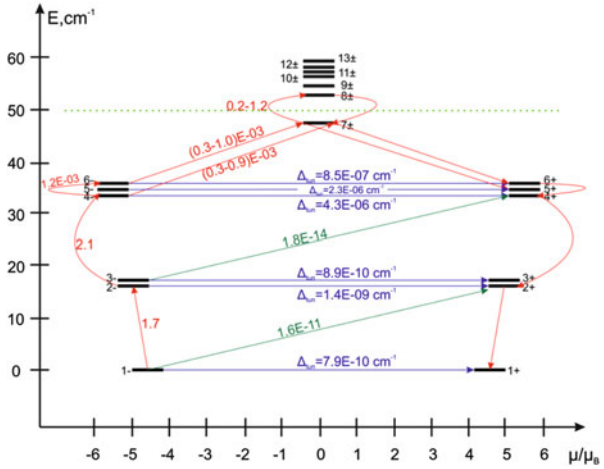

Fig. 18 The structure of magnetization blocking barriers in the Cr_2Dy_2 complex. The *thick black lines* represent the exchange levels as a function of their magnetic moment along the principal magnetic axis of the complex. The *external red arrows* connecting the neighbor levels outline the relaxation path. The meaning of the *internal arrows* is the same as in Fig. 11. The *horizontal dashed line* corresponds approximately to the height of the calculated blocking barrier. Reproduced with permission from Langley et al. [106]. Copyright 2013 John Wiley & Sons, Inc

on exchange multiplets originating from ground-state Kramers doublets on Dy sites. The many states involved in the relaxation path make this barrier opaque at low temperatures (significantly lower than the height of the barrier), which explains the very good blocking properties of the complex [106]. On the other hand, the activation energy describing the intra-ionic relaxation of magnetization, which becomes operative at higher temperatures, corresponds to the second excited Kramers doublet on each Dy site which lies much higher in energy [106].

If the Ln ions in a mixed Ln–TM complex are characterized by non-collinear principal magnetic axes, then the arrangement of magnetic moments on the metal sites will also be non-collinear. This is because the isotropic spin of each TM site tends to align as parallel as possible to the principal magnetic axes of neighbor Ln ions and often ends up by choosing an intermediate orientation. For example, in the octanuclear Cr^{III}_4 Dy $^{III}_4$ complex of wheel type having an approximate fourfold symmetry axis [107], the principal magnetic axes on Dy sites lie in mutually orthogonal planes while the spin on each Cr lies in the bisecting plane between two neighbor dysprosium ions. Among the mixed complexes, the Ln–R compounds, where R is a radical, are viewed nowadays as the most perspective ones for the design of efficient SMMs. The main advantage of these complexes is their ability to exhibit a very strong Ln–R exchange interaction, which can overcome the Ln–TM complexes by an order of magnitude. This has been recently demonstrated on the example of N_2^{3-} radical-bridged lanthanide complexes [108], which have

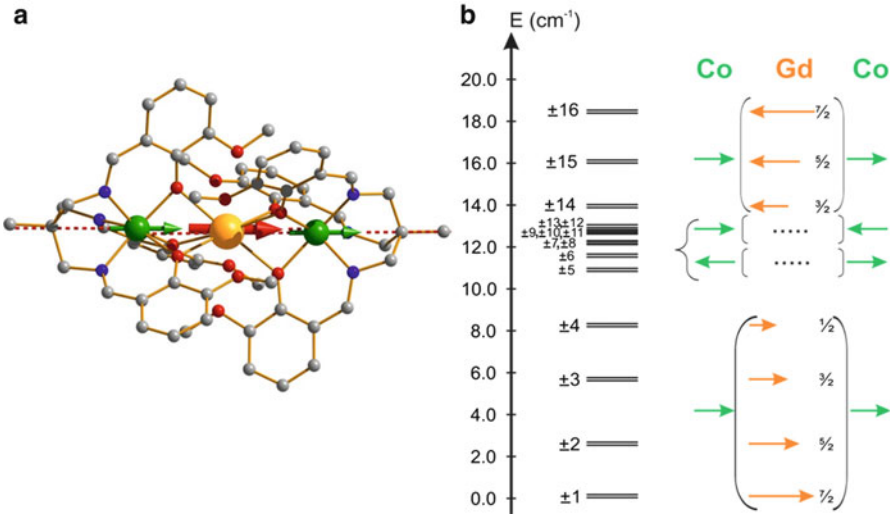

Fig. 19 (**a**) Molecular structure $[LCoGdCoI]^+$ complex. *Color legend*: Gd yellow, Co green, C gray, N blue, O red. *Dashed lines* show principal magnetic axes on Co sites and *arrows* show the local magnetic moment in the ground exchange doublet. (**b**) Spectrum of exchange levels originating from the ground KDs on Co(II) sites (*left*) and the value/orientation of local magnetic moments on metal sites in the corresponding states. Reprinted with permission from Ungur et al. [102]. Copyright 2013 American Chemical Society

shown a record for the height of blocking barrier of exchange type and the highest to date blocking temperature among the existent SMMs [109].

Finally, one notices that SMM complexes combining strongly anisotropic and isotropic magnetic sites should not necessarily include lanthanide ions. As an example of a "non-lanthanide" mixed complex, Fig. 19a shows a trinuclear complex from the series $[LCo^{II}LnCo^{II}L]^+$ [110], where L = N,N′,N″-tris(2-hydroxy-3-methoxybenzylidene)-2-(aminomethyl)-2-methyl-1,3-propanediamine, for Ln = Gd. In this series, owing to the structure of L, the complexes possess an almost ideal trigonal axis connecting the three metal ions. The trigonal symmetry of the complex gives rise to a twofold orbital degeneracy of the two Co(II) centers allowing for unquenched projection of orbital momentum, $L_z \approx \pm 2$, on the common symmetry axis (z) [102]. Spin–orbit coupling of L_z with the S_z projection of ground spin $S = 3/2$ on cobalt leads to four equidistant Kramers doublets on each Co site, separated by $\approx 2\zeta/3$, where ζ is the spin–orbit coupling constant of Co(II) ion. The ab initio calculation has confirmed this structure of low-lying Kramers doublets on the Co sites, giving for the energy separation between them an average value of 280 cm^{-1} [102]. This allows to describe the magnetic properties of the complex in terms of exchange interaction between the ground-state Kramers doublets on each Co center ($\widetilde{s}_i = 1/2$, $i = 1, 2$) and the isotropic spin $S = 7/2$ of the Gd ion. The important feature is the obtained relatively strong axiality ($g_Z \approx 9.3$, g_X, $g_Y \approx 0.3$) of the ground Kramers doublet of Co(II) sites. This is the result of predominant contribution of the projections of the total angular momentum $M_J = 7/2$

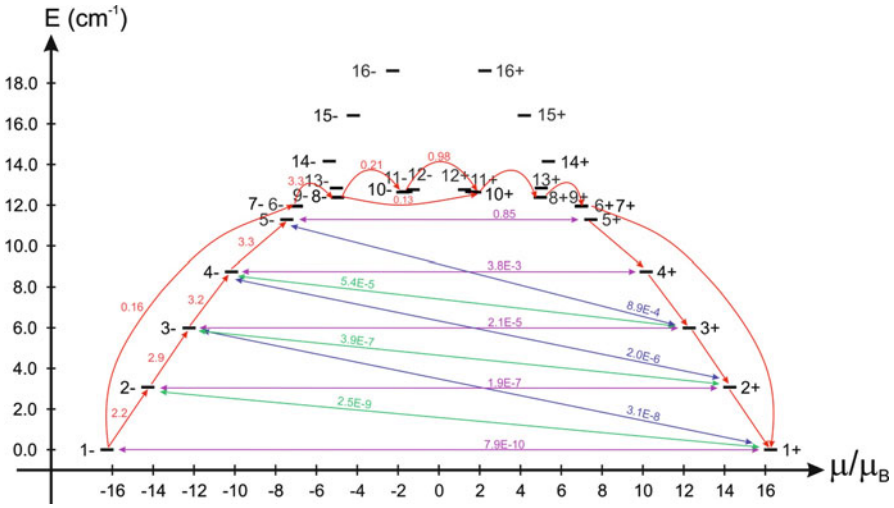

Fig. 20 Magnetization blocking barrier in $[LCoGdCoL]^+$. The exchange states are arranged according to the values of their magnetic moments. The *external red arrows* connecting the neighbor levels outline the relaxation path. The meaning of the *internal arrows* is the same as in Fig. 11. Reprinted with permission from Ungur et al. [102]. Copyright 2013 American Chemical Society

and $M_J = -7/2$, respectively, to the two wave functions of the Kramers doublet. The deviation from a perfect axiality (see Sect. 3.3) is due to the fact that other M_J components can admix in trigonal symmetry. Nevertheless, the axiality is sufficiently high ($g_{X,Y}/g_Z = 0.02$–0.04) in order to make the exchange interaction between Co and Gd mainly of collinear Ising type (Fig. 14b). This is confirmed by the spectrum of exchange multiplets (Fig. 19b) calculated with the interaction Hamiltonian involving exchange parameters extracted from the fitting of magnetic data (in analogy with Cr_2Dy_2 complex discussed above). We can see that the lowest four exchange multiplets are equidistant and correspond consecutively to the spin projections $M = 7/2$, 5/2, 3/2, and 1/2 on Gd site, respectively, under unchanged directions of local magnetization on Co sites. This gradual decrease of M with increasing the energy of the exchange doublet resembles much the structure of blocking barrier in the conventional SMMs for complexes in the strong exchange limit, like Mn_{12}ac.[1,3] The main difference is that in the later the splitting of the ground spin manifold follows a parabolic dependence, $E_M = |D|M^2$, while in the present case, it is almost equidistant. The analysis of the structure of the blocking barrier (Fig. 20) shows that its top corresponds to ca 12 cm^{-1} [102], which is in good agreement with the value extracted from experiment [110]. The high SMM performance of this complex [110] is explained by a multilevel structure of the exchange barrier, as was also the case of the Cr_2Dy_2 complex considered above.

5 Concluding Remarks

The understanding of mechanisms of magnetic anisotropy in molecular nanomagnets became a task of primary importance in the last decade. The description of the effects of magnetic anisotropy is relatively simple in complexes with weak spin–orbit coupling effects on the metal sites, corresponding to strong exchange limit in polynuclear compounds. The model parameters for such complexes can usually be extracted without problems from magnetic measurements. On the contrary, in complexes with strong spin–orbit coupling effects, leading to weak exchange limit in polynuclear compounds, the details of anisotropic magnetic interactions can be hardly revealed from experiment alone. The problem is in the large number of parameters describing the anisotropic magnetic interaction in this case. For such complexes, the theoretical description of magnetic anisotropy, especially, based on ab initio calculations of the complexes with nonperturbative treatment of spin–orbit coupling becomes indispensable. In this review, we presented several examples of such an approach allowing to extract details of anisotropic magnetic interaction which have not been available in the past. We also analyzed in detail the mechanisms leading to strong magnetic axiality in anisotropic magnetic complexes as being the necessary condition for the design of efficient SIMs and SMMs and emphasized the role of lanthanide-based complexes. Fast progress in this domain can be achieved by combining the refined spectroscopic methods, like INS, SQUID magnetometry, and infrared spectroscopy, with state-of-the-art ab initio approaches, as was demonstrated in very recent studies [111, 112].

Acknowledgments I would like to thank Dr. Liviu Ungur for the long-term collaboration on the theoretical description of magnetic anisotropy in molecular nanomagnets and Veaceslav Vieru for technical assistance. This work was supported by Methusalem and INPAC grants at KU Leuven and by FWO grants of Flemish Science Foundation.

References

1. Sessoli R, Gatteschi D, Caneschi A, Novak MA (1993) Nature 365:141
2. Christou G, Gatteschi D, Hendrickson DN, Sessoli R (2000) Mater Res Bull 25:66
3. Gatteschi D, Sessoli R, Villain J (2006) Molecular nanomagnets. Oxford University Press, Oxford
4. Aromi G, Brechin EK (2006) In: Winpenny REP (ed) Single-molecule magnets and related phenomena, vol 122. Structre Bonding, p 1
5. Woodruff DN, Winpenny REP, Layfield RA (2013) Chem Rev 113:5110
6. Kahn O, Larionova J, Quahab L (1999) Chem Commun 11:945
7. Bencini A, Gatteschi D (1990) Electron paramagnetic resonance of exchange coupled systems. Springer, Berlin
8. Kahn O (1993) Molecular magnetism. Wiley-VCH, Weinheim
9. Chibotaru LF, Ungur L, Soncini A (2008) Angew Chem Int Ed 47:4126

10. Görller-Warland C, Binnemans K (1998) Spectral intensities of f-f transitions. In: Gschneidner KA Jr, Eyring L (eds) Handbook on the physics and chemistry of rare earths, vol 25. Elsevier, Amsterdam, p 101
11. Bloor D, Copland GM (1972) Rep Prog Phys 35:1173
12. Furrer A, Waldmann O (2013) Rev Mod Phys 85:367
13. Mannini M, Pineider F, Danieli C, Totti F, Sorace L, Sainctavit PH, Arrio M-A, Otero E, Joly L, Cezar JC, Cornia A, Sessoli R (2010) Nature 468:417
14. Barra AL, Gatteschi D, Sessoli R (1996) Phys Rev B 56:8192
15. Abragam A (1961) The principles of nuclear magnetism. Clarendon, Oxford
16. Bernot K, Luzon J, Bogani L, Etienne M, Sangregorio C, Shanmugam M, Caneschi A, Sessoli R, Gatteschi D (2009) J Am Chem Soc 131:5573
17. Boulon M-E, Cucinotta G, Liu S-S, Jiang S-D, Ungur L, Chibotaru LF, Gao S, Sessoli R (2013) Chem Eur J 19:13726
18. Ishikawa N, Sugita M, Ishikawa T, Koshihara S, Kaizu Y (2004) J Phys Chem B 108:11265
19. AlDamen MA, Clemente-Juan JM, Coronado E, Martí-Gastaldo C, Gaito-Ariño A (2008) J Am Chem Soc 130:8874
20. Aquilante F, Vico LD, Ferré N, Ghigo G, Malmqvist PÅ, Neográdi P, Pedersen TB, Pitoňák M, Reiher M, Roos BO, Serrano-Andrés L, Urban M, Veryazov V, Lindh R (2010) J Comput Chem 31:224
21. Chibotaru LF, Ungur L (2012) J Chem Phys 137:064112
22. Weinberger P (2009) Magnetic anisotropies in nanostructured matter. CRC Press, Boca Raton
23. Néel L (1949) Annu Geophys 5:99
24. Coulon C, Miyasaka H, Clérac R (2006) Single-chain magnets: theoretical approach and experimental systems. In: Winpenny REP (ed) Single-molecule magnets and related phenomena, vol 122. Structure Bonding, p 163
25. Abragam A, Bleaney B (1970) Electron paramagnetic resonance of transition ions. Oxford University Press, Oxford
26. Landau LD, Lifshitz EM (1975) Quantum mechanics, 2nd edn. Pergamon, Oxford
27. Moriya T (1963) Weak ferromagnetism. In: Rado GT, Suhl H (eds) Magnetism, vol 1. Academic, New York, p 85
28. Ashcroft NW, Mermin ND (1976) Solid state physics. Saunders College, Philadelphia
29. Villain J, Hartmann-Boutron F, Sessoli R, Rettori A (1994) Europhys Lett 27:159
30. Garanin DA, Chudnovsky EM (1997) Phys Rev B 56:11102
31. Leuenberger MN, Loss D (1999) Europhys Lett 46:692
32. Stoner EC, Wohlfarth EP (1948) Phil Trans Lond Ser A 240:599
33. Beown WF Jr (1963) Phys Rev 130:1677
34. Frenkel J, Dorfman J (1930) Nature 126:274
35. Kittel C (1946) Phys Rev 70:965
36. Thompson DA, Best JS (2000) IBM J Res Dev 44:311
37. Wernsdorfer W (2001) Classical and quantum magnetization reversal studied in nanometer-sized particles and clusters. In: Rice SA, Dinner AR (eds) Advance in chemical physics, vol 118, p 99
38. Bedanta S, Kleemann W (2009) J Phys D Appl Phys 42:013001
39. Al'tshuler SA, Kozyrev BM (1974) Electron paramagnetic resonance in compounds of transition elements. Wiley, New York
40. Chibotaru LF (2013) *Ab initio* methodologies for pseudospin Hamiltonians of anisotropic magnetic complexes. In: Rice SA, Dinner AR (eds) Advance in chemical physics, vol 153, p 397
41. Figgis BN, Hitchman MA (1999) Ligand field theory and its applications. Wiley-VCH, New York
42. Neese F (2001) Int J Quant Chem 83:104

43. Kaupp M, Bühl M, Malkin VG (eds) (2004) Calculation of NMR and EPR parameters. Wiley-VCH, Weinheim
44. Maganas D, Sottini S, Kyritsis P, Groenen EJJ, Neese F (2011) Inorg Chem 50:8741
45. Arratia-Pérez R, Hernandez-Acevedo L, Malli GL (2001) J Chem Phys 121:7743
46. Quiney HM, Belanzoni P (2002) Chem Phys Lett 353:253
47. Neese F, Solomon E (1998) Inorg Chem 37:6568
48. Pederson MR, Khanna SN (1999) Phys Rev B 60:9566
49. Postnikov AV, Kortus J, Pederson MR (2006) Phys Stat Sol B 243:2533
50. Atanasov M, Comba P, Daul CA (2008) Inorg Chem 47:2449
51. Webb SP, Gordon MS (1998) J Chem Phys 109:919
52. Maurice R, Bastardis R, de Graaf C, Suaud N, Mallah T, Guihery N (2009) J Chem Theor Comp 5:2977
53. Maurice R, de Graaf C, Guihery NJ (2010) Chem Phys 133:084307
54. Cremades E, Ruiz E (2011) Inorg Chem 50:4016
55. Maurice R, Sivalingam K, Ganyushin D, Guihery N, de Graaf C, Neese F (2011) Inorg Chem 50:6229
56. Atanasov M, Ganyushin D, Pantazis DA, Sivalingam K, Neese F (2011) Inorg Chem 50:7460
57. Takeda R, Yamanaka S, Yamaguchi K (2005) Int J Quant Chem 102:80
58. Takeda R, Yamanaka S, Shoji M, Yamaguchi K (2007) Int J Quant Chem 107:1328
59. Maurice R, Pradipto AM, Guihery N, Broer R, de Graaf C (2010) J Chem Theor Comp 6:3092
60. Roos BO, Taylor PR, Siegbahn PEM (1980) Chem Phys 48:157
61. Andersson K, Malmqvist PÅ, Roos BO, Sadlej AJ, Wolinski K (1990) J Phys Chem 94:5483
62. Aquilante F, De Vico L, Ferre N, Ghigo G, Malmqvist PÅ, Neogrady P, Pedersen TB, Pitonak M, Reiher M, Roos BO, Serrano-Andres L, Urban M, Veryazov V, Lindh R (2010) J Comp Chem 31:224
63. Hess BA, Marian CM, Wahlgren U, Gropen O (1996) Chem Phys Lett 251:365
64. Malmqvist PÅ, Roos BO, Schimmelpfennig B (2002) Chem Phys Lett 357:2
65. Chibotaru LF, Hendrickx MFA, Clima S, Larionova J, Ceulemans A (2005) J Phys Chem A 109:7251
66. Bolvin H (2006) Chemphyschem 7:1575
67. Petit S, Pilet G, Luneau D, Chibotaru LF, Ungur L (2007) Dalton Trans 4582
68. Chibotaru LF, Ungur L, Aronica C, Elmoll H, Pilet G, Luneau D (2008) J Am Chem Soc 130:12445
69. Novitchi G, Wernsdorfer W, Chibotaru LF, Costes J-P, Anson CE, Powell AK (2009) Angew Chem Int Ed 48:1614
70. Cucinotta G, Perfetti M, Luzon J, Etienne M, Car PE, Caneschi A, Calvez G, Bernot K, Sessoli R (2012) Angew Chem Int Ed 51:1606
71. Aravena D, Ruiz E (2013) Inorg Chem 52:12777
72. Chibotaru LF, Ceulemans A, Bolvin H (2008) Phys Rev Lett 101:033003
73. Notter FP, Bolvin H (2009) J Chem Phys 130:184310
74. Ungur L, Chibotaru L (2014) Computational modeling of the magnetic properties of lanthanide compounds. In: Layfield RA, Murugesu M (eds) Lanthanides and actinides in molecular magnetism. Wiley
75. Boca R (2004) Coord Chem Rev 248:757
76. Griffith JS (1971) The theory of transition metal ions. Cambridge University Press, Cambridge
77. Bethe HA, Salpeter EE (1957) Quantum mechanics of one- and two-electron atoms. Springer, Berlin
78. McWeeny R (1992) Methods of molecular quantum mechanics. Academic, London
79. Neese F (2007) J Chem Phys 127:164112
80. Rogez G, Rebilly JN, Barra AL, Sorace L, Blondin G, Kirchner N, Duran M, van Slageren J, Parsons S, Ricard L, Marvilliers A, Mallah T (2005) Angew Chem Int Ed 44:1876
81. Stevens KWH (1952) Proc Phys Soc A 65:209

82. Reu OS, Palii AV, Ostrovsky SM, Tregenna-Piggott PL, Klokishner SI (2012) Inorg Chem 51:10955
83. Ungur L, Chibotaru LF (2014) Nat Comm, submitted
84. Le Roy JJ, Jeletic M, Gorelsky SI, Korobkov I, Ungur L, Chibotaru LF, Murugesu M (2013) J Am Chem Soc 135:3502
85. Liu J-L, Chen Y-C, Zheng Y-Z, Lin W-Q, Ungur L, Wernsdorfer W, Chibotaru LF, Tong M-L (2013) Chem Sci 4:3310
86. Ungur L, Chibotaru LF (2011) Phys Chem Chem Phys 13:20086
87. Blagg RJ, Ungur L, Tuna F, Speak J, Comar P, Collison D, Wernsdorfer W, McInnes EJL, Chibotaru LF, Winpenny REP (2013) Nat Chem 5:673
88. Ungur L, Le Roy JJ, Korobkov I, Murugesu M, Chibotaru LF (2014) Angew Chem Int Ed 53:4413
89. Ishikawa N, Sugita M, Wernsdorfer W (2005) Angew Chem Int Ed 44:2931
90. Rinehart JD, Long JR (2011) Chem Sci 2:2078
91. Meihaus KR, Long JR (2013) J Am Chem Soc 135:17952
92. Magnani N, Apostolidis C, Morgenstern A, Colineau E, Griveau J-C, Bolvin H, Walter O, Caciuffo R (2011) Angew Chem Int Ed 50:1696
93. King DM, Tuna F, McMaster J, Lewis W, Blake AJ, McInnes EJL, Liddle ST (2013) Angew Chem Int Ed 52:4921
94. Meihaus KR, Rinehart JD, Long JR (2011) Inorg Chem 50:8484
95. Moro F, Mills DP, Liddle ST, van Slageren J (2013) Angew Chem Int Ed 52:3430
96. Harman WH, Harris TD, Freedman DE, Fong H, Chang A, Rinehart JD, Ozarowski A, Sougrati MT, Grandjean F, Long GJ, Long JR, Chang CJ (2010) J Am Chem Soc 132:18115
97. Zadrozny JM, Xiao DJ, Atanasov M, Long GJ, Grandjean F, Neese F, Long JR (2013) Nat Chem 5:577
98. Dreiser J, Pedersen KS, Schnegg A, Holldack K, Nehrkorn J, Sigrist M, Tregenna-Piggott P, Mutka H, Weihe H, Mironov VS, Bendix J, Waldmann O (2013) Chem Eur J 19:3693
99. Qian K, Huang X-C, Zhou C, You X-Z, Wang X-Y, Dunbar KR (2013) J Am Chem Soc 135:13302
100. Barra AL, Debrunner P, Gatteschi D, Schulz CE, Seesoli R (1996) Europhys Lett 35:133
101. Gatteschi D, Sorace L (2001) J Solid State Chem 159:253
102. Ungur L, Thewissen M, Costes J-P, Wernsdorfer W, Chibotaru LF (2013) Inorg Chem 52:6328
103. Vieru V, Ungur L, Chibotaru LF (2014), unpublished
104. Anderson PW (1959) Phys Rev 115:1
105. Guo Y-N, Xu G-F, Wernsdorfer W, Ungur L, Guo Y, Tang J, Zhang H-J, Chibotaru LF, Powell AK (2011) J Am Chem Soc 133:11948
106. Langley SK, Wielechowski DP, Vieru V, Chilton NF, Moubaraki B, Abrahams BF, Chibotaru LF, Murray KS (2013) Angew Chem Int Ed 52:12014
107. Rinck J, Novitchi G, Van den Heuvel W, Ungur L, Lan Y, Wernsdorfer W, Anson CE, Chibotaru LF, Powell AK (2010) Angew Chem Int Ed 49:7583
108. Rinehart JD, Fang M, Evans WJ, Long JR (2011) Nat Chem 3:538
109. Rinehart JD, Fang M, Evans WJ, Long JR (2011) J Am Chem Soc 133:14236
110. Yamaguchi T, Costes J-P, Kishima Y, Kojima M, Sunatsuki Y, Bréfuel N, Tuchagues J-P, Vendier L, Wernsdorfer W (2010) Inorg Chem 49:9125
111. Pedersen KS, Ungur L, Sigrist M, Sundt A, Schau-Magnussen M, Vieru V, Mutka H, Rols S, Weihe H, Waldmann O, Chibotaru LF, Bendix J, Dreiser J (2014) Chem Sci 5:1650
112. Marx R, Moro F, Dörfel M, Ungur L, Waters M, Jiang SD, Orlita M, Taylor J, Frey W, Chibotaru LF, van Slageren J (2014) Chem Sci 5:3287

Struct Bond (2015) 164: 231–292
DOI: 10.1007/430_2014_155

Published online: 2 October 2014

Spectroscopy Methods for Molecular Nanomagnets

Michael L. Baker, Stephen J. Blundell, Neus Domingo, and Stephen Hill

Abstract This chapter provides a detailed overview of some of the primary spectroscopic methods that have contributed to the current understanding of molecular nanomagnets (MNs). These include: electron paramagnetic resonance (EPR); optical spectroscopy, including magnetic and X-ray magnetic circular dichroism (MCD/XMCD); inelastic neutron scattering (INS); and muon spin rotation (μ^+SR). For each technique, a historical survey of the most important discoveries is provided, up to and including the most recent developments. Each section gives an introduction to the theoretical principles underpinning the techniques, as well as a description of experimental requirements and protocols. A common theme among the described spectroscopies is the fact that state-of-the-art measurements typically have to be performed at major research facilities such as synchrotrons (terahertz EPR and XMCD), high magnetic field laboratories (EPR), and accelerator facilities or reactors (INS and μ^+SR). Details of such facilities are given where appropriate. Forefront issues that are addressed in the chapter include: the fundamental properties of both mono- and poly-nuclear single-molecule magnets (SMMs); the deployment of MNs in quantum information processing applications; the addressing of individual magnetic molecules on surfaces or in devices; the probing of spin dynamics in MNs using EPR, INS, and μ^+SR; and studies of long-range magnetic

M.L. Baker
Department of Physics, City College of New York, CUNY, New York, NY 10031, USA

Department of Physics, New York University, New York, NY 10003, USA

S.J. Blundell
Department of Physics, Clarendon Laboratory, University of Oxford, Oxford OX1 3PU, UK

N. Domingo
Centre d'Investigació en Nanociència i Nanotecnologia (ICN2-CSIC), Campus UAB, 08193 Bellaterra, Spain

S. Hill (✉)
Department of Physics and National High Magnetic Field Laboratory, Florida State University, Tallahassee, FL 32310, USA
e-mail: shill@magnet.fsu.edu

ordering in MN crystals. An extensive list of references is provided. The chapter is intended for physicists, chemists, and materials scientists, particularly junior researchers who are just starting work in the field.

Keywords Electron paramagnetic resonance · Inelastic neutron scattering · Magnetic circular dichroism · Muon spin rotation · X-ray magnetic circular dichroism

Contents

1 Introduction

The chapter begins by introducing electromagnetic/photon probes, starting with a section on electron paramagnetic resonance (EPR – Sect. 2), which was one of the first spectroscopic methods applied to the study of single-molecule magnets (SMMs) [1]. This is followed by a section on surface-sensitive magneto-optical techniques, including magnetic circular dichroism (MCD) and X-ray MCD (XMCD), which have found increased applicability in recent years as researchers have attempted to study the properties of individual molecules grafted onto surfaces (Sect. 3). The last two sections of the chapter switch to local probes that have mass – namely inelastic neutron scattering (INS – Sect. 4) and muon spin rotation (μ^+SR – Sect. 5) spectroscopy. Each of the described techniques offers advantages for studying various types of molecules in different environments. For example, high-field EPR is particularly suited to investigations of anisotropic molecules with large magnetic moments. For this reason, an extensive introduction to the spin-Hamiltonian formalism and the physics of SMMs is given in Sect. 2. Likewise,

INS is highly suited to studies of the collective excitations of spins in antiferromagnetically coupled molecules. Therefore, a more in-depth discussion of such systems is given in Sect. 4. Less detail is devoted to the deposition of molecules onto surfaces because this is discussed in detail elsewhere in this book.

2 Electron Paramagnetic Resonance

EPR and, in particular, high-field EPR (HFEPR [2]) have played a pivotal role in the study of SMMs and other molecule-based magnetic materials. Indeed, one of the very first papers on the prototypical SMM, $[Mn_{12}O_{12}(O_2CCH_3)_{16}(H_2O)_4]\cdot 2CH_3CO_2H\cdot 4H_2O$ ($Mn_{12}Ac$), included continuous-wave (cw) HFEPR data that confirmed the molecular spin $S = 10$ ground state and appreciable magnetic anisotropy [1]. This work was followed by more detailed measurements on both polycrystalline [3] and single-crystal [4] samples, enabling precise elucidation of a set of effective spin Hamiltonian parameters. Likewise, the first report of the magnetic properties of the widely studied Fe_8 SMM included detailed cw HFEPR measurements [5]. During the last decade, pulsed EPR measurements have played an increasingly important role in the study of molecular nanomagnets (MNs), with a view to their potential use in quantum information technologies (see, e.g., [6–10]). This section begins with an introduction and background to the use of cw EPR in the study of SMMs, followed by an extensive survey of the important applications. The section ends with a short review of recent pulsed EPR investigations of MNs.

2.1 Cw HFEPR

The importance of high magnetic fields and high EPR frequencies in the study of SMMs becomes apparent when one examines the simplest effective Hamiltonian describing the spin degrees of freedom of a well isolated orbital singlet ground state associated with a 3*d* transition metal ion [11]. Assuming the symmetry of the local coordination environment allows for such a description, one may introduce magnetic anisotropy by treating the spin-orbit interaction ($\lambda\vec{\mathbf{L}}\cdot\vec{\boldsymbol{s}}$) as a perturbation of the zeroth-order Hamiltonian describing the effects of electrostatic and ligand/crystal-field interactions on the basis of orbital states associated with the 3*d* ion. This procedure enables a description of the lowest orbital singlet in terms of an effective spin-only Hamiltonian (effective because the eigenstates are not pure spin states):

$$\widehat{H} = \mu_B \boldsymbol{B}\cdot\left(g_e\overleftrightarrow{\mathbf{I}} + 2\lambda\overleftrightarrow{\mathbf{\Lambda}}\right)\cdot\hat{\boldsymbol{s}} + \hat{\boldsymbol{s}}\cdot\lambda^2\overleftrightarrow{\mathbf{\Lambda}}\cdot\hat{\boldsymbol{s}}. \quad (1)$$

Here, λ is the spin-orbit coupling constant (which is typically reduced relative to the free-ion value), and $\overleftrightarrow{\mathbf{\Lambda}}$ parameterizes the matrix elements arising from the spin-orbit mixing between excited crystal-field states (at energy ε_i) and the orbital singlet ground state (at energy ε_o); it should be noted that $\overleftrightarrow{\mathbf{\Lambda}}$ contains the energy denominators, $\Delta_i = \varepsilon_i - \varepsilon_o$. The remaining quantities in Eq. (1) include the effective spin operator, $\hat{\boldsymbol{s}}$, the identity matrix, $\overleftrightarrow{\mathbf{I}}$, the free electron Landé g_e-value, and the Bohr-magneton, μ_B. Equation (1) simplifies to the more familiar form [11, 12]:

$$\widehat{H} = \mu_B \boldsymbol{B} \cdot \overleftrightarrow{g} \cdot \hat{\boldsymbol{s}} + \hat{\boldsymbol{s}} \cdot \overleftrightarrow{d} \cdot \hat{\boldsymbol{s}}, \tag{2}$$

where $\overleftrightarrow{g}$ and $\overleftrightarrow{d}$ represent effective Landé and zero-field-splitting (zfs) tensors, respectively; lowercase $\overleftrightarrow{d}$ is employed here to differentiate the single-ion case from the giant spin approximation (GSA) discussed below. The spin multiplicity of the ground state gives rise to $2s+1$ eigenstates that, in the absence of spin-orbit coupling, would be degenerate in zero applied magnetic field. In the typical cw EPR experiment, a swept magnetic field is employed in order to vary the Zeeman energy spacing between m_s spin-projection states. Resonant absorption of microwaves then occurs when the spacing between states connected by the magnetic dipole selection rule ($\delta m_s = \pm 1$) is equal to the microwave energy quantum, hv, resulting in $2s$ distinct EPR transitions. In the isotropic ($\lambda = 0$) case, these transitions would all occur at the same resonance field, $B_{res} = hv/g\mu_B$ ($\equiv 1$ T for a microwave frequency of 28 GHz), i.e., just a single resonance would be observed (neglecting electron-nuclear hyperfine couplings). For the anisotropic case, the second term in Eq. (2) lifts the zero-field degeneracies between states with different absolute m_s values, resulting in a separation of the $2s$ distinct EPR transitions observed in a field-swept single-crystal EPR experiment (see Fig. 1 and discussion below). For a tetragonal crystal-field, the separation between successive EPR peaks is given by $\Delta B_{res} = 2d_{zz}/g\mu_B$, where d_{zz} is the only non-zero (uniaxial) component of the $\overleftrightarrow{d}$ tensor. One thus sees that the more anisotropic the system, the greater the field range [$= (2s-1)\,\Delta B_{res}$] over which the full EPR spectrum extends. Moreover, in order to access many of the EPR transitions, the microwave quantum, hv, must exceed the zfs for cases with $s > ½$. For many transition metal complexes, these constraints require EPR spectrometers that operate over magnetic field and frequency ranges that far exceed those of commercial instruments. Hence, most of the data found in the literature on highly anisotropic molecular magnets have been recorded on home-built spectrometers, many of which are located at major user facilities such as the high magnetic field laboratories in Dresden/Grenoble [14] and Florida [15, 16], or terahertz light sources such as BESSY in Berlin [17].

The magnetic anisotropy discussed above also lies at the heart of SMM physics [12, 18]. Again, considering the uniaxial case with $d_{zz} < 0$ (easy-axis anisotropy), the spin "up" and "down" states with $m_s = \pm s$ lie lowest in energy. Therefore, in

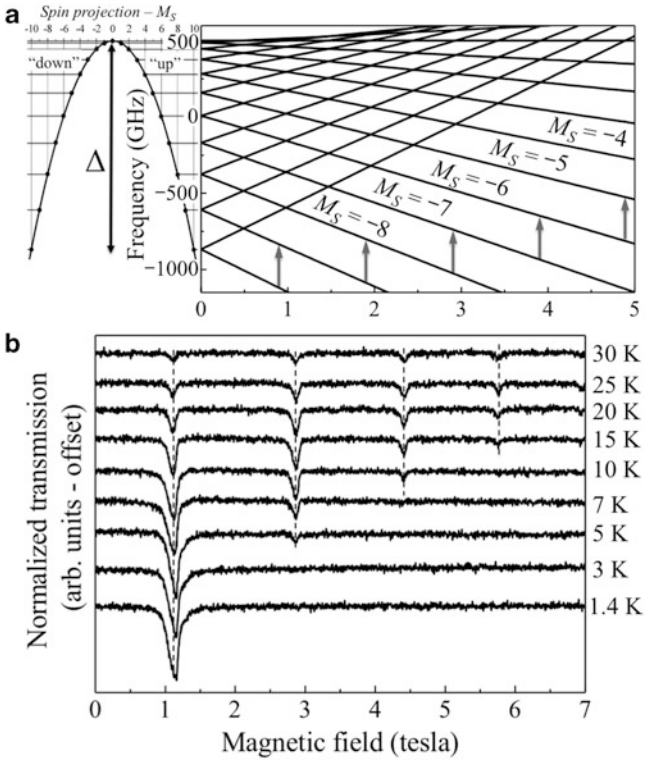

Fig. 1 (**a**) Zeeman diagram generated for spin $S = 10$ according to a purely second-order giant spin Hamiltonian, with $D = -0.66$ K, $E = 0$, and $H//z$. The eigenstates are plotted versus the spin projection, M_S, on the left to make a connection to the parabolic energy barrier (Δ) separating spin-up and down states. Several possible EPR transitions are marked by *vertical gray arrows* in the main panel. (**b**) Temperature dependence of the easy-axis ($H//c$) HFEPR spectra for $Mn_{12}Bu^tAc$ at a frequency of 336 GHz. Adapted with permission from [13]. Copyright 2013 American Chemical Society

order for an "up" spin to reverse its orientation, it must overcome an energy barrier created by the higher-lying intervening spin projection states with $|m_s| < s$. However, in nearly all cases [19], quantum fluctuations (through barrier tunneling) prevent complete blocking of the magnetic moment associated with a single 3*d* ion. For this reason, all of the early work on SMMs involved large, polynuclear transition metal clusters with giant ferro- or ferrimagnetically coupled spin ground states. The stabilization of a giant (~mesoscopic) spin moment suppresses quantum fluctuations, leading to the situation in which the $20\mu_B$ magnetic moment associated with the $S = 10$ $Mn_{12}Ac$ SMM completely blocks below ~4 K [1, 20, 21]. A full treatment of the exchange coupling between twelve anisotropic spins is computationally challenging [20]. However, in many SMMs (including Mn_{12} and Fe_8), these couplings are sufficiently strong that one may approximate the low-energy/low-temperature physics by assuming the spins to be rigidly coupled, giving rise to an effective molecular giant spin, *S*, ground state [3, 12].

The GSA allows for a description of the low-energy magnetic spectrum of a SMM using the Hamiltonian of Eq. (2), albeit with the single-ion spin operator, $\hat{\boldsymbol{s}}$, replaced by a corresponding giant spin operator, $\hat{\boldsymbol{S}}$ [12]. One can diagonalize (rotate) and renormalize the molecular $\overleftrightarrow{\boldsymbol{D}}$ tensor such that the second-order zfs is expressed in terms of just two parameters: the well known axial and rhombic anisotropy parameters D and E, respectively. When written in this form, the second term in Eq. (2) becomes $D\hat{S}_z^2 + E\left(\hat{S}_x^2 - \hat{S}_y^2\right)$. Figure 1a shows the Zeeman energy level diagram obtained using the above Hamiltonian for an easy-axis ($D < 0$) $S = 10$ system such as $Mn_{12}Ac$ (with E set to zero), with the magnetic field applied parallel to the easy-axis. The zero-field spectrum is shown to the left of the Zeeman diagram, illustrating the potential energy barrier ($\Delta = DS^2$) separating spin "up" and "down" states; the D ($= -0.66$ K) parameter employed for Fig. 1a was chosen to approximately mimic the $Mn_{12}Ac$ SMM [22] (note – 1,000 GHz $\equiv$ 48 K $\equiv$ 33.3 cm^{-1}). The first thing to note is the ~300 GHz zero-field separation between the $M_S = \pm 10$ and ± 9 states. Frequencies in excess this zfs are therefore required in order to excite EPR transitions from the lowest-lying $M_S = -10$ Zeeman level. A single-crystal EPR experiment performed in the high-field/frequency limit would result in $2S$ ($= 20$ for $Mn_{12}Ac$) evenly spaced easy-axis resonances, with a spacing given by $\Delta B_{res} = 2D/g\mu_B \approx D/\mu_B \approx 1$ T for the D parameter employed in Fig. 1a; representative transitions responsible for such resonances are indicated by vertical gray arrows in Fig. 1a.

Figure 1b shows actual 336.3 GHz absorption mode EPR spectra obtained for a single-crystal sample of the high-symmetry $[Mn_{12}O_{12}(O_2CCH_2Bu^t)_{16}(CH_3OH)_4]\cdot CH_3OH$ ($Mn_{12}Bu^tAc$) SMM, with the magnetic field applied parallel to its magnetic easy-axis [13, 22–26]. The first thing to note is the uneven spacing between EPR transitions, and the fact that these spacings significantly exceed the $\Delta B_{res} \approx 1$ T predicted above ($Mn_{12}Ac$ and $Mn_{12}Bu^tAc$ have virtually identical Hamiltonian parameters [22]). These observations immediately highlight limitations of the second-order perturbative Hamiltonian of Eq. (2). First and foremost, the second-order zfs Hamiltonian possesses rigorous D_{2h} symmetry (or $D_{\infty h}$ when $E = 0$) [12], which is incompatible with the local S_4 point group ($I\overline{4}$ space group) symmetry appropriate to many Mn_{12} SMMs [18, 22]. In particular, E is strictly forbidden for $Mn_{12}Bu^tAc$, and it is clear that a single D parameter cannot account for the uneven spacing of the EPR transitions seen in Fig. 1b. It was recognized early on [3, 4] that one could simulate the HFEPR spectra of $Mn_{12}Ac$ using extended Stevens operators to account for the zfs interactions [12], i.e.,

$$\hat{H}_{zfs} = \sum_{p}^{2S} \sum_{q=0}^{p} B_p^q \hat{O}_p^q, \tag{3}$$

where $\hat{O}_p^q\left(\hat{S}_x, \hat{S}_y, \hat{S}_z\right)$ represent the operators [27, 28], and B_p^q the associated phenomenological (or effective) zfs parameters. The subscript p denotes the order

of the operator, which must be even because of the time reversal invariance of the spin-orbit interaction; the order is also limited by the total spin of the molecule ($p \leq 2S$). The superscript q ($\leq p$) denotes the rotational symmetry of the operator about the quantization (z-) axis. The summation in Eq. (3) includes the second-order axial anisotropy with $D = 3B_2^0$ and $E = B_2^2$; therefore, the more general GSA Hamiltonian is obtained by replacing the last term in Eq. (2) by $\hat{H}_{\text{zfs}}$.

Use of extended Stevens operators enables application of the effective spin Hamiltonian formalism to almost any SMM, as well as many other MNs, irrespective of symmetry or spin state. A drawback of this approach is the fact that it can be challenging to relate the obtained phenomenological B_p^q parameters to the microscopic structural details of the molecule under investigation; we come back to this issue further below. Nevertheless, the GSA has proven remarkably successful in terms of explaining many low-temperature magnetic properties of SMMs, including spectacular effects due to quantum tunneling and quantum interference, as seen in magnetization hysteresis measurements [12]. HFEPR has played an essential role in understanding these phenomena by providing direct access to an underlying spin Hamiltonian (in this case the GSA). In fact, at a very basic level, quantum tunneling of magnetization (QTM [29, 30]) measurements can be thought of as a zero-frequency EPR experiment given that hysteresis loop steps are observed at the level-crossings seen in Fig. 1a [separated by $\Delta B_{\text{QTM}} \approx D/g\mu_B \approx 0.5$ T]. Thus, one can extract D and higher-order ($p > 2$) diagonal ($q = 0$) terms from the locations of magnetization steps seen in hysteresis loop measurements performed with the field applied parallel to the magnetic easy-axis [12]. Meanwhile, off-diagonal ($q \neq 0$, tunneling) terms can, in principle, be deduced from QTM rates and quantum interference measurements [31]. However, such studies have only been performed for a handful of SMMs to date, primarily because of the need to employ specialized high-sensitivity magnetometers (micro-SQUID [31] or micro-Hall [32]), and because experiments must be performed well below the blocking temperature (typically $\ll 1$ K) using dilution refrigerators.

A drawback of the magnetic measurements described above is that hysteresis loop steps occur at field locations that depend both on the field-independent interactions, $\hat{H}_{\text{zfs}}$, and the field-dependent Zeeman interaction. Thus, it can be difficult to simultaneously constrain both the g tensor and zfs parameters. This is where HFEPR becomes extremely powerful. By performing measurements at multiple high-frequencies, one can independently constrain the field-dependent (Zeeman) and field-independent (zfs) interactions [32]. For a uniaxial SMM, application of a field parallel to z (easy-axis) ensures that the Zeeman interaction appears on the diagonal of the spin Hamiltonian. The effects of the off-diagonal ($q \neq 0$) zfs interactions are negligible in this situation because the EPR spectrum is dominated by the lowest-lying Zeeman levels ($M_S = -10, -9, -8\ldots$), and these are mostly protected from each other, i.e., they do not cross. Even those low-lying states that do cross (e.g., $M_S = +10$ and -9, $M_S = +10$ and -8) are largely immune to the off-diagonal terms because of the enormous differences in spin projection: the symmetry-allowed $\hat{O}_4^4 \equiv \frac{1}{2}\left(\hat{S}_+^4 + \hat{S}_-^4\right)$ interaction connects $M_S = +10$ and -6

($\Delta M_S = 16$) only as a fourth-order perturbation; this is the reason why the quantum relaxation is so slow at these (avoided) level crossings, i.e., the tunneling rates (gaps) are incredibly small (~Hz for the first few resonances for Mn_{12}). Consequently, the easy-axis HFEPR peak positions vary linearly with applied field, as seen in Fig. 2a, which plots multi-frequency single-crystal data for $Mn_{12}Bu^tAc$ [26]. Fits to these data yield g_z, D, B_4^0 and, in principle, higher order $q = 0$ terms; g_z is constrained by the slope of the lines through the data points, while the remaining parameters dictate the field-independent spacings between the data points. Because these measurements are spectroscopic, they provide extremely tight constraints on the axial zfs parameters. As such the obtained values are far more reliable than those deduced from thermodynamic measurements (magnetization, susceptibility, etc.) that yield data sets with relatively little information content.

The remaining off-diagonal ($q \neq 0$) terms are obtained by applying a large magnetic field transverse to the easy axis. In this situation, the now dominant Zeeman interaction dictates the quantization axis so that previously off-diagonal terms appear along the diagonal of the spin Hamiltonian [32]. The components of the g- and zfs tensors can then be picked off by applying a magnetic field along different axes of a single crystal – see Fig. 2. In practice, such experiments are extremely challenging and time consuming, requiring a cavity (for sensitivity to small crystals) and two-axis rotation capabilities. Consequently, only a few such examples involving SMMs can be found in the literature [23, 32–40]. A more direct approach involves studying a finely ground powder sample. In this situation, all crystal orientations contribute equally to the EPR absorption (provided the powder is constrained). By recording the spectrum in derivative mode (using field modulation), features emerge that correspond to the turning points in the full two-axis, angle-dependent EPR spectrum, i.e., the hard, intermediate, and easy directions, corresponding to x, y, and z for a rhombic system. Example powder HFEPR spectra are displayed in Fig. 3 for the biaxial Fe_8 SMM [5], illustrating good separation of the x, y, and z components. However, powder measurements typically require a lot of sample (>50 mg) because the EPR absorption now extends over the entire spectrum [$\Delta B_{spec} = 2D\ (2S-1)/g\mu_B$], as opposed to being concentrated within just a few sharp resonances. Moreover, the act of making a powder can affect sample quality, particularly in cases involving volatile lattice solvent molecules (discussed below [41]). Lastly, one does not know a priori where the turning points in the spectrum should occur, thus making it difficult to know exactly which zfs interactions contribute to the anisotropy in the hard plane of a SMM [32]. One can, in principle, invoke symmetry arguments to eliminate certain possibilities. But this does not always work for low-symmetry crystals.

Using microwave resonators, HFEPR studies of very small (~0.1 mm^3 or ~100 μg) single-crystal samples of high quality become feasible [16]. Field rotation studies then provide direct information on the symmetries of the dominant transverse zfs operators, as illustrated by the data in Fig. 2c for $Mn_{12}Ac$ [34]. In this case, the HFEPR spectrum consists of several contributions due to the existence of multiple species of Mn_{12} molecule possessing different zfs parameters.

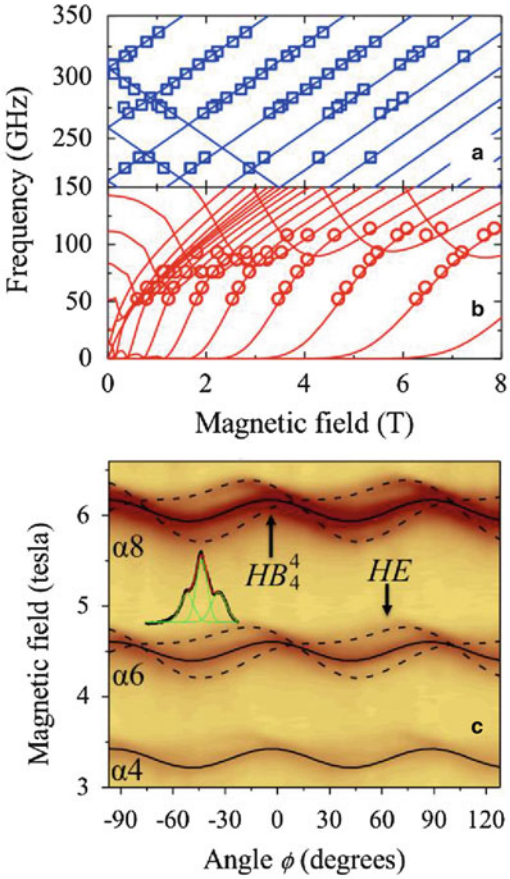

Fig. 2 (**a**) Fits to the frequency dependence of easy-axis HFEPR peak positions for a $Mn_{12}Bu^tAc$ single-crystal (see Fig. 1b and [24]); (**b**) corresponding fits to the hard-plane peak positions. The easy-axis data constrain the axial (*z*-) components of the spin Hamiltonian, while the hard-plane data constrain the transverse components (see main text). (**c**) 2D contour plot of the $T = 15$ K HFEPR absorption intensity versus magnetic field strength and its orientation, ϕ, within the hard (*xy*-) plane for a deuterated d-$Mn_{12}Ac$ single-crystal (from [24]). The *darker shades* correspond to stronger absorption and the resonances have been labeled according to the scheme described in [33]. Each resonance consists of multiple components (see *inset*): the central peak exhibits pure fourfold symmetry, whereas the low- and high-field shoulders exhibit a superposition of two and fourfold behavior. Fits to the central peak (*solid lines*) and the shoulders (*dashed lines*) are superimposed on the plot, and the approximate orientations of the hard-axes associated with the intrinsic B_4^4 (HB_4^4) and extrinsic E (HE) interactions are indicated. Adapted with permission from [24]. Copyright 2005 Elsevier

The dominant central portion of the spectrum (due to ~50% of the molecules) exhibits a fourfold rotational symmetry, with turning points separated by 45° [not the 90° expected on the basis of the second order rhombic Hamiltonian of Eq. (2)]. One would not know this from a powder measurement, although symmetry

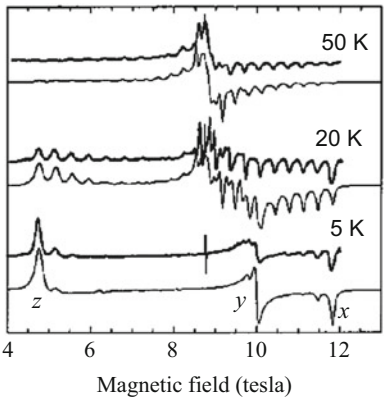

Fig. 3 Powder HFEPR spectra of the Fe_8 SMM at 245 GHz at the three indicated temperatures. The *upper curve* for each temperature corresponds to the experimental spectrum, while the *lower curve* is the simulated spectrum The x, y, and z components of the spectrum are labeled. Adapted with permission from [5]. Copyright 1996 EDP Sciences

considerations suggest that the dominant transverse zfs interactions should posses fourfold symmetry. Closer inspection of the edges of the spectrum reveals satellite peaks that exhibit a superposition of four and twofold rotation patterns [33]. There are two such components (each corresponding to ~25% of the molecules) shifted by 90° so that the summed spectrum retains overall fourfold symmetry. Therefore, roughly 50% of the molecules in a $Mn_{12}Ac$ crystal experience a significant rhombic zfs interaction: 25% with $E > 0$ and 25% with $E < 0$, so that the average rhombicity (symmetry) is zero (fourfold). Here, one sees the remarkable detail that one can obtain from such a spectroscopic measurement; there is no way this amount of information could be extracted from thermodynamic studies. The findings have been correlated both with structural studies [42], INS [43] and magnetic hysteresis measurements in which the rhombic interaction is found to influence the quantum relaxation behavior [44]. The rhombicity is attributed to a discrete disorder associated with an acetic acid solvent molecule that directly influences the coordination (and hence the Jahn-Teller distortion) at one of the Mn^{III} sites. Further details of this solvent induced disorder are given in the following section and can be found in [32–34, 42, 43].

2.2 *Applications of cw EPR*

In spite of the need for very high EPR frequencies (>300 GHz, or >3× the highest frequency available at the time commercially), the Mn_{12} family of SMMs has attracted by far the most interest up to now. There are many reasons for this, foremost among them being the fact that $Mn_{12}Ac$ was the first SMM, boasting the highest blocking temperature until just a few years ago. Indeed, $Mn_{12}Ac$ has sometimes been used as a model system for demonstrating the efficacy of newly developed terahertz spectrometers [17, 45] and EPR techniques [46, 47]. Meanwhile, $Mn_{12}Ac$ has presented many mysteries as well. For example, a complete microscopic understanding of resonant QTM rates remains elusive [12]. The S_4

symmetry of the idealized $Mn_{12}O_{12}$ core is so close to being cylindrical that one expects the quantum tunneling at most of the level crossings (QTM resonances) in Fig. 1 to be strictly forbidden. The reason for this can be traced back to the second order effective single-ion spin Hamiltonian of Eq. (2). When one projects the collective single-ion anisotropies onto the molecular spin $S = 10$ ground state, the transverse component of the second order molecular anisotropy $E\left(\hat{S}_x^2 - \hat{S}_y^2\right)$ exactly cancels [12], i.e., E is strictly forbidden on symmetry grounds (one can think of this as a vector addition in which the transverse components exactly sum to zero). Consequently, QTM would be strictly forbidden in all resonances for an ideal Mn_{12} molecule if the second order Hamiltonian told the entire story. As discussed below, there are several mechanisms that can give rise to higher order transverse anisotropies in the molecular Hamiltonian [Eq. (3)] that are compatible with S_4 symmetry, e.g., $B_4^4 O_4^4 \equiv \frac{1}{2} B_4^4 \left(\hat{S}_+^4 + \hat{S}_-^4\right)$. Nevertheless, these terms are quite weak, and they cannot explain the fact that QTM is observed at all resonances in Fig. 1. However, it does not require much of a distortion to the ideal molecular symmetry to result in a rapid re-emergence (non-cancelation) of the second-order transverse anisotropy, which can dramatically accelerate QTM rates. Therefore, many theoretical and experimental studies have focused on the role of disorder and other factors that influence the QTM relaxation in Mn_{12} SMMs [12, 13, 18, 22–26, 32–34, 42–62].

Perhaps the best illustration of the influence of disorder in SMM crystals involves an early curiosity associated with $Mn_{12}Ac$. It had been recognized since some of the first investigations that roughly 5–8% of the sample relaxes much faster than the canonical high-symmetry Mn_{12} species [63]. The faster relaxing molecules are found in all samples and are believed to be randomly distributed throughout the crystal [48, 64]. They can be detected either from AC susceptibility measurements, where they give rise to a small out-of-phase peak at temperatures well below that of the main species [26], or in low-temperature hysteresis studies where they relax at much lower fields than the main species [48]. Detailed synthetic work, involving ligand substitution and crystallization from a variety of solvents, resulted in the discovery of many different forms of Mn_{12} possessing the same neutral $Mn_{12}O_{12}$ core (see, e.g., [13, 22, 26, 38, 53, 65, 66], or [67] for a comprehensive review). These Mn_{12} complexes can be grouped broadly into two categories [38, 67]: (1) fast-relaxing (FR) and (2) slow relaxing (SR). Indeed, a histogram of the effective magnetization relaxation barriers (deduced from frequency-dependent AC susceptibility measurements), for around 20 different Mn_{12} complexes, reveals a bimodal distribution ([48] and Hendrickson, private communication) with values in the 25–45 K range for the FR species and the 60–80 K range for the SR species. In many of the cases where the FR species was obtained in single-crystal form, it was found that one or more of the Jahn-Teller elongation axes associated with the Mn^{III} atoms was abnormally oriented [38, 53, 65] in comparison to the usual SR form [1, 13, 22, 26], thereby significantly lowering the symmetry of the Mn_{12} core.

Single-crystal HFEPR studies provided crucial insights into the reduced relaxation barrier associated with the FR form of Mn_{12}, and the importance of lattice

solvent molecules [38]. Measurements were performed on a low-symmetry version of the $Mn_{12}Bu^tAc$ molecule (that co-crystallizes with $CH_2Cl_2/MeNO_2$ solvents [65]) in which the Jahn-Teller distortion associated with one of the Mn^{III} atoms has flipped so that it is close to parallel to the plane of the molecule, in contrast to the other seven which are roughly perpendicular to this plane. HFEPR studies revealed only a moderate (~10%) reduction in the molecular D parameter. However, a very significant molecular E value (~D/6) was found [38]. In other words, the axial anisotropy is only moderately reduced as a result of re-orienting the local anisotropy at one of the eight Mn^{III} sites. The very significant second-order rhombic molecular anisotropy emerges due to non-cancelation of the transverse components of the single-ion anisotropies. In this case, it is the transverse projection of the axial anisotropy (d) associated with the abnormally oriented Jahn-Teller axis that gives rise to the large molecular E value. In turn, this causes very strong mixing of (or tunneling between) M_S states well below the top of the barrier generated purely on the basis of the axial $D\hat{S}_z^2$ term (see Fig. 1a) [38]. Thus, spins can relax via states well below the top of the classical barrier, explaining the observed fast relaxation behavior. The HFEPR studies were extremely challenging due to the low symmetry structure and because the crystals rapidly lose solvent, leading to a loss of crystallinity. In fact, AC susceptibility studies show that the loss of volatile $CH_2Cl_2/MeNO_2$ solvent leads to a conversion of the FR species into the SR form, and subsequent recrystallization of the dried product from a CH_2Cl_2/MeCN mixture gives good crystals of the pure SR form [65]. Putting everything together, one clearly sees here the dramatic influence of the solvent and subtle crystal packing forces on the quantum properties of SMMs.

The quantum properties of the SR $Mn_{12}Ac$ species are also influenced by an intrinsic disorder associated with the co-crystallizing acetic acid solvent [32]. In fact, this disorder was recognized early on from EPR line-width studies that suggested significant strains (distributions) in the molecular D parameters for both the Fe_8 and $Mn_{12}Ac$ SMMs ($\sigma_D \sim 0.01 - 0.02D$) [45, 49–52]. However, the importance of the disordered solvent was made on the basis of combined X-ray and powder HFEPR studies [42]. The acetic acid forms a hydrogen-bond to the $Mn_{12}O_{12}$ core, resulting in a distortion of the coordination environment around one of the eight Mn^{III} atoms. Although each solvent molecule occupies a position between adjacent Mn_{12} molecules, it can hydrogen-bond to only one of them, resulting in a statistical distribution of solvent isomers with either 0, 1, 2, 3, or 4 hydrogen bonding interactions to the acetic acid. A small fraction of these isomers maintain S_4 symmetry, while the remainder adopt a lower symmetry. Ligand-field calculations show that the low-symmetry isomers acquire non-negligible molecular E values, again due to imperfect cancelation of the transverse components of the second-order single-ion anisotropies [42]. However, the Jahn-Teller axes remain approximately parallel, so the effect is far weaker than the case of the FR Mn_{12} species. Consequently, the influence of the disorder on the QTM relaxation is subtle, albeit measurable [32, 44]. Meanwhile, the solvent isomerism is very apparent in angle-dependent single-crystal HFEPR measurements (a subset of

these data are displayed in Fig. 2c [32–34]). In particular, it is found that the low-symmetry isomers have their easy-axes tilted slightly away from the average crystallographic S_4 (c-) axis; the half-width of the distribution is less than 1° [18, 33], illustrating the remarkable resolution of the EPR technique. Moreover, the tilting and rhombicity (see Fig. 2c) are correlated, as expected on the basis of the solvent isomer model [42].

The original $Mn_{12}Ac$ can be modified to obtain new high-symmetry Mn_{12} SMMs [13, 22–26]. Approaches include substitution of the acetate ligand with bulkier ones such as $BrCH_2CO_2^-$ (BrAc [23, 26]), or $Bu^tCH_2CO_2^-$ (Bu^tAc [13, 24, 25]); water molecules may also be exchanged with alcohols [22]. These modifications primarily influence the environment of the $Mn_{12}O_{12}$ molecule, without affecting internal couplings. Therefore, the $S = 10$ ground state is retained. To date, three new high-symmetry Mn_{12}s have been synthesized and interrogated by HFEPR. They include: $[Mn_{12}O_{12}(O_2CCH_2Br)_{16}(H_2O)_4]\cdot 4CH_2Cl_2$ ($Mn_{12}BrAc$ [23–26]), $[Mn_{12}O_{12}(O_2CCH_2Bu^t)_{16}(MeOH)_4]\cdot CH_3OH$ ($Mn_{12}Bu^tAc$ [13, 24, 25]), and $[Mn_{12}O_{12}(O_2CCH_3)_{16}(CH_3OH)_4]\cdot CH_3OH$ [$Mn_{12}Ac/CH_3OH$] [22]. The latter compound is essentially identical to the original $Mn_{12}Ac$ except that the acetic acid solvent is replaced by methanol. All three complexes possess fourfold symmetric crystal structures ($I4_1/a$ for the BrAc and $I\bar{4}$ for the other two). In the latter two compounds, both the Mn_{12} molecule and the single CH_3OH solvent reside on $I\bar{4}$ (S_4) axes and, although the solvent is disordered, it resides far from the Mn_{12} core [13, 18, 22]. Consequently, hydrogen bonding interactions of the kind found in the original $Mn_{12}Ac$ are absent. The situation in the BrAc complex is slightly different [26]. There are hydrogen bonding interactions between solvents and the Mn_{12} core. However, because of the 4:1 ratio of CH_2Cl_2 and Mn_{12}, these interactions do not perturb the S_4 symmetry of the core. Nevertheless, the CH_2Cl_2 solvent is quite volatile.

Careful studies of the three newer high-symmetry Mn_{12} complexes reveal remarkably clean HFEPR spectra, with absolutely no evidence for the solvent isomerism/disorder found in the original $Mn_{12}Ac$ [13, 22–26]. Angle-dependent single-crystal HFEPR spectra for the $Mn_{12}Bu^tAc$ complex exhibit the ideal fourfold behavior expected on the basis of the intrinsic S_4 symmetry of the $Mn_{12}O_{12}$ core [13, 24, 39]. However, measurements performed on the BrAc complex show a considerable degradation of the EPR spectra when the samples are exposed to air for an extended period [18, 22, 26]. This exposure (or, more precisely, removal from the mother liquid) results in a loss of the volatile CH_2Cl_2 solvent from the lattice. Over time, the HFEPR spectra start to resemble those of the original $Mn_{12}Ac$, with simulations suggesting that the solvent loss generates a similar orientational disorder. Moreover, comparisons of QTM measurements performed on pristine and dried samples reveal remarkable differences [26, 68], once again demonstrating that solvent disorder has a profound influence on the QTM dynamics of high-symmetry SMMs. Similar investigations for a Mn_{12} benzoate complex involving combined magnetic and frequency domain magnetic resonance (FDMR [69] – EPR performed in the frequency domain) measurements concluded that

disorder did not influence the QTM relaxation [57]. However, the Mn_{12} benzoate complex possesses a low symmetry structure to begin with, i.e., it belongs to the FR species [67]. Therefore, it would require an inordinate degree of disorder to accelerate the QTM relaxation beyond the rate dictated by the intrinsic second-order transverse anisotropy. In a related study, it was argued that differences in relaxation found for $Mn_{12}Ac$ and $Mn_{12}Bu^tAc$ are due to differences in dipolar field distributions [62], which are known to play a role in mediating the collective quantum dynamics in SMM crystals [70]. However, this study ignored the documented disorder in $Mn_{12}Ac$ [42]. Instead, comparisons between $Mn_{12}Ac$ and $Mn_{12}Ac/CH_3OH$ allow for an unbiased assessment of this controversy because they have the same structures and, hence, the same dipolar field distributions [12]. HFEPR studies reveal essentially identical axial anisotropy parameters (D and B_4^0), within the experimental uncertainty. Meanwhile, the measured effective relaxation barrier is measurably lower for $Mn_{12}Ac$, demonstrating that the intrinsic solvent disorder increases QTM (M_S state mixing) and promotes under-barrier relaxation [22].

Comparisons of EPR spectra obtained across families of closely related compounds (e.g., Ni_4, Mn_3, and Mn_4) demonstrate that the solvent-free complexes (when they exist) consistently exhibit much sharper spectral features [12, 41, 71]. Stated differently, solvent-containing compounds tend to suffer from disorder that causes significant inhomogeneous broadening (D, E, etc., strain) of the EPR spectra; in some cases, the differences in EPR line-widths can be a factor of 10 between the solvent-containing and solvent-free members of a family that otherwise possess identical molecular cores and identical axial anisotropy parameters [41]. It is assumed that the disorder is related primarily to the loss of solvent from the lattice, although the solvent molecules themselves can be disordered as well. Samples containing more volatile solvents tend to display more disorder [26, 72]. It is therefore not surprising that combined HFEPR and QTM investigations of solvent-free SMMs have revealed important new insights into the physics of SMMs [12, 73–79]. Foremost among these is the clear observation of QTM selection rules dictated by the intrinsic C_3 symmetry of a triangular Mn_3 SMM [75].

In comparison to other bulk low-energy spectroscopic probes (e.g., INS and FDMR), cw HFEPR offers exceptional sensitivity and energy resolution. Indeed, the instrument resolution is limited primarily by the specifications of the magnet (<10 ppm is achievable [80]). The true resolution is therefore usually limited by sample quality. The availability of solvent-free crystals combined with the high resolution of EPR has thus enabled many detailed studies (beyond those described so far) that have made important contributions to the current understanding of MNs. Several such studies have focused on the origin of higher order ($p > 2$) terms in the GSA (Eq. (3) [12, 35, 37, 39, 40, 71, 74–78, 81]). Ligand-field calculations based on non-perturbative methods are known to generate fourth order corrections to Eq. (2) [82], and these terms can in principle survive when projected onto the ground spin state of a multinuclear SMM. However, single-ion zfs interactions of order greater than 2 are strictly forbidden for a spin $s = 1$ ion such as Ni^{II} due to the limited

dimension (3×3) of the Hamiltonian matrix. The S_4-symmetric solvent-free $[Ni(hmp)(dmb)Cl]_4$ (Ni_4) cluster therefore serves as an interesting case study, given that single-crystal HFEPR studies similar to those presented in Fig. 2 reveal significant fourth-order GSA parameters (both B_4^0 and B_4^4) associated with the $S = 4$ ground state [35–37]. Due to the relatively small size of this molecule one can employ a microscopic Hamiltonian that separately takes into account the local spin-orbit anisotropy at each Ni^{II} site, together with the exchange coupling between the ions [74]:

$$\widehat{H} = \sum_{i=1}^{4} \left(\mu_B \boldsymbol{B} \cdot \overleftrightarrow{g}_i \cdot \hat{\boldsymbol{s}}_i + \hat{\boldsymbol{s}}_i \cdot \overleftrightarrow{d}_i \cdot \hat{\boldsymbol{s}}_i \right) + \sum_{i<j}^{4} \hat{\boldsymbol{s}}_i \cdot \overleftrightarrow{J}_{ij} \cdot \hat{\boldsymbol{s}}_j. \tag{4}$$

As can be seen from comparisons with Eq. (2), the first summation accounts for the second-order local anisotropy and Zeeman interaction at the four Ni^{II} sites (labeled by the index i). The second summation parameterizes the exchange interactions between spins i and j. Equation (4) perfectly reproduces the single-crystal HFEPR data for Ni_4, including the uneven easy-axis peak spacings (attributed to B_4^0 within the GSA description), and the fourfold symmetry obtained from angle-dependent measurements (attributed to B_4^4 within the GSA) [35–37]. Moreover, independent HFEPR measurements of the $\overleftrightarrow{d}_i$ tensors, including their orientations, was made possible by studying a solid solution sample of $[Ni_xZn_{1-x}(hmp)(dmb)Cl]_4$ ($x = 0.02$) [83]. Therefore, the only adjustable parameter in the fits to the HFEPR data was the exchange coupling constant, J, which was assumed to be isotropic and the same for all contacts. In other words, the apparent fourth order anisotropy is connected with the exchange coupling within the cluster.

As noted previously, one can determine the second-order anisotropy for a coupled spin system via a procedure that involves projecting the individual second-order anisotropies onto the molecular spin state [74, 84]. However, this procedure is only exact as long as the molecular spin quantum number is exact. If the exchange coupling within a molecule is weak, excited spin states will mix with the ground state. In such situations, the projection method is approximate. One still expects the second-order transverse components to cancel for situations in which the molecular symmetry forbids a rhombic anisotropy, e.g., tetragonal Mn_{12} and Ni_4, or trigonal Mn_3 [12]. However, the transverse components can emerge at higher orders in these situations via the mixing with excited states. By performing a numerical mapping between the parameters employed in the two models [Eqs. (3) and (4)], one finds that the higher order GSA terms scale as inverse powers of the exchange coupling, i.e., $|J|^{-n}$, where $2n = p - 2$ [74, 77]. In essence, the interaction (mixing) between spin multiplets renormalizes the energies within each multiplet. The extent of the mixing depends on the proximity of excited spin states. The renormalization is then captured by adding higher order terms to the GSA Hamiltonian: fourth-order terms arise through first-order mixing, with the energy denominator given by the appropriate multiplet spacing, which is proportional to J, i.e.,

$B_4^4 \propto |J|^{-1}$; sixth-order terms arise through second-order mixing, i.e., $B_6^6 \propto |J|^{-2}$, and so on [12, 77]. These ideas have been beautifully verified through detailed HFEPR studies on Ni_4 [35–37], Fe_3Cr [40], Mn_3 [73–77], Mn_4 [78, 79], a $Mn_{3\times3}$ grid [81], and even Mn_{12} [38]. Importantly, these findings demonstrate that EPR can provide detailed information about the exchange interactions within a SMM, something that was previously thought to be possible only via INS. The magnetic dipole selection rules forbid inter-spin-state transitions. However, the aforementioned spin-state mixing provides indirect access to the exchange physics, and inter-spin transitions can even become allowed in situations where the mixing is strong [81, 85, 86]. Another important conclusion concerns situations with little or no symmetry, where it is clear that any of the terms in Eq. (3) can exist [77]. This has important implications for QTM selection rules, suggesting that disorder can cause tunneling in any resonance, thereby perhaps explaining why intrinsic symmetry enforced QTM selections rules were only observed recently in a solvent free SMM [12, 87]. On the flip side, these investigations demonstrate that one should in principle be able to completely switch off quantum tunneling in high symmetry SMMs if strong enough exchange coupling can be achieved, because all of the symmetry allowed transverse GSA interactions scale as $|J|^{-n}$.

Until fairly recently, most SMM research was directed towards polynuclear 3*d* transition metal clusters, with the synthetic goal of maximizing both the molecular spin state and the cluster anisotropy [88, 89]. However, a number of factors have limited progress based on this strategy, with the record blocking temperature for a Mn_6 cluster [88] only just surpassing that of the original Mn_{12} SMM [1]. Limiting factors include: (1) a tendency for exchange interactions to be both weak (few cm^{-1}) and often antiferromagnetic; (2) the fact that orbital momentum is usually quenched, thus significantly suppressing the magnetic anisotropy; and (3) the difficulties associated with maximally projecting any remaining (second order spin-orbit) axial anisotropy onto the ground spin state of a SMM. HFEPR studies have addressed the latter issue by focusing on families of closely related Mn_3 and Mn_6 SMMs [76, 84, 90, 91], where the Mn_6 molecule can be thought of as a ferromagnetically coupled $[Mn_3]_2$ dimer. A particular attraction is the fact that one can switch the sign of the exchange within the triangular $[Mn^{III}]_3$ units, thereby achieving both high-spin ($S = 6$) and low-spin ($S \lesssim 2$) states (or $S = 12$ and $S = 4$ states in the case of Mn_6). Extensive studies of spin states ranging from $S = 4$ to 12 (also including Mn_{12}) reveal experimental anisotropy barriers that vary by no more than a factor of 2 [76], in spite of the fact that the Jahn-Teller axes on the Mn^{III} ions are reasonably parallel in all cases. The reason for this is again related to the projection of the single-ion anisotropies onto the molecular spin ground state. The molecular *D* value is given by a weighted sum of the anisotropies of the constituent ions (d_i), where the weighting is inversely proportional to the total molecular spin, *S* [84, 92]. Thus, *D* decreases as *S* increases. If all spins are coupled ferromagnetically and their $\overleftrightarrow{d}$ tensors parallel, the theoretical best that one can hope to achieve is a molecular barrier ($\sim DS^2$) that scales linearly with *S* or *N* (the number of spins in the molecule) [76]. Experiments comparing Mn_3 ($S = 6$) and Mn_6 ($S = 12$)

broadly agree with this rule, even though it is exact only in the large N limit. The situation is worse when comparing low-spin and high-spin molecules, where theory predicts a weaker dependence of the barrier on S [84], i.e., the barrier is almost S independent [92]. Again, this is borne out by experiment [76]. Therefore, it is no surprise that the optimum $[Mn^{III}]_N$ SMM has a nuclearity of just six [89]!

Given the above situation, it has become clear that the more direct route to SMMs that can be used in practical devices involves the use of magnetic ions that exhibit considerably stronger magneto-anisotropies than those that have traditionally been used in the synthesis of large polynuclear clusters, e.g., orbitally degenerate transition metal ions, or heavier elements with Hund's-coupled ($\mathbf{J} = \mathbf{L} + \mathbf{S}$) moments and strong crystal-field interactions. Examples include certain high-symmetry and/or low-coordinate 3*d* transition metal complexes (Fe^{I} [19], Fe^{II} [93, 94], Co^{II} [95–97], even Ni^{II} [98]), as well as elements further down the periodic table such as the 4*d*, 5*d*, 4*f,* and 5*f* elements [99–102]. The discovery in 2003 of a SMM comprising just a single lanthanide ion sandwiched within a bis-phthalocyanine structure clearly justifies this approach [99], resulting in an explosion of activity focused mononuclear SMMs. More recent efforts have focused on achieving strong exchange within low-nuclearity complexes (dimers, trimers, etc. [103–107]) of highly anisotropic magnetic ions. This has resulted in SMMs with quite dramatic increases in both their anisotropy barriers and the technologically relevant blocking temperature. The current benchmark is an N_2^{3-} radical bridged Tb_2 complex that exhibits hysteresis all the way up to 14 K and a barrier of ~330 K [106], i.e., a factor of 4 to 5 higher than Mn_{12}.

In spite of the relative simplicity of some of the more recent SMMs in comparison to, e.g., Mn_{12}, the strong anisotropy presents a considerable challenge to the HFEPR community because zfs energies often exceed 20 cm^{-1} ($\cong 0.6$ THz). The FDMR [69] and frequency domain fourier transform (FDFT [17, 108]) techniques both represent forms of broadband low-frequency (THz or far-infrared) optical spectroscopy that can provide access to excitations in this range (up to about 1.5 THz). Moderate magnetic fields may also be applied to distinguish magnetic excitations from electronic ones. This approach is becoming more applicable as more labs acquire/develop the appropriate hardware to perform such measurements. Some representative examples where magnetic excitations in the 20−40 cm^{-1} range have been reported include: hexaaqua Fe^{II} [109]; pentacoordinate Ni^{II} [110]; square planar Co^{III} [111]; and low-spin pseudo-octahedral Mn^{III} [112].

An orthogonal approach to the frequency-domain techniques described above involves taking advantage of very high-field magnets. The idea here is to compete the Zeeman interaction against the field-independent terms in Eq. (2), thereby providing access to HFEPR transitions that are highly constrained by the zero-field anisotropy [97, 98, 113]. Two examples of such measurements are given in Fig. 4: the first involves an octahedral $s = {}^3/_2$ Re^{IV} complex with a biaxial magnetic anisotropy [113]. In this situation, a ground state level-crossing ($m_s = -{}^3/_2, -½$) can be induced upon application of a magnetic field parallel to the hard (z-) axis. The location of the level crossing is directly related to the zero-field gap between

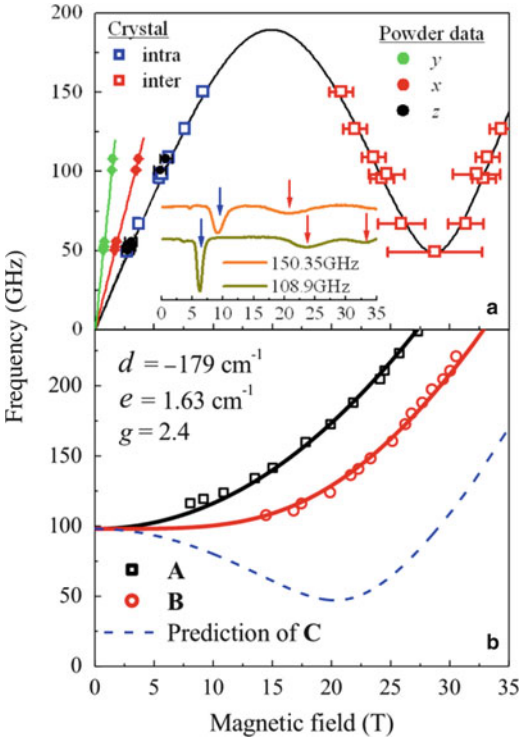

Fig. 4 (**a**) *Main panel*: HFEPR peak positions for a single-crystal of $(NBu_4)_2[ReCl_4(CN)_2]$ at 1.3 K (*open squares*), with the field aligned close to the *z*-axis of the $\overleftrightarrow{d}$ tensor. Intra-Kramers powder peak positions are also included in the low-field region (*solid circles*). The *solid lines* are the best simulations of the peak positions employing Eq. (2). *Inset*: representative high-field spectra obtained at the two indicated frequencies. Reprinted with permission from [113]. Copyright 2012 American Chemical Society. (**b**) HFEPR peak positions for a single crystal of [Ni(Me_6tren)Cl](ClO_4), with the field aligned within the hard plane. A Jahn-Teller distortion gives rise to three molecular orientations, *A*, *B*, and *C*, resulting in multiple resonance branches (see [98] for details). The *solid lines* represent the best fit to Eq. (2) for peaks *A* and *B*, with the obtained zfs parameters given in the figure; the *dashed line* represents the predicted locations of transitions associated with the *C* orientation. Reprinted with permission from [98]. Copyright 2013 American Chemical Society

the two Kramers doublets. Importantly, EPR transitions can be detected at relatively low frequencies (50–100 GHz), in the vicinity of the level-crossing, enabling the use of highly sensitive cavity perturbation methods [16, 114]. Cw HFEPR facilities exist at the US National High Magnetic Field Laboratory (NHMFL) in Florida [115], providing magnetic fields up to 45 T, while experiments at the Dresden High Magnetic Field Laboratory in Germany can be performed in pulsed magnetic fields of up to 70 T [14, 116]. A rough rule of thumb gives 28 GHz/T (~1 cm^{-1}/T for $g = 2$) of tuning, i.e., ~1.3 THz (or 45 cm^{-1}) in Florida and ~2 THz

(or 70 cm^{-1}) in Dresden. These ranges can be extended by combining high-fields and high frequencies (up to 1 THz at both facilities); under the right conditions, the two can add so that zfs energies of order 80–100 cm^{-1} become directly accessible [98]. One may obtain exceptionally tight constraints on all of the relevant parameters of the spin Hamiltonian by conducting measurements over a wide range of frequencies, then performing fits to so-called "Florida Maps" (see, e.g., Fig. 4).

Figure 4b displays a second example involving an orbitally degenerate trigonal-bipyramidal Ni^{II} (d^8) complex with easy-axis anisotropy [98]. The zero-field spectrum consists of a pair of low-lying singlets that are very well isolated from the next singlet on account of an unusually high axial anisotropy associated with this coordination geometry. The low-lying singlets are split by a rhombic e term, which can be directly measured from the zero-field intercept ($=2e$) in Fig. 4b. However, the third singlet is estimated to lie >3 THz above the low-lying singlets, rendering it inaccessible to essentially any currently available EPR spectrometer. A solution to this problem involves application of a magnetic field transverse to the easy-axis, with the goal of reaching a regime where the transition energy/frequency between the low-lying singlet levels depends linearly on the applied field. Extrapolation of the linear region back to zero-field provides a direct measure of the axial anisotropy, in this case the axial d parameter if one chooses to approximate the ion as a spin-only $s = 1$ species. The linear regime has not yet been reached, even at the highest field in Fig. 4b. However, fits to the data suggest a huge d value in the range from -120 to -180 cm^{-1}, which may be a record determination on the basis of EPR [98].

We conclude this section with an example involving a Ho^{III} ($4f^{10}$) SMM encapsulated within a high symmetry polyoxometallate (POM) cage [102]. The encapsulation preserves the intrinsic properties of the nanomagnet outside of a crystal. Consequently, these compounds are of potential interest in terms of the types of molecular spintronics applications discussed in the following section [8, 9]. A significant magnetic anisotropy arises due to a splitting of the Hund's coupled total angular momentum ($\mathbf{J} = \mathbf{L} + \mathbf{S} = 8$) ground state in the POM ligand field. The high symmetry again gives rise to a pair of isolated low-energy singlets, akin to the preceding Ni^{II} example. EPR studies at 50.4 GHz (Fig. 5) reveal a highly anisotropic eight line spectrum corresponding to transitions between the low-lying Zeeman-split $m_J = \pm 4$ components of the $J = 8$ multiplet, split by a strong hyperfine interaction with the $I = 7/2$ Ho nucleus (100% natural abundance) [102]. Meanwhile, X-band (9 GHz) studies reveal the presence of an appreciable zero-field tunneling gap of ~9 GHz between the $m_J = \pm 4$ states, leading to a highly non-linear field-dependence of the spectrum at low-energies (see Fig. 5 [102]). The tunneling gap provides important information concerning the transverse components of the ligand-field that are inaccessible by other experimental methods. It has been postulated that the tunneling gap could provide an optimal operating point for coherent spin manipulations at X-band, which leads naturally into the next section dealing with pulsed EPR applications.

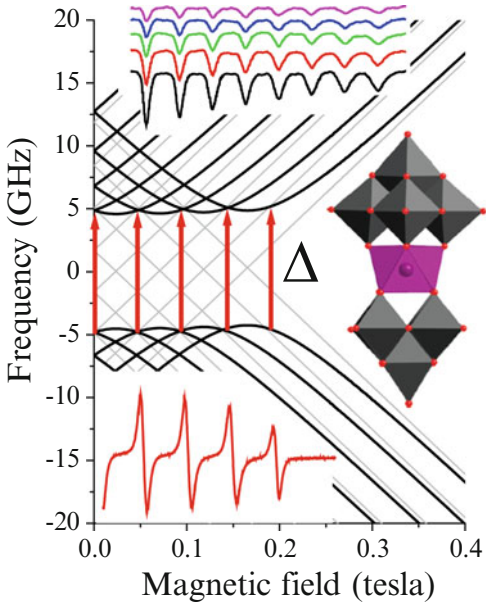

Fig. 5 Multi-frequency, single-crystal EPR spectra for a $Na_9[Ho_{0.25}Y_{0.75}(W_5O_{18})_2]$ complex (*right inset*), with the field applied parallel to the *z*-axis of the zfs tensor. Measurements at 50.4 GHz (*top*) reveal an eight-line spectrum corresponding to transitions within the lowest $m_J = \pm 4$ crystal field levels of the Hund's coupled $J = 8$ ground state, split by a strong hyperfine interaction with the $I = 7/2$ Ho^{III} nucleus. 9.7 GHz measurements (*lower-left*) reveal the presence of an appreciable tunneling gap, $\Delta \approx 9$ GHz, between the $m_J = \pm 4$ states, leading to a highly non-linear field-dependence of the Zeeman levels at low-frequencies (main panel – *dark curves*). The 50.4 GHz data constrain the *z*-components of the Landé and hyperfine tensors, while the 9.7 GHz data indicate the existence of a significant off-diagonal $B_4^4 \hat{O}_4^4$ crystal-field interaction (*faint lines* denote the Zeeman levels in the absence of this interaction). Reprinted with permission from [102]. Copyright 2012 Royal Society of Chemistry

2.3 Pulsed EPR

We conclude this section on EPR by briefly reviewing the growing number of recent pulsed EPR studies involving MNs. These methods are employed primarily to obtain dynamical information related to molecular spin dynamics, as opposed to the static spectroscopic details described in the preceding sections. Nevertheless, one can often infer important information concerning the static spin Hamiltonian based on, e.g., a theoretical understanding of the magnetic field or temperature dependence of relaxation times. More importantly, knowledge of these relaxation times/mechanisms is of crucial importance if one is to eventually employ MNs in spintronics applications. Experiments involve the use of coherent pulses of microwave radiation that are tailored to produce controlled rotations of the magnetization within a sample. The basic principles of pulsed EPR [117] are similar to pulsed NMR. The main challenge concerns the much faster electronic relaxation rates in

paramagnetic solids, requiring large microwave powers in order to achieve coherent operations on sufficiently short timescales. For this reason, applications of pulsed EPR have significantly lagged those of NMR. Nevertheless, recent advances in microwave technologies have translated into significant increases in the performance of pulsed EPR spectrometers. For the most part, commercial systems operating at relatively low frequencies (9/34 GHz) have led the way. Sophisticated spectrometers operating at higher frequencies (>90 GHz) are now becoming available – both home-built [118–120] and from commercial vendors.

Most of the employed pulsed EPR methods rely on the Hahn-echo sequence in which a $\pi/2$ pulse first rotates the magnetization into the *xy*-plane. This magnetization is then allowed to evolve for a time τ, after which it is refocused by means of the π pulse, resulting in an echo at a time 2τ after the initial tipping pulse. Refocusing only occurs if the spins retain phase coherence during the 2τ evolution time. Indeed, by measuring the echo amplitude as a function of the delay time τ, one can directly measure the phase memory time T_2. Variations on the Hahn-echo sequence enable measurements of many other quantities such as the longitudinal relaxation time, T_1, and dipolar couplings to nearby nuclei and other electron spins [117]. Because of the need to retain phase coherence during the Hahn-echo portion of the sequence, one usually has to go to considerable lengths to ensure that the T_2 times in the sample of interest are as long as possible. Thus, experiments are typically performed at low temperatures. However, strong decoherence may remain even at liquid helium temperatures, due to fluctuating dipolar fields generated via energy conserving electron and nuclear spin-spin cross relaxation (so-called flip-flop) processes [121]. Consequently, many other measures are often taken to improve the outcomes of such measurements such as dilution of the paramagnetic species and deuteration of solvents.

The use of pulsed EPR in the study of paramagnetic molecules (including many polynuclear transition metal complexes) goes back well over 25 years [122–124], predating even the discovery of SMMs [1]. These earlier investigations focused on obtaining structural information from biochemically important molecules, e.g., the Mn_4 cluster within the photosynthetic reaction center of Photosystem II [123]. Because of the need for long coherence times, many of the tricks employed in more recent EPR studies have been known to the biochemistry community for a long time, e.g., the use of deuterated solvents to reduce the amplitude of nuclear dipolar field fluctuations [125–127]. The first pulsed EPR study that focused specifically on the possible application of MNs in quantum information processing (QIP) targeted frozen solutions of antiferromagnetically coupled Cr_7M rings (<0.2 mg/ml in Toluene, with M = Ni and Mn) [128, 129]. Measurements were performed in a commercial X-band (9 GHz) spectrometer, and a phase memory time of $T_2 \approx 3$ μs was deduced in deuterated samples of the spin $S = ½$ Cr_7Ni compound at low temperatures [128], comparable to results found in biochemical studies [123, 127]. On the basis of these measurements, it was concluded that the deployment of MNs in QIP applications would be feasible, opening the door to many similar investigations. Subsequent chemical modifications of the molecular structure of the Cr_7Ni compound, aimed at minimizing environmental decoherence

sources, have demonstrated phase memory times of up to 15 μs [130]. Meanwhile, the possibility of propagating quantum information between Cr_7Ni molecules via aromatic linkers has also been explored in-depth [131].

The next milestone involved the observation of Rabi oscillations – quantum oscillations resulting from the coherent absorption and emission of photons. The first such study concerned a trinuclear oxo-centered Fe^{III} ($s = {}^5/_2$) complex that possesses a well-isolated collective $S = ½$ ground state [132]. The complex was again diluted into a frozen acetone solution in order to achieve long phase memory times (2.6 μs at 5 K). Although Rabi oscillations were observed, they decayed rather rapidly (in less than 120 ns). Shortly thereafter, results were reported for a much larger antiferromagnetic V_{15}^{IV} MN embedded within a non-magnetic host (a surfactant that envelops the V_{15} cluster, thereby ensuring that molecules do not interact strongly with each other) [133, 134]. This work was motivated by a much earlier theoretical proposal suggesting that the highly symmetric V_{15} molecule could be a suitable prototype for QIP [6]. In spite of its large size and complexity, the low energy spectrum is relatively simple, consisting of two doublets ($S = ½$) and a quartet ($S = {}^3/_2$), well isolated from a quasi-continuum of states some 250 K above. The main goal of this work was to observe Rabi oscillations associated with the collective $S = ½$ ground spin states, since these are the ones that would be employed for QIP. In fact, in the original studies, performed at a relatively high temperature of ~4 K, Rabi oscillations corresponding to both the $S = {}^3/_2$ and $S = ½$ states were observed; the Rabi oscillation frequencies, Ω_R, differ considerably for the two cases, so they can be selectively excited. However, the authors were subsequently unable to confirm that the $S = ½$ signal was intrinsic to the V_{15} molecule after suggestions that it might be due to a paramagnetic background signal associated with the X-band cavity [135, 136]. More recent studies, performed at a lower temperature of 2.4 K, have definitively shown evidence for the $S = ½$ oscillations, thereby demonstrating the possibility of QIP in the ground states of V_{15} [137].

The early pulsed investigations focused mainly on antiferromagnetic molecules with spin-½ ground states, in part because this is the simplest possible quantum system that can easily be studied using commercial pulsed X-band EPR spectrometers, but also because the small magnetic moment provides maximal protection against environmental decoherence. However, it had previously been proposed that one could implement Grover's search algorithm using the eigenstates of high-spin SMMs such as Mn_{12} and Fe_8 [7]. The first major challenge in cases involving SMMs is the strong magnetic anisotropy, which dramatically broadens the EPR spectrum. Thus, a pulsed measurement performed (in field) on a frozen solution of randomly oriented SMMs would address only a tiny fraction of the molecules in the sample (due to the finite bandwidth of the pulses). Moreover, a high frequency pulsed EPR spectrometer is a prerequisite for studies of most SMMs, for which the technology lags significantly behind that of X-band instruments. A clever solution to these problems involved selecting a SMM for which the EPR excitation frequency from the ground state (the zfs) matched that of a commercial W-band

(94 GHz) instrument in zero applied magnetic field. The chosen compound was $[Fe_4^{III}(acac)_6(Br\text{-}mp)_2]$ (Fe_4 [138]), which possesses a spin $S = 5$ ground state and easy-axis anisotropy. Experiments were again performed on dilute solutions to mitigate molecular spin-spin decoherence, yielding a maximum phase memory time of 630 ns at 4.3 K. Rabi oscillations were also clearly observed. Because the measurements were performed without an external magnetic field, the orientational disorder did not affect the distribution (spread) of excitation frequencies. Thus, a large fraction of the molecules lie within the excitation bandwidth of the employed pulses. However, the orientational disorder does influence the Rabi frequencies, likely explaining the short-lived Rabi oscillations.

An obvious solution to the problem of orientational disorder would be to study single crystals. However, one then runs into the problem of strong electron spin-spin decoherence due to the high concentration of molecules. An ingenious trick that more-or-less completely suppresses this decoherence involves performing EPR measurements at high frequencies and low temperatures [121]. The high frequency (f) ensures that the ground state is well separated from the first excited state. If the temperature (T) is then reduced so that $k_BT \ll hf$, the molecular spin system will maintain near 100% spin polarization. Electronic spin flip-flop processes are completely suppressed in these circumstances (because all spins are aligned). In other words, even though the host crystal is highly magnetized, it is essentially non-magnetic insofar as its magnetization is completely static. The commercial W-band spectrometer employed in the preceding investigation does not meet the $k_BT \ll hf$ condition, because 94 GHz is equivalent to ~4.5 K and the base temperature of the system is not much below this. For this reason, such studies have only been possible up to now using home-built pulsed EPR spectrometers [118], with almost all of the work performed at the NHMFL. The landmark study involved the Fe_8 SMM, for which spin-echo measurements of T_1 and T_2 were performed on an oriented crystal at 240 GHz ($\cong 11.5$ K) and 1.27 ± 0.05 K, in a magnetic field of 4.566 T [139, 140]. A phase memory time of ~700 ns was obtained under these conditions. Although this high-field approach may not be as attractive for potential applications in comparison to the zero-field method described previously [138], it has enabled very detailed investigations of the underlying decoherence mechanisms in SMM crystals [140, 141].

One can take the single-crystal approach further by diluting magnetic molecules into an isostructural non-magnetic host crystal, thus ensuring good alignment of the magnetic species. This approach is challenging for polynuclear systems because the magnetic and non-magnetic elements tend to scramble during the formation of the crystal, leading to a mixture of various mixed-metal species [83]. However, there are a few examples where this can work without scrambling [142]. In one very recent example, spin-echo measurements were possible for Cr_7Zn ($S = {}^3/_2$ ground state) doped into the isostructural Ga_7Zn host (0.3% Cr_7Zn by mass) [143]. Phase memory times approaching 1 μs were found in this example, with good prospects for increasing this value upon further dilution. Rabi oscillations were also detected. By contrast, magnetic dilution of mononuclear species into non-magnetic host

crystals is typically more straightforward, particularly in the case of lanthanides [102]. Indeed, this approach has been widely employed for pulsed EPR studies of magnetic ions embedded into more traditional (non-molecular) solids (see, e.g., [144]). A few studies involving mononuclear lanthanide molecular magnets have recently been reported, particularly involving the isotropic Gd^{III} ion [145, 146]. The prospects for future advances involving related materials look particularly promising [8, 9].

3 Magneto-Optical Techniques

Applications of SMMs in fields such as spintronics and quantum computing will require, as a first step, the deposition of isolated molecules onto surfaces while retaining SMM behavior, so that individual molecules can be manipulated and their behavior specifically employed. In this sense, evolution of characterization tools is required to be able to determine magnetic properties at the nanoscale and, moreover, with surface sensitivity.

Magneto-optical and X-ray based techniques turn out to be very suitable for the spectroscopic characterization of MNs since they allow for high sensitivity and high spatial resolution. One can find different techniques according to the configuration and type of radiation used, either uv/visible or X-ray. In all cases, the magnetic signal is obtained from the dependence on the initial and final states of the transition associated with the absorbed wavelengths, being thus chemically selective in some cases, and also allowing for magnetic measurements as a function of an applied external field, e.g., magnetization hysteresis cycles.

3.1 Magnetic Circular Dichroism and Magneto-Optical Kerr Effect

MCD takes advantage of the differential absorption (dichroism) of left and right circularly polarized light by a sample under the presence of a magnetic field parallel to the propagation direction. It is typically applied in the visible to ultraviolet spectral range and, thus, requires molecular samples to be either transparent or in a solution state that allows for light transmission. By contrast, the magneto optical Kerr effect (MOKE) measures the rotation of the polarization angle after reflection of the electromagnetic wave from a magnetic sample under the presence of a magnetic field, allowing for the characterization of magnetic moments of molecular materials deposited onto opaque substrates, achieving sensitivities of up to 10^{-12} emu. The development of nanoMOKE technology has increased the spatial resolution, leading to surface mapping capabilities of magnetic properties with a resolution close to the intrinsic diffraction limit dictated by the employed

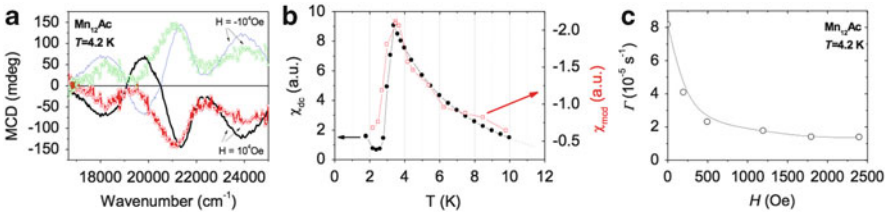

Fig. 6 (**a**) MCD spectra of $Mn_{12}Ac$ in a 1:1 frozen solution of CH_2Cl_2:toluene (*solid curves without symbols*) and 1:2 CH_3CN:dmf (*solid curves with open circles*), at applied magnetic fields of 10^4 Oe and -10^4 Oe (*labeled in the figure*). (**b**) Zero-field-cooled magnetization measurements of $Mn_{12}Ac$ in a 1:1 glass of CH_2Cl_2:toluene, in an applied field of 10^3 Oe; *solid circles* indicate SQUID measurements (referred to the *left axis*) and the *open squares* are the MCD measurements (referred to the *right axis*). (**c**) Magnetization relaxation rates determined from MCD measurements at $T = 4.2$ K, as a function of the applied magnetic field. The increase of the MCD signal decay rate at low fields is indicative of acceleration of the relaxation due to resonant quantum tunneling. Adapted with permission from [151]. Copyright 2004 American Physical Society

wavelength. Moreover, the degree of rotation of the polarization is sensitive to the orientation of the magnetic moment with respect to the surface, allowing for a determination of the orientation of the magnetic anisotropy of thin films of SMMs. Since this technique offers high temporal resolution, it is also highly suitable for studies of magnetization dynamics on surfaces. Some examples include the determination of magneto-optical constants of paramagnetic thin films of phthalocyanine (Pc) molecules such as CuPc by MOKE [147, 148], as well as the interaction of related molecules with a ferromagnetic substrate [149]. However, the use of MOKE for SMM characterizations has not been extended, mainly due to the requirement for low temperature measurements.

Coming back to measurements in absorption, the intensity of the MCD signal depends on the ground and excited state parameters, determined by the *g* factor and zfs, and is thus associated with the degree of spin-orbit coupling, varying with temperature and magnetic field strength. This technique, used initially to perform magnetic characterization of Mn_{12} derivatives isolated in different organic glasses, or embedded in polymeric films [150, 151], has been shown to be a powerful tool for revealing SMM behavior [151–153], and for determining zfs parameters [154]. It is thus complementary to EPR. The study of the thermal and field dependence of MCD signals at very low temperatures also led to the first observation of magnetic hysteresis cycles and relaxation rates of completely isolated SMMs, as shown in Fig. 6, demonstrating that the magnetic anisotropy, the SMM behavior, and also the QTM relaxation are not intrinsically lost when the molecules are isolated in an organic glass [150–152].

Nowadays, MCD is commonly used for the low temperature characterization of magnetic hysteresis cycles of many different types of SMM, generally in frozen solutions or transparent thin films. Several derivatives of Mn_{12} have been studied by MCD in different environments such as an amorphous matrix, Langmuir Blodgett films, directly grafted onto Au surfaces [155], and sprayed onto transparent LiF

substrates [156]. More recently, one can find other examples of molecular magnets studied by MCD: Fe_4 molecular clusters diluted in different polymeric matrices [157], weakly exchange coupled transition metal dimers [158], Ni_4 cubane molecular magnets in a dilute solution [154], mononuclear Dy^{III} SMMs in solution [159], as well as different examples of bis(phthalocyaninato)lanthanide SMM complexes [153, 160] and double decker systems [161]. In this latter case [160], it has been proven that the MCD technique can be used to determine the magnetic properties of different redox states of the same complex, without interference of the preparation of the solid state solution on the results. Moreover, MCD spectroscopy can be used to determine not only the single-ion anisotropy, but also the molecular zfs, which is crucial for understanding the origin of magnetic anisotropy in SMMs [149, 153, 154, 158, 160, 162–165].

Even though it is found that some of the MNs studied by MCD do not retain their SMM properties when deposited on surfaces [155], it is not thought that the absorbance of light resulting from the MCD measurement is responsible for perturbing the natural SMM behavior. Instead, major distortions have mainly been ascribed to critical molecule-surface interactions, or matrix-induced strains [157]. However, absorption of radiation at optical wavelengths can drive changes in the magnetization at low temperatures by triggering phonon-assisted spin-transitions that lead to fast relaxation rates [166]. This can result in the loss of hysteresis properties of SMMs at certain temperatures when measured by SQUID magnetometry under light irradiation (or even by XMCD – see below) that can be wrongly attributed to damage generated by the beam (since the electrons involved in the light absorption process lie at the very heart of the SMM behavior), or to an intrinsic loss of magnetic anisotropy due to the molecular environment [167].

3.2 X-Ray Magnetic Circular Dichroism

XMCD is a synchrotron spectroscopic technique based on the principle that resonant circularly polarized photons are differently absorbed by a magnetic material depending on their helicity relative to the sample magnetization. In XMCD, the photon propagation direction is aligned parallel to the magnetic field and, thus, the quantization (z) axis. In this case, following perturbation theory, the absorption cross-sections for left (L) and right (R) circularly polarized photons can be expressed as:

$$\sigma_{L,R}(\omega) = 4\pi^2 \alpha \hbar\omega \sum_{\phi,l} (l/d_l) \left| \langle \phi | \boldsymbol{\varepsilon}_{L,R} \cdot \mathbf{r} | l \rangle \right|^2 \delta\left(E_\phi - E_l - \hbar\omega\right). \tag{5}$$

Here, $\hbar\omega$ is the energy of the incoming X-rays, α is the fine structure constant, $|l\rangle$ and $|\phi\rangle$ are the initial and final state wave functions of the system, and the delta distribution insures energy conservation. The degeneracy of the ground state is d_l,

and $\boldsymbol{\varepsilon}_{L,R}$ are the polarization vectors [$\boldsymbol{\varepsilon}_L = \sqrt{2}(1/2, \mathrm{i}/2, 0)$ and $\boldsymbol{\varepsilon}_R = \sqrt{2}(1/2, -\mathrm{i}/2, 0) = (\boldsymbol{\varepsilon}_L)^*$] corresponding to the left and right circularly polarized photons propagating along z. The dichroic signal is the difference, $\sigma_L(\omega) - \sigma_R(\omega)$, and it is non-zero when time-reversal symmetry is broken by a net magnetic moment of the system, either due to spontaneous or field-induced magnetic order.

One of the advantages of this technique is its very high surface sensitivity since it has been used to study the magnetism of sub-monolayers of magnetic atoms and molecules on surfaces using the total electron yield (TEY) detection mode [168]. Even more important is its chemical sensitivity, which allows one to specifically probe the magnetic behavior of a given element in a molecule and, moreover, to determine element selective spin and orbital moments separately in heteronuclear systems. Another very appealing aspect that is very useful when studying fragile SMMs on surfaces is the fact that XMCD is a spectroscopic method and, thus, allows for verification of the integrity of the molecules under study by measuring their electronic structure, oxidation, and their magnetic properties [169].

The first examples of SMM characterization with XMCD are quite recent, focusing on Mn_{12} molecules adsorbed on gold surfaces [167, 170], for which a redox instability of the Mn_{12} complexes was observed due to partial reduction of Mn^{III} to Mn^{II}, accompanied by structural rearrangements. These initial studies launched a debate about the suitability of XMCD for SMM studies, since the excitation of core electrons of the molecule could be equivalent to demagnetization effects. However, the following explosion of experiments using XMCD to study a range of SMMs on surfaces, using various different deposition methods [171], provides clear evidence that the technique is *not* incompatible with such SMM characterizations. Examples include: Fe_4 (Fig. 7 and [172–177]) and the isostructural heterometallic Fe_3Cr complex [177, 178] deposited and grafted onto Au surfaces using different covalent groups; Cr_7Ni antiferromagnetic rings [179–182]; the endohedral SMM DyScN@C80 [183]; and double-decker Tb^{III} complexes with phthalocyanine ligands [184–188]. In fact, it seems that Mn_{12} is one of the more fragile examples when deposited on surfaces, showing a strong tendency for reduction of Mn^{III} to Mn^{II}, even in the presence of a buffer monolayer of acid that decouples the molecule from the substrate and minimizes induced perturbations [189]. It seems, therefore, that Mn_{12} is particularly unstable, and that it cannot survive many of the widely employed deposition processes such as sublimation. However, a very recent example of the observation of Mn_{12} on a Bi (111) surface deposited directly by gentle tip deposition using a scanning tunneling microscope (STM), as well as recent measurements of its quantum behavior when deposited on metallic and thin-insulating surfaces by optimized electrospray ion beam deposition [190], opens up new expectations for the assessment of magnetic properties of SMMs on solid surfaces [191]. Meanwhile, submonolayers of Mn_6 SMM derivatives deposited onto Au surfaces [192, 193] show a decrease of the average Mn^{III} spin moment when compared to relatively thick films [194]. However, in this case, the Mn^{III} oxidation state (and, hence, the local moment) is preserved, and the reduced average moment is attributed to local distortions of the Mn environment that modify the Mn-Mn exchange coupling.

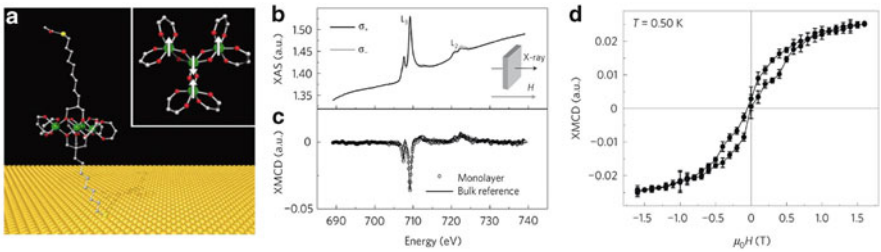

Fig. 7 (**a**) Schematic representation of a Fe_4 derivative bearing a thiolate-terminated aliphatic long chain attached to a gold surface; the *inset* depicts the magnetic core of the Fe_4 molecule with *arrows* indicating the ground-state spin arrangement. (**b**) The iron $L_{2,3}$-edge X-ray absorption spectra (*XAS*) using left-(σ_+) and right-(σ_-) circularly polarized photons, in a magnetic field of 3 T, recorded for a monolayer of the Fe_4 molecules at a temperature of 0.50 K. (**c**) XMCD spectra for a Fe_4 monolayer and a bulk sample. (**d**) A magnetic hysteresis loop obtained for the Fe_4 monolayer, monitored through the XMCD intensity, at a field sweep rate of 2 mTs^{-1}. Adapted with permission from [172]. Copyright 2009 Nature Publishing Group

In contrast to the Mn examples, the Fe_4 SMM seems to easily survive different deposition processes, and monolayers of Fe_4 on Au surfaces preserve their butterfly-shaped hysteresis cycles down to 0.5 K [172, 174, 175], either when adsorbed onto the surface or even when covalently grafted using appropriate ligands [176]. Examples of XMCD hysteresis cycles for Fe_4 derivatives covalently bonded onto Au surfaces are shown in Fig. 7d and in [195]. These results, together with the previously cited ones, demonstrate that there are no fundamental limitations that preclude the observation of magnetic hysteresis when SMMs are wired to a conducting substrate. Moreover, similar to the MCD results obtained for dilute frozen solutions, XMCD has been employed in order to demonstrate that SMMs preserve their quantum properties on surfaces: monolayers of oriented $Fe_4(L)_2(dpm)$ [where H_3L is 7-(acetylthio)-2,2-bis(hydroxymethyl)heptan-1-ol and HDPM is dipivaloylmethane] SMMs grafted onto Au with short aliphatic chains show evidence for resonant QTM by means of the characteristic steps in their hysteresis cycles (see [195, 196]). These investigations went as far as demonstrating that the QTM resonance fields (hysteresis loop steps) displayed the expected dependence on the orientation of the applied magnetic field relative to the normal to the surface, confirming the ordering of the magnetic easy-axis direction with respect to the Au surface. Finally, the element selective capabilities of XMCD allow for the determination of the relative alignment of the magnetic moments of different ions. As an example, it has been shown that the ferrimagnetic interaction between Fe and Cr moments in the Fe_3Cr complex is also preserved when deposited onto a surface [177, 178].

The advantage of element selectivity is a key factor in the study of the origin of magnetic anisotropy in MNs. Cr_7Ni antiferromagnetic rings deposited on surfaces are a paragon for the study of the interplay between single-ion and overall molecular anisotropy in complex polynuclear systems. Submonolayer depositions of Cr_7Ni rings on Au(111) surfaces [179] employing different functionalization

pathways [180], and even self-assembled monolayers deposited by UHV sublimation techniques [181], show very minor perturbations of their electronic structure and magnetic properties, i.e., the oxidation states, local environments, and crystal-field intensities at the Cr and Ni sites remain essentially unchanged. The element selectivity of XMCD also enables confirmation of the antiparallel arrangements of the Cr and Ni magnetic moments. A step forward in XMCD characterization has been achieved by studying the angular-dependence of the dichroic signal, which reveals the magnetic easy-axis direction of the rings with respect to the substrate. Specifically, deep analysis of the angular-dependence of the spectra of ordered monolayers of Cr_7Ni determined that, although the easy-axes of both the Ni and Cr ions are oriented perpendicular to the plane of the ring, the magnetization of the Cr_7Ni molecule is preferentially aligned within the plane of the ring [182]. This can be explained by considering the projection of the easy-axis anisotropy for each ion onto the lowest lying spin states of the molecule, for which the thermally populated $S = {}^3/_2$ multiplet dominates the collective cluster anisotropy at the field/temperature employed for the measurements; the projected anisotropy of this state turns out to be easy-plane. These studies demonstrate that, although XMCD probes the magnetic properties of individual ions, one can still deduce the magnetic anisotropy of an entire molecule via projection methods.

Finally, metal-porphyrins and metal-phthalocyanines are magnetic molecules that have also recently been explored as hybrid systems combining metal and molecular layers for possible use in molecule-based devices. These molecules show excellent chemical stability and, furthermore, they easily organize in perfect 2D networks by spontaneously ordering through lateral hydrogen bonds, thus becoming an archetypal family of metal-organic semiconductors. Initially, XMCD was used to study the interaction between different types of paramagnetic porphyrin molecules and ferromagnetic substrates [197–200]. More recently, XMCD has been applied to the study of slow relaxation of the magnetization of monolayers and sub-monolayers of the double decker $TbPc_2$ SMM deposited onto Cu [184], Au [185], and graphite surfaces [186, 187], together with its neutral and anionic derivatives and, more recently, sublimated onto $La_{0.7}Sr_{0.3}MnO_3$ (LSMO) and Co surfaces [188]. The typical butterfly shaped hysteresis curves are preserved for deposition onto Au and HOPG surfaces, as observed by XMCD at low temperatures, indicating that the intimate interaction with the substrate doesn't destroy the magnetic anisotropy in these cases. A decrease in anisotropy compared to the crystalline phase is observed for sub-monolayer deposition onto Au. Meanwhile, no hysteresis was observed for $TbPc_2$ molecules deposited onto Cu, LSMO, and Co. For Cu, this was attributed to the long times necessary to acquire a typical XMCD magnetization curve. However, it remains unclear as to the origin of the disappearance of the butterfly shaped hysteresis loops in the other cases.

4 Inelastic Neutron Scattering

The neutron, a charge-less particle with a quantum spin of one half, is highly penetrating in matter and an efficient microscopic probe of magnetism. Beams of neutrons for spectroscopy provide unique spatial and temporal information on interaction with magnetic materials. INS measures neutron energy and momentum transfer on interaction with the measured sample, from which the energy of magnetic excitations and aspects of their internal spin structure may be obtained directly. INS probes the magnetism of MNs in the same energy window where exchange interactions and anisotropies exist. The key advantages of a low energy microscopic probe relate to how measurements may be performed in zero or at fixed applied magnetic fields, with excited states being accessed directly along with detailed information relating to their wave functions.

Historically INS has maintained to be a somewhat specialist spectroscopic tool, as investigations of MNs were limited by the requirement of large sample quantities (typically of order 5 g), and the necessity of deuteration of all hydrogen atoms present within investigated samples. Recent advances in INS instrument technology mean that, today, samples on the order of 200 mg are often sufficient, opening up possibilities for the study of single crystal samples and the measurement of polycrystalline compounds with low synthetic yield. Furthermore there is an increasing realization that, in some energy ranges, deuteration is not always imperative as previously thought for the measurement of energy spectra in polycrystalline studies. Altogether, INS is more accessible for the study of MNs than ever before, and the first single crystal investigations have proven to permit the extraction of unprecedented information concerning the internal spin structure of MNs.

In the early days, magnetic dimers were prepared specifically for the investigation of exchange interactions in systems free from the cooperative magnetic effects present within extended magnetic systems. This is where the use of INS first took its foothold in the study of physical phenomena of MNs. These initial works provided a proof of principle, demonstrating how direct access to exchange interactions could be obtained, and how the different types of transitions could be distinguished via the momentum transfer of the INS intensity. Today, the physics of MNs has become a field of research in its own right, and INS plays an integral role in unraveling the properties of increasingly complex MN compounds. There are several reviews available presenting case studies of significant highlights in the application of INS for the study of MNs; see for example [201–204]. The aim of the present review is to outline some examples of seminal INS results, along with a selection of examples that benefited from the most up-to-date advances in instrumentation. Emphasis is made on how instrument development is driving higher levels of spectroscopic detail in magnetic characterization and outlining the new opportunities associated with the investigation of single-crystal MNs.

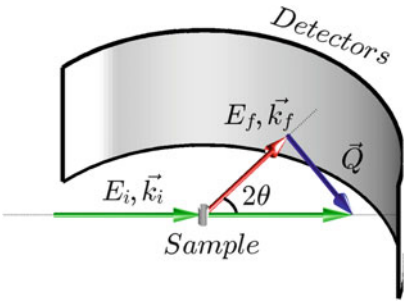

Fig. 8 Inelastic neutron scattering instrument setup; see text for explanation

4.1 General Background to INS

Neutrons provide a useful probe for the study of structure and dynamics in matter from a wide range of scientific disciplines. This is due to the extremely rich interactions that occur between the neutron and the sample under investigation. Neutrons, which have no electrical charge, may have their momenta adjusted to correspond with de Broglie wavelengths comparable to interatomic distances in matter, hence providing a tunable probe of spatial and dynamic correlations. Neutron beams are produced at specialist nuclear reactors or at spallation source facilities. Spallation is a technique where high-energy protons are accelerated into a heavy metal target driving neutrons from the target nuclei. Both spallation and nuclear fission create neutrons of high energy (MeV), and thus a moderator is required to reduce neutron energies appropriate for spectroscopy (typically 0.1–10 meV) [205]. Typically, the magnetic excitations (and zfs in SMMs) match this INS energy window, providing direct access to exchange interactions and anisotropy parameters. The neutron quantum spin angular momentum of $s = ½$ interacts with unpaired electrons of the investigated sample. Consequently when a low-energy neutron is inelastically scattered by unpaired electrons in the measured sample, the change in neutron energy is a large fraction of its initial energy. Measurements of changes in neutron energies upon interaction with the measured sample hence provide a direct probe of magnetic excitations. A typical INS instrument monochromates the incident neutron beam, selecting the initial neutron beam energy (E_i) and momentum ($\hbar \boldsymbol{k_i}$, where $\boldsymbol{k_i}$ is the initial wave vector). Scattered neutrons gain or loose energy on interaction, and arrive at a detector with a final energy (E_f) and momentum ($\hbar \boldsymbol{k_f}$). The energy transfer ($\hbar\omega$) between the measured sample and the interacting neutron beam is expressed in Eq. (6) and the momentum transfer vector ($\boldsymbol{Q}$) is deduced from the scattering angle with respect to the initial and final wave vectors, as expressed in Eq. (7) (see Fig. 8):

$$\hbar\omega = E_i - E_f = \frac{\hbar^2}{2m}\left(\boldsymbol{k}_i^2 - \boldsymbol{k}_f^2\right) \tag{6}$$

$$\hbar\boldsymbol{Q} = \hbar\left(\boldsymbol{k}_i - \boldsymbol{k}_f\right). \tag{7}$$

4.2 Neutron Scattering Cross Section

The cross section (σ) of neutrons with energy in the range from E_f to $E_f + dE_f$, scattering into an individual detector of area $d\Omega$, is expressed in terms of the partial differential cross-section. A general basic expression to describe this, applicable to both nuclear and magnetic scattering, can be derived from Fermi's Golden Rule and is equivalent to the first Born approximation, where the interaction between neutron and sample is considered small enough to be treated as a perturbation [205, 206]:

$$\frac{d^2\sigma}{d\Omega dE_f} = \left(\frac{m_N}{2\pi\hbar^2}\right)^2 \frac{k_f}{k_i} \sum_{nm} p_n \left| \left\langle \boldsymbol{k}_i, n \middle| \hat{O} \middle| \boldsymbol{k}_f, m \right\rangle \right|^2 \delta(E_n - E_m + \hbar\omega). \tag{8}$$

The neutron mass is given by m_N, and E_n and E_m are the eigenvalues for the initial (n) and final (m) states of the scattering system, respectively. The Kronecker delta function (δ) maintains energy conservation within the scattering process. The scattering system has to be in thermal equilibrium, where the occupation of a specified n state is based on the Boltzmann distribution function (p_n). The operator $\hat{O}$ represents the specific interaction between the neutron and the scattering system. Experimentally, large portions of $\boldsymbol{Q}$ and $\hbar\omega$ are measured. Hence it is convenient to express the neutron scattering as a function of these measured dimensions [Eq. (9)]:

$$S(\boldsymbol{Q}, \omega) = \left(\frac{2\pi\hbar^2}{m_N}\right)^2 \frac{k_i}{k_f} \frac{d^2\sigma}{d\Omega dE_f}. \tag{9}$$

Neutron scattering interactions within condensed matter include absorption, nuclear scattering (coherent and incoherent), and magnetic scattering.

4.2.1 Nuclear Scattering

Nuclear scattering is expressed by Eq. (8) with substitution of Eq. (10), the Fermi pseudo-potential for $\hat{O}$.

$$V_{\text{nuc}} = \frac{2\pi\hbar^2}{m_N} b_j \delta(\boldsymbol{r} - \boldsymbol{r}_j). \tag{10}$$

The Fermi pseudo-potential considers the interaction between a neutron (position, $\boldsymbol{r}$) and a nucleus (position, $\boldsymbol{r}_j$), where b_j is the scattering length of the jth nucleus. The scattering length depends on the specific nucleus. When the interacting nucleus (nuclei + neutron) is not near an excited state, the scattering length is real and depends on the neutron spin and the interacting nucleus spin. It is worth noting that, for interacting nuclei near excited states, the scattering length becomes imaginary. In this case, neutron absorption occurs; strong neutron absorbers include

metals such as ^{113}Cd [205] and Gd [207]. Coherent nuclear scattering gives Bragg diffraction peaks and phonons. Incoherent nuclear scattering gives an isotropic elastic contribution and an inelastic response proportional to the vibrational density of states. A large source of incoherent scattering in MNs is from hydrogen which has a particularly large incoherent cross-section. Large quantities of incoherent nuclear scattering can mask the observation of magnetic excitations. In many cases the incoherent nuclear scattering of ligand hydrogen within MNs does not become significant until energies greater than around 2 meV. To alleviate the contribution of incoherent nuclear scattering that sometimes does obscure magnetic scattering, the hydrogen within the investigated MN can be interchanged with deuterium. Deuterium exhibits an incoherent cross-section 40 times less than hydrogen. Distinction between incoherent phonons and magnetic excitation intensities can be made by analysis of the momentum transfer of the inelastic scattering intensity. The intensity of incoherent phonon scattering follows a Q^2 dependence, in contrast to magnetic excitations which exhibit more complex modulations of intensity with respect to Q.

4.2.2 Magnetic Scattering

The magnetic scattering interaction potential [Eq. (11)] resembles the nuclear potential; $F_j(Q)$ is the magnetic form factor, the Fourier transform of the normalized unpaired electron density of the jth atom at position $\boldsymbol{r}_j$ with linear momentum p_j.

$$V_{\text{mag}} = \frac{2\pi\hbar^2}{m_N} p_j F_j(Q)\delta\left(\boldsymbol{r} - \boldsymbol{r}_j\right). \tag{11}$$

The partial differential magnetic scattering cross-section can be determined as in the case of nuclear scattering by substitution of the magnetic interaction potential, Eq. (11), into Eq. (8). For a finite magnetic complex, where unpaired electrons are localized to positions $\boldsymbol{r}_j$, the partial differential magnetic scattering cross section can be written as:

$$\frac{d^2\sigma}{d\Omega dE_f} = \frac{A}{N}\frac{k_f}{k_i}\sum_{n,m} P_n I_{nm}(\boldsymbol{Q})\delta\left(E_i - E_f + \hbar\omega\right), \tag{12}$$

where A = 0.29 *barn* and N is the number of magnetic ions. The INS intensity has an orientation dependence given by the quantity $I_{nm}(\boldsymbol{Q})$, written explicitly in Eq. (13).

$$I_{nm}(\boldsymbol{Q}) = \sum_{jj'} F_j^*(Q) F_{j'}(Q) e^{i\boldsymbol{Q}\cdot(\boldsymbol{r}_j - \boldsymbol{r}_{j'})} \sum_{\alpha\beta} \left(\delta_{\alpha\beta} - \frac{Q_\alpha Q_\beta}{Q^2}\right) \times \langle n|\hat{s}_{j\alpha}|m\rangle\langle m|\hat{s}_{j'\beta}|n\rangle. \tag{13}$$

Equation (13) contains the space and time Fourier transform of the time dependent spin-spin correlations for all permutations of pairs of magnetic moment carrying ions ($\hat{s}_{j\alpha}$ and $\hat{s}_{j'\beta}$) within the MN, where α and β denote the Cartesian coordinates x, y, z. The $(\delta_{\alpha\beta} - Q_\alpha Q_\beta/Q^2)$ factor maintains that the neutron only couples to components of the magnetic moment which are perpendicular to the wave vector $\boldsymbol{Q}$ [205].

The intensity of each given magnetic excitation varies as a function of $\boldsymbol{Q}$ in the first case by the magnetic form factor, $F(Q)$, of the scattering magnetic ions, which results in a decrease in intensity for increasing magnitude of Q. Additionally, the relative positions of the moment carrying ions modulate the scatting intensity within the structure factor $e^{i\boldsymbol{Q}\cdot(\boldsymbol{r}_j - \boldsymbol{r}_{j'})}$ in numeration with the space and time Fourier transform of the time dependent spin–spin correlations, $\left\langle n|\hat{s}_{j\alpha}|m\right\rangle\left\langle m|\hat{s}_{j'\beta}|n\right\rangle$. These correlation terms exhibit all of the information associated with the spin dynamics of the specific excitation.

The correlations are the key quantities describing the detailed spin dynamics of the measured sample. It hence pertains that if large portions of the magnetic scattering contribution to $S^{\alpha\beta}(\boldsymbol{Q},\omega)$ are measured for a MN with a well-defined orientation (i.e., a single crystal), the specific two spin correlations for each magnetic excitation can be extracted directly. To date the majority of measurements concern the investigation of polycrystalline MN samples. In such events $I_{nm}(\boldsymbol{Q})$ is averaged over all spatial orientations of $\boldsymbol{Q}$, a procedure described explicitly in [208, 209]. The orientation averaged scattering function is, hence,

$$S(\boldsymbol{Q},\omega) = \sum_{n,m} P_n I_{nm}(\boldsymbol{Q}) \cdot \delta\big(E_i - E_f + \hbar\omega\big). \tag{14}$$

Selection rules derived from the magnetic scattering cross section, Eq. (12), dictate that neutron scattering transitions should obey the following: $\Delta S = 0, \pm 1$ and $\Delta m_s = 0, \pm 1$. These selection rules allow the energy between different spin multiplets to be probed directly. INS studies of orientation averaged samples still contain important information about the spin dynamics and spatial properties of magnetic excitations via their Q dependence.

4.2.3 Instrumentation

The most convenient means to access large portions of the magnetic scattering function, $S(\boldsymbol{Q},\omega)$, is via the time-of-flight (ToF) technique. Following monochromation, bursts of neutrons with a fixed velocity interact with the sample.

The time elapsed before neutrons arrive at the detectors, set at a fixed distance from the sample, is used to determine the change in neutron velocity and, hence, the energy transfer upon interaction with the measured sample. Similarly, the position of neutron detection resolves the change in neutron momentum on interaction with the sample. Figure 8 shows a schematic of a direct geometry INS instrument. Recently, the development of detector arrays with large position sensitive detectors allows for huge portions of $S(\boldsymbol{Q}, \omega)$ to be accessed, increasing detection sensitivity and special resolution. Conventionally, ToF spectroscopy is performed by selecting a single neutron pulse of monochromatic wavelength from a polychromatic source beam. Contrastingly, the recently developed repetition rate multiplication (RRM) method [210] makes more efficient use of source neutrons, especially at spallation facilities, selecting multiple monochromatic wavelengths at each source pulse, dramatically increasing the repetition rate of ToF. Several of the latest cold neutron spectrometers to come online at spallation source facilities (such as LET at the ISIS facility in the UK [211] and; AMATERAS at MLF, J-PARC in Japan [212]) include RRM, or *multi-*E_i options. These spectrometers enable several dynamical ranges to be measured simultaneously (see Fig. 11 below).

4.3 A Direct Probe of Exchange Interactions

The first investigation of magnetic exchange coupling in a molecule-based magnet by INS was reported by Güdel and Furrer in 1977 [214, 215]. The experiment outlined the measurement of exchange interactions in a dinuclear Cr^{III} complex, $[(NH_3)_5CrOHCr(NH_3)_5]^{5+}$. The complex exhibits antiferromagnetic (AF) coupling between the two Cr^{III} ions. The neutron energy loss showed clear, well defined peaks corresponding to $|S=0\rangle \rightarrow |S=1\rangle$, $|S=1\rangle \rightarrow |S=2\rangle$, and $|S=2\rangle \rightarrow |S=3\rangle$ transitions respectively, see Fig. 9a. The energetic sequence of the transition intensities was established by monitoring the temperature dependence of the observed transitions. At 5 K $|0\rangle \rightarrow |1\rangle$ is observed alone; with increasing temperature, further excited states are revealed. Measuring at different temperatures provides information to distinguish between magnetic and phonon excitations – phonons obeying Bose statistics, whereas electron population of exchange-split levels is governed by Boltzmann statistics. The momentum transfer of the $|0\rangle \rightarrow |1\rangle$ excitation is shown in Fig. 9b. The structure factor for the calculation of the Q dependence of the inelastic transition intensity, for the case of the dimer singlet to triplet excitation, simplifies to give:

$$I(Q) \propto F(Q)^2 \left(1 - \frac{\sin(Q \cdot R)}{Q \cdot R}\right), \tag{15}$$

where R is the distance between the two Cr ions and $F(Q)$ is the magnetic form factor of the Cr ions. Following this proof of principle investigation of 3*d*–3*d*

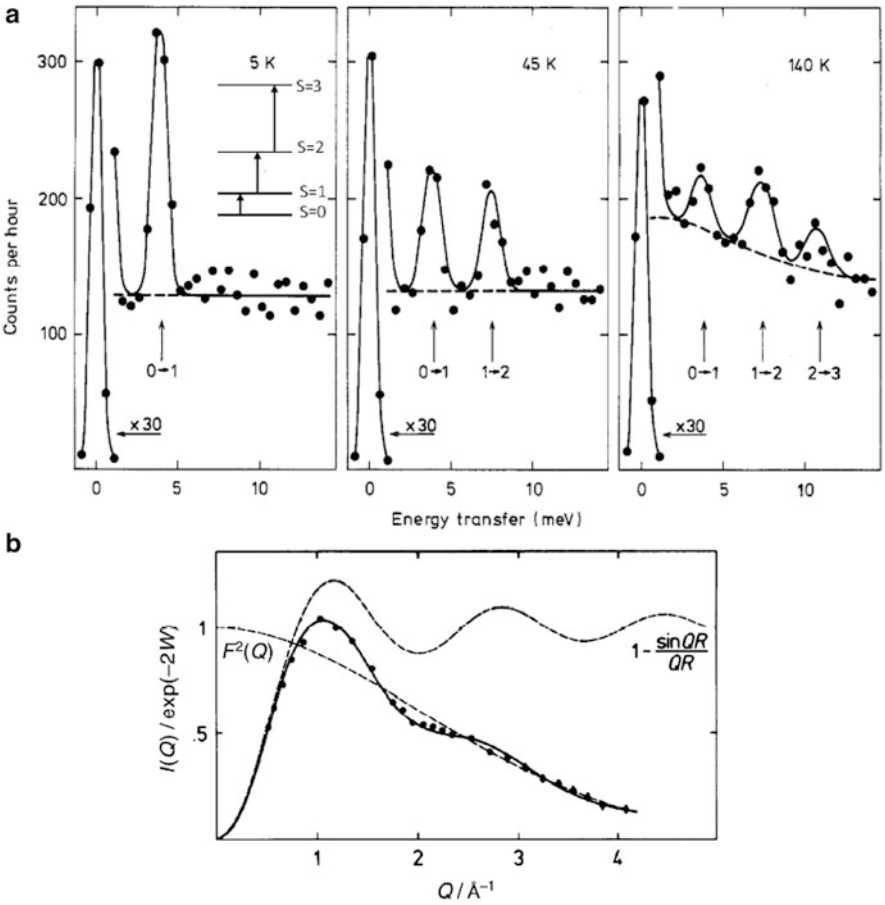

Fig. 9 Magnetic excitations of a polycrystalline sample of the dinuclear Cr^{III} complex, $[(NH_3)_5CrOHCr(NH_3)_5]^{5+}$. (**a**) Energy spectra show how variable temperature measurements access the energy gaps between successive spin states. (**b**) Momentum transfer associated with the transition from $S = 0$ to 1 at 5 K (*black circles*). The *solid* and *dashed curves* are calculations based on Eq. (15). Adapted with permission from [214, 215]. Copyright 1977 American Physical Society and Taylor & Francis

exchange interactions between Cr ions, INS was utilized to investigate the more complex exchange interactions of 4*f*–4*f* and 4*f*–3*d* exchange. Except for Gd^{III}, exchange concerning lanthanide metals (Ln) is complicated by the manifestation of ligand field effects within the same temperature range as the exchange interactions between the magnetic centers. Furthermore, the large spin-orbit coupling of Ln ions means that assumptions about *g* values in applied magnetic fields are not straightforward. For these reasons INS has proven a particularly well suited means for the investigation of Ln exchange. Initial studies concerned Ln^{III} dimers such as $Cs_3Tb_2Br_9$ [216, 217]. The nature and magnitude of Tb-Tb exchange was evaluated within the exchange coupled, lowest energy ligand-field states. Figure 10 shows the

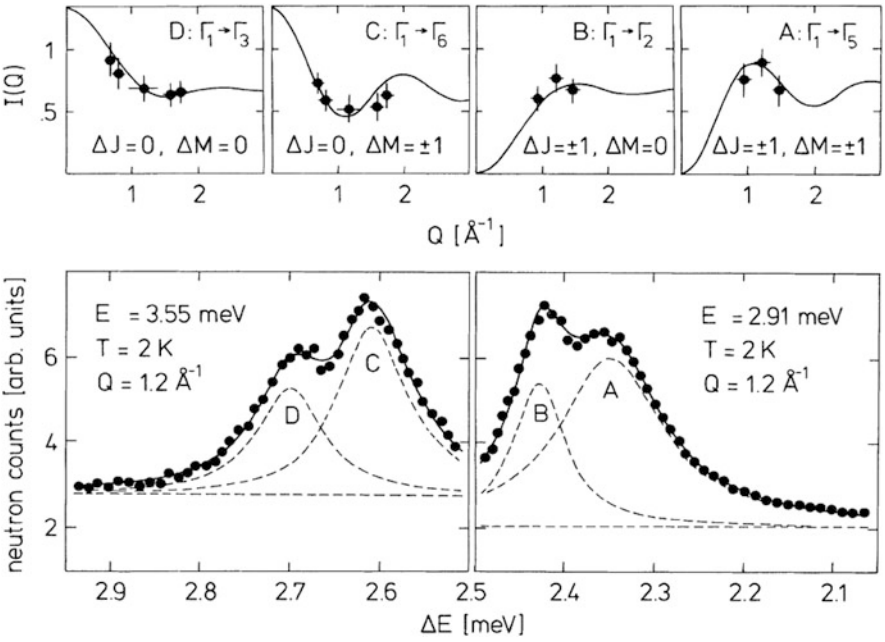

Fig. 10 *Main panel*: neutron energy spectra of a polycrystalline $Cs_3Tb_2Br_9$ dimer compound, resolving transitions to four excited states labeled *A* to *D*. The *top figures* show the different momentum transfers for each of the excitations, which depend on the transition selection rules. Reprinted with permission from [216]. Copyright 1989 American Physical Society

three excitations probed, and their specific Q dependences, measured on the ToF instrument IN5 at Institut Laue Langevin (ILL), Grenoble, France. The four transitions have their own characteristic Q-dependence corresponding to the different wave-functions of the relevant dimer states involved in the observed excitation. This information enabled the deduction of a weak antiferromagnetic Heisenberg exchange interaction of $\mathcal{J} = -0.0049\,\text{meV}$ $\left(\hat{H} = -2\mathcal{J}\boldsymbol{J}_1 \cdot \boldsymbol{J}_2\right)$. This method has proven valuable for detailed investigations of the magnitude, sign, and symmetry of exchange interactions in a wide variety of Ln pairs [218, 219] and mixed dimers of 4*f*–3*d* coupled ions [220].

4.4 Single-Molecule Magnets

4.4.1 Exchange Coupled Lanthanide Based SMMs

A renewed interest has formed in the characterization of Ln based MNs following their utilization for the design of SMMs with large blocking temperatures [99–107, 221, 222]. Since the early investigations of Ln exchange, instrumentation for ToF

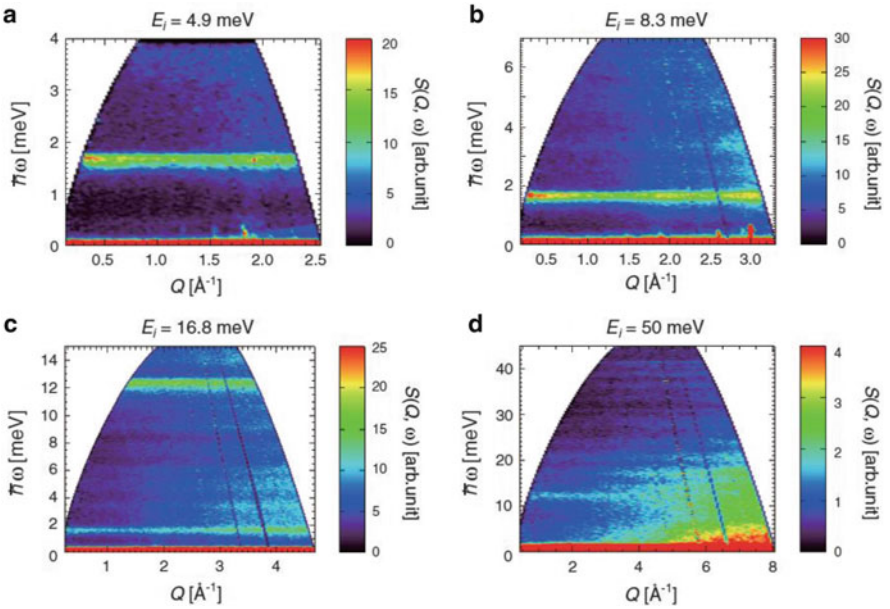

Fig. 11 INS intensity as functions of energy and momentum transfer measured on a Tb-Cu dimer. The respective $S(Q, \omega)$ maps correspond to incident neutron energies of 4.9, 8.3, 16.8, and 50 meV (**a**–**d**, respectively). Measurements were performed simultaneously at 3.5 K using the repetition rate multiplication spectrometer AMATERAS at MLF, J-PARC in Japan. Reprinted with permission from [213]. Copyright 2013 American Physical Society

INS has undergone marked development. The AMATERAS ToF spectrometer was utilized to investigate a Tb-Cu SMM [213] using RRM. In this investigation, four incident neutron energies and wave vectors were selected to probe four $S(Q, \omega)$ dynamic ranges simultaneously. Figure 11 shows the $S(Q, \omega)$ intensity maps measured for the Tb–Cu SMM: two clear magnetic excitation bands are observed at 1.7 and 12.3 meV corresponding to the energy of the Tb–Cu exchange interaction and the transition between the multiplets of the Tb ligand field states. The high instrumental resolution of the AMATERAS spectrometer ($\Delta E/E \sim 1\,\%$) permits resolution of the hyperfine interaction of Cu and Tb, observed as splitting within the 1.7 meV excitation.

4.4.2 Transition Metal SMMs and the Giant Spin Approximation

INS investigations on the first discovered SMMs resolved the zfs without the need for applied magnetic fields, aiding the development of simplified models necessary to understand the manifestation of slow magnetic relaxation and QTM. The first INS investigations were performed on $[Fe_8O_2(OH)_{12}(tacn)_6]^{8+}$ (Fe_8 [223]) and, shortly thereafter, on $[Mn_{12}O_{12}(CD_3COO)_{16}] \cdot 2D_3COOD \cdot 4D_2O$ (deuterated

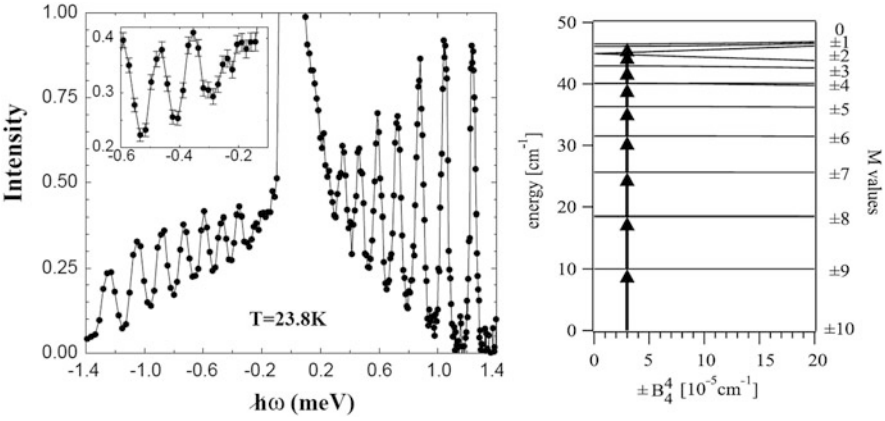

Fig. 12 (*Left*) Neutron scattering intensity as a function of energy transfer for $Mn_{12}Ac$. (*Right*) Zero-field-splitting eigenvalues within the ground state multiplet calculated as a function of the transverse anisotropy term (B_4^4) relevant to QTM. Adapted with permission from [224]. Copyright 1999 American Physical Society

$Mn_{12}Ac$) [224, 225]. In both cases, the advantage of a zero applied magnetic field approach to directly measure zfs within the ground spin multiplet was demonstrated. The observed transition energies and intensities were calculated within the approximation of a single $S = 10$ ground state (the giant spin approximation, or GSA – see Sect. 2.1). Figure 12 shows the neutron scattering energy spectrum for $Mn_{12}Ac$. The measurement determined irregular spacing of transition energies (related to B_4^0), and a reduction in transition intensities at the top of the energy barrier, providing direct spectroscopic access to the transverse Hamiltonian term coefficient (B_4^4) responsible, in part, for the manifestation of QTM. Figure 12b shows how the zero field eigenvalues vary as a function of the B_4^4 coefficient, with arrows labeling the observed INS transition intensities. The B_4^4 coefficient only accounts for QTM for even to even M_S applied field crossings (see Fig. 1), inconsistent with magnetization measurements where QTM is observed at every M_S crossing [29, 30]. Some 5 years later, following an upgrade of the IN5 spectrometer incident neutron flux in 2002 [226], further insight into the quantification of lower symmetry Hamiltonian terms within $Mn_{12}Ac$ could be resolved [43]. In this later investigation, evidence for rhombic anisotropy within a multi-isomer model was quantified, consistent with EPR results [33, 34, 42]. The inclusion of rhombic anisotropy is justified by low temperature X-ray and neutron diffraction analyses [227, 228] which identify hydrogen bonds responsible for transmitting lattice solvent disorder to $Mn_{12}Ac$ clusters, as discussed in detail in Sects. 1.1.1 and 1.1.2. Further INS studies of $Mn_{12}Ac$ went on to investigate pressure induced reduction of axial anisotropy [229] and investigations into the exchange interactions present within $Mn_{12}Ac$ resulting in the identification of several spin excited states [230, 231].

The ability to spectroscopically access exchange interactions and anisotropy based zfs has meant INS is appropriate for studying SMMs where the GSA is no longer appropriate (see also Sect. 2.2). This was the focus of an investigation into the breakdown of the GSA via the characterization of two Mn_6 complexes [232, 233]. The possibility to probe inter-multiplet transitions by INS enabled access to energy levels originating from the excited $S = 11$ manifold. Indeed, the $S = 11$ excited states were identified to be below the anisotropy barrier and nested within the $S = 12$ ground state multiplet. Using a microscopic spin Hamilton, considering exchange between Mn^{III} ions and their individual anisotropy contributions, the properties of the Mn_6 clusters could be described including the demonstration of tunneling pathways involving manifolds of different total spin S.

4.5 *Inelastic Neutron Scattering in Fixed Applied Magnetic Fields*

Elusive physical phenomena such as magnetic frustration induced ground state degeneracy [234–238], and the avoided spin state crossings at critical applied magnetic fields [239], are challenging to quantitatively examine. Understanding the composition of the state wave functions involved is imperative for the rationalization of such phenomena. The application of an applied static magnetic field provides a means to break magnetic frustration induced degeneracy such that the wave functions of the involved spin states can be probed by INS. Likewise, applied fields can be used to access critical points exhibiting interesting quantum tunneling phenomena. It is desirable that electromagnets for ToF INS do not restrict scattered neutron pathways, so as to maximize $S(\boldsymbol{Q}, \omega)$ coverage. The design of such setups in increasingly high magnetic fields, and with broader angular neutron detection ranges, is in continuous development [240] and will provide a marked advance for the study of condensed matter magnetism as a whole.

There have been several successful INS investigations of MNs in applied fields. The IN5 ToF spectrometer was used to investigate the antiferromagnetic molecule $K_6[V_{15}As_6O_{42}]\cdot H_2O$ [241] in applied fields of up to 2.5 T. The employed magnet reduced the vertically accessible detector coverage of the IN5 instrument. However, the portion of $S(\boldsymbol{Q}, \omega)$ obtained proved sufficient to determine the origin of wave function mixing in the frustrated ground state of this system. An isolated spin ½ trimer with equilateral AF exchange is the most fundamental model system to investigate the manifestation of magnetic frustration. If characterized in sufficient detail, the energy levels and wave functions of the system may be solved exactly, in contrast to extended frustrated systems with collective magnetic phenomena [242]. The V_{15} molecule has multi-layered exchange pathways with a V_3 triangle sandwiched between two V_6 rings. Magnetic susceptibility measurements and EPR show that, below 100 K, the two rings above and below a central triangle of V ions lock into a singlet state and, at lower temperatures, the spin dynamics of the system

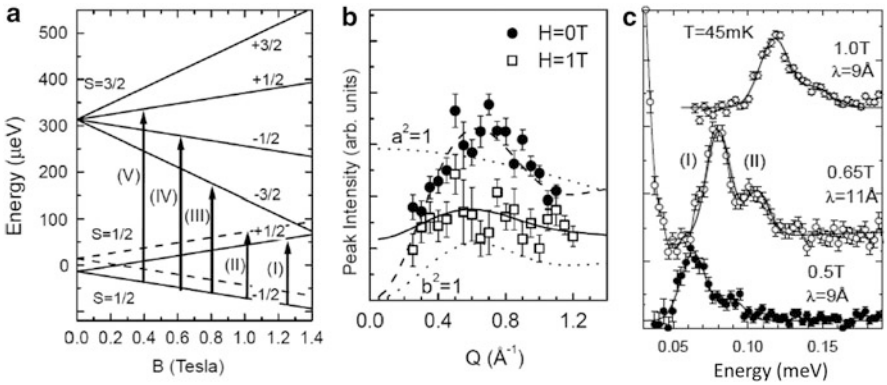

Fig. 13 (**a**) Energy level diagram of V_{15} in applied magnetic field with labels for the observed INS transitions. (**b**) Neutron intensity as a function momentum transfer, Q, for transitions I (at a field of 1 T – *open squares*) and $III + IV + V$ (at 0 T – *black circles* with a simulation denoted by the *dashed curve*); simulations of I were performed according to Eq. (16), both with the inclusion of state mixing (*solid line*) and without (*dotted lines*). (**c**) Use of magnetic field to resolve the low-energy transitions I and II. Adapted with permission from [247]. Copyright 2004 EDP Sciences

are governed by the V_3 triangle which rests on the C_3 symmetry axis of the molecule [243, 244]. A trigonal symmetry triangle of AF coupled spin-½ particles (s_a, s_b and s_c) has a ground state characterized by two degenerate Kramers doublets, $|0, ½, ½, \pm½\rangle$ and $|1, -½, ½, \pm½\rangle$, corresponding to the following basis $|S_{ab}, S_c, S_{\text{total}}, M_S\rangle$. However, low temperature magnetization measurements of V_{15} exhibit butterfly like hysteresis, suggesting a small degeneracy lifting within the ground state, and mixing between the two Kramers doublet states [245]. Initial attempts to account for this non-degeneracy were inconclusive [246]. Only by analysis of INS intensity as a function of Q with applied magnetic field could the internal spin structure of the frustrated triangle be deduced [247]. Figure 13a shows the energy level diagram as a function of applied field, with labels for the accessed INS excitations. With the application of the field, it is possible to resolve the non-degeneracy of the two Kramers doublets (27 μeV). In zero applied magnetic field, the intensity of a $\Delta S_{a,\,b} = 0$ transition is the same as a $\Delta S_{a,\,b} = \pm 1$ transition for an equatorially AF exchange coupled triangle. However, in an applied magnetic field, the intensity of a $\Delta S_{a,\,b} = 0$ transition is three times as intense as a $\Delta S_{a,\,b} = \pm 1$ transition. Figure 13c shows that the intensity of transitions I and II are different in applied field, but not by a factor of three. The Q dependence of transition I is used to quantify the origin of mixing between the $|0, ½, ½, \pm½\rangle$ and $|1, -½, ½, \pm½\rangle$ states. Equation (16) expresses the orientation averaged $I(Q)$ for the specific case of a triangle, where a^2 and b^2 are mixing coefficients for the $S_{a,\,b} = 0$ and 1 states, respectively, R is the interatomic distance, and I_0 is a normalization constant.

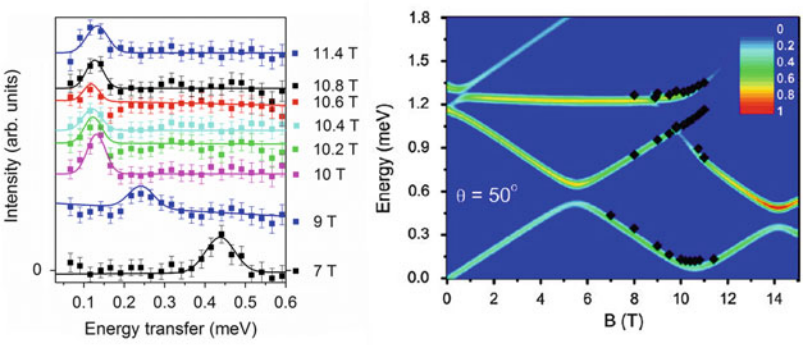

Fig. 14 (*Left*) INS energy spectra for a single crystal of Cr_7Ni, measured at 66 mK and at various fields in the vicinity of an avoided spin state crossing. (*Right*) Measured peak maxima (*black squares*) superimposed on a calculated INS intensity color plot of energy versus applied magnetic field. Adapted with permission from [248]. Copyright 2007 American Physical Society

$$I(Q) = I_0 F(Q)^2 \left[a^2 + \frac{b^2}{3} \left(1 - \frac{\sin(QR)}{QR} \right) \right]. \tag{16}$$

The proportion of mixing found to reproduce the measured Q dependence of I [solid line in Fig. 13b] was found to be represented by the inclusion of a small difference in the exchange coupling between sites s_a/s_b with respect to s_b/s_c and s_a/s_c. Quantification of the energy gap and its origin required neutron scattering. The study ruled out a long-standing theory that Dzyaloshinskii-Moriya (DM) interactions governed the non-degeneracy in V_{15}, showing that the energy gap between the doublets is field independent, in contradiction to a splitting originating from DM exchange.

Mixing between wave functions at avoided spin state crossings has been investigated by INS directly in the heterometallic AF ring $[(C_2D_5)_2NH_2Cr_7NiF_8(O_2CC(CD_3)_3)_{16}]$ (Cr_7Ni [248]). The inclusion of a Ni^{II} ion within an AF ring of 8 Cr^{III} ions breaks the ideal ring symmetry. The ToF Disk Chopper Spectrometer at the NIST Center for Neutron Research was used to probe a single crystal of Cr_7Ni in magnetic fields up to 11.4 T. The avoided crossing between the $S = ½$ ground state and the $S = {}^3/_2$ first excited state corresponds to a coherent oscillation in the total spin between $S = ½$ and ${}^3/_2$. To confirm this scenario experimentally the spin dynamics of the avoided crossing gap have to be directly probed in the frequency domain. INS is a measurement of this nature [cf. Eq. (13)] and was adopted to probe the energy gap between the $S = ½$ ground state and $S = {}^3/_2$ excited state as a function of magnetic field through the 10.5 T avoided crossing, proving that the associated oscillations occur coherently (see Fig. 14).

The study of relaxation in SMMs has also been investigated in applied magnetic fields using time resolved INS at the IN5 spectrometer ILL, France. The principle of this method was proven in the study on an array of aligned $Mn_{12}Ac$ single crystals [249]. In this investigation, the magnetic relaxation was probed by monitoring

changes in the population of states as a function of time via the INS intensity following a switch of field direction along the sample magnetic easy-axis. Additionally, the field dependent studies aided the identification of a minority $Mn_{12}Ac$ species present within samples (see also Sect. 2.2), providing quantification and additional explanation for the anomalous fast relaxation observed in AC susceptibility measurements [250].

4.6 Antiferromagnetic Molecular Clusters: AF Rings

The spin dynamics of AF rings with dominant nearest neighbor exchange have drawn considerable interest [251–254]. Experimental investigations have uncovered a wealth of interesting physical phenomena [255] in accordance with much of the theoretical speculation. Topics of interest include bipartite excitations [256], spin wave theory [257, 258], magnetic frustration [236, 259], and Néel vector tunneling [260, 261].

Even membered rings with nearest neighbor Heisenberg exchange have been found to follow a rotational-band-like energy dependence in accordance with the Landé interval rule [256, 262, 263]. This rule, $E_S = \Delta_0 S(S+1)/2$, gives the energy dependence of spin states with increasing S (known as the L-band), where Δ_0 is the energy gap between the ground and first excited spin state. An approximate Hamiltonian can be used to express this band of excitations, where an effective exchange (J_{eff}) between two sub-lattice spin vectors, S_A and S_B, is considered. Conformation to this bipartite model assumes collective behavior between sub-lattice spins in the absence of quantum fluctuations. Within this context the energy dependence can be considered semi-classical in nature [264], analogous to the magnetic bi-stability in SMMs. A second, higher energy band of excitations, the so-called E-band, also exhibits a parabolic energy dependence upon increasing spin, displaced in energy from the L-band of excitations. The difference between the two bands of increasing spin states reflects differences within their internal spin structure. One of the first AF rings to be studied was a polycrystalline sample of Cr_8, $[Cr_8F_8(tBuCO_2)_{16}]$ [256, 265]. The Cr_8 ring exhibits a singlet $S = 0$ ground state and, at 1.5 K, transitions to $S = 1$ excited states of the L and E bands were probed. The two bands of excitations exhibit different momentum transfer dependence, reflecting the differences in their internal structure. The effect of lowering the symmetry of the Cr_8 ring by inclusion of a diamagnetic Zn ion has also been investigated by INS, i.e., a similar Cr_8Zn ring [266]. The Zn ion breaks the translational invariance around the ring, making the L-band a worse approximation; thus, mixing of the characteristic L and E band neutron momentum transfers was observed.

Néel vector tunneling has been proposed for ring systems exhibiting bipartite properties in addition to a large axial anisotropy, where alignment of the Néel vector with the z-axis (either up, $|\uparrow\rangle$, or down, $|\downarrow\rangle$) becomes energetically favorable for sufficiently strong axial anisotropy. Many investigations have pursued the

observation of Néel vector tunneling – a coherent quantum oscillation between $|\uparrow\rangle$ and $|\downarrow\rangle$ – through the anisotropy barrier. Neutron scattering experiments have been conducted in search of this tunneling in Fe-based AF rings, exhibiting large dipolar anisotropies [260, 261, 267]. However, while parameterization of general theoretical criteria could be met [251], determination of whether the tunneling transition is a genuine combination of two Néel states remains unclear. The best evidence so far for Néel vector tunneling involves magnetic torque measurements [260].

4.7 Single Crystal ToF INS

The vast majority of ToF INS investigations on MNs have been of a polycrystalline form, where the modulus of Q is obtained from the scattering cross section. In this scenario, limited information regarding the internal spin structure of the measured MN may be extracted. This is because the polycrystalline scattering cross section depends only on distances between correlated magnetic ions, washing out the detailed information concerning the dynamic spin–spin correlations between particular pairs of spins within the studied MN. The orientation average of the so-called interference terms does provide valuable information, several examples of which have been discussed here. However, this represents only part of the potential information available in comparison to measuring the full four-dimensional $S(\boldsymbol{Q}, \omega)$ cross section [268]. In fact, such a measurement *is* possible with a single-crystal MN sample, where the Fourier components of the dynamic correlations between particular magnetic ion pairs are related to their vector separation in the scattering cross section, modulating the scattering intensity with respect to $\boldsymbol{Q}$. To gain access to such information requires the measurement of large portions of $S(\boldsymbol{Q}, \omega))$, which requires neutron detectors with position sensitivity in both the azimuthal and out of plane scattering angles. Until recently, cold source ToF INS spectrometers had just unitary detectors which measure on Debye-Scherrer rings. However, with the development of ^{3}He position sensitive detectors for cold source neutron ToF INS, the coverage of large detection solid angles, with full $S(\boldsymbol{Q}, \omega))$ analysis, is within reach [211, 212, 226, 269]. Embedded within the Fourier components of the dynamic spin correlations is detailed information regarding the low temperature dynamics. The measured correlations can be linked to the low temperature dynamics by linear response functions. These functions are represented by a set of susceptibilities, which provide the response of a spin d at time t to a magnetic field pulse vector to spin d' at time $t = 0$. Such information can provide critical information regarding the internal spin structure within a MN, enabling, e.g., a validation of the Néel vector tunneling regime within AF rings. Additionally, the sum of the full set of dynamical spin correlations gives the equal time correlation functions, which characterize the spin structure of the ground state [270].

Successful extraction of the dynamic spin pair correlations within a MN has been demonstrated in 2012 [270]. The measurements were performed on the IN5

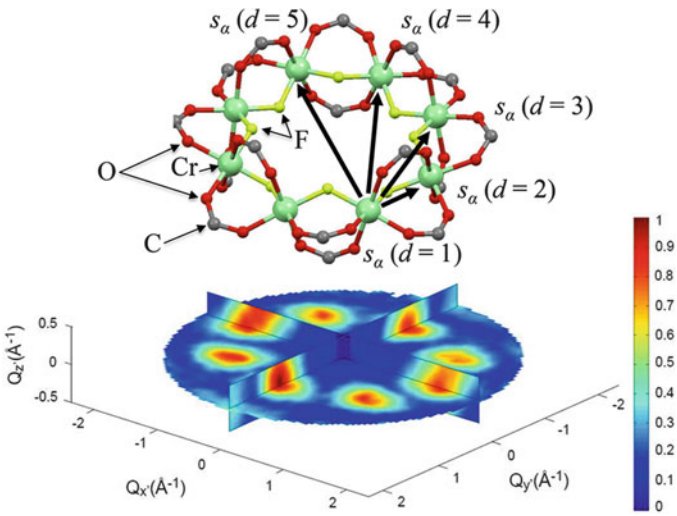

Fig. 15 (*Top*) Principal correlated spin pairs ($d=1$ to 5), with respect to vectors (*thick arrows*) within the Cr_8 MN. The Cr atom (*large balls*) pairs in the ring are bridged by fluorines and two $tBuCO_2$ groups, with carboxylates cropped for clarity (see labeling). (*Bottom*) Combined $S(\boldsymbol{Q})$ of Cr_8 for the *L*-band magnetic excitation, $p=1$. Adapted with permission from [270]. Copyright 2012 Nature Publishing Group

spectrometer following an upgrade which saw the installation of position sensitive detectors composed of 10^5 pixels covering a total of 30 m^2. A 240 mg single-crystal of the well characterized prototype AF ring Cr_8 was selected for the investigation. INS spectra were measured in one-degree steps, rotating the crystal to access a large range of momentum transfers. At 1.5 K, transitions from the $S=0$ ground state access three $S=1$ excited states labeled $p=1$, 2, and 3. The $p=1$ transition reaches into the $S=1$ first excited state (*L*-band), and $p=2$ and 3 go to $S=1$ excited states (*E*-band), while further transitions into additional excited states exhibit close to zero oscillator strength. An integrated energy cut displaying the measured neutron scattering momentum transfer for the $p=1$ transition is shown in Fig. 15. The magnetic neutron scattering cross section [Eq. (9)] for the specific case of a homometallic MN with axial anisotropy, as $T\rightarrow 0$, may be written as [206]:

$$S(\boldsymbol{Q},\omega) \propto \sum_{\alpha=x,y,z}\left(1-\frac{Q_\alpha^2}{Q^2}\right)\sum_p\sum_{d\geq d'}^{N} F_d(Q)\times F_{d'}(Q)\cos\left(\boldsymbol{Q}\cdot\boldsymbol{R}_{dd'}\right), \\ \times\left\langle 0\middle|s_\alpha(d)\middle|p\right\rangle\left\langle p\middle|s_\alpha\left(d'\right)\middle|0\right\rangle\delta\left(E_i-E_f+\hbar\omega_p\right) \tag{17}$$

where $F_d(Q)$ is the magnetic form factor of the dth ion in the ring, $\boldsymbol{R}_{dd'}$ is the vector between ion d with spin $s_\alpha(d)$ and ion d' with spin $s_\alpha(d')$, and $|0\rangle$ and $|p\rangle$ are the ground and excited eigen-functions of the magnetic transition p, with eigenvalue $\hbar\omega_p$. The $\langle 0|s_\alpha(d)|p\rangle\langle p|s_\alpha(d')|0\rangle$ terms represent the Fourier components of the

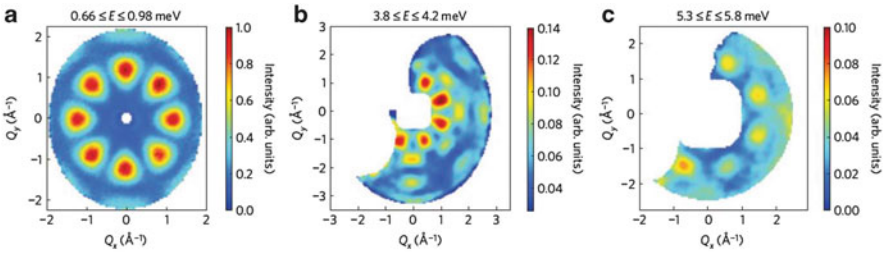

Fig. 16 Constant energy cuts for magnetic excitations $p = 1$, 2, and 3 [(**a**)–(**c**), respectively]. The maps show the Q_x–Q_y wave vector dependence lying in the plane of the Cr_8 ring. Adapted with permission from [270]. Copyright 2012 Nature Publishing Group

dynamical correlations between ions within the MN. Hence, by fitting [271] Eq. (17) to the measured $S(\boldsymbol{Q}, \omega)$ for excitations $p = 1$, 2, 3, the full set of Fourier components for the dynamical correlations may be extracted directly from the measurement without reliance on any spin Hamiltonian model. The Cr_8 molecule exhibits 5 principle correlations (see Fig. 15): the self-correlation $d = 1$, and pair correlations $d = 1$ to $2 \rightarrow 5$, where $d = 6$, 7, 8 are equivalents to $d = 4$, 3, 2, respectively. Figure 16 shows constant energy plots for the excitations $p = 1$, 2, 3, showing the momentum transfer for two wave-vector components, Q_x and Q_y, lying in the plane of the Cr_8 ring. Fits to the full three wave-vector components for each transition successfully extracted the Fourier components of the two spin dynamical correlations. The obtained values were found to correspond very well to exact values extracted from a microscopic Hamiltonian calculation solved for Cr_8 in [265].

4.8 Future Prospects

The selection of key studies reported here demonstrates that INS has played an integral role in the development of the MN research field. Today much effort goes into taking MNs out of the crystal for manipulation [272] of their quantum properties on surfaces [169] or within nanotubes [273]. However, before control of MNs can be achieved to such a precision that applications like QIP could become a reality, an extensive understanding of the structure of eigenstates within prototype clusters must be reached. The recent development of ToF INS spectrometers underpins a renaissance for the characterization of MNs, providing a way to probe detailed wave-function information for development of this research area. As exemplified in the single-crystal study of Cr_8 [270], extraction of two-spin dynamical correlations opens up new possibilities to access the internal spin structure of MNs. It will be fascinating to see the application of single crystal ToF INS to probe quantum entanglement within prototype qubits, composed of supramolecular complexes of linked MNs [274, 275]. Another field of interest

includes confirmation of Néel vector tunneling in AF rings. The extracted spin correlation information obtained from the single-crystal INS study of Cr_8 demonstrated that the degree of validity of the Néel vector tunneling framework can be tested directly.

A further instrumentation development will be the integration of large applied magnetic fields with ToF INS on single crystals of MNs. The evolution of MN cluster wave-functions with applied magnetic fields could be used to investigate quantum phenomena such as avoided spin state crossings, and the effect of magnetic fields on exchange biased qubit prototypes. Applied fields provide a means of accessing detailed information regarding the internal spin structure of the degenerate eigenstates in frustrated systems and MNs exhibiting magnetic vortex-spin chirality [276]. The Cr_8 single crystal study revealed how the propagation of quantum fluctuations can be observed. It was shown how the propagation of a local disturbance causes a wave-like motion of the magnetization around the ring, with the occurrence of constructive interference as both anti-clockwise and clockwise propagations meet at the opposite side of the ring. It will be of interest to obtain the same information for odd membered, frustrated rings [236, 277], where complex interference effects should occur as out-of-phase propagations of magnetization meet. Coupling single crystal studies with applied magnetic fields will open up further opportunities for probing elusive physical phenomena within MNs. Fields of just a couple of Tesla are enough to investigate phenomena such as entanglement or frustration-induced degeneracy; many spectrometers are already equipped and ready for such investigations.

In summary, single crystal INS changes the landscape in terms of the amount of detailed information that can be experimentally probed within MNs. The recent demonstration of this method on the prototypical AF ring, Cr_8, highlights what can be achieved. This method currently requires very large crystals – of order of 200 mg; additionally, the arrangements of molecules within the unit cell must be as simple as possible. In most cases, deuteration is required, introducing further complexity to chemical synthesis. However, it is frequently observed that incoherent scattering from hydrogen only becomes significant at energies greater than around 2 meV. The characterization of polycrystalline samples becomes an increasingly rapid method to investigate MNs, with greater energy resolutions enabling measurements of small zfs interactions. The latest cold source ToF INS spectrometers (LET and AMATERAS) present the possibility of measuring multiple dynamic ranges at the same time, known as RRM. This will enable the measurement of $S(\boldsymbol{Q}, \omega)$ over a broader dynamic range than possible with a single monochromating pulse rate, reducing the amount of time needed to obtain the three vector scattering intensities for all magnetic excitations over a broad energy range within a MN. ToF INS on single crystals of MNs represents the frontier of what is currently possible with today's neutron scattering technology. However, the construction of new neutron scattering facilities, such as the European Spallation source [278], should see increases of neutron beam intensities by many orders of magnitude, permitting the study of more complex high-nuclearity structures with much smaller crystal sizes.

5 Muon-Spin Rotation

In a μ^+SR experiment [279, 280], spin-polarized positively charged muons are stopped in a target sample. The time evolution of the muon spin polarization is probed via the positron decay asymmetry function $A(t)$ to which it is proportional. Such experiments can be carried out at muon sources which are available in various locations around the world (currently J-PARC in Japan, PSI in Switzerland, RAL in the UK, and TRIUMF in Canada). They give a means of measuring local magnetization and dynamics from the viewpoint of the implanted probe, the spin-polarized muon. A conventional magnetometry measurement of the magnetic susceptibility χ yields

$$\chi = \lim_{\delta H \to 0} \frac{\delta M_{\mathrm{av}}}{\delta H}, \tag{18}$$

where M_{av} is given by $M_{\mathrm{av}} = \frac{1}{V}\int_V M(\mathbf{r}) d^3 r$, a volume averaged magnetization. In contrast, from μ^+SR data one can extract the staggered magnetization distribution $\rho(M)$ in zero applied field; thus if there are N crystallographically independent muon sites (in most molecular magnetic materials that have been studied, it is found that N is 1, 2, or 3), such that a fraction f_i of the muons implant at the ith site, then one can assume that the measured muon polarization function $A(t)$ (neglecting weakly relaxing terms due to longitudinal relaxation) follows

$$A(t) \propto \sum_{i=1}^{N} f_i \int \rho(M) e^{-\lambda_i t} \cos\left(\alpha_i M t\right) dM, \tag{19}$$

where α_i is a constant which depends on the dipolar coupling between the local magnetization M and the muon at site i, and λ_i is a relaxation rate. If the sample has uniform staggered magnetization M_0 so that $\rho(M) = \delta(M - M_0)$, then

$$A(t) \propto \sum_{i=1}^{N} f_i e^{-\lambda_i t} \cos\left(\alpha_i M_0 t\right). \tag{20}$$

Muons can hence allow the temperature dependence of M_0 to be determined and have the useful advantage that they can demonstrate rather easily that M_0 is a characteristic of the entirety of the sample, and not of a minority impurity phase.

5.1 Applications of μ^+*SR*

Muons have a particular advantage in the case of low-dimensional magnets [281–283]. Because the correlation length ξ in an antiferromagnetic chain grows on cooling, the heat capacity exhibits a rather broad maximum as the entropy of the

spins consequently decreases with the increasing correlation. Thus, when 3D ordering sets in at T_N, the transition is associated only with a rather small change in entropy, thereby giving rise to a tiny peak in the heat capacity, the size of which decreases as $|J'/J|$ decreases. This effect is shown in recent Monte Carlo simulations for quasi-two-dimensional systems [284], and means that identifying 3D ordering in very anisotropic magnets using heat capacity can be challenging. In contrast, the transition from a non-long-range ordered state, even one with dynamic correlations of large spatial extent, to a 3D long-range ordered state is rather straightforward using μ^+SR [282].

However, for MNs, measurements made using μ^+SR have proven difficult to interpret, and the large number of muon sites within a complex molecule that will inevitably occur do not make the situation easy. Although initially it was thought that QTM should be measurable by implanting muons into MNs [285–287], the unambiguous detection of this effect proved elusive [288]. Instead, μ^+SR spectra obtained on high spin systems appeared to arise from dynamic fluctuations of a local magnetic field distribution at the muon sites, which persisted down to dilution refrigerator temperatures [286–289]. Muon results on MN systems all showed similar behavior but it was unclear whether the muon was probing the intrinsic behavior of the large electronic spin or some residual effect. It has been argued that μ^+SR is sensitive to the dephasing of the MN electronic spins caused by the incoherent fluctuations of nuclear moments in which the metal ions are embedded [290]. If this is the case then it makes the muon a valuable probe of the potential mechanism behind QTM. In order to address the question of what the muon probes in MN systems, identical μ^+SR measurements were performed [291] on protonated and deuterated samples of Cr_7Mn ($S = 1$) and Cr_8 ($S = 0$) [292, 293] [structure shown in the inset of Fig. 17a, b]. These measurements show (1) that the muon is controlled by the large electronic spin in a MN; (2) deuteration leads to a significant increase in the μ^+SR relaxation rate at low temperature in Cr_7Mn, implying that muons probe the dephasing of large electronic spins by the random magnetic fields due to the nuclei and; (3) that upon cooling, a magnetic ground state is reached by a freezing out of dynamic processes that leads to magnetic order in Cr_7Mn below 2 K [291]. Typical spectra measured for Cr_7Mn and Cr_8 are shown in Fig. 17. Above $T \approx 2$ K the spectra for all materials differ depending on whether protonated or deuterated.

In the temperature range $2 \leq T \leq 100$ K the spectra for $S = 1$ Cr_7Mn (Fig. 17a) were found to be described by the relaxation function $A(t) = A_1 \exp\left(-\sqrt{\lambda t}\right) + A_{bg}$; where A_{bg} accounts for any background contribution from muons that stop in the sample holder or cryostat tails. This behavior is typical of that observed previously in MN materials [286, 287, 290] and arises because of the complex dynamic distribution of local fields within the material sampled by the muon ensemble. The monotonic relaxation and the fact that the muons could not be decoupled with an applied magnetic field up to 0.6 T places the relaxation in the fast-fluctuation limit [294]. The spectra measured for the $S = 0$ Cr_8 samples are quite different (Fig. 17b). In this case the relaxation rate is far smaller and resembles a Kubo-Toyabe (KT) function with a distribution width given by $\Delta = \gamma_\mu \langle B^2 \rangle^{1/2}$, where

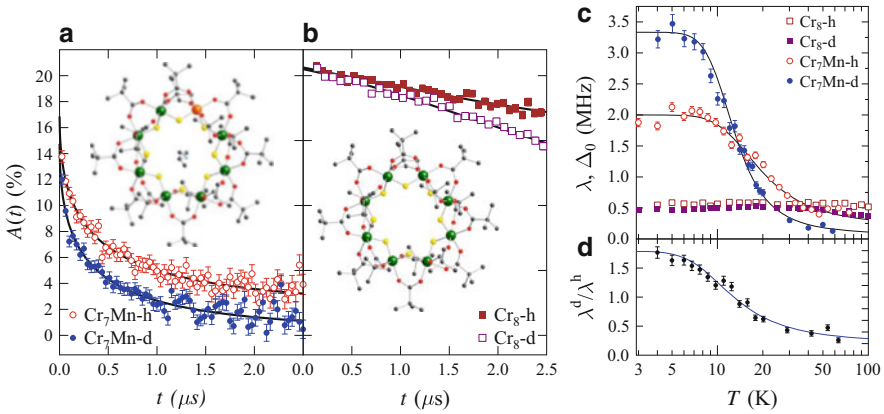

Fig. 17 Spectra for protonated and deuterated Cr_7Mn (**a**) and Cr_8 (**b**) materials, measured at $T = 4.5$ K. *Insets*: structures of the molecules. (**c**) Temperature evolution of the relaxation rates. (**d**) Ratio of the Cr_7Mn-h and -d relaxation rates. The *line* is a guide to the eye. Adapted with permission from [291]. Copyright 2010 American Physical Society

$\gamma_\mu = 2\pi \times 135.5$ MHz T^{-1} is the muon gyromagnetic ratio and B is the local magnetic field at a muon site [294]. In a MN there are many inequivalent classes of muon sites and this leads to a distribution of second moments $p(\Delta)$. The resulting muon relaxation is obtained by averaging the KT function over this distribution, and an analysis [291] shows that the muon is sensitive to the disordered nuclear moments in Cr_8. This is confirmed by the application of a small longitudinal magnetic field which quenches the relaxation. The larger Δ found in Cr_8-d compared to Cr_8-h reflects (albeit partially) the larger moment of the deuteron. Most importantly, the dramatic difference between the measured spectra and relaxation rates for $S = 0$ Cr_8 and $S = 1$ Cr_7Mn samples (Fig. 17a, b) strongly suggests that the muon response in MN systems with $S \neq 0$ stems from dynamic fluctuations of the *electronic* spin. In the absence of an electron spin in Cr_8, the muon spin is relaxed by quasistatic disordered nuclear moments.

The temperature dependence of the relaxation rate λ for the protonated (λ^h) and deuterated (λ^d) Cr_7Mn samples is shown in Fig. 17c. On cooling below $T \sim 50$ K, the relaxation rate λ increases before saturating below ~10 K, with the onset of the increase and the saturation occurring at similar values of T for both materials. This T-dependence is common to nearly all MN systems that have been previously measured with μ^+SR [286–288, 290] and is discussed in more detail below. At high temperature $\lambda^d > \lambda^h$. It is likely that at these high temperatures the electronic spins are fluctuating very fast and are at least partially motionally narrowed from the spectra. Upon cooling, the increase in λ is greater for the deuterated sample, with λ^d becoming greater than λ^h below $\approx$15 K. Most significantly, the saturation of the relaxation at $T \lesssim 10$ K occurs with $\lambda^d > \lambda^h$. The temperature dependence of the ratio λ^d/λ^h (Fig. 17d), which increases upon cooling, tends to $\approx$1.7 at the lowest temperature.

The muon relaxation rate is proportional to the electronic spin correlation time τ_e and $1/\tau_e \propto \langle B_n{}^2 \rangle \tau_n$, where τ_n is the correlation time of the nuclear stochastic field. It is probable that swapping protons for deuterons changes not only the local field distribution (via $\langle B_n{}^2 \rangle$) but also the correlation time of the nuclear stochastic field [291].

Measurements made down to 20 mK show heavily damped oscillations which are identical for -h and -d samples and lead to an estimate of a transition temperature of 1.9(1) K to a state of magnetic order. The heavily damped nature of the oscillations and the Cr_8 results suggest that there are many magnetically inequivalent muon sites in the system. μ^+SR is likely to be particularly effective in revealing transitions to long-range order in MNs and this is a fruitful area for future research. A second interesting topic is the recent observation using muons of electronic energy level crossings [295]. This gives further evidence that the spin relaxation of the implanted muon is sensitive to the dynamics of the electronic spin. The experiment was performed on a broken ring MN Cr_8Cd and the data show clear evidence for the $S = 0$ to $S = 1$ transition that takes place at $B_c = 2.3$ T. The crossing is observed as a resonance-like dip in the average positron asymmetry and also in the muon spin relaxation rate, which shows a sharp increase in magnitude at the transition and a peak centered within the $S = 1$ regime [295]. A third interesting new direction concerns the study of MNs on surfaces using the technique of proximal magnetometry [296] in which very low energy muons are used as a spin probe, implanting them in the substrate, just below the magnetic material. Such experiments are beginning to bear fruit [297].

Acknowledgements All of the authors are indebted to collaborators whose names can be found in a number of the references cited. MLB would especially like to thank Hannu Mutka, Hans-Uli Güdel, Tatiana Guidi, Stefano Carretta, and Paolo Santini; his recent research position is supported by the Army Research Office (W911NF-13-1-0125). SJB would like to thank Tom Lancaster, Francis Pratt, Richard Winpenny and Arzhang Ardavan; his research is supported by EPSRC and STFC (UK). ND acknowledges the Ministerio de Ciencia e Innovación of Spain for a grant under the program Ramón y Cajal. SH would like to acknowledge the NSF (DMR 1309463) and the Air Force (AOARD grant #134031) for financial support. Work at the NHMFL is supported by the NSF (DMR 1157490) and the State of Florida.

References

1. Caneschi A, Gatteschi D, Sessoli R, Barra AL, Brunel LC, Guillot M (1991) J Am Chem Soc 113:5873
2. Brunel L-C, van Tol J, Angerhofer A, Hill S, Krzystek J, Maniero AL (2004) In: Grinberg O, Berliner LJ (eds) Very high frequency EPR, vol 22, Biological magnetic resonance. Springer, New York, p 465
3. Barra AL, Gatteschi D, Sessoli R (1997) Phys Rev B 56:8192
4. Hill S, Perenboom JA, Dalal NS, Hathaway T, Stalcup T, Brooks JS (1998) Phys Rev Lett 80:2453
5. Barra A-L, Debrunner P, Gatteschi D, Schulz CE, Sessoli R (1996) Europhys Lett 35:133
6. Dobrovitski VV, Katsnelson MI, Harmon BN (2000) Phys Rev Lett 84:3458

7. Leuenberger MN, Loss D (2001) Nature 410:789
8. Lehmann J, Gaita-Ariño A, Coronado E, Loss D (2007) Nat Nanotechnol 2:312
9. Lehmann J, Gaita-Ariño A, Coronado E, Loss D (2009) J Mater Chem 19:1672
10. Troiani F, Bellini V, Candini A, Lorusso G, Affronte M (2010) Nanotechnology 21:274009
11. Rudowicz C, Misra SK (2001) Appl Spectrosc Rev 36:11
12. Liu J, del Barco E, Hill S (2014) In: Bartolomé J, Luis F, Fernández J (eds) Molecular magnets: physics and applications, Springer series on nanoscience and technology. Springer, Berlin, pp 77–110
13. Lampropoulos C, Murugesu M, Harter AG, Wernsdofer W, Hill S, Dalal NS, Abboud KA, Christou G (2013) Inorg Chem 52:258
14. Barra A-L, Goiran M, Sessoli R, Zvyagin SA (2013) C R Phys 14:106
15. Hassan AK, Pardi LA, Krzystek J, Sienkiewicz A, Goy P, Rohrer M, Brunel LC (2000) J Magn Reson 142:300
16. Mola M, Hill S, Goy P, Gross M (2000) Rev Sci Instrum 71:186
17. Schnegg A, Behrends J, Lips K, Bittl R, Holldack K (2009) Phys Chem Chem Phys 11:6820
18. Hill S (2013) Polyhedron 64:128
19. Zadrozny JM, Xiao DJ, Atanasov M, Long GJ, Grandjean F, Neese F, Long JR (2013) Nat Chem 5:577
20. Sessoli R, Tsai H-L, Schake AR, Wang S, Vincent JB, Folting K, Gatteschi D, Christou G, Hendrickson DN (1993) J Am Chem Soc 115:1804
21. Sessoli R, Gatteschi D, Caneschi A, Novak M (1993) Nature 365:141
22. Redler G, Lampropoulos C, Datta S, Koo C, Stamatatos TC, Chakov NE, Christou G, Hill S (2009) Phys Rev B 80:094408
23. Petukhov K, Hill S, Chakov NE, Christou G (2004) Phys Rev B 70:054426
24. Hill S, Anderson N, Wilson A, Takahashi S, Petukhov K, Chakov NE, Murugesu M, North JM, del Barco E, Kent AD, Dalal NS, Christou G (2005) Polyhedron 24:2284
25. Hill S, Anderson N, Wilson A, Takahashi S, Chakov NE, Murugesu M, North JM, Dalal NS, Christou G (2005) J Appl Phys 97:10M510
26. Chakov NE, Lee S-C, Harter AG, Kuhns PL, Reyes AP, Hill SO, Dalal NS, Wernsdorfer W, Abboud KA, Christou G (2006) J Am Chem Soc 128:6975
27. Rudowicz C, Chung CY (2004) J Phys Condens Matter 16:5825
28. Stoll S, Schweiger A (2006) J Magn Reson 178:42
29. Friedman JR, Sarachik MP, Tejada J, Ziolo R (1996) Phys Rev Lett 76:3830
30. Thomas L, Lionti F, Ballou R, Gatteschi D, Sessoli R, Barbara B (1996) Nature 383:145
31. Wernsdorfer W, Sessoli R (1999) Science 284:133
32. del Barco E, Kent AD, Hill S, North JM, Dalal NS, Rumberger EM, Hendrickson DN, Chakov N, Christou G (2005) J Low Temp Phys 140:119
33. Takahashi S, Edwards RS, North JM, Hill S, Dalal NS (2004) Phys Rev B 70:094429
34. Hill S, Edwards RS, Jones SI, North JM, Dalal NS (2003) Phys Rev Lett 90:217204
35. Wilson A, Lawrence J, Yang E-C, Nakano M, Hendrickson DN, Hill S (2006) Phys Rev B 74, R140403
36. Kirman C, Lawrence J, Hill S, Yang E-C, Hendrickson DN (2005) J Appl Phys 97:10M501
37. Lawrence J, Hill S, Yang E-C, Hendrickson DN (2009) Phys Chem Chem Phys 2009:6743
38. Hill S, Murugesu M, Christou G (2009) Phys Rev B 80:174416
39. Barra A-L, Caneschi A, Cornia A, Gatteschi D, Gorini L, Heiniger L-P, Sessoli R, Sorace L (2007) J Am Chem Soc 129:10754
40. Sorace L, Boulon M-E, Totaro P, Cornia A, Fernandes-Soares J, Sessoli R (2013) Phys Rev B 88:104407
41. Lawrence J, Yang E-C, Edwards R, Olmstead MM, Ramsey C, Dalal NS, Gantzel PK, Hill S, Hendrickson DN (2008) Inorg Chem 47:1965
42. Cornia A, Sessoli R, Sorace L, Gatteschi D, Barra AL, Daiguebonne C (2002) Phys Rev Lett 89:257201
43. Bircher R, Chaboussant G, Sieber A, Güdel HU, Mutka H (2004) Phys Rev B 70:212413

44. del Barco E, Kent AD, Rumberger EM, Hendrickson DN, Christou G (2003) Phys Rev Lett 91:047203
45. Parks B, Loomis J, Rumberger E, Hendrickson DN, Christou G (2001) Phys Rev B 64:184426
46. Macia F, Lawrence J, Hill S, Hernandez JM, Tejada J, Santos PV, Lampropoulos C, Christou G (2008) Phys Rev B 77:020403(R)
47. van Slageren J, Vongtragool S, Gorshunov B, Mukhin A, Dressel M (2009) Phys Rev B79:224406
48. Wernsdorfer W, Sessoli R, Gatteschi D (1999) Europhys Lett 47:254
49. Maccagnano S, Achey R, Negusse E, Lussier A, Mola MM, Hill S, Dalal NS (2001) Polyhedron 20:1441
50. Park K, Novotny MA, Dalal NS, Hill S, Rikvold PA (2001) Phys Rev B 65:014426
51. Park K, Novotny MA, Dalal NS, Hill S, Rikvold PA (2002) Phys Rev B 66:144409
52. Hill S, Maccagnano S, Park K, Achey RM, North JM, Dalal NS (2002) Phys Rev B 65:224410
53. Takeda K, Awaga K, Inabe T, Yamaguchi A, Ishimoto H, Tomita T, Mitamura H, Goto T, Mori N, Nojiri H (2002) Phys Rev B 65:094424
54. Vongtragool S, Mukhin A, Gorshunov B, Dressel M (2004) Phys Rev B 69:104410
55. van Slageren J, Vongtragool S, Mukhin A, Gorshunov B, Dresses M (2005) Phys Rev B 72:020401
56. El Hallak F, van Slageren J, Gómez-Segura J, Ruiz-Molina D, Dressel M (2007) Phys Rev B 75:104403
57. Carbonera C, Luis F, Campo J, Sánchez-Marcos J, Camón A, Chaboy J, Ruiz-Molina D, Imaz I, van Slageren J, Dengler S, González M (2010) Phys Rev B 81:014427
58. Chudnovsky EM, Garanin DA (2001) Phys Rev Lett 87:187203
59. Mertes KM, Suzuki Y, Sarachik MP, Paltiel Y, Shtrikman H, Zeldov E, Rumberger E, Hendrickson DN, Christou G (2001) Phys Rev Lett 87:227205
60. Garanin DA, Chudnovsky EM (2002) Phys Rev B 65:094423
61. Wen B, Subedi P, Bo L, Yeshurun Y, Sarachik MP, Kent AD, Millis AJ, Lampropoulos C, Christou G (2010) Phys Rev B 82:014406
62. Burzurí E, Carbonera C, Luis F, Ruiz-Molina D, Lampropoulos C, Christou G (2009) Phys Rev B 80:224428
63. Sessoli R, Gatteschi D, Caneschi A, Novak M (1993) Nature 365:141
64. Wernsdorfer W, Chakov NE, Christou G. arXiv:cond-mat/0405014v2 (unpublished)
65. Soler M, Wernsdorfer W, Sun Z, Huffman JC, Hendrickson DN, Christou G (2003) Chem Commun 2003:2672
66. Lampropoulos C, Redler G, Data S, Abboud KA, Hill S, Christou G (2010) Inorg Chem 49:1325
67. Bagai R, Christou G (2009) Chem Soc Rev 38:1011
68. del Barco E, Kent AD, Chakov NE, Zakharov LN, Rheingold AL, Hendrickson DN, Christou G (2004) Phys Rev B 69:020411
69. van Slageren J, Vongtragool S, Gorshunov B, Mukhin AA, Karl N, Krzystek J, Telser J, Müller A, Sangregorio C, Gatteschi D, Dressel M (2003) Phys Chem Chem Phys 5:3837
70. Prokof'ev NV, Stamp PCE (1998) Phys Rev Lett 80:5794
71. Liu J, Beedle CC, Quddusi HM, del Barco E, Hendrickson DN, Hill S (2011) Polyhedron 30:2965
72. Ferguson A, Lawrence J, Parkin A, Sanchez-Benitez J, Kamanev KV, Brechin EK, Wernsdorfer W, Hill S, Murrie M (2008) Dalton Trans 2008:6409
73. Feng PL, Koo C, Henderson JJ, Nakano M, Hill S, del Barco E, Hendrickson DN (2008) Inorg Chem 47:8610
74. Feng PL, Koo C, Henderson J, Manning P, Nakano M, del Barco E, Hill S, Hendrickson DN (2009) Inorg Chem 48:3480

75. Henderson JJ, Koo C, Feng PL, del Barco E, Hill S, Tupitsyn IS, Stamp PCE, Hendrickson DN (2009) Phys Rev Lett 103:017202
76. Hill S, Datta S, Liu J, Inglis R, Milios CJ, Feng PL, Henderson JJ, del Barco E, Brechin EK, Hendrickson DN (2010) Dalton Trans 39:4693
77. Liu J, del Barco E, Hill S (2012) Phys Rev B 85:014206
78. Quddusi HM, Liu J, Singh S, Heroux KJ, del Barco E, Hill S, Hendrickson DN (2011) Phys Rev Lett 106:227201
79. Heroux KJ, Quddusi HM, Liu J, O'Brien JR, Nakano M, del Barco E, Hill S, Hendrickson DN (2011) Inorg Chem 50:7367
80. Stoll S, Shafaat HS, Krzystek J, Ozarowski A, Tauber MJ, Kim JE, Britt RD (2011) J Am Chem Soc 133:18098
81. Datta S, Waldmann O, Kent AD, Milway VA, Thompson LK, Hill S (2007) Phys Rev B 76:052407
82. Bencini A, Ciofini I, Uytterhoeven MG (1998) Inorg Chim Acta 274:90
83. Yang E-C, Kirman C, Lawrence J, Zakharov LN, Rheingold AL, Hill S, Hendrickson DN (2005) Inorg Chem 44:3827
84. Datta S, Bolin E, Inglis R, Milios CJ, Brechin EK, Hill S (2009) Polyhedron 28:1911
85. Hill S, Edwards RS, Aliaga-Alcalde N, Christou G (2003) Science 302:1015
86. Liu J, Koo C, Amjad A, Feng PL, Choi E-S, del Barco E, Hendrickson DN, Hill S (2011) Phys Rev B 84:094443
87. Liu J, Hill S (2013) Polyhedron 66:147
88. Ako AM, Hewitt IJ, Mereacre V, Clerac R, Wernsdorfer W, Anson CE, Powell AK (2006) Angew Chem Int Ed 45:4926
89. Milios CJ, Vinslava A, Wernsdorfer W, Moggach S, Parsons S, Perlepes SP, Christou G, Brechin EK (2007) J Am Chem Soc 129:2754
90. Inglis R, Taylor SM, Jones LF, Papaefstathiou GS, Perlepes SP, Datta S, Hill S, Wernsdorfer W, Brechin EK (2009) Dalton Trans 2009:9157
91. Inglis R, Jones LF, Milios CJ, Datta S, Collins A, Parsons S, Wernsdorfer W, Hill S, Perlepes SP, Piligkos S, Brechin EK (2009) Dalton Trans 2009:3403
92. Waldmann O (2007) Inorg Chem 46:10035
93. Harman WH, Harris TD, Freedman DE, Fong H, Chang A, Rinehart JD, Ozarowski A, Sougrati MT, Grandjean F, Long GJ, Long JR, Chang CJ (2010) J Am Chem Soc 132:18115
94. Zadrozny JM, Atanasov M, Bryan AM, Lin C-Y, Rekken BD, Power PP, Neese F, Long JR (2013) Chem Sci 4:125
95. Lawrence J, Beedle C, Ma J, Hill S, Hendrickson DN (2007) Polyhedron 26:2299
96. Liu J, Datta S, Bolin E, Lawrence J, Beedle CC, Yang E-C, Goy P, Hendrickson DN, Hill S (2009) Polyhedron 28:1922
97. Zadrozny JM, Liu J, Piro NA, Chang CJ, Hill S, Long JR (2012) Chem Commun 48:3927
98. Ruamps R, Maurice R, Batchelor L, Boggio-Pasqual M, Guillot R, Barra A-L, Liu J, Bendief E-E, Pillet S, Hill S, Mallah T, Guihery N (2013) J Am Chem Soc 135:3017
99. Ishikawa N, Sugita M, Ishikawa T, Koshihara S, Kaizu Y (2003) J Am Chem Soc 125:8694
100. Ishikawa N, Sugita M, Wernsdorfer W (2005) J Am Chem Soc 127:3650
101. AlDamen MA, Clemente-Juan JM, Coronado E, Martí-Gustaldo C, Gaita-Ariño A (2008) J Am Chem Soc 130:8874
102. Ghosh S, Datta S, Friend L, Cardona-Serra S, Coronado E, Hill S (2012) Dalton Trans 41:13697
103. Tang J, Hewitt I, Madhu NT, Chastanet G, Wernsdorfer W, Anson CE, Benelli C, Sessoli R, Powell AK (2006) Angew Chem Int Ed 45:1729
104. Long J, Habib F, Lin PH, Korobkov I, Enright G, Ungur L, Wernsdorfer W, Chibotaru LF, Murugesu M (2011) J Am Chem Soc 133:5319
105. Rinehart JD, Fang M, Evans WJ, Long JR (2011) Nat Chem 3:538
106. Rinehart JD, Fang M, Evans WJ, Long JR (2011) J Am Chem Soc 133:14236

107. Mills DP, Moro F, McMaster J, van Slageren J, Lewis W, Blake AJ, Liddle ST (2011) Nat Chem 3:454
108. Dreiser J, Schnegg A, Holldack K, Pedersen KS, Schau-Magnussen M, Nehrkorn J, Tregenna-Piggott P, Mutka H, Weihe H, Bendix J, Waldmann O (2011) Chem Eur J 17:7492
109. Telser J, van Slageren J, Vongtragool S, Dressel M, Reiff WM, Zvyagin SA, Ozarowski A, Krzystek J (2005) Magn Reson Chem 43:S130
110. Rebilly J-N, Charron G, Rivière E, Guillot R, Barra A-L, Durán Serrano M, van Slageren J, Mallah T (2008) Chem Eur J 14:1169
111. Ray K, Begum A, Weyhermüller T, Piligkos S, van Slageren J, Neese F, Wieghardt K (2005) J Am Chem Soc 127:4403
112. Forshaw AP, Smith JM, Ozarowski A, Krzystek J, Smirnov D, Zvyagin SA, Harris TD, Karunadasa HI, Zadrozny JM, Schnegg A, Holldack K, Jackson TA, Alamiri A, Barnes DM, Telser J (2013) Inorg Chem 52:144
113. Feng X, Liu J, Harris TD, Hill S, Long JR (2012) J Am Chem Soc 134:7521
114. Takahashi S, Hill S (2005) Rev Sci Instrum 76:023114
115. Brooks JS, Crow JE, Moulton WG (1998) J Phys Chem Solids 59:569
116. Zvyagin SA, Ozerov M, Cizmar E, Kamenskyi D, Zherlitsyn S, Heransdorfer T, Woznitsa J, Wunsch R, Seidel W (2009) Rev Sci Instrum 80:073102
117. Schweiger A, Jeschke G (2001) Principles of pulse electron paramagnetic resonance. Oxford University Press, New York
118. Morley GW, Brunel L-C, van Tol J (2005) Rev Sci Instrum 79:064703
119. Hofbauer W, Earle KA, Dunnam CR, Moscicki JK, Freed JH (2004) Rev Sci Instrum 75:1194
120. Cruikshank PAS, Bolton DR, Robertson DA, Hunter RI, Wylde RJ, Smith GM (2009) Rev Sci Instrum 80:103102
121. Takahashi S, Hanson R, van Tol J, Sherwin M, Awschalom D (2008) Phys Rev Lett 101:047601
122. Thomann H, Morgan TV, Jin H, Burgmayer SJN, Bare RE, Stiefel EI (1987) J Am Chem Soc 109:7913
123. Britt RD, Zimmermann J-L, Sauer K, Klein MP (1989) J Am Chem Soc 111:3522
124. Hagen WR, van den Berg WAM, van Dongen WMAM, Reijerse EJ, van Kan PJM (1998) J Chem Soc Faraday Trans 94:2969
125. Milov AD, Maryasov AG, Tsvetkov YD (1998) Appl Magn Reson 15:107
126. Huber M, Lindgren M, Hammarstrom P, Martensson LG, Carlsson U, Eaton GR, Eaton SS (2001) Biophys Chem 94:245
127. Borbat PP, Davis JH, Butcher SE, Freed JH (2004) J Am Chem Soc 126:7764
128. Ardavan A, Rival O, Morton JL, Blundell SJ, Tyryshkin AM, Timco GA, Winpenny REP (2007) Phys Rev Lett 98:057201
129. Wernsdorfer W (2007) Nat Mater 6:174
130. Wedge CJ, Timco GA, Spielberg ET, George RE, Tuna F, Rigby S, McInnes EJL, Winpenny REP, Blundell SJ, Ardavan A (2012) Phys Rev Lett 108:107204
131. Bellini V, Lorusso G, Candini A, Wernsdorfer W, Faust TB, Timco GA, Winpenny REP, Affronte M (2011) Phys Rev Lett 106:227205
132. Mitrikas G, Sanakis Y, Raptopoulou CP, Kordas G, Papavassiliou G (2008) Phys Chem Chem Phys 10:743
133. Bertaina S, Gambarelli S, Mitra T, Tsukerblat B, Müller A, Barbara B (2010) Nature 453:1006
134. Winpenny REP (2008) Angew Chem 47:7992
135. Bertaina S, Gambarelli S, Mitra T, Tsukerblat B, Müller A, Barbara B (2008) Nature 466:203
136. Shim JH, Bertaina S, Gambarelli S, Mitra T, Müller A, Baibekov EI, Malkin BZ, Tsukerblat B, Barbara B (2012) Phys Rev Lett 109:050401
137. Yang J, Wang Y, Wang Z, Rong X, Duan C-K, Su J-H, Du J (2012) Phys Rev Lett 108:230501

138. Schlegel C, van Slageren J, Manoli M, Brechin EK, Dressel M (2008) Phys Rev Lett 101:147203
139. Takahashi S, van Tol J, Beedle CC, Hendrickson DN, Brunel L-C, Sherwin MS (2009) Phys Rev Lett 102:087603
140. Takahashi S, Tupitsyn IS, van Tol J, Beedle CC, Hendrickson DN, Stamp PCE (2011) Nature 476:76
141. Wang Z, Datta S, Papatriantafyllopoulou C, Christou G, Dalal NS, van Tol J, Hill S (2011) Polyhedron 30:3193
142. Vergnani L, Barra A-L, Neugebauer P, Rodriguez-Douton MJ, Sessoli R, Sorace L, Wernsdorfer W, Cornia A (2012) Chem Eur J 18:3390
143. Moro F, Kaminski D, Tuna F, Whitehead GF, Timco GA, Collison D, Winpenny REP, Ardavan A, McInnes EJL (2014) Chem Commun 50:91
144. Bertaina S, Gambarelli S, Tkachuk A, Kurkin IN, Malkin B, Stepanov A, Barbara B (2007) Nat Nanotechnol 2:39
145. Martínez-Perez MJ, Cardona-Serra S, Schlegel C, Moro F, Alonso PJ, Prima-García H, Clemente-Juan JM, Evangelisti M, Gaita-Ariño A, Sesé J, van Slageren J, Coronado E, Luis F (2012) Phys Rev Lett 108:247213
146. Baldoví JJ, Cardona-Serra S, Clemente-Juan JM, Coronado E, Gaita-Ariño A, Prima-García H (2013) Chem Commun 49:8922
147. Fronk M, Bräuer B, Kortus J, Schmidt OG, Zahn DRT, Salvan G (2009) Phys Rev B 79:235305
148. Bräuer B, Fronk M, Lehmann D, Zahn DRT, Salvan G (2009) J Phys Chem B 113:14957
149. Ishii K, Ozawa K (2009) J Phys Chem C 113:18897
150. Cheesman MR, Oganesyan VS, Sessoli R, Gatteschi D, Thomson AJ (1997) Chem Commun 1997:1677
151. Domingo N, Williamson BE, Gómez-Segura J, Gerbier P, Ruiz-Molina D, Amabilino DB, Veciana J, Tejada J (2004) Phys Rev B 69:052405
152. McInnes EJL, Pidcock E, Oganesyan VS, Cheesman MR, Powell AK, Thomson AJ (2002) J Am Chem Soc 124:9219
153. Gonidec M, Davies ES, McMaster J, Amabilino DB, Veciana J (2010) J Am Chem Soc 132:1756
154. Moro F, Piga F, Krivokapic I, Burgess A, Lewis W, McMaster J, van Slageren J (2010) Inorg Chim Acta 363:4329
155. Bogani L, Cavigli L, Gurioli M, Novak RL, Mannini M, Caneschi A, Pineider F, Sessoli R, Clemente-León M, Coronado E, Cornia A, Gatteschi D (2007) Adv Mater 19:3906
156. Moroni R, Buzio R, Chincarini A, Valbusa U, de Mongeot FB, Bogani L, Caneschi A, Sessoli R, Cavigli L, Gurioli M (2008) J Mater Chem 18:109
157. Novak RL, Pineider F, de Julián Fernández C, Gorini L, Bogani L, Danieli C, Cavigli L, Cornia A, Sessoli R (2008) Inorg Chim Acta 361:3970
158. Piligkos S, Slep LD, Weyhermüller T, Chaudhuri P, Bill E, Neese F (2009) Coord Chem Rev 253:2352
159. da Cunha TT, Jung J, Boulon M-E, Campo G, Pointillart F, Pereira CLM, Le Guennic B, Cador O, Bernot K, Pineider F, Golhen S, Ouahab L (2013) J Am Chem Soc 135:16332
160. Gonidec M, Krivokapic I, Vidal-Gancedo J, Davies ES, McMaster J, Gorun SM, Veciana J (2013) Inorg Chem 52:4464
161. Malavolti L, Mannini M, Car P-E, Campo G, Pineider F, Sessoli R (2013) J Mater Chem C 1:2935
162. Collison D, Oganesyan VS, Piligkos S, Thomson AJ, Winpenny REP, McInnes EJL (2003) J Am Chem Soc 125:1168
163. Bradley JM, Thomson AJ, McInnes EJL, Winpenny REP, Timco G (2008) Dalton Trans 2008:3311
164. Bradley JM, Thomson AJ, Inglis R, Milios CJ, Brechin EK, Piligkos S (2010) Dalton Trans 39:9904

165. van Slageren J, Piligkos S, Neese F (2010) Dalton Trans 39:4999
166. Donnio B, Rivière E, Terazzi E, Voirin E, Aronica C, Chastanet G, Luneau D, Rogez G, Scheurer F, Joly L, Kappler JP, Gallani JL (2010) Solid State Sci 12:1307
167. Grumbach N, Barla A, Joly L, Donnio B, Rogez G, Terazzi E, Kappler JP, Gallani JL (2010) Eur Phys J B 73:103
168. Gambardella P, Stepanow S, Dmitriev A, Honolka J, de Groot FMF, Lingenfelder M, Gupta SS, Sarma DD, Bencok P, Stanescu S, Clair S, Pons S, Lin N, Seitsonen AP, Brune H, Barth JV, Kern K (2009) Nat Mater 8:189
169. Cornia A, Mannini M, Sainctavit P, Sessoli R (2011) Chem Soc Rev 40:3076
170. Mannini M, Sainctavit P, Sessoli R, Cartier dit Moulin C, Pineider F, Arrio M-A, Cornia A, Gatteschi D (2008) Chem Eur J 14:7530
171. Domingo N, Bellido E, Ruiz-Molina D (2012) Chem Soc Rev 41:258
172. Mannini M, Pineider F, Sainctavit P, Danieli C, Otero E, Sciancalepore C, Talarico AM, Arrio M-A, Cornia A, Gatteschi D, Sessoli R (2009) Nat Mater 8:194
173. Mannini M, Pineider F, Sainctavit P, Joly L, Fraile-Rodríguez A, Arrio M-A, Moulin CCD, Wernsdorfer W, Cornia A, Gatteschi D, Sessoli R (2009) Adv Mater 21:167
174. Mannini M, Pineider F, Sainctavit P, Cartier dit Moulin C, Arrio M-A, Cornia A, Gatteschi D, Sessoli R (2009) Eur Phys J Spec Top 169:167
175. Pineider F, Mannini M, Danieli C, Armelao L, Piras FM, Magnani A, Cornia A, Sessoli R (2010) J Mater Chem 20:187
176. Rodriguez-Douton MJ, Mannini M, Armelao L, Barra A-L, Tancini E, Sessoli R, Cornia A (2011) Chem Commun 47:1467
177. Mannini M, Tancini E, Sorace L, Sainctavit P, Arrio M-A, Qian Y, Otero E, Chiappe D, Margheriti L, Cezar JC, Sessoli R, Cornia A (2011) Inorg Chem 50:2911
178. Tancini E, Mannini M, Sainctavit P, Otero E, Sessoli R, Cornia A (2013) Chem Eur J 19:16902
179. Corradini V, Moro F, Biagi R, De Renzi V, del Pennino U, Bellini V, Carretta S, Santini P, Milway VA, Timco G, Winpenny REP, Affronte M (2009) Phys Rev B 79:144419
180. Corradini V, Ghirri A, Pennino UD, Biagi R, Milway VA, Timco G, Tuna F, Winpenny REP, Affronte M (2010) Dalton Trans 39:4928
181. Ghirri A, Corradini V, Bellini V, Biagi R, del Pennino U, De Renzi V, Cezar JC, Muryn CA, Timco GA, Winpenny REP, Affronte M (2011) ACS Nano 5:7090
182. Corradini V, Ghirri A, Garlatti E, Biagi R, De Renzi V, del Pennino U, Bellini V, Carretta S, Santini P, Timco G, Winpenny REP, Affronte M (2012) Adv Funct Mater 22:3706
183. Westerström R, Dreiser J, Piamonteze C, Muntwiler M, Weyeneth S, Brune H, Rusponi S, Nolting F, Popov A, Yang S, Dunsch L, Greber T (2012) J Am Chem Soc 134:9840
184. Stepanow S, Honolka J, Gambardella P, Vitali L, Abdurakhmanova N, Tseng T-C, Rauschenbach S, Tait SL, Sessi V, Klyatskaya S, Ruben M, Kern K (2010) J Am Chem Soc 132:11900
185. Margheriti L, Chiappe D, Mannini M, Car PE, Sainctavit P, Arrio M-A, de Mongeot FB, Cezar JC, Piras FM, Magnani A, Otero E, Caneschi A, Sessoli R (2010) Adv Mater 22:5488
186. Biagi R, Fernandez-Rodriguez J, Gonidec M, Mirone A, Corradini V, Moro F, De Renzi V, del Pennino U, Cezar JC, Amabilino DB, Veciana J (2010) Phys Rev B 82:224406
187. Gonidec M, Biagi R, Corradini V, Moro F, De Renzi V, del Pennino U, Summa D, Muccioli L, Zannoni C, Amabilino DB, Veciana J (2011) J Am Chem Soc 133:6603
188. Malavolti L, Poggini L, Margheriti L, Chiappe D, Graziosi P, Cortigiani B, Lanzilotto V, de Mongeot FB, Ohresser P, Otero E, Choueikani F, Sainctavit P, Bergenti I, Dediu VA, Mannini M, Sessoli R (2013) Chem Commun 49:11506
189. Moro F, Biagi R, Corradini V, Evangelisti M, Gambardella A, De Renzi V, del Pennino U, Coronado E, Forment-Aliaga A, Romero FM (2012) J Phys Chem C 116:14936
190. Kahle S, Deng Z, Malinowski N, Tonnoir C, Forment-Aliaga A, Thontasen N, Rinke G, Le D, Turkowski V, Rahman TS, Rauschenbach S, Ternes M, Kern K (2011) Nano Lett 12:518
191. Sun K, Park K, Xie J, Luo J, Yuan H, Xiong Z, Wang J, Xue Q (2013) ACS Nano 7:6825

192. del Pennino U, Corradini V, Biagi R, De Renzi V, Moro F, Boukhvalov DW, Panaccione G, Hochstrasser M, Carbone C, Milios CJ, Brechin EK (2008) Phys Rev B 77:085419
193. Moro F, Corradini V, Evangelisti M, Renzi VD, Biagi R, Pennino UD, Milios CJ, Jones LF, Brechin EK (2008) J Phys Chem B 112:9729
194. Moro F, Corradini V, Evangelisti M, Biagi R, De Renzi V, del Pennino U, Cezar JC, Inglis R, Milios CJ, Brechin EK (2010) Nanoscale 2:2698
195. Cornia A, Mannini M (2014) Single-molecule magnets on surfaces. Struct Bond. doi:10.1007/430_2014_150
196. Mannini M, Pineider F, Danieli C, Totti F, Sorace L, Sainctavit P, Arrio MA, Otero E, Joly L, Cezar JC, Cornia A, Sessoli R (2010) Nature 468:417
197. Scheybal A, Ramsvik T, Bertschinger R, Putero M, Nolting F, Jung TA (2005) Chem Phys Lett 411:214
198. Wende H, Bernien M, Luo J, Sorg C, Ponpandian N, Kurde J, Miguel J, Piantek M, Xu X, Eckhold P, Kuch W, Baberschke K, Panchmatia PM, Sanyal B, Oppeneer PM, Eriksson O (2007) Nat Mater 6:516
199. Bernien M, Miguel J, Weis C, Ali ME, Kurde J, Krumme B, Panchmatia PM, Sanyal B, Piantek M, Srivastava P, Baberschke K, Oppeneer PM, Eriksson O, Kuch W, Wende H (2009) Phys Rev Lett 102:047202
200. Stepanow S, Mugarza A, Ceballos G, Moras P, Cezar JC, Carbone C, Gambardella P (2010) Phys Rev B 82:014405
201. Baker ML, Mutka H (2012) Eur Phys J Spec Top 213:53
202. Amoretti G, Caciuffo R, Carretta S, Guidi T, Magnani N, Santini P (2008) Inorg Chim Acta 361:3771
203. Basler R, Boskovic C, Chaboussant G, Güdel HU, Murrie M, Ochsenbein ST, Sieber A (2003) Chem Phys Chem 4:910
204. Furrer A, Waldmann O (2013) Rev Mod Phys 85:367
205. Squires GL (1996) Introduction to the theory of thermal neutron scattering. Dover, Mineola
206. Marshall W, Lovesey SW (1971) Theory of thermal neutron scattering. Oxford University Press, Oxford
207. Dianoux AJ, Lander G (2003) Neutron data booklet. OCP Science, Grenoble
208. Waldmann O (2003) Phys Rev B 68:174406
209. Caciuffo R, Guidi T, Amoretti G, Carretta S, Liviotti E, Santini P, Mondelli C, Timco G, Muryn CA, Winpenny REP (2005) Phys Rev B 71:174407
210. Russina M, Mezei F (2009) Nucl Instr Meth Phys Res Sect A Accelerators Spectrometers Detectors Assoc Equip 604:624
211. Bewley RI, Taylor JW, Bennington SM (2011) Nucl Instr Meth Phys Res Sect A Accelerators Spectrometers Detectors Assoc Equip 637:128
212. Nakajima K, Ohira-Kawamura S, Kikuchi T, Nakamura M, Kajimoto R, Inamura Y, Takahashi N, Aizawa K, Suzuya K, Shibata K, Nakatani T, Soyama K, Maruyama R, Tanaka H, Kambara W, Iwahashi T, Itoh Y, Osakabe T, Wakimoto S, Kakurai K, Maekawa F, Harada M, Oikawa K, Lechner RE, Mezei F, Arai M (2011) J Phys Soc Jpn 80:SB028
213. Kofu M, Yamamuro O, Kajiwara T, Yoshimura Y, Nakano M, Nakajima K, Ohira-Kawamura S, Kikuchi T, Inamura Y (2013) Phys Rev B 88:064405
214. Furrer A, Güdel HU (1977) Phys Rev Lett 39:657
215. Güdel HU, Furrer A (1977) Mol Phys 33:1335
216. Furrer A, Güdel HU, Blank H, Heidemann A (1989) Phys Rev Lett 62:210
217. Furrer A, Güdel HU, Darriet J (1985) J Less Common Metals 111:223
218. Guedel HU, Furrer A, Blank H (1990) Inorg Chem 29:4081
219. Furrer A, Güdel HU, Krausz ER, Blank H (1990) Phys Rev Lett 64:68
220. Aebersold MA, Güdel HU, Hauser A, Furrer A, Blank H, Kahn R (1993) Phys Rev B 48:12723
221. Sessoli R, Powell AK (2009) Coord Chem Rev 253:2328

222. Rinehart JD, Long JR (2011) Chem Sci 2:2078
223. Caciuffo R, Amoretti G, Murani A, Sessoli R, Caneschi A, Gatteschi D (1998) Phys Rev Lett 81:4744
224. Mirebeau I, Hennion M, Casalta H, Andres H, Güdel HU, Irodova AV, Caneschi A (1999) Phys Rev Lett 83:628
225. Zhong Y, Sarachik MP, Friedman JR, Robinson RA, Kelley TM, Nakotte H, Christianson AC, Trouw F, Aubin SMJ, Hendrickson DN (1999) J Appl Phys 85:5636
226. Ollivier J, Mutka H (2011) J Phys Soc Jpn 80:SB003
227. Cornia A, Fabretti AC, Sessoli R, Sorace L, Gatteschi D, Barra A-L, Daiguebonne C, Roisnel T (2002) Acta Cryst C 58:m371
228. Farrell AR, Coome JA, Probert MR, Goeta AE, Howard JAK, Lemee-Cailleau M-H, Parsons S, Murrie M (2013) Cryst Eng Commun 15:3423
229. Sieber A, Chaboussant G, Bircher R, Boskovic C, Güdel HU, Christou G, Mutka H (2004) Phys Rev B 70:172413
230. Chaboussant G, Sieber A, Ochsenbein S, Güdel HU, Murrie M, Honecker A, Fukushima N, Normand B (2004) Phys Rev B 70:104422
231. Hennion M, Pardi L, Mirebeau I, Suard E, Sessoli R, Caneschi A (1997) Phys Rev B 56:8819
232. Carretta S, Guidi T, Santini P, Amoretti G, Pieper O, Lake B, van Slageren J, Hallak FE, Wernsdorfer W, Mutka H, Russina M, Milios CJ, Brechin EK (2008) Phys Rev Lett 100:157203
233. Pieper O, Guidi T, Carretta S, van Slageren J, El Hallak F, Lake B, Santini P, Amoretti G, Mutka H, Koza M, Russina M, Schnegg A, Milios CJ, Brechin EK, Julià A, Tejada J (2010) Phys Rev B 81:174420
234. Garlea VO, Nagler SE, Zarestky JL, Stassis C, Vaknin D, Kögerler P, McMorrow DF, Niedermayer C, Tennant DA, Lake B, Qiu Y, Exler M, Schnack J, Luban M (2006) Phys Rev B 73:024414
235. Schnack J (2010) Dalton Trans 39:4677
236. Baker ML, Timco GA, Piligkos S, Mathieson JS, Mutka H, Tuna F, Kozłowski P, Antkowiak M, Guidi T, Gupta T, Rath H, Woolfson RJ, Kamieniarz G, Pritchard RG, Weihe H, Cronin L, Rajaraman G, Collison D, McInnes EJL, Winpenny REP (2012) Proc Natl Acad Sci 109:19113
237. Iida K, Qiu Y, Sato TJ (2011) Phys Rev B 84:094449
238. Kögerler P, Tsukerblat B, Möller A (2010) Dalton Trans 39:21
239. Affronte M, Carretta S, Timco GA, Winpenny REP (2007) Chem Commun 2007:1789
240. Steiner M, Tennant DA, Smeibidl P (2006) J Phys Conf Ser 51:470
241. Müller A, Döring J (1988) Angew Chem Int Ed 27:1721
242. Mourigal M, Fuhrman WT, Sheckelton JP, Wartelle A, Rodriguez-Rivera JA, Abernathy DL, McQueen TM, Broholm CL (2014) Phys Rev Lett 112:027202
243. Barra AL, Gatteschi D, Pardi L, Mueller A, Doering J (1992) J Am Chem Soc 114:8509
244. Gatteschi D, Pardi L, Barra AL, Muller A, Doring J (1991) Nature 354:463
245. Chiorescu I, Wernsdorfer W, Müller A, Bögge H, Barbara B (2000) Phys Rev Lett 84:3454
246. Chaboussant G, Basler R, Sieber A, Ochsenbein ST, Desmedt A, Lechner RE, Telling MTF, Kögerler P, Müller A, Güdel HU (2002) Europhys Lett 59:291
247. Chaboussant G, Ochsenbein ST, Sieber A, Güdel H-U, Mutka H, Müller A, Barbara B (2004) Europhys Lett 66:423
248. Carretta S, Santini P, Amoretti G, Guidi T, Copley JRD, Qiu Y, Caciuffo R, Timco G, Winpenny REP (2007) Phys Rev Lett 98:167401
249. Waldmann O, Carver G, Dobe C, Biner D, Sieber A, Güdel HU, Mutka H, Ollivier J, Chakov NE (2006) Appl Phys Lett 88:042507
250. Waldmann O, Carver G, Dobe C, Sieber A, Güdel HU, Mutka H (2007) J Am Chem Soc 129:1526
251. Chiolero A, Loss D (1998) Phys Rev Lett 80:169
252. Normand B, Wang X, Zotos X, Loss D (2001) Phys Rev B 63:184409

253. Bärwinkel K, Hage P, Schmidt H-J, Schnack J (2003) Phys Rev B 68:054422
254. Bärwinkel K, Schmidt HJ, Schnack J (2000) J Magn Magn Mater 212:240
255. Timco GA, McInnes EJL, Winpenny REP (2013) Chem Soc Rev 42:1796
256. Waldmann O, Guidi T, Carretta S, Mondelli C, Dearden AL (2003) Phys Rev Lett 91:237202
257. Dreiser J, Waldmann O, Dobe C, Carver G, Ochsenbein ST, Sieber A, Güdel HU, van Duijn J, Taylor J, Podlesnyak A (2010) Phys Rev B 81:024408
258. Ummethum J, Nehrkorn J, Mukherjee S, Ivanov NB, Stuiber S, Strässle T, Tregenna-Piggott PLW, Mutka H, Christou G, Waldmann O, Schnack J (2012) Phys Rev B 86:104403
259. Baker ML, Waldmann O, Piligkos S, Bircher R, Cador O, Carretta S, Collison D, Fernandez-Alonso F, McInnes EJL, Mutka H, Podlesnyak A, Tuna F, Ochsenbein S, Sessoli R, Sieber A, Timco GA, Weihe H, Güdel HU, Winpenny REP (2012) Phys Rev B 86:064405
260. Waldmann O, Stamatatos TC, Christou G, Güdel HU, Sheikin I, Mutka H (2009) Phys Rev Lett 102:157202
261. Waldmann O, Dobe C, Mutka H, Furrer A, Güdel HU (2005) Phys Rev Lett 95:057202
262. Furukawa Y, Kiuchi K, Kumagai K-I, Ajiro Y, Narumi Y, Iwaki M, Kindo K, Bianchi A, Carretta S, Timco GA, Winpenny REP (2008) Phys Rev B 78:092402
263. Taft KL, Delfs CD, Papaefthymiou GC, Foner S, Gatteschi D, Lippard SJ (1994) J Am Chem Soc 116:823
264. Honecker A, Meier F, Loss D, Normand B (2002) Eur Phys J B 27:487
265. Carretta S, van Slageren J, Guidi T, Liviotti E, Mondelli C, Rovai D, Cornia A, Dearden AL, Carsughi F, Affronte M, Frost CD, Winpenny REP, Gatteschi D, Amoretti G, Caciuffo R (2003) Phys Rev B 67:094405
266. Bianchi A, Carretta S, Santini P, Amoretti G, Guidi T, Qiu Y, Copley JRD, Timco G, Muryn C, Winpenny REP (2009) Phys Rev B 79:144422
267. Santini P, Carretta S, Amoretti G, Guidi T, Caciuffo R, Caneschi A, Rovai D, Qiu Y, Copley JRD (2005) Phys Rev B 71:184405
268. Waldmann O, Bircher R, Carver G, Sieber A, Güdel HU, Mutka H (2007) Phys Rev B 75:174438
269. Ehlers G, Podlesnyak AA, Niedziela JL, Iverson EB, Sokol PE (2011) Rev Sci Instrum 82:085108
270. Baker ML, Guidi T, Carretta S, Ollivier J, Mutka H, Gudel HU, Timco GA, McInnes EJL, Amoretti G, Winpenny REP, Santini P (2012) Nat Phys 8:906
271. Perring TG, Ewings RA, Duijn JV Visualising and manipulating $S(\boldsymbol{q}, \omega)$ measured in all four dimensions (unpublished). http://horace.isis.rl.ac.uk
272. Zyazin AS, van den Berg JWG, Osorio EA, van der Zant HSJ, Konstantinidis NP, Leijnse M, Wegewijs MR, May F, Hofstetter W, Danieli C, Cornia A (2010) Nano Lett 10:3307
273. del Carmen Giménez-López M, Moro F, La Torre A, Gómez-García CJ, Brown PD, van Slageren J, Khlobystov AN (2011) Nat Commun 2:407
274. Wernsdorfer W, Aliaga-Alcalde N, Hendrickson DN, Christou G (2002) Nature 416:406
275. Timco GA, Carretta S, Troiani F, Tuna F, Pritchard RJ, Muryn CA, McInnes EJL, Ghirri A, Candini A, Santini P, Amoretti G, Affronte M, Winpenny REP (2009) Nat Nanotechnol 4:173
276. Luzon J, Bernot K, Hewitt IJ, Anson CE, Powell AK, Sessoli R (2008) Phys Rev Lett 100:247205
277. Cador O, Gatteschi D, Sessoli R, Larsen FK, Overgaard J, Barra A-L, Teat SJ, Timco GA, Winpenny REP (2004) Angew Chem Int Ed 43:5196
278. Lindroos M, Bousson S, Calaga R, Danared H, Devanz G, Duperrier R, Eguia J, Eshraqi M, Gammino S, Hahn H, Jansson A, Oyon C, Pape-Møller S, Peggs S, Ponton A, Rathsman K, Ruber R, Satogata T, Trahern G (2011) Nucl Instr Meth Phys Res Sect B Beam Interact Mater Atoms 269:3258
279. Blundell SJ (1999) Contemp Phys 40:175
280. Blundell SJ (2004) Chem Rev 104:5717
281. Lancaster T, Blundell SJ, Brooks ML, Baker PJ, Pratt FL, Manson JL, Landee CP, Baines C (2006) Phys Rev B 73, R020410

282. Lancaster T, Blundell SJ, Pratt FL (2013) Phys Scr 88:068506
283. Blundell SJ, Lancaster T, Pratt FL, Baker PJ, Brooks ML, Baines C, Manson JL, Landee CP (2007) J Phys Chem Solids 68:2039
284. Sengupta P, Sandvik AW, Singh RRP (2003) Phys Rev B 68:094423
285. Lascialfari A, Jang ZH, Borsa F, Carretta P, Gatteschi D (1998) Phys Rev Lett 81:3773
286. Salman Z, Keren A, Mendels P, Marvaud V, Scuiller A, Verdaguer M, Lord JS, Baines C (2002) Phys Rev B 65:132403
287. Blundell SJ, Pratt FL, Marshall IM, Steer CA, Hayes W, Letard JF, Heath SL, Caneschi A, Gatteschi D (2003) Synth Met 133–134:531
288. Lancaster T, Blundell SJ, Pratt FL, Brooks ML, Manson JL, Brechin EK, Cadiou C, Low D, McInnes EJL, Winpenny REP (2004) J Phys Condens Matter 16:S4563
289. Salman Z, Kiefl RF, Chow KH, MacFarlane WA, Keeler TA, Parolin TJ, Tabbara S, Wang D (2008) Phys Rev B 77:214415
290. Keren A, Shafir O, Shimshoni E, Marvaud V, Bachschmidt A, Long J (2007) Phys Rev Lett 98:257204
291. Lancaster T, Blundell SJ, Pratt FL, Franke I, Steele AJ, Baker PJ, Salman Z, Baines C, Watanabe I, Carretta S, Timco GA, Winpenny REP (2010) Phys Rev B 81:140409(R)
292. Larsen FK, McInnes EJL, El Mkami H, Overgaard J, Piligkos S, Rajaraman G, Rentschler E, Smith AA, Smith GM, Boote V, Jennings M, Timco GA, Winpenny REP (2003) Angew Chem Int Ed 42:101
293. van Slageren J, McInnes EJL, El Mkami H, Overgaard J, Piligkos S, Rajaraman G, Rentschler E, Smith AA, Smith GM, Boote V, Jennings M, Timco GA, Winpenny REP (2002) Chem Eur J 8:277
294. Hayano RS, Uemura YJ, Imazato J, Nishida N, Yamazaki T, Kubo R (1979) Phys Rev B 20:850
295. Lancaster T, Möller JS, Blundell SJ, Pratt FL, Baker PJ, Guidi T, Timco GA, Winpenny REP (2011) J Phys Condens Matter 23:242201
296. Salman Z, Blundell SJ (2012) Phys Proc 30:168
297. Hofmann A, Salman Z, Mannini M, Amato A, Malavolti L, Morenzoni E, Prokscha T, Sessoli R, Suter A (2012) ACS Nano 6:8390

Struct Bond (2015) 164: 293–330
DOI: 10.1007/430_2014_150

Published online: 4 July 2014

Single-Molecule Magnets on Surfaces

Andrea Cornia and Matteo Mannini

Abstract Encoding and manipulating information through the spin degrees of freedom of individual magnetic molecules or atoms is one of the central challenges in the continuing trend towards molecular/atomic scale electronics. With their large magnetic moment and long spin relaxation time, single-molecule magnets (SMMs) are of special importance in this emerging field. Their electrical addressing at the molecular level appears now well within reach using STM methods, which require to organize SMMs on a conducting surface. In this chapter, we present a critical overview of the latest achievements in the deposition of SMMs as monolayers or submonolayers on native or prefunctionalized surfaces. Special emphasis is placed on the selection and design of molecular structures that withstand solution or vapour-phase processing and that maintain their magnetic functionality on a surface. Chemical strategies to control the strength of molecule–substrate interaction and the molecular orientation on the surface are also illustrated. Rewardingly, these efforts have shown that the distinctive properties of SMMs, i.e. slow spin relaxation and quantum tunnelling of the magnetic moment, persist in metal-wired molecules.

Keywords Molecular assembling • Molecular magnetism • Spintronics • Surface science • X-ray absorption spectroscopy

A. Cornia (✉)
Dipartimento di Scienze Chimiche e Geologiche, Università degli Studi di Modena e Reggio Emilia & INSTM Research Unit of Modena and Reggio Emilia, Via G. Campi 183, 41125 Modena, Italy
e-mail: acornia@unimore.it

M. Mannini
Dipartimento di Chimica "Ugo Schiff", Università degli Studi di Firenze & INSTM Research Unit of Firenze, Via della Lastruccia 3-13, 50019 Sesto Fiorentino (FI), Italy
e-mail: matteo.mannini@unifi.it

Contents

Abbreviations

4-mobca	4′-Mercapto-octafluorobiphenyl-4-carboxylic acid
4-mtba	4-Mercapto-tetrafluorobenzoic acid
AC	Alternating current
DFT	Density functional theory
DPN	Dip-pen nanolithography
EPR	Electron paramagnetic resonance
ESI-MS	Electrospray ionization mass spectrometry
Et-saoH_2	2-Hydroxyphenylpropanone oxime
H_2hmb	*N*′-(2-hydroxy-3-methoxybenzylidene)benzhydrazide
H_2Pc	Phthalocyanine
H_2sao	2-Hydroxybenzaldehyde oxime
Hbiph	Biphenyl-4-carboxylic acid
Hdmbz	3,5-Dimethylbenzoic acid
Hdpm	Dipivaloylmethane
Hhfac	Hexafluoroacetylacetone
HOPG	Highly oriented pyrolitic graphite
Hpfb	4-Fluorobenzoic acid
Hpta	Pivaloyl trifluoromethyl acetone
Hth	3-Thiophene-carboxylic acid
Htpc	*p*-Terphenyl-4-carboxylic acid
LnDD	Lanthanide double-decker
ML	Monolayer
NP	Nanoparticle

PyNO	Pyridine *N*-oxide
QT	Quantum tunnelling
SAM	Self-assembled monolayer
SH	Spin hamiltonian
SMM	Single-molecule magnet
SQUID	Superconducting quantum interference device
STM	Scanning tunnelling microscope/scanning tunnelling microscopy
STS	Scanning tunnelling spectroscopy
T_B	Blocking temperature
TEY	Total electron yield
ToF-SIMS	Time of flight secondary ion mass spectrometry
UHV	Ultra-high vacuum
VSM	Vibrating sample magnetometer
XAS	X-ray absorption spectroscopy
XMCD	X-ray magnetic circular dichroism
XNLD	X-ray natural linear dichroism
XPS	X-ray photoelectron spectroscopy
ZFS	Zero-field splitting
μSR	Muon spin relaxation

1 Twenty Years of Magnetic Bistability in Single-Molecule Magnets

1.1 Introductory Remarks

Twenty years after the seminal paper by Sessoli and co-workers [1] the field of single-molecule magnets (SMMs) remains a lively crossroad between chemistry, physics and materials science, but has undergone extensive reshaping and refocussing. The underlying physics governing magnetic moment reversal in bulk crystalline samples is fairly well understood now [2], thanks to fundamental studies [1, 3, 4] that are considered milestones in the history of spin [5]. Moreover, it has become evident that SMMs are not expected to replace or compete with bulk magnets for traditional applications. Rather, the unique potential of SMMs lies in their utmost versatility in chemical composition and structure, close to perfect monodispersity and small size [6]. In particular, shrinking components to the scale of molecules or atoms does not merely mean to approach the ultimate miniaturization limit and the highest conceivable storage densities. Reaching the "difficult middle ground" defined by molecular sizes [5] leads to the emergence of a new physics dominated by quantum effects, which hold promise for information storage and processing using nonclassical (i.e. quantum) schemes. For this reason, SMMs and more generally molecule-based magnets are the target of active investigation as candidate materials for molecule-based spintronics [7–11] and quantum

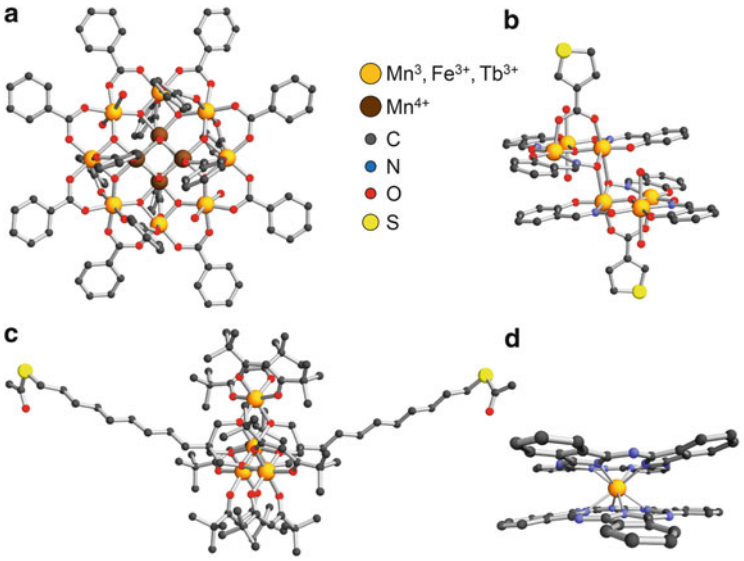

Fig. 1 Molecular structure of SMM complexes relevant to deposition on surfaces: Mn_{12}bz (**a**), Mn_6th (**b**), Fe_4C9 (**c**) and $TbPc_2$ (**d**). Hydrogen atoms are omitted

computing[1] [13–16]. However, exploiting SMM functionality for practical purposes still poses many theoretical and experimental challenges. Any real development in such a direction in fact demands SMMs with operating temperatures at least above 4.2 K (the boiling temperature of helium at ambient pressure). In addition, it asks for a much deeper understanding of the interaction between localized molecular spins and electric currents. It is precisely on these two tasks that a large part of the SMM community is now concentrating their efforts.

1.2 Towards High-Temperature SMMs

Other contributions in this volume cover the recent advances in the design and synthesis of SMMs, as well as the physical origin of SMM behaviour. Here we just stress that the use of exotic spin carriers and unusual coordination geometries has been essential to escape the "3 K trap" as defined by the blocking temperature (T_B) of the first discovered SMM, $[Mn_{12}O_{12}(OAc)_{16}(H_2O)_4]$ (Mn_{12}ac) [1]. For almost fifteen years after this discovery, derivatives of Mn_{12}ac like $[Mn_{12}O_{12}(O_2CPh)_{16}(H_2O)_4]$ (Mn_{12}bz) in Fig. 1a have maintained a central role in the field and have contributed to building up a large portion of our current knowledge on SMM behaviour. For this reason, they were called "the *Drosophila*

[1] In 2009, Journal of Materials Chemistry has published a themed issue on molecular spintronics and quantum computing. See ref. [12].

of single-molecule magnetism" by Bagai and Christou [17]. However, Mn_{12}ac has been holding the record for the largest anisotropy barrier ($U_{eff}/k_B = 62$ K) until 2006, when it was surpassed by another dodecamanganese complex, $[Mn_{12}O_{12}(O_2CCH_2Br)_{16}(H_2O)_4]$, with $U_{eff}/k_B = 74.4$ K [18]. After one year, elegant work in manganese chemistry afforded a complex with formula $[Mn_6O_2(Et\text{-}sao)_6(dmbz)_2(EtOH)_6]$ (Mn_6dmbz) that exhibited the largest barrier known at that time for a polynuclear SMM ($U_{eff}/k_B = 86.4$ K) [19]. These small advances turn into minimal when comparing T_B values rather than anisotropy barriers, as recommended by Rinehart et al. [20]: after almost one decade and a half of skillful molecular engineering and inspired serendipitous assembly, T_B was increased from 3.1 K in Mn_{12}ac to 3.2 K in Mn_6dmbz.[2]

A couple of important contributions were crucial to resolve this *impasse*. As pointed out by Waldmann [21] and later by Neese and Pantazis [22], most synthetic approaches aimed at maximizing the spin in the ground state. The underlying argument was that, in the strong-exchange approximation, the "spectroscopic" anisotropy barrier takes the form $U = |D|S^2$ for integer S and $U = |D|(S^2 - 1/4)$ for half-integer S, where S and D are the total spin quantum number and axial ZFS parameter for the ground state, respectively. However, the D parameter displays a hidden dependence to S through projection coefficients[3] and, for a given structure, U turns out to depend only weakly on S. Enhancing U then requires either more anisotropic constituents or higher-nuclearity species.

Evidence for a crucial role of large single-site anisotropies was available since 2003, when Ishikawa and co-workers reported that individual lanthanide ions sandwiched by two Pc^{2-} ligands could work as SMMs with anisotropy barriers up to 330 K [24]. Such lanthanide double-decker (LnDD) complexes were the first examples of slowly relaxing mononuclear species, although with a fast tunnelling of the magnetic moment in zero field. This unusual behaviour arises directly from the crystal-field splitting of the ground J manifold in the particular coordination environment defined by the two Pc^{2-} ligands [25]. Since then, lanthanide ions have become important ingredients in the SMM field, both as single-ion complexes and as components of polynuclear species [26–34]. This is no surprise, since the strongest magnets known like $SmCo_5$ and $Nd_2Fe_{14}B$ are lanthanide-based materials [25]. Encouraging results were also reported on actinide-based SMMs [35, 36].

Polynuclear lanthanide complexes pose a particularly important challenge: special structural design is required to promote a sizeable interaction between rare earth ions, whose 4*f* electrons have a very limited radial extension. In 2011 Long et al. described dimeric dysprosium(III) and terbium(III) complexes

[2] Here we adopt Rinehart definition of T_B as the temperature affording a relaxation time of 100 s in zero applied field. The need for a reference relaxation time arises from the fact that different techniques have different measurement times and, consequently, detect blocking of the magnetic moment at different temperatures.

[3] Projection coefficients define the relationship between local anisotropic contributions (among which single-ion terms) and the overall anisotropy (D) associated with each total spin state. They can be computed using recursive relations. For details see [23].

containing a N_2^{3-} radical bridge ($s = ½$) which exhibit record T_B's of 6.7 and 13.9 K, respectively [20, 37] (see footnote 1). Such remarkable T_B's, which are the largest ever detected in an SMM, arise from the very diffuse orbital hosting the unpaired electron in N_2^{3-}, which promotes exceptionally strong magnetic coupling between the two lanthanide ions. The compounds are however extremely air sensitive, as is the latest product of creative work in Long's group: an SMM based on a mononuclear complex of iron(I) with linear coordination [38]. The low oxidation state and coordination number result in a very weak crystal field, which leaves a large unquenched orbital momentum on the metal ion. Despite the modest spin-orbit coupling constant in first-row transition-metal ions like iron(I), such a combination yields a record anisotropy barrier for a transition-metal-based SMM (325 K) [38]. Spurred by these and other findings, mononuclear transition-metal SMMs are becoming a fertile area of investigation [39–41] where theoretical methods give considerable aid to molecular design [42].

1.3 SMMs on Surfaces: the Hows and Whys

The second important task is the realization of proof-of-principle devices to demonstrate how the spin state of a molecule can influence electron transport and, conversely, how a molecular spin can be manipulated by an electric current. To this aim, two main configurations were proposed: the current can be driven either through a conductor laterally coupled to the nanomagnet or directly across the molecule [8].

Concerning the former configuration (Fig. 2a), the conductance of a gold quantum dot bridging nonmagnetic electrodes was theoretically predicted to depend on the relative orientation of the magnetic moment of two Mn_{12} complexes linked to it [43]. A similar *spin-valve* effect was invoked to explain the conductance of single-walled carbon nanotubes [44–47] and of graphene nanoconstrictions [48] decorated with LnDD nanomagnets.

To study the interplay between the giant spin of an SMM and an electric current driven *through* it, molecules have to be wired either permanently or temporarily to external electrodes.

Permanent wiring is achieved, for instance, by skillfully embedding SMMs in metal-molecule-metal nanojunctions (Fig. 2b) [49]. Once the device has been assembled, state-of-the-art equipment allows to carry out transport measurements down to subkelvin temperatures while externally tuning the molecular energy levels with a gate potential. In addition, magnetic fields up to several teslas can be applied to identify magnetic excitations [50–56]. The magnetic field can be directed at different angles from the junction axis, allowing angle-resolved characterizations that are extremely useful for strongly anisotropic molecules like SMMs [57, 58]. By entrapping a $TbPc_2$ nanomagnet (Fig. 1d) in such a three-terminal device, Vincent et al. were able to detect QT of the magnetic moment coupled to the nuclear spin of Tb and to reconstruct the hysteresis loop of a single molecule [58].

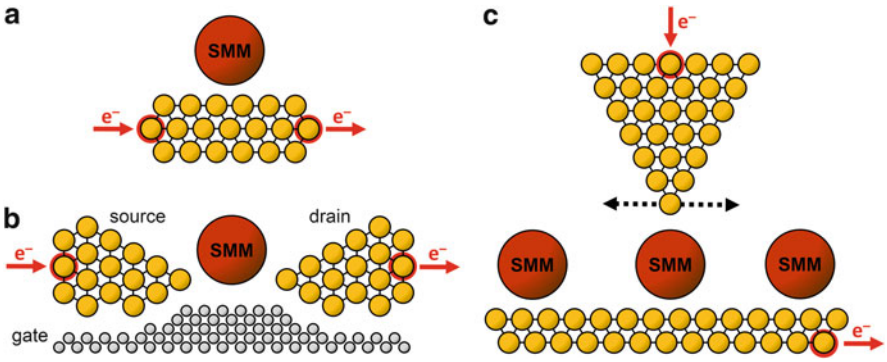

Fig. 2 Different approaches to the electrical addressing of SMMs. In (**a**) the electrons flow through a conductor (metal dot, carbon nanotube, graphene nanoconstriction) that is laterally coupled to the SMM. In (**b**) the current is driven through the molecule itself which is embedded in a three-terminal device comprising source and drain electrodes and a gate terminal. In (**c**) electrons also flow through the molecule which is deposited on an atomically flat surface and contacted by the movable tip of an STM

Molecules can be temporarily connected to external leads by first depositing them on a conductive surface. The tip of an STM is then used as a second, movable electrode to detect and control the electronic spin (Fig. 2c), as suggested by massive theoretical work [59–63]. Two indications show that such experiments may now be within reach. Groundbreaking results were obtained in the electrical addressing, spin detection and spin manipulation of individual metal atoms or arrays thereof (so-called artificial molecules) [64–71]. Furthermore, submolecular resolution was achieved even on complex and delicate molecules, like Mn_{12} complexes (Fig. 3) [72, 73]. These impressive advances in STM methods are further motivating efforts to deposit SMMs on surfaces, an activity that started in 2003 [74, 75].

1.4 Outline

Excellent reviews are available which describe the evolution of research as reported in papers that appeared until the beginning of 2011 [76–81]. Here, we will focus on the structural and electronic properties of surface-supported SMM ensembles by covering the latest advances and highlighting some of the earlier turning points in the field. It is our personal view that investigating the collective properties of molecules on surfaces is an important prerequisite for subsequent in-depth studies at the single-molecule level (we are aware that many influent scientists working in the field of scanning probe methods have strong arguments against our choice). In consequence, our accent will be on the chemical design of SMMs, on their organization at solid interfaces as MLs or subMLs and on the application of spectroscopic and magnetic techniques to study these arrays, which typically

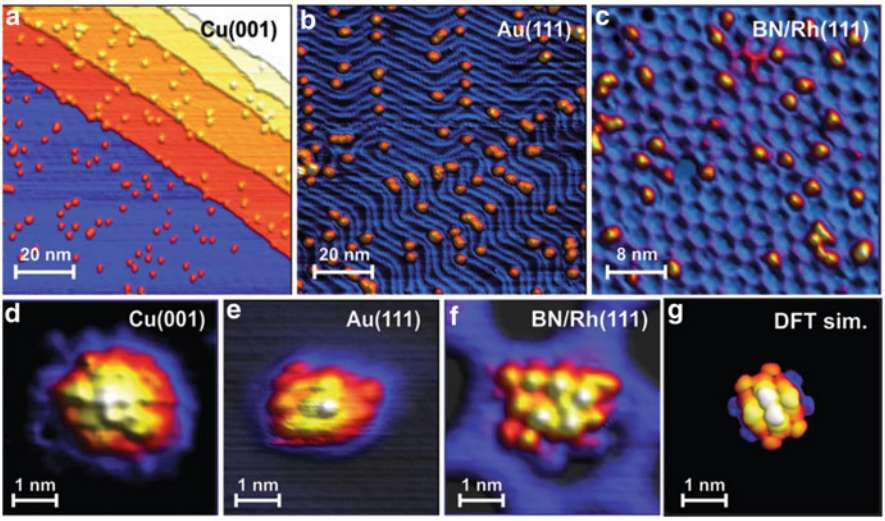

Fig. 3 STM topographic images of mass-selected Mn_{12} complexes deposited on various substrates, recorded over wide areas (**a**–**c**) and with submolecular resolution (**d**–**f**). Image (**g**) shows the response of an individual molecule as predicted by DFT calculations. Reprinted with permission from [72]. Copyright © 2012 American Chemical Society

comprise about 10^{13} molecule/cm^2. The reader more specifically interested in STM/STS studies or in the physical basis of molecular spintronics is addressed to specialistic reviews that have appeared in the recent literature [8, 10, 11], as well as to other contributions in this volume.

A large portion of this review (Sects. 2–4) deals with the organization of SMMs on atomically flat metal surfaces. For simplicity, the text is structured according to the different chemical classes of SMMs, starting from Mn_{12} and Mn_6 clusters and then covering Fe_4 and LnDD systems. Incidentally, this allows to most easily follow the chronological evolution of the field in terms of concepts and techniques. A separate section (Sect. 5) is devoted to SMMs interfaced with metal NPs as a convenient strategy to investigate surface-induced effects. In the final Sect. 6 we draw conclusions and highlight perspectives and future developments.

2 The Weak Sides of Mn-Based SMMs

2.1 Mn_{12} Complexes

The gold surface was the substrate of choice in the earliest investigations on SMM arrays [74, 75]. The main advantage is that gold films and gold crystals can exhibit clean and atomically flat Au(111) terraces hundred nanometers wide after proper

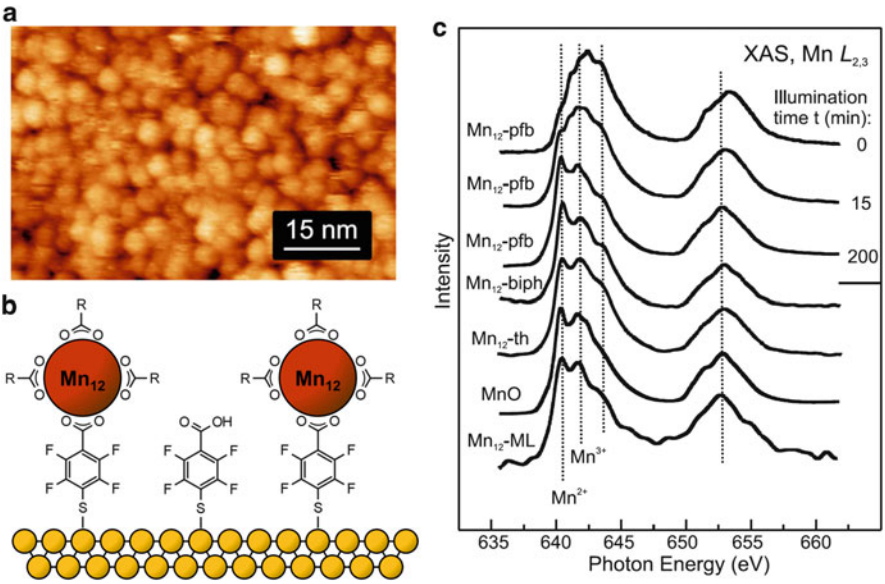

Fig. 4 STM topographic image (**a**) and sketched structure (**b**) of a ML of $[Mn_{12}O_{12}(pfb)_{16}(EtOH)_4]$ (Mn_{12}pfb) grafted on 4-mtba/Au(111) (R = 4-fluoro-phenyl). Panel (**c**) compares the XAS profiles recorded on crystals of Mn_{12}pfb as a function of X-ray exposure time with the final spectra from crystals of $[Mn_{12}O_{12}(biph)_{16}(H_2O)_4]$ (Mn_{12}biph) and $[Mn_{12}O_{12}(th)_{16}(H_2O)_4]$ (Mn_{12}th). Spectra labelled as MnO and Mn_{12}-ML were recorded on non-sputtered MnO (which includes Mn^{2+} and Mn^{3+} contributions) and on the ML in (**a**), respectively. Panels (**a**) and (**c**) reprinted with permission from [85]. Copyright 2008 Springer-Verlag

treatment. Furthermore, gold surfaces display a well-known reactivity towards functional groups carrying "soft" donor atoms (thiolates, phosphines, etc.), as emerging from decades of studies on the adsorption of simple organic species as SAMs [82–84].

Holding a long-standing record for the highest anisotropy barrier, Mn_{12} complexes were at that time considered the most appealing candidates for deposition on either native or prefunctionalized Au(111) surfaces. In the former case ("direct deposition") the interaction with the surface was promoted by introducing S-containing groups at the cluster's periphery. On the other hand, surface prefunctionalization was normally accomplished using aliphatic or aromatic carboxylates that can act as linkers between the substrate and the Mn_{12} core (Fig. 4a, b). As an important and unexpected lesson, these early attempts soon revealed a tendency of Mn_{12} complexes to undergo systematic alterations at surfaces. A posteriori, surface-induced structural distortions or even more dramatic chemical changes are hardly unexpected when considering the richness of manganese carboxylate cluster chemistry [86]. However, they were completely overlooked in the course of initial studies, that were largely based on standard techniques for surface analysis like XPS and scanning probe methods [74].

Compositional data determined by quantitative XPS analysis do not in general provide unique structural information, in part because of their large associated

uncertainty. Furthermore, owing to the limited spectral resolution of XPS experiments, it is quite hard or impossible to distinguish between different oxidation states of Mn ions with this technique. Trying to overcome this difficulty, Fleury and co-workers used the exchange splitting of Mn 3*s* photoelectron peak to infer the oxidation state of Mn in two Mn_{12} derivatives deposited on prefunctionalized silicon [87, 88]. Such a correlation was established by previous work on manganites and other Mn oxides, but its applicability to Mn_{12} compounds seems questionable; in fact both grafted and bulk reference samples display Mn 3*s* splittings of 5.4–5.6 eV, which would indicate an average oxidation state lower than 3.0.

Scanning probe methods like STM, sometimes aided by STS, were useful to find synthetic routes to the highest-quality MLs as well as to reveal the existence of a gapped energy spectrum typical of molecular species [78, 85, 89–94]. However, although STM/STS experiments can be informative even under ambient conditions at room temperature [95], the relevant energy scale for magnetic molecules can be addressed only at low temperature (4.2 K or below [72, 73]). Furthermore, it is only by application of a magnetic field that signatures of quantum magnetism can be identified, as reported for Mn_{12} molecules deposited on BN/Rh(111) [72].

2.1.1 Studies by X-ray Absorption Spectroscopy

A turning point in the field was represented by the introduction of techniques based on XAS to directly probe the electronic structure and magnetic behaviour of SMM arrays with the required surface sensitivity. These methods demand synchrotron-light sources and specially designed end-stations working in UHV, so that they cannot be considered as routine characterization techniques. The experiments are normally carried out at the absorption edges of the metal ions. For manganese and other first-row transition metals it is customary to choose the $L_{2,3}$ edges, which correspond to 2*p*-3*d* transitions.

It was soon found that the Mn $L_{2,3}$ edge spectra of Mn_{12} MLs on gold significantly deviate from those of bulk crystalline samples due to the appearance of a Mn^{2+} signal (Fig. 4c) [85, 89, 96]. Notice that exposure to an X-ray beam of sufficient intensity causes progressive photoreduction even in bulk samples. This problem is commonplace in the spectroscopic investigation of metal-organic compounds using soft X-rays as well as in protein crystallography [97, 98]. However, with a proper choice of measurement conditions (e.g. low photon flux and short irradiation times), the spectra of the MLs become time independent while still displaying a Mn^{2+} component from the very beginning of the experiment. The details of the reduction (e.g. proportion of Mn in the different oxidation states) are however influenced by the particular Mn_{12} derivative used [89, 96], by the adopted deposition protocol (direct deposition vs. surface prefunctionalization) [89], by the specific prefunctionalizing layer used [99], as well as by the solvent [96] and by the presence of moisture [85]. The many factors involved may offer a possible explanation for some conflicting reports present in the literature [78, 85].

From the available data, the surface prefunctionalization approach seems superior to direct deposition in terms of surface coverage and quality of the MLs [90], although partial reduction to Mn^{2+} takes place in both cases. However, recent studies by Saywell, Handrup and collaborators at the University of Nottingham have contributed to stir things up in the field and to revitalize deposition on native gold surfaces. In a series of papers [100–102], these authors investigated three Mn_{12} derivatives featuring protective ligand shells of different thickness: Mn_{12}ac, Mn_{12}bz (Fig. 1a) and $[Mn_{12}O_{12}(tpc)_{16}(H_2O)_4]$ (Mn_{12}tpc). The complexes were brought onto the Au(111) surface by the non-thermal technique of UHV electrospray deposition. In such a way, the intrinsic thermal instability of Mn_{12} complexes was circumvented and contaminations arising from chemical manipulations were minimized. Layers of Mn_{12}ac with coverage ranging from 2.5 to 0.2 MLs revealed a dramatic increase of Mn^{2+} contribution with decreasing surface coverage [100]. No improvement in the fraction of undamaged complexes was achieved using Mn_{12}bz, which features a bulkier ligand shell [101]. Rewardingly, the XAS profiles of Mn_{12}tpc were virtually coverage independent in the range 1.7–0.3 ML and closely matched those of "intact", bulk-phase complexes [102]. Replacing Au(111) with rutile TiO_2 (110), a wide band gap semiconductor, introduced no appreciable changes in the behaviour of Mn_{12}bz and Mn_{12}tpc: only in the latter compound were the correct oxidation states preserved at subML coverage. A very low Mn^{2+} content was also reported by Grumbach et al. for another Mn_{12} derivative carrying bulky mesogenic ligands and deposited as a thin film approximately one-molecule thick on SiO_2/Si [103].

It can be concluded that, all other conditions being the same, a bulky ligand shell can minimize reduction of Mn^{3+} and/or Mn^{4+} ions to Mn^{2+}. Furthermore, the aforementioned coverage-dependent studies demonstrated that reduction is a surface-mediated effect and that overlayers remain largely unaffected. Unfortunately, it is still unproven whether such a reduction occurs upon adsorption or takes place instantaneously upon irradiation with X-rays. Both mechanisms would in fact be mitigated by bulky organic ligands, which decouple the core from the surface. Voss et al. pointed out that MLs and deliberately beam-damaged bulk samples have remarkably similar XAS profiles [85]. However, the fact that time-independent spectra are observed for low photon fluxes suggests that photoreduction may not be the primary source of Mn^{2+}. Such a view is confirmed by recent STM/STS studies and DFT calculations on Mn_{12} complexes deposited on Bi(111). In these conditions, the molecules exhibit a greatly reduced HOMO-LUMO gap (ca. 40 % of the value found in free Mn_{12} complexes), a result attributed to charge transfer from the substrate [73].

2.1.2 Studies by X-ray Magnetic Circular Dichroism and microSQUID Susceptometry

Evidence of a strongly perturbed electronic structure in Mn_{12} complexes at surfaces has emerged in the clearest fashion from magnetic studies [96]. The magnetic

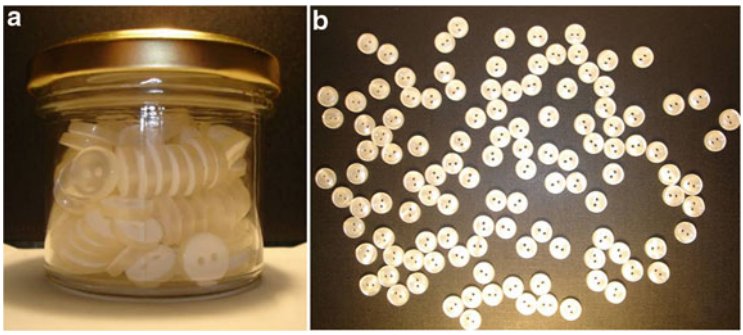

Fig. 5 Buttons filling a jar resemble tightly packed molecules in a crystal (**a**); when spread on a surface, buttons and molecules can extend over very large areas (**b**). As a sample calculation, a 0.1 mg single crystal is just enough for detailed magnetic studies using a SQUID magnetometer; for a molar mass of 2,000 g/mol it comprises about $3{\cdot}10^{16}$ molecules. If each molecule covers a 2-nm^2 area, 1 cm^2 of a ML contains about $5{\cdot}10^{13}$ molecules, i.e. three orders of magnitude less material than the single crystal

characterization of MLs is complicated by the fact that manageable ML samples typically comprise submicrogram amounts of magnetic material (Fig. 5). Unless piled substrates are used [104], traditional magnetometry must then be abandoned and replaced by other methods, such as XMCD. XMCD is a spectroscopic technique that relies on the different absorption of right and left circularly polarized X-rays by a magnetized sample [105–107].[4] The amplitude of the XMCD signal is often simply proportional to the magnetic polarization at the absorbing element, so that XMCD is most conveniently measured at the absorption edges of the metal ions. To enhance magnetic polarization in paramagnetic systems, low temperatures and high magnetic fields are in general used. In these conditions, XMCD allows field- and temperature-dependent magnetic studies with a much higher sensitivity than traditional magnetometry. In particular, X-ray absorption can be monitored by measuring the drain current caused by the emission of secondary electrons from the sample (TEY detection mode). Because of the low penetration depth of these electrons, TEY-XMCD is a surface sensitive technique and can probe down to 0.01 MLs of Mn atoms on a surface.

XMCD profiles, along with their temperature or field dependence, were found much more informative than XAS spectra when looking for small differences in the electronic structure. As an example, a single Mn^{2+} ion per Mn_{12} is difficult to be detected in XAS but is well visible in the XMCD profile [96]. In consequence,

[4] In an XMCD experiment, absorption cross sections for photon helicity parallel (σ^+) and antiparallel (σ^-) to the applied field are separately measured and the XMCD signal is defined as the difference ($\sigma^- - \sigma^+$). It is usually expressed as percentage of the maximum in the isotropic spectrum, that can be estimated as $(\sigma^+ + \sigma^-)/2$ in the case of transition metals. Since the isotropic spectrum intensity is proportional to the number of absorbing atoms, the XMCD signal so defined (XMCD%) provides the dichroic response *per* atom.

apparently intact samples (according to "XAS criterion") may have XMCD responses that differ substantially from those of bulk phases [99]. In this sense, the previously mentioned MLs of Mn_{12} metallomesogens reported by Grumbach et al. are unique, as their XMCD response is bulk-like in both lineshape and intensity [103]. XMCD-detected magnetization curves recorded at 2 K are also compatible with a high-spin ground state. As disappointing as it may be, these MLs exhibit simple paramagnetic behaviour at 2 K, while the bulk material has an open hysteresis loop with a coercive field of around 3 kOe in SQUID measurements. Altogether, these results evidence an adverse effect of the surface environment on the magnetic behaviour of Mn_{12} complexes, affecting static properties, dynamic properties or both.

Remarkably, even bulk samples may exhibit a compromised electronic structure in their topmost layers. In 2009, a Mn_{12} derivative was investigated in the bulk phase using, in parallel, a VSM and TEY-XMCD [108]. Samples were prepared by drop-casting millimolar solutions of the compound on Au(111) to achieve films with thickness of a few hundred nanometers. When the magnetism of the entire film was probed by a VSM, a temperature-dependent hysteresis loop was detected below 3 K, the typical T_B of Mn_{12} derivatives. When the topmost layers of the film were investigated by TEY-XMCD, the spectral profile was in agreement with the one expected for an "intact" Mn_{12} core. However, the field dependence of isothermal magnetization revealed reduced anisotropy and simple paramagnetic behaviour, with no hysteresis down to 0.75 K. These data indicate that the first few nanometers of the deposit show drastically altered static magnetic properties and a much faster spin dynamics than the bulk phase.

Trying to explain these and other disappointing results, Grumbach, Donnio and collaborators [103, 109] invoked a possible intrinsic inability of XMCD to probe magnetization dynamics in molecular systems, as opposed to low-dimensional metallic ferromagnets [110]. The reason why such an interpretation can now be safely ruled out is twofold. First, slow magnetic relaxation was indeed detected by XMCD in Fe_4 and other SMMs (see below). Second, in an elegant piece of work Bellido et al. [111] used DPN to deposit Mn_{12}bz complexes (Fig. 1a) on the sensitive area of a microSQUID susceptometer. The sample was nanostructured in the form of a continuous film or of a dot pattern with thickness of 3–8 molecular layers on SiO_2/Si. The magnetic characterization of bulk samples, carried out under the same conditions and with the same setup, showed the typical magnetization dynamics of Mn_{12}bz complexes. However, magnetic relaxation was much faster in the nanostructured samples, which displayed normal paramagnetic behaviour in the accessible frequency range. Many environmental factors can contribute to this drastic alteration of the spin dynamics. The amorphous nature of the deposits seems unimportant, as previous studies evidenced only minor differences in the behaviour of crystalline and amorphous phases of the same material [112]. On the other hand, molecules lying at interfaces may experience severe distortions [113] and have their anisotropy parameters modified [96, 99]. For instance, flipping of the Jahn–Teller axis of just one Mn^{3+} ion in the core causes a dramatic decrease of the anisotropy barrier [114]. Supporting this interpretation is the 13 % lower anisotropy

barrier observed in crystalline Mn_{12}bz when the particle size is reduced from 11.5 to 0.4 μm [115]. Other less investigated aspects are the role of molecule–substrate electronic interaction and possible differences in spin-phonon coupling at the surface.

2.1.3 Orientation Control Over Mn_{12} Monolayers

Owing to the strong anisotropy of SMMs, orientation control over surface grafting is crucial to retrieve a well-defined response from surface-supported molecules. In the case of Mn_{12} complexes, a strategy for promoting an oriented grafting was proposed based on previous, elegant work by Christou's group [116, 117]. The structure of Mn_{12} complexes can be most simply described as a fragment of a manganese oxide surrounded by sixteen carboxylate or related ligands. These sixteen carboxylates can be partitioned into two structurally distinct groups – axial and equatorial – that display Mn–O bonds of different strength. Such differences are useful to carry out site-selective carboxylate abstraction [116] or to control ligand distribution in mixed-carboxylate complexes [117]. In fact, the more basic ligands show a preference for equatorial sites whereas the less basic ones occupy axial sites. When a Si surface covalently prefunctionalized with long-chain (C11) alkanecarboxylic acids was treated with a solution of $[Mn_{12}O_{12}(O_2CCHCl_2)_{16}(H_2O)_4]$, XPS showed that the Cl/Mn ratio in the adsorbate was halved with respect to the solid complex [87]. By contrast, $[Mn_{12}O_{12}(O_2CCHCl_2)_8(O_2CCH_2{}^tBu)_8(H_2O)_3]$ (with dichloroacetate ligands in axial positions) maintained its Cl/Mn ratio after grafting [88]. From these results and from the higher pK_a of 1-undecanoic vs. dichloroacetic acid it was inferred that the anchoring process involves the eight equatorial sites and that molecules are oriented with their fourfold axis normal to the surface. Such a chain of arguments is weakened by the tendency of mixed-ligand Mn_{12} complexes to undergo ligand redistribution in solution, as noted by Soler et al. [117]. Moreover, the spatial distribution of alkanoic units on the surface is fixed at the stage of surface prefunctionalization and cannot undergo any later rearrangement to ensure coordination to all eight equatorial sites in each cluster.

The molecular height measured by STM/STS methods in high-quality MLs was also used to infer the absence of a preferred molecular orientation in a Mn_{12} derivative containing diphenylphosphinate ligands and grafted on a gold-supported ML of 4-mobca [118]. In contrast to this, data collected on $[Mn_{12}O_{12}(th)_{16}(H_2O)_4]$ (Mn_{12}th) would suggest a preference for binding through axial positions, i.e. with the molecular axis along the surface normal [93]. It was noted that such differences match the trend in relative ligand basicity [118]. However, because of the aforementioned difficulties in retrieving precise structural and electronic information from XPS and STM/STS techniques, claims of structural control over Mn_{12} MLs should be critically reconsidered.

A careful examination of the Mn_{12} core shows that another approach to orientation control may be feasible: site-specific insertion of rigid dicarboxylates whose

geometry exactly matches the spatial arrangement of two axial sites. Such an idea found a practical realization in 2004 [119] but was not developed any further owing to growing evidence of electronic instability and loss of SMM behaviour in Mn_{12} complexes at surfaces. However, it turned out to be a key strategy when applied to a different family of SMMs, namely Fe_4 propeller-like complexes, as described in Sect. 3.4.

2.2 *Mn_6 Complexes*

As mentioned in Sect. 1.2, Mn_6 complexes are excellent SMMs and some derivatives even outperform the Mn_{12} family in terms of T_B [19, 120]. Although much less studied than Mn_{12} species, they are also emblematic of adverse surface effects on the electronic structure and magnetic response. Sulphur-functionalized derivatives containing th^- ligands like $[Mn_6O_2(sao)_6(th)_2(H_2O)_4]$ (Mn_6th) (Fig. 1b) form adsorbates on Au(111) with the correct composition according to XPS analysis [121]. XAS studies also suggested no significant reduction of the hexamanganese (III) core, but the spectral profiles of bulk samples and adsorbates are nevertheless not identical, hinting to subtle structural differences [122]. Variable temperature and variable field XMCD spectra in fact revealed a drastic decrease of the magnetic moment residing on Mn^{3+} ions in the adsorbates [123].

Summarizing, state-of-the-art diagnostic tools like XAS/XMCD or microSQUID susceptometry showed that only in special cases is the electronic structure of manganese-based SMMs maintained at surfaces in terms of correct oxidation states and static magnetic response. Bulky ligands at the cluster's periphery help decoupling the core from the surface, although they are expected to decrease electrical conductivity and to hamper electrical addressing of individual molecules. Even though a compromise can always be sought, there is at present no single experiment proving that individual Mn_{12} or Mn_6 complexes (or small groups thereof) can maintain their memory effect when lying on a surface. This failure to observe slow magnetic relaxation has long puzzled scientists and has represented a major blocking point for years. As described in Sect. 3.3, in 2009 it was finally demonstrated that slow magnetic relaxation is compatible with the surface environment, thereby "turning a nightmare into a vision" [124]. To achieve this, it was essential to abandon manganese chemistry and to focus on propeller-like complexes of a different transition-metal ion: iron(III).

3 The Iron Option

The structure of tetrametallic propellers of direct interest to this review is shown in Fig. 6. It entails a metal-centred triangular arrangement of metal ions and two different types of ligands: peripheral β-diketonates and bridging alkoxides. In stark

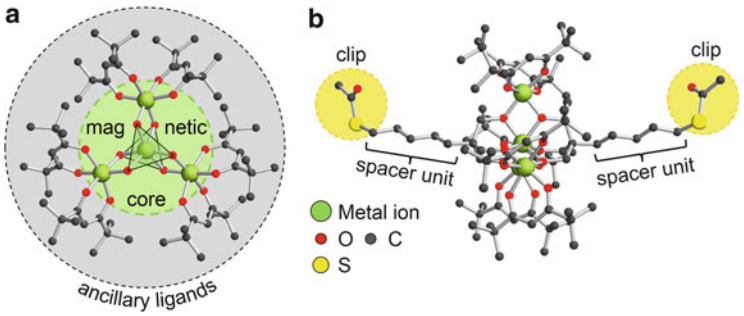

Fig. 6 Structure of heteroleptic tetrametallic propellers viewed along the idealized threefold axis (**a**) and perpendicular to it (**b**). Three main structural components are susceptible of chemical tailoring: the magnetic core, the ancillary ligands and the axial groups, here comprising a surface-binding "clip" and a spacer unit. *Triangles* in (**a**) connect the three O donors of each tripodal ligand. Hydrogen atoms are omitted

contrast with their homoleptic analogues [125–128], these simple SMMs are extremely versatile from the chemical point of view, since terminal and bridging ligands can be varied independently.

Their precursor, $[Fe_4(OMe)_6(dpm)_6]$, has a magnetic core supported by six methoxide ligands [129]. By carefully examining its structure, it was soon realized that the O–O separation between methoxide bridges lying on the same side of the molecular plane (2.92–2.95 Å) closely matches the geometry of tripodal alkoxides H_3L=R-C$(CH_2OH)_3$ [130]. In accordance with this simple idea, the reaction of $[Fe_4(OMe)_6(dpm)_6]$ with H_3L ligands afforded a pool of heteroleptic tetrairon(III) systems with formula $[Fe_4(L)_2(dpm)_6]$.[5] The ligand replacement reaction, which leaves the shell of dpm^- ligands untouched, has important consequences on the chemical properties and physical behaviour of the material.

First, ^{1}H- and ^{2}H-NMR showed that while the precursor rapidly decomposes in organic solvents like Et_2O [132] and toluene [133], complexes incorporating tripodal alkoxides remain stable in solution for up to several days [53, 134, 135]. Molecular-ion peaks are easily detected by ESI-MS [133, 136, 137] and some derivatives can even be thermally evaporated in high vacuum with full retention of their structure and magnetic properties [138]. Second, the tripodal ligands do not alter the ground spin state value ($S = 5$) but afford a twofold larger $|D|$ parameter (from $D = -0.21$ to $-0.41/-0.45$ cm^{-1}, depending on the derivative). Owing to the enhanced anisotropy the spectroscopic anisotropy barrier also increases, although differences stand out most clearly when comparing effective barriers: $U_{eff}/k_B = 3.5$ K in $[Fe_4(OMe)_6(dpm)_6]$ vs. 14–17 K in complexes $[Fe_4(L)_2(dpm)_6]$ [139]. The improved magnetic properties were related to the different helical pitch and to the more closely axial symmetry imposed by the tripodal ligands [139].

[5] Similar complexes can also be prepared in a single step, as described for related systems containing acetylacetonato ligands [131].

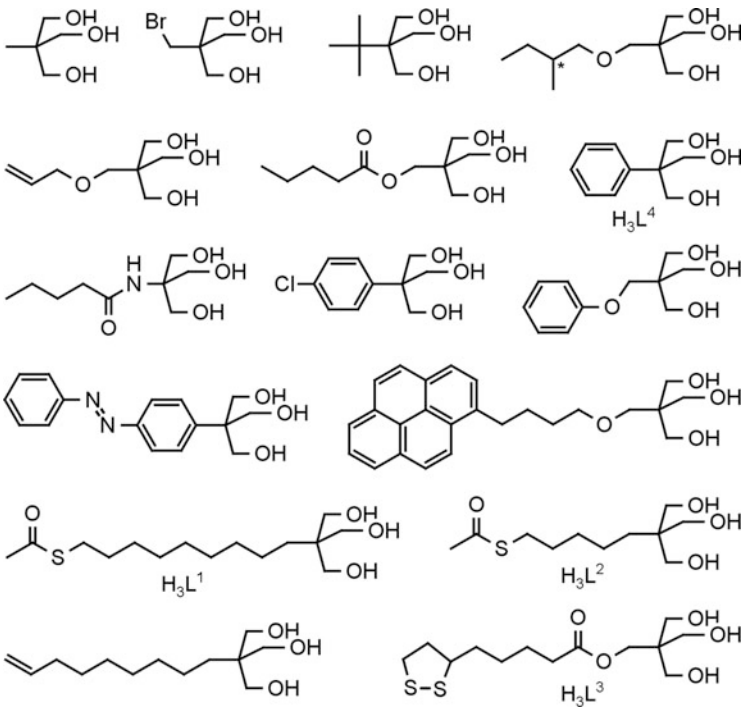

Fig. 7 Tripodal ligands that afforded crystalline Fe_4 complexes

Third, the R group is bound to lie along the idealized threefold molecular axis and opens the way to the deliberate functionalization of the molecules. As a further advantage, the nature of the R group does not affect much the crystal packing and solubility, which are mainly determined by the ancillary ligands.

A collection of ligands used for functionalizing tetrairon(III) complexes are shown in Fig. 7. Some of them contain fluorescent or photoactive units that afforded multifunctional materials [140]. Derivatives suitable for deposition on noble-metal substrates, like those carrying thioacetyl or disulphide groups, were also prepared as detailed in the next sections.

Separate tailoring of the ancillary ligands is of course possible to convey special properties to the molecules, such as improved processability by thermal evaporation (see Sect. 6) [141]. Finally, homo- or heterometallic complexes with the same structure were prepared using other trivalent metal ions, like Ga^{3+} [142], Cr^{3+} [142–144] and V^{3+} (Westrup et al. unpublished results). Especially important are Fe_3Cr species, which retain the same "ferrimagnetic" spin structure as Fe_4 complexes but contain a central Cr ion that can be separately probed by XMCD experiments (see Sect. 3.2).

3.1 XMCD-Detected Slow Magnetic Relaxation of Fe_4 Complexes in the Bulk Phase

Although their T_B's remain well below 1 K, Fe_4 clusters display much enhanced structural and redox stability as compared with Mn_{12} and Mn_6 species. That the surface environment may not have a dramatic effect on these small SMMs was first evident by investigating microcrystalline samples of compound $[Fe_4(L^1)_2(dpm)_6]$ (Fe_4C9), which contains long-chain SAc-terminated ligands (Figs. 1c and 7). TEY-XMCD data recorded as a function of temperature and field were found to closely match the magnetic behaviour of bulk phases. More important, both TEY-XMCD (which is surface sensitive) and microSQUID magnetometry (which is bulk sensitive) detected magnetic bistability and a waist-restricted hysteresis loop when experiments were carried out at 0.55(5) K and with the same field sweep rate [108]. This finding demonstrated that the XMCD technique can correctly probe slow magnetic relaxation in molecular systems, contrary to previous interpretations [103, 109] and in agreement with pioneering work by Létard et al. [145]. Additionally, by showing that the surface layers in a microcrystalline sample of Fe_4C9 behave similarly to the bulk, it marked the emergence of Fe_4 propellers as benchmark systems to investigate slow magnetic relaxation at surfaces. Since then, XAS/XMCD experiments have maintained a central role not only to prove retention of the correct oxidation states but also to probe the electronic structure over very different energy scales, as defined by superexchange interactions, magnetic anisotropies and tunnel splittings.

3.2 Fe_4 and Fe_3Cr Complexes at Surfaces: Superexchange Interactions Detected by XMCD

After deposition on Au(111) from dichloromethane solution, the XAS profile of Fe_4C9 is indeed superimposable to that of bulk samples, allowing to rule out any surface-induced reduction or beam damage [135]. The XMCD line shape and intensity also match well the response of the bulk phase and are in agreement with theoretical predictions [108].

Further experiments proved that the observed XMCD profile and intensity are reliable signatures of the "ferrimagnetic" spin arrangement in the ground $S = 5$ state of Fe_4 complexes. In fact, the dichroic response per Fe atom (as measured by the XMCD% signal) (see footnote 3) is expected to change dramatically when the central iron(III) ion, which provides a field-opposing magnetic contribution, is replaced by a different metal ion (M^{3+}) while preserving an antiferromagnetic M-Fe coupling (Fig. 8a). Starting from this idea, Cr^{3+} was selectively incorporated as a central ion using either a one-pot reaction from mixed metal salts [142, 143] or a sequential assembly protocol [144]. In this way, a crystalline complex $[Fe_3Cr(L^1)_2(dpm)_6]$ (Fe_3CrC9) isomorphous to Fe_4C9 was prepared which features

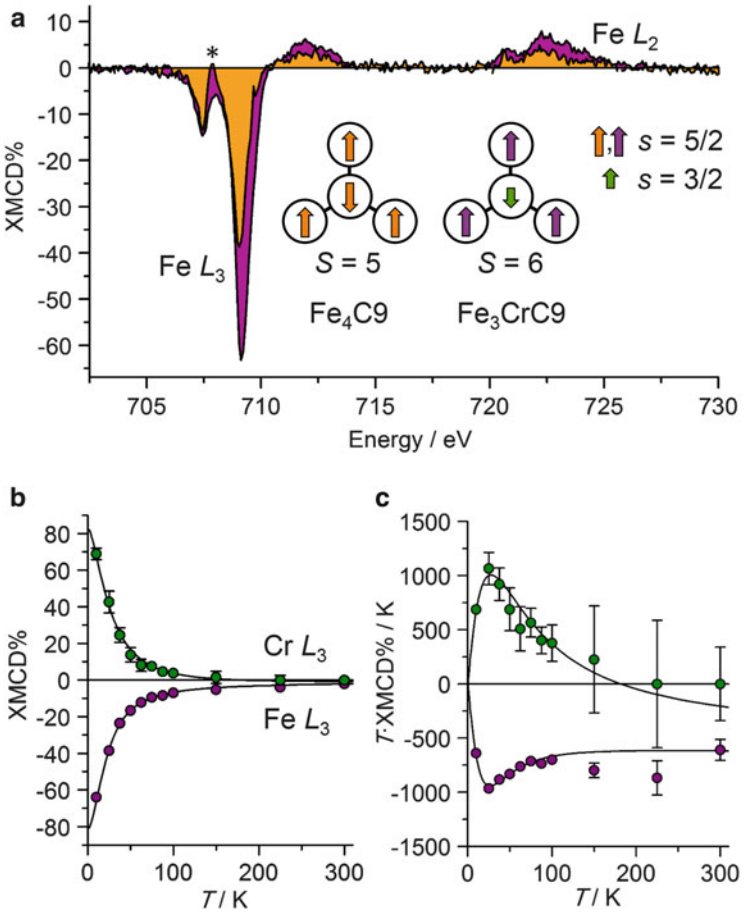

Fig. 8 XMCD% signal (see footnote 3) at the Fe $L_{2,3}$ edges measured on MLs of Fe_3CrC9 and Fe_4C9 complexes on Au(111) at 30 kOe and 7 K (**a**). The *inset* explains the enhanced magnetic polarization per iron ion found in Fe_3CrC9, where the field-opposing contribution of the central metal is missing; this contribution is also responsible for the vanishing XMCD% signal at 707.9 eV (marked by an *asterisk*). Temperature-dependent XMCD response of ML samples of Fe_3CrC5 at the Fe and Cr L_3 edges measured in a 50 kOe applied field (**b**, **c**). Error bars are omitted when smaller than the symbol size. *Solid lines* represent best-fit calculated curves. Panel (**a**) adapted with permission from [143]. Copyright 2011 American Chemical Society. Panels (**b**) and (**c**) adapted with permission from [146]. Copyright 2013 WILEY-VCH Verlag GmbH & Co. KGaA, Weinheim

antiferromagnetic Cr–Fe interactions and an $S = 6$ ground state. Bulk-phase samples and MLs on Au(111) were analysed by XMCD, which evidenced signals of expectedly opposite signs at the Fe and Cr $L_{2,3}$ edges [143]. More important, the dichroic response of Fe_3CrC9 and Fe_4C9 at the Fe $L_{2,3}$ edges was substantially different in both lineshape and intensity. The XMCD amplitude in the Cr-containing complex was enhanced by a factor about two, in accordance with

the approximately doubled magnetic polarization per Fe ion (Fig. 8a). Careful comparison of XMCD lineshapes also disclosed subtle differences between Fe_3CrC9 and Fe_4C9, suggesting that the peripheral and central iron(III) ions in Fe_4C9 may contribute to the overall XMCD response with non-identical profiles [143].

More recently, XMCD was utilized to measure the Fe-Cr superexchange coupling constant ($J_{Fe\text{-}Cr}$) in surface-wired complexes $[Fe_3Cr(L^2)_2(dpm)_6]$ (Fe_3CrC5) [146] (see Fig. 7 for ligand structure). As in traditional magnetometry, the determination of $J_{Fe\text{-}Cr}$ corresponds to evaluating the energy of excited spin states and requires temperature-dependent studies. Here, a major difficulty is represented by the rapid decrease of magnetic polarization and, concomitantly, of XMCD intensity as a paramagnet is heated, so that the XMCD signal remains detectable only in a limited temperature range. This explains why only few molecular materials have been studied by temperature-dependent XMCD as bulk phases [147–149] or MLs [150–152]. Figure 8b presents the T-dependent XMCD intensity at the Fe and Cr L_3 edges recorded on MLs of Fe_3CrC5 at a constant field of 50 kOe. In the temperature range where they could be reliably measured (10–100 K for Cr and 10–300 K for Fe), XMCD% vs. T data evidenced the expected rapid decrease of magnetic polarization as temperature is increased. Furthermore, the magnetic polarization has an opposite sign at Fe and Cr sites: it is field parallel (XMCD% < 0) on Fe and field-antiparallel (XMCD% > 0) on Cr, hinting to dominant antiferromagnetic correlations. As commonplace in traditional magnetometry, a plot of XMCD%·T vs. T is however much more informative about superexchange interactions. As shown in Fig. 8c, the |XMCD%·T| values increase upon cooling below 100 K, before saturation effects set in at the lowest temperatures. The ability of XMCD to probe magnetism in an element-specific manner further reveals a strikingly different temperature dependence for the two signals, in agreement with expectations.[6] The two curves were simultaneously fitted to reliably determine $J_{Fe\text{-}Cr} = 14.7$ (7) cm^{-1}, in excellent agreement with the value found in the bulk phase by the same method as well as by SQUID magnetometry [146]. With this $J_{Fe\text{-}Cr}$ value the magnetic polarization on chromium(III) is expected to switch from field-antiparallel to field parallel around 180 K. Unfortunately, at this T the XMCD signal at the Cr $L_{2,3}$ edges is already zero within experimental error. These findings show that the electronic structure of the complexes is maintained over the energy scale of superexchange interactions, which remain antiferromagnetic and of the

[6] In the absence of superexchange interactions and saturation effects, both the overall magnetization (as probed by traditional magnetometry) and the local magnetic polarizations at metal sites (as probed by XMCD) follow the Curie law. When superexchange interactions are switched on, the local magnetic polarizations are not necessarily proportional to each other and to molecular magnetization [147, 153]. In Fe_3Cr systems, the magnetic polarization at Fe sites is always parallel to the applied field, while that at the Cr site must switch from field antiparallel to field parallel with increasing T. The corresponding XMCD signals are thus expected to exhibit completely different T dependences. Notice that in the temperature range of interest magnetic anisotropy has no effect on magnetic behaviour and can be neglected.

same magnitude as in the bulk phase. This situation is rare among complex molecular architectures deposited on surfaces, as shown by work on Fe_{14} [150] and Cr_7Ni [151, 152] species.

3.3 *Magnetic Anisotropy and Memory Effect in Surface-Wired Fe_4 Complexes*

The next relevant energy scale is defined by magnetic anisotropy, which determines the value of U and, in bulk samples, is usually probed by isothermal field-dependent magnetization curves. In MLs of Fe_4C9, XMCD-detected magnetization data recorded at 1.5 and 4.5 K in fields up to 55 kOe displayed a pronounced nesting when plotted as a function of H/T, pointing to a sizeable magnetic anisotropy. This static magnetic response of the sample matched rewardingly well the prediction based on the SH parameters for the bulk phase [135].

The last, crucial energy scale covers the tunnel splittings arising from non-diagonal SH terms, which have a direct bearing on slow magnetic relaxation. In the most critical part of the experiment, XMCD indicated that MLs of Fe_4C9 follow paramagnetic behaviour down to 0.70 K, but that a hysteresis loop opens at 0.50(5) K, the lowest temperature that could be reached [135]. Slow relaxation of the magnetization was also directly measured as a function of time in a static field of 2.5 kOe and found to follow a mono-exponential law [135]. The characteristic decay time of 220(15) s at 0.50(5) K is comparable to that observed at the surface of thick films, i.e. 285(10) s at 0.55(5) K [108]. These findings provided the first clear demonstration that metal-wired SMMs can retain their most distinctive feature, i.e. slow magnetic relaxation. Because SMM behaviour is exceedingly sensitive to structural distortions as well as to environmental effects, the detection of a memory effect also provides a smoking-gun proof of intact molecules.

Subsequent investigations by XNLD were used to probe the structural order in the MLs of Fe_4C9.[7] Data showed that the MLs are completely disordered [154], as a likely consequence of the long and flexible alkyl chains, which can promote surface binding through one or both SAc groups (Fig. 9a) [155]. Shorter tethers are expected to limit the interaction with the surface to one thioacetyl group only (Fig. 9b) and to promote a partially oriented grafting, as described in the next section.

[7] While XMCD utilizes circularly polarized X-rays to study magnetism, XNLD uses linearly polarized radiation to probe structural order. In an XNLD experiment, the beam is tilted from the surface normal and the XNLD signal is defined as the difference in response to vertically (σ_V) and horizontally (σ_H) polarized radiation, ($\sigma_V - \sigma_H$). Normalization of the XNLD signal is carried out as described for XMCD (see footnote 3).

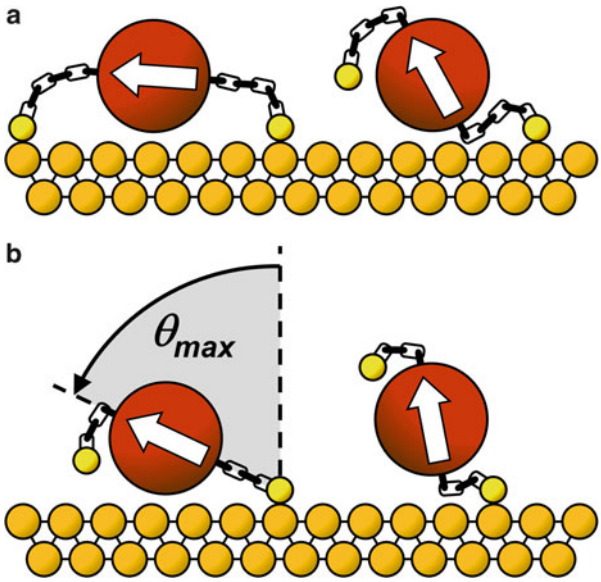

Fig. 9 Long flexible tethers allow surface binding in any orientation (**a**), but sufficiently short linkers. (**b**) impose a maximum tilting angle (θ_{max}). The easy magnetic axis is drawn as a *white arrow*

3.4 Orientation Control and Resonant Quantum Tunnelling in Surface-Wired Fe_4 Complexes

To prove that shorter spacers limit orientational freedom on the surface, the ligand H_3L^2 (Fig. 7) was deliberately prepared and used to assemble $[Fe_4(L^2)_2(dpm)_6]$ (Fe_4C5), whose structure is depicted in Fig. 6b. Its MLs on Au(111) showed a nonzero XNLD signal (Fig. 10a), suggesting partial orientational ordering (see footnote 6). With the aid of DFT calculations, the easy magnetic axis was found to withstand a maximum tilting angle (θ_{max}) of approximately 35° from the surface normal if an S-Au linkage has to be maintained (Fig. 9b). Consistent with this, an XMCD investigation at 0.65(5) K with fields applied at different angles (θ_H) from the surface normal revealed an anisotropic magnetic response (Fig. 10b). More important, as a consequence of the partially ordered layers, a spectacular waist-restricted hysteresis loop was detected with clear signatures of resonant QT effects [154]. Faster relaxation was in fact observed (Fig. 10b) in zero field and at two nonzero field values (±4.5 kOe). It is now well established [2] that such steps occur whenever the magnetic field causes the states with $m = S$ and $m = -S + n$ to be quasi-degenerate (n positive integer or zero), i.e. at $H = \pm n|D|/(g\mu_B)$. Using the bulk-phase value $D/k_B = -0.60(1)$ K one gets (in kOe) $H = \pm 4.47(7)n$, in complete accordance with experiment. These findings demonstrate that Fe_4 complexes remain fully functional when chemically grafted to gold and that orientation control can be achieved by a rational chemical approach. We foresee that further shortening of the alkyl spacers will decrease the tilt angle on the surface and provide even better oriented layers.

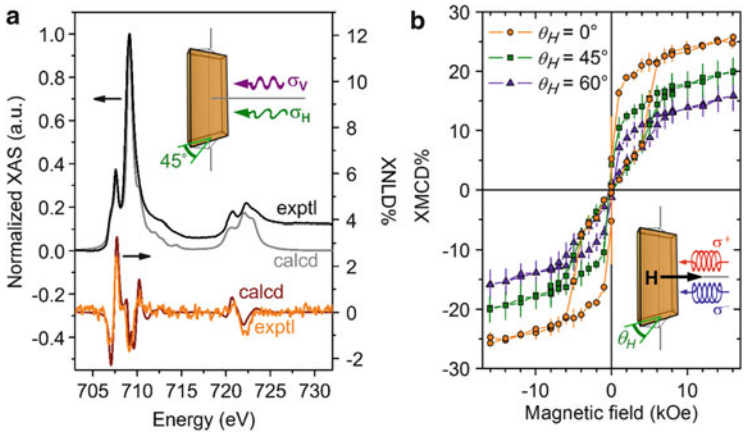

Fig. 10 Experimental and calculated XAS and XNLD profiles (see footnote 6) for Fe_4C5 on Au (111) (**a**). The *inset* shows the geometry of the experiment, which encompasses a 45° tilting of the substrate with respect to the incoming beam. XMCD-detected magnetization curves (see footnote 3) measured on the same sample at 0.65(5) K for different angles (θ_H) between the applied magnetic field and the surface normal (**b**). Adapted with permission from [154]. Copyright 2010 Nature Publishing Group

4 Lanthanide Double-Deckers

LnDD systems [156] have been the target of a number of investigations in surface science and molecular spintronics, starting from pioneering studies by Gómez-Segura et al. [157]. Interest was mostly geared towards the neutral complex $TbPc_2$ (Fig. 1d) and its derivatives, which exhibit a slower magnetization dynamics in the bulk phase as compared with the corresponding anions [158, 159]. In analogy to simpler metal phthalocyaninato systems [160], the flat structure of LnDDs facilitates addressing by STM [161]. Furthermore, a crucial property of these complexes is their remarkable thermal stability. For instance, $TbPc_2$ can be sublimated slightly below 700 K in high vacuum and is thus suitable for deposition by thermal evaporation, one of the cleanest methods in surface science. The earliest report of this kind was by Souto et al. who evaporated a 200-nm thick film of $TbPc_2$ working as a NO_x sensor [162]. In the same paper the authors described also the preparation of Langmuir–Blodgett films, a strategy later optimized using a derivative functionalized with long alkyl chains [163]. Since then, the thermal evaporation technique was extensively used to obtain both (sub)MLs and thick deposits on various surfaces ranging from diamagnetic metals [161, 164–166] and metal oxides [162, 165] to magnetic substrates [167–171].

Alternatively, solution methods were employed to anchor derivatized $TbPc_2$ complexes to specific substrates. A diluted (10^{-6} M) solution of a butoxy-functionalized derivative was drop-cast on HOPG to give regular arrays of molecules interacting with the surface via Van der Waals forces [157]. Similar structures

were observed for other LnDD systems at the liquid–solid interface [172] as well as for simpler metal phthalocyaninates deposited by drop casting [173]. However, the adsorbates of the butoxy-derivative were found to collapse within a few hours [157]. In contrast, the corresponding isopropylidenedioxy derivative forms sub-micrometric crystals epitaxially grown on HOPG [174, 175]. This Volmer-Weber-like growth mode allows to obtain bar-shaped islands approximately one-molecule thick and provides a low cost alternative to UHV to prepare ultra-thin films. Notice that, unlike the neutral complex, the anionic form does not assemble in an ordered fashion on the HOPG surface [174].

Chemisorption is of course also feasible for LnDD derivatives and a $TbPc_2$ complex functionalized with alkylthio-substituents was successfully grafted on Au (111), as confirmed by XPS and XAS [176]. More sophisticated synthetic strategies afforded a heteroleptic derivative bearing one 4-pyren-1-ylbutoxy group suitable for selective grafting on single-walled carbon nanotubes [177] and graphene [178]. In both cases the pyrenyl-terminated linker is preferentially adsorbed on the carbon-based frameworks as demonstrated by Raman microscopy; the deposition of a single layer of molecules on graphene was confirmed by the enhanced molecular polarizability caused by charge transfer effects [179]. The ability in producing these hybrid structures has led to some breakthrough results in SMM-based spintronics, already mentioned in Sect. 1.3 [44, 46–48].

As for Mn- and Fe-based SMMs, XAS and XMCD techniques have provided considerable insight into the electronic structure of surface-supported LnDDs, such as $TbPc_2$. In this case, experiments are conveniently carried out at the Tb $M_{4,5}$ edges and are facilitated by the strong dichroic response of rare earths. From the beginning, a very critical aspect was however evident when examining thermally evaporated films [164, 165]: a subML coverage results in faster spin dynamics at temperatures well below the T_B of bulk samples [165]. As a possible explanation, hybridization between the ligand molecular orbitals and the electronic states of the metal surface may have an impact on the spin dynamics of molecules in contact with the substrate. Such electronic interactions were modeled by Vitali et al. on the basis of STS measurements on a subML of $TbPc_2$ [180] and confirmed by local spin-resolved point-mode spectroscopy [171]. It has to be mentioned, however, that even the magnetic behaviour of bulk phases, which are customarily used as reference samples, is not fully understood. In recent studies, $TbPc_2$ molecules were embedded in different solid matrices and found to exhibit an erratic magnetization dynamics [181]. These findings suggest that crystal packing and intermolecular interactions may not have an innocent role in the SMM properties of bulk $TbPc_2$.

In an additional investigation, spin fluctuations at low temperature were monitored by μSR spectroscopy in bulk samples of $TbPc_2$ and in evaporated films of different thickness (1 μm and 100 nm). The slowest and the fastest fluctuation rates were found in bulk samples and in thin films, respectively (Fig. 11). Furthermore, depth-resolved studies showed an increasing fluctuation rate with decreasing distance from a gold substrate [182]. The origin of such a behaviour may lie in a depth-dependent structure of the $TbPc_2$ film, which influences the magnetic properties via intermolecular interactions.

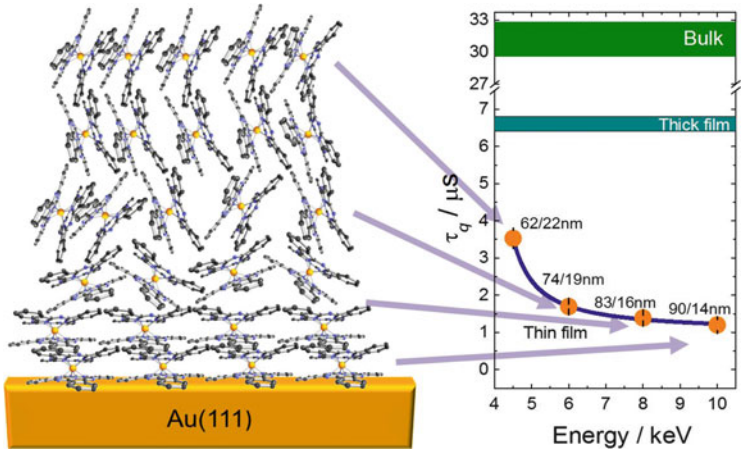

Fig. 11 Relaxation time of $TbPc_2$ in a thin (100 nm) film evaporated on gold as locally detected in a low-energy μSR experiment as a function of muon energy. The mean/rms implantation depth of muons is indicated for each data point. For comparison, the behaviours of a bulk powder sample and of a 1-μm thick film are also presented. Adapted with permission from [182]. Copyright 2012 American Chemical Society

When the substrate is magnetic, the aforementioned hybridization effects allow communication between a quantum magnet (the molecule) and a traditional magnet (the substrate), possibly affording exotic behaviours. Work in this area is in its infancy, but promising results have already been achieved. An antiferromagnetic coupling between $TbPc_2$ and a ferromagnetic Ni substrate was first detected in XMCD experiments by Lodi Rizzini et al. who also reported a dependence of the superexchange interaction on substrate doping [167]. These new behaviours on ferromagnetic surfaces were only partially confirmed by other groups and found to strongly depend on the particular substrate used [169, 170]. We notice here that the presence of [TbPc] fragments directly interacting with the substrate might explain the observed antiferromagnetic coupling, as reported for bridged 3*d*-4*f* systems [153]. In a subsequent paper, Lodi Rizzini and coworkers claimed the observation of an exchange bias at the interface between $TbPc_2$ and an antiferromagnetic layer of Mn, but not of CoO, grown on Ag(100) [168]. More systematic investigations and additional efforts in the development of higher sensitivity setups are now required to shed light on these latest findings, which define a new avenue of research.

5 SMM-Nanoparticle Hybrids

Metal NPs are ideal benchmark systems to gain insight into slow magnetic relaxation of metal-wired molecules. They have a high surface-to-volume ratio and can be easily prepared in batches of several hundred milligrams. In consequence,

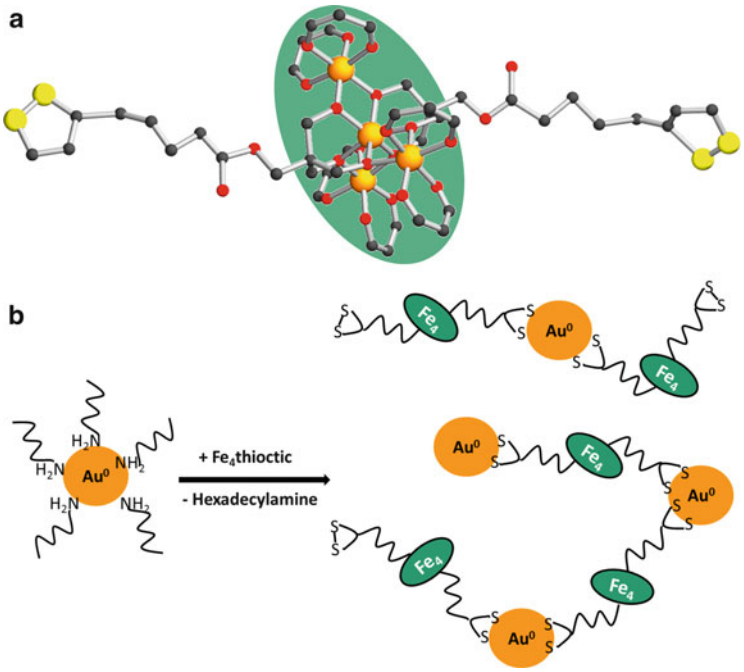

Fig. 12 Molecular structure of Fe_4thioctic derivative (**a**) and chemical route to SMM-NP hybrids (**b**). In (**a**) the colour code is the same as in Fig. 1 and hydrogen atoms as well as C atoms of ^{t}Bu groups are omitted for simplicity. Adapted with permission from [183]. Copyright 2013 WILEY-VCH Verlag GmbH & Co. KGaA, Weinheim

SMM-functionalized NPs comprise enough magnetic material for traditional magnetometry to be applicable. Starting from such an idea, 5-nm gold nanoparticles capped by hexadecylamine were reacted with a Fe_4 derivative (Fig. 12a) carrying two 1,2-dithiolane rings derived from thioctic acid, $[Fe_4(L^3)_2(dpm)_6]$ (Fe_4thioctic) [183] (see Fig. 7 for ligand structure). Owing to the excellent Au-binding properties of the 1,2-dithiolane group, the replacement of the surfactant by sulphur-terminated ligands is favoured and causes extensive aggregation of the NPs, suggesting that Fe_4 units act as bridges between NPs (Fig. 12b). The intactness of the tetrairon(III) core in this hybrid material was proved by a combination of techniques which included XAS/XMCD, EPR spectroscopy and AC susceptometry. In particular, EPR spectra indicated that the anisotropy parameters of Fe_4 complexes interacting with Au NPs remain quite close to bulk-phase values, implying similar spectroscopic barriers (14.9 vs. 15.5 K). However, the activation parameters for zero-field magnetic relaxation ($U_{eff}/k_B = 8.0(1)$ K and $\tau_0 = 1.20(6)\cdot10^{-6}$ s) are rather distinct from those found in the bulk phase ($U_{eff}/k_B = 14.0(1)$ K and $\tau_0 = 6.6(3)\cdot10^{-8}$ s). A lower anisotropy barrier and a larger preexponential factor, which combine to give faster relaxation, are typical signatures for an increased efficiency of QT effects. A similar acceleration of relaxation was detected, although only qualitatively, by

Holmberg et al. working on $[Dy_2(Hhmb)_3(NCS)_3]$. This dinuclear species contains three thiocyanate ligands available to bind Au NPs via their sulphur atoms. It was grafted on naked gold nanocrystals (8.3 nm average size) prepared by laser ablation [184], thereby merging *top-down* and *bottom-up* routes to nanostructures. The different magnetic behaviour in these hybrid materials may simply originate from strain-induced structural distortions or, more intriguingly, from the metallic nature of the substrate, in ways that deserve further studies. Worth investigating is also a possible interplay between slow magnetic relaxation and the plasmonic properties of the NPs.

6 Conclusions and Perspectives

On-surface deposition of complex molecular architectures working as SMMs had to face serious challenges arising from the chemical and magnetic fragileness of the prototypal family of Mn_{12} clusters. These blocking points have been partially overcome now by a careful selection and chemical tailoring of molecules that remain intact upon deposition: Fe_4 systems (among polynuclear SMMs) and LnDDs (among mononuclears). Such an experimental *tour de force*, aided by state-of-the-art methods for electronic and magnetic characterization (XAS, XMCD, XNLD), showed that the most distinctive properties of SMMs are compatible with the surface environment, be it an atomically flat substrate or the surface atoms of NPs. Exploiting the surface sensitivity and element specificity of XMCD, the electronic structure of surface-supported Fe_4 SMMs was probed over different energy scales, as defined by superexchange interactions, magnetic anisotropies and tunnel splittings. The static and dynamic magnetic behaviour was found to largely conform to bulk-phase properties and clear observations were made of slow spin relaxation and resonant QT of the magnetic moment in surface-wired molecules. Developing chemical complementarities with the surface by skillful molecular design enabled to gain control over adsorption geometry, with great improvement of the magnetic response of the layers.

Since XMCD experiments at subkelvin temperatures are extremely demanding, this overlap area between molecular magnetism and surface science would greatly benefit from any progress in the design of new SMMs featuring higher T_B's (say, above 4.2 K). In this direction, the recent spectacular advances based on exotic oxidation states and unusual coordination geometries (see Sect. 1.2) hold real promises, provided that sufficient chemical stability is also achieved.

A large amount of work has relied on solution methods. Though simple and extremely cost-effective, these wet-chemistry approaches have severe drawbacks. Samples prepared ex situ and involving extensive chemical manipulations are prone to contamination. For this reason, an increasing attention is now devoted to "cleaner" deposition methods where all steps (substrate cleaning, deposition and characterization) are carried out in an UHV chamber, thereby minimizing chemical operations. The particular technique to be used for deposition is however dictated

by stability issues. DPN was applied to transfer the very fragile Mn_{12} complexes from HOPG to the target Bi(111) substrate under UHV [73]. The related method of dry imprinting was used as a very soft technique to ensure deposition of intact $TbPc_2$ molecules [180]. Electrospray deposition is another soft method to bring delicate molecules like Mn_{12} derivatives on surfaces, although it still implies preparation of a solution [72, 100–102].

Vacuum sublimation methods are normally inadequate due to the thermal instability of most polynuclear species, but work well for mononuclear SMMs like LnDD complexes [164]. Notable exceptions are the dimer $[Dy_2(hfac)_6(PyNO)_2]$ [185] and two tetrairon(III) derivatives, $[Fe_4(L^4)_2(dpm)_6]$ [138] and $[Fe_4(L^4)_2(pta)_6]$ [141] (see Fig. 7 for ligand structure). These two isostructural complexes sublimate at different temperatures [(500 ± 10) K and (440 ± 5) K, respectively, at 10^{-7} mbar] as a likely consequence of fluorination of ancillary ligands in the latter compound. Evaporated films were probed by XPS, ToF-SIMs and AC susceptibility measurements, which coherently demonstrated the presence of intact molecules and the persistence of slow magnetic relaxation.

More efforts are now needed to further develop SMM systems that withstand thermal evaporation and to build up proof-of-principles devices suitable for STM addressing in UHV conditions. These thermally resistant SMMs will also be essential for the clean assembling of MLs on the reactive surfaces of ferromagnetic metals to give hybrid materials conjugating classical and quantum magnetism. In this case, the element-specificity of XMCD will be crucial to independently probe the magnetism of the molecules and of the substrate. Additional important challenges are still open and will certainly spur future research in the field. They include gaining better control over surface coverage, lateral ordering, molecular orientation and electronic coupling to the substrate via molecular design or by developing ad hoc deposition protocols.

Acknowledgments We are indebted to many colleagues that have substantially contributed to our scientific activity over the years. We especially wish to thank Dante Gatteschi, Roberta Sessoli and Andrea Caneschi (Università degli Studi di Firenze and INSTM Research Unit of Firenze, Sesto Fiorentino, Italy) as invaluable teachers and endless sources of ideas and illuminating suggestions. Many groundbreaking experiments were only possible thanks to Wolfgang Wernsdorfer (Institut Néel-CNRS, Grenoble, France), Anne-Laure Barra (LNCMI-CNRS, Grenoble, France), Philippe Sainctavit (IMPMC, Université Pierre et Marie Curie, Paris, France) and Zaher Salman (PSI, Villigen, Switzerland). This work was financially supported by European Union through an ERANET project "NanoSci-ERA: Nanoscience in European Research Area" (SMMTRANS), by European Research Council through the Advanced Grant MolNanoMas (267746) and by Italian MIUR through PRIN (2008FZK5AC) and FIRB (RBAP117RWN, RBFR10OAI0) projects.

References

1. Sessoli R, Gatteschi D, Caneschi A, Novak MA (1993) Magnetic bistability in a metal-ion cluster. Nature 365:141–143

2. Gatteschi D, Sessoli R, Villain J (2006) Molecular nanomagnets. Oxford University Press, Oxford
3. Friedman JR, Sarachik MP (1996) Macroscopic measurement of resonant magnetization tunneling in high-spin molecules. Phys Rev Lett 76:3830–3833
4. Thomas L, Lionti F, Ballou R, Gatteschi D, Sessoli R, Barbara B (1996) Macroscopic quantum tunnelling of the magnetization in a single crystal of nanomagnets. Nature 383:145–147
5. Ziemelis K (2008) Nature Milestones Spin, Milestone 22: (1996) Mesoscopic tunnelling of magnetization. http://www.nature.com/milestones/milespin/full/milespin22.html
6. Caneschi A, Gatteschi D, Sangregorio C, Sessoli R, Sorace L, Cornia A, Novak MA, Paulsen C, Wernsdorfer W (1999) The molecular approach to nanoscale magnetism. J Magn Magn Mater 200:182–201
7. Chappert C, Fert A, Nguyen Van Dau F (2007) The emergence of spin electronics in data storage. Nat Mater 6:813–823
8. Bogani L, Wernsdorfer W (2008) Molecular spintronics using single-molecule magnets. Nat Mater 7:179–186
9. Sanvito S (2011) Molecular spintronics. Chem Soc Rev 40:3336–3355
10. Katoh K, Isshiki H, Komeda T, Yamashita M (2012) Molecular spintronics based on single-molecule magnets composed of multiple-decker phthalocyaninato terbium(III) complex. Chem Asian J 7:1154–1169
11. Jiang SD, Goß K, Cervetti C, Bogani L (2012) An introduction to molecular spintronics. Sci China Chem 55:867–882
12. Coronado E, Epstein AJ (2009) J Mater Chem 19:1670–1671
13. Timco GA, Faust TB, Tuna F, Winpenny REP (2011) Linking heterometallic rings for quantum information processing and amusement. Chem Soc Rev 40:3067–3075
14. Troiani F, Affronte M (2011) Molecular spins for quantum information technologies. Chem Soc Rev 40:3119–3129
15. Aromí G, Aguilà D, Gamez P, Luis F, Roubeau O (2012) Design of magnetic coordination complexes for quantum computing. Chem Soc Rev 41:537–546
16. Wedge CJ, Timco GA, Spielberg ET, George RE, Tuna F, Rigby S, McInnes EJL, Winpenny REP, Blundell SJ, Ardavan A (2012) Chemical engineering of molecular qubits. Phys Rev Lett 108:107204
17. Bagai R, Christou G (2009) The *Drosophila* of single-molecule magnetism: $[Mn_{12}O_{12}(O_2CR)_{16}(H_2O)_4]$. Chem Soc Rev 38:1011–1026
18. Chakov NE, Lee SC, Harter AG, Kuhns PL, Reyes AP, Hill SO, Dalal NS, Wernsdorfer W, Abboud KA, Christou G (2006) The properties of the $[Mn_{12}O_{12}(O_2CR)_{16}(H_2O)_4]$ single-molecule magnets in truly axial symmetry: $[Mn_{12}O_{12}(O_2CCH_2Br)_{16}(H_2O)_4]\cdot 4CH_2Cl_2$. J Am Chem Soc 128:6975–6989
19. Milios CJ, Vinslava A, Wernsdorfer W, Moggach S, Parsons S, Perlepes SP, Christou G, Brechin EK (2007) A record anisotropy barrier for a single-molecule magnet. J Am Chem Soc 129:2754–2755
20. Rinehart JD, Fang M, Evans WJ, Long JR (2011) A N_2^{3-} radical-bridged terbium complex exhibiting magnetic hysteresis at 14K. J Am Chem Soc 133:14236–14239
21. Waldmann O (2007) A criterion for the anisotropy barrier in single-molecule magnets. Inorg Chem 46:10035–10037
22. Neese F, Pantazis DA (2011) What is not required to make a single molecule magnet. Faraday Discuss 148:229–238
23. Bencini A, Gatteschi D (1990) EPR of exchange-coupled systems. Springer, Berlin
24. Ishikawa N, Sugita M, Ishikawa T, Koshihara S, Kaizu Y (2003) Lanthanide double-decker complexes functioning as magnets at the single-molecular level. J Am Chem Soc 125:8694–8695
25. Rinehart JD, Long JR (2011) Exploiting single-ion anisotropy in the design of f-element single-molecule magnets. Chem Sci 128:2078–2085

26. Chilton NF, Collison D, McInnes EJL, Winpenny REP, Soncini A (2013) An electrostatic model for the determination of magnetic anisotropy in dysprosium complexes. Nat Commun 4:2551
27. Blagg RJ, Ungur L, Tuna F, Speak J, Comar P, Collison D, Wernsdorfer W, McInnes EJL, Chibotaru LF, Winpenny REP (2013) Magnetic relaxation pathways in lanthanide single-molecule magnets. Nat Chem 5:673–678
28. Woodruff DN, Winpenny REP, Layfield RA (2013) Lanthanide single-molecule magnets. Chem Rev 113:5110–5148
29. Habib F, Murugesu M (2013) Lessons learned from dinuclear lanthanide nano-magnets. Chem Soc Rev 42:3278–3288
30. Zhang P, Guo YN, Tang J (2013) Recent advances in dysprosium-based single molecule magnets: structural overview and synthetic strategies. Coord Chem Rev 257:1728–1763
31. Sorace L, Benelli C, Gatteschi D (2011) Lanthanides in molecular magnetism: old tools in a new field. Chem Soc Rev 40:3092–3104
32. Sessoli R, Powell AK (2009) Strategies towards single molecule magnets based on lanthanide ions. Coord Chem Rev 253:2328–2341
33. Jiang SD, Wang BW, Sun HL, Wang ZM, Gao S (2011) An organometallic single-ion magnet. J Am Chem Soc 133:4730–4733
34. Lucaccini E, Sorace L, Perfetti M, Costes JP, Sessoli R (2014) Beyond the anisotropy barrier: slow relaxation of the magnetization in both easy-axis and easy-plane Ln(trensal) complexes. Chem Commun 50:1648–1651
35. Mougel V, Chatelain L, Pécaut J, Caciuffo R, Colineau E, Griveau JC, Mazzanti M (2012) Uranium and manganese assembled in a wheel-shaped nanoscale single-molecule magnet with high spin-reversal barrier. Nat Chem 4:1011–1017
36. Baldoví JJ, Cardona-Serra S, Clemente-Juan JM, Coronado E, Gaita-Ariño A (2013) Modeling the properties of uranium-based single ion magnets. Chem Sci 4:938–946
37. Rinehart JD, Fang M, Evans WJ, Long JR (2011) Strong exchange and magnetic blocking in N_2^{3-}-radical-bridged lanthanide complexes. Nat Chem 3:538–542
38. Zadrozny JM, Xiao DJ, Atanasov M, Long GJ, Grandjean F, Neese F, Long JR (2013) Magnetic blocking in a linear iron(I) complex. Nat Chem 5:577–581
39. Martínez-Lillo J, Mastropietro TF, Lhotel E, Paulsen C, Cano J, De Munno G, Faus J, Lloret F, Julve M, Nellutla S, Krzystek J (2013) Highly anisotropic rhenium (IV) complexes: new examples of mononuclear single-molecule magnets. J Am Chem Soc 135:13737–13748
40. Vallejo J, Pascual-Álvarez A, Cano J, Castro I, Julve M, Lloret F, Krzystek J, De Munno G, Armentano D, Wernsdorfer W, Ruiz-García R, Pardo E (2013) Field-induced hysteresis and quantum tunneling of the magnetization in a mononuclear manganese(III) complex. Angew Chem Int Ed 42:14075–14079
41. Dey M, Gogoi N (2013) Geometry-mediated enhancement of single-ion anisotropy: a route to single-molecule magnets with a high blocking temperature. Angew Chem Int Ed 52:12780–12782
42. Gomez-Coca S, Cremades E, Aliaga-Alcalde N, Ruiz E (2013) Mononuclear single-molecule magnets: tailoring the magnetic anisotropy of first-row transition-metal complexes. J Am Chem Soc 135:7010–7018
43. Rostamzadeh Renani F, Kirczenow G (2013) Switching of a quantum dot spin valve by single molecule magnets. Phys Rev B 87:121403(R)
44. Urdampilleta M, Klyatskaya S, Cleuziou JP, Ruben M, Wernsdorfer W (2011) Supramolecular spin valves. Nat Mater 10:502–506
45. Hong K, Kim WY (2013) Fano-resonance-driven spin-valve effect using single-molecule magnets. Angew Chem Int Ed 52:3389–3393
46. Ganzhorn M, Klyatskaya S, Ruben M, Wernsdorfer W (2013) Carbon nanotube nanoelectromechanical systems as magnetometers for single-molecule magnets. ACS Nano 7:6225–6236

47. Ganzhorn M, Klyatskaya S, Ruben M, Wernsdorfer W (2013) Strong spin-phonon coupling between a single-molecule magnet and a carbon nanotube nanoelectromechanical system. Nat Nanotechnol 8:165–169
48. Candini A, Klyatskaya S, Ruben M, Wernsdorfer W, Affronte M (2011) Graphene spintronic devices with molecular nanomagnets. Nano Lett 11:2634–2639
49. Osorio EA, Bjørnholm T, Lehn JM, Ruben M, van der Zant HSJ (2008) Single-molecule transport in three-terminal devices. J Phys Condens Matter 20:374121
50. Jo MH, Grose JE, Baheti K, Deshmukh MM, Sokol JJ, Rumberger EM, Hendrickson DN, Long JR, Park H, Ralph DC (2006) Signatures of molecular magnetism in single-molecule transport spectroscopy. Nano Lett 6:2014–2020
51. Heersche HB, de Groot Z, Folk JA, van der Zant HSJ, Romeike C, Wegewijs MR, Zobbi L, Barreca D, Tondello E, Cornia A (2006) Electron transport through single Mn_{12} molecular magnets. Phys Rev Lett 96:206801
52. Grose JE, Tam ES, Timm C, Scheloske M, Ulgut B, Parks JJ, Abruña HD, Harneit W, Ralph DC (2008) Tunnelling spectra of individual magnetic endofullerene molecules. Nat Mater 7:884–889
53. Zyazin AS, van den Berg JWG, Osorio EA, van der Zant HSJ, Konstantinidis NP, Leijnse M, Wegewijs MR, May F, Hofstetter W, Danieli C, Cornia A (2010) Electric field controlled magnetic anisotropy in a single molecule. Nano Lett 10:3307–3311
54. Osorio EA, Moth-Poulsen K, van der Zant HSJ, Paaske J, Hedegård P, Flensberg K, Bendix J, Bjørnholm T (2010) Electrical manipulation of spin states in a single electrostatically gated transition-metal complex. Nano Lett 10:105–110
55. Haque F, Langhirt M, del Barco E, Taguchi T, Christou G (2011) Magnetic field dependent transport through a Mn_4 single-molecule magnet. J Appl Phys 109:07B112
56. Wagner S, Kisslinger F, Ballmann S, Schramm F, Chandrasekar R, Bodenstein T, Fuhr O, Secker D, Fink K, Ruben M, Weber HB (2013) Switching of a coupled spin pair in a single-molecule junction. Nat Nanotechnol 8:575–579
57. Burzurí E, Zyazin AS, Cornia A, van der Zant HSJ (2012) Direct observation of magnetic anisotropy in an individual Fe_4 single-molecule magnet. Phys Rev Lett 109:147203
58. Vincent R, Klyatskaya S, Ruben M, Wernsdorfer W, Balestro F (2012) Electronic read-out of a single nuclear spin using a molecular spin transistor. Nature 488:357–360
59. Kim GH, Kim TS (2004) Electronic transport in single-molecule magnets on metallic surfaces. Phys Rev Lett 92:137203
60. Misiorny M, Barnaś J (2007) Magnetic switching of a single molecular magnet due to spin-polarized current. Phys Rev B 75:134425
61. Misiorny M, Weymann I, Barnaś J (2010) Spin diode behavior in transport through single-molecule magnets. Europhys Lett 89:18003
62. Wang RQ, Shen R, Zhu SL, Wang B, Xing DY (2012) Inelastic transport detection of spin quantum tunneling and spin relaxation in single-molecule magnets in the absence of a magnetic field. Phys Rev B 85:165432
63. Misiorny M, Barnaś J (2013) Effects of transverse magnetic anisotropy on current-induced spin switching. Phys Rev Lett 111:046603
64. Hirjibehedin CF, Lin CY, Otte AF, Ternes M, Lutz CP, Jones BA, Heinrich AJ (2007) Large magnetic anisotropy of a single atomic spin embedded in a surface molecular network. Science 317:1199–1203
65. Meier F, Zhou L, Wiebe J, Wiesendanger R (2008) Revealing magnetic interactions from single-atom magnetization curves. Science 320:82–86
66. Loth S, von Bergmann K, Ternes M, Otte AF, Lutz CP, Heinrich AJ (2010) Controlling the state of quantum spins with electric currents. Nat Phys 6:340–344
67. Serrate D, Ferriani P, Yoshida Y, Hla SW, Menzel M, von Bergmann K, Heinze S, Kubetzka A, Wiesendanger R (2010) Imaging and manipulating the spin direction of individual atoms. Nat Nanotechnol 5:350–353

68. Loth S, Etzkorn M, Lutz CP, Eigler DM, Heinrich AJ (2010) Measurement of fast electron spin relaxation times with atomic resolution. Science 329:1628–1630
69. Khajetoorians AA, Wiebe J, Chilian B, Wiesendanger R (2011) Realizing all-spin-based logic operations atom by atom. Science 332:1062–1064
70. Loth S, Baumann S, Lutz CP, Eigler DM, Heinrich AJ (2012) Bistability in atomic-scale antiferromagnets. Science 335:196–199
71. Khajetoorians AA, Baxevanis B, Hübner C, Schlenk T, Krause S, Wehling TO, Lounis S, Lichtenstein A, Pfannkuche D, Wiebe J, Wiesendanger R (2013) Current-driven spin dynamics of artificially constructed quantum magnets. Science 339:55–59
72. Kahle S, Deng Z, Malinowski N, Tonnoir C, Forment-Aliaga A, Thontasen N, Rinke G, Le D, Turkowski V, Rahman TS, Rauschenbach S, Ternes M, Kern K (2012) The quantum magnetism of individual manganese-12-acetate molecular magnets anchored at surfaces. Nano Lett 12:518–521
73. Sun K, Park K, Xie J, Luo J, Yuan H, Xiong Z, Wang J, Xue Q (2013) Direct observation of molecular orbitals in an individual single-molecule magnet Mn_{12} on Bi(111). ACS Nano 7:6825–6830
74. Cornia A, Fabretti AC, Pacchioni M, Zobbi L, Bonacchi D, Caneschi A, Gatteschi D, Biagi R, del Pennino U, De Renzi V, Gurevich L, Van der Zant HSJ (2003) Direct observation of single-molecule magnets organized on gold surfaces. Angew Chem Int Ed 42:1645–1648
75. Clemente-León M, Coronado E, Forment-Aliaga A, Romero FM (2003) Organized assemblies of magnetic clusters. C R Chimie 6:683–688
76. Domingo N, Bellido E, Ruiz-Molina D (2012) Advances on structuring, integration and magnetic characterization of molecular nanomagnets on surfaces and devices. Chem Soc Rev 41:258–302
77. Gómez-Segura J, Veciana J, Ruiz-Molina D (2007) Advances on the nanostructuration of magnetic molecules on surfaces: the case of single-molecule magnets (SMM). Chem Commun 3699–3707
78. Voss S, Burgert M, Fonin M, Groth U, Rüdiger U (2008) A comparative study on the deposition of Mn_{12} single molecule magnets on the Au(111) surface. Dalton Trans 499–505
79. Gatteschi D, Cornia A, Mannini M, Sessoli R (2009) Organizing and addressing magnetic molecules. Inorg Chem 48:3408–3419
80. Cornia A, Mannini M, Sainctavit P, Sessoli R (2011) Chemical strategies and characterization tools for the organization of single molecule magnets on surfaces. Chem Soc Rev 40:3076–3091
81. Cavallini M, Facchini M, Albonetti C, Biscarini F (2008) Single molecule magnets: from thin films to nano-patterns. Phys Chem Chem Phys 10:784–793
82. Ulman A (1996) Formation and structure of self-assembled monolayers. Chem Rev 96:1533–1554
83. Love JC, Estroff LA, Kriebel JK, Nuzzo RG, Whitesides GM (2005) Self-assembled monolayers of thiolates on metals as a form of nanotechnology. Chem Rev 105:1103–1169
84. Vericat C, Vela ME, Benitez G, Carro P, Salvarezza RC (2010) Self-assembled monolayers of thiols and dithiols on gold: new challenges for a well-known system. Chem Soc Rev 39:1805–1834
85. Voss S, Fonin M, Burova L, Burgert M, Dedkov YS, Preobrajenski AB, Goering E, Groth U, Kaul AR, Ruediger U (2009) Investigation of the stability of Mn_{12} single molecule magnets. Appl Phys A 94:491–495
86. Aromí G, Aubin SMJ, Bolcar MA, Christou G, Eppley HJ, Folting K, Hendrickson DN, Huffman JC, Squire RC, Tsai HL, Wang S, Wemple MW (1998) Manganese carboxylate clusters: from structural aesthetics to single-molecule magnets. Polyhedron 17:3005–3020
87. Fleury B, Huc V, Catala L, Jegou P, Baraton L, David C, Palacin S, Mallah T (2009) Orientation of Mn_{12} molecular nanomagnets in self-assembled monolayers. CrystEngComm 11:2192–2197

88. Fleury B, Catala L, Huc V, David C, Zhong WZ, Jegou P, Baraton L, Palacin S, Albouy PA, Mallah T (2005) A new approach to grafting a monolayer of oriented Mn_{12} nanomagnets on silicon. Chem Commun 2020–2022
89. Voss S, Fonin M, Rüdiger U, Burgert M, Groth U, Dedkov YS (2007) Electronic structure of Mn_{12} derivatives on the clean and functionalized Au surface. Phys Rev B 75:045102
90. Burgert M, Voss S, Herr S, Fonin M, Groth U, Rüdiger U (2007) Single-molecule magnets: a new approach to investigate the electronic structure of Mn_{12} molecules by scanning tunneling spectroscopy. J Am Chem Soc 129:14362–14366
91. Voss S, Fonin M, Rüdiger U, Burgert M, Groth U (2007) Experimental observation of a band gap in individual Mn_{12} molecules on Au(111). Appl Phys Lett 90:133104
92. Voss S, Herr S, Fonin M, Rüdiger U, Burgert M, Groth U (2008) Identification of linker molecules suited for deposition and study of Mn_{12} single molecule magnets on Au surfaces. J Appl Phys 103:07B901
93. Voss S, Zander O, Fonin M, Rüdiger U, Burgert M, Groth U (2008) Electronic transport properties and orientation of individual Mn_{12} single-molecule magnets. Phys Rev B 78:155403
94. Meng L, Lin BF, Yang JY, Sun Y, Dou RF, Ma LX, Xiong CM, Nie JC (2012) Detection of the intrinsic two energy gaps in individual Mn_{12} single molecule magnets. Chem Phys Lett 542:81–84
95. Petukhov K, Alam MS, Rupp H, Strömsdörfer S, Müller P, Scheurer A, Saalfrank RW, Kortus J, Postnikov A, Ruben M, Thompson LK, Lehn JM (2009) STM spectroscopy of magnetic molecules. Coord Chem Rev 253:2387–2398
96. Mannini M, Sainctavit P, Sessoli R, Cartier dit Moulin C, Pineider F, Arrio MA, Cornia A, Gatteschi D (2008) XAS and XMCD investigation of Mn_{12} monolayers on gold. Chem Eur J 14:7530–7535
97. Helmstedt A, Sacher MD, Gryzia A, Harder A, Brechling A, Müller N, Heinzmann U, Hoeke V, Krickemeyer E, Glaser T, Bouvron S, Fonin M (2012) Exposure of $[Mn^{III}_6Cr^{III}]^{3+}$ single-molecule magnets to soft X-rays: the effect of the counterions on radiation stability. J Electron Spectros Relat Phenomena 184:583–588
98. Kuepper K, Derks C, Taubitz C, Prinz M, Joly L, Kappler JP, Postnikov A, Yang W, Kuznetsova TV, Wiedwald U, Ziemann P, Neumann M (2013) Electronic structure and soft-X-ray-induced photoreduction studies of iron-based magnetic polyoxometalates of type $\{(M)M_5\}_{12}Fe^{III}_{30}$ ($M=Mo^{VI}$, W^{VI}). Dalton Trans 42:7924–7935
99. Moro F, Biagi R, Corradini V, Evangelisti M, Gambardella A, De Renzi V, del Pennino U, Coronado E, Forment-Aliaga A, Romero FM (2012) Electronic and magnetic properties of Mn_{12} molecular magnets on sulfonate and carboxylic acid prefunctionalized gold surfaces. J Phys Chem C 116:14936–14942
100. Saywell A, Magnano G, Satterley CJ, Perdigão LMA, Britton AJ, Taleb N, del Carmen G-LM, Champness NR, O'Shea JN, Beton PH (2010) Self-assembled aggregates formed by single-molecule magnets on a gold surface. Nat Commun 1:75
101. Saywell A, Britton AJ, Taleb N, del Carmen Giménez-López M, Champness NR, Beton PH, O'Shea JN (2011) Single molecule magnets on a gold surface: in situ electrospray deposition, X-ray absorption and photoemission. Nanotechnology 22:075704
102. Handrup K, Richards VJ, Weston M, Champness NR, O'Shea JN (2013) Single molecule magnets with protective ligand shells on gold and titanium dioxide surfaces: in situ electrospray deposition and X-ray absorption spectroscopy. J Chem Phys 139:154708
103. Grumbach N, Barla A, Joly L, Donnio B, Rogez G, Terazzi E, Kappler JP, Gallani JL (2010) Loss of single-molecule-magnet behavior of a Mn_{12}-based compound assembled in a monolayer. Eur Phys J B 73:103–108
104. Naitabdi A, Bucher JP, Gerbier P, Rabu P, Drillon M (2005) Self-assembly and magnetism of Mn_{12} nanomagnets on native and functionalized gold surfaces. Adv Mater 17:1612–1616
105. Stöhr J (1999) Exploring the microscopic origin of magnetic anisotropies with X-ray magnetic circular dichroism (XMCD) spectroscopy. J Magn Magn Mater 200:470–497

106. Thole BT, Carra P, Sette F, van der Laan G (1992) X-Ray circular dichroism as a probe of orbital magnetization. Phys Rev Lett 68:1943–1946
107. Wende H (2004) Recent advances in X-ray absorption spectroscopy. Rep Prog Phys 67:2105–2181
108. Mannini M, Pineider F, Sainctavit P, Joly L, Fraile-Rodríguez A, Arrio MA, Cartier dit Moulin C, Wernsdorfer W, Cornia A, Gatteschi D, Sessoli R (2009) X-ray magnetic circular dichroism picks out single-molecule magnets suitable for nanodevices. Adv Mater 21:167–171
109. Donnio B, Rivière E, Terazzi E, Voirin E, Aronica C, Chastanet G, Luneau D, Rogez G, Scheurer F, Joly L, Kappler JP, Gallani JL (2010) Magneto-optical interactions in single-molecule magnets: low-temperature photon-induced demagnetization. Solid State Sci 12:1307–1313
110. Gambardella P, Dallmeyer A, Maiti K, Malagoli MC, Eberhardt W, Kern K, Carbone C (2002) Ferromagnetism in one-dimensional monatomic metal chains. Nature 416:301–304
111. Bellido E, González-Monje P, Repollés A, Jenkins M, Sesé J, Drung D, Schurig T, Awaga K, Luis F, Ruiz-Molina D (2013) Mn_{12} single molecule magnets deposited on μ-SQUID sensors: the role of interphases and structural modifications. Nanoscale 5:12565–12573
112. Carbonera C, Luis F, Campo J, Sánchez-Marcos J, Camón A, Chaboy J (2010) Effect of crystalline disorder on quantum tunneling in the single-molecule magnet Mn_{12} benzoate. Phys Rev B 81:014427
113. Otero G, Evangelio E, Rogero C, Vázquez L, Gómez-Segura J, Martín-Gago JA, Ruiz-Molina D (2009) Morphological investigation of Mn_{12} single-molecule magnets adsorbed on Au(111). Langmuir 25:10107–10115
114. Aubin SMJ, Sun Z, Eppley HJ, Rumberger EM, Guzei IA, Folting K, Gantzel PK, Rheingold AL, Christou G, Hendrickson DN (2001) Single-molecule magnets: Jahn-Teller isomerism and the origin of two magnetization relaxation processes in Mn_{12} complexes. Inorg Chem 40:2127–2146
115. Domingo N, Luis F, Nakano M, Muntó M, Gómez J, Chaboy J, Ventosa N, Campo J, Veciana J, Ruiz-Molina D (2009) Particle-size dependence of magnetization relaxation in Mn_{12} crystals. Phys Rev B 79:214404
116. Artus P, Boskovic C, Yoo J, Streib WE, Brunel LC, Hendrickson DN, Christou G (2001) Single-molecule magnets: site-specific ligand abstraction from $[Mn_{12}O_{12}(O_2CR)_{16}(H_2O)_4]$ and the preparation and properties of $[Mn_{12}O_{12}(NO_3)_4(O_2CCH_2Bu^t)_{12}(H_2O)_4]$. Inorg Chem 40:4199–4210
117. Soler M, Artus P, Folting K, Huffman JC, Hendrickson DN, Christou G (2001) Single-molecule magnets: preparation and properties of mixed-carboxylate complexes $[Mn_{12}O_{12}(O_2CR)_8(O_2CR')_8(H_2O)_4]$. Inorg Chem 40:4902–4912
118. Fonin M, Voss S, Herr S, de Loubens G, Kent AD, Burgert M, Groth U, Rüdiger U (2009) Influence of the ligand shell on the surface orientation of Mn_{12} single molecule magnets. Polyhedron 28:1977–1981
119. Pacchioni M, Cornia A, Fabretti AC, Zobbi L, Bonacchi D, Caneschi A, Chastanet G, Gatteschi D, Sessoli R (2004) Site-specific ligation of anthracene-1,8-dicarboxylates to an Mn_{12} core: a route to the controlled functionalisation of single-molecule magnets. Chem Commun 2604–2605
120. Inglis R, Milios CJ, Jones LF, Piligkos S, Brechin EK (2012) Twisted molecular magnets. Chem Commun 48:181–190
121. Moro F, Corradini V, Evangelisti M, De Renzi V, Biagi R, del Pennino U, Milios CJ, Jones LF, Brechin EK (2008) Grafting derivatives of Mn_6 single-molecule magnets with high anisotropy energy barrier on Au(111) surface. J Phys Chem B 112:9729–9735
122. del Pennino U, Corradini V, Biagi R, De Renzi V, Moro F, Boukhvalov DW, Panaccione G, Hochstrasser M, Carbone C, Milios CJ, Brechin EK (2008) Electronic structure of a Mn_6 (S=4) single molecule magnet grafted on Au(111). Phys Rev B 77:085419

123. Moro F, Corradini V, Evangelisti M, Biagi R, De Renzi V, del Pennino U, Cezar JC, Inglis R, Milios CJ, Brechin EK (2010) Addressing the magnetic properties of sub-monolayers of single-molecule magnets by X-ray magnetic circular dichroism. Nanoscale 2:2698–2703
124. Wende H (2009) How a nightmare turns into a vision. Nat Mater 8:165–166
125. Saalfrank RW, Bernt I, Chowdhry MM, Hampel F, Vaughan GBM (2001) Ligand-to-metal ratio controlled assembly of tetra- and hexanuclear clusters towards single-molecule magnets. Chem Eur J 7:2765–2769
126. Saalfrank RW, Scheurer A, Bernt I, Heinemann FW, Postnikov AV, Schünemann V, Trautwein AX, Alam MS, Rupp H, Müller P (2006) The $\{Fe^{III}[Fe^{III}(L^1)_2]_3\}$ star-type single-molecule magnet. Dalton Trans 2865–2874
127. Zhu YY, Guo X, Cui C, Wang BW, Wang ZM, Gao S (2011) An enantiopure Fe^{III}_4 single-molecule magnet. Chem Commun 47:8049–8051
128. Singh R, Banerjee A, Colacio E, Rajak KK (2009) Enantiopure tetranuclear iron(III) complexes using chiral reduced Schiff base ligands: synthesis, structure, spectroscopy, magnetic properties, and DFT studies. Inorg Chem 48:4753–4762
129. Barra AL, Caneschi A, Cornia A, Fabrizi de Biani F, Gatteschi D, Sangregorio C, Sessoli R, Sorace L (1999) Single-molecule magnet behavior of a tetranuclear iron(III) complex. The origin of slow magnetic relaxation in iron(III) clusters. J Am Chem Soc 121:5302–5310
130. Cornia A, Fabretti AC, Garrisi P, Mortalò C, Bonacchi D, Gatteschi D, Sessoli R, Sorace L, Wernsdorfer W, Barra AL (2004) Energy-barrier enhancement by ligand substitution in tetrairon(III) single-molecule magnets. Angew Chem Int Ed 43:1136–1139
131. Schlegel C, Burzurí E, Luis F, Moro F, Manoli M, Brechin EK, Murrie M, van Slageren J (2010) Magnetic properties of two new Fe_4 single-molecule magnets in the solid state and in frozen solution. Chem Eur J 16:10178–10185
132. Accorsi S, Barra AL, Caneschi A, Chastanet G, Cornia A, Fabretti AC, Gatteschi D, Mortalò C, Olivieri E, Parenti F, Rosa P, Sessoli R, Sorace L, Wernsdorfer W, Zobbi L (2006) Tuning anisotropy barriers in a family of tetrairon(III) single-molecule magnets with an S=5 ground state. J Am Chem Soc 128:4742–4755
133. Danieli C, Cornia A, Cecchelli C, Sessoli R, Barra AL, Ponterini G, Zanfrognini B (2009) A novel class of tetrairon(III) single-molecule magnets with graphene-binding groups. Polyhedron 28:2029–2035
134. Vergnani L, Barra AL, Neugebauer P, Rodriguez-Douton MJ, Sessoli R, Sorace L, Wernsdorfer W, Cornia A (2012) Magnetic bistability of isolated giant-spin centers in a diamagnetic crystalline matrix. Chem Eur J 18:3390–3398
135. Mannini M, Pineider F, Sainctavit P, Danieli C, Otero E, Sciancalepore C, Talarico AM, Arrio MA, Cornia A, Gatteschi D, Sessoli R (2009) Magnetic memory of a single-molecule quantum magnet wired to a gold surface. Nat Mater 8:194–197
136. Barra AL, Bianchi F, Caneschi A, Cornia A, Gatteschi D, Gorini L, Gregoli L, Maffini M, Parenti F, Sessoli R, Sorace L, Talarico AM (2007) New single-molecule magnets by site-specific substitution: incorporation of "alligator clips" into Fe_4 complexes. Eur J Inorg Chem 4145–4152
137. Bogani L, Danieli C, Biavardi E, Bendiab N, Barra AL, Dalcanale E, Wernsdorfer W, Cornia A (2009) Single-molecule-magnet carbon-nanotube hybrids. Angew Chem Int Ed 48:746–750
138. Margheriti L, Mannini M, Sorace L, Gorini L, Gatteschi D, Caneschi A, Chiappe D, Moroni R, Buatier de Mongeot F, Cornia A, Piras FM, Magnani A, Sessoli R (2009) Thermal deposition of intact tetrairon(III) single-molecule magnets in high-vacuum conditions. Small 5:1460–1466
139. Gregoli L, Danieli C, Barra AL, Neugebauer P, Pellegrino G, Poneti G, Sessoli R, Cornia A (2009) Magnetostructural correlations in tetrairon(III) single-molecule magnets. Chem Eur J 15:6456–6467
140. Prasad TK, Poneti G, Sorace L, Rodriguez-Douton MJ, Barra AL, Neugebauer P, Costantino L, Sessoli R, Cornia A (2012) Magnetic and optical bistability in tetrairon(III) single molecule magnets functionalized with azobenzene groups. Dalton Trans 41:8368–8378

141. Rigamonti L, Piccioli M, Malavolti L, Poggini L, Mannini M, Totti F, Cortigiani B, Magnani A, Sessoli R, Cornia A (2013) Enhanced vapor-phase processing in fluorinated Fe_4 single-molecule magnets. Inorg Chem 52:5897–5905
142. Tancini E, Rodriguez-Douton MJ, Sorace L, Barra AL, Sessoli R, Cornia A (2010) Slow magnetic relaxation from hard-axis metal ions in tetranuclear single-molecule magnets. Chem Eur J 16:10482–10493
143. Mannini M, Tancini E, Sorace L, Sainctavit P, Arrio MA, Qian Y, Otero E, Chiappe D, Margheriti L, Cezar JC, Sessoli R, Cornia A (2011) Spin structure of surface-supported single-molecule magnets from isomorphous replacement and X-ray magnetic circular dichroism. Inorg Chem 50:2911–2917
144. Totaro P, Westrup KCM, Boulon ME, Nunes GG, Back DF, Barison A, Ciattini S, Mannini M, Sorace L, Soares JF, Cornia A, Sessoli R (2013) A new approach to the synthesis of heteronuclear propeller-like single molecule magnets. Dalton Trans 42:4416–4426
145. Létard I, Sainctavit P, Cartier dit Moulin C, Kappler JP, Ghigna P, Gatteschi D, Doddi B (2007) Remnant magnetization of Fe8 high-spin molecules: X-ray magnetic circular dichroism at 300 mK. J Appl Phys 101:113920
146. Tancini E, Mannini M, Sainctavit P, Otero E, Sessoli R, Cornia A (2013) On-surface magnetometry: the evaluation of superexchange coupling constants in surface-wired single-molecule magnets. Chem Eur J 19:16902–16905
147. Arrio MA, Scuiller A, Sainctavit P, Cartier dit Moulin C, Mallah T, Verdaguer M (1999) Soft X-ray magnetic circular dichroism in paramagnetic systems: element-specific magnetization of two heptanuclear $Cr^{III}M^{II}_6$ high-spin molecules. J Am Chem Soc 121:6414–6420
148. Lorusso G, Corradini V, Ghirri A, Biagi R, del Pennino U, Siloi I, Troiani F, Timco G, Winpenny REP, Affronte M (2012) Magnetic and entanglement properties of molecular Cr_2nCu_2 heterometallic spin rings. Phys Rev B 86:184424
149. Ghigna P, Campana A, Lascialfari A, Caneschi A, Gatteschi D, Tagliaferri A, Borgatti F (2001) X-ray magnetic-circular-dichroism spectra on the superparamagnetic transition-metal ion clusters Mn_{12} and Fe_8. Phys Rev B 64:132413
150. Corradini V, Ghirri A, Candini A, Biagi R, del Pennino U, Dotti G, Otero E, Choueikani F, Blagg RJ, McInnes EJL, Affronte M (2013) Magnetic cooling at a single molecule level: a spectroscopic investigation of isolated molecules on a surface. Adv Mater 25:2816–2820
151. Corradini V, Ghirri A, Garlatti E, Biagi R, De Renzi V, del Pennino U, Bellini V, Carretta S, Santini P, Timco G, Winpenny REP, Affronte M (2012) Magnetic anisotropy of Cr_7Ni spin clusters on surfaces. Adv Funct Mater 22:3706–3713
152. Corradini V, Moro F, Biagi R, De Renzi V, del Pennino U, Bellini V, Carretta S, Santini P, Milway VA, Timco G, Winpenny REP, Affronte M (2009) Successful grafting of isolated molecular Cr_7Ni rings on Au(111) surface. Phys Rev B 79:144419
153. Dreiser J, Pedersen KS, Piamonteze C, Rusponi S, Salman Z, Ali ME, Schau-Magnussen M, Thuesen CA, Piligkos S, Weihe H, Mutka H, Waldmann O, Oppeneer P, Bendix J, Nolting F, Brune H (2012) Direct observation of a ferri-to-ferromagnetic transition in a fluoride-bridged 3d–4f molecular cluster. Chem Sci 3:1024–1032
154. Mannini M, Pineider F, Danieli C, Totti F, Sorace L, Sainctavit P, Arrio MA, Otero E, Joly L, Cezar JC, Cornia A, Sessoli R (2010) Quantum tunnelling of the magnetization in a monolayer of oriented single-molecule magnets. Nature 468:417–421
155. Pineider F, Mannini M, Danieli C, Armelao L, Piras FM, Magnani A, Cornia A, Sessoli R (2010) Deposition of intact tetrairon(III) single molecule magnet monolayers on gold: an STM, XPS, and ToF-SIMS investigation. J Mater Chem 20:187–194
156. Ishikawa N (2007) Single molecule magnet with single lanthanide ion. Polyhedron 26:2147–2153
157. Gómez-Segura J, Díez-Pérez I, Ishikawa N, Nakano M, Veciana J, Ruiz-Molina D (2006) 2-D Self-assembly of the bis(phthalocyaninato)terbium(III) single-molecule magnet studied by scanning tunnelling microscopy. Chem Commun 2866–2868

158. Ishikawa N, Sugita M, Tanaka N, Ishikawa T, Koshihara S, Kaizu Y (2004) Upward temperature shift of the intrinsic phase lag of the magnetization of bis(phthalocyaninato) terbium by ligand oxidation creating an S=1/2 spin. Inorg Chem 43:5498–5500
159. Ganivet CR, Ballesteros B, de la Torre G, Clemente-Juan JM, Coronado E, Torres T (2013) Influence of peripheral substitution on the magnetic behavior of single-ion magnets based on homo- and heteroleptic Tb^{III} bis(phthalocyaninate). Chem Eur J 19:1457–1465
160. Gimzewski JK, Stoll E, Schlittler RR (1987) Scanning tunneling microscopy of individual molecules of copper phthalocyanine adsorbed on polycrystalline silver surfaces. Surf Sci 181:267–277
161. Katoh K, Yoshida Y, Yamashita M, Miyasaka H, Breedlove BK, Kajiwara T, Takaishi S, Ishikawa N, Isshiki H, Zhang YF, Komeda T, Yamagishi M, Takeya J (2009) Direct observation of lanthanide(III)-phthalocyanine molecules on Au(111) by using scanning tunneling microscopy and scanning tunneling spectroscopy and thin-film Field-Effect Transistor properties of Tb(III)- and Dy(III)-phthalocyanine molecules. J Am Chem Soc 131:9967–9976
162. Souto J, de Saja JA, Aroca R, Rodriguez ML (1993) Langmuir-Blodgett and vacuum sublimed films of terbium bisphthalocyanine. Synth Met 54:229–235
163. Wang X, Chen Y, Liu H, Jiang J (2006) Spectroscopic and structural characteristics of Langmuir-Blodgett films of bis[2,3,9,10,16,17,24,25-octakis(octyloxy)phthalocyaninato] rare earth complexes. Thin Solid Films 496:619–625
164. Stepanow S, Honolka J, Gambardella P, Vitali L, Abdurakhmanova N, Tseng TC, Rauschenbach S, Tait SL, Sessi V, Klyatskaya S, Ruben M, Kern K (2010) Spin and orbital magnetic moment anisotropies of monodispersed bis(phthalocyaninato)terbium on a copper surface. J Am Chem Soc 132:11900–11901
165. Margheriti L, Chiappe D, Mannini M, Car PE, Sainctavit P, Arrio MA, Buatier de Mongeot F, Cezar JC, Piras FM, Magnani A, Otero E, Caneschi A, Sessoli R (2010) X-ray detected magnetic hysteresis of thermally evaporated terbium double-decker oriented films. Adv Mater 22:5488–5493
166. Fu YS, Schwöbel J, Hla SW, Dilullo A, Hoffmann G, Klyatskaya S, Ruben M, Wiesendanger R (2012) Reversible chiral switching of bis(phthalocyaninato) terbium(III) on a metal surface. Nano Lett 12:3931–3935
167. Lodi Rizzini A, Krull C, Balashov T, Kavich JJ, Mugarza A, Miedema PS, Thakur PK, Sessi V, Klyatskaya S, Ruben M, Stepanow S, Gambardella P (2011) Coupling single molecule magnets to ferromagnetic substrates. Phys Rev Lett 107:177205
168. Lodi Rizzini A, Krull C, Balashov T, Mugarza A, Nistor C, Yakhou F, Sessi V, Klyatskaya S, Ruben M, Stepanow S, Gambardella P (2012) Exchange biasing single molecule magnets: coupling of $TbPc_2$ to antiferromagnetic layers. Nano Lett 12:5703–5707
169. Malavolti L, Poggini L, Margheriti L, Chiappe D, Graziosi P, Cortigiani B, Lanzilotto V, Buatier de Mongeot F, Ohresser P, Otero E, Choueikani F, Sainctavit P, Bergenti I, Dediu VA, Mannini M, Sessoli R (2013) Magnetism of $TbPc_2$ SMMs on ferromagnetic electrodes used in organic spintronics. Chem Commun 49:11506–11508
170. Klar D, Klyatskaya S, Candini A, Krumme B, Kummer K, Ohresser P, Corradini V, De Renzi V, Biagi R, Joly L, Kappler JP, del Pennino U, Affronte M, Wende H, Ruben M (2013) Antiferromagnetic coupling of $TbPc_2$ molecules to ultrathin Ni and Co films. Beilstein J Nanotechnol 4:320–324
171. Schwöbel J, Fu Y, Brede J, Dilullo A, Hoffmann G, Klyatskaya S, Ruben M, Wiesendanger R (2012) Real-space observation of spin-split molecular orbitals of adsorbed single-molecule magnets. Nat Commun 3:953
172. Takami T, Arnold DP, Fuchs AV, Will GD, Goh R, Waclawik ER, Bell JM, Weiss PS, Sugiura K, Liu W, Jiang J (2006) Two-dimensional crystal growth and stacking of bis (phthalocyaninato) rare earth sandwich complexes at the 1-phenyloctane/graphite interface. J. Phys Chem B 110:1661–1664

173. Qiu X, Wang C, Yin S, Zeng Q, Xu B, Bai C (2000) Self-assembly and immobilization of metallophthalocyanines by alkyl substituents observed with scanning tunneling microscopy. J Phys Chem B 104:3570–3574
174. Biagi R, Fernandez-Rodriguez J, Gonidec M, Mirone A, Corradini V, Moro F, De Renzi V, del Pennino U, Cezar JC, Amabilino DB, Veciana J (2010) X-ray absorption and magnetic circular dichroism investigation of bis(phthalocyaninato)terbium single-molecule magnets deposited on graphite. Phys Rev B 82:224406
175. Gonidec M, Biagi R, Corradini V, Moro F, De Renzi V, del Pennino U, Summa D, Muccioli L, Zannoni C, Amabilino DB, Veciana J (2011) Surface supramolecular organization of a terbium(III) double-decker complex on graphite and its single molecule magnet behavior. J Am Chem Soc 133:6603–6612
176. Glebe U, Weidner T, Baio JE, Schach D, Bruhn C, Buchholz A, Plass W, Walleck S, Glaser T, Siemeling U (2012) Self-assembled monolayers of single-molecule magnets [Tb $\{Pc'(SR)_8\}_2$] on gold. Chem Plus Chem 77:889–897
177. Kyatskaya S, Galán Mascarós JR, Bogani L, Hennrich F, Kappes M, Wernsdorfer W, Ruben M (2009) Anchoring of rare-earth-based single-molecule magnets on single-walled carbon nanotubes. J Am Chem Soc 131:15143–15151
178. Lopes M, Candini A, Urdampilleta M, Reserbat-Plantey A, Bellini V, Klyatskaya S, Marty L, Ruben M, Affronte M, Wernsdorfer W, Bendiab N (2010) Surface-enhanced Raman signal for terbium single-molecule magnets grafted on graphene. ACS Nano 4:7531–7537
179. Ling X, Xie L, Fang Y, Xu H, Zhang H, Kong J, Dresselhaus MS, Zhang J, Liu Z (2010) Can graphene be used as a substrate for Raman enhancement? Nano Lett 10:553–561
180. Vitali L, Fabris S, Mosca Conte A, Brink S, Ruben M, Baroni S, Kern K (2008) Electronic structure of surface-supported bis(phthalocyaninato) terbium(III) single molecular magnets. Nano Lett 8:3364–3368
181. Malavolti L, Mannini M, Car PE, Campo G, Pineider F, Sessoli R (2013) Erratic magnetic hysteresis of $TbPc_2$ molecular nanomagnets. J Mater Chem C 1:2935–2942
182. Hofmann A, Salman Z, Mannini M, Amato A, Malavolti L, Morenzoni E, Prokscha T, Sessoli R, Suter A (2012) Depth-dependent spin dynamics in thin films of $TbPc_2$ nanomagnets explored by low-energy implanted muons. ACS Nano 6:8390–8396
183. Perfetti M, Pineider F, Poggini L, Otero E, Mannini M, Sorace L, Sangregorio C, Cornia A, Sessoli R (2014) Grafting single molecule magnets on gold nanoparticles. Small 10:323–329
184. Holmberg RJ, Hutchings AJ, Habib F, Korobkov I, Scaiano JC, Murugesu M (2013) Hybrid nanomaterials: anchoring magnetic molecules on naked gold nanocrystals. Inorg Chem 52:14411–14418
185. Yi X, Bernot K, Pointillart F, Poneti G, Calvez G, Daiguebonne C, Guillou O, Sessoli R (2012) A luminescent and sublimable Dy^{III}-based single-molecule magnet. Chem Eur J 18:11379–11387

Struct Bond (2015) 164: 331–382
DOI: 10.1007/430_2014_170

Published online: 22 November 2014

Experiments on Molecular Magnets for Molecular Spintronics

Lapo Bogani

Abstract We present a review of the experimental state of the art of molecular spintronics, as obtained with molecular magnetic materials. After a brief introduction about the fundamental concepts in the field, we consider experiments performed with all the approaches attempted up to date. We eventually provide a brief discussion of the future directions and the considerable challenges that remain unexplored in the field and of the possible evolutions of this quickly developing area of research.

Keywords Carbon nanomaterials • Molecular cluster compounds • Molecular magnets • Molecular spintronics • Nanospintronics

Contents

L. Bogani (✉)
Physikalisches Institut, Universität Stuttgart, Stuttgart, Germany
e-mail: lapo.bogani@pi1.physik.uni-stuttgart.de

1 Introduction

In other chapters of this volume, the fundaments for the synthesis and understanding of molecular magnetic materials have been laid out. In this chapter we will consider one emerging area of investigation of these materials, where the creation of devices and the study of novel fundamental effects are strongly intertwined: molecular spintronics.

The field of molecular spintronics arises from the combination of two traditionally distinct areas: molecular magnetism and molecular electronics. Spintronics, which studies how the magnetisation state of a device can influence the current that is passed through it, has gained enormous attention since the discovery of giant effects in very thin structures [1, 2]. Spintronic devices now routinely run in the logical and memory units of computers. As many reviews and books on the subject are readily available ([3]; see, e.g. the dedicated issue on [4], [5]), here we will only sketch out the main concepts of the area, necessary for the understanding of the basics of molecular spintronics. Since a few years, much of the research in spintronics has aimed at reducing the size of the components to nanoscale dimensions [5, 6]. Even though the fabrication and characterisation of such systems has mainly been carried out via physical methods, the opportunity of using elements with the size of single molecules will likely represent the final attainable level of miniaturisation. Thus, there is a hugely fecund research field that is just appearing on the horizon, where the chemical design of the system will eventually determine the functionality of the devices.

On the other hand, when reaching such extremely small sizes, the electronic behaviour of the devices is strikingly different than that of bulk circuits, and one must understand the effect of transport through molecules themselves. This is the domain of molecular electronics [7, 8], which studies what happens when one part of an electric circuit is a single-molecule element. Whatever the approach used to create the molecular electronic devices, the system has to be interfaced with standard electronics, and the resulting device will contain bulk leads, which can act as reservoirs of electrons, while the molecule will act as a quantised system, with discrete energy levels. Again, several excellent reviews and books on the field already exist [7–10], showing the many interesting physical phenomena that have been found to determine the behaviour of such systems. Here we will just explain the basic concepts of this area, in a way that should be accessible to chemists and

material scientists alike, so as to prepare the basis for the following discussion of molecular spintronic effects. It should be understood, anyway, that the physics of these devices constitutes a very active field of research in itself, which will offer a very fertile ground when mixed with spintronics.

The additional key element of molecular spintronic devices is constituted by the presence of magnetic molecules, which saw a very fast development following the rise of molecular magnetism (see, e.g. the dedicated focus on [11]), in the last three decades. In this sense, the particular appeal of molecular magnetism lies in the fact that it allows creating magnetic materials whose properties can be tuned with the means of classical synthetic chemistry, for example, changing the ligands surrounding a metal centre or their disposition, or by tuning the molecular bridges that link two magnetic centres. As shown in the other chapters of this volume, chemists have developed a huge library of ligands and compounds to choose from to design the magnetic properties of these systems. They have also been able to relate many magnetic properties, such as the exchange interaction or the magnetic anisotropy, to structural features and thus managed to rationalise the behaviour of entire classes of compounds. The second important feature is the possibility, as displayed by some molecules called single-molecule magnets (see, e.g. the dedicated focus on [11]), of retaining the same magnetisation state for long times at sufficiently low T, as a consequence of the opening of a hysteresis cycle of dynamical origin. This opens the possibility of storing information at the single-molecule level and also allows studying dynamical magnetic processes and quantum effects, such as quantum tunnelling and Berry phase interference. These characteristics also indicate the possible use of molecular clusters as computational units for quantum logics and solid-state memory systems (see, e.g. the dedicated focus on [11]). All these possibilities are clearly extremely appealing, if they can be integrated into an electronic device. In the following, we will show the progress made in this direction, calibrating the review so as to allow the interested reader into the field, even if his background is in synthetic chemistry.

2 Spin Electronics: An Essential Introduction

Spin electronics starts with the idea that moving electrons do not only transport charges but also carry a spin and thus a magnetic part. While it had been known since decades that a current can be altered by the magnetic state of the electronic elements, it was only at the end of the 1980s that it became clear that the effect could become enormous, when using nanostructured devices [1, 2]. This discovery led to the award of Nobel Prize to Grünberg and Fert, only 12 years after the discovery, and to applicative possibilities in an even shorter timescale. While the initial, breakthrough discovery was made on thin layers of ferromagnets, Fe, and antiferromagnets, Cr, the field is naturally moving towards nanoscale elements. The most basic and general scheme encountered in spintronics is that of a spin valve (SV) ([3]; see, e.g. the dedicated issue on [4]), i.e. a device composed of two

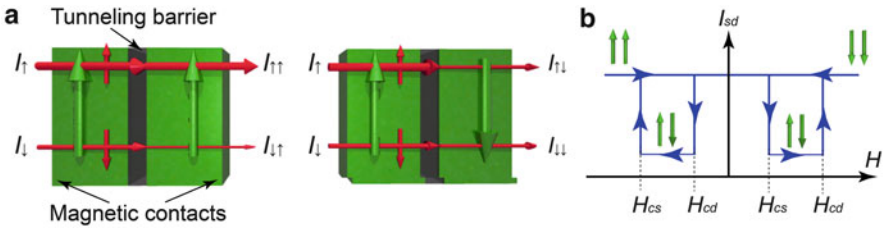

Fig. 1 A schematic diagram of the core of a spin valve. (**a**) The elements that make up a spin valve (in *green arrow* representing the magnetisation) and their effects on the spin-polarised currents (in *red*, *vertical arrows* representing the spin polarisation of the current). The parallel spin alignment (*left*) presents a higher analyser resistance towards the minority spin-down current and lower resistance for the more relevant spin-up current. The antiparallel disposition leads to: (**b**) resulting source–drain current vs. magnetic field diagram for an SV. The parallel spin alignment, in this case, leads to higher currents

magnetic elements through which an electronic current can flow. The first element is considered as a polariser, as it allows to select a majority of electrons flowing with a certain spin: in standard currents half of the spins have up spin and half have a down spin; the polariser unbalances this ratio between up and down spins towards one spin orientation, so that the current flowing has a net spin polarisation. The second element is called an analyser and filters the incoming spin-polarised electrons in function of its magnetisation state. As an example, an up-magnetised analyser electrode will be more transparent to electrons having the same spin polarisation "up" and will offer less resistance to their flow, with respect to the incoming electrons with "down" spin. An SV used both a polariser and an analyser (Fig. 1), typically with different coercive fields. This can be obtained by using two different materials or by nanostructuring the materials in different ways (e.g. by making them of different thicknesses or sizes) so that the coercivity is affected. When the magnetic field is then swept, the device will offer the minimum resistance when both the polariser and analyser electrodes are magnetised in the same direction, and it will display a maximum resistance for the field ranges where the magnetisation directions of the two elements are antiparallel (Fig. 1b).

Standard materials are characterised by few per cent variations of resistance at room temperature, too small a variation for applications, while the multilayer structures of nanoscale thickness studied by Fert and Grünberg [1, 2] can show much higher effects. Such systems possess magnetic electrodes (Fe layers) and a tunnelling element, such as very thin Cr or insulating layer, and have naturally high resistances. The resulting magnetoresistance ratio is enhanced to 1,800% at low temperatures, and up to 400% at room temperatures, a phenomenon aptly called giant magnetoresistance. Devices built on this principle now constitute the core of many logic and memory units, and they are routinely fabricated using top-down techniques and purely inorganic materials.

The challenge is now to understand the processes that rule the behaviour of spintronic devices when they are scaled down to a single-molecule level. In principle, similar effects can be expected (and have been claimed), but the

interactions that mediate them remain to be understood. The promise is to create molecular spintronic systems that may possess very large magnetoresistance effects even in such molecular structures and, hopefully, to devise novel schemes that allow operation at high temperatures.

3 A Brief Introduction to Quantum Transport

Electrons in bulk metals are, usually, fairly well described by band theory. On the contrary, the electronic states of molecules are strongly quantised, with delocalisation playing a role almost exclusively in the presence of groups and functionalities involving π orbitals. When a molecule is sandwiched between two bulk electrodes, the electronic reservoirs of the leads interact with the discrete and quantised energy levels of the central molecule. It should be understood that the same situation can be produced also by sandwiching a sufficiently small (nanoscale) piece of conducting or semiconducting material between the electrodes, as obtained, for example, when using carbon nanotubes (CNTs) or semiconducting islands at the core of nanoelectronic devices. If the dimensions of the central system connected to the macroscopic leads are reduced to such a small size as to lead to a quantisation of the electronic band structure, we will obtain a quantum dot (QD), i.e. an electronic element that has a set of discrete energy levels, exactly as for what is naturally found in molecules. QDs can be assimilated to "artificial molecules" and form good quasi-zero-dimensional systems, but it is important to clearly state some differences: in molecules the energy-level spacing is defined by the choice of the system and can be varied using different chemical constituents and arrangements of the molecular structure; in QDs the level spacing largely depends on the material chosen and the size of the system. The typical dimensions necessary to observe quantum effects are between tens and several hundreds of nanometres, depending on the material. While quantum behaviour appears for a few atoms of a metal [3, 5], it can emerge in structures that are several nanometres large for semiconducting systems [3], while several hundreds of nanometres are sufficiently small to achieve quantisation of the energy levels in CNTs.

The fundamental mechanisms that control electron flow through such devices are rather different than those of standard, classical electronic systems. The electronic properties of electronic devices based on single molecules or QDs are usually investigated via transport measurements by connecting them to leads. The following discussion about quantum transport holds equally for devices with a molecule or any other kind of quantum dot. Hence, the two terms can be used interchangeably. It must be stressed, here, that a sizeable energy barrier can develop between the QD (or the molecule) and the leads themselves. At low temperatures the presence or absence of the barrier can lead to a completely different response of the molecule sandwiched between the leads. As a rule of thumb, different mixings of the molecular electronic states with the delocalised wave function of the electrodes will cause different barrier heights, and we can distinguish three main regimes ([3];

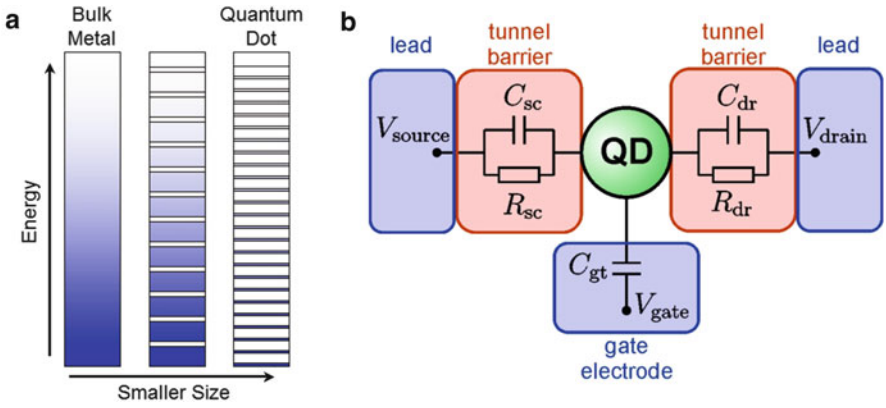

Fig. 2 (**a**) Finite-size effects leading to the creation of a set of quantised energy levels from a metallic band structure when the system is reduced to nanoscopic dimensions. In the original band structure (*left*), a number of small energy gaps start appearing when the dimension of the system is progressively reduced, creating a number of small energy bands (*centre*). Reducing the size of the system even further leads to the presence of only a small number of allowed occupational states, which are differently spaced based on the actual dimension of the system (*right*). (**b**) Circuit diagram of a typical nanoelectronic device. The molecule or quantum dot is connected to two leads – source (*sc*) and drain (*dr*) – via tunnel barriers, each represented by a capacitance $C_{sc/dr}$ and a tunnel resistance $R_{sc/dr}$. A gate electrode is capacitively coupled to the dot C_{gt}. A bias voltage can be applied via V_{source} and V_{drain} and the electrostatic potential on the dot can be tuned by V_{gate}

see, e.g. the dedicated issue on [4], [5–10]): (1) a strong-coupling regime, where the molecular states are strongly hybridised with those of the bulk metal, leading to small barriers; (2) a weak-coupling regime, where the molecular states are well separated and distinct from those of the leads, and the barriers are high; (3) a physically very rich and interesting intermediate regime, where the molecular/QD levels are only partially mixed with those of the leads, and the molecule can still retain its identity, but can be easily accessed by the lead electrons.

As the height of the barrier will generally lead to different regimes, it is thus important to understand, at least intuitively, what is its origin. For molecules the barrier height is usually varied using one of two strategies: the first approach involves changing the metal of the contact [10] or the group responsible for the grafting onto the lead; a second approach involves inserting a non-conjugated molecular spacer, e.g. an alkyl chain, between the grafting group and the molecule itself [12], as schematised in Fig. 2. The proof of principle of the strategies has been implemented experimentally, the first using different sulphonated ligands to Single Molecule Magnets (SMMs) to Au leads [13] and the second using alkyl spacers between strongly binding thiol groups and a central molecular core, constituted by a $Co(terpy)_2$ complex, as discussed in Sect. 6.1 [12].

In addition to the source and drain electrodes, a gate electrode is usually added to the device, so as to be able to tune the electrostatic potential by a capacitive coupling. Experimentally, this is usually implemented by building the devices over doped Si wafers with a 100–300 nm SiO_2 layer on top creating a back-gated

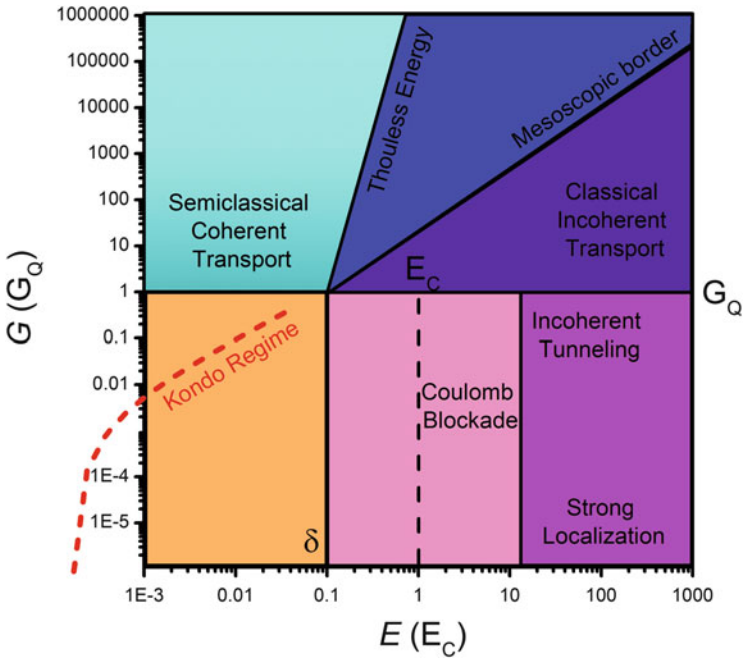

Fig. 3 Diagram of the most important regimes attainable for electronic and nanoelectronic devices, depending on the size of the components and their electronic characteristics. The vertical energy scale is given in units of the quantum of conductance, G_Q, while the horizontal scale defines the level statistics and is provided in terms of Coulomb charging energy, E_C, for reasons of generality

device. The same effect can also be obtained using top-gates or side-gates, as sometimes necessary when the device includes more than one QD. The final circuit diagram representing a typical three-terminal device is sketched in Fig. 2b.

The behaviour of the system shall then be schematised by introducing a quantity called the quantum of conductance $G_Q = 2e^2/h$, which can be used to classify the characteristics of our devices. The second range that defines the transport characteristics of our devices is the energy of the conduction channels. Two main quantities will define the behaviour of our system: the spacing of the quantised levels, δ, discussed above and the energy E_C which needs to be spent to overcome the Coulomb repulsion when adding an electron to a system already containing some. The absolute energy scale will depend on the level of confinement of the electrons and on the system in consideration and is usually of the order of eV for single atoms (Fig. 3).

Once these scales are defined, we can draw, following previous considerations, a rather general and basic sketch of the different regimes in which an electronic device can operate (Fig. 4). Several boundaries can be defined. Let us consider the limiting situations first. If the conductance G through the device is large and $G \gg G_Q$, a large number of electrons are travelling through our device simultaneously, and this will happen via a number of ways, called transport channels. If, on

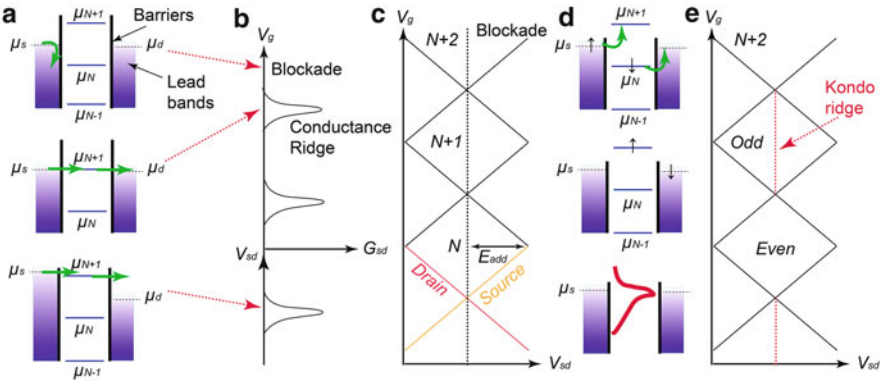

Fig. 4 (**a**) Schematic of the quantised states of the electrochemical potential of a quantum dot for three different level alignments. If no potential is applied, the dot levels are, in general, not aligned with the chemical potential of the leads. If the dot is not within the bias window, the number of electrons on the dot is fixed (N) and it is in Coulomb blockade. No current can be measured. Increasing V_{gate} (the gate voltage is increased going from the top position to the middle one) lowers the dot chemical potentials, and when one of the levels is aligned within the Fermi energy of the leads, electrons can tunnel across the dot. A nonzero current I_{dot} is thus measured. The same current can be measured when changing the source–drain potential so that one dot level falls into the bias window (*bottom*). (**b**) Coulomb oscillations in the differential conductance $\mathrm{d}I/\mathrm{d}V$ as measured across the QD. The same schematic differential conductance $\mathrm{d}I/\mathrm{d}V_{\mathrm{sd}}$ plot is shown in the *bottom part*, where the voltage variation is the bias. (**c**) Resulting Coulomb diamonds, as obtained plotting the differential conductance as a function of V_{g} and V_{sd}. The addition energy E_{add} and the energy E_{exc} of an excited state are indicated. (**d**) Schematic depiction of the Kondo effect, displaying the basic co-tunnelling processes that change the spin on the QD. The result is that a finite density of states at the Fermi level arises (*bottom*). (**e**) The resulting scheme for a strongly coupled quantum dot, showing nonzero conductance (Kondo ridges) in the Coulomb diamonds corresponding to an odd number of electrons on the dot

the contrary, $G \gg G_{\mathrm{Q}}$, the electrons will get through the QD only very rarely in discrete events. The regime for which $G \sim G_{\mathrm{Q}}$ is still under intense theoretical and experimental investigation and constitutes one of the boundaries of our diagram.

For $G \gg G_{\mathrm{Q}}$ the electrons can spend different amounts of time on the QD, and as any timescale is related to a corresponding energy scale by the Heisenberg uncertainty principle, we can define a so-called Thouless boundary around $2\Delta E \Delta t \sim \hbar$. This boundary provides an upper energy limit for coherent transport with multiple channels, which is a semi-classical regime. At energies higher than this boundary, we will find a region where electron–electron interactions, which work destructively against any form of coherence, become dominant. This second boundary will be found when the time that the electron spends on the QD is approximately the same as the inelastic scattering time. Above this energy we will thus operate in a completely classical regime, while below this energy the conductors are better described as a collection of smaller nanostructures, so that the boundary region is usually called the mesoscopic border.

Once the three main regions with many transport channels are defined, we now move to devices in which there is only one quantum of conductance or less. The region defined by $G \gg G_Q$ and $E \gg E_C$ is characterised by a strong localisation of the electronic excitations and a conduction mechanism dominated by electron hopping and is usually called the strong-localisation regime. The most important region, for our purposes, is the one at lower energies, where the charging energy becomes the fundamental energy scale, which is called the Coulomb blockade regime of a nanodevice. When we are in this region and close to G_Q, we can place the electrons one by one onto the QD during our transport measurements ([3]; see, e.g. the dedicated issue on [4], [5]). This means that we will have incoherent tunnelling of the electrons onto the molecule through the aforementioned energy barriers with the leads, and one can manipulate electrons one by one. The energy scale $\sqrt{E_C \delta}$ will define a boundary between regions where this tunnelling happens elastically and where inelastic tunnelling effects dominate. It should be noticed that if one can operate in the coherent tunnelling region and build devices with superconducting electrodes, one can create quantum devices of almost macroscopic size. As we discussed above, the barrier energy between the QD and the leads is fundamental. When its transparency becomes high enough that the electromagnetic environment can affect the QD, we fall into the bottom-left region of the diagram. In this region the distinction between the states of the QD and the leads becomes blurred. In certain cases the electrons that pass through the magnetic QD will perceive it only as a magnetic impurity, which screens the electron flow. This regime, which is of high theoretical and experimental interest, is called the Kondo regime ([3]; see, e.g. the dedicated issue on [4], [5–10]) and is obtained only for strong coupling of the QD to the leads.

Now that we have defined this general background, we will ignore most of the mentioned areas and we will concentrate on two of them: the Coulomb blockade regime and the region to its left – the Kondo regime.

Let us examine the Coulomb blockade first. In the three-terminal set-up of a quantum dot, two voltages are available to manipulate the electronic environment of the QD/molecule: the bias voltage V_{sd}, i.e. the difference in chemical potentials of the source and the drain electrode, and the gate voltage V_g. In the linear response regime, only a small bias voltage is applied and the current via the QD is measured as a function of gate voltage. In the case of a weak coupling and sufficiently low T, generally, no state of the QD is aligned within the small bias window, as sketched in the left panel of Fig. 4a, so that the number of electrons on the dot, N, is fixed and no current is measured. Increasing V_g lowers the QD potential, and when a level is aligned within the bias window, one electron can tunnel from the source onto the dot and off into the drain. In this way a nonzero current is measured only in the proximity of the QD energy levels (centre panel of Fig. 4a). Increasing V_g further fills the dot with one more electron from the source, and, by sweeping the voltage, we can subsequently fill the dot with electrons. The conductance measurement thus exhibits so-called Coulomb oscillations [7] in the current across the QD, as in Fig. 4b.

Another way to measure transport via the quantum dot is by changing V_{sd}. Keeping V_g constant and increasing V_{sd}, the changes in the number of available states in the bias window can be monitored by the differential conductance dI/dV_{sd}. Whenever one additional dot level falls into resonance with the Fermi energy, one more transport channel opens up and the current increases, observed as peaks in the differential conductance. By varying both available voltages, a conductance map can be constructed as function of V_g and V_{sd}, forming the stability diagram of a quantum dot. As sketched in Fig. 4c, the diagram consists of diamond-shaped regions, called Coulomb diamonds, where the number of electrons on the dot is fixed. The diamonds are connected by ridges where the differential conductance is high and which follow the evolution of the energy level of the QD when we are applying potentials to the leads and/or gates.

It should be stressed here that this map is a *form of spectroscopy* of the QD/molecule: in standard spectroscopy one sends photons onto the system and measures absorption or transmission at different energies of the incoming particles. Here we can observe the excitations of one single molecule and its electronic, vibrational and spin energy levels by measuring the transmission of electrons through it. Analogously to other forms of spectroscopy, from the V_g and V_{sd} potentials, one can extract the essential information of the molecule. The energy needed to add one electron to the molecule and the gate coupling parameter can be extracted from the height and the width of the Coulomb diamonds (Fig. 5b, c). In general, the two slopes forming the edges of the Coulomb diamonds are not symmetric and depend on the dimensionless coupling parameters $\alpha_i = C_i/C$ ($i = $ sc, dr, gt; $C = C_{sc} + C_{dr} + C_{gt}$), which hence can also be extracted [7, 13]. Along the edge of the diamond with positive (negative) slope, the dot level is aligned with the

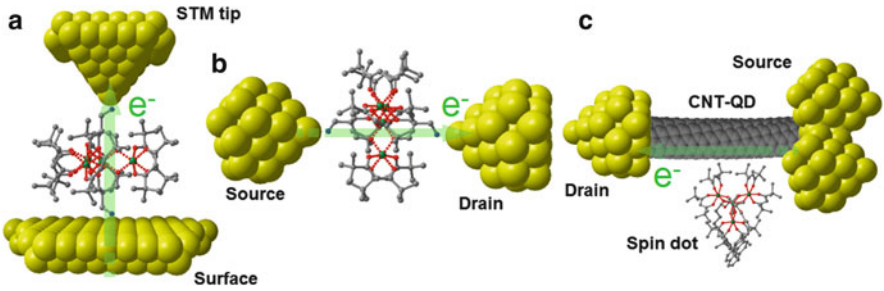

Fig. 5 Three main detection schemes in molecular spintronics. All schemes are shown as implemented with Fe_4 molecular magnetic clusters, for reasons of schematicity. (**a**) Detection scheme using a conducting tip, as in a scanning tunnelling microscope. (**b**) Molecular junction device, to which a third terminal can be added by building the device on a highly doped Si wafer covered with SiO_2, as commonly used in the electronics industry. (**c**) Double-dot scheme. The molecule (i.e. a spin QD) is attached onto a second, electronic QD (in this case a carbon nanotube). The effect of the molecular spin onto the current flowing into the QD is then felt and detected, leading to single-molecule detection without flowing electrons directly through the spin system and thus avoiding strong perturbations. Again a back-gate electrode can be added by building the device on a Si wafer covered with SiO_2

Fermi level of the source (drain), and such regions are called source (drain) resonances. The transitions involving vibrational or spin excited states of the single-particle energy spectrum are found as resonance lines running parallel to the diamond edges. The energy-level spacing can be extracted from the bias window at the meeting point of an excited state resonance line with a diamond edge. Following these lines as a function of some other external parameters, such as magnetic field, allows observing spin or other effects that affect the QD. For example, a splitting of a resonance line associated with spin excitations is usually expected when applying a magnetic field and can provide information on the spin system under investigation. In summary, it is possible to fully characterise a QD/molecule from its stability diagram. The capacitances which couple the dot to the environment can be determined, as well as the quantum level structure and the excited state spectrum including spin excitations. In this sense, quantum transport serves as a spectroscopic method, capable of detecting single molecules and their properties.

The second regime which we are concerned about is the one in which the transparency of the barriers becomes very high. One can picture this situation as similar to the case in which one atom (which has a quantised energy spectrum when alone) is bound to a bulk metal, which has a continuum of states defined by its band structure. Until now we have considered the situation when the interaction is not so strong (e.g. when depositing *n*-heptane on Au). Then, the energy levels of the molecule remain well defined, in a situation similar to our case of high-energy barriers. On the other hand, it is clear that if their bonding is good (e.g. adding a Co atom to an Au surface), the atom will then become part of the metal and the individuality of its energy states will be lost, which is equivalent to saying that the barrier is low, in our case. This second situation is usually schematised using the Kondo regime for QDs, where co-tunnelling effects are possible. That means that an electron may tunnel onto the QD while another electron tunnels off, as sketched in Fig. 4d. In this case, the electronic states of the QD/molecule become strongly hybridised with those of the leads and a quasi-continuum of states will develop. This many-body state leads to a peak in the density of states at the Fermi level (Fig. 4e), which will be detected as a characteristic peak of conduction at zero-bias voltage, often called a "Kondo ridge" (Fig. 4e). Following the initial assumption made by Kondo to explain the resistivity of metals with magnetic impurities at low T, one starts considering that the spin S associated with the QD is coupled with the electrons on the conduction band, S, and the spins of the conduction electrons have to align antiparallel to minimise the total energy. This leads to a screening of the electrons flowing through the device by the spin S when there is an odd number of electrons on the QD, while an even number of electrons usually produces no effect.

4 The Different Paths Towards Molecular Spintronics

Over time, three essentially different schemes to organise and address single molecules for transport have been developed:

1. By organising the molecules on conducting surfaces and then using the conducting tip of a scanning tunnelling microscope (STM) as a lead (Fig. 5a).
2. By breaking a tiny metal strip so as to create a nanoscopic gap, in which a molecule can be placed, usually by random methods.
3. By grafting the molecule onto another nanoscopic electronic device, such as a QD. This is also known as the double-dot scheme, because it makes use of an electronic QD (the device) and a spin QD (the molecule).

In this section we present the general rationale of these possible schemes, with their advantages and disadvantages, while the details of the observed results will be provided in the following sections, together with a discussion of the molecular magnetic materials that have been used to implement them.

The first approach (Fig. 5a) constitutes the most basic approach and requires the immobilisation of molecules onto a conducting surface, so as to probe the energy levels on the system using a conducting tip, as in a STM. This approach has the advantage of being more easily implementable than the other two, as it only needs the deposition of molecules on the metal surface. This has been achieved via a number of different functionalisations of SMM clusters to bind on gold and other metals [14]. The main disadvantage of this approach is the fact that one can investigate the properties of the molecules as a function of the surface-tip voltage but no external voltage source can be applied, i.e. no gate voltage is present. This is a major disadvantage because it basically restricts the investigation onto one line of the Coulomb diagram (as mentioned in the previous section) and prevents a complete spectroscopic characterisation of the system. Such limitations are overcome by the second type of measurements, albeit at some price.

The second, more advanced and more challenging approach (Fig. 5b) is to immobilise a molecule between two electrodes and then measure the current through it. Such experiments have in fact been the first to be attempted, because they offer the possibility of fully characterising the system, even though the devices are more challenging to produce. They have the important drawback that, in contrast to STM imaging, only one molecule can be investigated, and this particular molecule cannot be investigated with other means and will be imprisoned in one unique, random orientation with respect to the leads and the current flow. The experiments thus suffer from a lack of reproducibility, and it is also difficult to state clearly what is in fact being probed, in the absence of clear magnetic fingerprints. The most used junctions are electromigrated or break-junction devices [15], which can integrate a back-gate electrode, usually buried below the junction itself. As usual, two experimental regimes can be distinguished, depending on the strength of the coupling to the electrodes: the weak-coupling (or Coulomb) limit or the strong-coupling limit, where Kondo effects can be probed.

The third detection scheme, which is growing in interest and relevance, consists of using a multi-dot device in a three-terminal scheme [16], where the current passes through a non-magnetic QD only weakly coupled to the SMM. Recently the double QD scheme has been implemented using CNT contacted by non-magnetic electrodes, as discussed in Sect. 7.2, and could also be relevant for apparent single-molecule measurements, as explained in Sect. 6.2. In this set-up, the CNT forms a non-magnetic quantum dot, while the switching of the magnetic moment of the molecules grafted onto it causes changes in the electronic transport depending on the applied magnetic field. The reasons for the choice of such electronic elements are described in Sect. 7 in more detail.

5 The Surface-Deposition Approach

One major issue for the development of this approach has been the possibility of placing intact molecular magnets on surfaces, without having them destroyed by the deposition method, the surface reactivity or the interaction with air and other contaminants. The different deposition strategies that have been developed, and the degree of success that they have met, have constituted a particular subfield of molecular magnetism [14]. The interested reader is redirected to the several very complete and detailed reviews [14, 17] of these efforts, for reference. Here we will only resume the main conclusions and lines that can be extrapolated from this mass of work and the issues that are still relevant to the field.

The first point to be considered is the choice of the deposition method. Two main avenues have been followed: one relies on binding the molecular materials onto the surface with suitable chemical groups (e.g. thiols for Au surfaces), while the second one relies on the immobilisation of the molecules via evaporation and/or direct drop casting methods.

The second issue that has emerged is the need for a correct choice of the active molecules, which need to be stable enough to survive the deposition. This implies the possibility to withstand ultra-high vacuum or high temperatures, or to remain stable in solution, depending on the method chosen. One of the most famous and investigated molecular magnets, Mn_{12} (see dedicated chapter in [11]), has been found to be quite unstable in solution and to undergo partial reduction when grafted on surfaces and conducting materials [18]. Another factor determining the molecular choice is the fact that it is desirable to be able to obtain a preferential orientation of the molecules on the surface. In this sense molecules with particular, asymmetrical shapes can be preferred over larger and more symmetric systems.

The third parameter to be considered is the substrate. The substrate must present low surface reactivity, in order to maintain the properties of the molecular system, but must also be sufficiently reactive as to allow the grafting of the molecular objects. The substrate must also be a good conductor, to allow the transport experiments, and the effects of the symmetry of the surface electronic states seem to be playing a more and more important role. Eventually, depending on the

experiments, magnetic or non-magnetic substrates can be preferred. The substrate must also allow the cleaning and fabrication procedures necessary to tunnelling microscopies and must present a relatively low roughness, in order to permit the investigations.

It is extremely important to stress, here, that two points have attracted most of the attention of the researchers in this area and currently constitute fundamental and only partially solved steps for the creation of molecular spintronic devices. The first is that the integrity of the systems investigated has to be proved and checked with extreme accuracy, not only on the structural but also at the electronic level. This is of paramount importance for the study of single-molecule effects. The first check to be performed is if the molecules retain the structural and chemical features of the bulk crystals, without becoming fragmented, heavily distorted, electronically reduced or oxidised by the interaction with the surface. Such structural and chemical characterisations, at the very low concentrations typical of the surface-assembled systems, are extremely challenging. Techniques such as surface Fourier-transformed infrared spectroscopy and Raman spectroscopy have seen little use in molecular magnetism, while other techniques such as mass spectrometry have shown their full potential. Time-of-flight secondary ion mass spectrometry, for example, can detect the mass of the adsorbed system for depths of 1–2 nm and allows identifying the presence of intact molecules, without providing any knowledge of the electronic states. Indications on the integrity of the electronic structure of the systems can be obtained using X-ray-based spectroscopies, such as X-ray photoelectron spectroscopy, X-ray absorption spectroscopy and X-ray magnetic circular dichroism. All these techniques, by involving electronic reorganisation processes, can provide valuable information on the oxidation state of the deposited systems. These techniques can also be used to control the relative elemental abundance of different metals, if the situation occurs, which is useful to extract information on the presence of the molecular composition and its chemical environment. The second problem is the operation of the devices themselves, which currently requires very low temperatures, extreme mechanical stabilities and high magnetic fields. Such conditions are extremely challenging to meet and often lead to difficulties in obtaining statistically relevant results and stable devices.

5.1 Some Examples of Relevant Molecules and Surfaces

Surface chemistry has been a major research field in chemistry [19], way before the appearance of spintronics, because of the interest in catalysis [20] and related surface processes. Molecules can interact with surfaces only weakly (e.g. via van der Waals interactions), and the corresponding surface deposition process is called physisorption, or they can interact more strongly and form true bonds, leading to a surface functionalisation process called chemisorption [19]. Physisorption can be achieved using high vacuum chambers, and this method is gaining prominence in molecular magnetism [14, 17], although some molecular magnets are unstable in

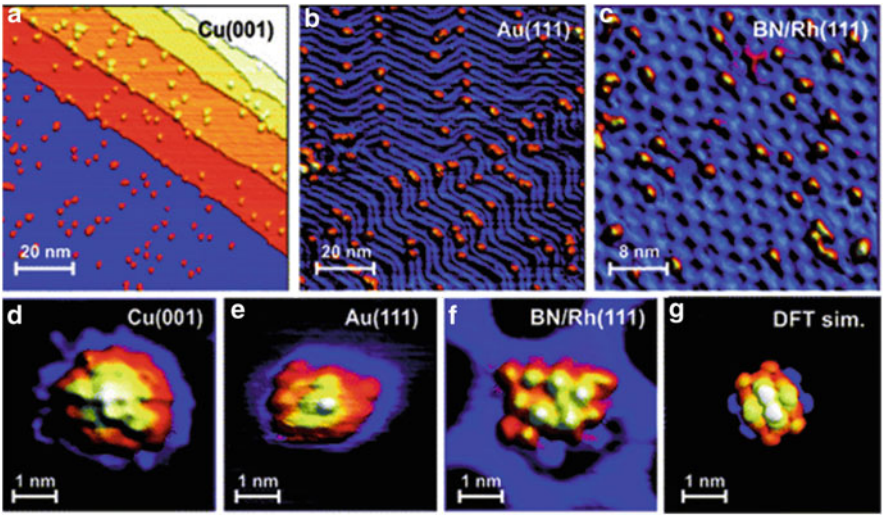

Fig. 6 Scanning tunnelling microscope topographic images of Mn_{12} molecules deposited on different surfaces. (**a**) On Cu(001) immobile molecules are randomly distributed over the surface at 300 K. (**b**) On Au(111), molecules are found preferably at the elbow sites of the herringbone reconstruction ($T = 40$ K). (**c**) On the BN/Rh(111) surface, molecules adsorb in the depressions of the BN corrugation ($T = 1.5$ K). (**d**–**f**) Images of individual molecules reveal an intramolecular structure identified as the acetate groups. Different adsorption geometries can be observed. (**g**) Comparison with the DFT calculation of the free molecule. Reproduced with permission from Warner [25]. Copyright 2011 American Chemical Society

such conditions. Some examples of simple molecules physisorbed on Au surfaces are metal phthalocyaninate and porphyrinate and metal Pc systems, whose deposition has been the subject of detailed studies for at least the case of CuPc, which has been deposited on Au, ITO, Si and SiO_2 [21–23]. Ordered assemblies have been obtained, and the layers have revealed exceptionally interesting properties for quantum information processing [24].

Weak interactions have also been used to keep molecules on a variety of surfaces after bombardment. In this sense a particularly interesting example is that of the soft-landing of Mn_{12} molecules on a variety of surfaces, as obtained with unique instrumentation at the MPI für Festkörperforschung in Stuttgart [25]. The result is obtained using electrospray ion beam deposition, a very gentle technique, which allows deposition of Mn_{12} clusters onto several supports, including Cu(001), Au (111) and thin BN on Rh(111) [25]. The chemical composition and the amount of deposited material can then be compared to expectations, and the results confirm the deposition of intact Mn_{12}. An example of the resulting systems on surfaces, as observed with STM, is provided in Fig. 6. A second interesting example is that of Co-based complexes, such as Co-Salen ones, deposited over insulating surfaces, such as NaCl [26]. The deposition of intact systems was proved using nonconventional surface techniques, and the results can in part be admired in

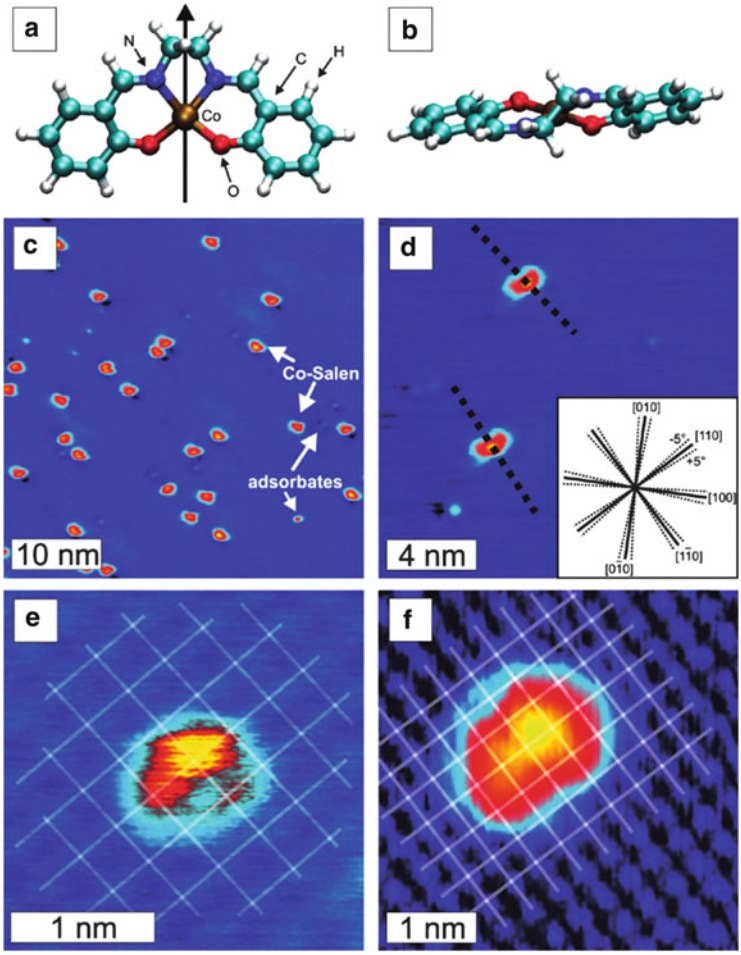

Fig. 7 Top (**a**) and side (**b**) of the free Co-Salen molecule, with the tilted $-C_2H_4-$ bridge resulting in a C_2 symmetry. (**c**) Overview NC-AFM image after deposition of Co-Salen molecules on NaCl (001). (**d**) Two individual Co-Salen molecules. The angle between their axis is approximately $\pm 5^\circ$ away from the [1–10] substrate direction. (**e**, **f**) show high-resolution NC-AFM images showing a single molecule and atomic resolution on the substrate simultaneously using a Cr coated tip. Reproduced with permission from Kahle et al. [26]. Copyright 2010 American Chemical Society

Fig. 7, showing the orientation of the molecules with respect to the crystallographic axes of the substrate and the typical "banana" shape of the molecular complex.

Chemisorption allows creating a great variety of structures on surfaces, by taking advantage of both the substrate structure and the possible presence of molecular appendages to create ordered structures. Most of the attention has been focused on anchoring chemical groups that contain sulphur atoms to perform grafting of the molecule to Au surface [14, 17]. This strategy can be pursued by pre-functionalising the surface with the thiols, so as to anchor groups that then

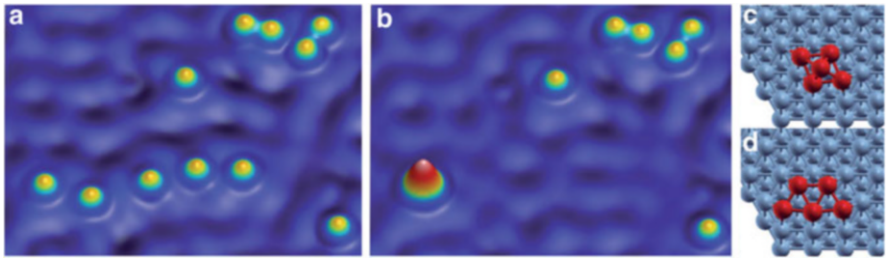

Fig. 8 Constant current STM images of single Fe atoms on the surface of Cu(111) (**a**) before and (**b**) after construction of a five-atom Fe magnet. (**c**, **d**) DFT calculations of the relaxed geometry of the two possible configurations (pyramid and flat, respectively) of the penta-atomic Fe magnet (*red spheres*) on Cu(111) (*blue spheres*) constructed in (b). Reproduced with permission from Lämmle et al. [27]. Copyright 2013 American Association for the Advancement of Science

allow grafting of the molecular magnets, or by pre-functionalising the molecules and then performing the deposition [14]. While the creation of fully formed and ordered self-assembled monolayers would, in principle, be possible [19], such geometrically ordered states have not been achieved for molecular magnets on surfaces.

Eventually we would like to stress the recent possibility of creating quantum magnetic materials directly on the surface [27], so as to produce small aggregates of magnetic atoms with a strong interatomic coupling. The resulting nanostructure (Fig. 8) behaves in a way very similar to that of molecular magnets and allows the observation of quantum tunnelling of the magnetisation.

5.2 Transport Through Deposited Molecular Magnetic Systems

The main problem with experiments conducted using scanning tunnelling spectroscopy is the lack of a gating voltage to tune the levels of the quantum dot. On the other hand, it is often possible to tune the coupling of the molecule to one of the leads (the tip) so as to achieve different coupling regimes and be able to observe Kondo features. Additionally, it is possible to move the tip so as to explore the different behaviours in different parts of the molecule, thus achieving a different level of characterisation, as shown below.

Some of the most prominent current examples consider organic radicals, because of the implicit advantage in considering a $S = 1/2$ system with low spin–orbit interactions. One attempt used verdazyl radical derivatives (Fig. 9) [28]. This well-known radical was one of the first to be used to obtain ferromagnetic coupling in purely organic magnets, and many of its derivatives are known to exist and have been investigated [29]. The radical clearly showed a Kondo resonance when deposited onto gold, and its structures could be optimised in vacuum chambers

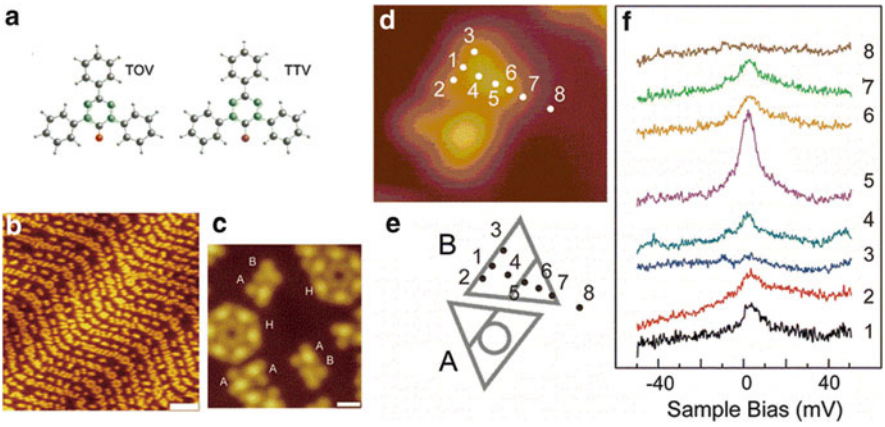

Fig. 9 (**a**) Optimised model of a verdazyl derivative molecules used in the study in vacuum conditions (*grey*, *green*, *white*, *red* and *purple balls* represent C, N, H, O and S, respectively). (**b**) Large area image of verdazyl TOV molecules on Au(111). Scale bar is 200 Å. (**c**) TOV dimers and hexamers. *A*, *B* and *H* represent type *A*, type *B* TOV molecules and hexamers, respectively. Scale bar is 20 Å. (**d**) STS detection positions on type *B* molecule in *A*–*B* dimer. (**e**) Illustration of (a). (**f**) Changes of the Kondo resonance of the TOV molecule with the detection positions. Numbers for the positions in all panels are synchronised. Reproduced with permission from Khajetoorians et al. [28]. Copyright 2013 American Chemical Society

and using soft deposition techniques. STM was used to monitor the organisation of the molecules on the gold surface Au(111). Two different types of configurations that the same molecule (TOV) can acquire on the surface could be detected.

The two configurations, labelled A and B in Fig. 9, were shown to have distinct characteristics, revealing the fragility of spintronic behaviour with respect to the environmental factors. Scanning tunnelling spectroscopy allowed observing distinct spectra depending on the particular radical used and also on the conformation adopted by the radical itself, with only one form allowing for the identification of the zero-bias Kondo resonance. The effect could be attributed to the presence of a high delocalisation of the unpaired π electron, which enhances the Kondo resonance.

The second class of radicals that has received attention for such studies [30] is the well-known nitronyl nitroxide radicals, which have often been used for organic ferromagnets and also for the creation of molecular coordination compounds [31]. Some of the most prominent results are reported in Fig. 10, showing the radicals used and the scanning tunnelling microscopy data [30]. Again, a clear Kondo feature was observed at zero bias, and the full temperature and magnetic field evolution could be followed. The features showed remarkable agreement only when using a weak-coupling interpretation of the data and a perturbative approach to the system, contrarily to previous studies that concentrated on spins in strongly coupled electron baths.

The other class of molecules that has attracted a lot of interest for surface spin-dependent characterisations is that of rare-earth double deckers. The discovery of

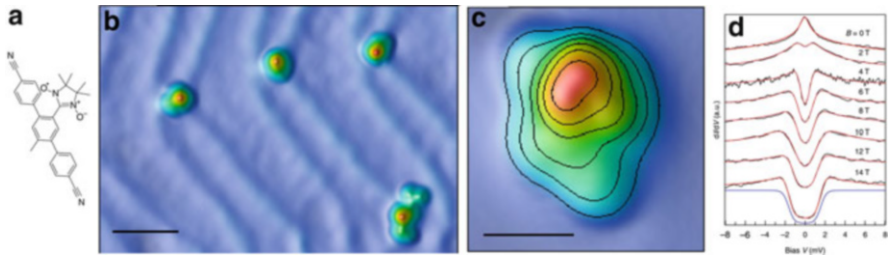

Fig. 10 (**a**) Chemical structure of the studied organic radical molecule with a nitronyl nitroxide side group that contains a delocalised singly occupied molecular orbital. The molecule is drawn with a similar orientation as in the topography in (c). (**b**) Overview topography at $T = 6.7$ K of individual molecules on Au(111). The *bottom right* molecule is decorated by three neighbouring dichloromethane molecules. The scale bar corresponds to 5 nm. (**c**) High-resolution topography of one organic radical molecule, with *contour lines* at height intervals of 50 pm and the scale bar corresponding to 1 nm. (**d**) Differential conductance measurements taken at successively increased magnetic fields on the radical side group of the molecule ($T = 1.8$ K). All spectra are normalised and offset for clarity. *Red curves* are fits modelling the conductance using perturbation theory up to third order in the exchange interaction J. The *blue curve* at $B = 14$ T shows exemplarily the contribution of the second order in J to the differential conductance. Reproduced with permission from Koivisto and Hicks [30]. Copyright 2013 Nature Publishing Group

single-centre molecules with slow relaxation [32] of the magnetisation has prompted strong attention, and attempts were promptly performed to investigate the charge transport mechanisms in such systems. Again, the study of Kondo resonances has been of particular importance in this early stage of research [33–35]. The double-decker derivatives are formed by a single rare-earth centre (Ln) sandwiched between two phthalocyanine (Pc) molecules and are stable in two oxidation states, namely, $[LnPc_2]^-$ and $[LnPc_2]$. The electronic oxidation and reduction of the molecule happens at the PC moiety, and the neutral $[LnPc_2]$ complex has an open shell π electron system. $[LnPc_2]$ molecules thus possess two spin centres: an unpaired electron delocalised over the π orbitals of the Pc ligands and the Ln(III) ion, whose properties are determined by the magneto-chemistry of 4f electrons. Measurements were conducted with scanning tunnelling microscopy on $[TbPc_2]$ molecules deposited onto the Au(111) surface. Again, two types of molecules were observed: with four lobes and with eight lobes (Fig. 11), corresponding to a broken complex, where a Pc ligand is lost, and to the intact [TbPc2] system.

The identification of the molecular species then allowed a dI/dV mapping of the molecules with four lobes, which lead to the observation of Kondo features in about half of the systems, while the remaining molecules showed no relevant features in the dI/dV curves, possibly owing to the detachment of the metal ion from the adsorbed systems. Fitting the curves, and in particular of the energy width of the feature, led to the estimation of a Kondo temperature of ca 250 K [33], which is similar to those of analogous 3d metal complexes. Similar experiments performed using other rare earths, such as in $[DyPc_2]$ and $[YPc_2]$, revealed the lack of any

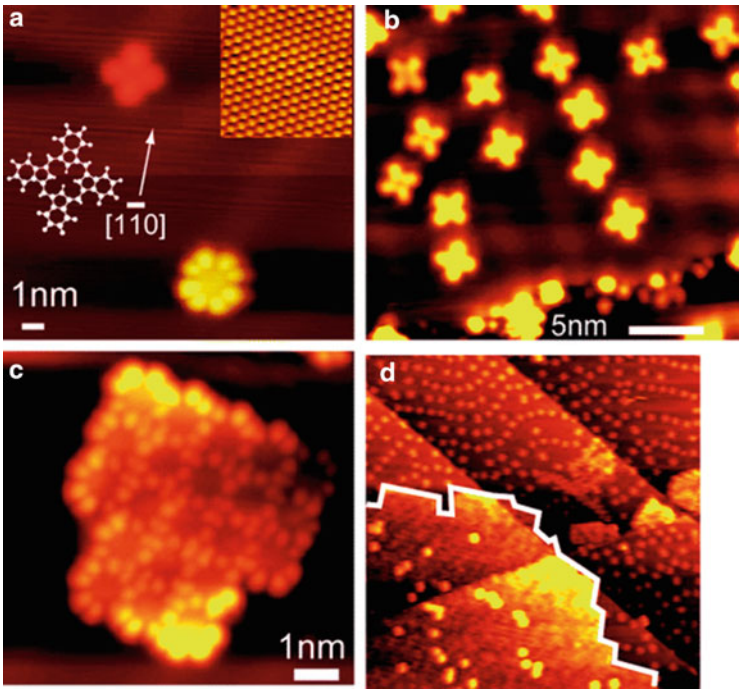

Fig. 11 (**a**) STM images of [$TbPc_2$] and [TbPc]. (a) Single molecules of [TbPc] (*upper*) and $TbPc_2$ (*lower*). An atomic image of the Au(111) is shown in the *inset*. The [$1\bar{1}0$] direction is marked by the *arrow*. Schematic models of the Pc plane of the observed [TbPc] and [$TbPc_2$] molecules are superimposed. (**b**) [TbPc] molecules on the terrace part of the Au(111) surface ($25 \times 23\ nm^2$). (**c**) [$TbPc_2$] film composed of 21 molecules ($7.8 \times 7.8\ nm^2$). (**d**) Coexisting [$TbPc_2$] island and isolated [TbPc] molecules. The boundary of the former is highlighted by the white line in the image (area $80 \times 80\ nm^2$). Reproduced with permission from Ishikawa et al. [33]. Copyright 2009 American Chemical Society

Kondo feature for such systems, in agreement with the expected parity of the spin state in such complexes.

Another beautiful example [36] of such experiments has employed a heteroleptic double-decker complex, where the rare earth is sandwiched between two different phthalocyaninato molecules. In particular the Pc and naphthalocyanate (NPc) ligands were found to be attractive, as they can be easily distinguished (Fig. 12). Two configurations of the intact molecule on the surface can then be considered: the PcUp, in which the molecule is attached to the surface with the NPc face, and the NPcUp, in which the molecule rests with the Pc face attached onto the surface. Once again, a Kondo resonance is observed for the two molecules, with different signals for NPcUP and PcUp. In both cases spin-resolved DFT techniques allowed assigning the Kondo peaks to the unpaired electron in the organic π orbital. Excellent agreement between the observed and simulated features could be achieved using sophisticated techniques that allow including the surface density

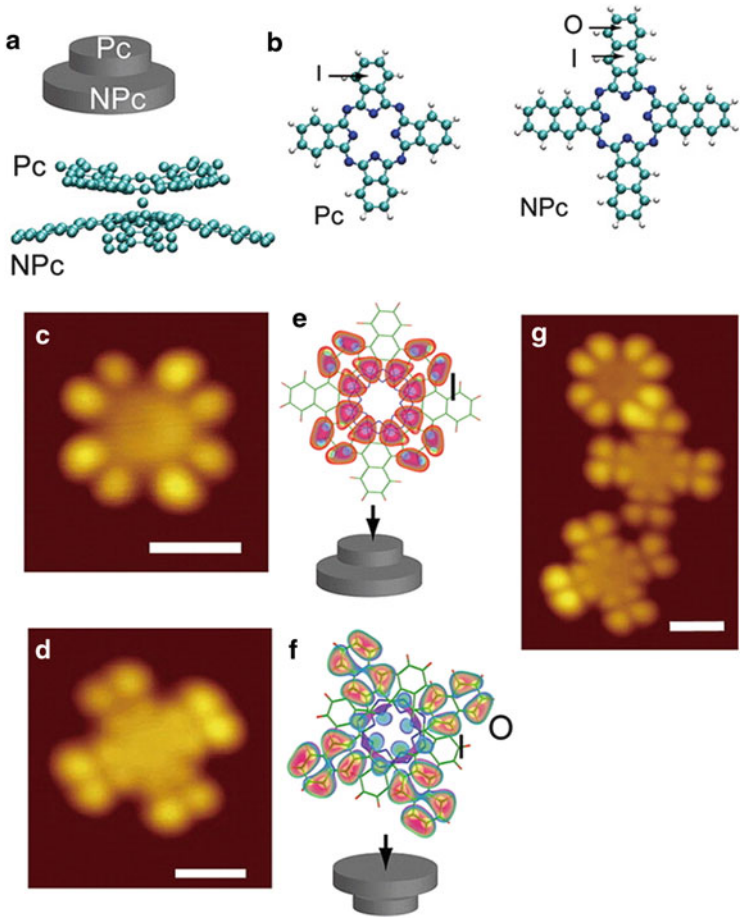

Fig. 12 (**a**, **b**) Models of the heteroleptic double-decker molecules used for STM investigations. "I" and "O" in (b) specify the position of the outer phenyl rings. (**c**–**f**) STM images and DFT simulated images of isolated Pc-up and NPc-up molecules. (**g**) STM image of aggregates. *White bars* in (c), (d) and (g) are 1 nm. Reproduced with permission from Katoh et al. [36]. Copyright 2013 American Chemical Society

of states, which were performed on mechanically deposited double-decker complexes [37] (Fig. 13).

The same group, after overcoming the important difficulties in the deposition of Mn_{12} molecules (see Sect. 5.1 and Fig. 6), also managed to characterise the surface-deposited cluster molecules. While in the previous section we discussed the challenges in overcoming the stability problems, here we describe the end result of the inspection of the magnetic behaviour, measured at 1.5 K by inelastic spin flip spectroscopy [25]. The technique consists in measuring the differential conductance as the voltage is tuned through the excitation energy and allows precise characterisation of several types of excitation, including vibrational, electric and

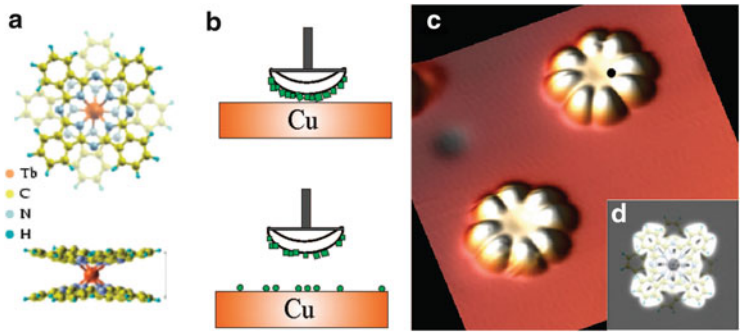

Fig. 13 (**a**) Structure of the [$TbPc_2$] molecule. (**b**) Scheme of the dry-imprinting technique (see text). (**c**) Constant current topography of two isolated [$TbPc_2$] molecules supported by the Cu(111) surface (image size, 7×7 nm); the *black dot* indicates the position where the dI/dV spectrum in Fig. 2 was obtained. (**d**) Simulated STM image of an isolated [$TbPc_2$] molecule. Reproduced with permission from Komeda et al. [37]. Copyright 2008 American Chemical Society

magnetic ones. The measurements revealed that the magnetic properties of the bulk could still be observed for molecules deposited on the insulating BN layers, which allow partial decoupling of the molecular magnets that form the conducting substrate. Comparison of several experiments performed with and without an applied magnetic field revealed several transitions of magnetic origin. A careful attribution of all the transitions could be performed by combining analytical and numerical treatment of the data, and the technique allowed the observation of the transitions between different sublevels of the $S = 10$ ground-state multiplet [25]. The analysis of the linewidths of the peaks also allowed probing the dynamics, and the spin state lifetimes were estimated to be in 2–4 ps range. This leads to the conclusion that in order to achieve current-induced spin pumping, currents of ca 100 nA would be needed, higher than what can be sustained by the fragile Mn_{12} clusters [25].

We also wish to highlight here emerging reports about the possibility of measuring the spatial distribution of the Landé g-factor [38]. In this case, the factor should be considered as a conceptually different quantity than the standard factor that is encountered in the Spin Hamiltonian. It is more related to a measure of how the local electron spin density reacts to an externally applied magnetic field and how this changes, locally, the relative transport properties of the electronic system. The experiments have been conducted using STM and MnPc complexes deposited on Au(111). The atomic g-factors, measured extended Kondo effect arising from charge-transfer-induced spin polarisation (Fig. 14), were found to be inhomogeneously distributed within the molecules. Compared to spin-polarised tunnelling measurements of the spatial resolution of the spin polarisations, this approach seems to provide an easier way to obtain an excellent, sub-molecular resolution of the magnetic behaviour.

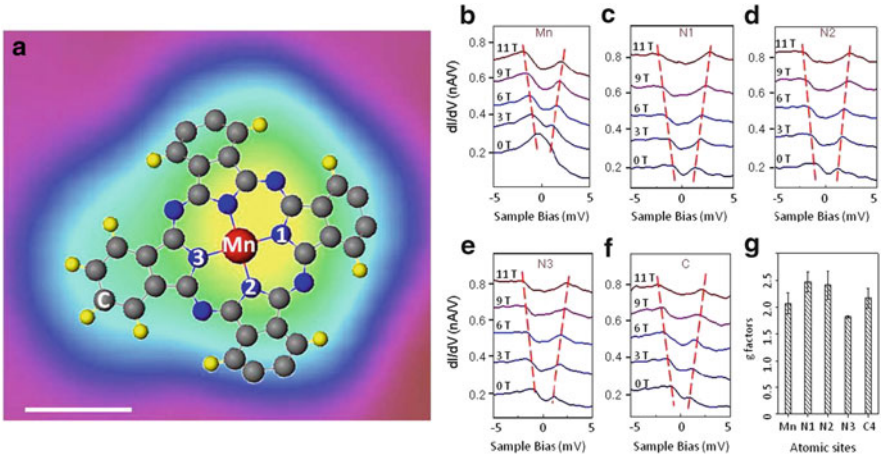

Fig. 14 *g*-factor mapping within a -6H-MnPc molecule. (**a**) Topography of a -6H-MnPc molecule and overlay of corresponding model. Scale bar, 0.5 nm. (**b**–**f**) d*I*/d*V* spectra taken on different sites corresponding to the positions of the -6H-MnPc molecule in (a). All d*I*/d*V* spectra were measured at the sample temperature of 0.4 K under a magnetic field of $Bz = 0 \sim 11$ T. The Kondo peaks split at higher magnetic fields. The asymmetric peak intensity of the split peaks arises from the asymmetric Fano-shaped Kondo resonance at zero magnetic field. Each successive plot is vertically shifted by 0.2 nA/V for clarity. (**g**) *g*-factors calculated from the Kondo splitting from (b) to (f). Reproduced from Vitali et al. [38]

5.3 *Controlling Molecular Spins on Surfaces*

The possibilities opened by this first approach to manipulate and use the spins states stored in single molecules are well exemplified by a number of studies in the literature. Three experiments seem particularly noteworthy for our present discussion. The first one is an approach that uses the application of radiofrequency pulses together with an STM detection [39]. This allows exciting the resonances in single molecules by placing the STM tip at a fixed position over the molecule. In the experiments, the continuous tunnelling conductance, d*I*/d*V*, is then measured while simultaneously modulating the sample bias at a variable radio frequency. The conductance of the molecule is then modulated by the excitation of hyperfine-split electronic states of the Tb ion, produced by the radiofrequency-tunnelling electrons (Fig. 15a). This process is not restricted by the selection rules of photon-induced magnetic dipole transitions, and the possible transitions are then shown in Fig. 15b.

Distinct peaks can then be observed at certain frequency values, while a constant signal is obtained over bare Au(111), with the experimental peak positions being in very good agreement with the calculated frequency values of the hyperfine transitions. Compared to more standard magnetic resonance methods, the method employs tunnelling electrons at radio frequencies and is not restricted by the standard magnetic resonance selection rules. This technique thus promises to

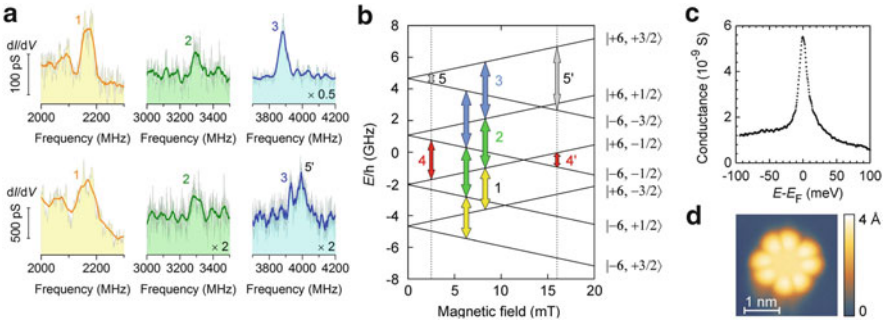

Fig. 15 (**a**) Single-molecule resonance spectra by rf-STM. Conductance ($dI = dV$) resonance peaks obtained by rf-STM over single [TbPc2] molecules adsorbed on Au(111) at 5 K and a static magnetic field of (*top*) 2.5 mT and (*bottom*) 16.1 mT applied perpendicular to the sample surface; the STM tip was placed over the ligand; *solid line* indicates averaged adjacent data points in each single spectrum; labels *1–3* and *5′* relate to selected spin transitions marked by *arrows* in panel (b). (**b**) Zeeman diagram of the lowest 6 substrates of the electronic ground state of Tb in a neutral [$TbPc_2$] molecule; nuclear hyperfine interaction with the $I = 3 = 2$ Tb nucleus splits each electronic level J_z into four hyperfine levels; *yellow*, *green* and *blue arrows* mark purely nuclear hyperfine transitions with $\Delta J_z = 0$ and $\Delta J_z = \pm 1$, labelled *1–3*; *red arrows* mark a purely electronic hyperfine transition with $\Delta J_z = \pm 12$ and $\Delta I_z = 0$ at two different field values, labelled *4* and *4′*, respectively; *grey arrows* mark a selected mixed electronic-nuclear transition at different field values, labelled *5* and *5′*, respectively; *dotted lines* indicate two field values realised in the experiments. (**c**) Kondo signature in tunnelling conductance spectrum characteristic of [TbPc2] adsorbed on Au(111). (**d**) STM topographic image of a single [TbPc2] molecule on Au(111) used in the study. Reproduced from Liu et al. [39]

open new possibilities for characterising and controlling single magnetic molecules on surfaces.

A second possibility is the use of molecules that have, themselves, more than one stable state. This has been achieved by using molecular systems that can assume more than one spin state, such as the complexes of the Fe phenanthroline family, which are known to undergo a low- to high-spin state transition at a certain temperature. One prominent study [40] used the [Fe(1,10-phenanthroline)$_2$(NCS)$_2$] complex, a very well-known molecule that exhibits a LS → HS transition when heated above 175 K, which is accompanied by a concomitant change in the distances and angles of the Fe–N coordination bonds. The molecule could be observed, together with its switching, by measuring the current flowing through the device with an STM tip. Selective switching was observed above a certain voltage threshold, with the resulting molecular state remaining stable on sweeping back the applied voltage. At a corresponding negative voltage, the state could be switched back, obtaining a molecular behaviour and a current that depend on the history of the device. These resistive properties with a memory of the previous history thus produce a so-called memristive behaviour. The magnetic states of the system were, on the other hand, strongly hybridised with those of the substrate, and a Kondo peak could be observed for the high-spin state ($S = 2$). Although this was also reported in other Fe-based molecules on Cu(II), the observation is unexpected

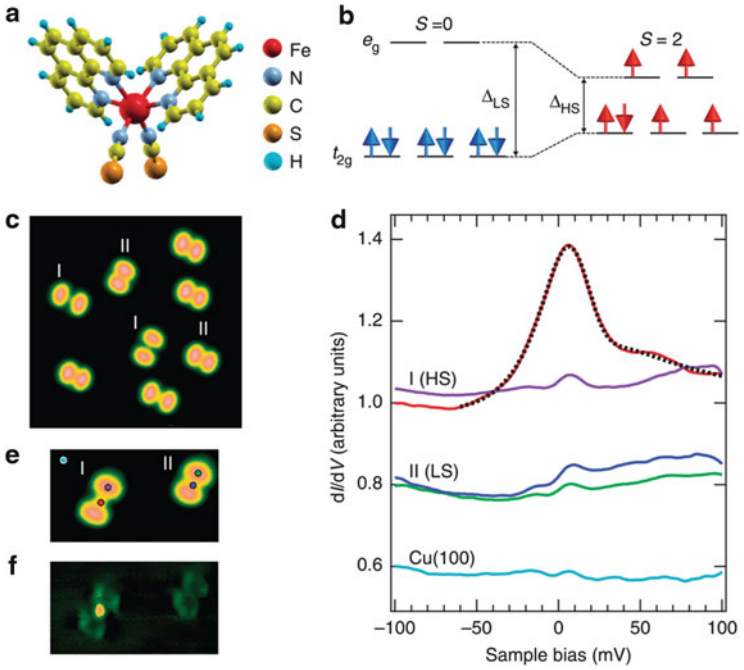

Fig. 16 (**a**) Three-dimensional model of the [Fe(1,10-phenanthroline)$_2$(NCS)$_2$] molecule. (**b**) Simplified electronic configuration of the Fe(II) 3d states in the ligand field. For large ligand fields (Δ_{LS}), the electrons fully occupy the t_{2g} states and the total spin S is quenched, while for low ligand fields (Δ_{HS}), the Fe(II) ion is in the spin state $S = 2$. (**c**) STM image of isolated [Fe(1,10-phenanthroline)$_2$(NCS)$_2$] molecules on the Cu(100) surface with two conformations denoted as I (HS) and II (LS). Image size is 13×13 nm^2. (**d**) dI/dV spectra recorded on the centre of type I (HS) and type II (LS) molecules and Cu(100) surface. The *colours* indicate the position, where the spectra were taken and are marked as *coloured dots* of (e). The *black dotted line* denotes a Fano fit to the Kondo resonance. (**e**) STM topography of a pair of type I (HS) and type II (LS) molecules and (**f**) corresponding dI/dV map (*bottom*) obtained at +10 mV showing the position of the Kondo resonance at the centre of the HS molecule. Image sizes are 6.7×3.7 nm^2. Reproduced with permission from Müllegger et al. [40]. Copyright 2012 Nature Publishing Group

because Kondo features usually appear only for semi-integer spin states, and the mechanism and states involved in the process are still not perfectly understood. The important point is, on the other hand, that, in this case, the conformational switching of the system still produces a variation of the current through the molecular system. Similar observations and confirmation of the effect could be obtained also on molecular bilayers made of [Fe(1,10-phenanthroline)(dihydro-bis-pyrazolyl-borate)$_2$] [41] (Fig. 16).

A third option was to use the conformational rotational switching of the phthalocyanine deckers in the already discussed [TbPc$_2$] complexes [42]. The lower Pc ligand is likely immobile, owing to interaction with the underlying substrate, while the upper one can be moved between two possible conformations by applying a current pulse (see Fig. 17). The rotation of the ligand molecule can be monitored by

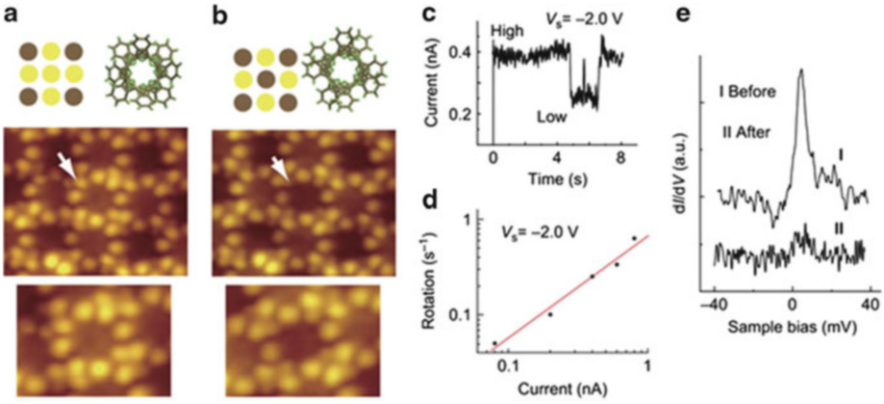

Fig. 17 (**a**, **b**) Conversion of the centre molecule from (b) ($\theta = 45°$) to (d) ($\theta = 30°$) by applying a current pulse. The target molecule is marked by an *arrow*, and magnified images are shown in the *bottom panel*. Changes in the contrast and the top view of the centre molecule are schematically illustrated. (**c**) Current during a −2.0 V voltage pulse over a [$TbPc_2$] molecule initially in the b state; the tip remained fixed over a lobe position with the feedback loop open. Each jump in the current indicates the moment of rotation of the molecule and the low state corresponds to the (d) state. (**d**) Rotations per electron as a function of tunnelling current for $V = -2.0$ V. Both axes are in log scale. Data shown are for rotation from (b) to (d). The *red line* corresponds to a least squares fit. (**e**) Comparison of the Kondo peaks before I and after II of the application of the pulse. Reproduced with permission from Gopakumar et al. [42]. Copyright 2011 Nature Publishing Group

the variation of the tunnelling current change. Figure 17c shows changes in the current during injection of a current pulse, showing two (high and low) tunnelling current states, with a sharp change indicating that rotation occurs. Analysis of the mechanism suggests that the current-induced rotation is a single-electron phenomenon. Once the molecule is switched by the pulse, it remains in the same state in a timescale of hours, and the Kondo peak is dramatically changed as a result, as shown in Fig. 17e, with an almost complete disappearance of the sharp Kondo feature typical of these systems.

While some other reports have appeared, and some of these results have something in common with previous research on multistable conformational changes in molecular adsorbates on surfaces, these three examples show well the possibilities that have been explored, so far, for the control of molecular systems on surfaces. One of the next issues is then to develop switching mechanisms for correlated systems, such as chains. It would be extremely interesting to understand if the mechanisms that have been evidenced in atomic chains assembled on surfaces [43], or that have been devised for crystalline molecular materials [44], can also be exported to molecular magnetic chains on surfaces and thus introduce correlated molecular magnetic materials in molecular spintronics.

6 The Junction Approach

This approach is the one that allows using also a gate voltage, and thus it allows a complete spectroscopic investigation of the molecular system, tuning both the potential at the extremes of the molecule and the position of the molecular levels. While this detection scheme presents several advantages over the first one, it still suffers from several drawbacks, the most important of which is probably the fact that the electron flow can directly pass through the molecule, thus strongly perturbing the spin state. Such drawbacks can be further overcome by using the third detection scheme, discussed in the next section. On the other hand, several recent experiments have shown how this detection scheme can be applied for maximum efficacy to characterise molecular magnetic materials in the junction, thus extracting valuable information on the systems.

As Mn_{12} was the archetypical and most studied single-molecule magnet (see, e.g. the dedicated focus on [11]), at least for many years, it also was the first molecular magnet studied in a three-terminal geometry and showed signatures of sequential electron transport and even signatures of its magnetic properties in transport experiments conducted with the second approach [45, 46]. The first experimental realisation of the weak-coupling limit was achieved using a Mn_{12} derivative functionalised with thiol groups, which provides strong and reliable covalent bonds to the electrodes [45] but, on the other hand, also creates relatively high Schottky barriers. As the Coulomb blockade involves the sequential charging of the molecular magnet, the magnetic properties of the negatively and positively charged species must be considered, in addition to those of the ground state. This introduces an important difference with respect to standard molecular electronics, where charging of the molecule usually does not significantly alter the interesting degrees of freedom. Positively charged Mn_{12} clusters have a lower D anisotropy [45], and the presence of these charged states is fundamental to explain the electronic transport and in particular the observed negative G values. Studies as a function of applied magnetic field H have shown a first evidence of the spin transistor properties [46] as well as the lack of a hysteretic response, which can be due to the breaking of the molecular magnet during the grafting and to the population of excited states or might also be a consequence of the interaction with the metallic electrodes, similarly to the observed interaction with conducting surfaces in the scanning tunnelling experiments described above. The result can also be a consequence of the aforementioned difficulties in keeping the molecular system intact under deposition conditions, and several experiments now show that the magnetic properties of the Mn_{12} magnetic core are not preserved when the molecule is in direct contact with metals, so that the thin insulating layer in scanning tunnelling experiments may have been of fundamental importance for the observations [47].

In the following we will first consider the cases where nice signatures of the molecular properties have been obtained, and we will then move to recent advances in probing the relaxation times of the molecular systems. Eventually we will

consider more advanced cases that consider multiple-spin centres and start emerging in the field.

6.1 Measurements of Transport Through Magnetic Molecules

The strong electronic coupling remains unachieved for magnetic systems that show slow relaxation of the magnetisation but has been obtained with mono- and dinuclear centres. The mononuclear paramagnetic molecule investigated in this regime [48] is the magnetic molecule $Co(TerPyridine(CH_2)_nSH)_2^{2+}$, with $n = 0$, 5. The metal thiolates have the function of grafting groups, as they had extensively been used to produce self-assembled monolayers on gold. The resulting systems (Fig. 18a) show a Kondo peak when the thiol is directly connected to the terpyridine ligand ($n = 0$), while the system with the longer alkyl spacer ($n = 5$) displays low-transparency barriers and Coulomb blockade. Characterisation as a function of H reveals the presence of spin excitations and agrees with the effective $S = 1/2$ state attributed to Co^{2+} ions at low T. On the other hand, a Landé factor $g = 2.1$ is found, which is unexpected for Co^{2+} ions, characterised by high spin–orbit coupling and magnetic anisotropy, and this point needs further investigation.

The possibilities offered by a simple dimeric molecule, i.e. containing two magnetic centres, have also been investigated using the divanadium molecule [(*N*,*N*′,*N*″-trimethyl-1,4,7-triazacyclononane)$_2V_2(CN)_4(\mu\text{-}C_4N_4)$] (Fig. 18b) [49]. This is again directly grafted to the electrodes and produces very high transparencies. Via the gate voltage, one can tune the molecule into different charged states: a neutral state with $S = 0$ and a positively charged state with $S = 1/2$. The Kondo resonance is found only for the state in which the molecule has a half-integer spin moment and the current is screened by the magnetic impurity, as otherwise expected ([3]; see, e.g. the dedicated issue on [4], [5–10]). This nicely

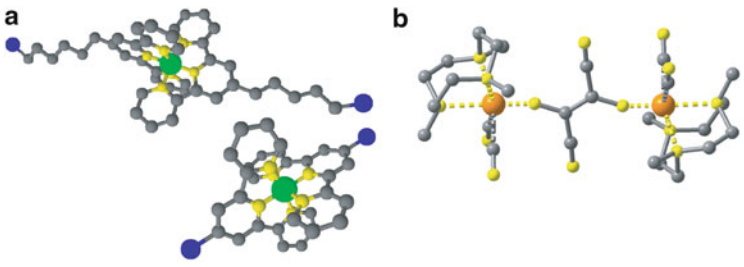

Fig. 18 (**a**) Scheme of the structure of $[Co(terpy\text{-}(CH_2)_5\text{-}SH)_2]^{2+}$ (tpy-$(CH_2)_5$-SH = 4′-(5-mercaptopentyl)-2,2′:6′,2″-terpyridinyl) and $[Co(terpy\text{-}SH)_2]^{2+}$ (tpy-SH = 4′-(mercapto)-2,2′:6′,2″-terpyridinyl) (*left*). Molecular structure of $[(Me_3tacn)_2V_2(CN)_4(\mu\text{-}C_4N_4)]$ (Me_3tacn = N,N′,N″-trimethyl-1,4,7-triazacyclononane) (Shores and Long, 2002). Reproduced with permission from Park et al. [16]. Copyright 2008 Nature Publishing Group

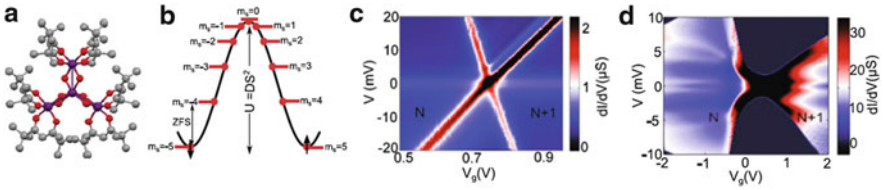

Fig. 19 (**a**) Crystal structure of the magnetic core of Fe_4 including some peripheral ligands. (**b**) Energy-level diagram for the molecular system, showing the splitting of the spin ground state into $2S+1$ states distributed over an energy barrier that prevents the spontaneous reversal of the magnetisation. (**c**) dI/dV colour map versus Vg and V_{sd} for a junction containing an individual Fe_4 molecular magnet. High-conductance lines mark the onset of single-electron tunnelling that separates two charge states. Kondo correlations in adjacent charge states are fingerprint of a high-spin state. (**d**) Charge-degeneracy point for a different device with larger barriers, so that co-tunnelling excitations appear. The colour scale is saturated as to highlight the co-tunnelling lines. Measurement temperature is $T = 1.9$ K and $T = 1.6$ K, respectively. Reproduced with permission from Mannini et al. [51], copyright 2006 American Chemical Society, and from Accorsi et al. [52], copyright 2014 Springer

demonstrates that magnetic molecules with multiple centres and antiferromagnetic interactions permit to switch the Kondo effect on and off, depending on the charging state of the QD itself. The temperatures at which Kondo features are found in such systems are much higher than those obtained for quantum dots and CNTs, as probably due to the stronger localisation effects.

Later attempts then switched to molecular magnets of the Fe_4 family, as these systems meet the same requirements of Mn_{12}, while retaining the magnitude and orientation of the magnetic anisotropy when deposited on conducting surfaces [13, 50]. Fe_4 single-molecule magnets are made out of a core of four Fe^{3+} ions and peripheral ligands that keep them in a star-shaped configuration, as illustrated in Fig. 19a. The central ion is connected to the peripheral ones via a strong antiferromagnetic exchange interaction and, as each centre has spin $S = 5/2$, a total molecular spin $S = 5$ is then produced. The molecular magnetic anisotropy lifts the degeneracy of the spin ground state into five doublets and a singlet (Fig. 19b). In crystals the height of the barrier is ca 1.4 meV [51, 52], with a zero-field splitting of 0.5 meV.

A number of experiments were then performed in different devices, where the height of the Schottky barrier is different and the system is found to be in different transport regimes. Figure 14c, d shows the differential conductance maps ($G = dI/dV$) of two different junctions containing an individual Fe_4 molecule with different barriers separating it from the leads. Figure 14c shows ridges of high differential conductance, which is characteristic of single-electron transport. The low differential conductance regions (blue in the figure) correspond to charge states N and $N+1$, as schematised in Fig. 4. Strong excitations appear at energies of 4.8 meV, a value compatible to the calculated energy of the next spin multiplet ($S = 4$) [50]. High-order excitations are also visible around zero bias, which was interpreted as a fingerprint of high-spin Kondo correlations. These results confirmed the presence of an anisotropic magnetic molecule sandwiched between source and drain, and in

the latter sample, spin excitations in the co-tunnelling regime thus became accessible [53, 54]. Both inelastic spin flip tunnelling and gate-voltage spectroscopy in field were used to characterise the system, revealing the nature of the spin states and their field behaviour. In the Kondo regime, a Kondo temperature was obtained from the temperature-dependent evolution of the full width half maximum of the Kondo. The results indicate a Kondo temperature of ca. 10 and 13 K for different charge states.

These molecules have also allowed measuring the transverse and axial anisotropy of the system sandwiched between the leads [55]. These results (see Fig. 20) have shown extremely good correspondence between the theoretical and experimental results and indicate a first attempt of addressing a fundamental question: what happens to the molecular system when it is between the leads and taken away from its more standard crystalline environment? A very detailed and statistically relevant study showed that the presence of the leads induces strong transverse anisotropy terms in the single molecule, which, in principle, can strongly alter the quantum tunnelling properties. These results are in agreement with investigations on molecular clusters on graphene (see Sect. 5.3) and contrast somehow with the behaviour observed for [$TbPc_2$] systems on CNTs and in junctions.

It should eventually be mentioned that the junction approach has recently allowed controlling the magnetic anisotropy of Fe_4 molecular magnets by using the electric fields present in the nanoscale device [56]. The investigation included two different molecular species (Fig. 21a). One features an Fe_4 derivative containing two phenyl groups on both sides, and the other features a long alkyl chain (see Fig. 21 for the structures). Three inelastic co-tunnelling lines are visible for the former species, with the nanodevice being in the single-electron transistor regime and medium coupling to the leads. For the latter system, on the contrary, the presence of the bulkier alkyl chains leads to a weaker coupling, and inelastic co-tunnelling excitations have the form of conductance steps. Information on the nature of the low-energy excitations was obtained by measuring the evolution of the lines in an applied magnetic field. Reduction and oxidation of the molecules inevitably change their magnetic properties, although it is not a priori clear in which way, a question that can be investigated using three-terminal spectroscopic measurements. First, the difference in spin values of adjacent charge states was determined from the shift of the degeneracy point in a magnetic field. From the measured splitting, enhanced axial anisotropy value was observed for the electronically excited state of the phenyl compound. For the alkyl-containing sample, the bulk zero-field splitting value and the neutral charge state were observed, with $S = 5$ and $D = 0.06$ meV. A clearly nonlinear Zeeman effect was also observed, allowing to estimate the angle between the easy axis and the field. In this way, electric-field control over the anisotropy of a single magnetic molecule was demonstrated using a three-terminal junction. A stronger magnetic anisotropy upon both reduction and oxidation, as induced by the gate voltage, was observed. This enhancement may be related to the alteration of single-ion anisotropy, which should be substantial when changing the redox state. These results open the way to the possibility of

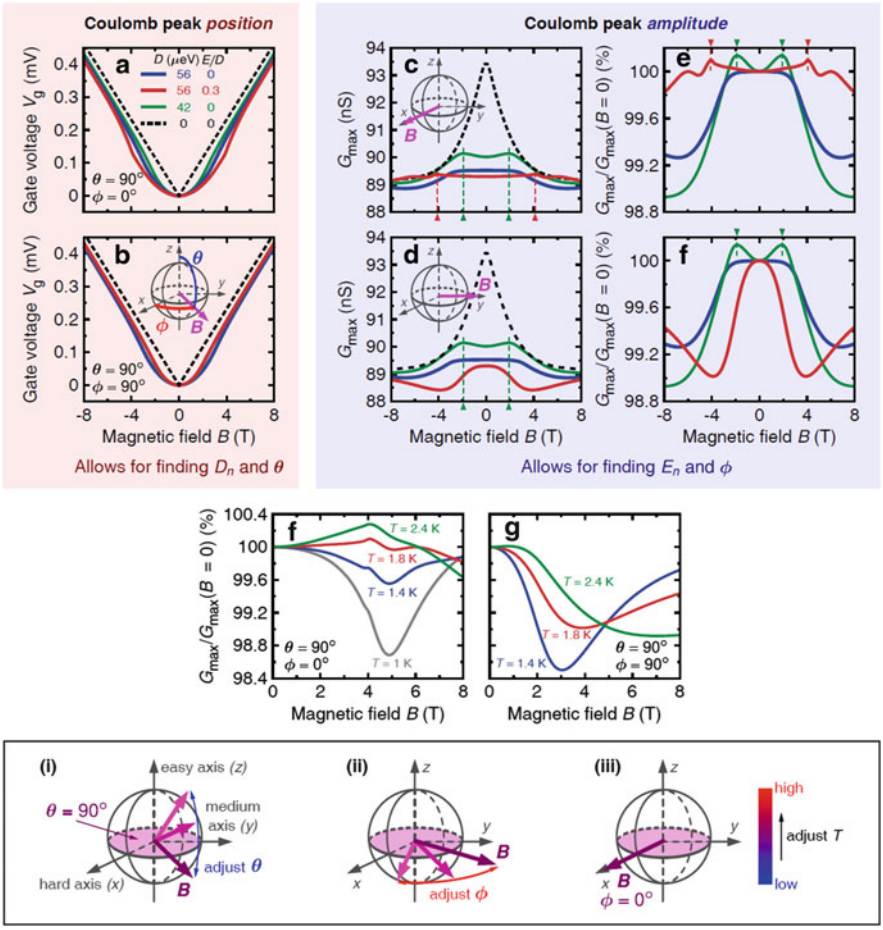

Fig. 20 How to determine the transverse magnetic anisotropy constant E of an individual molecular magnet from its transport characteristics: The position (**a**, **b**) and amplitude (**c**–**f**) of the Coulomb peak are shown for different values of the parameters D and E of the SMM model with $S_N = 5$ and $S_{N+1} = 9/2$ for $T = 1.8$ K. Note that we employ the assumption for the Fe_4 molecule from the main text, that is, $D = D_N = D_{N+1}/1.2$ and $E = E_N$ with $E_N/E_{N+1} = D_N/D_{N+1}$, and a relatively large value of E/D (*red lines*) is used for clear illustration of the effects under discussion. In panels (a, c, e) the external magnetic field B is oriented along the SMM hard axis x [see *inset* in (c)], whereas in panels (b, d, f) the field is parallel to the medium axis y [see *inset* in (d)]. In panel (**g**) we present how temperature affects the occurrence of characteristic peaks associated with the presence of transverse magnetic anisotropy for B along the hard axis x. To make the discussion complete, in panel (**h**), we show analogous dependencies but in the case when the field lies along the medium axis y. Finally, the frame at the bottom contains a schematic summary of the procedure leading to estimation of E: i) Using the analysis of the Coulomb peak position, find D and adjust the magnetic field B so that it is contained in the hard plane, i.e. the plane perpendicular to the easy axis z. (ii) Rotating systematically the magnetic field B in the hard plane, analyse the Coulomb peak amplitude to find the direction of the molecule's hard axis. This will be characterised by occurrence of additional peaks in the amplitude, whose field position allows for estimating E_n. (iii) If no local maxima in the amplitude can be seen, adjust (try increasing) the temperature. Reproduced from Burzuri et al. [55]

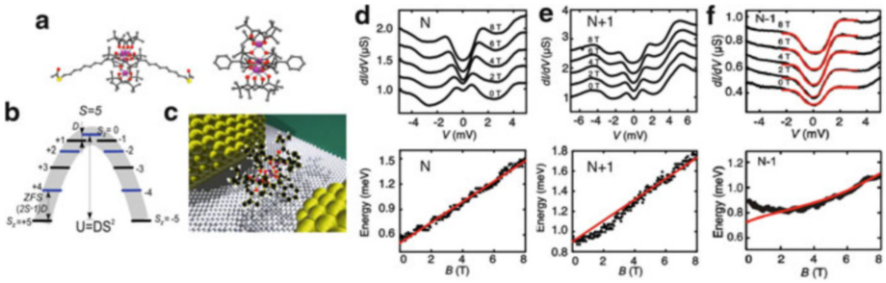

Fig. 21 (**a**) Structure of the Fe_4 molecules (colour code: iron = *purple*, oxygen = *red*, carbon = *grey*, sulphur = *yellow*). *Left*: Fe_4C_9SAc derivative, *right*: Fe_4Ph derivative. (**b**) Energy diagram of the ground spin multiplet at zero field. The S_z levels corresponding to different orientations of the spin vector along the easy axis of the molecule are doubly degenerate. The $S_z = +5$ and $S_z = -5$ states are separated by a parabolic anisotropy barrier. An important property of the Fe_4 molecule is the large exchange gap to the next $S = 4$ high-spin multiplet in the neutral state. Transport below a bias voltage of a few mV therefore only probes magnetic excitations of the ground high-spin multiplet, in contrast to the Mn_{12} derivatives. (**c**) Drawing of a three-terminal junction with a single Fe_4Ph molecule bridging two gold electrodes (*yellow*) on top of an oxidised aluminium gate (*grey*). (**d**) $dI = dV$ as a function of V for the neutral state in various magnetic field values (*top*) and excitation energy as a function of magnetic field for the same gate voltage (*bottom*); (**e**) same as (d) but with a different oxidation state; (**f**) same as (d) and e but with the Fe_4C_9SAc derivative and a different oxidation state. Reproduced with permission from Misiorny et al. [56]. Copyright 2010 American Chemical Society

manipulating individual magnetic molecules using electric fields in molecular spintronic devices.

6.2 Measuring Coherence Times

In the experiments above, we only considered signatures accounting for the electronic magnetic moment of the molecules. On the other hand, when the current can pass through the molecule, it is possible to probe also the interaction with the nuclear spin bath. Recently, transport measurements taken through a single $[TbPc_2]$ molecular magnet were studied in a three-terminal geometry obtained by electromigration (Fig. 22) [57, 58]. As the Tb(III) centre is very stable towards reduction and oxidation, it was suggested that a direct current flow through the Tb ion is highly unlikely. On the contrary, the two Pc ligands sport a conjugated π system, which can conduct electrons, as also shown by the transport experiments reported in Sect. 5. When the $[TbPc_2]$ molecular magnet was directly inserted into the electromigrated gold junction, the dI/dV curve vs. V_{sd} and V_g exhibits a single charge-degeneracy point with a weak spin $S = 1/2$ Kondo effect. A detailed study of the magnetic field dependence of the Kondo peak shows a ferromagnetic exchange interaction of about 0.35 T was measured between the spin 1/2 of the Pc and the spin of the Tb ion. While alternative coupling mechanisms (dipolar,

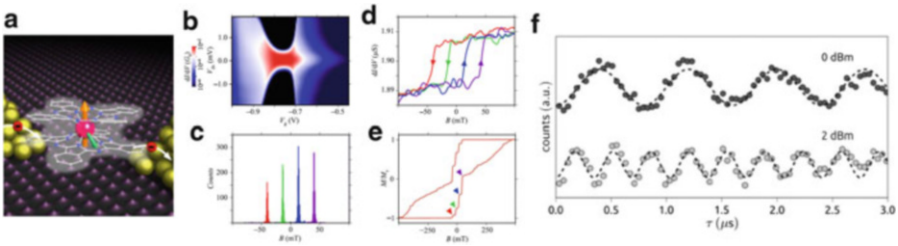

Fig. 22 (**a**) Schematic and idealised representation of the measurement system with the complex between the two electrodes. (**b**) Stability diagram of the Pc readout quantum dot exhibiting the differential conductance, dI/dV, in units of the quantum of conductance, G_Q, as a function of gate voltage, Vg, and bias voltage, V_{sd}, at 0.1 K. (**c**) dI/dV measurements for a given working point ($V_g = -0.9$ V; $V_{ds} = 0$ V) as function of the magnetic field B. The *arrows* indicate the field sweep direction. Abrupt jumps in the differential conductance, attributed to the switching of the Tb^{3+} magnetic moment, are visible for all traces of B, showing a clear hysteresis in the dI/dV characteristics. (**d**) Histogram of switching field obtained for 11,000 field sweeps showing four preferential field values that are assigned to QTM events. (**e**) Normalised hysteresis loop of a single [TbPc2] SMM obtained by integration of 1,000 field sweeps and performed for trace and retrace on a larger magnetic field range than in (c). The *four arrows on the trace curve* show the four preferential field values associated to QTM (*red*, −40 mT; *green*, −14 mT; *blue*, 14 mT; *purple*, 40 mT). (**f**) Rabi oscillation of a single nuclear spin. The transition probability from a nuclear spin state mI to a nuclear spin state $m'_I = m_I \pm 1$, obtained from 400 repetitions of the measurement procedure and plotted as a function of the applied pulse length τ for a microwave power of 0 and 2 dBm. Reproduced with permission from ref [57], copyright 2012 Nature Publishing Group, and Vincent et al. [58], copyright 2014 American Association for the Advancement of Science

magneto-Coulomb and flux coupling) were also considered, as in Sect. 7, the relatively high interaction value was attributed to pure exchange, as expected for the aromatic Pc ligand. In this schematisation, even when sandwiching a single molecule between two leads, the schematisation is rather that of a double quantum dot, as discussed in Sect. 7, with the Pc ligands forming a molecular quantum dot coupled to the magnetic moment of the Tb(III) ion[57]. The magnetic properties of the Tb(III) centre have been stated to be independent of the charging state of the Pc system. This is quite surprising, considering the high spin–orbit coupling of rare earths and the extreme sensitivity of these systems to all forms of perturbation in the shell of the coordinating ligands.

Based on these observations, electronic readout was carried out close to the charge-degeneracy point ($V_g = -0.9$ V and $V_{sd} = 0$ V in Fig. 22b). When the magnetic field is swept from negative to positive values, a single abrupt jump of the differential conductance is observed, and this feature is reversed if the field is swept in the opposite direction (Fig. 22c). These jumps are attributed to the reversal of the Tb^{3+} magnetic moment, which slightly influences the chemical potential of the Pc quantum dot through the exchange interaction [57]. Statistics on the switching fields shows a magnetisation reversal at four distinct magnetic fields (Fig. 22d) that are in perfect quantitative agreement with theoretical predictions and observations of the four avoided energy-level crossings with the nuclear spin states

−3/2, −1/2, 1/2 and 3/2. By integrating the normalised switching histograms, a magnetic hysteresis loop can be extracted (Fig. 22e). Again the agreement with measurements of crystals of [$TbPc_2$] is strikingly good. The lifetimes of the nuclear states were then measured by sending a radiofrequency pulse on the device [58], showing nuclear spin lifetimes T_1 of tens of seconds. The coherent properties were then probed by looking at the Rabi oscillations of the nuclear spin. The experiments were achieved by mounting a radiofrequency antenna in close proximity to the device and apply microwave pulses to induce coherent oscillations between the nuclear spin ground state and the first excited state. This allowed observing the coherence time of the nuclear spin, T_2, which was found to be in the order of μs, as also in other comparable systems.

6.3 Measuring Multi-centre Molecules

More recent experiments have attempted a further step forward, i.e. the use of molecules with multiple-spin centres. A mechanically controlled break-junction technique was used to sandwich between two gold electrodes a single molecule containing two coupled spin centres that are confined on two Co^{2+} ions [59]. The molecular complex is composed of a bipyrimidine wire with two thiol groups at the ends, which are used to attach it to the electrodes (Fig. 23). The wire forms coordination bonds to two Co^{2+} ions and allows magnetic interaction between the two spin centres. The threefold degeneracy of the $^4T_{1g}$ state, present in a perfect octahedron, is lifted by the ligand field and by spin–orbit coupling. The ground state of the system, as calculated by complete active space self-consistent field calculations taking into account the zero-field splitting of Co(II) and the exchange interactions, is found to be a pseudo-singlet, while the first excitations behave as a pseudo-triplet [59]. This schematisation, in agreement with the bulk magnetic data, shows the presence of four relevant states with a very weak antiferromagnetic coupling. With subtle geometrical variations, a shift of the ground state to the pseudo-triplet state (Fig. 23d) has been proposed as a consequence of an electric or magnetic field, with subtle changes in the local environment. When measuring the conductance through the system, two phenomenologically different behaviours were indeed observed, labelled type I and type II. Experimentally, these states can be assigned to the absence and occurrence of a Kondo-like zero-bias anomaly in the low-temperature conductance data, respectively (Fig. 23). By applying finite bias, one can repeatedly switch between the pseudo-singlet state and the pseudo-triplet state. The microscopic origin of this bias-induced switching could be found in an electric-field-induced asymmetry (caused by the irregular shape of the junction) that could drive the singlet–multiplet transitions.

Although this still represents only one particular case, at the moment, we are quite confident that the relevance of multiple-spin systems with weak intramolecular spin–spin coupling will grow in the future, as these systems offer very

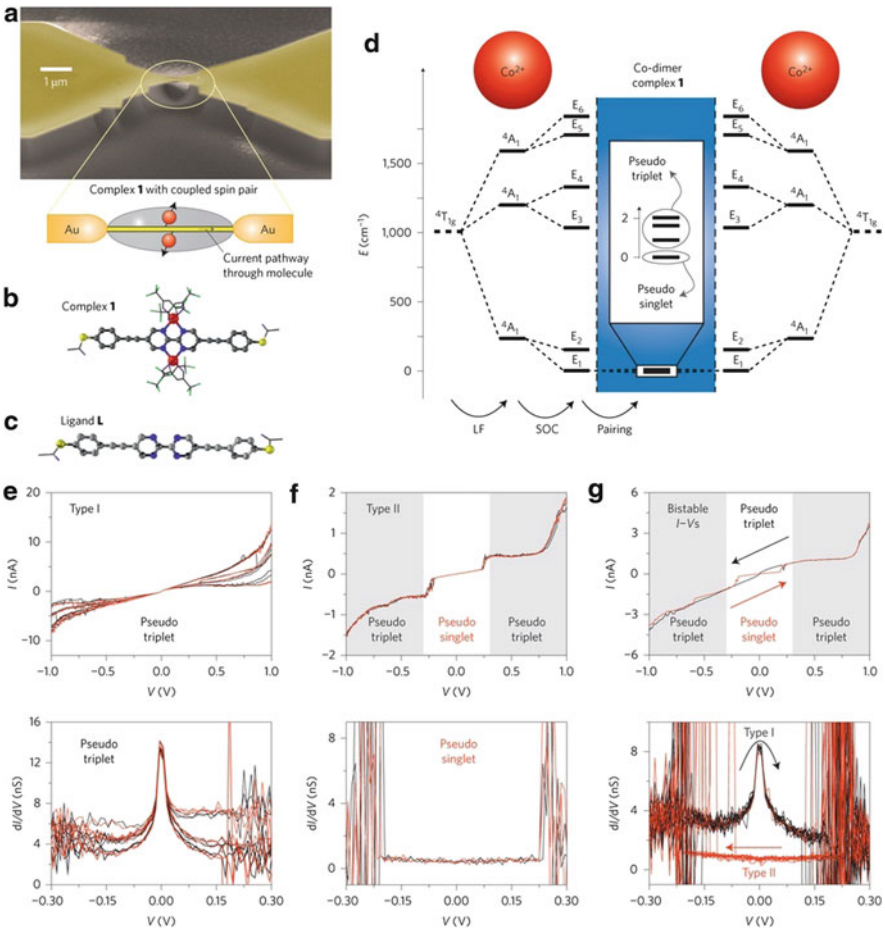

Fig. 23 (**a**) Scheme of the experiment. A molecule with a pair of spin centres is contacted in a single-molecule junction (SEM micrograph of a break-junction set-up). The magnetic ion pair is attached orthogonally to the current pathway. (**b**) Molecular structure of the complex used, from single-crystal X-ray diffraction. The Co^{2+} ions are marked in *red*, carbon in *grey*, nitrogen in *blue*, oxygen in *violet* and sulphur in *yellow*; hydrogen atoms are omitted for clarity. (**c**) Molecular structure of the bare bipyrimidine wire used for control experiments. (**d**) Electronic states of the coupled spin system, as obtained from quantum chemical calculations. *First column*: Co^{2+} in octahedral surrounding ($^4T_{1g}$). *Second column*: splitting as a consequence of the ligand field in the complex. *Third column*: influence of spin–orbit coupling. The *central column* indicates the consequence of pairing the two Co centres: a pseudo-singlet and a pseudo-triplet state arise, further split by zero-field splitting. (**e**) Curves displaying a Kondo-like zero-bias anomaly, but no discontinuity, classified as type *I* (up-sweeps are marked in *black* and down-sweeps in *red*). This is identified as the electrical fingerprint of the pseudo-triplet state. (**f**) Set of data displaying no Kondo-like anomaly, but a discontinuity at ~0.2 V, termed type *II* and assigned, for the inner part, to the pseudo-singlet. (**g**) Bistable *I*–*V* characteristics due to hysteresis of the coupled spin pair. Down-sweeps are similar to f and up-sweeps to (e). Reproduced with permission from Thiele et al. [59]. Copyright 2013 Nature Publishing Group

interesting experimental systems for the investigation of electron-induced spin effects in molecular spintronics.

7 The Double-Dot Approach

This scheme requires the presence of the spin quantum dot on another, electronic quantum dot. The behaviour of the spin dot is then probed via its effect on the current that flows through the electronic quantum dot. This scheme has the advantage that the current is not passed directly through the spin centre, thus avoiding the problems connected to the continuous reduction and oxidation of the magnetic centre. On the other hand, other control schemes, such as the electric field control discussed at the very end of Sect. 6.2, also become problematic to put in place. The scheme has still some unclear points that will need further inspection about the fundamental mechanisms that lead to the spin dot–electronic dot interaction.

In particular, a few ways in which the spin can influence the transport properties of the conducting QD can be envisaged (Fig. 24): the first is by simple dipolar coupling between the molecular magnet magnetic dipole and the electrons flowing in the electronic QD, and does not require any particular form of chemistry, as non-covalent grafting should be sufficient; the second is the magneto-Coulomb effect [60], which might possibly be responsible for some of the observed effects on molecular magnets; the third possibility, i.e. direct exchange coupling between the spin quantum dot and the electronic one [45], requires a covalent functionalisation that allows some form of overlap between the orbitals of the two dots, and this has only been achieved when using two moieties of the same molecule, as in Sect. 6.3; the fourth option is to use the electronic quantum dot as a detector of the magnetic flux variation, and this necessitates the creation of a superconducting quantum interference device.

It should be noticed, anyway, that in known cases the exact mechanism leading to the observation of the signal remains unknown and the underlying physics shall likely become the subject of future investigation. Spin valve-like mechanisms have been proposed [61], but they remain to be confirmed using the tools that normally identify such behaviours, e.g. Hanle precession.

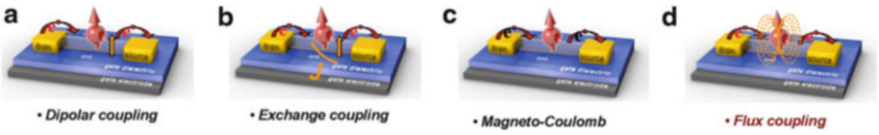

Fig. 24 Different coupling schemes between a QD (here represented as a carbon nanotube) and a molecular magnet that can lead to the observation of spin effects on the electron flow of the carbon nanotube (*red*). The schemes of dipolar coupling (**a**), exchange coupling (**b**) and magneto-Coulomb interaction (**c**) can all work using metallic leads, while the flux-coupling scheme (d, *in red*) sees the necessity of superconducting leads and the creation of a superconducting quantum interference device ring

The use of carbon nanomaterials has been dominant, in the double-dot approach, because such materials have a very good electronic channel that is directly exposed to external objects. In this regard both CNTs and graphene constitute excellent substrates, where the delocalised band is created by the p orbitals of the carbon sp^3 hybridisation, that stick out of the plane of the honeycomb network created. As the study of such materials constitutes a fecund field of its own, here we will focus only on the approaches that have been developed to connect this area with that of molecular magnetism. The chemistry of such carbon materials also allows using the tools of synthetic chemistry to functionalise the electronic quantum dot with the spin one. Both covalent and non-covalent functionalisation are then possible, and the development of the necessary chemistry has been the focus of no little attention recently, as described in Sect. 7.1. We then move to the observations made using CNTs and graphene systems, in Sects. 7.2 and 7.3, respectively.

7.1 Chemical Challenges

In this section, due to the growing relevance of the third detection method, we quickly review the possibilities in the chemistry of carbon nanomaterials and molecular nanomagnets. The bulk of the work has been performed on CNTs, while some recent works point in the direction of graphene-based hybrids and devices, which can exploit the presence of Dirac electrons in the graphene structures.

The chemistry of CNTs has been well developed since their discovery and leads to some fundamental advances in functionalisation and chemical manipulation [63]. It is worth reviewing briefly these modification methods to develop suitable means for the functionalisation of CNT and graphene with molecular magnets. Basically, the chemistry of CNTs often revolves around introducing defects on the sidewall of the CNTs to perform further reaction with target molecules. However, the defects on a CNT constitute scattering sites that severely limit the performance of electronic devices. Therefore it is of fundamental importance to reduce the defects of a CNT to a minimum level during the development of CNT-molecular magnets hybrid electronics devices.

Basically, there are two strategies to develop hybrid devices with different outcomes on the electronic properties: non-covalent and covalent binding to CNT or graphene. For the non-covalent binding to CNTs, the grafted molecule will locally alter the electron density of the CNT and thus generate a scattering centre. It can also be expected that the interaction between the CNT and the molecular magnet is very weak, and this strategy is a good way to develop a weak-coupling hybrid. The weak-coupling hybrid electronic devices, if operated with sufficient sensitivity, can detect the presence of one or several grafted molecules even at room temperature. It is very important to use stable molecules so as to avoid a loss of molecules from the grafting ligand attached to the CNT, which will generate unnecessary scattering centres.

Two ways are usually employed to modify the molecular magnets in order to graft them on CNTs with a non-covalent binding. The first one is to modify the ligand with tails containing polycyclic aromatic groups, like pyrene. These aromatic groups are able to form relatively strong π–π stacking with a CNT and have been used to attach Fe_4 molecular clusters to CNTs from solutions (Fig. 26). For the purposes of molecular spintronics, it became important to understand how many molecules were on the CNT system [64]. A method to determine the distribution of those molecules on CNTs was also developed. The modified molecules are assumed to stick onto the CNT randomly. Then, the probability of having two molecules at a distance L is $P(C, L) = Ce^{-LC}$, where C is the linear concentration of the molecules on the CNT. Statistical analysis of the distribution of L, performed on CNTs, revealed good agreement with the predicted law and allowed C to be extracted for each repetition. The results show that C varies linearly with the repetition times. This allows determining the linear concentration of grafted molecules on CNTs, so as to optimise the experimental conditions before proceeding to electronic devices.

Additionally double-decker molecules modified with pyrene were also used [65]. High-resolution transmission electron microscopy, emission spectroscopy and atomic force spectroscopy confirm grafting onto the CNTs using π–π stacking interactions. Additionally, due to the reducing intermolecular interaction, the anisotropy energy barrier and the magnetic relaxation time of the hybrid are both increased in comparison with the modified complex.

Another way to modify the molecular magnets is by addition of long alkyl chains. Such groups can form van der Waals interactions with the hydrophobic wall of a CNT, either with the chains lying along the CNT axis or by wrapping around its circumference. In both cases, the interactions are likely lower than in the previous case and can introduce lower perturbations on the electronic structure of the CNT.

The strategy of a covalent binding to CNTs is based on the presence of defects occurring inside CNTs (see Fig. 25). In the previous section, we assumed that the CNT walls are formed by a perfect honeycomb lattice, but present synthetic method does not usually yield perfect CNTs without defects. The defective sites can be used to form covalent bonds with modified molecular magnets, to obtain a stronger coupling between the molecular magnets and the CNTs than with non-covalent methods [66]. Defects are partly constituted by dislocations or changes in diameter or by missing carbon atoms inside the CNT walls and by the local severing of carbon bonds. Alternatively, pentagon–heptagon pairs (also known as Stone–Wales defects) and vacancies can be used as suitable reactive sites on the CNT walls. Treatment with inorganic acids, often performed in order to eliminate the catalyst used in the fabrication, can also cause a large amount of defects and should be considered with care. Even nonchemical treatments, such as ultra-sonication, electron beam imaging and AFM microscopy, can damage the CNTs and introduce additional defects.

Defective sites can be divided into three types: (i) sites of sp^3 hybridisation with hydrogen or hydroxide groups inserted into the defective site and oxidative defective sites with carbon atoms replaced by carboxylic groups on (ii) sidewalls or

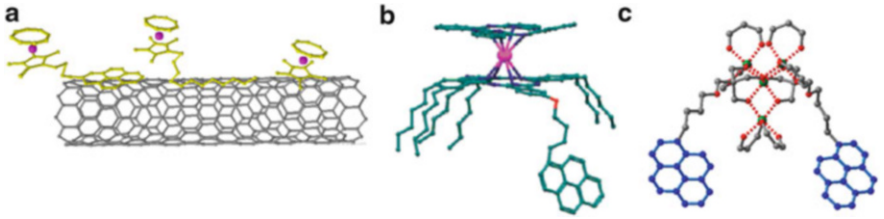

Fig. 25 (**a**) Strategies to graft molecular magnets onto a CNT using non-covalent binding. Modifying the ligands with tails containing polycyclic aromatic groups, i.e. pyrene, can attach the molecules via π–π stacking onto a CNT. Another way to modify the molecular magnets is by adding long alkyl chains to form van der Waals interactions with the hydrophobic wall of a CNT. Employing molecular magnets with aromatic substituents on the outer ligand shell can generate a comparable stronger interaction between the target molecule and the CNT. (**b**) The structure of the double-decker molecule with a terbium ion sandwiched in *centre*. One of the deckers is modified with pyrenyl and hexyl substitutions which is able to maximise the interaction with CNTs. (**c**) The structure of modified Fe_4 molecule using with pyrenyl substitutions which is able to maximise the interaction with CNTs and graphene

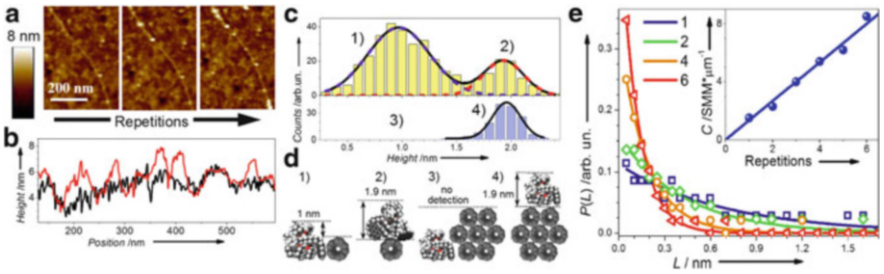

Fig. 26 (**a**) Sequential grafting of the Fe_4 molecular magnets with pyrene side groups on a single-walled carbon nanotube, as obtained from solution and observed with AFM topographic analysis. The same CNT is observed on repeating the grafting process: *left* one time, *centre* four times and *right* ten times. (**b**) Section profile along the same CNT before (*black line*) and after (*red line*) multiple grafting of 1. (**c**) Heights of the grafted objects. The statistics acquired on single CNTs or small bundles with diameter <1 nm (*yellow*; *1* and *2*; see (d)) differs from that acquired on CNTs or bundles with larger diameter (*blue*; *3* and *4*; see (d)). Lines are fittings with Gaussian distributions. (**d**) Corresponding different dispositions of (*1*) with respect to CNTs (*1* and *2*) or bundles (*3* and *4*). (**e**) Probability of finding a distance *L* between SMMs grafted on CNTs for sequential repetitions of the process. *Symbols* are experimental data for *1*, *2*, *4* and *6* repetition and lines are the corresponding fits. *Inset*: extracted linear concentration as a function of the number of repetitions of the process and linear fit. Reproduced with permission from Balasubramanian and Burghard [64]. Copyright 2009 John Wiley and Sons

(iii) terminal sites. Normally, terminal groups cannot be exploited for molecular spintronic devices for their difficulty in creating a two-lead device. Defects of sp^3 hybridisation can be difficult to exploit, because their chemistry has only been explored to attach organic appendages to a CNT but remain unused for binding metals or ligands. The most valuable defects are probably those terminating with

carboxylic group on the sidewall of CNTs. Little is known on how different chemical groups transmit spin interactions, and the chemistry of these different centres, together with that of molecular magnets, can be an invaluable tool to this aim.

These carboxylic groups can be de-protonated to afford a negative charge and can be used to obtain an electrostatic interaction with positively charged groups such as protonated amines. Molecular magnets with positively charged ligands are available, and they have been exploited to graft on the surface of CNT [67].

Ligand exchange reactions could also be used to bind a metal ion centre, e.g. a lanthanide one, to the carboxylic group. This can probably yield the highest possible coupling with the CNT.

One of the most important chemical properties of carboxylic groups is that they are able to form esters with hydroxyl groups and to form amides with amines, and both reactions can be used to graft molecular magnets that sport –OH or $–NH_2$ groups onto defective sites. The interesting point of this strategy is that, beyond forming a relatively strong coupling, by varying the spacer ligand containing hydroxyl or amine group, one can tune the coupling between the molecular magnets and the CNTs, which, as aforementioned, is a rather important goal in the creation of novel molecular spintronic materials.

7.2 Using Carbon Nanotubes

Most of the experiments carried out, until now, on the double-dot approach were performed using CNTs. In this scheme the molecular magnet is coupled to a state-of-the-art CNT transistor, composed of a single CNT, with good contacts to the leads and with a single-walled structure. The electric current in the nanotube is then used to probe and manipulate the spin of the molecular magnet, and the basic behaviour of the device will thus be connected to the physics of carbon-nanotube-based electronic devices. A CNT that behaves as a quantum dot may show, at low temperatures, an electronic behaviour connected to Coulomb blockade or Kondo effect (see Sect. 3). In this regime, the CNT is extremely sensitive to even the smallest fluctuations in its environment, such as the magnetisation reversal of a molecular magnet grafted onto it, with the means described in Sect. 7.1. The molecular magnets grafted for experiments in this direction were heteroleptic [$TbPc_2$] molecules functionalised with pyrene appendages on one of the deckers, as in Figs. 27c and 28a. The main observation performed up to now is the fact that the system can behave as a spin valve device (Fig. 28b), with a high-resistance and a low-resistance state available that can be tuned via the external magnetic field [61]. The main issue in these observations is that the system does not have any magnetic leads that can introduce a spin-polarised current into the device (as in Fig. 1). The observed data have thus been interpreted as a signature of the presence of multiple molecular magnets onto the nanotube. It has then been proposed that if two molecular magnets are coupled to a CNT via a π–π interaction, one can act as a

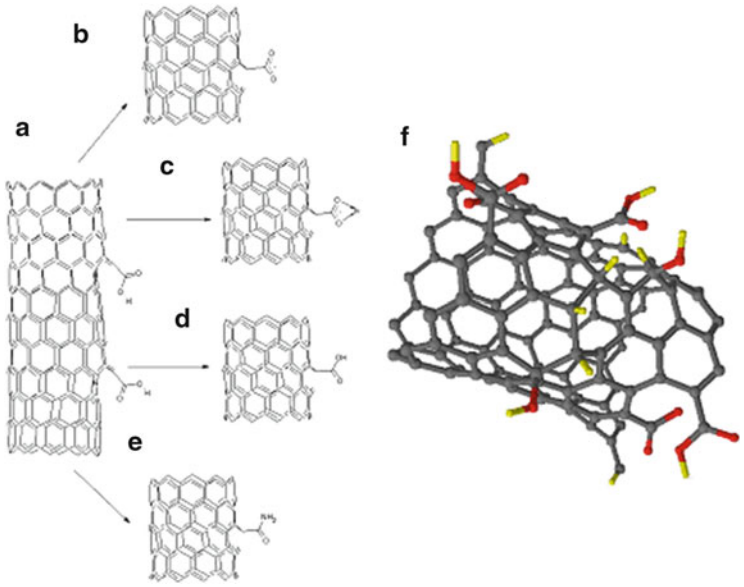

Fig. 27 (*Left*) Scheme of a number of useful reactions for the covalent binding of a group or a metal ion to defective sites of the CNT. (**a**) Carboxyl defects on a single-walled CNT exploitable for the grafting of molecular magnets. (**b**) Electrostatic interactions with positively charged molecules, i.e. protonated amines, used for anchoring nanomaterials to CNTs. (**c**) Direct ligand exchange interactions to bind complexes of metal ions. (**d**) Formation of an ester to covalently bind a ligand or desired molecule. (**e**) Formation of an amide group to form a covalent bond binding a molecular magnet. (**f**) Defects on a single-walled CNT exploitable for the grafting of molecular magnets. Oxygen atoms are depicted in *red*. Three types of defects are represented: sites maintaining sp^3 hybridisation with –H and –OH groups inserted into the defective site, oxidative defective sites with carbons replaced by –COOH groups on sidewalls and terminal sites, normally terminating in carboxyl groups

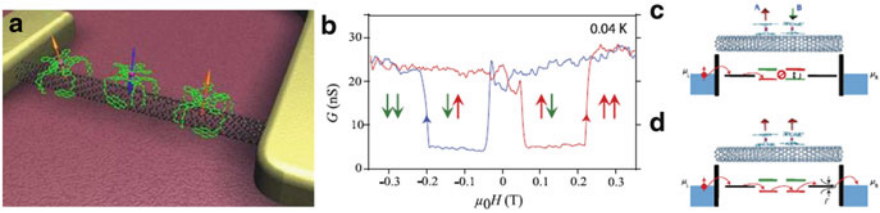

Fig. 28 (**a**) Spin valve configuration in a supramolecular spintronic device based on a carbon nanotube quantum dot functionalised with modified heteroleptic [$TbPc_2$] molecular magnets. (**b**) Butterfly hysteresis loop of the resulting spin valve behaviour at $T = 40$ mK. (**c**) Proposed mechanism for the switching of the device. Antiparallel spin configuration: the spin state in one dot is reversed with respect to that of the other dot. The energy mismatch between levels with identical spin results in a current blockade. (**d**) Parallel spin configuration for both molecular magnets. Energy levels with same spin are aligned, allowing electron transport through the carbon nanotube. Reproduced with permission from Shimada et al. [61]. Copyright 2011 Nature Publishing Group

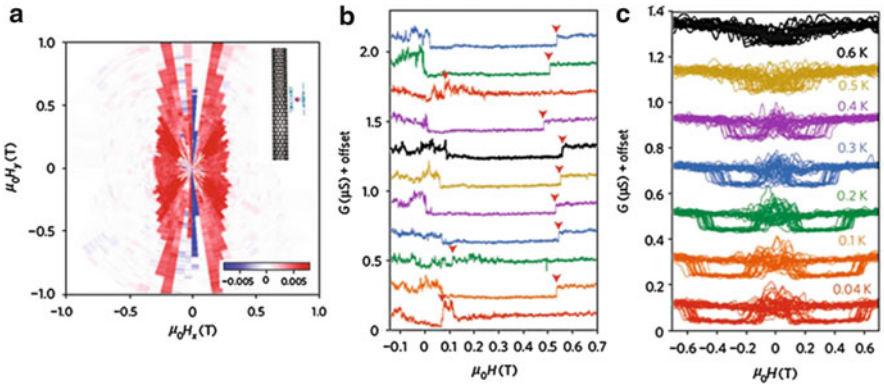

Fig. 29 Supramolecular spin valve and molecular fingerprint. (**a**) Angular dependence of the spin valve behaviour. The difference in conductance between the up- and downward magnetic field sweep in a hysteresis loop is plotted as a function of the magnetic field angle. For spins oriented parallel, the difference is negligible (*white*), whereas in an antiparallel configuration, the difference is nonzero (*red*). The *red–white boundary* corresponds to the switching field of the second molecule B and is consistent with the uniaxial anisotropy of the [$TbPc_2$] SMM. (**b**) Stochastic switching of molecule B. Three times out of 11, the molecule can switch its magnetisation by quantum tunnelling magnetisation, while 8 times out of 11, the reversal occurs by phonon-assisted magnetic relaxation as predicted by the Landau–Zener model. (**c**) 20 hysteresis loops at different temperatures. Reproduced with permission from Shimada et al. [61]. Copyright 2011 Nature Publishing Group

spin polariser and the other as an analyser, while both are sitting on the conducting channel where the electrons are transmitted through the CNT. This would imply that, despite the discrete level structure of the quantum dot, the magnetic moment of each molecule can locally induce a spin polarisation in the CNT, mediated by exchange interactions. At large negative magnetic fields, both molecular spins are oriented in the same direction and the quantum dot is in a high-conductance state. Upon increasing the magnetic field (red trace in Fig. 28b), one molecular spin is reversed by quantum tunnelling of magnetisation, resulting in an antiparallel spin orientation and lower conductance. When the external field is increased even further, the second molecular spin also flips, restoring a parallel spin orientation and raising, once again, the device conductance. The characteristic butterfly hysteresis loop of a spin valve could then be observed, and the extracted magnetoresistance ratio is up to 300% [61].

The presence of the characteristic magnetic behaviour of spin valve effect and the current switching exhibits the fingerprint like characteristics of the [$TbPc_2$] molecular magnets was then checked via repeated sweeping of the devices. Figure 29a shows the difference between upward (red) and downward (blue) sweeps of the magnetic field for different angles of application of the magnetic field. In the white regions (no difference), the two molecular magnets have the same polarisation, while in the red regions, the spins are oriented in opposite directions. The switching fields then become visible, and from the angular dependence, it can

be observed that the projection of the switching field along one axis (the easy axis) is constant, as expected for the uniaxial magnetic anisotropy of [$TbPc_2$]. The inherently stochastic character of the magnetisation reversal is shown by multiple hysteresis acquisitions (Fig. 29b), where the jumps are randomly distributed around certain positions. The temperature dependence also shows that the spin valve effect becomes less pronounced at higher temperatures, disappearing at 1 K. This behaviour shows strikingly good consistency to the one of crystalline [$TbPc_2$] molecular magnets [61]. In particular the exact coincidence of the blocking temperature with that of the thermal activation of the crystalline system is surprising, as one might expect the different phononic bath present in the device to play a role as observed, for example, for graphene (see Sect. 7.3). This and the exact source of the coupling mechanisms constitute stimulating points that warrant further investigation into such double-dot devices.

7.3 Using Graphene

In addition to CNTs, another useful substrate for the creation of molecular spintronic devices with the double-dot scheme is graphene. Graphene displays several unique properties, such as the presence of extremely high electron mobilities, interesting mechanical and optical properties and relativistic-like particles [68–70]. Several reviews on graphene are available, for the interested reader [68–70], and here we will simply state the presence of the behaviours of interest, when necessary, without explaining their origin.

The creation of hybrid materials containing graphene and molecular magnets has followed the directions shown in Sect. 7.1. In particular, pyrene groups and stacking interactions have mainly been used for the grafting of the molecular objects on surfaces, and all molecular materials shown in Fig. 27 have led to the creation of molecular hybrids based on graphene. The Tb double-decker complexes [$TbPc_2$] have been deposited onto graphene, although with multilayers and aggregated formations on the surfaces. As graphene usually has very high mobility, it is very difficult to obtain a direct effect of the adsorbate on the electron transport, without resorting to special techniques. The present approach has focused on confining the graphene electrons via nanostructuring (Fig. 30). A graphene nanostriction was developed via nanofabrication techniques, and a multilayer system was then deposited on the device [71]. The resulting electronic properties showed the influence of the spin states of the molecular complexes. In particular, a spin valve-like effect could be observed, with varying conduction depending on the magnetisation state of the deposited molecules. A hysteresis loop was then observed at very low temperatures, again with characteristics that match perfectly those of the homologous crystalline compound. The behaviour of the device was interpreted as due to interaction with the graphene layer through a dipolar magnetic field. The Tb(III) ion would then produce a dipolar stray field of about 2 kOe. The resulting magnetic

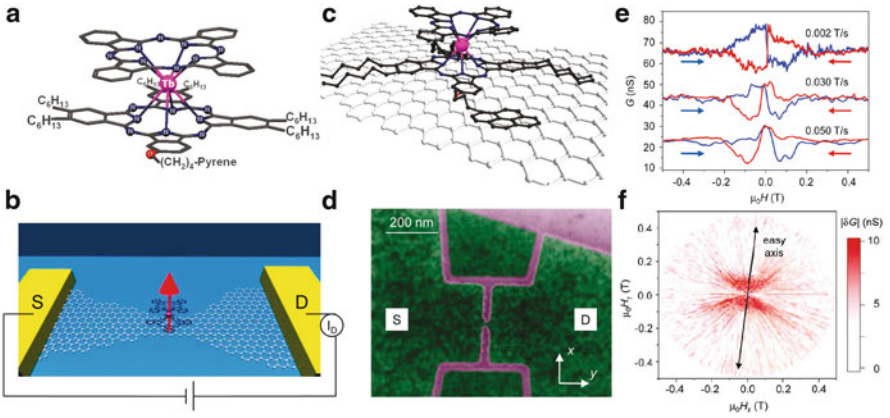

Fig. 30 (**a**) Schematic representation of the [$TbPc_2$] single-molecule magnet used for grafting. (**b**, **c**) Schematic view of the device, showing in (b) the molecule attached to graphene and in (c) the nanoconstriction contacted by source and drain electrodes. (**d**) False-colour SEM image of the device. SiO_2 substrate and etched graphene are coloured in *purple*. Graphene conductive regions are coloured in *green*, with source and drain electrodes indicated. (**e**) Differential magnetoconductivity *G* obtained at fixed back-gate voltage *Vg* for different field sweep rates. The curves are shifted vertically for clarity. The hysteresis loops are weakly depending on the field sweep rates and remain open for very slow rates. When the field is swept very slowly, the jump of the conductivity is straighter and the hysteresis can begin even before zero field. The behaviour is in agreement with what is expected from magnetisation measurements on crystal samples. (**f**) *Colour plot* of the difference between trace and retrace for different directions of the magnetic field in the plane of graphene. The *border between the red regions and the non-coloured ones* represents the fields at which the hysteresis loop is closing. The behaviour is typical for magnetic systems with uniaxial anisotropy and the easy axis is indicated. Along the hard direction (perpendicular to the easy axis) no hysteresis is observed as the magnetic field is not high enough to reverse the magnetisation of the system. Reproduced with permission from Geim and Novoselov [71]. Copyright 2011 American Chemical Society

field profile for a large ensemble of molecules would be highly inhomogeneous and would influence the tunnelling of the conducting electrons through striction [71].

Other magnetic hybrids made of graphene and Fe_4-based molecular magnets showed a marked effect of the Dirac electrons on the magnetic properties of the system [72]. In particular, the zero-field tunnelling rate was shown to be strongly affected by the interaction with graphene, with fingerprints of the threefold symmetry of the electronic density of states of the layer. Such interactions were shown to amplify the tunnelling rate by orders of magnitude, leading to an increased quantum relaxation. The particularly strong effects produced by Dirac electrons were shown to lead the molecular magnet system into a different tunnelling regime, called Villain's tunnelling, where the spin coherently resonates between the two energy potential wells. Additionally, a clear effect of the modified phononic bath could be observed, and a general relation connecting the thermal relaxation of molecular magnets in a three-dimensional crystal to that of a deposited system could be obtained. All these effects were shown to be suppressed as soon as the

system is aggregated on the graphene surface, so that the electronic potential is partially shielded and the phononic bath is closer to that of a crystalline system.

8 Conduction Paths in Multi-molecule Systems

It should be noticed, anyway, that there is no absolute necessity to use single molecules to have a spintronic device based on molecular magnets. The main reason to use single molecules lies in the clarity of the information gained and in the interest of obtaining devices that are truly working at the molecular basis. On the other hand, in principle, several of the effects discussed can also be observed for multi-molecule assemblies. If the assembly is small enough, i.e. in the nanometre scale, the behaviour can even differ markedly from that of bulk systems, and even from that of single-molecule electronics, as discussed in Sect. 2. In this intermediate regime, the conductance of the devices is not purely quantistic but is also still affected by the very small distances between electrodes and the presence of strong confinement effects.

One of the first approaches, and an elegant one, was creating an organic field-effect transistor, i.e. an organic element whose transport characteristics can be modulated by an external electrical field. Top- and bottom-contacted thin-film organic field-effect transistors could be made out of [$TbPc_2$] systems [33], showing p-channel characteristics, and out of [$TbPc_2$], showing amphi-polar behaviour. This provides a very good starting point for the conception and design of molecular magnets with electron transport properties for organic field-effect transistors. On the other hand, the relationship between the observed electronic transport properties and the thin-film structure will likely necessitate further investigation. The possibility of obtaining spintronic properties is appealing and seems particularly promising because of the presence of a conduction path that includes radical systems with unpaired electrons.

Additional studies have focused on the possibility of using organic radical systems. Usually, molecular crystals of organic radicals are Mott insulators because of their large on-site Coulomb repulsion, notwithstanding the presence of a singly occupied molecular orbital. When radicals are partially doped, the unpaired electron of the radical usually becomes oxidised, and the resulting material is diamagnetic. The “spin-polarised donor” approach has allowed solving some of these issues, by using one-electron oxidation at the highest unoccupied molecular orbital, rather than at the singly occupied molecular orbital [73]. This produces a ground-state triplet diradical cation. The most notable example of such systems, in our opinion, is the diselena analogue, a dibrominated benzo-tetrathiafulvalene containing a nitronyl nitroxide (NN) group (Fig. 31).

The temperature dependence of the magnetic susceptibility was well explained by considering one-dimensional ferromagnetic chains with intra-chain and interchain interactions. Crystals of the material were found to be conductive upon hole injection from electrodes, even at low temperatures, and it is remarkable that

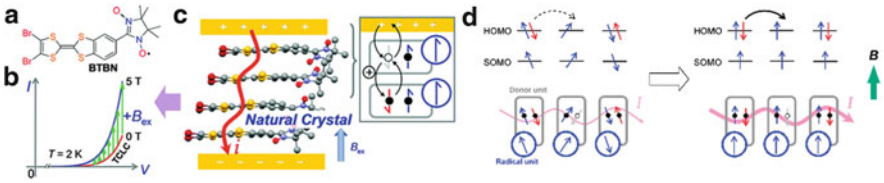

Fig. 31 (**a**) Structure of the molecular conductor based on nitronyl nitroxide and tetrathiafulvalene moieties that displays the negative magnetoresistance properties. (**b**) Magnetoresistance effect measured at 2 K, showing the increase in conductance at 50 kOe. (**c**) Sketch of the geometry used for the transport experiments, showing the arrangement of the molecular film between the electrodes and the electron transfer processes occurring. (**d**) Scheme of the proposed different spin scattering mechanisms occurring in the system without (*left*) and with (*right*) the external magnetic field. Reproduced with permission from Cervetti et al. [73]. Copyright 2010 American Chemical Society

the conductance of the crystal could be controlled by the application of an external magnetic field [73]. Below 30 K the resistance of the sample decreased upon application of a magnetic field, and the sample exhibited negative magnetoresistance of 76% at 2 K (Fig. 31b). The temperature at which the magnetoresistance appears, 30 K, was observed to correspond to the degree of interaction between the conduction electrons and the organic localised spins. Conduction electrons, which can be scattered by the thermally fluctuating paramagnetic spins of the radical sites, can become less scattered when the external magnetic aligns the localised spins parallel to the external field. Control experiment using crystals of the non-radical precursor exhibited very low positive magnetoresistance.

Very recent results have also been capable of distinguishing the presence of intra- and intermolecular conduction pathway effect. Such investigations have been carried out with combined ultrafast optical measurements and high-resistivity transport measurements [74] on molecular magnetic tori composed of Fe and rare-earth metallic centres, connected by organic ligands in a rather complex and beautiful pattern (Fig. 32). The relevant electronic processes were identified as vibrational cooling and fast conversion towards shallow states, followed by electron-hole recombination modulated by the presence of the rare earths. Space-charge limited currents were identified as fundamental processes in such magnetic molecular crystals. The hopping mechanism from one molecule to another was found to be strongly affected by the presence of traps, and several types of traps were identified. By changing the rare-earth places into the molecular tori, a clear distinction between Kramers and non-Kramers ions could be observed, with the former showing much higher charge densities and electron mobilities. This intriguing distinction holds for both intra- and intermolecular processes and remains to be investigated in detail by theoretical methods.

Eventually it is fundamental to observe that the use of multimolecular assemblies can allow the creation of molecular spintronic devices working at room temperature. A brilliant experiment was designed using a neutral planar phenalenyl-based molecule, zinc methyl phenalenyl (ZMP, $C_{14}H_{10}O_2Zn$;

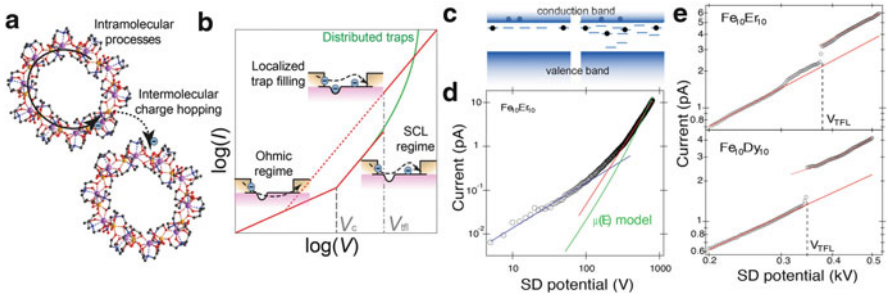

Fig. 32 (**a**) Scheme of the molecular tori investigated and of the hopping transport mechanism, showing the intra- and intermolecular electron mobility. (**b**) Expected behaviour for space-charge limited transport, with the schematic representation of the relevant effects observed in different voltage regions. The effects of exponentially distributed (*green*) and localised-energy (*red*) traps are also shown. Examples of trapping effects, as observable in the *I*/*V* characteristic curve. (**c**) Schematic depiction of localised traps (*left*) and energetically distributed traps (*right*) placed between the valence and conduction bands of the system. (**d**) Exponentially distributed traps in $Fe_{10}Er_{10}$ inducing a voltage dependence with an exponent larger than 2. Comparison between a trap-free surface-charge-limited (SCL) (*red line*) and a field-dependent mobility model (*green line*) is provided. (**e**) Localised electron traps in $Fe_{10}Er_{10}$ (*top*) and $Fe_{10}Dy_{10}$ (*bottom*). The trapped-charge limited regime (*solid red*) and the trap-free SCL regime (*dotted red*) are shown, and the trap-filled limit V_{TFL} is highlighted with *dashed vertical lines*. Reproduced with permission from Komatsu et al. [74]. Copyright 2014 John Wiley and Sons

Fig. 33a), that has no net spin [75]. By growing these molecules on a ferromagnetic surface, interface spin transfer causes a hybridised organometallic supramolecular magnetic layer to develop, which shows a very large magnetic anisotropy and spin-filter properties. This interface layer creates a spin-dependent resistance and gives rise to an interface magnetoresistance effect. The interface magnetoresistance response was observed in a vertical device made of a ZMP thin film on a Co surface connected with Cu on top. The nonlinear current–voltage behaviour of the device shows that tunnelling is the dominant transport mechanism, providing a magnetoresistance signal close to 25%. As bulk magnetism in ZMP can be ruled out, the observations indicate an interfacial phenomenon as responsible for the interface magnetoresistance effect. Magnetoresistance measurements performed on a magnetic junction structure, made by replacing Cu with permalloy (Fig. 33c) and by inserting an ultrathin Al_2O_3 layer at the bottom interface, indicate a nonconventional switching behaviour with the necessity of a direct contact between the molecular layer and the ferromagnetic surface. The behaviour could be modelled by ab initio methods, showing that the presence of an interaction between the magnetic surface and the molecular multilayer is fundamental to observe the interface magnetoresistance. In particular the presence of more than one molecule along the conduction channel is fundamental for the development and the magnitude of the behaviour. In this sense, the effect could not exist if a monolayer or a single molecule were employed in the device, nicely showing how a molecular spintronic device can be built out of multimolecular devices. As the behaviour was

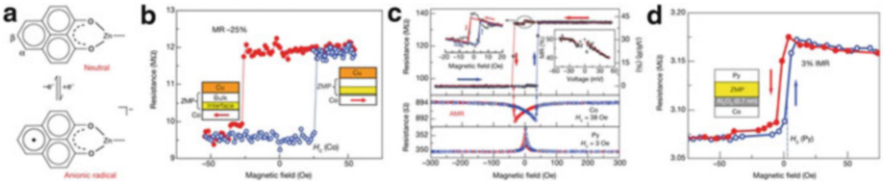

Fig. 33 (**a**) Molecular structure of zinc methyl phenalenyl (*ZMP*) in a neutral state with no net spin (*top*). Charge transfer processes through hybridisation on the ferromagnet surface can change the chemical state of the phenalenyl moiety from neutral to an anionic radical (*bottom*) with net moment. (**b**) Magnetoresistance measurements (data points) of a device with a single ferromagnetic electrode (Co (8 nm)/ZMP (40 nm)/Cu(12 nm)), measured at 15 mV after cooling the device to 4.2 K in a 550 Oe magnetic field. *Blue* and *red data points* refer to positive and negative field sweeps respectively. The *solid lines* are guides to the eye. The magnetoresistance loop corresponds to the switching of the Co magnetisation, as shown in the two *insets*, with respect to the hard magnetic layer forming at the interface (*yellow*). *Left* and *right insets* show the Co magnetisation pointing in the negative and positive directions, respectively. (**c**) *Top panel*, magnetoresistance measurements (*black data points*) on a Co (8 nm)/ZMP (35 nm)/Py (12 nm) device (at 25 mV) show independent interface magnetoresistance response of both the *bottom* Co/ZMP interface and the *top* ZMP/Py interface around zero field. *Left inset*, zoomed-in view showing low field scan. *Right inset*, IMR of bottom Co/ZMP interface versus applied bias shows a flat response under low bias conditions with a maximum of 50% in negative bias. *Middle* and *bottom panels* show AMR measurements of Co and Py electrode, respectively. (**d**) Magnetoresistance measurements on an interface-modified junction, Co (8 nm)/Al_2O_3 (0.7 nm)/ZMP (30 nm)/Py (12 nm), due only to Py switching (data points). The *blue* and *red curves* refer to positive and negative field sweeps, respectively, and *arrows* show sweep direction. Reproduced with permission from Baniodeh et al. [75]. Copyright 2013 Nature Publishing Group

observed up to near room temperature (~250 K), these results indicate a possible way of obtaining molecular spintronic devices with real-life and immediate applications [75].

Conclusions

In this chapter we have shown some of the bulk of results that start appearing about molecular spintronic devices. The results already allowed implementing most of the detection schemes that were predicted to exist, indicating that single-molecule effects are observable. Several problems remain open, though. The main issue, in our view, is related to the fact that the mechanisms via which the spin can exert an influence on the transport properties are not univocally determined. Several future studies will likely focus on this. At the same time, the effect of the environment seems to have been underrated, in previous studies, and might constitute a fundamental point of great interest for both the chemistry and physics communities. A few perspectives in this direction already exist [76], and the interested reader is redirected to them for details.

(continued)

Another important point that is surfacing is the fact that, despite all the attention focused on single-molecule effects, multimolecular systems can actually produce extremely valuable effect, which may open the way to room-temperature applications of molecular magnets for spintronics. The investigation of the intra- and intermolecular transport channels and of the interface effects in molecular materials may thus become of primary importance for the creation of novel functional molecular spintronic systems.

Eventually we wish to mention that this large amount of experimental work has been continuously sustained by a concomitant theoretical effort, which we did not cover here. In several cases the new theoretical schemes have been directly compared to the data, by using numerical calculations or analytical theories. On some other occasions, on the other hand, theoretical work has been faster than the experimental one, mainly owing to the many difficulties in obtaining clean experiments, to the time required by setting up systems capable of measuring the molecular properties in the desired way, and by the general slow pace of investigations that require careful checks over purity and stability conditions. It will be extremely interesting to see if the theoretical and experimental results can be positively intertwined, as already happened for the case of the study of molecular anisotropy via transport measurements, for example. Such a synergy, which is already showing its effects also for room-temperature molecular effects, could soon determine an even faster growth in this already fast paced and extremely challenging area.

Acknowledgements We acknowledge financial support from German DFG, the BW Stiftung (Kompetenznetz Funktionelle Nanostrukturen), the AvH Stiftung (Sofja Kovalevskaja Award), the IMPRS-AM and EU ERC-StG-338258-"OptoQMol".

References

1. Baibich MN et al (1988) Phys Rev Lett 61:2472
2. Binasch G et al (1988) Phys Rev B 39:4828
3. Žutić I, Fabian J, Das Sarma S (2004) Rev Mod Phys 76:323
4. Nature Materials (2012) http://www.nature.com/nmat/insight/spintronics/index.html
5. Felser C, Fecher GH (eds) (2013) Spintronics: from materials to devices, vol XXI. Springer, Netherlands, p 369
6. Popa PL et al (2014) Proc Natl Acad Sci USA 111:10433
7. Seneor P, Bernand-Mantel A, Petroff F, Phys J (2007) Condens Matter 19(165222)
8. Cuevas JC, Sheer E (2010) Molecular electronics: an introduction to theory and experiment, World scientific series in nanotechnology and nanoscience. World Scientific Publishing Company, Singapore
9. Launay JP, Verdaguer M (2014) Electrons in molecules: from basic principles to molecular electronics. Oxford University Press, Oxford
10. Kouwenhoven LP et al (2001) Rep Prog Phys 64:701

11. Nature Nanotechnology (2013) http://www.nature.com/nnano/focus/molecular-electronics/index.html
12. Gatteschi D, Sessoli R, Villain J (2006) Molecular nanomagnets. Oxford University Press, New York
13. Liang W et al (2002) Nature 417:725–729
14. Kastner MA (1993) Phys Today 46:24
15. Domingo N et al (2012) Chem Soc Rev 41:258–302
16. Park H et al (1999) Appl Phys Lett 75:301
17. Bogani L, Wernsdorfer W (2008) Nat Mater 7:179–186
18. Cornia A et al (2011) Chem Soc Rev 40:3076
19. Mannini M et al (2008) Chemistry 14:7530–7535
20. Barth JV et al (2005) Nature 437:671
21. Ertl G (2008) Angew Chem Int Ed 47:3524
22. Buchholtz J et al (1977) J Chem Phys 66:573–580
23. Kanai M et al (1995) Surf Sci 329:L619–L623
24. Lippel PH et al (1989) Phys Rev Lett 62:171
25. Warner M et al (2013) Nature 503:504–508
26. Kahle S et al (2011) Nano Lett 12:518–521
27. Lämmle K et al (2010) Nano Lett 10:2965
28. Khajetoorians AA et al (2013) Science 339:55–59
29. Liu J et al (2013) J Am Chem Soc 135:651
30. Koivisto BD, Hicks RG (2005) Coord Chem Rev 249:2612–2630
31. Zhang Y et al (2013) Nat Commun 4:2110
32. Caneschi A et al (1991) Prog Inorg Chem 39:331–429
33. Ishikawa N et al (2003) J Am Chem Soc 125:8694–8695
34. Katoh K et al (2009) J Am Chem Soc 131:9967–9976
35. Katoh K et al (2010) Dalton Trans 39:4708–4723
36. Katoh K et al (2012) Chem Asian J 7:1154
37. Komeda T et al (2013) ACS Nano 7:1092
38. Vitali L et al (2008) Nano Lett 8:3364
39. Liu L et al. http://arxiv.org/ftp/arxiv/papers/1310/1310.8436.pdf
40. Müllegger S et al. http://arxiv.org/pdf/1403.7035.pdf
41. Miyamaki T (2012) Nat Commun 3:938
42. Gopakumar TG et al (2012) Angew Chem Int Ed 52:3796
43. Komeda T et al (2011) Nat Commun 2:217
44. Loth S et al (2012) Science 335:196
45. Heintze E et al (2013) Nat Mater 12:202
46. Heersche HB et al (2006) Phys Rev Lett 96:206801
47. Jo MH et al (2006) Nano Lett 6:2014
48. Mannini M et al (2008) Chem Eur J 14:7530
49. Park J et al (2002) Nature 417:722–725
50. Mannini M et al (2009) Phys Rev Lett 8:194
51. Mannini M et al (2010) Nature 468:417
52. Accorsi S et al (2006) J Am Chem Soc 128:4742
53. Bartolomé J et al (eds) (2014) Molecular magnets, nanoscience and technology. Springer, Berlin
54. Zyazin AS et al (2011) Synth Met 161:591
55. Burzuri E et al (2012) Phys Rev Lett 109:147203
56. Misiorny M et al. http://arxiv.org/pdf/1407.5265v1.pdf
57. Zyazin AS et al (2010) Nano Lett 10:3307–3311
58. Vincent R et al (2012) Nature 488:357
59. Thiele S et al (2014) Science 344:6188
60. Wagner S et al (2013) Nat Nanotechnol 8:575

61. Shimada H et al (2003) J Appl Phys 93:8259–8264
62. Urdampilleta M (2011) Nat Mater 10:502
63. Sun YP et al (2002) Acc Chem Res 35:1096–1104
64. Balasubramanian K, Burghard M (2005) Small 1:180–192
65. Bogani L et al (2009) Angew Chem Int Ed 48:746–750
66. Klyatskaya S et al (2009) J Am Chem Soc 131:15143–15151
67. Da Jiang S et al (2012) Sci China Chem 55:867
68. Bosch-Navarro C et al (2012) Adv Funct Mater 22:373
69. Castro Neto AH et al (2009) Rev Mod Phys 81:109–162
70. Das Sarma S et al (2011) Rev Mod Phys 83:407–470
71. Geim AK, Novoselov KS (2007) Nat Mater 6:183–191
72. Candini A et al (2011) Nano Lett 11:2634–2639
73. Cervetti C et al (to appear) Nat Mater
74. Komatsu H et al (2010) J Am Chem Soc 132:4528–4529
75. Baniodeh A et al Adv Funct Mater 24:6280–6290. doi:10.1002/adfm.201400336
76. Raman KV et al (2013) Nature 493:509–513
77. Cervetti C et al (2014) Dalton Trans 43:4220–4232

Struct Bond (2015) 164: 383–430
DOI: 10.1007/430_2014_145

Published online: 22 May 2014

Quantum Computation with Molecular Nanomagnets: Achievements, Challenges, and New Trends

Alberto Ghirri, Filippo Troiani, and Marco Affronte

Abstract Molecular nanomagnets exhibit quanto-mechanical properties that can be nicely tailored at synthetic level: superposition and entanglement of quantum states can be created with molecular spins whose manipulation can be done in a timescale shorter than their decoherence time, if the molecular environment is controlled in a proper way. The challenge of quantum computation is to exploit the similarities between the coherent manipulation of molecular spins and algorithms used to process data and solve problems. In this chapter we shall firstly introduce basic concepts, stressing analogies between the physics and the chemistry of molecular nanomagnets and the science of computing. Then we shall review main achievements obtained in the first decade of this field and present challenges for the next future. In particular we shall focus on two emerging topics: quantum simulators and hybrid systems made by resonant cavities and molecular nanomagnets.

Keywords Decoherence and relaxation times · Hybrid quantum systems · Molecular spin qubits · Quantum simulators · Quantum Computation

Contents

A. Ghirri and F. Troiani
Istituto Nanoscienze – CNR, Centro S3, via Campi 213/a, 41125 Modena, Italy

M. Affronte (✉)
Istituto Nanoscienze – CNR, Centro S3, via Campi 213/a, 41125 Modena, Italy

Dipartimento di Fisica, Informatica e Matematica, Università di Modena e Reggio Emilia, via Campi 213/a, 41125 Modena, Italy
e-mail: marco.affronte@unimore.it

1 Introduction

Quantum computation exploits tight similarities between the time evolution of a quantum system and some algorithms. This parallelism is essentially given by the mathematical description that accounts – at the same time – for the dynamics of the quantum system and for the calculation rules on which the algorithm relies. Experimentally, performing quantum computation implies to control the dynamics of the quantum system under the action of an external stimulus. Thus, defining the *input* of the calculation means to prepare our system in a given quantum state, processing data means to let our system evolve under the action of a given stimulus and reading the *output* stands for measuring the final quantum state of our system. It is clear that basic requirements for a system to be used as quantum computer are the description of its states and the full control of its dynamics in terms of both modeling and experimental procedures. On the other hand, quantum computation exploits specific characteristics of quanto-mechanics, like superposition and entanglement of quantum states; thus, it results to be more efficient than classical computers in solving a number of computationally complex problems. Starting from the suggestive intuition (the aforementioned parallelism) of Richard Feynman in the 1980s, several quantum systems, such as isolated atoms or ions, photons, electrons in quantum dots or superconducting circuits, have been successfully used to encode quantum bits (*qubit*). Spins are also excellent quantum systems for which both mathematical description and experimental tools for their manipulation have been largely developed.

The spin of molecular clusters may also work well for qubit encoding if we are able to manipulate them as quantum objects. As a matter of fact, the first proposal to

use molecular nanomagnets for quantum computation appeared in 2001 when the field of molecular magnetism achieved its maturity with the Agilent Technology Europhysics Prize awarded to Sessoli, Gatteschi, Wernsdorfer, Barbara, and Friedman for their discovery of Quantum Phenomena in molecular nanomagnets (2002). At that time quantum phenomena were primarily studied by magnetization measurements in different conditions. Pulsed ESR experiments at very low temperatures are required to manipulate electron spins in molecules and this introduced new experimental challenges. On the other hand, theoreticians immediately realized the huge potentialities of arranging spins in well-defined architectures like those provided by molecular assemblies and new challenges have been proposed to synthetic chemists since then. After one decade from its start, several important results have been obtained: the decoherence time has been measured on several molecular nanomagnets and different molecules have been designed and synthesized with inspiration to computing schemes.

In this chapter, we firstly introduce some fundamentals and then we review achievements obtained so far. No ambition to be exhaustive since this new field is strongly interdisciplinary and in rapid evolution. We shall rather focus on these questions: how a given molecular spin cluster fits a specific quantum scheme? Which are the advantages in using molecular spins with respect to other quantum systems to encode qubits? How far can a molecule be engineered in order to preserve the spin dynamics from the environmental noise? How should we assemble molecular spins in order to fabricate complex quantum devices?

The chapter is organized as follows: in Sect. 2 we summarize some basic concepts while we refer the reader to textbooks for a systematic presentation of quantum computation [1, 2] and for a detailed description of the spin dynamics [2, 3]. In Sect. 3 we discuss the problem of understanding and controlling the mechanisms of decoherence which limit the spin dynamics in molecular nanomagnets; in Sect. 4 we introduce concept of entanglement and we discuss superposition of quantum states in molecular spin clusters. In Sect. 5 we review results and specific proposals involving molecular spin clusters. The last two paragraphs are devoted to two emerging areas (trends): in Sect. 6 we introduce the idea of quantum simulators, i.e. small quantum computers dedicated to efficiently solve specific problems; finally in Sect. 7 we overview the possibility to link molecular spin clusters with other quantum systems in order to realize hybrid quantum devices. Finally, in the last paragraph we summarize the results and try to highlight open questions.

2 Spin Qubits

While for classical bits only two states 0 or 1 are possible, a qubit can exist as a superposition states: $|\Psi\rangle = \alpha|0\rangle + \beta|1\rangle$, being $|0\rangle$ and $|1\rangle$ two eigenvalues representing a basis of the two-level system. In this representation, any unitary transformation that acts on the wavefunction $|\Psi\rangle$ can work as a quantum gate. A spin 1/2 is a

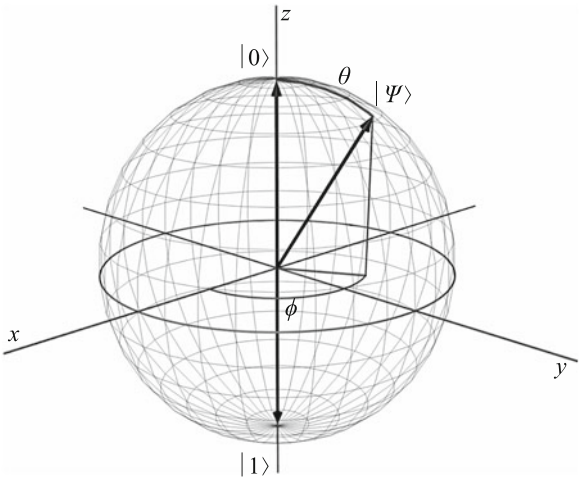

Fig. 1 Representation of the Hilbert space of a two-level system on the Bloch sphere. The eigenstates $|\uparrow\rangle$ and $|\downarrow\rangle$ of the Pauli matrix σ_z correspond to the basis states $|0\rangle$ and $|1\rangle$. A point on the Bloch sphere with polar coordinates θ and ϕ corresponds to a superposition of $|0\rangle$ and $|1\rangle$

prototypical case. The spin components along three perpendicular directions follow the commutation rules given for angular momentum. The Pauli operator $\hat{\sigma}$ with components:

$$\sigma_x = \begin{pmatrix} 0 & 1 \\ 1 & 0 \end{pmatrix}, \quad \sigma_y = \begin{pmatrix} 0 & -i \\ i & 0 \end{pmatrix}, \quad \sigma_z = \begin{pmatrix} 1 & 0 \\ 0 & -1 \end{pmatrix},$$

satisfy such conditions and are the proper tools to describe the spin operator $\hat{\mathbf{S}} = \hbar\hat{\sigma}/2$. We can fix the z-direction by an applied magnetic field $\mathbf{B}_0$. Two eigenstates of the σ_z operator are the $|\uparrow\rangle$ and $|\downarrow\rangle$ states, i.e. the spin lying along or opposite to the magnetic field direction. In this context, qubits are well represented by spinors, i.e. any superposition: $|\Psi\rangle = \alpha|\uparrow\rangle + \beta|\downarrow\rangle$ with $|\alpha|^2 + |\beta|^2 = 1$. It is also convenient to visualize spinors by points on a Bloch sphere profiting from the correspondence with vectors $\sin(\theta/2)|\uparrow\rangle + \cos(\theta/2)e^{i\phi}|\downarrow\rangle$ (Fig. 1).

Quantum gates operating on single-spin qubit are elementary rotations along particular directions as we shall see in Sects. 5 and 7 in more detail. We can now realize that spin impurities in solids and nuclear spins in solution can be considered as natural candidates for qubits encoding and the required tools – algebra and experiments – to control their dynamics have been largely developed. Nuclear spins are generally well isolated from the environment and can maintain free rotation for seconds even at room temperature, but it is hard to detect their small magnetic moment. Electron spins can be detected more easily but they are linked to the environment more closely and several damping mechanisms limit their free rotations.

We mentioned $S = 1/2$ but one may wonder whether *higher* spins can also be used to encode quantum bit. Certainly yes, if we identify two sub-levels, for instance two m-states of the ground multiplet and the allowed transition related to these sub-levels. There are also (quantum) algorithms that require multi-level

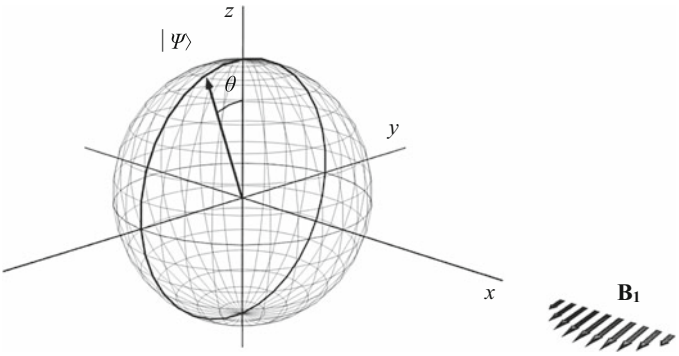

Fig. 2 Representation of spin rotation using the Bloch sphere. This rotation can be generated by the action of a magnetic pulse $\mathbf{B}_1$. In this case, for $\theta = \pi$, the rotation represents a NOT-gate inducing a spin flip

registers, thus one can also try to exploit more sub-levels in a high-spin multiplet. Generally speaking, the use of high spin may facilitate the manipulation and the measurement of the final state but high spins are more sensible to the environment, thus a tradeoff needs to be found taking into account also the specific computational scheme.

A quantum computer can be designed to solve different types of problems. Similarly to classical computers, two possible strategies can be adopted: the first one is to build a "universal" computing machine versatile enough to solve – in principle – any type of problem. Alternatively, one can identify specific classes of problems and design specialized quantum machines that result in being more efficient than any classical analogue for that task. In both cases, quantum computers are designed to perform sophisticated quantum algorithms. Like for the classical ones, it is convenient to decompose complex algorithms in sequences of elementary (quantum) gates. Thus the first problem is to identify a set of gates which can be combined to perform more complex algorithms and therefore to constitute the basis for a universal quantum computer. Keeping this scheme in mind, we can now describe quantum operations with spins.

Basic operations on single qubit are given by rotations of the spin about arbitrary directions in the space. Elementary rotations of an angle θ around the x-axis can be described by using the Pauli matrices:

$$R_x(\theta) = e^{-i\theta\sigma_x/2}; \tag{1}$$

or – equivalently – by the matrix:

$$R_x(\theta) = \begin{bmatrix} \cos(\theta/2) & -i\sin(\theta/2) \\ -i\sin(\theta/2) & \cos(\theta/2) \end{bmatrix}. \tag{2}$$

Again, the Bloch sphere helps us to visualize these rotations (Fig. 2) and this is a useful tool to understand how a simple quantum gate actually works on a spin qubit.

Table 1 Truth table of the Controlled-NOT gate. The first qubit acts as control while the second is the target: the target qubit is flipped if and only if the control is set to 1

Input	Output
$\|00\rangle$	$\|00\rangle$
$\|01\rangle$	$\|01\rangle$
$\|10\rangle$	$\|11\rangle$
$\|11\rangle$	$\|10\rangle$

In practice, a spin flip is obtained by electromagnetic pulses with the magnetic field component along the suited axis (see Sect. 7 for further discussion).

In analogy with the classical ones, a convenient way to represent gates is to provide the so-called *truth table* which gives the final state for each possible combination of initial states.

Next we need to perform gates involving two or more qubits. One qubit is chosen as *control* while the other(s) are considered as *target*(*s*) in such a way that the final state of target is determined also as a function of the initial state of the control. For instance, a basic two-qubit gate is the control-NOT (CNOT) that operates as described by the truth table (see Table 1). Qubit–qubit coupling is an essential resource to build multi-bit quantum gates. That is why it is important to control inter-molecular interaction and spin entanglement in molecular assemblies as described in the Sect. 4. Moreover since the implementation of both single- and multi-qubit gates requires a dynamical control of such interactions, fast molecular switches or protocols to switch the coupling between spin clusters are also of great interest for the realization of multi-bit gates.

The key point here is that it is demonstrated that any unitary operation on *n*-qubits can be implemented by a sequence of single-qubit and CNOT gates. Equivalent universality can be proved with other sets of elementary operations of one- and two-qubit gates [1]. This is an important result that suggests to focus effort in proving the feasibility of elementary quantum gates with new qubit candidates like molecular nanomagnets.

In principle, there are many other quantum algorithms of interest. Yet, not for many of them it has been proved that they are more efficient than classical analogues. That's why the interest is generally focused on few of them which become popular for their proven efficiency.

A first one is the Shor's algorithm that is based on the quantum Fourier transform of a given set of N states. The algorithm increases exponentially its efficiency with respect to a classical computer by exploiting both the superposition and the entanglement of quantum states. The Fourier transform allows to solve a large class of problems including the factoring in prime numbers. Worth to be mentioned here is a very nice experiment that proved the ability to factorize the number 15 has been realized by NMR with nuclear spins [4]. Factorization of larger numbers (143) has been recently demonstrated by implementing an adiabatic approach [5].

A second class of problems that quantum computers have been proved to solve more efficiently than classical ones is the search of items in an unsorted database of N entries. Schematically the problem can be simplified as follows: suppose we have

to find a number in a phonebook. A classical computer splits the database into two and finds the part where the number is and it will proceed like this until the requested number is found. In 1996, Lev Grover proposed an algorithm exploiting the superposition and interference of quantum states (but not the entanglement!). In this way, the quantum computer operates in parallel by exploring different possibilities at the same time. This requires $\sqrt{N}$ steps instead of N needed by a classical computer.

3 Decoherence Mechanisms in Molecular Nanomagnets

Communication and processing of quantum information is based on the coherent evolution of the system state vector: $|\Psi(t)\rangle = e^{-iHt/\hbar}|\Psi(0)\rangle$. In real systems, however, the coupling to the environment ($\mathcal{E}$) tends to spoil the coherent character of the system ($\mathcal{S}$) dynamics. This process is known as *decoherence* [6, 7], and its characteristic timescale is the (de)coherence time $\tau_{\rm d}$. The environment can induce transitions between different eigenstates of the system Hamiltonian, as in the relaxation and incoherent excitation. These processes can be made relatively inefficient by introducing a large energy mismatch between the system and the environment excitation energies. The most harmful form of decoherence is typically represented by dephasing, resulting from elastic interactions between $\mathcal{S}$ and $\mathcal{E}$. Dephasing consists in the loss of phase coherence between the components of a linear superposition and implies the evolution of a pure state into a statistical mixture: $|\Psi\rangle = \sum_i c_i|\phi_i\rangle \rightarrow \rho = \sum_i |c_i|^2|\phi_i\rangle\langle\phi_i|$. If relaxation and dephasing display exponential dependences on time, they can be characterized by the so-called longitudinal (T_1) and transverse (T_2) relaxation time constants. Decoherence is an ubiquitous phenomenon; yet, its features and timescales depend strongly on the system, the experimental conditions, and the specific linear superpositions under consideration.

In molecular nanomagnets, decoherence of the electron spin mainly arises from the coupling to phonons and nuclear spins [8, 9]. In addition, being most experiments performed on ensembles of nanomagnets, dipolar interactions between different replicas of the system can result in decoherence [10, 11]. While dipolar interactions and coupling to phonons depend on the arrangement of the nanomagnets within the sample, and can be possibly reduced by modifying such arrangement, the coupling between electron and nuclear spins of each molecule represents an intrinsic source of decoherence. Hyperfine interactions might therefore represent the fundamental limitation of the electron-spin coherence.

Let's consider the case of a nanomagnet with an $S = 1/2$ ground state doublet, that is initialized into a linear superposition: $|\Psi\rangle = (|\Psi_1\rangle + |\Psi_2\rangle)/\sqrt{2}$, where $|\Psi_1\rangle = |\Uparrow\rangle$ and $|\Psi_2\rangle = |\Downarrow\rangle$ are the lowest eigenstates of the molecule spin Hamiltonian H. In the presence of a static magnetic field $\mathbf{B}_0$ along z, the molecule spin tends to precess in the xy plane. The (contact and dipole–dipole) coupling between the electron ($\mathbf{s}_i$)

and the nuclear spins ($\mathbf{I}_k$) modifies such idealized picture in different respects. Firstly, the nuclear bath generates a magnetic field (the so-called Overhauser field $\mathbf{B}_N$); this adds to $\mathbf{B}_0$ a contribution that renormalizes the Larmor frequency of the nanomagnet spin $\mathbf{S}$ and depends on the state of the nuclei. The state of the nuclear bath is generally undefined and is thus represented by a statistical mixture of different states $|\mathcal{J}_\alpha\rangle$, each with probability p_α and each inducing a different renormalization δ_α of the Larmor frequency. As a consequence of such dispersion in the Larmor frequency, the state of the nanomagnet evolves from $|\Psi\rangle$ into a mixture $\rho = \sum_\alpha p_\alpha |\Psi_\alpha(t)\rangle\langle\Psi_\alpha(t)|$, with $|\Psi_\alpha(t)\rangle = \left[|\Uparrow\rangle + e^{i(\omega_L+\delta_\alpha)^t}|\Downarrow\rangle\right]/\sqrt{2}$. On timescales where the dynamics of the nuclear bath is frozen, the phase coherence can be ideally recovered by refocusing techniques. On timescales where the nuclear bath dynamics can't be neglected, the electron-spin decoherence tends to be irreversible. In fact, even if the nuclei cannot efficiently induce transitions between electron-spin states (due to the large mismatch between the electron and the nuclear Zeeman energies), these can in turn affect the nuclear dynamics. In first order in the hyperfine coupling, such dependence results from the chemical and Knight shifts, i.e. from the magnetic field generated by the spins $\mathbf{s}_i$ on the $\mathbf{I}_k$. Higher-order processes can also contribute, such as those where a (real) transition between nuclear states involves a virtual transition of the electron state. The evolution of the nuclear-bath state, resulting from the interplay between such hyperfine interactions and the (dipole–dipole) ones between the nuclei, nuclei is different if the electron spin of the nanomagnet points in one direction or in the opposite one. As a consequence, electron-nuclear correlations arise, and an initial state which is factorizable into the product of an electron and a nuclear state (e.g., $(|\Uparrow\rangle + |\Downarrow\rangle) \otimes |\mathcal{J}\rangle$, evolves into an entangled state $|\Uparrow\rangle \otimes |\mathcal{J}_\Uparrow\rangle + |\Downarrow\rangle \otimes |\mathcal{J}_\Downarrow\rangle$, where $|\mathcal{J}_{\chi=\Uparrow,\Downarrow}\rangle$ are the states of the nuclei conditioned upon the electron spins being in either of the two eigenstates). The state of the electron spins alone is defined by the reduced density matrix, which is obtained by tracing away the nuclear degrees of freedom, i.e. by averaging over the nuclear spins state. One can show that the stronger the dependence of the nuclear state on the electron state, the smaller $|\langle\mathcal{J}_\Uparrow|\mathcal{J}_\Downarrow\rangle|$, the smaller the modulus of the electron-spin coherence.

The control of decoherence represents indeed one of the key challenges for the implementation of quantum-information processing. In order to maximize the decoherence time, a detailed understanding of the process is required [9]. This represents the prerequisite for engineering the system by chemical synthesis; besides, it allows one to identify the degrees of freedom that are more robust with respect to decoherence and that are thus more suitable for encoding quantum information. The simulation of the nuclear dynamics in Cr_7Ni rings, for example, has allowed one to highlight the dominant role played by the H nuclei that represent the majority of the nuclear spins in the molecule [12].

Quantum-information processing heavily relies on linear superpositions of multi-qubit states. The decoherence of such states is therefore also relevant and in general cannot be simply reduced to that of the single qubit. Let's consider the case of two exchange-coupled Cr_7Ni rings. A linear superposition of two eigenstates of the dimer such as $(|\Uparrow\Uparrow\rangle + |\Downarrow\Downarrow\rangle)/\sqrt{2}$, which is also an entangled state, decoheres

under the effect of hyperfine interactions with the same characteristic timescales of linear superpositions in the single ring. Two (effective) 1/2 spins can also be used to encode a single qubit. In the singlet–triplet qubit, for example, the logical states 0 and 1 are identified with the singlet and triplet (with $M = 0$ states). In the dimer of Cr_7Ni rings, a linear superposition between these two states is much more robust than that between the polarized states ($M = \pm 1$) [13]. In fact, for both the $M = 0$ states, the expectation values of the electron spins vanish. As a consequence, neither state induces a shift of the nuclear energies. The main contribution to the electron-nuclear entanglement is thus represented by processes that are second order in the hyperfine couplings, which are orders of magnitude smaller. These processes consist of flip-flop transitions between pairs of nuclei, mediated by virtual transitions of the electron-spin state. The comparison between these two linear superpositions in the ring dimer shows how decoherence can depend not only quantitatively but also qualitatively on the state in question.

A similar argument applies to the eigenstates of the chirality qubit, where the logical states coincide with eigenstates of opposite spin chirality $C_z = \left(4/\sqrt{3}\right)\mathbf{s}_1 \cdot \mathbf{s}_2 \times \mathbf{s}_3$. If C_z is used for the qubit encoding, the states $|0\rangle$ and $|1\rangle$ also correspond to identical expectation values of the spin projections, both of the total and of the individual spins. As a consequence, the timescale related to nuclear-induced decoherence is enhanced by at least two orders of magnitude with respect to the value of S_z [14]. Such a robustness with respect to decoherence represents a potential advantage of the chirality qubit, along with the possibility of performing the manipulation through electric – rather than magnetic – fields.

Experimentally a first estimation of decoherence effects can be obtained by measuring the line-width of continuous-wave EPR spectra. However this includes several effects and more detailed information can be obtained by pulsed ESR experiments, as also explained in another chapter of this book. Specific pulse-sequences are adopted in order to minimize some contingent effects – like inhomogeneity – and evidence intrinsic dephasing effects. These techniques are normally used to evaluate T_2. Experimental values measured on specific molecular nanomagnets are reported in Sect. 5.

4 Linear Superpositions and Entanglement of Quantum States in Molecular Nanomagnets

In order to outperform classical devices, quantum computers need to exploit quantum interference and entanglement. A preliminary condition for implementing quantum-information processing is thus represented by the capability of understanding and controlling such quantum-mechanical effects in the systems of interest. In this perspective, we introduce hereafter criteria for quantitatively investigating linear superpositions and entanglement in molecular nanomagnets.

4.1 How Large Is a Linear Superposition?

Quantum mechanics allows superpositions of quantum states in systems of – in principle – arbitrary dimensions. This leads to admit the paradoxical possibility that a macroscopic system be suspended between two classically incompatible states. In the last decades, the controlled generation of linear superpositions in systems of increasing sizes has also gained a practical relevance, especially in the fields of quantum-information processing and quantum metrology. However, the question on whether or not a linear superposition is truly macroscopic, or, more generally, on how large a linear superposition actually is, doesn't admit a simple and general answer.

This issue was first addressed by Leggett [15], who introduced the so-called *disconnectivity* as a possible measure of the size of a quantum state. The disconnectivity essentially corresponds to the number of particles within the system that are quantum correlated with each other. Other measures have been proposed in the last years, with reference to a more specific class of linear superpositions, namely that between two semiclassical states: $|\Psi\rangle = (|\Psi_1\rangle + |\Psi_2\rangle)/\sqrt{2}$. One possible starting point for quantifying the size of $|\Psi\rangle$ is represented by the observation that linear superpositions of this kind tend to be extremely fragile with respect to decoherence. In fact, the rate at which the phase coherence between the components decays is expected to increase exponentially with the number of particles that form the system (Quantum mechanics would thus explain why linear superpositions in the macroscopic world, though possible in principle, are generally not observable). Therefore, the decoherence rate itself can be used to quantify the size of the linear superposition [16]. Another possible criterion is based on the use of macroscopic linear superpositions to increase the sensitivity of interferometric experiments. Here, the typical experimental setting includes a quantum system that evolves in time under the effect of a single-particle Hamiltonian αH, where α is the parameter to be estimated. One can show that the sensitivity of the interferometric estimation of α depends on the time that the quantum system takes to evolve into a state orthogonal to the initial state and is maximized by linear superpositions of semiclassical states [17]. The measures that have been introduced according to this criterion are closely related to the ones that are discussed in the second part of the present paragraph.

Hereafter, we consider pure quantum states of the form $|\Psi\rangle = (|\Psi_1\rangle + |\Psi_2\rangle)/\sqrt{2}$, where $|\Psi_1\rangle$ and $|\Psi_2\rangle$ are two ground states of the nanomagnet of interest, and, more specifically, of its spin Hamiltonian. In particular, we shall assume that these ground states have well-defined values of the total spin (S) and of its projection along z (M_1 and M_2, respectively). Linear superpositions of this kind can be dynamically generated by pulsed magnetic fields, or statically induced by resonant tunneling.

There are at least two simple and intuitive ways to quantify the size of such a linear superposition. The first one would be to identify the size of the linear superposition with the number of spins that form the cluster (N). The second way would be to quantify the size of $|\Psi\rangle$ in terms of the spin length S, or of the difference

between the total-spin projections corresponding to the two components ($|M_1 - M_2|$). The shortcomings of such approaches are, however, quite apparent. The first criterion only depends on the structure of the nanomagnet and therefore doesn't discriminate between any two linear superpositions generated within a given system. On the opposite side, the second criterion leaves completely out of consideration the number of constituent spins involved in the linear superposition, as well as the features of $|\Psi_1\rangle$ and $|\Psi_2\rangle$ that depend on any quantum number but S and M. In the following, we discuss two ways to measure the size of linear superpositions, which can be regarded as two refined versions of the above ones.

In the first measure we consider the size of the linear superposition corresponds to the number N' of units (or subsystems) into which the spin cluster can be partitioned, such that one can discriminate between the states $|\Psi_1\rangle$ and $|\Psi_2\rangle$ with a probability P larger than some fixed threshold $1-\varepsilon$, by performing arbitrary measurements within each subsystem [18]. The definition of such units, and the value of N', is thus state-dependent. According to such a criterion, the fact that a linear superposition $|\Psi\rangle$ is large requires not only large values of N, but also that the which-component information is available within each few microscopic units. In the limiting case where the single-spin states corresponding to $|\Psi_1\rangle$ and $|\Psi_2\rangle$ are orthogonal, the corresponding size attains its theoretical maximum $N = N'$. This would be the case, for example, with a linear superposition between fully polarized states ($|\Psi_1\rangle = |\uparrow\uparrow\uparrow\ldots\rangle$ and $|\Psi_2\rangle = |\downarrow\downarrow\downarrow\ldots\rangle$), or between two states with maximum values of the staggered magnetization ($|\Psi_1\rangle = |\uparrow\downarrow\uparrow\ldots\rangle$ and $|\Psi_2\rangle = |\downarrow\uparrow\downarrow\ldots\rangle$).

The second measure we consider can be traced back to the intuitive idea that a large linear superposition $|\Psi\rangle$, and more specifically a Schrödinger-cat state, is characterized by a high degree of *quantumness*, while its components $|\Psi_1\rangle$ and $|\Psi_2\rangle$ are classical-like states. A classical-like state of a spin cluster is possibly one where each of the spins is in a defined state, and more specifically one that minimizes the overall fluctuations in the spin-component operator. Conversely, a nonclassical (pure) state is identified by the fact that the state of each spin is undefined, being the spin entangled with the rest of the system. As a result, the fluctuations of any single-spin operator tend to be large. The size of the linear superposition can thus be quantified by the variance of an operator that can be written as the sum of single-spin operators: $\mathcal{V}(X,\Psi) = \langle\Psi|X^2|\Psi\rangle - \langle\Psi|X|\Psi\rangle^2$, where $X = \sum_{i=1}^{N} \hat{\mathbf{n}}_i \cdot \mathbf{s}_i$ [19]. If $\Psi_{k=1,2}$ is given by the product of single-spin coherent states, one can always find a set of versors $\hat{\mathbf{n}}_i$ such that $\mathcal{V}(X,\Psi_k)$ vanishes. In general, the versors $\hat{\mathbf{n}}_i$ are chosen so as to maximize the fluctuations of X for each given linear superposition. In the simplest case, $\hat{\mathbf{n}}_i = \hat{\mathbf{z}}$, the operator X reduces to S_z and its variance coincides with $(M_1 - M_2)^2/4$. In other cases of interest, $\hat{\mathbf{n}}_i = \pm\hat{\mathbf{z}}$, and X coincides with the staggered magnetization $S_z^* = S_z^A - S_z^B$, being A and B two sublattices into which the spin cluster is partitioned. In any case, in order to single out the degree of quantumness which specifically comes from the linear superposition of $|\Psi_1\rangle$ and $|\Psi_2\rangle$, rather than from the components themselves, the fluctuations of X in $|\Psi\rangle$ can be normalized to those in the states $|\Psi_{k=1,2}\rangle : \mathcal{V}_n(X,\Psi) = 2\mathcal{V}(X,\Psi)/[\mathcal{V}(X,\Psi_1) + \mathcal{V}(X,\Psi_2)]$.

The two criteria outlined above have been used to quantify the size of linear superpositions that have been – or might be – generated in a number of noticeable molecular nanomagnets [20]. Here, a major distinction is that between high-spin molecules, such as Mn_{12} and Fe_8 ground state, and low-spin systems, such as Cr_7Ni or V_{15} ($S = 1/2$). The former ones are characterized by more classical-like ground states (in particular, those with $M = \pm S$) In the latter ones, the ground states are highly nonclassical, and a large amount of quantum fluctuations of the single-spin operators results from the competing exchange interactions. These general features are clearly reflected by the values of N' and $\mathcal{V}(X, \Psi)$ obtained for the different nanomagnets.

The largest linear superpositions can be generated in high-spin molecules, by linearly combining states of maximum spin projection ($M = \pm S$). Here, the size based on the distinguishability of $|\Psi_1\rangle$ and $|\Psi_2\rangle$ by local measurements corresponds to $N' = 8$ and $N' = 5$ for Mn_{12} and Fe_8, respectively (Fig. 3). In the case of Mn_{12}, the spins at the center of the sides (even-numbered, blue circles) are highly polarized – and in opposite directions – in the $M = \pm 10$ ground states. Therefore, one can discriminate between the two ground states with high probability through local measurements performed on each of these spins. In the remaining spins, the dependence of the state on M is less pronounced. The minimum subsystem that carries the required amount of which-component information is represented by spin pairs (green areas in the Fig. 3). In the case of Fe_8, the only spins that are highly polarized in the $M = \pm 10$ ground states are the four external ones: these can thus form a subsystem each. The state of the spins that form the central core is instead less defined and weakly dependent on M. Therefore, one needs to measure the state of the whole central core in order for the measurement to provide the required which-component information, and this should be regarded as a single subsystem. In both cases, the size N' of the linear superposition remains below the theoretical maximum N. One can show that, without changing the geometry and the pattern of exchange couplings within these clusters, nor the partition in sublattices of (approximately) antiparallel spins, one could increase the value of N' by modifying the values of the Js [20].

The values obtained for the measure N' in Cr_7Ni and V_{15} are much smaller, and non-proportionate to the number of spins that compose the two nanomagnets. In both cases, the considered linear superpositions are those between ground states with $M = \pm 1/2$. The size of $|\Psi\rangle$ in Cr_7Ni (which is formed by seven spins $s = 3/2$ and one spin $s = 1$) is $N' = 2$. This is essentially due to the fact that each spin is highly entangled with its nearest neighbors, such that its state is highly mixed. As a consequence, the spin states corresponding to the two components are hardly distinguishable, and the smallest subsystem that contains enough which-component information is formed by (any) four spins. The case of V_{15} is in some sense even more instructive. Here, 12 of the 15 $s = 1/2$ spins (those belonging to the two hexagons) are practically frozen in a singlet state in the low-energy sector of the system. They thus have (approximately) identical states in the two ground states $|\Psi_1\rangle$ and $|\Psi_2\rangle$ and carry no which-component information. This is distributed amongst the remaining three spins, such that the system cannot be partitioned at

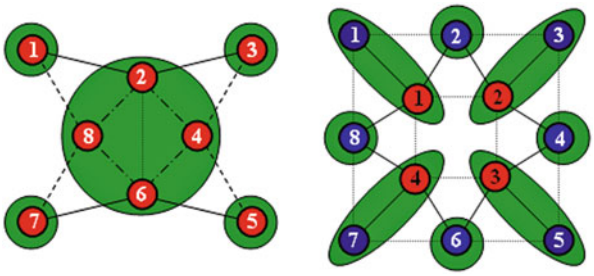

Fig. 3 Schematic view of the Fe_8 (*left*) and Mn_{12} (*right*) molecular nanomagnets. The magnetic core of Fe_8 is formed by $N = 8$ spins $s = 5/2$, while that of Mn_{12} consists of eight external $s = 2$ spins and four internal $s = 3/2$ spins. The shaded areas define the subsystems into which each spin cluster can be partitioned, such that the local measurement within each of them allows the discrimination between $|\Psi_1\rangle (M_1 = -10)$ and $|\Psi_2\rangle (M_2 = +10)$ with a probability higher than 0.99

all, and $N' = 1$. This measure thus gives the same value that would be obtained in a single $s = 1/2$ spin, in spite of the large number of spins that form the V_{15} cluster.

The characterization of the above linear superpositions in terms of quantum fluctuations of single-spin operators leads to qualitatively similar results. For the high-spin molecules Mn_{12} and Fe_8, the values of $\mathcal{V}_n$ are 45.4 and 48.7, respectively, denoting that the linear superposition $|\Psi\rangle$ of the ground states with $M = \pm 10$ has a highly nonclassical character, with respect to the components. This is not the case with Cr_7Ni and V_{15}, where the size $\mathcal{V}_n$ of the linear superpositions between the ground states $M = \pm 1/2$ is given by 2.7 and 1.1, respectively. In these systems, linear combinations of the ground states are not significantly more quantum than the ground states themselves.

4.2 Which and How Much Entanglement?

Entanglement has been recognized as one of the most peculiar features of quantum mechanics already in its early days. In the last decades, both the theoretical understanding of entanglement and the capability of generating and detecting it in diverse physical system have known a rapid development [21, 22]. This interest has been partly fueled by the identification of entanglement as a fundamental resource in quantum-information processing.

Hereafter, we recall some basic notions on entanglement. Given a two-spin system in some pure state $|\Psi_{12}\rangle$, the spins are entangled if it is impossible to write the overall state as a product of single-spin states (i.e., in a factorized form $|\Psi_{12}\rangle = |\psi_1\rangle \otimes |\psi_2\rangle$). Here, the presence of entanglement can be inferred from the mixed character of the single-spin reduced density matrices ρ_1 and ρ_2. In fact, entanglement measures such as the von Neumann entropy quantify entanglement between s_1 and s_2 in terms of the degree of disorder of their states: $S = -\mathrm{tr}\,(\rho_k \log\ \rho_k)$ $(k = 1, 2)$. If the overall state is not pure, then the spins are entangled

if the overall density matrix ρ_{12} can't be written as a mixture of factorized states. If, instead, $\rho_{12} = \sum_l p_l |\psi_l^1\rangle\langle\psi_l^1| \otimes |\psi_l^2\rangle\langle\psi_l^2|$, then the two spins are said to be in a *separable state*. Deciding whether or not a mixed state ρ_{12} is entangled is in general a nontrivial problem. This is because any given density matrix can in general be obtained by mixing different set of states: the decomposition of the density matrix is not unique. As a consequence, it is not easy to exclude that, e.g., a mixture ρ of entangled states cannot be obtained also by combining factorizable states, in the which case ρ would be separable. Measures such as those used for pure overall states can still be applied, through the so-called *convex-roof construction*. This corresponds to taking averaging the measure over the states $|\Psi_l\rangle$ that define a given decomposition of ρ_{12}, and minimizing over all possible decompositions. Such a procedure can be computationally very demanding and the relevant quantities are in general not directly accessible by experimental means. We note that one often deals with mixed two-spin states. This can result from the finite temperature of the system or, if the two spins in question are part of a larger system, by the partial trace performed on the state of the remaining spins in order to obtain ρ_{12}.

The above considerations apply to other forms of *bipartite entanglement*, such as that between two generic subsystems A and B. In this case, each of the two parties is itself a composite system, rather than an individual spin. The so-called *multipartite entanglement*, instead, is substantially different. The state $|\Psi_{123}\rangle$ of three spins, for example, is multipartite entangled if it can't be written in a fully factorized form ($|\psi_1\rangle \otimes |\psi_2\rangle \otimes |\psi_2\rangle$), nor in any biseparable form (such as $|\psi_{12}\rangle \otimes |\psi_3\rangle$, or $|\psi_1\rangle \otimes |\psi_{23}\rangle$). Prototypical examples of three-spin multipartite entangled states are the so-called GHZ and W states, defined for qubit systems: $|\mathrm{GHZ}\rangle = (|\uparrow\uparrow\uparrow\rangle + |\downarrow\downarrow\downarrow\rangle)/\sqrt{2}$ and $|\mathrm{W}\rangle = (|\uparrow\uparrow\downarrow\rangle + |\uparrow\downarrow\uparrow\rangle + |\downarrow\uparrow\uparrow\rangle)/\sqrt{3}$. The above definition can be generalized to the case of a mixed state ρ_{123} along the same lines of the bipartite case. In particular, three spins are considered multipartite entangled if ρ_{123} cannot be written as a mixture of factorized and biseparable states. A three-spin cluster is thus the smallest system where one can discuss multipartite entanglement. In a cluster formed by $N > 3$ spins, one can investigate a hierarchy of multipartite entanglement states, involving k spins at a time, with $2 < k \leq N$. A particularly useful notion in this respect is represented by the so-called *k-producibility*. A state ρ of the N-spin system is k-producible if it can be written as the mixture of states $|\Psi\rangle$, corresponding to a product of n states, $|\phi_1^l\rangle \otimes \ldots \otimes |\phi_n^l\rangle$, each involving no more than k spins. A state ρ of the N-spin clusters contains k-spin entanglement if it is not $(k-1)$-producible.

Molecular spin clusters with dominant antiferromagnetic interactions can be regarded as prototypical examples of strongly correlated systems [23]. The ground state of such system generally exhibits highly nonclassical features and different forms of entanglement (Fig. 4). In the following, we briefly review these forms, as well as the experimental and theoretical tools that can be used to detect and quantify them.

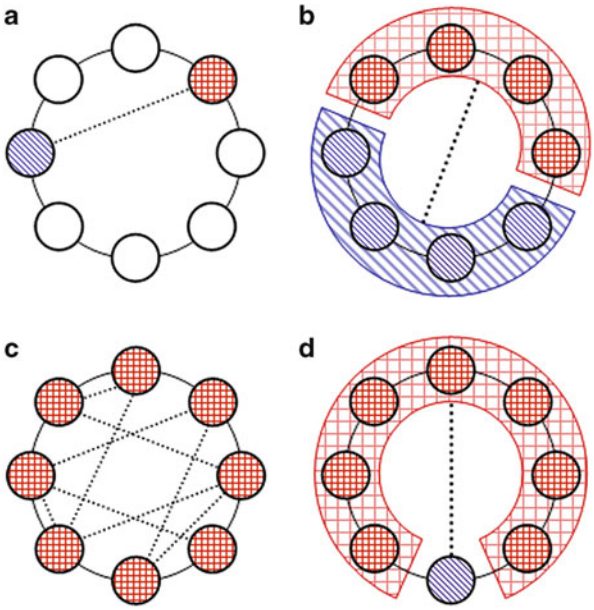

Fig. 4 Different forms of entanglement that can be investigated within a molecular spin cluster: (**a**) entanglement between two individual spins (circles with squared and linear patterning), tracing out the remaining $N-2$ spins (*empty circles*); (**b**) entanglement between complementary subsystems A (*squared*) and B (*linear*), formed by more than one spin each; (**c**) k-partite entanglement, involving more than $k>2$ spins at a time (and all of them, in the case $k=N$); (**d**) entanglement between one spin and the rest of the system

4.2.1 Entanglement Between Individual Spins

Possibly the simplest form of entanglement is that between individual spins. An antiferromagnetic interaction between two spins s_i and s_j ($J\mathbf{s}_i \cdot \mathbf{s}_j$), with $J>0$, tends to entangle them. In particular, if $s_i = s_j$, the exchange energy is minimized if the two spins are in a singlet state. If s_i and s_j are part of a wider spin cluster, then the exchange interaction between the two will generally compete with that between $s_i(s_j)$ and other spins $s_k \neq s_j$ ($s_k \neq s_i$), and none of these contributions to the overall exchange energy will be minimized in the system ground state. Correspondingly, at low temperatures ($T<J$), spin-pair entanglement tends to be present, though not maximum, in pairs of exchange-coupled spins.

Given the reduced two-spin density matrix ρ_{ij}, the entanglement between s_i and s_j can be quantified by functions such as negativity ($\mathcal{N}$), which measures the violation of the positive partial transpose separability criterion [21]. Unfortunately, the only way to derive $\mathcal{N}$ by experimental means is to perform the full tomography of ρ_{ij}, which is generally unfeasible with the experimental techniques available in molecular magnetism. There are, however, experimentally accessible quantities that allow the detection of spin-pair entanglement, the so-called *entanglement*

witnesses. One such observables is represented by the exchange operator $\mathbf{s}_i \cdot \mathbf{s}_j$ itself, which is now accessible in four-dimensional inelastic neutron scattering [24]. In fact, one can easily show that the expectation value of the above operator corresponding to (mixtures of) factorizable states $|\psi_i\rangle \otimes |\psi_j\rangle$ of the two spins cannot be lower than a given threshold: $\langle \mathbf{s}_i \cdot \mathbf{s}_j \rangle \geq -s_i s_j$. From the violation of such inequality, one can thus infer the presence of entanglement between the two spins.

With these simple tools, one can investigate the presence of spin-pair entanglement in molecular nanomagnets and its dependence on the tunable physical parameters. For example, one can show that in an antiferromagnetic wheel such as Cr_8 entanglement is only present between nearest neighbors and at temperatures $T < 1.5$ J (this should be contrasted with the classical correlations that are instead present in such a system between any two spins and at any finite temperature). Besides, the controlled introduction of a chemical substitutions allows one to investigate the effect of magnetic defects on the distribution of entanglement. In particular, the replacement of a spin s within a ring with an $s' \neq s$ reduces the amount of frustration (in terms of both energy and entanglement) and tends to induce an oscillating dependence of entanglement as a function of the distance from the defect [25]. These features can be clearly observed in the molecules of the Cr_7M series (with M = Zn, Cu, Ni, Cr, Fe, Mn), together with the dependence of the sign and amplitude in such oscillations on the length of the spin s_M (with respect to $s_{Cr} = 3/2$). An analogous effect can be produced by a different kind of magnetic defect, namely the introduction of an exchange coupling $J' \neq J$. In the presence of two (or more) substitutions, one can observe a constructive or a destructive interference between the oscillations induced by each defect separately, depending on the distance between the two. This can be observed in the molecules of the series $Cr_{2n}Cu_2$ [26]. Finally, a suitable engineering of the exchange couplings (in particular, of the ratio between the Cr–Cu coupling J' and the Cr–Cr coupling J) also allows one to induce entanglement between distant and uncoupled spins, which is generally absent in homometallic rings with nearest-neighbor interactions.

4.2.2 Multipartite Entanglement

There are forms of entanglement that cannot be traced back to entanglement between spin pairs, for they involve more than two spins at a time. As a limiting case, the state $|\Psi\rangle$ of an N-spin cluster is said to be N-partite entangled if it can't be factorized into the any product $|\Psi_A\rangle \otimes |\Psi_B\rangle$ of states of N_A and $N_B = N - N_A$ spins. Rather counterintuitively, such a form of entanglement can be detected through the expectation value of the exchange Hamiltonian, even though this only includes spin-pair operators. In fact, one can show that the ground state of a ring or chain of N spins is N-partite entangled, and that its energy is separated from that of the lowest biseparable state by a finite gap [27]. More generally, for any given system, one can calculate a number of lower bounds E_k for $\langle H \rangle$, such that the condition $\langle H \rangle < E_k$ implies the presence of k-spin entanglement in the systems state, where larger values of k correspond to lower thresholds E_k. Therefore, as the system

temperature decreases, the expectation value of the exchange energy progressively violates all lower bounds E_k, thus demonstrating the presence – in the equilibrium state – of higher and higher orders of multipartite entanglement. The approach developed for calculating the lower bounds E_k of a given system applies to arbitrary spins and to spin clusters that include spins of different lengths (such as heterometallic rings) [28].

4.2.3 Entanglement Between Subsystems

Another form of entanglement that is not conceptually reducible to that between spin pairs is that between two subsystems A and B into which the spin cluster can be partitioned. Some molecular systems, such as the dimer of Cr_7Ni nanomagnets, can be naturally thought in terms of two weakly coupled subsystems: in this case, A and B would in fact coincide with the two rings [29]. However, physically motivated bipartitions can be identified in a variety of spin clusters, such as those with ferrimagnetic ordering, where spins belonging to different sublattices point in opposite directions. Entanglement between all these subsystems can be quantified by means of the negativity or, if the overall state is pure, by entropic measures, such as the von Neumann entropy. As already mentioned, the practical disadvantage presented by these quantities is that they cannot be expressed as simple combinations of observable quantities and are therefore difficult to estimate experimentally. A possible solution to this problem is represented by the generalization to the case of composite spins of criteria – based on the use of entanglement witnesses – that allow the detection of entanglement between individual spins. For the sake of simplicity, we refer specifically to the already mentioned inequality, namely $\langle \mathbf{S}_A \cdot \mathbf{S}_B \rangle \geq -S_A S_B$, whose violation implies entanglement between the two spins, and consider the case where S_A and S_B are not individual spins, but partial spin sums ($\mathbf{S}_\chi = \sum_{i=1}^{N_\chi} \mathbf{s}_i^\chi$, where $\chi = A, B$), corresponding to subsystems of the spin cluster, which are formed by N_A and N_B spins, respectively. The fact that the spin lengths S_A and S_B are state-dependent quantities, and no longer intrinsic properties of the system, makes the application of the above inequality less straightforward. However, one can show that the criterion can be generalized to the case of composite spins, exploiting the fact that the witness $\mathbf{S}_A \cdot \mathbf{S}_B$ commutes with the partial spin sums $\mathbf{S}_{\chi=A,B}^2$ [30]. The generalized inequality reads: $\langle \mathbf{S}_A \cdot \mathbf{S}_B \rangle \geq -\sum_{S_A, S_B} p(S_A S_B) S_A S_B$, where $p(S_A \cdot S_B)$ is the probability corresponding to each pair of values of the partial spin sums. As a further step, one can show that such probabilities can be expressed in terms of experimentally accessible quantities, and specifically of spin-pair correlation functions. This can be done for a finite but limited amount of fluctuations of $\mathbf{S}_A^2$ and $\mathbf{S}_B^2$ in the (equilibrium) state of interest. Such condition turns out to be satisfied in a number of system and bipartitions, well beyond the limit where A and B are weakly coupled subsystems (i.e., the couplings between the spins of A, or B, are much larger than those between the spins of A and B, as is the case in typical dimer-like structures).

A particular case of bipartition into complementary subsystems is that where one of the two consists of a single spin. In this case, along the lines of the discussed above, one can derive the minima of exchange energy corresponding to states where the single-spin $\mathbf{s}_i$ isn't entangled with all the others. In the case where the spin clusters are formed by inequivalent spins (as for rings with a magnetic defect, or for spin segments), different minima e_i correspond to different spins. One can thus extract a local, spin-selective information by the measurement of a nonlocal quantity, such as the expectation value of the exchange Hamiltonian H. In fact, the violation of the inequality $\langle H \rangle \geq e_i$ allows one to infer that the spin $\mathbf{s}_i$ is entangled with the rest of the system.

5 Molecular Nanomagnets for Quantum Computation

Molecular spin systems have attracted much interest for the almost-unlimited number of possibilities they offer to engineer functionalities at molecular level as extensively presented also in the other chapters of this book. They also constitute an ideal playground for observing quantum phenomena [31]. They possess both electron and nuclear spins. Clusters of transition metals (or lanthanides) are bound together by superexchange interactions in such a way that is possible to define, on the one hand, the pattern of the low-lying molecular states and their relative energy splittings and, on the other hand, the environment in proximity of the magnetic core, an essential ingredient to control decoherence mechanisms as discussed in the previous paragraph. If sufficiently isolated from excited states, the ground S multiplet of one molecule can be used as register for the encoding of quantum information. Chemistry also allows one to control the external part of the molecule by introducing functional organic groups. These allow one to stick two or more molecules together with some control on the magnetic coupling. For instance, the use of organic conjugated groups can induce a permanent super-exchange interaction at supramolecular level [32]. Alternatively, the use of molecular switches between two-spin qubits allows one to create – at the synthetic level! – simple molecular architectures suitable for the implementation of quantum gates.

The independent control on the external ligands also allows the use of functional groups that can stick onto different surface (for a review, see [33] and other chapters of this book). For instance, the use of thiol groups exploits the affinity of the terminal sulfur to bind to gold surface, while the use of cyclic organic terminations, like pyridine or benzene, favors the sticking of the molecule to carbon-based surface (graphite, nanotubes, fullerenes, graphene). Alternatively, the use of polar terminations may allow the exact positioning of molecules on a surface prepared with the corresponding counter-ion. Further examples can be found in another chapter of this book dedicated to the deposition and characterization of molecular spin clusters on surface. All these points indicate clear advantages in using molecular spins, instead of spin impurities, for the design and the realization of architectures for computation. In the following, we review some recent achievements and

list real examples of molecular spin systems of interest for data processing. As discussed in the previous paragraphs, it is worth to point out, however, that a systematic investigation is required to consider a system suitable for the encoding of qubits, as clearly spelled out by the DiVincenzo criteria [34] listed here below:

- Individuation of well-defined quantum states for the qubit encoding and scalability of the system.
- Definition of a protocol to initialize the system.
- Ability to perform a set of quantum gates.
- Robustness of the system with respect to decoherence mechanisms and long coherence time as compared to the gating time.
- Definition of read-out of the final state.

5.1 Radicals

Simple molecules provide already the possibility to encode qubits. Radicals with one delocalized electron have a $S = 1/2$ net spin per molecule. They are well known to spectroscopists to provide very sharp line-width in EPR even at room temperature. For instance, the diphenyl-1-picrylhydrazyl (DPPH) that is commercially available normally shows $S = 1/2$, $g = 2.0037$ and about 2.4 gauss line-width in X-band EPR spectroscopy. Among a large variety of radicals the attention is focused on those that are stable in ambient conditions and can be dispersed in solution or safely deposited on surface. The group of Prof. Gatteschi in Florence works on nitronyl nitroxides and measured $T_2 = 0.9$ μs at 300 K (5 μs at 80 K) by pulsed ESR [35] (Fig. 5a). The group of Prof. T. Takui at Osaka City University is working on malonyl [36] or TEMPO [37] radicals reporting μs lifetimes at room temperature. Finally, the application of optimal dynamical decoupling was shown to allow an enhancement of the decoherence time of three orders of magnitude, achieving the value of 30 μs at 50 K [38].

5.2 Single-Ion Molecules

Next step is the use of single-ion magnets comprising one single lanthanide per molecule.

After the publication of Ishikawa et al. [40], single-ion magnets comprising one lanthanide sandwiched in a bis-phthalocyanine complex (Fig. 5b) have attracted much attention for the huge energy barrier due to magnetic anisotropy they offer and the versatility and robustness they show when deposited on surfaces. Quantum tunneling of the magnetization has been observed in $TbPc_2$ [41] which presents well-defined split of the ground $J = 6$ electronic state due to the hyperfine interaction with $I = 3/2$ nuclear spin. These features make it an ideal molecule for the realization of molecular quantum spintronic devices as presented in another chapter

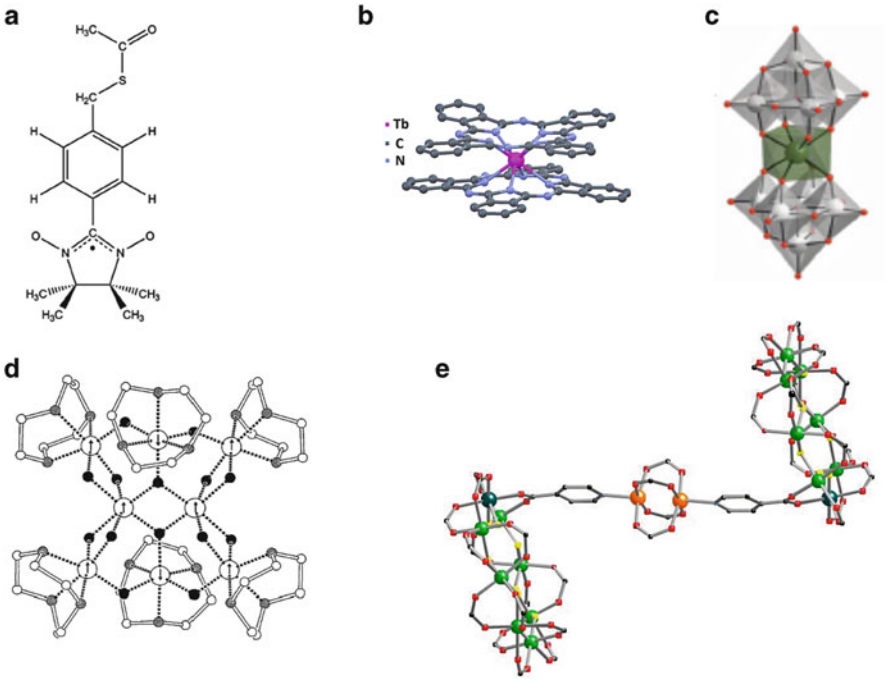

Fig. 5 Some examples of molecular spin qubits: (**a**) S-4-(nitronyl nitroxide) benzyl ethanethioate (NitSAc) radical. (**b**) Mononuclear Tb bis-phthalocyanine. (**c**) Mononuclear LnW_{10} polyoxometallate. (**d**) High spin ($S = 10$) Fe_8 $[(tacn)_6Fe_8O_2(OH)_{12}]$. (**e**) Supramolecular dimer of low-spin Cr_7Ni rings

of this book. Very interestingly, lifetimes exceeding 10 s for nuclear spin states have been measured on a single $TbPc_2$ molecule in a spin transistor setup [42].

The group of Prof. Coronado at University of Valencia isolated mononuclear Gd polyoxometallates (POM), namely GdW_{10} and GdW_{30} (Fig. 5c) for which two states of the ground $S = 7/2$ multiplet have been identified for the qubit encoding and a transverse relaxation time $T_2 = 410$ ns has been measured [39]. POMs offer wide possibilities to control the crystal field acting on the lanthanide magnetic center and to drastically reduce the number of nuclear spins in its environment.

5.3 *Molecular Spin Clusters*

The possibility to choose among an almost-endless catalog of molecules with core made by several transition metals (or lanthanides) tightly bound each other by ferro- or antiferromagnetic superexchange interactions allows to find molecules with quite different ground state, i.e. with magnetic moment ranging from 0 to values much higher than what is possible to find with a single magnetic ion.

In 2001, Leuenberger and Loss noticed that the M-states of the ground $S = 10$ multiplet of Mn_{12} and Fe_8. Single Molecule Magnet are not regularly spaced in

energy and they can be addressed separately by microwave radiation. Based on this consideration they proposed to perform the Grover's algorithm with these molecules [43]. Up to now, the experimental implementation of this proposal has not been realized probably due to the tough experimental requirements. That was, however, the first proposal for using molecular spins for quantum computation in which specific quantum algorithm fits the features of a given molecule, and it drove the attention and curiosity for exploiting molecular spin clusters for quantum computation as promptly realized by Tejada and co-workers [44].

5.4 *Low-Spin Molecular Clusters*

Few years later, Loss and co-workers proposed to consider antiferromagnetic spin arrangements in order to isolate molecular $S = 1/2$ qubits [45]. Low-spin ($S = 1/2$) molecular clusters certainly represent nice examples of two-level systems. Following this line of reasoning, in 2005 we proposed to consider heterometallic rings as suitable candidates for a specific qubit encoding [46]. Heterometallic Cr_7Ni rings with a well-isolated doublet as ground state have been synthesized by Dr. G. Timco in the group of Prof. R.E.P. Winpenny at Manchester University [47]. Coherent spin oscillations within the ground doublet have been shown to persist for timescales as long as 10 μs at 2 K by the group of Dr. A. Ardavan in Oxford [48, 49] (Fig. 6). In these antiferromagnetic rings, the main mechanism for decoherence at low temperature is related to the hyperfine coupling between electron and nuclear spins. The motion of the nuclei can provide an additional decoherence channel, whose presence can, however, be controlled by changing the external organic groups [49]. This molecule can be successfully grafted on different substrates, including gold and graphite, showing to be robust enough to suffer only minor changes in the pattern of its low-lying levels when single units are anchored on surface [50]. Due to the flat ring shape, Cr_7Ni self-assemble when gently sublimed on gold surface [51]. More recently, two or more Cr_7Ni rings have been linked together (see Fig. 6e) and the chemistry behind this seems to provide great flexibility in the choice of the linker (including switchable ones) and therefore in the tunability of the magnetic coupling [52]. Spin entanglement at supramolecular level has been proven and discussed in different cases [23]. Thus, it seems that all the prerequisites for the implementation of universal set of one- and two-qubit gates are present for this family of molecules.

Another prototypical example of low-spin molecule is V_{15} whose ground state is given by the coupling of 15 V^{4+} in spherical arrangement. The lowest lying states are two $S = 1/2$ doublets, split by only 80 mK and separated by 3.8 K from the first $S = 3/2$ excited state. Rabi oscillations within these low-lying multiplets have been observed on V_{15} with a coherence time estimated to be few hundreds of ns at 2.4 K [53] (Fig. 7). More recently, Rabi oscillations have been measured on low-spin Cu_3 antiferromagnetic trimers [54] dispersed in nanoporous Si: the spin coherence time was found to be $T_2 = 1.066$ μs at 1.5 K in this case.

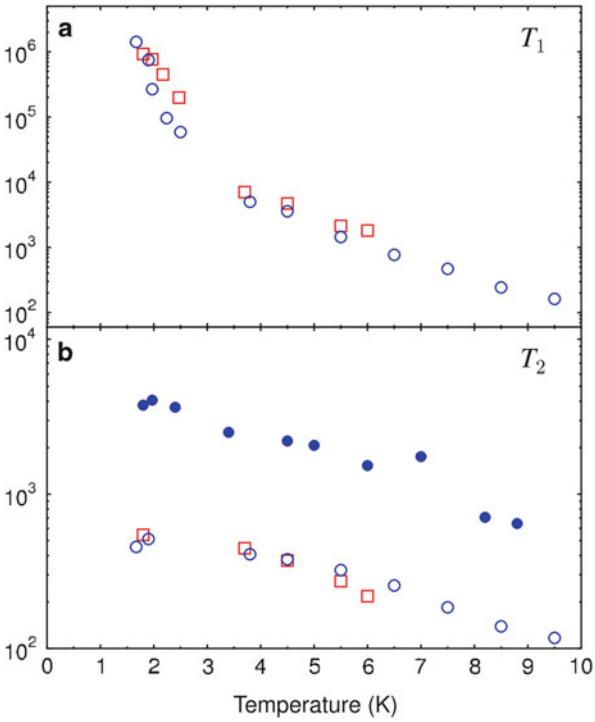

Fig. 6 Hahn-echo pulsed-ESR technique was used in these experiments to evaluate the spin relaxation times as a function of temperature for Cr_7Ni (*open circles*), Cr_7Mn (*open squares*), and perdeuterated Cr_7Ni (*filled circles*). (**a**) Spin–phonon relaxation T_1 (expressed in ns). (b) Spin–spin relaxation T_2 (in ns). Reprinted with permission from Ardavan et al. [48]. Copyright 2007 by American Physical Society

5.5 *High-Spin Molecular Clusters, SMM*

Coherent oscillations have also been measured in high-spin molecules considering transitions between two M-states of the ground multiplet. For Fe_8 (Fig. 5d) a decoherence time T_2 of 712 ns at 1.3 K was reported [55]. Similar experimental values have been reported for Fe_4 SMM for which direct experimental evidence for long-lasting, $T_2 = 640$ ns, quantum coherence and quantum oscillations between two M-states has been reported by using pulsed W-band ESR spectroscopy [56].

All these results show that the search of molecular spin qubits is at present a very effervescent field. Since the time to manipulate an electronic (molecular) spin range between 1 and 10 ns in real experimental conditions, the above mentioned experimental results demonstrate that the typical figure of merit for molecular spin qubit, i.e. the ratio between the coherence time and the manipulation time $Q = T_2/\tau$ ranges between 10^2 and 10^3. This figure of merit is comparable to what found in other solid state qubits and it is a good starting point to consider the molecular spins suitable for the implementation of one-qubit gate.

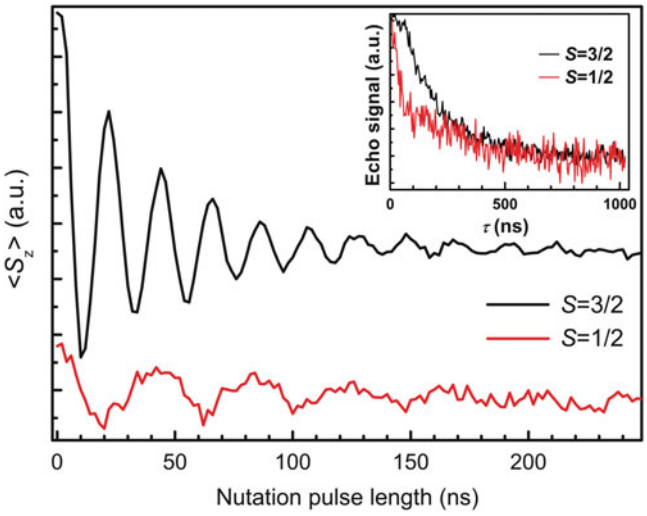

Fig. 7 Time dependence of the average $\langle S_z \rangle$ component after a spin-echo sequence. The lower curve shows the Rabi oscillations of the $S = 1/2$ ground state, while the upper one displays the Rabi oscillations of the $S = 3/2$ first excited state. Measurements were performed by spin-echo spectroscopy on V_{15} single crystals at 2.4 K. The inset shows the T_2 decay measured with Hahn-echo sequence. Reprinted with permission from Yang et al. [53]. Copyright 2012 by American Physical Society

5.6 *Molecules for the Implementation of Multiple-Qubit Gates*

Considerable effort has also been recently devoted to identify and synthesize supramolecular structures comprising two or more molecular qubits (or, more simply, bi- or poly-nuclear clusters). A prototypical example is the $(Mn_4)_2$ dimer comprising two Mn_4 moieties weakly coupled one to another [57, 58]. The family of Cr_7 Ni rings offers a great deal of possibilities to realize supramolecular architectures, including molecular spin qubits linked by organometallic switches [47]. In 2007, the groups of Coronado and Loss proposed to exploit the properties of $[PMo_{12}O_{40}(VO)_2]^{q-}$ POM comprising two $S = 1/2$ spins to perform the $\sqrt{\text{SWAP}}$ gate. Other proposals for the implementation of two-qubit gates with bi-nuclear molecules have been reported for the Tb_2 [59] and manolyn bi-radical [37]. Finally, it is worth mentioning the activity of the group of Dr. G. Aromi who is using β-diketonates ligands to synthesize linked SMMs designed for the implementation of different (multi-)gate schemes [60, 61]. These achievements indicate that the bottom-up – synthetic – approach allows one to assemble complex molecular architectures reflecting the scheme of quantum computers, and many conditions to perform multi-qubit gates appear to be met by different molecular systems. Yet, at the time of writing, no experiments have been successfully completed to prove the functioning of a molecular multi-bit gate. The use of – at least – two frequencies

in the pulse sequence (e.g., for separately addressing the qubits, or switching their interaction) requires noncommercial setups, and this is certainly one of the main experimental limitations at the moment. Further difficulties in combining different experimental conditions (low temperature, high power pulse, finite relaxation time) and fitting the properties (frequency) of a specific molecular system need to be overcome in future in order to achieve this fundamental goal and bring this field to maturity.

6 Quantum Simulators

Generally speaking, a simulator is a device able to reproduce the dynamics of a different system. Similarly, a *quantum* simulator is a device designed to efficiently reproduce the time evolution induced by a given target Hamiltonian, describing the behavior of a specific *quantum* system (for an extensive review, see [62, 63]). This is a very difficult task for a classical computer. For instance, to simulate a system with few quantum objects it requires an incredibly large amount of power, time and registers to a classical computer and, as soon as the size of the quantum system increases, the problem becomes intractable. In 1982, Richard Feynman firstly pointed out that a specifically designed set of quantum registers and processors may – instead – well do this job [64]. Since then, the idea of using quantum computers to solve problems in quantum physics and chemistry has been identified as one of the most intriguing problems in the field of quantum computation. More recently, simulation of simple quantum systems has become an achievable goal with current technology and a race in this direction has started with interesting proposals and results.

Typical problems that are treated by quantum simulators are those related to basic models in quantum magnetism and phase transitions of frustrated systems, or models for electron pairing in high temperature superconductors. Simulation of many-body fermionic systems is one of the most difficult tasks for a classical computer, also due to the change of sign of the wavefunction when two particles are swapped. Problems such as those related to the Hubbard Hamiltonian could instead be addressed by quantum simulators. Another typical many-body problem is the pairing mechanism at the basis of the BCS theory of superconductivity. In quantum chemistry, quantum simulators have been proposed for the design of new molecules as complex as those used for drugs.

Quantum simulators are nothing but quantum computers designed to solve specific problems. As such, they may not be able to perform a universal set of operations; yet, they can be extremely efficient in performing their specific task. Efficiency is indeed one crucial aspect. In 1996 Lloyd clearly presented cases for which a quantum simulator requires resources (registers and processors) increasing in polynomial way with the size of the simulated system, whilst a classical computer would require a number of resources increasing exponentially [65].

As mentioned above, the typical problem addressed by quantum simulators is the time evolution of a quantum system described by a wavefunction $|\Psi(t)\rangle$ under the action of the Hamiltonian $\hat{H}$ ($\hbar \equiv 1$):

$$|\Psi(t)\rangle = e^{-i\hat{H}t}|\Psi(0)\rangle. \tag{3}$$

Different ways to simulate the time evolution of the quantum system have been proposed, but an efficient strategy, if $\hat{H} \Sigma \hat{H}_i$ only includes local terms $\hat{H}_i$, is that to split the overall time evolution into a discrete sequence of simple steps [65], where the total simulation time T is then divided into N intervals $\tau = T/N$ and the overall time evolution is approximated by the so-called Trotter–Suzuki formula:

$$e^{-i\hat{H}t} \simeq \left(e^{-i\hat{H}_1\tau} \ldots e^{-i\hat{H}_N\tau}\right)^N, \tag{4}$$

where terms of higher order can be neglected for sufficiently large N. Thus, the general time-evolution operator is decomposed in a set of gates $e^{-i\hat{H}_1\tau}, \ldots, e^{-i\hat{H}_N\tau}$, each operating on a few qubits, and whose number scales favorably with both the time T and the number of qubits. Since elementary gates are known to form basis for a universal computation, each $e^{-i\hat{H}_i\tau}$ can be in turn expressed as a sequence of logical gates. We just notice that the type of the interaction between qubits that are exploited in the elementary gates $e^{-i\hat{H}_i\tau}$ as well as the architecture of the quantum simulator, need not reflect those of the system to be simulated.

Like in any other (quantum) computer, for quantum simulators we need to define both the preparation of the initial state and the measurement of the final state. The simplest way to initialize a quantum simulator is to let it cool down into its ground state. Another possibility is to measure and project it into a specific state. Besides these simple methods, one might need to define specific sequences of gates to prepare the simulator into the desired state. Measuring the output is also not a trivial task.

From the experimental point of view, the main problem is to engineer the interactions between qubits and at the same time to build up the scalable architectures required to simulate the target system. In the last years, simple quantum simulators have been realized and successfully tested with the most advanced quantum technologies. We can find examples of quantum simulators made of only few qubits, as well as extended architectures.

Nuclear spins benefit from their long coherence time and implementation of elementary and complex algorithms has been extensively carried out in the last two decades [66]. Effective nearest-neighbor Heisenberg interactions are naturally set between nuclear spins, and numerous groups have already attempted to simulate the three- and four-body problem as well as the behavior of spin chains [62]. Simulation of both fermionic and bosonic systems has been successfully performed by NMR [67–69].

The technology to realize arrays of *cold atoms* with optical lattices, as well as that to trap ions in architectures suitable for quantum simulators, is certainly one of the most advanced in the field. For *trapped ions* the mutual interaction can also be controlled, and simulation of spin systems has been designed and successfully performed by this technology [70, 71]. *Nitrogen vacancies* in diamond are one of the most promising ways for the implementation of quantum computation, due to their long coherence time – even at room temperature – and to the advanced optical techniques for the read-out. Recently, important progresses have been made in controlling the position of such vacancies and this opens the way for the fabrication of scalable architectures. Also, a quantum simulator using nuclear spins in diamond has been realized, where nitrogen vacancies have been implanted in a controlled manner [72]. Phase transitions of a frustrated magnetic system have been simulated and successfully tested [72].

Solid state qubits have also been used to realize quantum simulators. For instance, the basic problem of the hydrogen molecule has been simulated by using three *quantum dots* [73, 74]. Yet, for quantum dots, as well as for *superconducting circuits*, the main problem for the realization of large simulators remains the fabrication of identical qubits by lithographic methods and bottom-up approaches. The synthesis of molecular qubits looks very appealing in this respect.

In this context, proposals for the realization of quantum simulators with *molecular spins* have recently appeared [75]. Santini and co-workers considered an infinite chain of alternating *A*–*B* molecules, both with spin 1/2 but addressable separately and effectively coupled with each other through antiferromagnetic dimers that may switch on and off such coupling. They demonstrated that the dynamics of such a spin system may actually map different Hamiltonians, including those of fermionic systems or that describing the quantum tunneling of a spin 1. One peculiarity of this simulator is that there is no need to use local fields, thus operations can be run in parallel by microwave pulses [75]. This work has immediately inspired the synthesis of polymeric structures comprising the Cr_7Ni molecular qubits like those reported in [76], and efforts are currently on the way in order to synthesize metallo-organic frameworks fulfilling all the conditions to realize a quantum simulator with molecular qubits.

A different approach has been proposed by the Osaka group who focus the attention to air-stable *radicals* (hexa-methoxyphenalenyl) with an extremely well-resolved ESR hyperfine splittings a very small line-width in solution. Although the Hamiltonian description still needs to be defined, this molecule provides a specific cluster of both electron and nuclear spins interacting with each other. This suggests that ENDOR technique can also be used in order to exploit the long coherence time of nuclear spins and combine it with the easy read-out of electrons to realize a quantum simulator within only one molecule [77]. Indeed, hyperfine interactions represent one of the major obstacles in many electron-spin-based approaches to quantum computation. However, alternative schemes have been developed where the coupling between electron and nuclear spins represents a key ingredient for the quantum-gate implementation [78, 79].

7 Hybrid Quantum Systems and Devices

So far, the physical implementation of quantum-information processing has been pursued by using different quantum systems and techniques. Hybrid devices, in which different elements are assembled to exploit the best characteristic of each of them, are today considered promising in this perspective. Engineering the interaction of single photons with isolated quantum objects (atoms, ions, spins, etc.) is a fundamental goal in quantum mechanics, as testified by the 2012 Nobel Prize in Physics to Haroche and Wineland. The physics and technology associated with cavity quantum electrodynamics (cavity-QED) [80] has largely contributed to the development of quantum information.

In 2004 the Schoelkopf's group at the Yale University demonstrated that it is possible to implement cavity-QED on a chip by means of superconducting resonators and qubits [81]. In this approach, planar resonators substitute the 3D mirror cavities, thus opening the way to efficiently couple photons with any two-level systems lying on the same substrate. Hybrid circuits that incorporate superconducting hardware and spin systems were soon proposed to exploit the fast manipulation of superconducting qubits and the long decoherence times of electronic spins [82]. Moreover, superconducting lines can act as a quantum bus, linking different subsystems on the same chip by means of the coherent exchange of microwave radiation.

In this context, molecular nanomagnets can provide alternative elements of hardware. This is an emerging field for which theoretical proposals and experiments started to appear very recently. Besides the coherent coupling between molecular spins and photons in cavities, planar resonators are of interest for magnetic resonance experiments, since they allow measurements on thin films or nanostructured molecular nanomagnets. The purpose of the next paragraphs is to give an overview of these topics and to figure out possible scenarios in which molecular nanomagnets can play a role.

7.1 Coupling a Single Spin to Electromagnetic Radiation

We consider here a prototypical experiment where photons in a cavity interact with a two-level quantum system. An electromagnetic cavity is a physical constriction with mirrors that forces photons to multiple reflections, allowing the electromagnetic (e.m.) field to resonate as a stationary wave. Under appropriate experimental conditions the field has a single harmonic mode at frequency ω. Although the problem can be treated in general terms (the two-level quantum system can be either a cold atom (ion) or a superconducting qubit, a quantum dot, etc.), we consider more specifically the case of an isolated spin 1/2 placed in a static magnetic field $\mathbf{B}_0$ oriented, let's say, along the z-axis. When the temperature is sufficiently low, the Boltzmann population of the two levels is different. The spin

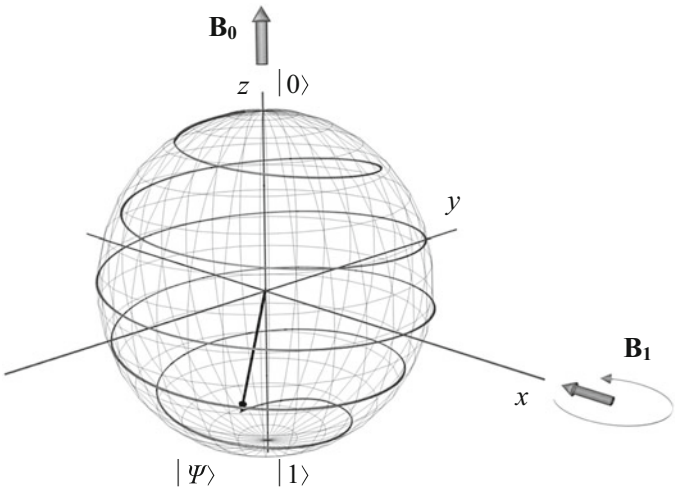

Fig. 8 Graphical representation of the Rabi nutation of $|\Psi\rangle$ in the laboratory frame. The spin, initially in the $|0\rangle$ state, evolves under the effect of the static field $\mathbf{B}_0$ and the oscillating field $\mathbf{B}_1$

precesses at the Larmor frequency $\omega_0 = -\gamma B_0$ about $\mathbf{B}_0$ and the degeneracy of the two eigenstates $|\uparrow\rangle = |0\rangle$ and $|\downarrow\rangle = |1\rangle$ is lift by the corresponding energy splitting $\hbar\omega_0 = g\mu_B B_0$.

The application of an oscillating magnetic field $\mathbf{B}_1$ induces a change of the magnetic moment $\mu = \gamma\hbar\mathbf{S}$ associated with the spin $\mathbf{S}$, which is given by

$$\frac{d\mu}{dt} = \gamma\mu \wedge \mathbf{B}_1. \tag{5}$$

When $\mathbf{B}_1$ is oriented in the x–y plane and oscillates with angular frequency $\omega \simeq \omega_0$, it can induce dipole transitions between the $|\uparrow\rangle$ and $|\downarrow\rangle$ states and change the relative populations (Fig. 8). This problem was first treated by Rabi and it is still a milestone for the spin resonance techniques [83]. The semiclassical model that describes the motion of a spin 1/2 under the action of a classical e.m. radiation field at the resonant frequency can be easily found in textbooks [2]. The probability $P(t)$ to find the spin in its eigenstates oscillates as:

$$P(t) = \frac{\Omega_R^2}{\Delta_c^2 + \Omega_R^2} \sin^2\left[\sqrt{\Delta_c^2 + \Omega_R^2}\,\frac{t}{2}\right], \tag{6}$$

where $\Delta_c = \omega - \omega_0$ is the detuning of the e. m. field frequency (ω) from ω_0 and $\Omega_R = -\gamma B_1$ is the Rabi frequency.

When the intensity of the e.m. radiation is progressively decreased, only few photons (n) statistically interact with the two-level system and the quantum mechanical features of the field come into play. These can be described by the

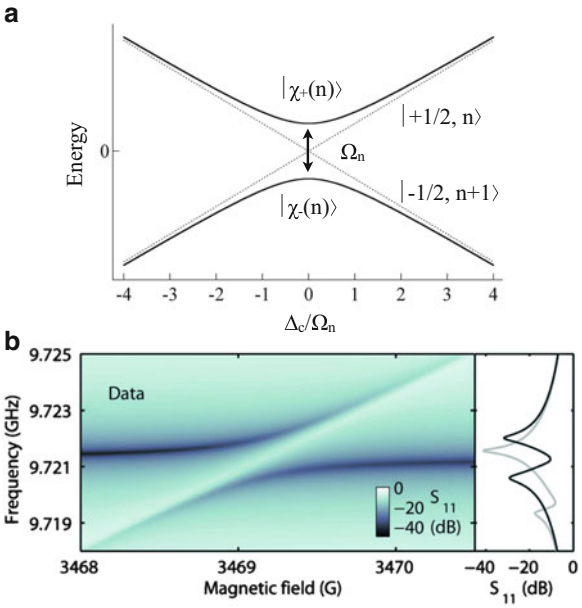

Fig. 9 (**a**) Vacuum Rabi splitting. The repulsion between the dressed states $|\chi_+(n)\rangle$ and $|\chi_-(n)\rangle$ determines an anticrossing for $\Delta_c = 0$ (see Appendix 1 for definitions). The energy splitting on resonance is related to the Rabi frequency $\hbar\Omega_n$. (**b**) Reflection spectrum of lithium phthalocyanine ($N = 2.2 \times 10^{12}$) measured for varying frequency and applied field by means of a three-dimensional cavity. The anticrossing behavior is well visible and theoretical fitting gives $g_c/2\pi = 0.71$ MHz and $\kappa_c = 2\pi = 5.4$ MHz. *Right panel* shows the cross sections measured for 3,469.2 G (*black*, on resonance) and 3,468.5 G (*gray*). Reprinted with permission from Abe et al. [84]. Copyright 2011 by American Institute of Physics

Jaynes–Cummings model in which the e.m. field is quantized. These conditions are typically encountered in cavity-assisted experiments, where few photons are confined in a limited space by multiple reflections at the cavity walls. This topic is described more in detail in Appendix 1 and here we simply summarize the main results. The spin–photon states tend to cross each other as the ω and/or $\mathbf{B}_0$ change. As ω approach $\omega_0(\Delta_c = 0)$ they strongly interact giving rise to a level repulsion (anticrossing) centered at resonance (Fig. 9a). The energy gap at resonance, known as Rabi splitting, quantifies this interaction. Photon and spin states become tightly correlated and for $n = 1$ and $\Delta_c = 0$, the eigenstates of the whole system correspond to the entangled states

$$|\chi_+\rangle = \frac{1}{\sqrt{2}}[|-1/2, 1\rangle + |+1/2, 0\rangle] \tag{7}$$

$$|\chi_-\rangle = \frac{1}{\sqrt{2}}[|-1/2, 1\rangle - |+1/2, 0\rangle]. \tag{8}$$

In realistic physical situations, the effect of the environment on the quantum states of both cavity and spin system is relevant and finite lifetimes must be considered. Photons are either absorbed by the environment or they escape from the feedlines. The decay rate κ is related to the quality factor Q of the resonator $\kappa = \frac{1}{\tau_p} = \frac{\omega}{Q}$. When Q is sufficiently high, the photon can be absorbed and emitted many times before escaping from the cavity and the corresponding lifetime τ_p is long. Similarly, the effects of the environment to the spin dynamics can be taken into account by considering the decoherence mechanism characterized by the rate $\gamma_s = 1/T_2$ at sufficiently low temperature (see Sect. 3). To observe the coherent dynamics of the coupled spin–photons system, the Rabi frequency must be faster than γ_s and κ, more specifically the coupling strength g_c between spin and photons must be $g_c \gg \gamma_s, \kappa$. When this condition is met, the system is in the so-called *strong-coupling regime*. A dimensionless measure of the coupling strength is the cooperativity, defined as $\mathcal{C} = \frac{g^2}{\gamma_s \kappa}$ such that the strong-coupling regime corresponds to $\mathcal{C} \gg 1$.

The strong-coupling regime has been observed in several experiments on Rydberg atoms, cold atoms, Coulomb crystals, or semiconductors by exploiting the electric coupling with the electromagnetic radiation. Coupling strengths in the 100 MHz range have been reported, thanks to either the strong electric dipole or the strong electric component of the cavity field. Conversely the strong coupling of a single spin to electromagnetic radiation is more difficult to observe, as the magnetic dipole gives only fairly weak $g_c \sim 1$ Hz. However, this value can be enhanced by using high-spin states, although higher magnetic moments would also result in stronger dipolar coupling to the environment and faster decoherence. Alternatively, the spin photon coupling can be enhanced by using spin ensembles as described in the following.

7.2 Spin Ensembles in a Cavity

Following Dicke [85] who considered the spin ensemble as a single quantum-mechanical system, Tavis and Cummings [86] generalized the problem to an ensemble of N independent two-level (spins) systems (Fig. 10). When the number of photons in the cavity is $n \ll N$, the excitations of the spin ensemble can be described in terms of non-interacting spin waves. Due to the constructive interference between single-spin transitions, the effective coupling of the spin ensemble with the field is enhanced to $g_{\mathrm{ens}} = g_c \sqrt{N}$. The strong coupling between spin ensemble and e.m. field can be achieved for $\boldsymbol{N}$ sufficiently high [84, 87].

For an increasing number of photons that populate the cavity, a transition from pure quantum to classical dynamics is predicted [87]. For $n = 1$, the ensemble oscillates between two available spin–photon states with energy separation given by the vacuum Rabi splitting $\hbar\sqrt{\Delta_c^2 + \Omega_n^2}$ (Fig. 9a). Each progressive addiction of a photon to the cavity creates a transition whose Rabi splitting depends on n.

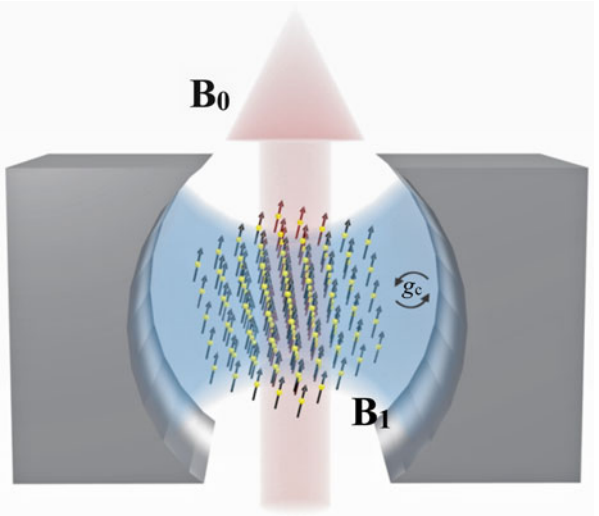

Fig. 10 Pictorial representation of a N-spin system coupled to the e.m. field of a three-dimensional cavity. The level structure within the spin ensemble has a harmonic character, where the excitation energy is determined by the Zeeman splitting due to the static field $\mathbf{B}_0$. The coupling strength g_c between the oscillating field ($\mathbf{B}_1$) and the collective spin system is enhanced by a factor $\sqrt{N}$

Experimentally, the occurrence of the vacuum Rabi splitting in experiments involving spin ensembles is detected by microwave spectroscopy by looking at both dispersive and absorptive signals. The former (usually neglected in conventional EPR spectrometers by locking the source to the central frequency of the resonator) is associated with the frequency shift with respect to the resonance frequency of the unperturbed cavity (ω).

$$\omega_c = \omega - \frac{g^2 \Delta_B}{\Delta_B^2 + \gamma_s^2}, \tag{9}$$

where $\Delta_B = m_0(B - B_0)/\hbar$ is the field detuning. The absorption signal is associated with an increase of the Q-factor

$$\kappa' = \kappa + \frac{g^2 \gamma_s}{\Delta_B^2 + \gamma_s^2}. \tag{10}$$

The full frequency and magnetic field spectrum shows by the appearance of two branches in the spectrum.

$$\omega_\pm = \omega_c + \frac{\Delta_B}{2} \pm \frac{\sqrt{\Omega_n^2 + \Delta_B^2}}{2} \tag{11}$$

This behavior is well visible in Fig. 9b, which shows the EPR signal measured for a lithium phthalocyanine with very narrow line-width (0.0083 G). The anticrossing is seen at about 3,469 G where the absorption line of the cavity meets that of the spin doublets.

The main complication of using ensembles is probably represented by the need of replacing single spin with collection of spins in the physical implementation of each qubit, in order to achieve the strong-coupling regime with the cavity modes. The source of the complication is twofold. On the one hand, spin ensembles behave (in the low-excitation regime) as harmonic systems: the qubit, whose logical states correspond to the presence in the ensemble of 0 or 1 excitations, is not naturally protected from population leakage to states with a higher number of excitations, as is the case for single $S = 1/2$ spin systems. On the other hand, small differences between the nominally identical systems within the ensemble, as well as inhomogeneities in the applied fields, can result in additional sources of qubit dephasing, with respect to single-spin (cluster) qubits.

7.3 Superconducting Hardware and Spin Ensembles

Hybrid circuits composed by superconducting and spin qubits are intensively studied in order to exploit the best of both worlds. The strong coupling constant of superconducting qubits to external fields makes them easy and fast to manipulate, while the long coherence times of electronic spins, as long as 2 s at room temperature for isolated impurities in crystals [88], make them ideal as quantum memories. Hybrid circuit-QED devices have been proposed in different schemes [89–92], with spin ensembles as quantum memories [93] to complete an architecture formed by the coplanar quantum bus and the superconducting qubits.

The experimental demonstration of the strong coupling with the cavity field is the first, necessary, step for spin ensemble to enter in the realm of circuit-QED. Exploiting the magnetic dipolar interactions, crystals of – typically 10^{12} – non-interacting magnetic entities can be placed on the planar resonator directly above the region where the magnetic field antinode is localized (Fig. 11). Different systems have been investigated, namely N–V centers [94–96], ruby [94], Er: Y_2SiO_5 [97] with coupling strengths g_{ens} ranging between 10 and 65 MHz. Recently, strong-coupling regime has been reported for ferrimagnetic Ga-doped $Y_3Fe_5O_{12}$($g_{ens} = 4{,}540$ MHz) [98].

In the strong-coupling regime, the resonator can be implemented to work as a "quantum bus" that coherently transfers the qubit state. Seminal experiments, performed in non-resonant strong dispersive regime, have, for instance, demonstrated the possibility to couple two qubits placed few millimeters apart by means of virtual photons [99]. The controlled phase interaction among the qubits has allowed the production of Bell states with concurrence up to 94%, reporting 1 μs of coherence time of the two-qubit device [100]. The exploitation of these quantum protocols also relies on the generation of a single or few microwave photons [101, 102] and controlled photon states [103], as well as on the possibility to detect the entanglement by means of a two-state tomography [104]. The successful execution of the Grover and Deutsch–Jozsa quantum algorithms has been carried out in proof-of-concept experiments [100].

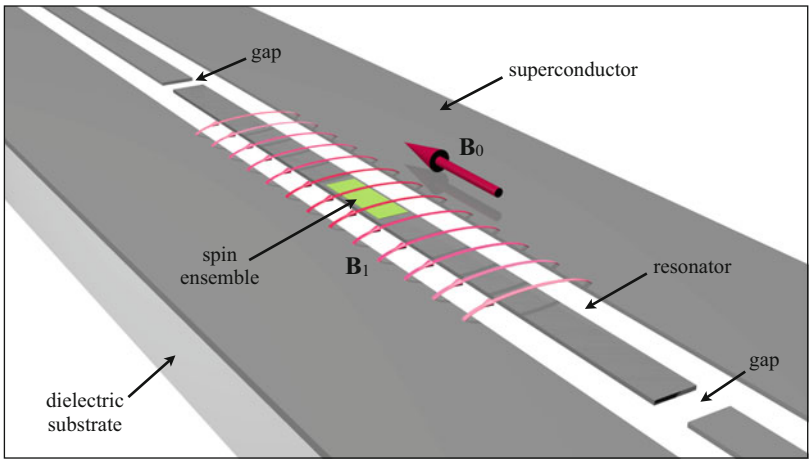

Fig. 11 Schematic representation of a coplanar waveguide microwave resonator realized by conducting strips on a dielectric substrate. For a quasi-TEM e.m. wave, the magnetic field component ($\mathbf{B}_1$) is maximized at the center of the resonator and the flux lines are perpendicular to the central strip conductor. The physical dimension of the capacitance gaps determines the coupling degree of the resonator to the feedlines

The storage and retrieval of a quantum state from photons to a spin ensemble has been achieved by means of suitable sequences of magnetic pulses in pulsed EPR experiments by Wu et al. [105]. In a planar device, the direct transfer of a single photon between a superconducting qubit and an ensemble of NV centers has been assessed by the observation of vacuum Rabi oscillations when the qubit is brought to resonance with the spin ensemble [106]. A variable frequency superconducting resonator has been employed by Kubo et al. as quantum bus to perform a SWAP operation. An arbitrary qubit state $\alpha|g\rangle + \beta|e\rangle$ has been transferred into a corresponding photonic state $\alpha|0\rangle + \beta|1\rangle$ of the bus. The adiabatic SWAPgate has been performed by sweeping the resonance frequency of the bus across the qubit frequency. The resonance frequency of the bus is then tuned to resonance with the spin ensemble for a certain interaction time; hence, it is tuned back to the qubit frequency and the quantum tomography is performed. The fidelity was of about 10% only, limited by hyperfine effects and by the inhomogeneous broadening at resonance. Julsgaard et al. [107] have recently proposed a restoring protocol, based on magnetic resonance refocusing methods, reporting an improved fidelity of 80% for a storage time of 10 μs.

7.4 Molecular Spins in Hybrid Quantum Circuits

The idea to combine molecular spins with resonant cavities has naturally risen in this context. *Organic radicals* provide narrow EPR lines and long spin–spin

decoherence times; thus, they can be used as first testbed. Chiorescu and co-workers studied the spin–photon coupling in a cylindrical cavity exploiting the doublet transition of DPPH radicals, showing the occurrence of a Rabi splitting of 10.9 MHz [87]. The Oxford team (Ardavan, Morton, and others) obtained the strong-coupling regime by using DPPH and lithium phthalocyanine in an X-band cylindrical dielectric ring resonator and they showed the $\sqrt{N}$ dependence of the coupling g-factor to the number of spins N [84]. In Stuttgart, superconducting striplines have been used to demonstrate frequency-swept EPR on organic radicals of the nitronyl-nitroxide family, as well as on Cr^{3+} atoms in ruby [108].

7.4.1 High-Spin Molecular Clusters

High-spin molecular clusters have been theoretically considered by Jenkins et al. [109] for use in hybrid quantum circuits. High spin can actually favor the establishment of strong coupling with modes in a resonating cavity. Thus, allowed transitions in high-spin clusters of Fe_8, GdW_{10}, GdW_{30}, TbW_{30} have been theoretically investigated in order to find optimal conditions for coupling with superconducting coplanar resonators. Hybrid circuits made of high-spin clusters and flux qubits have also been considered. The authors concluded that high-spin ensembles tend to couple more strongly to flux qubits than to resonators and they demonstrated that coupling strength of 10% of the qubit natural frequency could be obtained under realistic experimental conditions [109].

The case of Mn_{12} in a resonant superconducting cavity has been theoretically considered by Tsang et al. (private communication) in order to find conditions for strong coupling and then study the Quantum Tunneling of magnetization in this regime. From this study, it turns out that the molecule-cavity system exhibits a three-well potential with tunable inter-well interactions making conditions accessible for novel process of photon-assisted tunneling. Interestingly, this hybrid molecule-cavity system can be further exploited for simulating similar quantum systems.

7.4.2 Low-Spin Molecular Clusters

In the schemes based on the use of molecular nanomagnets, the interaction between the qubits is induced by superexchange bridges (see Sect. 4). It thus has a permanent and short-range character. Therefore, a suitable engineering of the intermolecular bridges is required in order to allow the switching of the effective qubit–qubit coupling or, alternatively, global-field approaches might be needed in order to bypass the requirement of an individual addressing of the nanomagnets [110]. In both these instances, the use of planar cavities offers the possibility of different solutions and suggests the development of different schemes. In particular, cavity photons can be used as bus qubits that possibly induce an effective coupling

between distant qubits within the array. Also, neighboring qubits can be separated by larger distances, so as to facilitate their selective addressing.

In schemes based on the use of planar cavities, spins are generally used as quantum memories. The quantum processors are instead represented by systems that can be manipulated on shorter timescales, such as (different kinds of) superconducting qubits. Within such an approach, the role of the cavity is that of coupling the quantum memory and the quantum processor, i.e. the spin and the superconducting qubits. Starting from a similar hybrid device, a different approach to the implementation of quantum-information processing has been theoretically proposed [111]. This is based on a hybrid dual-rail encoding, where each qubit is physically implemented by a spin ensemble and a mode of the stripline resonator, and the logical states 0 and 1 correspond to the localization of an excitation, respectively, in the spin ensemble and in the cavity mode. Therefore, spins and photons don't have distinct roles, but rather enter on the same footing. The possible advantage resulting from such an encoding is represented by the fact that all the manipulation is performed by the same means, namely the dynamical tuning of the resonator frequency. In particular, the single-qubit rotations of the form $e^{i\phi\sigma_x/2}$ can be implemented by putting in resonance the cavity mode with the lowest excitation mode of the spin ensemble for a defined time interval, thus allowing an excitation transfer between the two. Rotations around the z axis result instead from the modulation of the cavity frequency alone. The harmonic character of the spin-ensemble qubit represents a potential limitation in the implementation of conditional dynamics, and thus of the two-qubit gates. In order to introduce the required nonlinearity, a Cooper-pair box is added to the hardware, with three relevant energy levels. A suitable sequence of pulses (i.e., variations of the cavity frequencies) transfers the excitations of the two neighboring cavities to such three-level system and back to the qubits, thus adding a phase factor to the two qubits, only if these were initially in the logical state 11. This operation, combined with single-qubit gates, implements the CNOT gate.

In most of the developed schemes, the spin degree of freedom that is considered is the projection along z of the molecule spin. This choice implies the use of the magnetic component of the confined field for the spin manipulation. An alternative possibility is provided by *spin chirality*, which represents a good quantum number in odd-numbered spin rings with antisymmetric exchange. It has been predicted that such degree of freedom can be manipulated by means of pulsed electric fields [112, 113]. The actual value of the *spin-electric coupling* has been theoretically estimated in the case of some specific nanomagnets [114]. In suitably chosen molecules, such coupling might exceed that of the magnetic component, thus allowing the achievement of the strong-coupling regime with the cavity mode with smaller ensembles. As another possible advantage, spin chirality is expected to couple weakly to the nuclear-spin environment, and thus to present much longer decoherence times [14].

8 Conclusions and Perspectives

In Sect. 1 we rose some questions at which we can now try to answer.

8.1 Molecules Fitting Quantum Schemes

Many good examples of $S = 1/2$ molecules are available: while simple radicals provide sharper EPR lines, metallo-organic molecules look more appealing for their extraordinary ability to be functionalized and assembled in complex architectures. While experiments have assessed the feasibility of single-qubit gates, the next goal is the implementation of two-qubit gates with molecular nanomagnets. Noncommercial setups are required for this and dedicated effort should be devoted in order to open the way to more complex algorithms. Alternatively the use of high-spin molecules may allow the implementation of nontrivial qubits but these also require dedicated experiments.

8.2 Advantages in Using Molecular Qubits

One advantage of molecular nanomagnets is related to their functionalization, which opens to the control in positioning and linking them each other or to the surface. From this point of view, molecular nanomagnets are clearly superior with respect to spin impurities. This aspect may really open the way for the design and the synthesis of *complex quantum devices* being them either purely molecular or hybrid if molecules are further attached to solid state nano-objects. This looks like a real peculiarity of molecular nanomagnets which may give a *plus* to these systems to solve the problem of scalability.

8.3 Control of Decoherence at Molecular Level

The possibility to have a huge number of identical replicas makes molecular qubits robust with respect to inhomogeneities. However, in order to avoid pairwise dipolar interaction, diluted crystals need to be grown. Coherent dynamics of electron spins is quite sensitive to any excitation from the environment. To avoid incoherent relaxation processes, molecular spins work well only at very low temperature, like most of solid state quantum devices. Dephasing by interaction with nuclear spins remains the main source of noise at low temperature. Here the synthesis of derivatives with suitable ligands of nuclear-free isotopes has proved to be a viable route to improve the coherence time. As a matter of fact, the best T_2 values

measured on molecular spins now range between 1 and 10 μs at 2 K giving up to 10^3 as figure of merit for electron-spin manipulation. This is a good starting point that should be used as benchmark for new molecular candidates to quantum computation. Since nuclear spins have much longer coherent lifetime (range of seconds even at room temperature), an interesting route – not yet fully explored – is to use them as qubits instead of trying to avoid them.

In this chapter we have also presented two emerging trends in the field: quantum simulators and spin in QED cavities as example of hybrid devices. Quantum technologies are now pushing in many other interesting directions, for instance, quantum communication and quantum cryptography for which application of molecular nanomagnets has been not explored yet. Very impressive are, at the time of writing, pioneering experiments on single-spin transistors and molecular spin valves: if quantum properties and spin dynamics can be controlled at single molecule level, this can overcome several problems encountered with spin ensembles and open an alternative way to quantum computation with molecular nanomagnets as discussed in another chapter of this book (Molecular Spintronics).

Acknowledgments We wish to thank Dr. A. Candini, Dr. V. Corradini, Dr. V. Bellini, Dr. I. Siloi (CNR and University of Modena and Reggio E., I), Prof. S. Carretta, Prof. P. Santini and Prof. G. Amoretti (University of Parma, I), Prof. A. Lascialfari (University of Milano, I), Dr. D. Gerace and Dr. S. Sanna (University of Pavia, I), Prof. A. Cuccoli, and Dr. P. Verrucchi (University of Firenze, I) for stimulating discussions. We also wish to thank Dr. Grigore Timco and Prof. Richard Winpenny (University of Manchester, UK) for all their hints and synthesis and structural characterization of molecular spin clusters. This work was supported by FIRB project RBFR12RPD1 of the Italian Ministry of Research and by the US AFOSR/AOARD program, contract FA2386-13-1-4029.

Appendix 1: Quantum Description of the Spin Dynamics in a Resonant Cavity

In this section we provide further formalism to describe the interaction of single spin with a quantized electromagnetic field following the quantum approach [80, 87, 115]. We consider a cavity in which the field has a single harmonic mode of frequency ω. The intensity of the electromagnetic field determines the number n of photons in the cavity and we consider the situation for which few photons are present in the resonator. Let's assume that the quality factor of the cavity Q is very high so that the photons lifetime is very long. Such a quantized electromagnetic field can be described as $\mathcal{H}_c = \hbar\omega\left(a^\dagger a + \frac{1}{2}\right)$, where a and $a^\dagger$ are the creation and annihilation operators for photons, in analogy with a quantum one-dimensional oscillator [116]. The dipolar spin–photon interaction $\mathcal{H}_{cs} = -\mu \cdot \mathbf{B}$ can be written as:

$$\mathcal{H}_{cs} = \hbar g_c\left[(\mathbf{e}\cdot\mathbf{S})a + (\mathbf{e}^*\cdot\mathbf{S})a^\dagger\right]. \tag{12}$$

For this expression we make use of the Rotating Wave Approximation (RWA) that consists in neglecting fast-oscillating, non-energy-conserving terms which play a minor role in the dynamics of the system. The prefactor g_c is the coupling strength of the magnetic moment with the oscillating magnetic component of the electromagnetic field $\mathbf{B}_1(t)$ The unitary vector $\mathbf{e}$ describes the polarization of $\mathbf{B}_1(t)$, which can be conveniently chosen to obtain the circular polarization σ_+ or σ_- with respect to the static field $\mathbf{B}_0$ along the z-axis. Being $S_\pm = S_x \pm iS_y$, we have thus

$$\mathcal{H}_{\sigma+} = \hbar g_c \left(aS_+ + a^\dagger S_-\right), \tag{13}$$

for photons with helicity $+\hbar$ along z, and

$$\mathcal{H}_{\sigma-} = \hbar g_c \left(aS_- + a^\dagger S_+\right), \tag{14}$$

for photons with helicity $-\hbar$ along z. The Jaynes–Cummings model [117] considers the full Hamiltonian $\mathcal{H} = \mathcal{H}_c + \mathcal{H}_s + \mathcal{H}_{cs}$, i.e.:

$$\mathcal{H} = \hbar\omega\left(a^\dagger a + \frac{1}{2}\right) + \hbar\omega_0 S_z + \hbar g_c \left(aS_\pm + a^\dagger S_\mp\right). \tag{15}$$

being $\mathcal{H}_s = \mu_B B_0 S_z = \hbar\omega_0 S_z$ the term describing the spin precession about $\mathbf{B}_0$. The interaction term $\mathcal{H}_{cs}$ imposes the conservation of the z component of the total angular momentum since it has nonzero matrix element only between eigenstates of $\mathcal{H}_c + \mathcal{H}_s$ that are characterized by the same value of $m_s + n$. This reproduces the selection rules $\Delta m_s = 1$ for σ_+ and $\Delta m_s = -1$ for σ_- expected for conventional perpendicular-mode EPR [118]. Since $m_s = \pm\frac{1}{2}$, we have only two possible values $-1/2 + n + 1$ and $+1/2 + n$, so the diagonalization of Eq. (15) can be carried out separately in each of the two-dimensional subspaces. It is convenient to make use of the dressed atom approach to describe the evolution of an isolated system composed by n photons and one spin [115]. Each subspace is represented by the photon *plus* spin states:

$$|\varphi_a\rangle = \left|-\frac{1}{2}, n+1\right\rangle \quad |\varphi_b\rangle = \left|+\frac{1}{2}, n\right\rangle \tag{16}$$

related to the two allowed conditions, ground $-1/2$ spin state *plus* $n+1$ photons and exited $+1/2$ spin state *plus* n photons. The correspondent eigenvalues

$$E_a = (n+1)\hbar\omega - (\hbar\omega_0/2) \tag{17}$$

$$E_b = n\hbar\omega + (\hbar\omega_0/2) \tag{18}$$

are separated by the detuning frequency $\Delta_c = \frac{1}{\hbar}(E_a - E_b) = \omega - \omega_0$. At resonance ($\Delta_c = 0$), the unperturbed levels would be degenerate. The matrix elements of the interaction potential $\mathcal{H}_{\sigma_+}$ result

$$\langle \varphi_a | \mathcal{H}_{\sigma_+} | \varphi_a \rangle = \langle \varphi_b | \mathcal{H}_{\sigma_+} | \varphi_b \rangle = 0 \tag{19}$$

$$\langle \varphi_b | \mathcal{H}_{\sigma_+} | \varphi_a \rangle = \hbar g_c \sqrt{n+1}. \tag{20}$$

showing that for a system with n photons, the coupling strength scales nonlinearly as $\sqrt{n+1}$. By defining the n-photon Rabi frequency as $\Omega_n = 2g_c\sqrt{n+1}$, the eigenvalues of Eq. (15) read

$$E_+(n) = \hbar\left(n+\frac{1}{2}\right)\omega + \frac{\hbar}{2}\sqrt{\Delta_c^2 + \Omega_n^2} \tag{21}$$

$$E_-(n) = \hbar\left(n+\frac{1}{2}\right)\omega - \frac{\hbar}{2}\sqrt{\Delta_c^2 + \Omega_n^2}. \tag{22}$$

They form two branches of hyperbola with the unperturbed energies as asymptotes (see Fig. 9a). With respect to the unperturbed states, the interaction potential determines the formation of an anticrossing centered on resonance. The minimum gap between E_1 and E_2 is $\hbar\Omega_n$ for $\Delta_c = 0$. The corresponding eigenstates, expressed as function of the unperturbed basis, result

$$|\chi_+(n)\rangle = \sin\ \theta \left|-\frac{1}{2}, n+1\right\rangle + \cos\ \theta \left|+\frac{1}{2}, n\right\rangle \tag{23}$$

$$|\chi_-(n)\rangle = \cos\theta \left|-\frac{1}{2}, n+1\right\rangle + \sin\theta \left|+\frac{1}{2}, n\right\rangle \tag{24}$$

with mixing angle

$$\tan(2\theta_n) = -\frac{\Omega_n}{\Delta_c} \quad 0 \le 2\theta_n < \pi. \tag{25}$$

Each added photon creates a two-dimensional subspace, the complete manifold is a ladder of the two-level states shifted in energy by $\hbar\omega$.

Let's now focus on the resonant case. For $\Delta_c = 0$ the mixing angle is $\theta_n = \pi/4$ and the perturbed states result

$$|\chi_+(n)\rangle = \frac{1}{\sqrt{2}}\left[\left|-\frac{1}{2}, n+1\right\rangle + \left|+\frac{1}{2}, n\right\rangle\right] \tag{26}$$

$$|\chi_-(n)\rangle = \frac{1}{\sqrt{2}}\left[\left|-\frac{1}{2}, n+1\right\rangle - \left|+\frac{1}{2}, n\right\rangle\right]. \tag{27}$$

The time evolution can be calculated by applying the unitary evolution operator to the perturbed dressed states and by recasting in the $|-1/2\rangle$ or $|+1/2\rangle$ unperturbed basis. The time evolution of the ground $|\Psi_-\rangle$ state is

$$|\Psi_-(t)\rangle = \cos\left(\frac{\Omega_n t}{2}\right)\left|-\frac{1}{2}, n+1\right\rangle - i\sin\left(\frac{\Omega_n t}{2}\right)\left|+\frac{1}{2}, n\right\rangle \tag{28}$$

while the excited state evolves as

$$|\Psi_+(t)\rangle = \cos\left(\frac{\Omega_n t}{2}\right)\left|-\frac{1}{2}, n+1\right\rangle + i\sin\left(\frac{\Omega_n t}{2}\right)\left|+\frac{1}{2}, n\right\rangle \tag{29}$$

These expressions describe the dynamics of entangled spin and photon states which have a time evolution that recalls the beat signal of two coupled degenerate quantum oscillators. The eigenmodes are a symmetric and antisymmetric combination of the independent modes of the free oscillators. The cavity and the spin coherently exchange a photon, which is absorbed and then emitted following the spin flip.

The population of the $|-1/2, n+1\rangle$ and $|+1/2, n\rangle$ states oscillates and for $n \gg 1$ the transition probability can be written as

$$P_{ba}(t) = \frac{\Omega_n^2}{\Delta_c^2 + \Omega_n^2}\sin^2\left[\sqrt{\Delta_c^2 + \Omega_n^2}\,\frac{t}{2}\right]. \tag{30}$$

This formula reproduces the classical result of Eq. (6) with $\Omega_n = \Omega_{\mathrm{R}}$.

Appendix 2: Planar Resonators

Fabrication of Microstrip and Coplanar Resonators

Planar transmission lines are commonly used in microwave technology as they provide a simple way to transmit electromagnetic waves on a printed board circuit realized by standard lithographic methods. Among many different geometries, microstrip and coplanar waveguides are the most frequent choices. *Microstrip lines* are constituted by a dielectric substrate having a metal strip on the top and a ground plane on the bottom side. *Coplanar waveguides* differ from microstrips for the presence of two ground planes placed beside the central strip on the top side. The ground conductor in the backside can also be removed. With these geometries, it is possible to match the impedance of the feeding coaxial lines (usually $50\,\Omega$) with relative physical dimensions that spans from millimeter to micron size. By design, the transmission of quasi-transverse electromagnetic modes (TEM) can be achieved, while higher-order non-TEM modes can be appropriately suppressed [119].

Coplanar waveguides are the best choice for minimizing the irradiation of the microwave field outside the surface and to arrange ground electrodes close to the central signal line. A coplanar resonator of length l is realized when the central strip is interrupted in correspondence to two selected positions. These dielectric gaps are

capacitors that electrically couple resonator and transmission line, acting like mirrors do in an optical cavity. Resonant conditions are met when input and reflected wave signals give constructive interference into the cavity. The value of the resonant frequency ω_c is determined by the length l of the resonator and by the speed of propagation of the electromagnetic wave in the coplanar waveguide. The latter is related to the effective dielectric constant ε_{eff} of the insulator. For a cavity resonating at half wavelength $\lambda/2$ [120], the resonance frequency is:

$$\omega_c = \frac{2\pi c}{\sqrt{\varepsilon_{\text{eff}}}} \frac{1}{2l} \tag{31}$$

As mentioned in the previous sections, the quality factor of the resonator must be maximized to reduce the decay rate of the cavity κ and to increase the photon lifetime. The Q-factor is defined as the ratio between the energy stored in the cavity and the power dissipated in a time interval $1/\omega$ or, alternatively as the width of the resonance $\Delta\omega_c$ since $Q = \omega_c/\Delta\omega_c$. For a resonator coupled to the feedlines, the loaded quality factor must be considered

$$\frac{1}{Q} = \frac{1}{Q_{\text{ext}}} + \frac{1}{Q_{\text{int}}}, \tag{32}$$

which is calculated by including the external quality factor (Q_{ext}) related to the coupling capacitances and the intrinsic Q_{int}, due to the internal losses of the resonators.

The capacitance of the input and output gaps controls the coupling with the transmission line and consequently the power flow κ_{in} and κ_{out} along the waveguide. The maximum transfer of microwave energy is obtained when the impedance of the resonator is matched to the feedline. This corresponds to the condition $Q_{\text{ext}} = Q_{\text{int}}$ and the resonator is said to be critically coupled. For $Q_{\text{ext}} < Q_{\text{int}}$ the resonator is undercoupled. This configuration corresponds to reduced transmission, thus lower signal-to-noise ratio, but maximum Q. In the experiments it is often reported because the low output signals can be restored by a low noise microwave amplifier inserted along the output line. Conversely, in the overcoupling regime ($Q_{\text{ext}} > Q_{\text{int}}$) high κ_{in} and κ_{out} are obtained, thus lower Q. This configuration has been used to get fast measurement rates of the cavity photon states [81].

Intrinsic losses often determine the loaded quality factor of the resonator. They are related to different dissipation mechanisms that finally determine the performances of the coplanar resonator. Losses depend on the geometry, material choice, temperature, frequency range, and applied magnetic field. Resonators are rather susceptible to their environment, so they are usually enclosed in metal boxes. Without applied magnetic field, three are the main dissipation mechanisms: resistive, dielectric, and radiative losses [121].

Resistive losses are due to energy dissipated by an electromagnetic wave traveling along a waveguide with finite conductance. Just considering resistive losses, the Q factor passes from ~10^1 to 10^2, typically obtained for resistive cavities, up to $Q \sim 10^7$ for superconducting resonators [122]. Niobium is commonly

employed for its relatively high critical temperature ($T_c \simeq 9.2$ K) and critical field. Superconducting films of TiN, Al, Ta, Re, or YBCO are also reported. Spin systems usually require the application of static magnetic fields to split the degeneracy of the energy levels. For instance, X-band resonance of a spin 1/2 paramagnet requires about 340 mT. Trapping of magnetic flux can be minimized by aligning the field parallel to the resonator surface and experiments report limited degradation of Q up to 350 mT [123]. For higher field or other orientations the penetration of magnetic flux determines a decrease of the quality factor down to 10^3 or lower values. Strategies for the reduction of the magnetic losses have been applied, for instance, by pinning the vortex motion by patterning of slots or microdots [124–126]. Magnetic hysteresis effects are also present and determine the dependence of the Q-factor on the magnetic history of the sample [127].

Dielectric losses are due to absorption of the electromagnetic power by the dielectric substrate. For a lossy material the complex dielectric constant $\varepsilon = \varepsilon_r + i\varepsilon_i$ has a finite imaginary part ε_i and loss tangent ($\tan\delta$). The quality factor associated with the dielectric losses is $Q_{\text{diel}} = 1/\tan\delta$, thus it is desirable to choose insulating substrates with low loss tangent. Sapphire has very low losses with $\tan\delta \sim 10^{-8}$ in high-purity crystals [128]. High resistivity silicon and thermally grown SiO_2 provide a valid alternative [129]. Fabrication strategies, like suspended resonators with grooves etched in the regions of high electric field, have been proposed for reducing the dielectric losses [130].

Radiative losses are an additional contribution due to the emission of electromagnetic radiation in the free space. The associated quality factor is $Q_{\text{rad}} \sim (l/b)^2$, where l and b are, respectively, the length and the distance between the ground electrodes in the top plane [131]. For a typical coplanar waveguide resonator $Q_{\text{rad}} \sim 10^6$.

The temperature dependence of the Q-factor shows a sudden increase below T_c reaching a maximum value for $T \simeq T_c/10$ ($T \simeq 1$ K for Nb). At lower temperature, Q progressively decreases due to a further loss mechanism inducted by the two-level (spin) transitions. These losses, which dominate in the millikelvin range, are ubiquitously reported in lithographed resonators and they are independent by the materials used. They have been assigned to oxides or impurities located close to the active region of the resonator [132–135]

The fundamental resonance frequency of planar resonators is usually located in the 2–15 GHz range by appropriate choice of l. Higher-order harmonics provides further resonances, although the quality factor progressively deteriorates by increasing the mode number [136]. Tunable superconducting resonators have been realized by means of Josephson junctions demonstrating large tunable range and high quality factor [137–139], and the possibility to tune ω_c faster than photon lifetime [140].

Planar Resonators for Magnetic Resonance Experiments

Modern conventional three-dimensional EPR spectrometers report a spin sensitivity up to ~10^9 spins $Hz^{-1/2}$ thanks to the high quality factor of cavity. The minimum detectable number of spins of an EPR cavity depends also on a set of different parameters, such as cavity volume and strength of the microwave field [118]. For small samples, such as thin films or nanostructures, an efficient way to improve the sensitivity of the EPR measurement is to increase the filling factor

$$\eta = \frac{\int_{V_s} |B_1|^2 dV}{\int_{V_c} |B_1|^2 dV} \tag{33}$$

being V_c and V_s respectively, the e.m. mode and sample volume [141], by fabricating resonators that match the sample size and that can concentrate the microwave field in the sample space.

Planar resonating circuits show microwave fields confined in a small V_c, limited to about 100 μm above the surface, where the intensity of B_1 can reach the 0.1 mT range with a limited input power (~100 μW). These devices have been proposed as EPR cavities [142, 143], also because they are suitable for low temperature experiments where microwave heating must be avoided. With the purpose to maximize the power to field conversation efficiency on the sample volume, several designs have been studied, including microstrips [144], planar microcoils [145, 146], and surface loop-gap microresonators [147]. These devices, investigated by means of both continuous-wave and pulsed EPR experiments, report an increase of the sensitivity up to ~10^6 spins $Hz^{-1/2}$ [147]. Similar resonators were also used for ferromagnetic resonance measurements [148–150]. In addition, cross-shaped resonators were proposed for controlling the polarization of the microwave mode [151].

Continuous-wave EPR of different spin ensembles has been exploited for strong-coupling experiments with coplanar waveguide resonators [94–97, 152]. Superconducting resonators have also been studied for pulsed EPR [123, 153] or non-resonating frequency-sweeping EPR [108]. Optimized resonators made with parallel arrays of superconducting microstrip have been also developed for improving the homogeneity of B_1 over a large region [123].

References

1. Nielsen MA, Chuang IL (2010) Quantum computation and quantum information. Cambridge University Press, Cambridge
2. Bandyopadhyay S, Cahay M (2008) Introduction to spintronics. CRC, Boca Raton
3. Blundell S, Thouless D (2001) Magnetism in condensed matter, vol 1. Oxford University Press, New York

4. Vandersypen LM, Steffen M, Breyta G, Yannoni CS, Sherwood MH, Chuang IL (2001) Nature 414:883
5. Xu N, Zhu J, Lu D, Zhou X, Peng X, Du J (2012) Phys Rev Lett 108:130501
6. Zurek W (2003) Rev Mod Phys 75:715
7. Schlosshauer M (2005) Rev Mod Phys 76:1267
8. Stamp PC, Gaita-Arino A (2009) J Mater Chem 19:1718
9. Takahashi S, Tupitsyn I, van Tol J, Beedle C, Hendrickson D, Stamp P (2011) Nature 476:76
10. Prokof′ev N, Stamp P (2000) Rep Prog Phys 63:669
11. Morello A, Stamp P, Tupitsyn IS (2006) Phys Rev Lett 97:207206
12. Troiani F, Bellini V, Affronte M (2008) Phys Rev B 77:054428
13. Szallas A, Troiani F (2010) Phys Rev B 82:224409
14. Troiani F, Stepanenko D, Loss D (2012) Phys Rev B 86:161409
15. Leggett AJ (1980) Prog Theor Phys Suppl 69:80
16. Dür W, Simon C, Cirac JI (2002) Phys Rev Lett 89:210402
17. Björk G, Mana PGL (2004) J Opt B Quantum Semiclassical Opt 6:429
18. Korsbakken JI, Whaley KB, Dubois J, Cirac JI (2007) Phys Rev A 75:042106
19. Fröwis F, Dür W (2012) New J Phys 14:093039
20. Troiani F, Zanardi P (2013) Phys Rev B 88:094413
21. Horodecki R, Horodecki P, Horodecki M, Horodecki K (2009) Rev Mod Phys 81:865
22. Gühne O, Tóth G (2009) Phys Rep 474:1
23. Troiani F, Bellini V, Candini A, Lorusso G, Affronte M (2010) Nanotechnology 21:274009
24. Baker ML, Guidi T, Carretta J, Ollivier S, Mutka H, Güdel HU, Timco GA, McInnes EJL, Amoretti G, Winpenny REP, Santini P (2012) Nat Phys 8:906
25. Siloi I, Troiani F (2012) Phys Rev B 86:224404
26. Lorusso G, Corradini V, Ghirri A, Biagi R, del Pennino U, Siloi I, Troiani F, Timco G, Winpenny REP, Affronte M (2012) Phys Rev B 86:184424
27. Troiani F, Siloi I (2012) Phys Rev A 86:032330
28. Siloi I, Troiani F (2013) Eur Phys J B 86
29. Candini A, Lorusso G, Troiani F, Ghirri A, Carretta S, Santini P, Amoretti G, Muryn C, Tuna F, Timco G, McInnes EJL, Winpenny REP, Wernsdorfer W, Affronte M (2010) Phys Rev Lett 104:037203
30. Troiani F, Carretta S, Santini P (2013) Phys Rev B 88:195421
31. Gatteschi D, Sessoli R, Villain J (2006) Molecular nanomagnets. Oxford University Press, New York
32. Bellini V, Lorusso G, Candini A, Wernsdorfer W, Faust T, Timco G, Winpenny R, Affronte M (2011) Phys Rev Lett 106:227205
33. Domingo N, Bellido E, Ruiz-Molina D (2012) Chem Soc Rev 41:258
34. DiVincenzo DP (2000) Fortschr Phys 48:771
35. Collauto A, Mannini M, Sorace L, Barbon A, Brustolon M, Gatteschi D (2012) J Mater Chem 22:22272
36. Sato K, Nakazawa S, Rahimi R, Ise T, Nishida S, Yoshino T, Mori N, Toyota K, Shiomi D, Yakiyama Y et al (2009) J Mater Chem 19:3739
37. Nakazawa S, Nishida S, Ise T, Yoshino T, Mori N, Rahimi RD, Sato K, Morita Y, Toyota K, Shiomi D, Kitagawa M, Hara H, Carl P, Hfer P, Takui T (2012) Angew Chem Int Ed 51:9860
38. Du J, Rong X, Zhao N, Wang Y, Yang J, Liu RB (2009) Nature 461:1265
39. Martínez-Pérez MJ, Cardona-Serra S, Schlegel C, Moro F, Alonso PJ, Prima-García H, Clemente-Juan JM, Evangelisti M, Gaita-Ariño A, Sesé J, van Slageren J, Coronado E, Luis F (2012) Phys Rev Lett 108:247213
40. Ishikawa N, Sugita M, Ishikawa T, Koshihara SY, Kaizu Y (2004) J Phys Chem B 108:11265
41. Ishikawa N, Sugita M, Wernsdorfer W (2005) Angew Chem Int Ed 44:2931
42. Vincent R, Klyatskaya S, Ruben M, Wernsdorfer W, Balestro F (2012) Nature 488:357
43. Leuenberger MN, Loss D (2001) Nature 410:789
44. Tejada J, Chudnovsky E, Del Barco E, Hernandez J, Spiller T (2001) Nanotechnology 12:181

45. Meier F, Levy J, Loss D (2003) Phys Rev B 68:134417
46. Troiani F, Ghirri A, Affronte M, Carretta S, Santini P, Amoretti G, Piligkos S, Timco G, Winpenny R (2005) Phys Rev Lett 94:207208
47. Timco GA, Faust TB, Tuna F, Winpenny RE (2011) Chem Soc Rev 40:3067
48. Ardavan A, Rival O, Morton JJ, Blundell SJ, Tyryshkin AM, Timco GA, Winpenny RE (2007) Phys Rev Lett 98:057201
49. Wedge C, Timco G, Spielberg E, George R, Tuna F, Rigby S, McInnes E, Winpenny R, Blundell S, Ardavan A (2012) Phys Rev Lett 108:107204
50. Corradini V, Ghirri A, del Pennino U, Biagi R, Milway VA, Timco G, Tuna F, Winpenny RE, Affronte M (2010) Dalton Trans 39:4928
51. Ghirri A, Corradini V, Bellini V, Biagi R, del Pennino U, De Renzi V, Cezar JC, Muryn CA, Timco GA, Winpenny RE et al (2011) ACS Nano 5:7090
52. Timco GA, Carretta S, Troiani F, Tuna F, Pritchard RJ, Muryn CA, McInnes EJ, Ghirri A, Candini A, Santini P et al (2009) Nat Nanotechnol 4:173
53. Yang J, Wang Y, Wang Z, Rong X, Duan CK, Su JH, Du J (2012) Phys Rev Lett 108:230501
54. Choi KY, Wang Z, Nojiri H, van Tol J, Kumar P, Lemmens P, Bassil B, Kortz U, Dalal N (2012) Phys Rev Lett 108:067206
55. Takahashi S, van Tol J, Beedle CC, Hendrickson DN, Brunel LC, Sherwin MS (2009) Phys Rev Lett 102:087603
56. Schlegel C, van Slageren J, Manoli M, Brechin E, Dressel M (2008) Phys Rev Lett 101:147203
57. Hill S, Edwards R, Aliaga-Alcalde N, Christou G (2003) Science 302:1015
58. Wernsdorfer W, Aliaga-Alcalde N, Hendrickson DN, Christou G (2002) Nature 416:406
59. Luis F, Repollés A, Martínez-Pérez MJ, Aguilà D, Roubeau O, Zueco D, Alonso PJ, Evangelisti M, Camón A, Sesé J, Barrios LA, Aromí G (2011) Phys Rev Lett 107:117203
60. Sañudo EC, Cauchy T, Ruiz E, Laye RH, Roubeau O, Teat SJ, Aromí G (2007) Inorg Chem 46:9045
61. Barrios L, Aguil D, Roubeau O, Gamez P, Ribas-Ario J, Teat S, Aromi G (2009) Chem Eur J 15:11235
62. Brown KL, Munro WJ, Kendon VM (2010) Entropy 12:2268
63. Buluta I, Nori F (2009) Science 326:108
64. Feynman RP (1982) Int J Theor Phys 21:467
65. Lloyd S et al (1996) Science 1073–1077
66. Jones J (2000) Fortschr Phys 48:909
67. Brown KR, Clark RJ, Chuang IL (2006) Phys Rev Lett 97:050504
68. Negrevergne C, Somma R, Ortiz G, Knill E, Laflamme R (2005) Phys Rev A 71:032344
69. Somaroo S, Tseng CH, Havel TF, Laflamme R, Cory DG (1999) Phys Rev Lett 82:5381
70. Deng XL, Porras D, Cirac JI (2005) Phys Rev A 72:063407
71. Porras D, Cirac JI (2004) Phys Rev Lett 93:263602
72. Cai J, Retzker A, Jelezko F, Plenio MB (2013) Nat Phys 9:168
73. Gaudreau L, Studenikin SA, Sachrajda AS, Zawadzki P, Kam A, Lapointe J, Korkusinski M, Hawrylak P (2006) Phys Rev Lett 97:036807
74. Vidan A, Westervelt R, Stopa M, Hanson M, Gossard A (2004) Appl Phys Lett 85:3602
75. Santini P, Carretta S, Troiani F, Amoretti G (2011) Phys Rev Lett 107:230502
76. Whitehead GF, Cross B, Carthy L, Milway VA, Rath H, Fernandez A, Heath SL, Muryn CA, Pritchard RG, Teat SJ et al (2013) Chem Commun 49:7195
77. Ueda A, Suzuki S, Yoshida K, Fukui K, Sato K, Takui T, Nakasuji K, Morita Y (2013) Angew Chem Int Ed 52:4795
78. Hodges JS, Yang JC, Ramanathan C, Cory DG (2008) Phys Rev A 78:010303
79. Zhang Y, Ryan CA, Laflamme R, Baugh J (2011) Phys Rev Lett 107:170503
80. Haroche S, Raimond JM (2006) Exploring the quantum: atoms, cavities and photons. Oxford University Press, Oxford

81. Wallraff A, Schuster DI, Blais A, Frunzio L, Huang RS, Majer J, Kumar S, Girvin SM, Schoelkopf RJ (2004) Nature 431:162
82. Xiang ZL, Ashhab S, You JQ, Nori F (2013) Rev Mod Phys 85:623
83. Rabi I (1937) Phys Rev 51:652
84. Abe E, Wu H, Ardavan A, Morton JJ (2011) Appl Phys Lett 98:251108
85. Dicke RH (1954) Phys Rev 93:99
86. Tavis M, Cummings FW (1968) Phys Rev 170:379
87. Chiorescu I, Groll N, Bertaina S, Mori T, Miyashita S (2010) Phys Rev B 82:024413
88. Tyryshkin AM, Tojo S, Morton JJ, Riemann H, Abrosimov NV, Becker P, Pohl HJ, Schenkel T, Thewalt ML, Itoh KM et al (2011) Nat Mater 11:143
89. Rabl P, DeMille D, Doyle JM, Lukin MD, Schoelkopf RJ, Zoller P (2006) Phys Rev Lett 97:033003
90. Tordrup K, Negretti A, Mølmer K (2008) Phys Rev Lett 101:040501
91. Imamoğlu A (2009) Phys Rev Lett 102:083602
92. Wesenberg JH, Ardavan A, Briggs GAD, Morton JJL, Schoelkopf RJ, Schuster DI, Mølmer K (2009) Phys Rev Lett 103:070502
93. Simon C, Afzelius M, Appel J, de La Giroday AB, Dewhurst S, Gisin N, Hu C, Jelezko F, Kröll S, Müller J et al (2010) Eur Phys J D 58:1
94. Schuster DI, Sears AP, Ginossar E, DiCarlo L, Frunzio L, Morton JJL, Wu H, Briggs GAD, Buckley BB, Awschalom DD, Schoelkopf RJ (2010) Phys Rev Lett 105:140501
95. Kubo Y, Ong FR, Bertet P, Vion D, Jacques V, Zheng D, Dréau A, Roch JF, Auffeves A, Jelezko F, Wrachtrup J, Barthe MF, Bergonzo P, Esteve D (2010) Phys Rev Lett 105:140502
96. Amsüss R, Koller C, Nöbauer T, Putz S, Rotter S, Sandner K, Schneider S, Schramböck M, Steinhauser G, Ritsch H, Schmiedmayer J, Majer J (2011) Phys Rev Lett 107:060502
97. Probst S, Rotzinger H, Wünsch S, Jung P, Jerger M, Siegel M, Ustinov AV, Bushev PA (2013) Phys Rev Lett 110:157001
98. Huebl H, Zollitsch C, Lotze J, Hocke F, Greifenstein M, Marx A, Gross R, Goennenwein ST (2013) Phys Rev Lett 111:127003
99. Majer J, Chow J, Gambetta J, Koch J, Johnson B, Schreier J, Frunzio L, Schuster D, Houck A, Wallraff A et al (2007) Nature 449:443
100. DiCarlo L, Chow J, Gambetta J, Bishop LS, Johnson B, Schuster D, Majer J, Blais A, Frunzio L, Girvin S et al (2009) Nature 460:240
101. Houck A, Schuster D, Gambetta J, Schreier J, Johnson B, Chow J, Frunzio L, Majer J, Devoret M, Girvin S et al (2007) Nature 449:328
102. Schuster D, Houck A, Schreier J, Wallraff A, Gambetta J, Blais A, Frunzio L, Majer J, Johnson B, Devoret M et al (2007) Nature 445:515
103. Hofheinz M, Weig E, Ansmann M, Bialczak RC, Lucero E, Neeley M, Oconnell A, Wang H, Martinis JM, Cleland A (2008) Nature 454:310
104. Filipp S, Maurer P, Leek PJ, Baur M, Bianchetti R, Fink JM, Göppl M, Steffen L, Gambetta JM, Blais A, Wallraff A (2009) Phys Rev Lett 102:200402
105. Wu H, George RE, Wesenberg JH, Mølmer K, Schuster DI, Schoelkopf RJ, Itoh KM, Ardavan A, Morton JJL, Briggs GAD (2010) Phys Rev Lett 105:140503
106. Zhu X, Saito S, Kemp A, Kakuyanagi K, Karimoto SI, Nakano H, Munro WJ, Tokura Y, Everitt MS, Nemoto K et al (2011) Nature 478:221
107. Julsgaard B, Grezes C, Bertet P, Mølmer K (2013) Phys Rev Lett 110:250503
108. Clauss C, Bothner D, Koelle D, Kleiner R, Bogani L, Scheffler M, Dressel M (2013) Appl Phys Lett 102:162601
109. Jenkins M, Hmmer T, Martnez-Prez MJ, Garca-Ripoll J, Zueco D, Luis F (2013) New J Phys 15:095007
110. Troiani F, Affronte M, Carretta S, Santini P, Amoretti G (2005) Phys Rev Lett 94:190501
111. Carretta S, Chiesa A, Troiani F, Gerace D, Amoretti G, Santini P (2013) Phys Rev Lett 111:110501
112. Trif M, Troiani F, Stepanenko D, Loss D (2008) Phys Rev Lett 101:217201

113. Trif M, Troiani F, Stepanenko D, Loss D (2010) Phys Rev B 82:045429
114. Nossa JF, Islam MF, Canali CM, Pederson MR (2012) Phys Rev B 85:085427
115. Cohen-Tannoudji GGC, Dupont-Roc J (2004) Atom-photon interactions. Wiley-VCH, Weinheim
116. Gerry CC, Knight PL (2004) Introductory quantum optics. Cambridge University Press, Cambridge
117. Jaynes ET, Cummings FW (1963) Proc IEEE 51:89
118. Weil JA, Bolton JR (2008) Electron paramagnetic resonance, 2nd edn. Wiley, New York
119. Gupta K, Garg R, Bahl I, Bhartia P (1996) Microstrip lines and slotlines. Artech House, Boston
120. Pozar DM (1998) Microwave engineering. Wiley, New York
121. Lancaster MJ (1997) Passive microwave device applications of high-temperature superconductors. Cambridge University Press, Cambridge
122. Vissers MR, Gao J, Wisbey DS, Hite DA, Tsuei CC, Corcoles AD, Steffen M, Pappas DP (2010) Appl Phys Lett 97:232509
123. Benningshof O, Mohebbi H, Taminiau I, Miao G, Cory D (2013) J Magn Reson 230:84
124. Song C, Heitmann TW, DeFeo MP, Yu K, McDermott R, Neeley M, Martinis JM, Plourde BLT (2009) Phys Rev B 79:174512
125. Song C, DeFeo M, Yu K, Plourde B (2009) Appl Phys Lett 95:232501
126. Bothner D, Gaber T, Kemmler M, Koelle D, Kleiner R (2011) Appl Phys Lett 98:102504
127. Bothner D, Gaber T, Kemmler M, Koelle D, Kleiner R, Wünsch S, Siegel M (2012) Phys Rev B 86:014517
128. Creedon DL, Reshitnyk Y, Farr W, Martinis JM, Duty TL, Tobar ME (2011) Appl Phys Lett 98:222903
129. Frunzio L, Wallraff A, Schuster D, Majer J, Schoelkopf R (2005) IEEE Trans Appl Supercond 15:860
130. Barends R, Vercruyssen N, Endo A, De Visser P, Zijlstra T, Klapwijk T, Diener P, Yates S, Baselmans J (2010) Appl Phys Lett 97:023508
131. Mazin B (2004) Microwave kinetic inductance detectors. Ph.D. thesis, California Institute of Technology
132. Gao J, Daal M, Vayonakis A, Kumar S, Zmuidzinas J, Sadoulet B, Mazin BA, Day PK, Leduc HG (2008) Appl Phys Lett 92:152505
133. Wang H, Hofheinz M, Wenner J, Ansmann M, Bialczak R, Lenander M, Lucero E, Neeley M, OConnell A, Sank D et al (2009) Appl Phys Lett 95:233508
134. Lindström T, Healey JE, Colclough MS, Muirhead CM, Tzalenchuk AY (2009) Phys Rev B 80:132501
135. Macha P, van Der Ploeg S, Oelsner G, Ilichev E, Meyer HG, Wunsch S, Siegel M (2010) Appl Phys Lett 96:062503
136. Goppl M, Fragner A, Baur M, Bianchetti R, Filipp S, Fink J, Leek P, Puebla G, Steffen L, Wallraff A (2008) J Appl Phys 104:113904
137. Osborn K, Strong J, Sirois A, Simmonds R (2007) IEEE Trans Appl Supercond 17:166
138. Castellanos-Beltran M, Lehnert K (2007) Appl Phys Lett 91:083509
139. Palacios-Laloy A, Nguyen F, Mallet F, Bertet P, Vion D, Esteve D (2008) J Low Temp Phys 151:1034
140. Sandberg M, Wilson C, Persson F, Bauch T, Johansson G, Shumeiko V, Duty T, Delsing P (2008) Appl Phys Lett 92:203501
141. Poole CP (1983) Electron spin resonance: a comprehensive treatise on experimental techniques. Wiley, New York
142. Johansson B, Haraldson S, Pettersson L, Beckman O (1974) Rev Sci Instrum 45:1445
143. Wallace W, Silsbee R (1991) Rev Sci Instrum 62:1754
144. Torrezan A, Mayer Alegre T, Medeiros-Ribeiro G (2009) Rev Sci Instrum 80:075111
145. Narkowicz RSR, Suter D (2005) J Magn Reson 175:275284
146. Narkowicz R, Suter D, Niemeyer I (2008) Rev Sci Instrum 79:084702

147. Twig Y, Suhovoy E, Blank A (2010) Rev Sci Instrum 81:104703
148. Goglio G, Pignard S, Radulescu A, Piraux L, Huynen I, Vanhoenacker D, Vander Vorst A (1999) Appl Phys Lett 75:1769
149. Giesen F, Podbielski J, Korn T, Steiner M, Van Staa A, Grundler D (2005) Appl Phys Lett 86:112510
150. Liu Y, Chen L, Tan C, Liu H, Ong C (2005) Rev Sci Instrum 76:063911
151. Henderson J, Ramsey C, Quddusi H, Del Barco E (2008) Rev Sci Instrum 79:074704
152. Bushev P, Feofanov AK, Rotzinger H, Protopopov I, Cole JH, Wilson CM, Fischer G, Lukashenko A, Ustinov AV (2011) Phys Rev B 84:060501
153. Malissa H, Schuster D, Tyryshkin A, Houck A, Lyon S (2013) Rev Sci Instrum 84:025116

Struct Bond (2015) 164: 431–460
DOI: 10.1007/430_2014_152

Published online: 4 July 2014

Magnetic Refrigeration and Spin–Lattice Relaxation in Gadolinium-Based Molecular Nanomagnets

Fernando Luis and Marco Evangelisti

Abstract We review history, materials and underlying physics that form a background common to magnetic refrigeration and spin–lattice relaxation. To illustrate how these subjects are profoundly interrelated with each other, we describe studies performed on the molecular nanomagnets with formula $[Gd(W_5O_{18})_2]^{9-}$ and $[Gd(P_5W_{30}O_{110})]^{12-}$. Each molecular unit carries a single ion of gadolinium, which is coordinated to different polyoxometalate moieties, respectively. Each Gd^{3+} spin is magnetically isolated and maintains thermal equilibrium with the lattice down to temperatures close to absolute zero. For $T \lesssim 200$ mK, the spin–lattice relaxation becomes dominated by pure quantum tunneling events. We discuss these properties with a keen eye for promising applications of molecular nanomagnets, namely, as magnetic refrigerants for attaining such low temperatures and spin qubits in quantum information processing.

Keywords Cryogenics · Gadolinium · Magnetism · Magnetocaloric effect · Molecular nanomagnet · Polyoxometalate · Quantum tunneling · Qubit · Spin dynamics

Contents

F. Luis and M. Evangelisti (✉)
Departamento de Física de la Materia Condensada, Instituto de Ciencia de Materiales de Aragón, CSIC and Universidad de Zaragoza, 50009 Zaragoza, Spain
e-mail: evange@unizar.es

Abbreviations

χ	Magnetic susceptibility
τ^{-1}	Spin–lattice relaxation rate
ac	Alternating current
B	Applied magnetic field
C_{m}	Magnetic specific heat
EPR	Electron paramagnetic resonance
g_J	Gyromagnetic ratio
Gd	Gadolinium
k_{B}	Boltzmann constant
L	Orbital angular momentum
MCE	Magnetocaloric effect
MNM	Molecular nanomagnet
MR	Magnetic refrigeration
POM	Polyoxometalate
R	Gas constant
SLR	Spin–lattice relaxation
S_{m}	Magnetic entropy
T	Temperature

1 Introduction

The relationship between magnetic refrigeration (MR) and spin–lattice relaxation (SLR) is evident by considering the basic principle of MR, which reflects temperature variations following a change of the applied magnetic field under adiabatic conditions (see, e.g., [1]). This phenomenon, known as the magnetocaloric effect (MCE), is associated with the fact that changes in the entropy associated with the lattice compensate equal but opposite changes in the magnetic entropy, thus resulting in a change in temperature of the material (see, e.g., [2]). Therefore, a sine-qua-non condition for achieving optimum cooling is the thermodynamic equilibrium of the spins with the lattice.

Lanthanide ions are close to ideal workbench materials to test the validity of crystal-field and SLR theories (see, e.g., [3]). Among them, gadolinium occupies a special position because its orbital angular momentum (L) is zero and it has the largest entropy per single ion. Besides, gadolinium is the most widespread element among magnetic refrigerant materials. In spite of $L = 0$, some weak anisotropy can

be experimentally detected, though typically at very low temperatures. Coulomb interactions with ions in its close neighborhood are the electrostatic forces that almost exclusively determine such anisotropy. Therefore, this element is a model crystal-field probe. This enables a fine tuning of its magnetic properties by engineering its local coordination sphere by molecular chemistry. The importance of molecular nanomagnets (MNMs) has surged in recent years because of their record performances as magnetic coolers at cryogenic temperatures [4–7] and their potential use as qubits in quantum information processing [8–11].

In Sect. 2, we introduce the reader to the subject of magnetic anisotropy of lanthanide ions, with special emphasis on gadolinium. Then, we describe the fundamentals of the MR (Sect. 3) and the physical models that are at the basis of the SLR (Sect. 4). In Sect. 5, we review case examples from the recent literature on mononuclear MNMs, namely gadolinium polyoxometalates (Gd-POMs) [12, 13]. In addition to containing gadolinium, the advantage of these materials resides in an utterly effective screening of all magnetic interactions, which ultimately facilitates our purpose of shedding light on how MR and SLR relate with each other. In Sect. 6, we discuss the use of Gd-POMs as magnetic coolers, while we dedicate Sect. 7 to describe the dynamics of the Gd^{3+} spins in these materials. These studies reveal that the precise mechanism by which spins exchange energy with the lattice near zero magnetic field, i.e., the one that accounts for the observation of Curie law, is not yet fully understood. Section 8 explores the suitability of Gd-POMs to function as qubits at very low temperatures. We aim at presenting the state-of-the-art understanding of these phenomena and applications, while singling out challenges and open questions (Sect. 9).

2 Magnetic Anisotropy and Spin Hamiltonian of Lanthanide Ions

The magnetic properties of lanthanide Ln^{3+} ions are determined by the strong coupling between the orbital $\boldsymbol{L}$ and spin $\boldsymbol{S}$ angular momenta, which results in a total angular momentum $\boldsymbol{J} = \boldsymbol{L} + \boldsymbol{S}$. Given the energy differences between levels of different J, the magnetic behavior can often be accurately described by considering only the ground state multiplet. The magnetic moment of a lanthanide free ion is given by $\boldsymbol{\mu} = g_J \mu_B \boldsymbol{J}$, where g_J is the gyromagnetic ratio and μ_B is the Bohr magneton. The $2J + 1$ magnetic levels of this ground multiplet are split by the magnetic anisotropy, arising from the interaction with the crystal field. Time-reversal symmetry imposes some restrictions. Electronic energy levels of Kramers ions, having half-odd spin values, are, at least, doubly degenerate. The remaining degeneracy is lifted by the Zeeman interaction with magnetic fields. In addition, most lanthanides have stable isotopes with nonzero nuclear spin I, thus the hyperfine interactions must also be taken into account. In the case of gadolinium, the isotope ^{155}Gd has

$I = 3/2$ and a natural abundance of about 15 %. Within the ground multiplet, the spin Hamiltonian can be written in terms of Steven's operators, as follows [14]

$$\mathcal{H} = \sum_{n,m} B_n^m O_n^m - g_J \mu_B \left(B_x J_x + B_y J_y + B_z J_z \right) + \vec{J} A_{\rm hf} \vec{I} \qquad (1)$$

where, B_n^m, with n even and $m \leq n$, are numerical coefficients (or anisotropy constants), O_n^m are effective spin operators containing powers of J_x, J_y, and J_z, and $A_{\rm hf}$ is an hyperfine coupling tensor. The anisotropy terms that do actually appear in the spin Hamiltonian in Eq. (1) are determined by the local coordination, while their sign and magnitude vary also depending on each particular lanthanide ion. The energies and wave functions of Eq. (1) depend on the orientation of the external magnetic fields with respect to the crystal axes.

Figure 1 shows the typical energy level scheme of a lanthanide ion with $J = 7/2$ (like Gd^{3+}). However, it turns out that Gd^{3+} represents an exceptional situation. According to Hund's rules, its $4f^7$ electronic configuration results in a total spin $S = 7/2$ and angular momentum $L = 0$, with a g_J very close to the free electron value $g_J = 2$. The electronic wave function possesses spherical symmetry and the magnetic anisotropy vanishes, in first order. However, the crystal field induces some mixing of the ground state multiplet with excited multiplets having $L \neq 0$. The ensuing electronic orbital distortion results in a weak, but measurable, magnetic anisotropy that strongly depends on the local coordination. For instance, B. Bleaney and co-workers [15] studied Gd^{3+} ions located in a sixfold symmetry crystal field and found a zero-field level splitting of ~0.35 K, whereas W. Low and K. Shaltiel [16] found an overall splitting of ~0.25 K for Gd^{3+} ions located in a cubic field. S. Geschwind and co-workers [17] reported one of the largest splitting ever measured for gadolinium, using a sample of Al_3O_4 doped with Gd^{3+} impurities. In this case, the Gd^{3+} ion sits in a threefold coordinated site, giving rise to an overall level splitting of ~1.8 K.

3 Magnetic Refrigeration and the Magnetocaloric Effect

Nobel laureate Giauque and his student MacDougall were the first to attain sub-Kelvin temperatures by magnetic refrigeration [18, 19]. They reached 0.25 K by making use of 61 g of a paramagnetic material, namely $Gd_2(SO_4)_3 \cdot 8H_2O$, starting from the temperature of 1.5 K and the applied magnetic field of 0.8 T. At the basis of this achievement is the MCE, i.e., the isothermal change of magnetic entropy ($\Delta S_{\rm m}$) and adiabatic change of temperature ($\Delta T_{\rm ad}$) that follow a change of the applied magnetic field (ΔB). Figure 2 provides a graphical description of this effect and the associated principle of adiabatic demagnetization for a mole of paramagnetic material. The system is initially in A($T_{\rm i}$, $B_{\rm i}$), at temperature $T_{\rm i}$ and field $B_{\rm i}$. Under adiabatic conditions, i.e., when the total entropy of the system

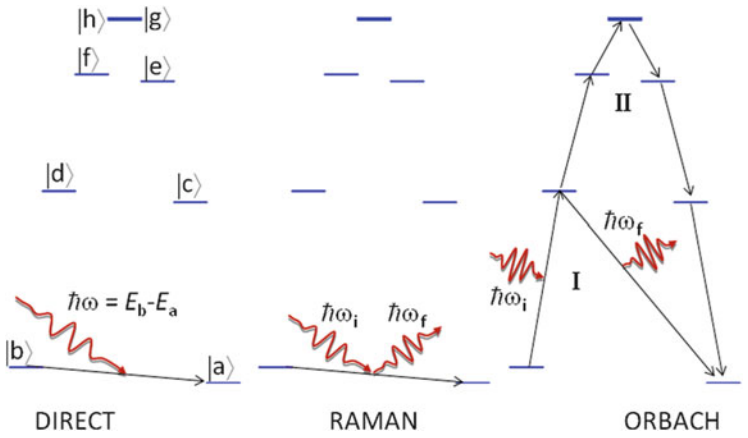

Fig. 1 Energy level scheme of a lanthanide ion with $J = 7/2$, resulting from the combined actions of the magnetic anisotropy and the Zeeman coupling to an external magnetic field. Each of the three panels shows schematically a different spin-phonon process linking the two lowest lying states $|a\rangle$ and $|b\rangle$. In a direct process, the spin system undergoes a transition from state $|b\rangle$ to state $|a\rangle$ induced by either the absorption or emission of a resonant phonon. The Raman process is an inelastic scattering of an incident phonon with the spin system, leading to a magnetic transition from $|b\rangle$ to $|a\rangle$ and a change in the frequency of the phonon. The Orbach process is a thermally activated two-phonon process. An incident phonon induces a transition to an intermediate excited spin state $|c\rangle$, which then decays to state $|b\rangle$ by re-emitting another phonon

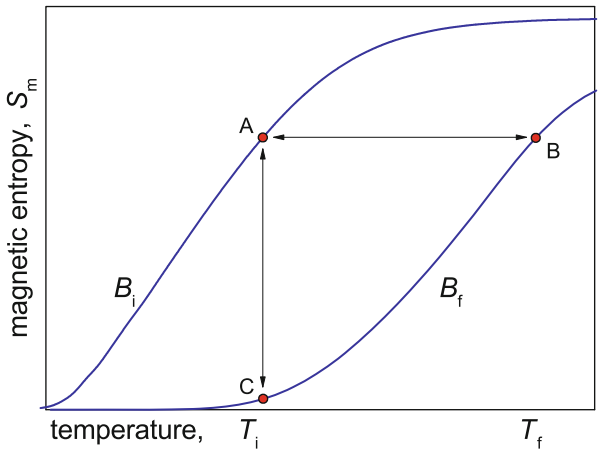

Fig. 2 Temperature-dependence of the molar magnetic entropy of a paramagnetic system for magnetic fields B_i and $B_f > B_i$. AB process: adiabatic magnetization (A → B) or demagnetization (B → A), providing ΔT_{ad}. AC process: isothermal magnetization (A → C) or demagnetization (C → A), providing ΔS_m

remains constant, the adiabatic field change $B_i \rightarrow B_f$, where $B_f > B_i$, brings the system to B(T_f, B_f) with a temperature increase $\Delta T_{ad} = T_f - T_i$ (horizontal arrow). On the other hand, adiabatically demagnetizing from B(T_f, B_f) to A(T_i, B_i) results in a temperature decrease $\Delta T_{ad} = T_i - T_f$. If the magnetic field is isothermally changed, as between A(T_i, B_i) and C(T_i, B_f), then there is an entropy change ΔS_m (vertical arrow), whose upper limit is the full magnetic entropy content at $T = \infty$, i.e., $S_m/R = \ln(2S + 1)$, where R is the gas constant and S the spin value (e.g., $S = 7/2$ for Gd^{3+}).

Both ΔS_m and ΔT_{ad} are the characteristic parameters of the MCE. All magnetic materials show the MCE, although the intensity of the effect depends on the properties of each material [2]. The exploitation of this effect requires large changes of magnetic entropy and adiabatic temperature within the working temperature range of interest. Molecular nanomagnets are promising refrigerant materials at cryogenic temperatures [4–7], since they can be synthetized as such to combine a large spin ground state, with weak ferromagnetic exchanges between the constituent magnetic ions, in addition to a relatively large metal:non-metal mass ratio, i.e., a large magnetic density [20]. All these characteristics favor the enhancement of the MCE at very low temperatures. As regards applications, best performing astronomical instruments rely on sensors cooled to milliKelvin temperatures. Contrary to ^{3}He-^{4}He dilution refrigerators, adiabatic demagnetization refrigerators are suitable for operations in a gravity-free environment, which is a requirement for space-borne missions. Furthermore, over the last few years we have witnessed a rise in the production of security instruments for nuclear detection that has ultimately led to a worldwide shortage of ^{3}He. It is then important to secure an efficient alternative to ^{3}He-based technology for ultra-low temperatures.

We shall pointing out that the magnetic anisotropy plays an important role, the more so the lower is the target T_f. The crystal-field effects arising from the metal oxidation states and surrounding organic ligands, concurrently with anisotropic magnetic interactions, set in a preferential direction for the spins. Therefore, the larger is the magnetic anisotropy, the less sensitive to the applied field is the polarization of the spins, hence resulting in a relatively smaller MCE [4]. This also suggests that the magnetic anisotropy contributes to determine the lowest temperature in an adiabatic demagnetization, likewise the magnetic interactions or their absence thereof (see Sect. 6).

4 Spin–Lattice Relaxation

4.1 Historical Background

The need of understanding the magnetism of diluted paramagnetic salts stimulated the early studies on the SLR. In 1929, Paul Ehrenfest argued that the polarization of paramagnetic moments under the action of an external magnetic field, that is, the processes described by Curie and Brillouin laws, must involve some transfer of

energy to the crystal lattice [21]. Such coupling is also necessary for the application of magnetic cooling to attain temperatures close to the absolute zero, when spins and lattice need to be in mutual thermal equilibrium.

In 1936, the Dutch physicist C. J. Gorter became the first to measure, using a calorimetric method, the heating of the crystal lattice following the relaxation of the spins of transition metal and Gd^{3+} ions [22]. Later, methods that are more powerful were developed to determine the characteristic spin–lattice relaxation times τ. The first of these was ac magnetic susceptibility. In analogy with the relaxation of electric dipoles, studied by P. Debye [23], the response of paramagnetic spins to an alternating magnetic field $\boldsymbol{h} = \boldsymbol{h}_0 \cos(\omega\tau)$ is described by a complex magnetic susceptibility, with real χ' and imaginary χ'' components that depend on frequency according to the following (Debye) equations [24]

$$\begin{aligned} \chi' &= \chi_S + \frac{\chi_T - \chi_S}{1 + (\omega\tau)^2} \\ \chi'' &= \frac{\chi_T - \chi_S}{1 + (\omega\tau)^2}\omega\tau \end{aligned} \tag{2}$$

where χ_T and χ_S are, respectively, the thermal equilibrium and adiabatic susceptibilities. If the system is characterized by a distribution of relaxation times (as it is the case in, e.g., a powdered sample of a paramagnetic material subject to a dc magnetic field), the above expressions have to be integrated over such distribution. Cole and Cole [25] proposed a useful analytical form, i.e.:

$$\begin{aligned} \chi' &= \chi_S + \frac{(\chi_T - \chi_S)\left[1 + (\omega\tau)^\beta \cos(\beta\pi/2)\right]}{1 + 2(\omega\tau)^\beta \cos(\beta\pi/2) + (\omega\tau)^{2\beta}} \\ \chi'' &= \frac{(\chi_T - \chi_S)(\omega\tau)^\beta \sin(\beta\pi/2)}{1 + 2(\omega\tau)^\beta \cos(\beta\pi/2) + (\omega\tau)^{2\beta}} \end{aligned} \tag{3}$$

where $\beta \leq 1$ is a new parameter that parameterizes the distribution width ($\beta = 1$ recovers Debye law).

After World War II, the first experiments of electron paramagnetic resonance (EPR) were performed [26, 27] This technique soon became very useful to determine spin-relaxation times. Ac susceptibility and EPR data of transition metal [28, 29] and lanthanide salts [30, 31] provided a solid basis for the development of theories accounting for the mechanism of SLR. It became clear that the coupling was dominated by the modulation of the magnetic anisotropy by lattice vibrations, or phonons. In this context, lanthanide ions are model systems because the magnetic anisotropy of localized 4f electrons is simpler to treat than that of transition metal ions.

This field of research received a big boost in 2005, when Ishikawa and co-workers discovered magnetic hysteresis, i.e. magnetic memory effects, in molecules comprising a lanthanide ion (Tb^{3+}) sandwiched between two flat

phthalocyanine molecules [32]. The hysteresis loops revealed the existence of quantum tunneling between different spin states, a phenomenon discovered earlier in polynuclear transition metal clusters [33–35]. In the last decade, many new molecules showing similar properties have been synthesized and their magnetic relaxation studied in detail [36–39]. In the following sub-sections, we briefly review the theoretical description of SLR and quantum spin dynamics of nearly isolated lanthanide ions.

4.2 Mechanisms of Spin–Lattice Relaxation

In 1932, I. Waller introduced the first mechanism [40]. He suggested that lattice vibrations modulate spin–spin dipolar interactions and can therefore induce transitions between different spin states. Spin lattice relaxation times calculated with this model were, however, found to be much longer than those measured by Gorter [22]. As an alternative, W. Heitler and E. Teller [41] proposed that the dominant coupling mechanism involves the modulation of the magnetic anisotropy, much stronger than dipolar interactions. Their theory was later elaborated by R. de L. Kronig [42], J. H. Van Vleck [43] and R. Orbach [44]. It extends the crystal-field theory by introducing the changes in the electric field caused by deformations of the local coordination. Combined with the spin-orbit interaction, such deformations introduce a dynamic spin–lattice interaction. This interaction can be expanded in terms of powers of the lattice strains ε and rotations ω. Up to first order, the spin–lattice interaction reads as follows [44, 45]

$$\mathcal{H}_{S-\mathrm{latt}} = \mathcal{H}^{(0)}_{S-\mathrm{latt}} + \sum_{n,m} g_{\mathrm{strain}}(n,m) O_n^m \varepsilon_{nm} + \sum_{n,m} g_{\mathrm{rot}}(n,m) O_n^m \omega_{nm} \qquad (4)$$

where $\mathcal{H}^{(0)}_{S-\mathrm{latt}}$ is the unperturbed magnetic anisotropy, i.e., the first term in Eq. (1), $g_{\mathrm{strain}}(n,m)$ and $g_{\mathrm{rot}}(n,m)$ are constant coefficients and ε_{nm} and ω_{nm} are linear combinations of strains and rotations that are appropriate to the spin operator ${O_n}^m$.

Because vibrations lower the local coordination symmetry, the spin–lattice Hamiltonian in Eq. (4) contains terms that are forbidden for the static lattice. A general treatment of these effects is a complicated and cumbersome problem and involves a large number of unknown parameters. However, in most situations, it is possible to achieve a reasonably good description by considering only the dominant terms. As an example, we consider an ion with a predominantly uniaxial magnetic anisotropy, given by the term ${B_2}^0 {O_2}^0$. We can then write the spin–lattice Hamiltonian as follows [45]

$$\mathcal{H}_{S-\text{latt}} = \frac{1}{2}\left(g_{\text{strain}}\varepsilon_{xz} + g_{\text{rot}}\omega_{xz}\right) \otimes \{J_x, J_z\} + \frac{1}{2}\left(g_{\text{strain}}\varepsilon_{yz} + g_{\text{rot}}\omega_{yz}\right) \otimes \{J_y, J_z\}. \tag{5}$$

In [45] (see also [46] and [47]), it was shown that $g_{\text{rot}}/2 = 3{B_2}^0$ and it was argued that $g_{\text{strain}} \approx g_{\text{rot}} = 6{B_2}^0$. Additional terms, such as $3{B_2}^0(\varepsilon_{xx} - \varepsilon_{yy})({J_x}^2 - {J_y}^2)$, can also be present in $\mathcal{H}_{S\text{-latt}}$ (see, e.g., [46]), although their physical basis has been the subject of some debate [48, 49]. Lattice strains and rotations can be expressed in terms of operators that create and annihilate normal vibration modes, or phonons. Therefore, the spin–lattice Hamiltonian introduces finite probabilities for transitions between different energy states of the unperturbed spin Hamiltonian, accompanied by changes in the populations $n_{\boldsymbol{k},s}$ of phonon modes. Here, $\boldsymbol{k}$ and s denote, respectively, the wave vector and polarization mode of each phonon.

At sufficiently low temperatures, SLR is dominated by transitions linking the two lowest-lying magnetic states $|\text{a}\rangle$ and $|\text{b}\rangle$. The simplest relaxation process is a transition, depicted in the left-hand panel of Fig. 2, between these two states induced by the creation or annihilation of a phonon with energy $\hbar\omega_{\text{ab}} \equiv E_{\text{b}} - E_{\text{a}}$. The rate of this first-order *direct process* can be calculated using Fermi golden rule. Using a simple linear phonon dispersion relation $\omega_{\boldsymbol{k}s} = ck$, where c is the average speed of sound, and the spin–lattice Hamiltonian given in Eq. (5), leads to the following expressions

$$\begin{aligned} W_{\text{a}\leftarrow\text{b}} &= \frac{(E_{\text{b}} - E_{\text{a}})^3}{6\pi\rho c^5\hbar^4}\left(|\langle\text{a}|V_{xz}|\text{b}\rangle|^2 + |\langle\text{a}|V_{yz}|\text{b}\rangle|^2\right)\left(\langle n_{\text{ab}}\rangle_T + 1\right) \\ W_{\text{b}\leftarrow\text{a}} &= \frac{(E_{\text{b}} - E_{\text{a}})^3}{6\pi\rho c^5\hbar^4}\left(|\langle\text{a}|V_{xz}|\text{b}\rangle|^2 + |\langle\text{a}|V_{yz}|\text{b}\rangle|^2\right)\langle n_{\text{ab}}\rangle_T \end{aligned} \tag{6}$$

where ρ is the density, $V_{\alpha z} = 3{B_2}^0\{J_\alpha, J_z\}$, with $\alpha = x$ or y are spin operators, and $\langle n_{\text{ab}}\rangle_T = [\exp(\hbar\omega_{\text{ab}}/k_{\text{B}}T) - 1]^{-1}$ is the thermal population of resonant phonon modes. The overall spin–lattice relaxation is then given by

$$\begin{aligned} \tau_{\text{D}}^{-1} &= W_{\text{a}\leftarrow\text{b}} + W_{\text{b}\leftarrow\text{a}} \\ &= \frac{(E_{\text{b}} - E_{\text{a}})^3}{6\pi\rho c^5\hbar^4}\left(|\langle\text{a}|V_{xz}|\text{b}\rangle|^2 + |\langle\text{a}|V_{yz}|\text{b}\rangle|^2\right) \times \coth\left(\frac{\hbar\omega_{\text{ab}}}{2k_{\text{B}}T}\right). \end{aligned} \tag{7}$$

The matrix elements in Eq. (7), thus also τ^{-1}, would vanish if $|\text{a}\rangle$ and $|\text{b}\rangle$ were eigenstates $|m\rangle$ and $|m'\rangle$ of J_z, i.e., if they corresponded to classical angular momentum orientations, unless $m = \pm 1/2$ and $m' = \mp 1/2$. The direct process is made possible by the presence of off-diagonal terms in the spin Hamiltonian (3). It is, therefore, a phonon-induced spin tunneling process. The rate also vanishes, at zero field, in the case of Kramers ions for which $E_{\text{a}} = E_{\text{b}}$ and matrix elements are equal to zero. This selection rule is broken by the Zeeman interaction with a

magnetic field. It follows then that $\langle a|V_{\alpha z}|b\rangle$ and $E_b - E_a \propto B$, which therefore introduces a stronger dependence of ${\tau_D}^{-1}$ on B with respect to that found for non Kramers ions.

For more complex spin–lattice Hamiltonians, the derivation of ${\tau_D}^{-1}$ can proceed along analogous (although mathematically more involved) lines. The relaxation rate can be written as

$$\tau_D^{-1} = (E_b - E_a)^d R_D \coth\left(\frac{\hbar\omega_{ab}}{2k_B T}\right) \tag{8}$$

where $d = 3$ and 5 for non Kramers and Kramers ions, respectively, and R_D is a coefficient that depends on the matrix elements of $\mathcal{H}_{S\text{-latt}}$ between $|a\rangle$ and $|b\rangle$.

Transitions between $|a\rangle$ and $|b\rangle$ can also proceed via two-phonon processes. These processes arise from the application of the spin–lattice interaction Hamiltonian in Eq. (4) up to second order of time-dependent perturbation theory. One of these, known as the Raman process due to its analogy with the Raman process in optics, is shown in the center panel of Fig. 2. It involves the inelastic scattering of an incoming phonon, of frequency ω_i, and the emission of another of frequency $\omega_f = \omega_i \pm \omega_{ab}$. Notice that both ω_f and ω_f can be $\gg\omega_{ab}$. Compared with the direct process, the Raman mechanism benefits from the increase of the phonon density of states with energy. Its relaxation rate ${\tau_R}^{-1}$ can be written as

$$\tau_R^{-1} = R_R \frac{b + pCB^2}{b + CB^2} T^r, \tag{9}$$

where $r = 7$ and 9 for non Kramers and Kramers ions, respectively, and R_R includes second-order matrix elements of $\mathcal{H}_{S\text{-latt}}$, b is constant describing the high-T specific heat dependence ($C_m = bT^{-2}$), C is the Curie constant and p is a material-dependent parameter.

The strong temperature dependence of ${\tau_R}^{-1}$ can make Raman processes dominant over direct processes at sufficiently high temperatures. Yet, experiments performed on cerium magnesium nitrate [50] revealed the existence of another two-phonon relaxation mechanism, the Orbach process, which is illustrated in the right-hand panel of Fig. 2. Unlike the Raman process, it involves a real, direct transition from state $|b\rangle$ to an intermediate excited spin state $|c\rangle$, followed by another transition from $|c\rangle$ to $|a\rangle$. This process is allowed provided that $(E_c - E_a)/\hbar$ falls within the spectrum of vibration frequencies. Its relaxation rate is given by

$$\tau_O^{-1} = R_O (E_c - E_a)^3 \exp\left(-\frac{E_c - E_a}{k_B T}\right), \tag{10}$$

where R_O is a coefficient that depends on the matrix element of $\mathcal{H}_{S\text{-latt}}$ between states $|c\rangle$ and $|a\rangle$. The intermediate state $|c\rangle$ needs not be the lowest lying excited state. Rather, the most efficient relaxation path is associated with excitations to the lowest lying state that has a sufficiently large overlap with the ground state $|a\rangle$. The

Orbach process is a thermally activated spin tunneling process, fully analogous to that found in polynuclear single molecule magnets such as Mn_{12} and Fe_8.

Summarizing, the classic theories predict that the overall spin–lattice relaxation rate can be estimated adding the contributions of the three different mechanisms shown in Fig. 2, thus it reads

$$\tau^{-1} = (E_b - E_a)^d \; R_{\mathrm{D}} \; \coth\left(\frac{\hbar\omega_{\mathrm{ab}}}{2k_{\mathrm{B}}T}\right) + R_{\mathrm{R}}\frac{b + pCB^2}{b + CB^2}T^r + R_{\mathrm{O}}(E_{\mathrm{c}} - E_a)^3 \exp\left(-\frac{E_{\mathrm{c}} - E_a}{k_{\mathrm{B}}T}\right). \tag{11}$$

At sufficiently low temperatures, only direct processes retain a finite probability. Furthermore, this probability can be very small at low magnetic fields, especially so in the case of Kramers ions. These two facts account for the existence of magnetization hysteresis and magnetic memory effects over long time scales in lanthanide single-ion magnets. Under these conditions, magnetic memory turns out to be limited by a different process, of a pure quantum nature, which was not contemplated by early models of spin lattice interaction.

4.3 Quantum Spin Tunneling

Quantum tunneling between angular momentum orientations $|m\rangle$ and $|m'\rangle$ is induced by off-diagonal terms in the spin Hamiltonian. This phenomenon can take place if the local magnetic bias $\xi = g_J\mu_{\mathrm{B}}|m - m'|B_z$ is smaller than the quantum tunnel splitting Δ of the two states at $B_z = 0$. Typical values of Δ for the ground state of lanthanide ions are of the order or smaller than 1 mK. This is much larger than the minute Δ of polynuclear MNMs, which lie well below the micro-K range, but still smaller than the energy scales of hyperfine couplings and of dipolar interactions with neighboring molecules. In analogy with the Landau-Zener model [51], tunneling can be induced externally by sweeping a magnetic field along the anisotropy axis that compensates the effect of these "environmental" perturbations. The first experimental evidences were found in a dilute crystal of Ho^{3+} ions diluted in inorganic fluoride crystals [52], whose hysteresis loop shows steps at magnetic fields that bring states of the same nuclear polarization into resonance conditions. Latter, the same phenomenon was found in $TbPc_2$ molecules [32].

Yet, ac susceptibility experiments suggest that tunneling can also occur near zero field in concentrated samples of lanthanide ions, for which dipolar interactions are expected to be much stronger than Δ [53]. A solution to this puzzle was found by Prokof'ev and Stamp [54], who studied the influence of time-dependent hyperfine and dipolar fields on spin tunneling. The situation is sketched in Fig. 3. For any lanthanide ion experiencing a local *static* $\xi_0 > \Delta$, tunneling would be forbidden.

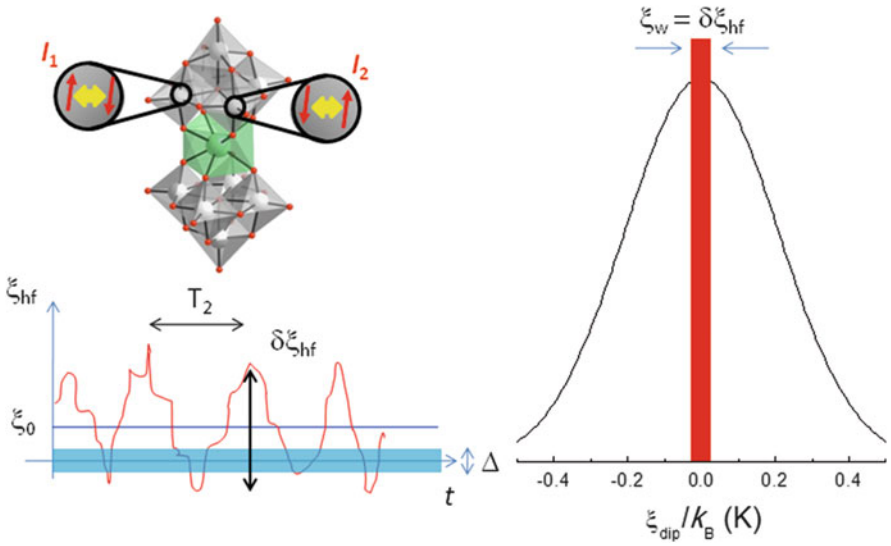

Fig. 3 Simple picture of quantum tunneling of an electronic spin induced by nuclear spin bath fluctuations. Quantum tunneling of an isolated electronic spin is allowed if the local bias ξ is smaller than the quantum tunnel splitting Δ. Flip-flop nuclear spin fluctuations give rise to a time-dependent component $\delta\xi_{hf}$ of the local hyperfine bias experienced by the lanthanide ion and can, therefore, broaden this tunneling energy "window". The right-hand panel shows the distribution P_{dip} of magnetic energy bias ξ_{dip} associated with intermolecular dipolar interactions

Yet, flip-flop transitions between nuclear spins in the same or neighboring molecules generate a *dynamic* component $\delta\xi_{hf}$, which can be larger than Δ. Like in a hysteresis measurement, these local field fluctuations can take the electronic spin to resonance conditions and enable it to flip by tunneling. The second ingredient of this model is the back action of the reversed spin on its neighbors. Each spin flip modifies the dipolar bias at any other crystal site. As a result, some spins that initially lie outside the tunneling energy "window" are brought into resonance. This self-organized process gives all spins a chance to tunnel. The average tunneling rate is then given by i.e.,

$$\Gamma = \frac{\Delta^2}{\hbar} P\left(\xi_{dip} = -\xi_Z\right), \tag{12}$$

where $P(\xi_{dip})$ is the distribution of dipolar bias (see Fig. 3) and ξ_Z is the Zeeman bias associated with external magnetic fields. An intriguing, and still open, question refers to the possible contribution of these tunneling flips to SLR. This question is addressed, from an experimental perspective, in Sect. 7.

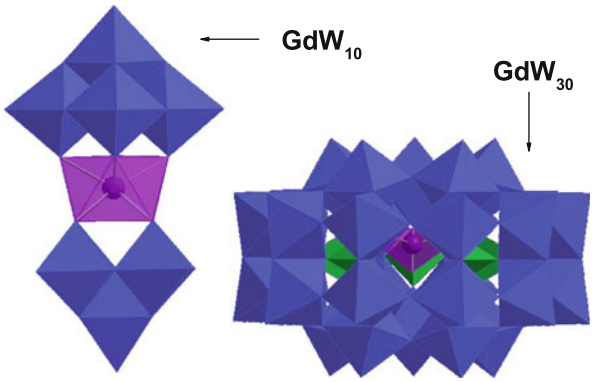

Fig. 4 Molecular structures of the two polyoxometalates, namely GdW_{10} (*left*) and GdW_{30} (*right*)

5 Mononuclear Gd-Based Polyoxometalates: Molecular Design of the Magnetic Anisotropy

To illustrate the close relationship between MR and SLR, we select two MNMs based on polyoxometalate (POM) salts with general formula $Na_9[Gd(W_5O_{18})_2]\cdot 35H_2O$ (hereafter shortened as GdW_{10}) and $K_{12}(GdP_5W_{30}O_{110})\cdot 54H_2O$ (hereafter shortened as GdW_{30}), respectively. Both compounds have a single Gd^{3+} ion per molecular unit, encapsulated by a closed polyoxowolframate framework that acts as a capping ligand (Fig. 4). Examples of Gd-based mononuclear MNMs other than Gd-POMs were recently studied in the context of MR and SLR [55]. A major characteristic of GdW_{10} and GdW_{30} is the significantly large intermolecular distance. The compound GdW_{10} crystallizes in space group triclinic with $a = 12.7417(3)$ Å, $b = 13.0815(3)$ Å, $c = 20.4366(5)$ Å, whereas GdW_{30} crystallizes in space group monoclinic with $a = 17.5255(10)$ Å, $b = 21.0554(2)$ Å, $c = 35.5201(2)$ Å [13]. From the unit cell volumes, one can obtain the mean values of the intermolecular separations, r, that are, 10 Å for GdW_{10} and 20 Å for GdW_{30}. Intermolecular dipolar interactions are therefore very weak, even in non-diluted samples.

These systems are appealingly simple and, as we show in this Section, offer possibilities for the chemical design of relevant physical parameters that are very difficult to achieve with polynuclear molecular clusters. The choice of Gd^{3+} is a natural one. As a free ion, it has an electronic ground state with $L = 0$ and $S = 7/2$. Its magnetic anisotropy is therefore very weak, which enhances SLR and MCE, and it is fully determined by the local coordination. In order to show the connection between structure and magnetic anisotropy, we compare the magnetic properties of GdW_{10} and GdW_{30}, which, as can be seen in Fig. 4, have very different molecular structures.

Magnetic susceptibility χ measurements show that both samples behave as quasi-ideal paramagnets [13]. The room-temperature χ_T value is 7.88 $cm^3\ K\ mol^{-1}$, as expected for the Curie law of a $S = 7/2$ system with $g_J = 2.00$. Furthermore, χ_T

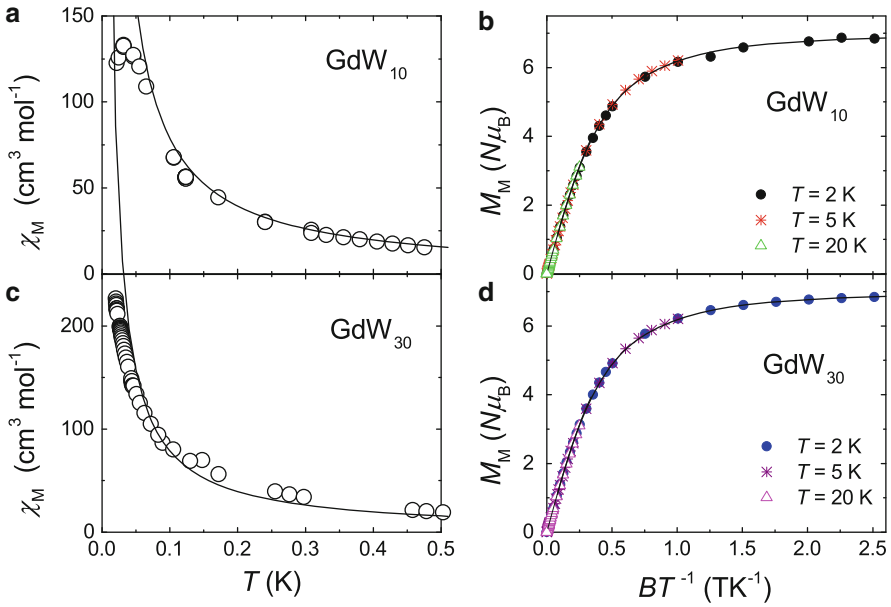

Fig. 5 Experimental zero-applied-field susceptibility of GdW_{10} (panel **a**) and GdW_{30} (panel **b**) versus temperature for the lowest investigated temperatures, together with Curie law for $S = 7/2$ and $g_J = 2.00$ (*solid lines*). Experimental magnetization of GdW_{10} (panel **c**) and GdW_{30} (panel **d**) versus B/T for 2 K $< T <$ 20 K and $0 < B < 5\,T$, together with the Langevin function (*solid lines*)

stays constant on decreasing temperature down to ≈0.1 K. Anticipating the discussion on the magnetic specific heat (C_m) and EPR experiments, we attribute the slight deviation from the Curie law observed below 0.1 K to the presence of a weak magnetic anisotropy, which becomes observable only at these very low temperatures. Besides, $\chi(T)$ of GdW_{10} shows a maximum centered at ≈36 mK (Fig. 5) that can be attributed to the onset of long-range magnetic order induced solely by dipole-dipole interactions. By contrast, GdW_{30} remains paramagnetic in the whole temperature range (Fig. 5). This difference can be accounted for by looking in detail at the crystal structures of both compounds. While the shortest Gd–Gd distance in the GdW_{10} lattice is 1.12 nm, it is 1.56 nm in the case of GdW_{30}. As the strength of the dipolar interaction is proportional to r^{-3}, we expect the spin ordering temperatures to scale accordingly. This argument enables us to estimate a critical temperature of $36/23 \approx 4$ mK for GdW_{30}, which is below the experimental base temperature (≈10 mK).

Magnetization isotherms, collected for 2 K $< T <$ 20 K and B up to 5 T (Fig. 5), corroborate the paramagnetic behavior of both compounds for this temperature range. These curves saturate to the value of $7N\mu_B$ and their field-dependence is well described by the Brillouin function for $S = 7/2$ and $g_J = 2.00$ (solid line).

Differences between these two MNMs become apparent if one looks at quantities, such as the specific heat or the microwave absorption, that strongly depend on

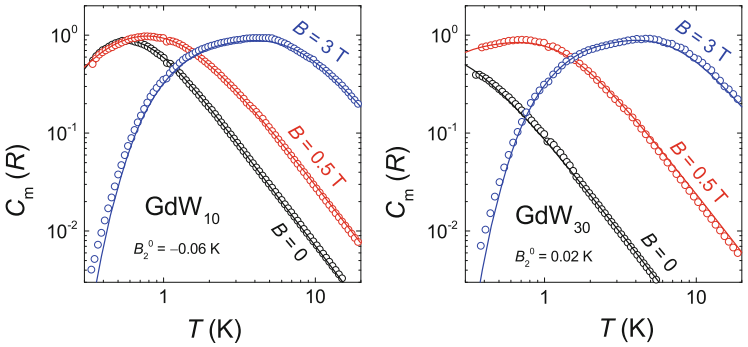

Fig. 6 Experimental magnetic specific heat of GdW_{10} (*left panel*) and GdW_{30} (*right panel*), normalized to the gas constant R, versus temperature, for $B = 0$, 0.5 and 3 T, as labeled. *Solid lines* are the calculated Schottky-like contributions, see main text

the intensity and sign of the magnetic anisotropy. Figure 6 compares C_m of GdW_{10} and GdW_{30}, measured between 0.35 and 20 K for $B = 0$, 0.5 and 3 T. As anticipated by the susceptibility results, these measurements do not show any signature of a phase transition. Instead, they show a broad Schottky-type anomaly that shifts towards higher temperatures on increasing applied magnetic field for both compounds. We associate this feature to the splitting of the $S = 7/2$ multiplet of the Gd^{3+} ion. The fact that the zero-field C_m also shows such behavior denotes the presence of an internal field, b_0, which acts locally on the Gd^{3+} ions, caused either by magnetic anisotropy or by magnetic interactions. We disregard the latter because the weak dipolar interactions should not be effective at these relatively high temperatures. This is further corroborated by the fact that magnetically dilute samples, like the isostructural $Gd_{0.3}Y_{0.7}W_{10,}$ in which a fraction of Gd^{3+} ions are replaced by diamagnetic Y^{3+}, show the same C_m [13]. The experimental curves can be fitted using the single-spin Hamiltonian in Eq. (1) with a nonzero B_2^0 anisotropy constant. The best fits are obtained for $B_2^0 = -0.06$ K and $B_2^0 = 0.02$ K for GdW_{10} and GdW_{30}, respectively. The different sign of the magnetic anisotropy show the crucial influence of the molecular structure on the magnetic properties. In the case of the "cigar-like" GdW_{10} molecule (Fig. 4), $B_2^0 < 0$. corresponds to an easy-axis magnetic anisotropy, which favors magnetization along the molecular axis. By contrast, the positive sign of B_2^0 found for the "donough-shaped" GdW_{30} implies that the z-axis is not a preferential spin orientation.

EPR experiments can provide complementary information on the magnetic anisotropy. Representative results for both materials, measured at $T = 10$ K and frequency of 25 GHz, are shown in Fig. 7 [12]. They confirm the existence of a finite magnetic anisotropy and corroborate the marked differences between the two MNMs. Fitting the spectra measured at different temperatures (between 2 and 20 K) and frequencies (from 15 GHz up to 35 GHz), enables the refinement of all relevant parameters of the spin Hamiltonian in Eq. (1). As anticipated in the discussion on

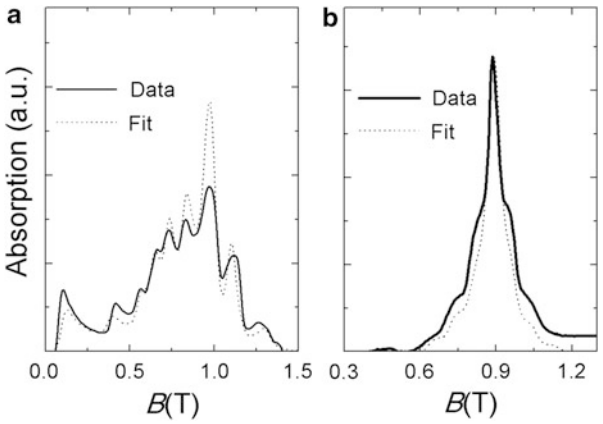

Fig. 7 Powder EPR absorption spectra of GdW_{10} (**a**) and GdW_{30} (**b**) measured at $T = 10$ K and $f = 25$ GHz, together with fits (*dashed lines*) obtained on basis of the spin Hamiltonian in Eq. (1)

the specific heat data, which parameters have nonzero values depends on the symmetry of the Gd^{3+} local coordination.

In the case of GdW_{10} (Fig. 4), the two anionic moieties that coordinate the central Gd^{3+}, are twisted to one another by 44.2°, leading to D_{4d} symmetry. Under these circumstances, the Hamiltonian in Eq. (1) has to include a term $B_4^4 O_4^4$, which does not commute with S_z. In the case of GdW_{30} (Fig. 4), a flat POM moiety encapsulates the Gd^{3+} ion with a close to C_{5v} symmetry, which allows the term $B_6^5 O_6^5$. Besides, ions located beyond the first coordination shell are likely causing a minor distortion from the ideal symmetry, which is accounted for by introducing a second-order term $B_2^2 O_2^2$. The results of the fits are as follows:

$$\frac{B_2^0}{k_B} = -0.059 \text{ K} \quad \text{and} \quad \frac{B_4^4}{k_B} = 4 \times 10^{-4} \text{ K} \quad \text{for } GdW_{10};$$

$$\frac{B_2^0}{k_B} = 0.019 \text{ K} \quad \text{and} \quad \frac{B_2^2}{k_B} = 0.019 \text{ K} \quad \text{for } GdW_{30}.$$

The inclusion of higher order terms does not improve the quality of the fits. These values corroborate, qualitatively and quantitatively, those obtained from the fit of specific heat data. The top panels of Fig. 8 show the classical magnetic energy landscapes of GdW_{10} and GdW_{30}, which correspond to an easy-axis and an easy-plane magnetic anisotropy, respectively. These results show that the design of the molecular structure by chemical engineering permits to modify the spin Hamiltonian, which governs the underlying physics. Finally, the determination of the anisotropy parameters enables calculating the energy level spectra that we show in the bottom panels of Fig. 8 for both compounds. The full spectra spread over relatively narrow energy ranges, e.g., not even exceeding 1 K in the case of GdW_{30}. As we shall see below, this has a profound influence in building solid foundations for exploiting these materials as effective magnetic coolers for the region of very low temperatures and as qubits.

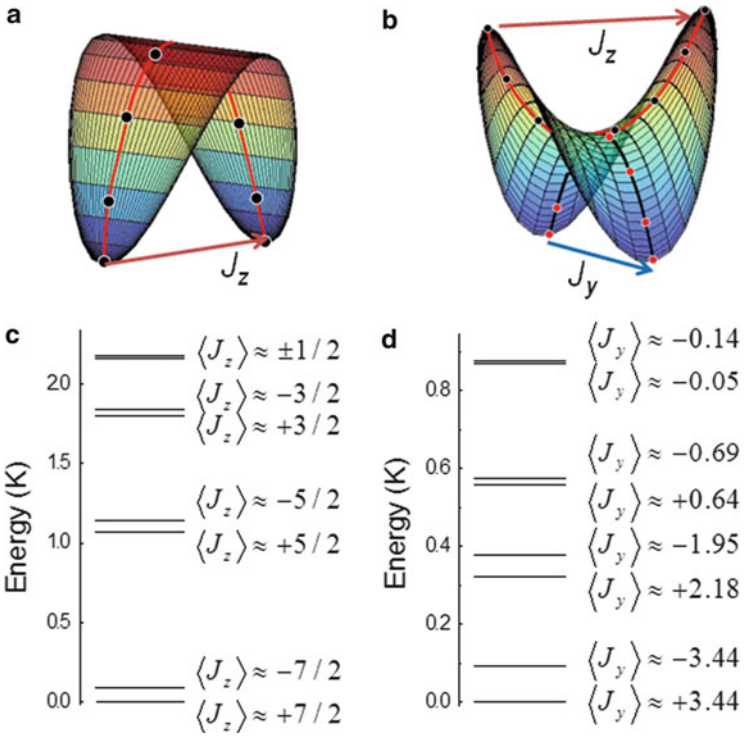

Fig. 8 Classical three-dimensional plots of the magnetic anisotropy energies of GdW_{10} (**a**) and GdW_{30} (**b**). Energy levels of GdW_{10} for $B_z = 10$ mT (**c**) and GdW_{30} for $B_y = 10$ mT (**d**) determined by diagonalization of the quantum spin Hamiltonian in Eq. (1)

6 Gd-POMs as Sub-Kelvin Magnetic Coolers

The lowest, final temperature that can be reached by adiabatically demagnetizing a system of paramagnetic spins, is

$$T_f = \frac{T_i}{B_i} \cdot B_f, \tag{13}$$

where T_i and B_i are the initial temperature and applied field, respectively, and B_f denotes the applied field at the end of the cooling procedure [1]. By letting $B_f \rightarrow 0$, the system becomes sensitive to any perturbation and Eq. (13) should become

$$T_f = \frac{T_i}{B_i} \cdot \sqrt{B_f^2 + b_0^2}, \tag{14}$$

where b_0 is the internal field, which results from magnetic anisotropy and/or spin-spin interactions [1]. Thus, minimizing any source of magnetic interactions is

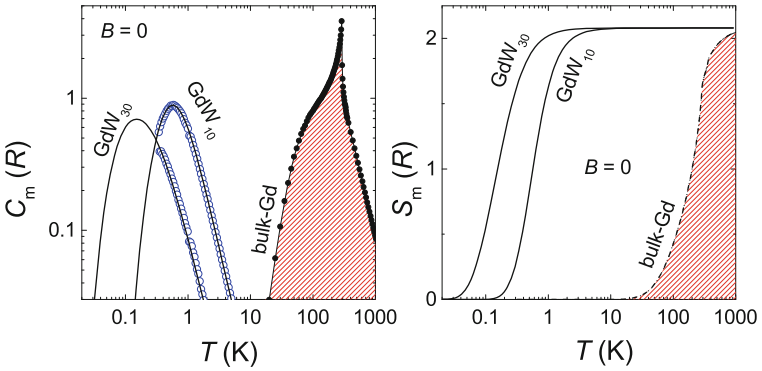

Fig. 9 Temperature-dependence of the zero-applied field magnetic specific heat, normalized to the gas constant R, for bulk gadolinium metal together with that of GdW_{10} and GdW_{30} for comparison (*left panel*). *Solid lines* are the calculated Schottky contributions for $B_2^0 = -0.06$ K (GdW_{10}) and $B_2^0 = 0.02$ K (GdW_{30}). Temperature-dependence of the zero-applied field magnetic entropy of, from left to right, GdW_{30}, GdW_{10} and bulk gadolinium metal, respectively, as obtained applying Eq. (15) to the C_m data (*right panel*)

among the simplest approaches that can be followed in order to design a magnetic refrigerant material suitable for attaining very low temperatures. Molecular nanomagnets are conceptually analogous to paramagnetic spins. Each molecular unit carries a magnetic moment that, in the cases of GdW_{10} and GdW_{30}, corresponds to an individual Gd^{3+} ion ($S = 7/2$). Gadolinium is a common constituent element for magnetic refrigerant materials, mainly because its $^8S_{7/2}$ ground state provides the largest entropy per single ion. Furthermore, its quenched orbital momentum implies that crystal field effects are extremely small, ultimately favoring a relatively larger MCE at very low temperatures, indeed [4].

Bulk gadolinium metal undergoes a ferromagnetic phase transition at $T_C \approx 294$ K, thus leaving no available magnetic disorder entropy at cryogenic temperatures. The direct comparison in Fig. 9 of the zero-field C_m for the bulk metal with that corresponding to the GdW_{10} and GdW_{30} compounds reveals a spectacular effect on the long-range magnetic ordering, i.e., the sharp λ-like feature at T_C. From the specific heat data, the temperature dependence of the magnetic entropies is obtained by integration, i.e.,

$$S_m(T) = \int_0^T \frac{C_m}{T} dT, \tag{15}$$

and depicted in Fig. 9. We note that the total molar entropy, gained by varying T from absolute zero to infinite, does not depend on whether we consider the isolated Gd^{3+} ions or the higher-temperature bulk ferromagnet. Indeed, this value depends on the number of all degrees of freedom involved, which is determined by the same spin value $S = 7/2$ for all these materials, thus providing

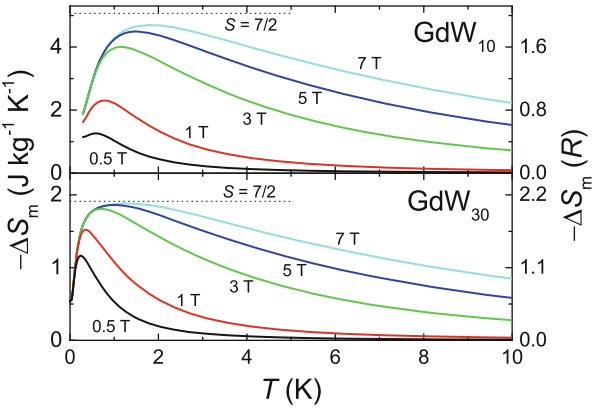

Fig. 10 Magnetic entropy changes, ΔS_m, of GdW_{10} (*top panel*) and GdW_{30} (*bottom panel*) for applied field changes ΔB, as labelled. The ΔS_m is in units of J kg^{-1} K^{-1} on the left vertical axis, whilst it is normalized to the gas constant R on the right vertical axis. The *dotted line* is the full entropy content for an $S = 7/2$ spin system

S_m $(\infty) = R\ln(2S+1) = 2.08R$. The difference stems from the strength of the energies involved. In bulk gadolinium metal, the magnetic exchange interactions are sufficiently strong as such that this material releases magnetic entropy near room temperature. In GdW_{10} and GdW_{30}, are the weak magnetic anisotropies and dipole–dipole interactions that lead to the release of magnetic entropy in the sub-Kelvin region.

Next, we evaluate the MCE for the GdW_{10} and GdW_{30} MNMs. This procedure includes the calculation from the entropy curves, viz., applying Eq. (15) to the measured specific heat curves depicted in Fig. 9, of the magnetic entropy change $\Delta S_m(T, \Delta B)$ for selected field changes $\Delta B = B_f - B_i$, between the final and initial applied field values, respectively (see Fig. 2). Figure 10 shows the so-obtained temperature dependencies of ΔS_m for several ΔB values. One can see that, for a maximum field change of $\Delta B = (7–0)$ T, $-\Delta S_m$ increases up to the value of 4.7 J kg^{-1} K^{-1} at $T \approx 1.8$ K and 1.9 J kg^{-1} K^{-1} at $T \approx 1.3$ K for GdW_{10} and GdW_{30}, respectively. The maximum value of ΔS_m for GdW_{30} compares well with the total molar entropy ($2.08R$), which indeed corresponds to 1.9 J kg^{-1} K^{-1}, considering its molecular weight ≈9,029 g/mol. In the case of GdW_{10}, a field change somewhat larger than 7 T is needed in order for $-\Delta S_m$ to reach its maximum value ($2.08R$), which in this latter case corresponds to 5.1 J kg^{-1} K^{-1}, according to the lighter molecular weight (≈3,410 g/mol). The relatively lower anisotropy in the case of GdW_{30} explains the stronger field dependence, taking place at lower temperatures [4].

It is worth pointing out that these effects take place at remarkably low temperatures. We consider the GdW_{10} and GdW_{30} molecular nanomagnets as ideal magnetic refrigerant materials for attaining milliKelvin temperatures. On the one hand, they show paramagnetism down to such low temperatures (Fig. 5), owed to the large spin–spin distances and relatively small single-ion anisotropies. On the other hand, the spin state, thus the entropy, is relatively large down to such low temperatures (Fig. 9). To our knowledge, GdW_{30} represents the best realization of a paramagnetic single-ion, gadolinium compound.

This analysis of the magnetocaloric properties would not be complete without a comparison of the aforementioned results with that reported for the best-known magnetic refrigerant materials for cryogenic temperatures. Gadolinium sulfate, $Gd_2(SO_4)_3 \cdot 8H_2O$, and gadolinium gallium garnet, $Gd_3Ga_5O_{12}$, are fine examples because of their large MCE. However, their magnetic ordering temperatures, i.e., $T_C = 0.18$ K for gadolinium sulfate [56] and $T_C = 0.9$ K for gadolinium gallium garnet [57], set the base temperature in an adiabatic demagnetization. Selected molecule-based magnetic coolers have similar properties. For instance, $[Gd(OAc)_3(H_2O)_2]_2 \cdot 4H_2O$ [20], $Gd_2(fum)_3(H_2O)_4 \cdot 3H_2O$ [58] and $Gd(HCOO)_3$ [59], show remarkably large values of the MCE but T_f is, again, limited by their critical temperatures, i.e., ≈0.2, 0.2 and 0.7 K, respectively. Mixed Gd^{3+}-Mn^{3+}, Gd^{3+}-Co^{2+} and Gd^{3+}-Ni^{2+} MNMs have been considered as magnetic coolers [60–64], but they are not suitable for very-low temperatures due to the anisotropy induced by the Mn^{3+}, Co^{2+} and Ni^{2+} ions, respectively. Diluted paramagnetic salts not-containing gadolinium, like cerium magnesium nitrate, $Ce_2Mg_3(NO_3)_{12} \cdot 24H_2O$ [65], and chromic potassium alum, $Cr_2K_2(SO_4)_4 \cdot 24H_2O$ [66], can achieve milliKelvin temperatures favored by the weak strength of the interactions between the paramagnetic ions. However, a strong magnetic anisotropy and relatively small spin-to-volume ratios, which characterize these commercially employed magnetic refrigerant materials, result in a low refrigeration power.

The almost totality of MNMs proposed as magnetic refrigerant materials are excellent candidates limitedly to temperatures between ≈1 and ≈10 K, for which their MCE per unit mass can be larger than that of conventional magnetic refrigerants. The GdW_{10} and GdW_{30} molecular nanomagnets represent rare and welcome exceptions. These results demonstrate that chemically engineering the molecules, e.g., to screen effectively all magnetic interactions, overcome limitations in the base temperature reachable by magnetic cooling. The inherent downside of such an effective screening is the heavy structural POM framework of each molecular unit that, being non-magnetic, ultimately lowers the cooling power. Indeed, a conventionally employed magnetic refrigerant for mK, such as $Ce_2Mg_3(NO_3)_{12} \cdot 24H_2O$, provides a magnetic entropy change which can be as large as $R\ln(2)$, corresponding to ≈7.5 J kg^{-1} K^{-1} [2]. Although this value is still relatively large, its strong dependency on the orientation of the applied field ($g_{//}/g_{\perp} < 0.014$) makes its application less efficient than that of the Gd-based POMs.

7 Spin–Lattice Relaxation and Quantum Spin Dynamics in Gd-POMs

The SLR of GdW_{30} and GdW_{10} can be explored by means of ac susceptibility experiments, performed in the region of very low temperatures. Figure 11 shows the real χ' and imaginary χ'' components measured on powdered samples of both compounds. Both set of data show the dependence on frequency that is

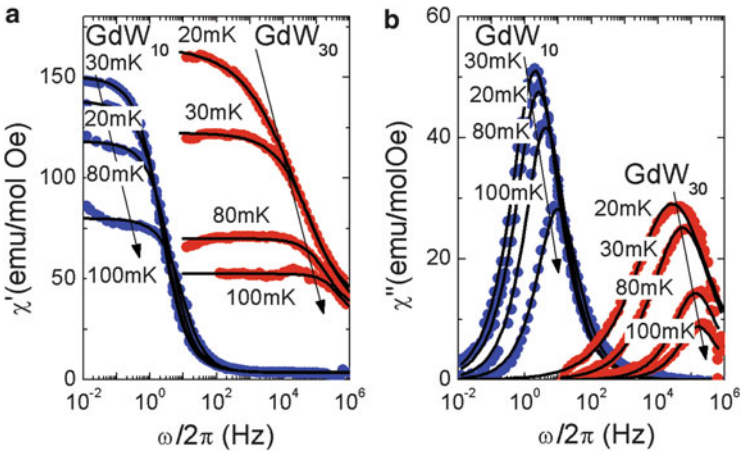

Fig. 11 Real (**a**) and imaginary (**b**) components of the ac magnetic susceptibility measured at different temperatures on GdW_{10} and GdW_{30} (scatter). The *solid lines* are least-squares Cole–Cole fits

characteristic of paramagnetic relaxation: an abrupt drop in χ' accompanied by a maximum of χ''. The low-frequency limit $\chi'(\omega \to 0)$ follows the Curie–Weiss law and, in the case of GdW_{10}, shows also signatures of magnetic order (see Fig. 5). The frequency dependence of the susceptibility reflects then relaxation of spins to thermal equilibrium with the lattice, i.e. the SLR process, and not spin–spin relaxation within the "spin bath". For GdW_{30}, this dependence shows up at much higher frequencies than in the case of GdW_{10}. This strong difference evidences that the coordination sphere determines not only the magnetic anisotropy but also the spin dynamics of Gd^{3+} ions [12].

The spin–lattice relaxation rates τ^{-1} can be determined, at each temperature, by fitting the frequency-dependent susceptibility data with a Cole–Cole law (3), as shown in Fig. 11. Values obtained by this method are shown in Fig. 12 as a function of temperature. Above $T \sim 200$ mK, the relaxation rate of GdW_{10} follows a thermally activated behavior $\tau^{-1} = {\tau_0}^{-1} \exp(-U/k_B T)$, characteristic of an Orbach process (Eq. (10)), with an activation energy $U/k_B = 2.2(2)$ K and a pre-factor ${\tau_0}^{-1} = 3 \times 10^9$ s^{-1}. The activation energy agrees with the classical anisotropy energy barrier $U_{cl}/k_B = 2.15$ K derived from the spin Hamiltonian in Eq. (1). Spin–lattice relaxation proceeds then via the highest energy excited states, thus following a relaxation path similar to that labeled II in Fig. 2. The pre-factor approximately corresponds to the direct decay to states lying immediately below the top of the anisotropy energy barrier. Using Eq. (6) and the anisotropy constants determined in Sect. 4 gives a speed of sound $c = 2 \times 10^5$ cm/s, in reasonably good agreement with that estimated from the lattice contribution to the specific heat. Below 200 mK, τ^{-1} becomes of order 20 s^{-1} and nearly independent of temperature. This regime is also characterized by a broader distribution of relaxation times, as revealed by the decrease of parameter β extracted from the Cole–Cole fits.

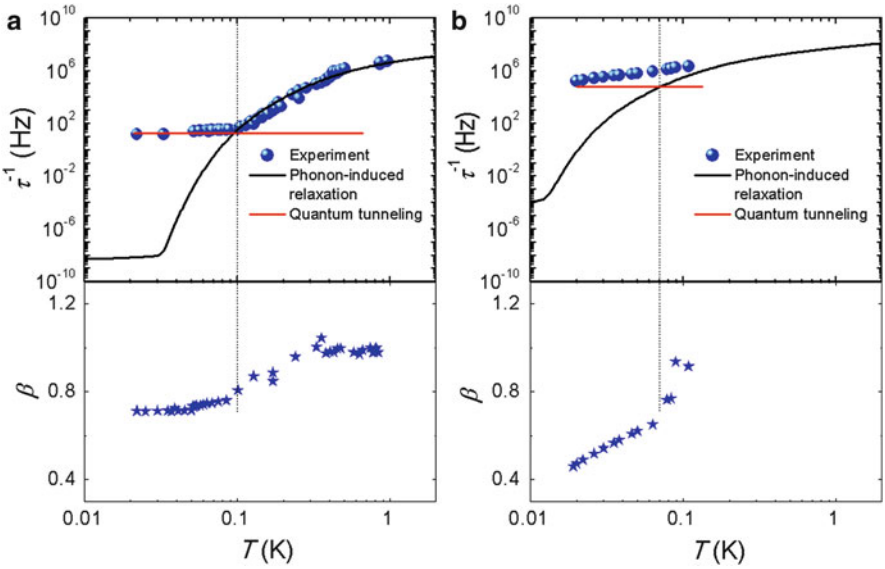

Fig. 12 Relaxation rates of GdW_{10} (**a**) and GdW_{30} (**b**) obtained from the Cole–Cole fits. The *bottom panels* show the respective values of the parameter β obtained from the same fits. The *solid line* shows the predictions for phonon-assisted relaxation. *Horizontal lines* show the spin tunneling rates that follow from the Prokof'ev and Stamp model, see Eq. (12)

The experimental spin–lattice relaxation rate can be compared with the rate of direct processes between states of the ground state doublet that, using the same parameters derived from the high-T relaxation, amounts to approximately $10^{-8}\,\mathrm{s}^{-1}$. This vanishingly small value can be associated with the fact that experiments are performed at very low magnetic fields, thus $E_\mathrm{b} - E_\mathrm{a} = 0$ and the density of phonons that are in "speaking terms" with the spin system is just very close to zero. In the same temperature region, τ^{-1} of GdW_{30} does not reach a pure quantum regime yet, although it depends weakly on temperature, showing a strong deviation from the expected thermally activated behavior. Furthermore, it is four orders of magnitude faster than τ^{-1} of GdW_{10}. These results clearly show that a different mechanism, much more efficient than the spontaneous emission of phonons, governs SLR at very low temperatures.

The obvious alternative to consider is pure quantum tunneling dynamics, that is, without the intervention of phonons. It might seem paradoxical, at first, that Gd^{3+} spins exhibit fast tunneling rates, as $\Delta = 0$, thus tunneling is strictly forbidden for Kramers ions at zero field. However, even if no external field is applied, each spin feels the dipolar magnetic field created by all other spins in the lattice that breaks Kramers degeneracy. The characteristic width σ_dip of the dipolar field distribution can be estimated using the approximate relation $2g_J\mu_\mathrm{B}\sigma_\mathrm{dip} \sim k_\mathrm{B}T_\mathrm{c}$, which for GdW_{10} ($T_\mathrm{C} \simeq 36$ mK, see Fig. 5a) gives $\sigma_\mathrm{dip} \simeq 3.8$ mT. Spin – spin interactions are weaker for GdW_{30} because of the larger intermolecular separations in this

material. As a first approximation, σ_{dip} can be estimated from that of GdW_{10}. The dipolar interaction energy decreases with r^{-3}, thus we expect $T_C \approx 4.5$ mK and $\sigma_{dip} = 0.5$ mT. Transverse dipolar fields $B_{dip;\perp}$, i.e. perpendicular to the magnetization easy axis, give rise to a finite quantum tunnel splitting Δ of the initially degenerate doublets. Inserting in Eq. (1) a magnetic field $B_{dip;\perp} = \sigma_{dip}$ oriented along the bisect of the hard and medium anisotropy axes gives $\Delta/k_B = 3.7 \times 10^{-6}$ K and $\Delta/k_B = 7.4 \times 10^{-5}$ K for the ground level doublets of GdW_{10} and GdW_{30}, respectively. With these values, the Prokof'ev and Stamp Eq. (12) gives for the former compound a quantum tunneling rate $\Gamma = 19\ s^{-1}$, which agrees remarkably well with the spin–lattice relaxation $\tau^{-1} \simeq 15\ s^{-1}$ measured below 200 mK (see Fig. 12). The same method gives $\Gamma = 6.4 \times 10^4\ s^{-1}$ for GdW_{30}, also in fair agreement with $\tau^{-1} \simeq 10^5\ s^{-1}$ measured at $T = 20$ mK. The tunneling rate of each molecule is determined by its local magnetic bias, which varies from one lattice site to another. This dependence accounts for the broader distribution of relaxation times (or, equivalently, the smaller parameter β) that characterizes the quantum relaxation regime as compared with that observed at higher temperatures.

These experiments show that Gd^{3+} spins attain thermal equilibrium via pure quantum tunneling processes, at rates that are many orders of magnitude faster than those predicted for direct phonon-induced processes [12]. Similar results have been found, in the course of the past few years, on other lanthanide ions [53] as well as on polynuclear MNMs [67–69]. Yet, the role played by this quantum process is somewhat puzzling, as according to existing theories it conserves the total energy of the ensemble of electronic and nuclear spins. Therefore, the precise mechanism by which the spins that flip by tunneling exchange energy with the lattice remains obscure and certainly deserves further attention in the future. The thermalization of spins plays a crucial role in fundamental phenomena, ranging from Curie law to the attainment of magnetically ordered states, as well as in their application as magnetic refrigerants or thermometers, thus its relevance can hardly be overestimated.

8 Gd-POMs as Quantum Hardware

Although most of the proposals for applications of MNMs in the field of quantum information processing are based on clusters with a polynuclear magnetic core [8–10, 70–73], mononuclear ones (or single-ion magnets) offer a better control over parameters that determine the energy level spectrum and wavefunctions as well as decoherence [12, 74]. Inorganic POM molecules can be prepared from elements with zero nuclear spin, thus giving access to nuclear-spin free systems. In addition, the replacement of the magnetic ion by a nonmagnetic one (e.g., replacing a lanthanide with Y^{3+}) enables the synthesis of magnetically diluted crystals. Well-known sources of decoherence [75] can therefore be reduced while preserving both the crystalline order and the molecular structure.

We here explore the suitability of Gd-POMs as spin qubits. The energy gap ΔE between the two qubit energy levels must fulfill the condition $\Delta E/h \leq 20$ GHz to comply with the requirements of radio frequency (RF) technologies and, in particular, with the resonance frequencies of superconducting microcavities. These devices are currently seen as one of the most promising technologies for the development of scalable quantum computation architectures [76–80]. Also, its coupling to a RF magnetic field $\boldsymbol{b}_{\rm rf}$ must be strong enough to ensure that the Rabi frequency $\Omega_R \equiv 2g_J\mu_B|\langle 1|\boldsymbol{b}_{\rm rf}\boldsymbol{S}|0\rangle|/h$ of coherent rotations between qubit states $|0\rangle$ and $|1\rangle$ be much larger than the decoherence rates.

Taking all these requirements into account, a sensible choice for the qubit definition is to associate $|0\rangle$ and $|1\rangle$ with spin states belonging to the ground and first excited doublets, respectively (see Fig. 13). The qubit energy gap is then defined by the zero-field energy splitting, which amounts to $\Delta E/h = 22$ GHz and $\Delta E/h = 6.3$ GHz, for GdW_{10} and GdW_{30}, respectively. With the above technical considerations in mind, GdW_{30} appears as a close to ideal candidate because of its weak magnetic anisotropy, resulting from its peculiar molecular structure. The twofold level degeneracies can be broken via the application of a weak magnetic field along the easy axis y. For instance, $B_y = 10$ mT splits the ground level doublet by 2 GHz, which would enable a ground state initialization of about 99.99 % at $T = 10$ mK. ΔE can be continuously tuned from 6.7 GHz, at $B_y = 10$ mT, up to 20 GHz, at $B_y = 465$ mT, becoming resonant with X-band (9.8 GHz) photons for $B_y \simeq 100$ mT. These qubits can therefore be manipulated with the electromagnetic radiation produced by any conventional EPR setup [81–83], a flux qubit [84] or a superconducting microcavity [77]. The fact that large magnetic fields are not required to tune ΔE might enable the integration of these lanthanide-based spin qubits into superconducting quantum circuits. For the frequency of coherent oscillations, we find, irrespective of B_y, $\Omega_R/b_{\rm rf} \simeq 60$ MHz/mT when $b_{\rm rf}$ is applied along the z axis, and $\Omega_R/b_{\rm rf} \simeq 90$ MHz/mT when $b_{\rm rf}$ is applied along the x axis. It might be noted here that if, by contrast, qubit states were associated with the ground state doublet $\langle S_y\rangle \approx \pm 3.5$, tuning $\Delta E/h$ to the adequate frequency range would lead to a strong suppression of Ω_R unless relatively large (of the order of 1 T) and extremely well oriented transverse magnetic fields (i.e., along either z or x) were applied [80].

The values of Ω_R need to be compared with the dominant decoherence rates. Pulsed X-band EPR experiments were performed on pure and magnetically diluted samples of $Gd_xY_{1-x}W_{30}$. Echo signals were observed for $x \leq 0.1$. As an illustrative example, we show in Fig. 13a the echo-detected EPR powder spectrum of $Gd_{0.001}Y_{0.999}W_{30}$ and $Gd_{0.01}Y_{0.99}W_{30}$, measured at $T = 6$ K. The qubit transition defined above corresponds to the lowest edge of the absorption band observed between 100 and 700 mT. For the lowest gadolinium concentration, $x = 0.001$, the relaxation of the echo signal gives $T_2 \simeq 410$ ns and $T_1 \simeq 1.6\,\mu$s as measured at $B = 100$ mT. Both relaxation times are observed to increase with decreasing concentration [12], suggesting that dipole–dipole interactions, albeit very weak, remain an important source of decoherence. The qubit figure of merit [82] is then $Q_M \equiv 2\Omega_R T_2 \approx 50$ for $b_{\rm rf} = 1$ mT. Rabi oscillations have recently been observed in this material [85]. The possibility of controlling the magnetic anisotropy via the

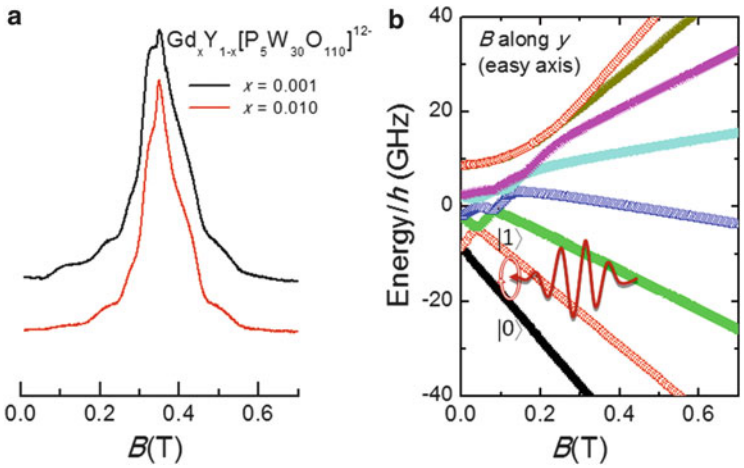

Fig. 13 (**a**) Echo-detected X-band EPR spectrum measured on powdered samples of $Gd_{0.001}Y_{0.999}W_{30}$ and $Gd_{0.01}Y_{0.99}W_{30}$ at $T = 6$ K using a two-pulses Hahn echo sequence with a $\pi/2$ pulse length of 16 ns and an interpulse delay of 180 ns. (**b**) Magnetic energy level structure of GdW_{30} for a magnetic field applied along the easy magnetization axis (y). The transition between the ground and first excited states becomes resonant with X-band photons (9.8 GHz) for $B_y \approx 0.11\,T$ and corresponds to the low-field edge observed in the EPR spectrum. These two states provide a proper definition for the two basis states $|0\rangle$ and $|1\rangle$ of a spin qubit

local coordination enables also the design of multi-qubit gates in clusters hosting several weakly coupled lanthanide ion [86]. These and related MNMs [11, 37, 86] are very promising candidates to take part of the hardware of future quantum computers.

9 Summary, Conclusions, Outlook

Over the last couple of decades, promising applications in magnetic data storage and processing boosted an intense research activity on molecular nanomagnets [87]. To this purpose, the main interest was the possibility of combining *large values of the magnetic anisotropy* and spin ground state within the same molecule. Using *nearly-magnetically-isotropic* MNMs for cryogenic MR has motivated a sea change in this trend, which has led to an impressive number of new molecular coolers during the last few years [4–7]. This line of research has been particularly successful for the temperature range between ≈1 and ≈10 K, which is strategically important since it covers the helium liquefaction temperature. However, the field of sub-Kelvin magnetic refrigeration with MNMs is still largely unexplored, both theoretically as well as experimentally. Ingredients for a successful recipe should guarantee that the rate of the SLR remains sufficiently fast down to such low temperatures. The Gd-POMs show that the molecular engineering of the local

coordination shell surrounding the magnetically shielded Gd^{3+} ions permits to accomplish such goal [13]. However, there are still challenges to overcome. For instance, the heavy structural non-magnetic POM framework of each molecule, ultimately, lowers the efficiency of these refrigerants. The search for other mononuclear isotropic MNMs having lighter capping ligands, yet effective in screening all magnetic interactions, should motivate further studies. Furthermore, the thermal conductivity of these MNMs should decrease drastically at such low temperatures, thus limiting their applicability. A promising alternative, which paves the way to on-chip microrefrigeration, is the grafting of MNMs to substrates with a relatively high thermal conductivity and low specific heat [88]. This is feasible because the cooling functionality is defined at the molecular scale and MNMs are stable in solution.

Exploiting the functionalities of MNMs by interfacing them with microdevices, recently opened a research trend with the promise of a bright future [89]. Implementing an all-spin quantum processor might soon become a reality. This challenge requires the strong coupling of suitably designed MNMs to on-chip superconducting circuits, which can be used to coherently manipulate and transfer information between spin qubits [80]. Initial efforts were devoted to the prototypical Fe_8 or Mn_{12} molecular spin qubits [71]. However, their strong magnetic anisotropy can likely lead to technical difficulties, which involve the need of very high frequencies and large, well-aligned applied magnetic fields. For these reasons, it seems more promising to operate with mononuclear molecular spin qubits, such as Gd-POMs, which offer a greater versatility for the modification of the spin Hamiltonian via molecular chemistry [12].

Finally, the molecular approach for the design of multifunctional materials is a long-term research activity (see, e.g., [90]). Since the processing of information using spin qubits requires very low temperatures, combining an effective cooler and qubit within the same and one molecule, as in Gd-POMs, can experimentally facilitate the implementation of a quantum processor.

Acknowledgements This work would not have been possible without the contribution of, in alphabetical order: P. J. Alonso, S. Cardona-Serra, J. M. Clemente-Juan, E. Coronado, A. Gaita-Ariño, M.-J. Martínez-Pérez, O. Montero, F. Moro, H. Prima-García, C. Schlegel, J. Sesé, J. van Slageren. We thank financial support from the Spanish MINECO (project MAT2012-38318-C03-01) and the Gobierno de Aragón (project MolChip).

References

1. Pobell F (2007) Matter and methods at low temperatures, 3rd edn. Springer-Verlag, Berlin, Heidelberg
2. Hudson RP (1972) Principles and application of magnetic cooling. North-Holland Publishing Company, Amsterdam
3. Abragam A, Bleaney B (1970) Electron paramagnetic resonance of transition ions. Clarendon Press, Oxford

4. Evangelisti M, Brechin EK (2010) Recipes for enhanced molecular cooling. Dalton Trans 39:4672
5. Sharples JW, Collison D (2013) Coordination compounds and the magnetocaloric effect. Polyhedron 54:91
6. Zheng Y-Z, Zhou G-J, Zheng Z, Winpenny REP (2014) Molecule-based magnetic coolers. Chem Soc Rev 43:1462
7. Evangelisti M (2014) Molecule-based magnetic coolers: measurement, design and application. In: Bartolomé J, Luis F, Fernández JF (eds) Molecular magnets, nanoscience and technology. Springer-Verlag, Berlin, Heidelberg
8. Stamp PCE, Gaita-Ariño A (2009) Spin-based quantum computers made by chemistry: hows and whys. J Mater Chem 19:1718
9. Affronte M (2009) Molecular nanomagnets for information technologies. J Mater Chem 19:1731
10. Ardavan A, Blundell SJ (2009) Storing quantum information in chemically engineered nanoscale magnets. J Mater Chem 19:1754
11. Aromí G, Aguilà D, Gamez P, Luis F, Roubeau O (2012) Design of magnetic coordination complexes for quantum computing. Chem Soc Rev 41:537
12. Martínez-Pérez MJ, Cardona-Serra S, Schlegel C, Moro F, Alonso PJ, Prima-García H, Clemente-Juan JM, Evangelisti M, Gaita-Ariño A, Sesé J, van Slageren J, Coronado E, Luis F (2012) Gd-based single-ion magnets with tunable magnetic anisotropy: molecular design of spin qubits. Phys Rev Lett 108:247213
13. Martínez-Pérez MJ, Montero O, Evangelisti M, Luis F, Sesé J, Cardona-Serra S, Coronado E (2012) Fragmenting gadolinium: mononuclear polyoxometalate-based magnetic coolers for ultra-low temperatures. Adv Mater 24:4301
14. Stevens KWH (1952) Matrix elements and operator equivalents connected with the magnetic properties of rare earth ions. P Phys Soc Lond A 65:209
15. Bleaney B, Scovil HED, Trenam RS (1954) The paramagnetic resonance spectra of gadolinium and neodymium ethylsulfates. P Roy Soc Lond A 223:15
16. Low W, Shaltiel D (1958) Paramagnetic resonance spectrum of gadolinium in single crystals of thorium oxide. J Phys Chem Sol 6:315
17. Geschwind S, Remeika JP (1961) Paramagnetic resonance of Gd^{3+} in Al_2O_3. Phys Rev 122:757
18. Giauque WF, MacDougall DP (1933) Attainment of temperatures below 1° absolute by demagnetization of $Gd_2(SO_4)_3 \cdot 8H_2O$. Phys Rev 43:768
19. Giauque WF, MacDougall DP (1935) The production of temperatures below one degree absolute by adiabatic demagnetization of gadolinium sulfate. J Am Chem Soc 57:1175
20. Evangelisti M, Roubeau O, Palacios E, Camón A, Hooper TN, Brechin EK, Alonso JJ (2011) Cryogenic magnetocaloric effect in a ferromagnetic molecular dimer. Angew Chem 123:6736; Angew Chem Int Ed 50:6606
21. Ehrenfest P (1920) Note on the paramagnetism of solids. Leiden Commun Suppl 44b:55
22. Gorter CJ (1936) Paramagnetic relaxation. Physica 3:503
23. Debye P (1935) The dielectrical saturation and interference of the free rotation in fluidity. Phys Zeits 36:193
24. Gorter CJ, Kronig R de L (1936) On the theory of absorption and dispersion in paramagnetic and dielectric media. Physica 3:1009
25. Cole KS, Cole RH (1941) Dispersion and absorption in dielectrics. I. Alternating current characteristics. J Chem Phys 9:341
26. Bagguley DMS, Griffiths JHE (1948) Paramagnetic resonance in copper sulphate. Nature (Lond) 162:538
27. Bleaney B, Stevens KWH (1953) Paramagnetic resonance. Rep Prog Phys 16:108
28. Gorter CJ, Dijkstra LJ, Groendijk H (1940) Paramagnetic absorption and dispersion in chromium potassium alum. Physica 7:625

29. Bagguley DMS, Griffiths JHE (1952) Paramagnetic resonance and spin–lattice relaxation times in the copper tutton salts. P Phys Soc Lond A 65:594
30. Van den Broek J, van der Marel LC (1963) Spin–lattice relaxation in rare earth ethyl-sulfates. I Physica 29:948
31. Larson GH, Jeffries CD (1966) Spin–lattice relaxation in some rare-earth salts. I. Temperature dependence. Phys Rev 141:461
32. Ishikawa N, Sugita M, Wernsdorfer W (2005) Quantum tunneling of magnetization in lanthanide single-molecule magnets: bis(phthalocyaninato)terbium and bis(phthalocyaninato)dysprosium anions. Angew Chem 117:2991; Angew Chem Int Ed 44:2931
33. Friedman JR, Sarachik MP, Tejada J, Ziolo R (1996) Macroscopic measurement of resonant magnetization tunneling in high-spin molecules. Phys Rev Lett 76:3830
34. Hernández JM, Zhang XX, Luis F, Bartolomé J, Tejada J, Ziolo R (1996) Field tuning of thermally activated magnetic quantum tunnelling in Mn_{12}-Ac molecules. Europhys Lett 35:301
35. Thomas L, Lionti F, Ballou R, Gatteschi D, Sessoli R, Barbara B (1996) Macroscopic quantum tunnelling of magnetization in a single crystal of nanomagnets. Nature (Lond) 383:145
36. AlDamen MA, Clemente-Juan JM, Coronado E, Martí-Gastaldo C, Gaita-Ariño A (2008) Mononuclear lanthanide single-molecule magnets based on polyoxometalates. J Am Chem Soc 130:8874
37. AlDamen MA, Cardona-Serra S, Clemente-Juan JM, Coronado E, Gaita-Ariño A, Martí-Gastaldo C, Luis F, Montero O (2009) Mononuclear lanthanide single molecule magnets based on the polyoxometalates $[Ln(W_5O_{18})_2]^{9-}$ and $[Ln(\beta_2\text{-}SiW_{11}O_{39})_2]^{13-}$ (Ln^{III} = Tb, Dy, Ho, Er, Tm, and Yb). Inorg Chem 48:3467
38. Jiang SD, Wang BW, Sun HL, Wang ZM, Gao S (2011) An organometallic single-ion magnet. J Am Chem Soc 133:4730
39. Sessoli R, Powell AK (2009) Strategies towards single molecule magnets based on lanthanide ions. Coord Chem Rev 253:2328
40. Waller I (1932) The magnetization of paramagnetic crystals in alternating fields. Zeitsch Phys 79:370
41. Heitler W, Teller E (1936) Time effects in the magnetic cooling method I. P Roy Soc Lond A 155:629
42. Kronig R de L (1939) On the mechanism of paramagnetic relaxation. Physica 6:33
43. Van Vleck JH (1940) Paramagnetic relaxation times for titanium and chrome alum. Phys Rev 57:426
44. Orbach R (1961) Spin–lattice relaxation in rare-earth salts. P Roy Soc Lond A 264:458
45. Dohm V, Fulde P (1975) Magnetoelastic interaction in rare earth systems. Z Phys B 21:369
46. Fort A, Rettori A, Villain J, Gatteschi D, Sessoli R (1998) Mixed quantum-thermal relaxation in Mn_{12} acetate molecules. Phys Rev Lett 80:612
47. Leuenberger MN, Loss D (2000) Spin tunneling and phonon-assisted relaxation in Mn_{12} acetate. Phys Rev B 61:1286
48. Chudnovsky EM, Garanin D (2000) Crystal field $-AD{S_z}^2$ does not produce one-phonon transitions with $\Delta S_z = \pm 2$. Europhys Lett 52:245
49. Leuenberger MN, Loss D (2000) Reply to the comment of E. M. Chudnovsky and D. Garanin on "Spin-relaxation in Mn_{12} acetate". Europhys Lett 52:247
50. Finn CB, Orbach R, Wolf WP (1961) Spin–lattice relaxation in cerium magnesium nitrate at liquid helium temperature - a new process. P Phys Soc Lond 77:261
51. Zener C (1932) Non-adiabatic crossing of energy levels. P Roy Soc Lond A 137:696
52. Giraud R, Wernsdorfer W, Tkachuk AM, Mailly D, Barbara B (2001) Nuclear spin driven quantum relaxation in $LiY_{0.998}Ho_{0.002}F_4$. Phys Rev Lett 87:057203
53. Luis F, Martínez-Pérez MJ, Montero O, Coronado E, Cardona-Serra S, Martí-Gastaldo C, Clemente-Juan JM, Sesé J, Drung D, Schurig T (2010) Spin–lattice relaxation via quantum tunneling in an Er^{3+}-polyoxometalate molecular magnet. Phys Rev B 82:060403

54. Prokof'ev NV, Stamp PCE (1998) Low-temperature quantum relaxation in a system of magnetic nanomolecules. Phys Rev Lett 80:5794
55. Qian K, Wang B, Wang Z, Su G, Gao S (2013) Field-dependent magnetic relaxation and magnetocaloric effect in mononuclear Gd complexes. Acta Chim Sinica 71:1022
56. Wielinga RF, Lubbers J, Huiskamp WJ (1967) Heat capacity singularities in two gadolinium salts below 1°K. Physica 37:375
57. McMichael RD, Ritter JJ, Shull RD (1993) Enhanced magnetocaloric effect in $Gd_3Ga_{5-x}Fe_xO_{12}$. J Appl Phys 73:6946
58. Sedláková L, Hanko J, Orendáčová A, Orendáč M, Zhou C-L, Zhu W-H, Wang B-W, Wang Z-M, Gao S (2009) Magnetism and magnetocaloric effect in $S = 7/2$ Heisenberg antiferromagnet $Gd_2(fum)_3(H_2O)_4 \cdot 3H_2O$. J Alloys Compd 487:425
59. Lorusso G, Sharples JW, Palacios E, Roubeau O, Brechin EK, Sessoli R, Rossin A, Tuna F, McInnes EJL, Collison D, Evangelisti M (2013) A dense metal-organic framework for enhanced magnetic refrigeration. Adv Mater 25:4653
60. Karotsis G, Evangelisti M, Dalgarno SJ, Brechin EK (2009) A calix[4]arene 3d/4f magnetic cooler. Angew Chem 121:10112; Angew Chem Int Ed 48:9928
61. Karotsis G, Kennedy S, Teat SJ, Beavers CM, Fowler DA, Morales JJ, Evangelisti M, Dalgarno SJ, Brechin EK (2010) $[Mn^{III}{}_4Ln^{III}{}_4]$ calix[4]arene clusters as enhanced magnetic coolers and molecular magnets. J Am Chem Soc 132:12983
62. Zheng Y-Z, Evangelisti M, Winpenny REP (2011) Co-Gd phosphonate complexes as magnetic refrigerants. Chem Sci 2:99
63. Zheng Y-Z, Evangelisti M, Winpenny RE (2011) Large magnetocaloric effect in a Wells-Dawson type $\{Ni_6Gd_6P_6\}$ cage. Angew Chem 123:3776; Angew Chem Int Ed 50:3692
64. Zheng Y-Z, Evangelisti M, Tuna F, Winpenny REP (2012) Co-Ln mixed-metal phosphonate grids and cages as molecular magnetic refrigerants. J Am Chem Soc 134:1057
65. Abraham BM, Brandt O, Eckstein Y, Ketterson JB, Kuchnir M, Roach P (1969) Heat capacity of diluted cerium magnesium nitrate and its potential for the production of very low temperatures. Phys Rev 187:273
66. Bleaney B (1950) Thermal properties of potassium chromic chromic alum between 0.05 and 1 degrees K. P Roy Soc Lond A 204:216
67. Evangelisti M, Luis F, Mettes FL, Aliaga N, Aromí G, Alonso JJ, Christou G, de Jongh LJ (2004) Magnetic long-range order induced by quantum relaxation in single-molecule magnets. Phys Rev Lett 93:117202
68. Evangelisti M, Luis F, Mettes FL, Sessoli R, de Jongh LJ (2005) Giant isotope effect in the incoherent tunneling specific heat of the molecular nanomagnet Fe_8. Phys Rev Lett 95:227206
69. Repollés A, Cornia A, Luis F (2014) Spin–lattice relaxation via quantum tunneling in diluted crystals of Fe_4 single-molecule magnets. Phys Rev B 89:054429
70. Leuenberger MN, Loss D (2001) Quantum computing in molecular magnets. Nature (Lond) 410:789
71. Tejada J, Chudnovsky EM, del Barco E, Hernández JM, Spiller TP (2001) Magnetic qubits as hardware for quantum computers. Nanotech 12:181
72. Troiani F, Ghirri A, Affronte M, Carretta S, Santini P, Amoretti G, Piligkos S, Timco G, Winpenny REP (2005) Molecular engineering of antiferromagnetic rings for quantum computation. Phys Rev Lett 94:207208
73. Santini P, Carretta S, Troiani F, Amoretti G (2011) Molecular nanomagnets as quantum simulators. Phys Rev Lett 107:230502
74. Bertaina S, Gambarelli S, Tkachuk A, Kurkin IN, Malkin B, Stepanov A, Barbara B (2007) Rare-earth solid-state qubits. Nat Nanotech 2:39
75. Prokof'ev NV, Stamp PCE (2000) Theory of the spin bath. Rep Prog Phys 63:669
76. Schoelkopf RJ, Girvin SM (2008) Wiring up quantum systems. Nature (Lond) 451:664
77. Schuster DI, Sears AP, Ginossar E, DiCarlo L, Frunzio L, Morton JJL, Wu H, Briggs GAD, Buckley BB, Awschalom DD, Schoelkopf RJ (2010) High-cooperativity coupling of electron-spin ensembles to superconducting cavities. Phys Rev Lett 105:140501

78. Kubo Y, Ong FR, Bertet P, Vion D, Jacques V, Zheng D, Dréau A, Roch J-F, Auffeves A, Jelezko F, Wrachtrup J, Barthe MF, Bergonzo P, Esteve D (2010) Strong coupling of a spin ensemble to a superconducting resonator. Phys Rev Lett 105:140502
79. Wu H, George RE, Wesenberg JH, Mølmer K, Schuster DI, Schoelkopf RJ, Itoh KM, Ardavan A, Morton JJL, Briggs GAD (2010) Storage of multiple coherent microwave excitations in an electron spin ensemble. Phys Rev Lett 105:140503
80. Jenkins M, Hümmer T, Martínez-Pérez MJ, García-Ripoll JJ, Zueco D, Luis F (2013) Coupling single-molecule magnets to quantum circuits. New J Phys 15:095007
81. Ardavan A, Rival O, Morton JJL, Blundell SJ, Tyryshkin AM, Timco GA, Winpenny REP (2007) Will spin-relaxation times in molecular magnets permit quantum information processing? Phys Rev Lett 98:057201
82. Bertaina S, Gambarelli S, Mitra T, Tsukerblat B, Muller A, Barbara B (2008) Quantum oscillations in a molecular magnet. Nature (Lond) 453:203
83. Schlegel C, van Slageren J, Manoli M, Brechin EK, Dressel M (2008) Direct observation of quantum coherence in single-molecule magnets. Phys Rev Lett 101:147203
84. Zhu X, Saito S, Kemp A, Kakuyanagi K, Karimoto S, Nakano H, Munro WJ, Tokura Y, Everitt MS, Nemoto K, Kasu M, Mizuochi N, Semba K (2011) Coherent coupling of a superconducting flux qubit to an electron spin ensemble in diamond. Nature (Lond) 478:221
85. Baldoví JJ, Cardona-Serra S, Clemente-Juan JM, Coronado E, Gaita-Ariño A, Prima-García H (2013) Chem Commun 49:8922
86. Luis F, Repollés A, Martínez-Pérez MJ, Aguilà D, Roubeau O, Zueco D, Alonso PJ, Evangelisti M, Camón A, Sesé J, Barrios LA, Aromí G (2011) Molecular prototypes for spin-based CNOT and SWAP quantum gates. Phys Rev Lett 107:117203
87. Sessoli R, Gatteschi D (2003) Quantum tunneling of magnetization and related phenomena in molecular materials. Angew Chem 115:278; Angew Chem Int Ed 42:268
88. Lorusso G, Jenkins M, González-Monje P, Arauzo A, Sesé J, Ruiz-Molina D, Roubeau O, Evangelisti M (2013) Surface-confined molecular coolers for cryogenics. Adv Mater 25:2984
89. Domingo N, Bellido E, Ruiz-Molina D (2012) Advances on structuring, integration and magnetic characterization of molecular nanomagnets on surfaces and devices. Chem Soc Rev 41:258
90. Ouahab L (ed) (2013) Multifunctional molecular materials. Pan Stanford Publishing, Singapore

Index